

Incremental sliding mode flight control

Wang, Sherry

DOI

[10.4233/uuid:c8259a08-bbee-4af0-b570-1350a2dd8d89](https://doi.org/10.4233/uuid:c8259a08-bbee-4af0-b570-1350a2dd8d89)

Publication date

2019

Document Version

Final published version

Citation (APA)

Wang, S. (2019). *Incremental sliding mode flight control*. [Dissertation (TU Delft), Delft University of Technology]. <https://doi.org/10.4233/uuid:c8259a08-bbee-4af0-b570-1350a2dd8d89>

Important note

To cite this publication, please use the final published version (if applicable).
Please check the document version above.

Copyright

Other than for strictly personal use, it is not permitted to download, forward or distribute the text or part of it, without the consent of the author(s) and/or copyright holder(s), unless the work is under an open content license such as Creative Commons.

Takedown policy

Please contact us and provide details if you believe this document breaches copyrights.
We will remove access to the work immediately and investigate your claim.

Incremental Sliding Mode Flight Control



Xuerui Wang

王雪蕊

INCREMENTAL SLIDING MODE FLIGHT CONTROL



Propositions

accompanying the dissertation

INCREMENTAL SLIDING MODE FLIGHT CONTROL

by

Xuerui WANG

1. Contrary to model-based sliding mode control methods, the sensor-based incremental sliding mode control framework proposed in this thesis can simultaneously reduce the model dependency and the control/observer gains. (*this thesis*)
2. Part of the system dynamics, external disturbances and the influences of faults can be captured by the measured or estimated output derivatives. (*this thesis*)
3. The incremental sliding mode flight control can help an aircraft resist a wide range of model uncertainties, atmospheric disturbances, actuator faults, and structural damages, without requiring fault detection and diagnosis or controller reconfiguration. (*this thesis*)
4. Fast and distributed wing-trailing-edge control surfaces are beneficial to multi-objective flexible aircraft flight control. (*this thesis*)
5. Similar as in control theory, also in everyday life it is true that although finite-time convergence is more challenging, it is also more appreciated than asymptotic convergence.
6. In meditation, one must fully observe and understand breaths and thoughts before controlling the mind; analogously, a successful controller cannot be designed without sufficiently observing and understanding its targeted physical system.
7. In our uncertain world, many policies deviate from their original intentions in practice because the “loop” is not closed, i.e., the feedback from society and the appropriate policy adaptations are missing.
8. The ultimate goal of debate is not to win but to reduce unconscious biases and create a more complete picture in people’s mind.
9. In yoga, relaxation is as important as tightening muscles; in scientific work, “clearing the mind” is as important as focusing.
10. Just as ideal sliding motions cannot be achieved without an ideal actuator, perfect life (without any flaw) cannot be achieved by mortals, but this should not prevent us from approaching the “boundary layer” of perfection.

These propositions are regarded as opposable and defensible, and have been approved as such by the promotor prof. dr. ir. M. Mulder.

INCREMENTAL SLIDING MODE FLIGHT CONTROL

Proefschrift

ter verkrijging van de graad van doctor
aan de Technische Universiteit Delft,
op gezag van de Rector Magnificus prof. dr. ir. T.H.J.J. van der Hagen,
voorzitter van het College voor Promoties,
in het openbaar te verdedigen op dinsdag 2 juli 2019 om 10:00 uur

door

Xuerui WANG

Bachelor of Engineering, Beihang University (Beijing University
of Aeronautics and Astronautics), Beijing, China
geboren te Qiangyang, Gansu, China

Dit proefschrift is goedgekeurd door de

promotor: Prof. dr. ir. M. Mulder

copromotor: Dr. ir. E. van Kampen

Samenstelling promotiecommissie:

Rector Magnificus,
Prof. dr. ir. M. Mulder,
Dr. ir. E. van Kampen,

voorzitter
Technische Universiteit Delft, promotor
Technische Universiteit Delft, copromotor

Onafhankelijke leden:

Prof. dr. B. Yao,
Prof. dr. C. Edwards,
Prof. dr. ing. F. Holzapfel,
Prof. dr. ir. J. W. van Wingerden,
Prof. dr. R. Curran,

Purdue University
University of Exeter
Technische Universität München
Technische Universiteit Delft
Technische Universiteit Delft, reservelid

Overige leden:

Dr. Q. P. Chu

Technische Universiteit Delft



Keywords: Incremental control; nonlinear control; fault-tolerant control; aeroservoelastic system; sliding mode control; sliding mode disturbance observer; quadrotor flight control

Printed by: Ipskamp Printing

Front & Back: designed by Sihao Sun and Xuerui Wang

Copyright © 2019 by Xuerui Wang. All rights reserved. No part of this publication may be reproduced, stored in a retrieval system, or transmitted, in any form or by any means, electronic, mechanical, photocopying, recording, or otherwise, without the prior permission in writing from the proprietor.

ISBN 978-94-6384-046-0

An electronic version of this dissertation is available at

<http://repository.tudelft.nl/>.

To my beloved parents

谨以此书献给我敬爱的父母



CONTENTS

Summary	xi
Samenvatting	xv
Nomenclature	xxi
1 Introduction	1
1.1 Threats to Flight Safety	1
1.1.1 Actuator Faults and Structural Damages	1
1.1.2 Atmospheric Disturbances	3
1.1.3 Increase of Structural Flexibility	4
1.1.4 Nonlinear Dynamics	5
1.2 Research Goal	6
1.3 Incremental Control	6
1.3.1 Literature Review on Incremental Control	6
1.3.2 Challenges in Incremental Control	8
1.4 Sliding Mode Control and Disturbance Observer	10
1.4.1 Aerospace Applications of SMC	10
1.4.2 Challenges in Sliding Mode Control	11
1.4.3 A Way to Reduce the Uncertainty in SMC	12
1.5 Research Approach and Contributions	13
1.5.1 Research Approach and Questions	13
1.5.2 Main Contributions	14
1.6 Outline of the Thesis	15
References	16
I Theoretical Development	27
2 Stability Analysis for Incremental Nonlinear Dynamic Inversion Control	29
2.1 Introduction	30
2.2 Reformulations of Incremental Nonlinear Dynamic Inversion	31
2.2.1 Input–Output Linearization	32
2.2.2 Output Tracking	34
2.2.3 Input-to-State Linearization under Disturbance Perturbations	35
2.3 Stability and Robustness Analysis	36
2.3.1 Stability Analysis	36
2.3.2 Robustness Analysis	40

2.4	Numerical Validation	45
2.4.1	Aircraft and Turbulence Models	45
2.4.2	Flight Control Design	47
2.4.3	Command Tracking in a Turbulence Field	47
2.4.4	Robustness Comparisons with Nonlinear Dynamic Inversion	50
2.5	Conclusions.	54
	References	55
3	Incremental Sliding Mode Fault-Tolerant Flight Control	59
3.1	Introduction	60
3.2	Comparisons between NDI and the Reformulated INDI	62
3.2.1	Problem Formulation	62
3.2.2	NDI and the Reformulated INDI	63
3.2.3	Comparisons between ϵ_{ndi} and ϵ_{indi}	64
3.3	Proposal of the Incremental Sliding Mode Control Framework	66
3.3.1	First-order Incremental Sliding Mode Control	67
3.3.2	Higher-order Incremental Sliding Mode Control	69
3.3.3	First-order INDI-SMC Driven by First-order Sliding Mode Disturbance Observers	70
3.3.4	Higher-order INDI-SMC Driven by Higher-order Sliding Mode Disturbance Observers	72
3.3.5	Advantages of the INDI-SMC Framework	72
3.4	Fault-Tolerant Flight Control Design	74
3.4.1	Nominal Equations of Motion	74
3.4.2	Actuator Faults.	74
3.4.3	Structural Damages	75
3.4.4	Aircraft Attitude Fault-Tolerant Control Design	76
3.5	Numerical Validation	78
3.5.1	Flight Control in the Nominal Case	78
3.5.2	Flight Control in the Presence of Actuator Faults	79
3.5.3	Flight Control in the Presence of Structural Damages	84
3.6	Conclusions.	88
	References	88
4	Incremental Backstepping Sliding Mode Fault-Tolerant Flight Control	93
4.1	Introduction	94
4.2	Incremental Backstepping Sliding Mode Control	96
4.2.1	Reformulation and Robustness Analysis for Incremental Backstepping	97
4.2.2	Proposal of Incremental Backstepping Sliding Mode Control.	100
4.2.3	Other Sliding Surface Designs	100
4.2.4	Comparisons between BSMC and IBSMC	102

4.3	Fault-Tolerant Flight Control System Design	104
4.4	Numerical Validation	104
4.4.1	Flight Control in the Nominal Case	105
4.4.2	Flight Control in the Presence of Model Uncertainties	105
4.4.3	Flight Control in the Presence of Actuator Faults	108
4.4.4	Flight Control in the Presence of Structural Damages	110
4.5	Conclusions	111
	References	112
5	Comparisons of Three Control Structures for Inducing Higher-Order Sliding Modes	115
5.1	Introduction	116
5.2	Three Control Structures for Inducing Higher-Order Sliding Modes	118
5.2.1	Nonlinear Dynamic Inversion based Control	119
5.2.2	Incremental Sliding Mode Control	119
5.2.3	Higher-order Sliding Mode Control with Artificially Increased Relative Degree	120
5.3	Analytical Comparisons	121
5.3.1	Comparisons of the Nominal Control	121
5.3.2	Comparisons of the Perturbation Terms	123
5.3.3	Perturbation Compensations and the Minimum Possible Gains	124
5.4	Numerical Comparisons	126
5.5	Conclusions	129
	References	130
II	Flight Control Applications	133
6	Quadrotor Fault-Tolerant Incremental Sliding Mode Control Driven by Sliding Mode Disturbance Observers	135
6.1	Introduction	136
6.2	Incremental Sliding Mode Control Driven by Sliding Mode Disturbance Observers	138
6.2.1	NDI-SMC/SMDO	139
6.2.2	INDI-SMC/SMDO	141
6.2.3	Comparisons between NDI and INDI based SMC/SMDO	145
6.3	Quadrotor Fault-tolerant Flight Control	147
6.3.1	Quadrotor Model	147
6.3.2	Controller Design	148
6.4	Numerical Validations	150
6.4.1	Simulation Results of NDI-SMC/SMDO	152
6.4.2	Simulation Results of INDI-SMC/SMDO	154
6.5	Experimental Validations	156
6.5.1	Experimental setup	156
6.5.2	Flights without Actuator Fault	158
6.5.3	Flights with Actuator Fault	158

6.6	Conclusions	163
	References	164
7	Flexible Aircraft Gust Load Alleviation with Incremental Nonlinear Dynamic Inversion	169
7.1	Introduction	170
7.2	Flexible Aircraft and Gust Models	172
7.2.1	Flexible Aircraft Equations of Motion	172
7.2.2	Unsteady Aerodynamic Models	175
7.2.3	Gust and Turbulence Models.	177
7.3	Flexible Aircraft Gust Load Alleviation Control	179
7.3.1	Incremental Nonlinear Dynamic Inversion Control	179
7.3.2	INDI for Flexible Aircraft GLA	181
7.3.3	Sensing and State Estimation	185
7.4	Simulation Results and Discussions.	187
7.4.1	Trim and Model Analysis.	187
7.4.2	Validation of the Model Simplification	190
7.4.3	State Estimation Results and Discussions	191
7.4.4	INDI GLA Simulation Results and Discussions.	193
7.4.5	Validation by a More Flexible Aircraft Model	197
7.4.6	Tolerance to Actuator Faults	201
7.4.7	Robustness to Aerodynamic Model Uncertainties	202
7.5	Conclusions.	203
	References	205
8	Conclusions and Recommendations	209
8.1	Conclusions.	209
8.1.1	Answers to Research Questions	209
8.1.2	Implementation Findings and Conclusions	212
8.1.3	Final Conclusions	213
8.2	Limitations and Recommendations.	214
	References	216
A	Definitions Used in Nonlinear Control Theory	219
	References	220
	Acknowledgements	221
	Curriculum Vitæ	225
	List of Publications	227

SUMMARY

The swift growth of air traffic volume stresses the importance of flight safety enhancement. Statistical data shows that fly-by-wire technology with automatic flight control systems can effectively reduce the fatal accident rate of loss of control in-flight. Although the dynamics of an aircraft are nonlinear and time-varying, it is common practice to design flight control laws based on local linear time-invariant (LTI) dynamic models, and apply gain-scheduling method. Here, the flight envelope is divided into many smaller operating regimes, and LTI model-based controllers are designed and tuned for each of them. However, this approach is cumbersome and cannot guarantee flight stability and performance in-between operational points.

In view of the challenges encountered by LTI model-based control, nonlinear control methods have attracted attention from the flight control community. Nonlinear dynamic inversion (NDI) and backstepping (BS) are two frequently used nonlinear control methods in flight control. These two approaches cancel the nonlinearities in the closed loop using a nonlinear model of the system. However, mismatches between the model and real dynamics inevitability exist, especially when an aircraft encounters atmospheric disturbances and when sudden actuator faults or even structural damages occur. To enhance the robustness of model-based nonlinear control methods to model mismatches, a commonly adopted approach is to augment them with online model identification. This process, however, is computational intensive and requires sufficient excitation, which can make an impaired aircraft fly out of the diminished safe flight envelope. In consideration of these challenges, the main goal of this thesis is:

To design a stability-guaranteed nonlinear flight control framework with reduced model dependency and enhanced robustness.

Since this thesis aims at designing a nonlinear control framework, Lyapunov stability criteria are adopted. The robustness to model uncertainties, external disturbances, sudden actuator faults and structural damages are all considered. Incremental nonlinear dynamic inversion (INDI) is a candidate to fulfill this goal. The core idea of INDI is to feed back angular accelerations and actuator positions to enhance the robustness of NDI to model mismatches. This idea has been applied to various flight control problems, and has shown promising effectiveness in rejecting disturbances and tolerating faults. However, this thesis reveals that existing derivations of INDI, which are based on the time-scale separation assumption and term omissions, have some limitations. The cascaded control structure of INDI used in flight control also restricts its applicability to more general nonlinear systems. More importantly, the stability and robustness analysis of INDI using transfer functions and the negative definiteness of the frozen-time eigenvalues are not rigorous, which leads to the first research question of this thesis:

How can the stability of incremental nonlinear dynamic inversion control be analyzed and expressed?

To address this question and to remedy the limitations of INDI control, this thesis first generalizes INDI for nonlinear uncertain systems with arbitrary input–output relative degrees, without using the time-scale separation assumption or term omissions. Then the stability of the generalized INDI control is analyzed using Lyapunov methods, considering the internal dynamics. Moreover, nonlinear system perturbation theory is adopted to analyze the robustness of INDI control to model uncertainties, external disturbances, and sudden changes in system dynamics. It is found that in the closed-loop system under INDI control, a perturbation term remains, which includes the influences of disturbances, dynamic variations, and the control effectiveness estimation errors.

One approach to enhance the robustness of INDI control is to augment it with adaptive parameter update laws, which requires to parameterize the perturbations using predefined model structures. This parameterization procedure can be tedious for external disturbances and dynamic variations remaining in the closed-loop of INDI. Furthermore, in these adaptation laws, the unknown parameters are assumed to be constant or slowly time-varying, which can become invalid when a sudden fault occurs. In addition, online parameter updates increase the computational load, which is unfavourable in flight control.

Another approach to enhance the robustness of INDI is to robustify it by using sliding mode control (SMC). The properties including finite-time convergence and the invariance (better than robust) to matched uncertainty have promoted the application of SMC to many aerospace control problems. Nonetheless, there is a contradiction between the reduction of model dependency and the reduction of uncertainty in existing SMC methods. Reducing the model dependency can simplify the implementation process and reduce the onboard computational load, while reducing the uncertainty decreases the SMC gains, which is crucial to chattering reduction. These observations raise the following research question:

How can the contradiction between the reduction of model dependency and the reduction of uncertainty in sliding mode control be solved?

Through the analysis of INDI control, it is found that a part of the input–output mapping of a nonlinear system is included in the estimated or directly measured output derivatives. This system information contained in sensor measurements can potentially solve the contradiction in SMC. Therefore, this thesis hybridizes (higher-order) SMC and sliding mode disturbance observers (SMDO) with the generalized INDI control for generic multi-input/multi-output nonlinear systems, named incremental sliding mode control (INDI-SMC). Theoretical analysis shows that this hybrid control framework inherits the advantages and remedies the drawbacks of both approaches. On the one hand, the incorporation of SMC and SMDO into INDI compensates for the influences of perturbations and also brings fixed/finite-time convergence property. On the other hand, by virtue of the sensor-based control structure of INDI, the model dependency and uncertainty are simultaneously reduced in INDI-SMC.

The theoretical developments in INDI and INDI-SMC also help to improve the concept of incremental backstepping (IBS) control. In the literature, IBS is proposed for second-order systems in the strict-feedback form. The outer-loop design of IBS is the same as standard model-based backstepping, while the inner-loop IBS design follows the idea of INDI control. As a consequence, the discussed limitations of INDI also exist

in IBS control. The closed-loop system using IBS control is also perturbed by uncertainties. These lead to the next research question:

How can the concept of incremental backstepping control be improved and how can its robustness be enhanced?

In this thesis, IBS is generalized for higher-order nonlinear uncertain systems in the strict-feedback form, without using the time-scale assumption or term omissions. It is then proposed to hybrid the generalized IBS with SMC, named incremental backstepping sliding mode control (IBSMC). Theoretical analysis shows that, on the one hand, IBSMC can compensate for the remaining uncertainty in IBS; on the other hand, as compared to backstepping sliding mode control in the literature, IBSMC can simultaneously reduce the model dependency and the minimum possible SMC gains. In addition, for nonlinear systems in the strict-feedback form, the recursive IBSMC design is simpler than INDI-SMC.

The INDI-SMC framework proposed in this thesis can induce both first- and higher-order sliding modes. In the literature, higher-order sliding modes can also be achieved by other control structures. This leads to the last research question of this thesis:

What is the relationship between the INDI-based SMC proposed in this thesis, the NDI-based SMC, and higher-order SMC with artificially increased relative degree?

In this thesis, analytical and numerical comparisons are made among these control structures. All of them can be used to induce higher-order sliding modes in finite time. It is found that only the estimated control effectiveness matrix is needed by the considered higher-order (HO) SMC and INDI-SMC, while NDI-SMC has higher model dependency. Moreover, although the considered HOSMC and INDI-SMC originate from completely different ideas, their nominal control increments are approximately equivalent if certain conditions are satisfied. Furthermore, the minimum possible switching gains needed by the considered HOSMC are approximately equal to those needed by INDI-SMC divided by the sample interval. Even so, these two control structures result in comparable chattering magnitudes, which are effectively reduced as compared to NDI-SMC.

The two hybrid control frameworks proposed in this thesis, INDI-SMC and IBSMC, are derived for generic nonlinear uncertain systems. Their effectiveness in flight control is evaluated by numerical simulations and quadrotor flight tests. When INDI-SMC and IBSMC are applied to fixed-wing aircraft fault-tolerant control problems, simulations show that a wide range of actuator faults and structural damages can be tolerated, without using additional fault detection and diagnosis (FDD) or online model identification. Even though the model dependencies of INDI-SMC and IBSMC are reduced, they present better robust performance than the NDI-SMC, BSMC, NDI, and BS control methods. Moreover, the SMC gains required by INDI-SMC and IBSMC are lower than those of NDI-SMC and BSMC, which mitigates the chattering effect.

To evaluate the effectiveness of the hybrid control in practice, this thesis implements INDI-SMC driven by a SMDO on a quadrotor. It is found that, in the presence of model uncertainties, wind disturbances, and actuator faults, INDI-SMC/SMDO has

better tracking performance than NDI-based SMC/SMDO. Moreover, the sliding mode control and observer gains needed by INDI-SMC/SMDO are lower, which alleviates the chattering effect. In addition, the onboard computational load is reduced by INDI-SMC/SMDO since a wide range of perturbations are passively resisted without adaptation, FDD or model identification. Last but not least, the implementation process of INDI-SMC/SMDO is simplified because of its reduced model dependency and smaller variations of the resulting uncertainty.

In the past decades, the trend of using composite materials to reduce airplane structural weight has emerged. This trend also brings challenges to flight control design because the accompanying increase in structural flexibility reduces the frequency separation between structural and rigid-body modes. This has been demonstrated by the loss of NASA's Helios Prototype aircraft. The design of highly flexible aircraft becomes a multidisciplinary problem, where the nonlinearities contributed by structural-, aero- and flight dynamics need to be considered. Therefore, this thesis proposes an integrated flexible aircraft flight control law based on incremental control. Numerical simulations show that the proposed control law can regulate rigid-body motions, alleviate gust loads, reduce the wing root bending moments, and suppress wing elastic modes. Furthermore, the proposed control law shows enhanced robustness to aerodynamic model uncertainties and actuator faults by virtue of its sensor-based nature.

In conclusion, guaranteed stability in the Lyapunov sense, reduced model dependency and computational load, reduced control and observer gains, as well as enhanced robustness to faults and disturbances, make the proposed incremental sliding mode control and incremental backstepping sliding mode control frameworks promising for enhancing flight safety in real life. The application of these two hybrid control frameworks to other nonlinear systems such as hydraulic systems and robotic manipulators are recommended as future work.

SAMENVATTING

De snelle groei van het luchtverkeersvolume benadrukt het belang van verbetering van de vliegveiligheid. Statistische gegevens tonen aan dat fly-by-wire technologie bij automatische vluchtbesturingsystemen het dodelijke ongevalspercentage van verlies van controle tijdens de vlucht effectief kan verminderen. Hoewel de dynamica van een vliegtuig niet-lineair is en in de tijd varieërd, is het in de praktijk gebruikelijk om vluchtregelwetten te ontwerpen op basis van lokale lineaire tijdsinvariabele (LTI) dynamische modellen, en om de gain-schedulingmethode toe te passen. Hier is de vluchtenvelop verdeeld in vele kleinere besturingsregimes, en zijn controllers gebaseerd op het LTI-model ontworpen en afgestemd voor elke hiervan. Deze aanpak is echter omslachtig en kan de vluchtstabiliteit en prestaties tussen operationele punten niet garanderen.

Met het oog op de uitdagingen die worden ondervonden door op LTI-modellen gebaseerde besturing, hebben niet-lineaire besturingsmethoden de aandacht getrokken van de vluchtbesturingsgemeenschap. Niet-lineaire dynamische inversie (NDI) en backstepping (BS) zijn twee vaak gebruikte niet-lineaire besturingsmethoden voor vluchtcontrole. Deze twee methodes annuleren de niet-lineariteiten in de closed-loop met een niet-lineair model van het systeem. Echter bestaan er onvermijdelijk mismatches tussen het model en de werkelijke dynamiek, vooral wanneer een vliegtuig atmosferische storingen tegenkomt en wanneer plotselinge actuatorfouten of zelfs structurele schade optreden. Om de robuustheid van modelgebaseerde niet-lineaire besturingsmethoden naar-model te verbeteren, is een algemeen geaccepteerde aanpak om ze te vergroten met online modelidentificatie. Dit proces is echter computationeel intensief en vereist voldoende excitatie, waardoor een beperkt vliegtuig uit de verminderde veilige vluchtenvelop kan vliegen. Met het oog op deze uitdagingen, is het belangrijkste doel van dit proefschrift:

Een stabiliteitsgegarandeerde niet-lineair vluchtcontrolekader te ontwerpen met verminderde modelafhankelijkheid en verbeterde robuustheid.

Aangezien dit proefschrift is gericht op het ontwerpen van een niet-lineair besturingskader, zijn de stabiliteitscriteria van Lyapunov aangenomen. De robuustheid-naar-model onzekerheden, externe verstoringen, plotselinge actuatorfouten en structurele schade zijn allemaal in beschouwing genomen. Incrementele niet-lineaire dynamische inversie (INDI) is een kandidaat om dit doel te bereiken. De kerngedachte van INDI is om hoekversnellingen en actuatorposities terug te koppelen om de robuustheid van NDI-naar-model mismatches te verbeteren. Dit idee is toegepast op verschillende vluchtcontroleproblemen en heeft veelbelovende resultaten laten zien bij het afwijzen van storingen en het tolereren van fouten. Dit proefschrift laat echter zien dat bestaande afwijkingen van INDI, die gebaseerd zijn op de time-scale separation aanname en term omissions, enkele beperkingen hebben. De gecascadeerde controlestructuur van INDI

gebruikt in vluchtcontrole beperkt ook de toepasbaarheid ervan tot meer algemene niet-lineaire systemen. Belangrijker nog is dat de stabiliteits- en robuustheidsanalyse van INDI met behulp van transferfuncties en de negatieve bepaaldheid van de frozen-time eigenwaarden niet rigoureuus zijn, wat leidt tot de eerste onderzoeksvraag van dit proefschrift:

Hoe kan de stabiliteit van incrementele niet-lineaire dynamische inversiebesturing worden geanalyseerd en uitgedrukt?

Om deze vraag te beantwoorden en de beperkingen van de INDI-besturing te verhelpen, generaliseert dit proefschrift eerst INDI voor niet-lineaire onzekere systemen met willekeurige relatieve input-output-graden, zonder gebruik te maken van de time-scale separation aanname of term omissions. Vervolgens wordt de stabiliteit van de gegeneraliseerde INDI-besturing geanalyseerd met behulp van Lyapunov-methoden, rekening houdend met de interne dynamiek. Bovendien wordt niet-lineaire systeemverstoringstheorie gebruikt om de robuustheid van de INDI-besturing-naar-model onzekerheden, externe verstoringen en plotselinge veranderingen in de systeemdynamiek te analyseren. Het is gebleken dat in het gesloten-lussysteem onder INDI-besturing een verstoringsterm overblijft die de invloeden van storingen, dynamische variaties en schattingsfouten voor de controle-effectiviteit omvat.

Eén benadering om de robuustheid van de INDI-besturing te verbeteren, is om deze te vergroten met adaptieve parameterupdatewetten, die vereist dat de verstoringen worden geparametreerd met behulp van vooraf gedefinieerde modelstructuren. Deze parameteringsprocedure kan tergend zijn voor externe verstoringen en dynamische variaties die overblijven in de closed-loop van INDI. Bovendien worden in deze aanpassingswetten de onbekende parameters verondersteld constant te zijn of langzaam in de tijd te variëren, wat ongelukkig kan worden als zich een plotselinge fout voordoet. Bovendien verhogen online parameterupdates de computationele belasting, wat ongunstig is voor de vluchtcontrole.

Een andere benadering om de robuustheid van INDI te verbeteren, is om het te versterken door gebruik te maken van sliding mode controle (SMC). De eigenschappen, waaronder ook eindige-tijdconvergentie en de invariantie (beter dan robuust) voor bijbehorende onzekerheid, hebben de toepassing van SMC bij vele problemen in de ruimtevaartcontrole bevorderd. Niettemin is er een tegenspraak tussen de vermindering van modelafhankelijkheid en de vermindering van onzekerheid in bestaande SMC-methoden. Het verminderen van de modelafhankelijkheid kan het implementatieproces vereenvoudigen en de computationele belasting aan boord verminderen, terwijl het verminderen van de onzekerheid de SMC gains verlaagt, wat cruciaal is voor het verminderen van chattering. Deze waarnemingen werpen de volgende onderzoeksvraag op:

Hoe kan de tegenstelling tussen de vermindering van de modelafhankelijkheid en de vermindering van onzekerheid in sliding mode controle worden opgelost?

Door de analyse van de INDI-besturing is gevonden dat een deel van de input-output mapping van een niet-lineair systeem is inbegrepen in de geschatte of direct gemeten

output derivatives. Deze systeem informatie in sensormetingen kan mogelijk de tegenstrijdigheid in SMC oplossen. Daarom hybridiseert dit proefschrift SMC- en sliding mode disturbance observers (SMDO) met de gegeneraliseerde INDI-besturing voor generieke multi-input / multi-output niet-lineaire systemen, genaamd incrementele sliding mode controle (INDI-SMC). Theoretische analyse laat zien dat dit hybride besturingskader de voordelen overneemt en de nadelen van beide benaderingen verhelpt. Aan de ene kant compenseert de opname van SMC en SMDO in INDI de invloeden van verstoringen en brengt ook vaste/eindige-tijdconvergentie-eigenschappen met zich mee. Aan de andere kant worden, op grond van de sensorgebaseerde besturingsstructuur van INDI, de afhankelijkheid van het model en de onzekerheid tegelijkertijd verminderd in INDI-SMC.

De theoretische ontwikkelingen in INDI en INDI-SMC helpen ook om het concept van incrementele backstepping (IBS)-besturing te verbeteren. In de literatuur wordt IBS voorgesteld voor systemen van de tweede orde in de strict-feedback vorm. Het outer-loop ontwerp van IBS is hetzelfde als standaard, op model gebaseerde backstepping, terwijl het inner-loop IBS-ontwerp het idee van INDI-besturing volgt. Als gevolg hiervan zijn de besproken beperkingen van INDI ook aanwezig in IBS-besturing. Het closed-loopsysteem met IBS-besturing is ook verstoord door onzekerheden. Deze leiden tot de volgende onderzoeksvraag:

Hoe kan het concept van incrementele backstepping-besturing worden verbeterd en hoe kan de robuustheid ervan worden verbeterd?

In dit proefschrift wordt IBS gegeneraliseerd voor hogere-orde, niet-lineaire onzekere systemen in de strict-feedback vorm, zonder gebruik te maken van de time-scale aanname of term omissions. Vervolgens wordt voorgesteld om de gegeneraliseerde IBS te hybridiseren met SMC, genaamd incrementele backstepping sliding mode controle (IBSMC). Theoretische analyse toont aan dat enerzijds IBSMC kan compenseren voor de resterende onzekerheid in IBS; anderzijds, in vergelijking met backstepping sliding mode controle in de literatuur, kan IBSMC tegelijkertijd de modelafhankelijkheid en de minimaal mogelijke SMC-gains verminderen. Voor niet-lineaire systemen in de strict-feedback vorm is het recursieve IBSMC-ontwerp bovendien eenvoudiger dan INDI-SMC.

Het INDI-SMC-raamwerk dat in dit proefschrift wordt voorgesteld, kan zowel eerste- als hogere orde sliding modi induceren. In de literatuur kunnen hogere-orde sliding modes ook worden bereikt door andere besturingsstructuren. Dit leidt tot de laatste onderzoeksvraag van dit proefschrift:

Wat is de relatie tussen de op INDI gebaseerde SMC zoals voorgesteld in dit proefschrift, de op NDI gebaseerde SMC, en hogere-orde SMC met een kunstmatig verhoogde relatieve graad?

In dit proefschrift worden analytische en numerieke vergelijkingen gemaakt tussen deze besturingsstructuren. Allen kunnen worden gebruikt om hogere orde sliding modi in eindige tijd te induceren. Het is gebleken dat alleen de geschatte matrix voor de controle-effectiviteit nodig is voor de hogere orde (HO) SMC en INDI-SMC, terwijl NDI-SMC een hogere modelafhankelijkheid heeft. Bovendien zijn, hoewel de beschouwde HOSMC en INDI-SMC hun oorsprong vinden in totaal verschillende ideeën, hun nominale besturingsincrementen ongeveer gelijkwaardig als aan bepaalde voorwaarden

is voldaan. Verder zijn de minimaal mogelijke switching-gains die nodig zijn voor de beschouwde HOSMC ongeveer gelijk aan die welke nodig zijn voor INDI-SMC gedeeld door het sample interval. Toch resulteren deze twee besturingsstructuren in vergelijkbare chattering groottes, die effectief worden verminderd in vergelijking met NDI-SMC.

De twee hybride besturingskaders voorgesteld in dit proefschrift, INDI-SMC en IBSMC, zijn afgeleid voor generieke niet-lineaire onzekere systemen. Hun effectiviteit in vluchtcontrole is geëvalueerd door numerieke simulaties en quadrotor-vluchttesten. Wanneer INDI-SMC en IBSMC worden toegepast op fixed-wing vliegtuig fouttolerante besturingsproblemen, laten simulaties zien dat een groot bereik aan actuatorfouten en structurele schade kan worden getolereerd, zonder gebruik van aanvullende foutdetectie en diagnose (FDD) of online-modelidentificatie. Hoewel de modelafhankelijkheid van INDI-SMC en IBSMC wordt verminderd, vertonen ze betere robuustheidsprestaties dan de NDI-SMC, BSMC, NDI en BS besturingsmethoden. Bovendien zijn de SMC-gains vereist door INDI-SMC en IBSMC lager dan die van NDI-SMC en BSMC, wat het chatteringeffect verminderd.

Om de effectiviteit van de hybride besturing in de praktijk te evalueren, implementeert dit proefschrift INDI-SMC, aangestuurd door een SMDO op een quadrotor. Het blijkt dat, in de aanwezigheid van modelonzekerheden, windverstoringen en actuatorfouten, INDI-SMC/SMDO betere trackingprestaties heeft dan op NDI-gebaseerde SMC/SMDO. Bovendien zijn de benodigde observer-gains en sliding mode controle voor INDI-SMC/SMDO lager, wat het chatteringeffect verlicht. Verder wordt de computationele belasting aan boord verminderd door INDI-SMC/SMDO, aangezien een groot bereik aan verstoringen passief wordt weerstaan zonder aanpassing, FDD of modelidentificatie. Ten slotte wordt het implementatieproces van INDI-SMC/SMDO vereenvoudigd vanwege de verminderde modelafhankelijkheid en kleinere variaties van de resulterende onzekerheid.

In de afgelopen decennia is de trend van het gebruik van composietmaterialen om het structurele gewicht van vliegtuigen te verminderen in opkomst geweest. Deze trend brengt ook uitdagingen met zich mee voor het ontwerp van de vluchtcontrole omdat de bijbehorende toename in structurele flexibiliteit de frequentiescheiding tussen structurele en rigid-body modi vermindert. Dit is aangetoond door het verlies van het Helios Prototype-vliegtuig van de NASA. Het ontwerp van zeer flexibele vliegtuigen wordt een multidisciplinair probleem, waarbij rekening moet worden gehouden met de niet-lineariteiten door de structurele-, aero- en vluchtdynamiek. Daarom stelt dit proefschrift een geïntegreerde flexibele vluchtregelwet voor vliegtuigen voor gebaseerd op incrementele besturing. Numerieke simulaties tonen aan dat de voorgestelde regelwet rigid-body bewegingen kan reguleren, last door windvlagen kan verlichten, de vleugelwortel buigmomenten kan verminderen en elastische modi van vleugels kan onderdrukken. Bovendien vertoont de voorgestelde regelwet een verbeterde robuustheid voor onzekerheden in aerodynamische modellen en actuatorfouten vanwege zijn sensor-gebaseerde aard.

Kortom, gegarandeerde stabiliteit in de Lyapunov-zin, verminderde modelafhankelijkheid en computationele belasting, verminderde besturings- en observer gains, evenals verbeterde robuustheid tegen fouten en verstoringen, zorgen ervoor dat de voorge-

stelde incrementele sliding mode besturing en incrementele backstepping sliding mode besturingskaders veelbelovend zijn voor het verbeteren van vliegveiligheid in het echte leven. De toepassing van deze twee hybride besturingskaders op andere niet-lineaire systemen zoals hydraulische systemen en robotachtige manipulators wordt aanbevolen als toekomstig werk.



NOMENCLATURE

Latin Letters

C_w	matrix of direction cosines between (x_w, y_w, z_w) and (x_f, y_f, z_f)
C_f	matrix of direction cosines between (x_f, y_f, z_f) and (X_E, Y_E, Z_E)
C_e	matrix of direction cosines between (x_e, y_e, z_e) and (x_f, y_f, z_f)
$\mathcal{C}_{uw}, \mathcal{C}_{\psi w}$	damping matrices for the bending and torsion of the wing
\mathbf{d}	vector of external disturbances
\mathbf{e}	vector of tracking errors
EI, GJ	bending and torsional stiffness, $\text{N}\cdot\text{m}^2$
E_f	matrix relating Eulerian velocities to angular quasi-velocities
f_s	sampling frequency
\mathbf{F}, \mathbf{M}	generalized resultant forces and moments, $\text{N}, \text{N}\cdot\text{m}$
$\mathcal{F}_{uw}, \mathcal{F}_{\alpha w}$	Rayleigh dissipation function densities
\mathbf{G}	control effectiveness matrix
\mathbf{J}	inertia matrix for the deformed aircraft
$\mathcal{K}_{uw}, \mathcal{K}_{\psi w}$	stiffness matrices for the bending and torsion of the wing
L	Lagrangian for the aircraft
\mathcal{L}, \mathcal{H}	matrices of stiffness differential operators for the wing
\mathbf{M}_{st}	system mass matrix
M_r	wing root bending moment, $\text{N}\cdot\text{m}$
n_z	vertical load factor, m/s^2
$\mathbf{p}_{V_f}, \mathbf{p}_{\omega_f}$	momentum vectors for aircraft translation and rotation
$\mathbf{p}_{uw}, \mathbf{p}_{\psi w}$	momentum vectors for bending and torsion
\mathbf{q}	vectors of generalized coordinates for bending
$\mathbf{r}_w, \mathbf{r}_f, \mathbf{r}_e$	nominal position vector of a point on the wing, fuselage, and tail, m
\mathbf{r}_{fw}	radius vector from O_f to O_w , m
\mathbf{r}_{fe}	radius vector from O_f to O_e , m
\mathbf{R}_f	position vector of the origin of (x_f, y_f, z_f) relative to (X_E, Y_E, Z_E) , m
\mathbf{s}	vectors of generalized coordinates for bending velocities, $\text{m}/\text{s}, \text{rad}/\text{s}$
$\tilde{\mathbf{S}}$	matrix of the first moments of inertia of the deformed aircraft
\mathcal{T}, \mathcal{V}	kinetic, potential energy of the aircraft
\mathbf{u}_w	bending displacements of the wing, m
\mathbf{u}	control input
\mathbf{u}_{eq}	the equivalent control
$\hat{\mathbf{U}}$	resultant of the force density vector
\mathbf{v}_w	bending velocities of the wing, m/s
\mathbf{V}_f	translational velocity vectors of (x_f, y_f, z_f) , m/s
\mathbf{x}_{rm}	state reference vector

$\mathbf{x}_r, \mathbf{x}_e$ rigid and elastic state vectors
 $\bar{\mathbf{v}}_w, \bar{\mathbf{v}}_f, \bar{\mathbf{v}}_e$ velocity of an arbitrary mass element on the wing, fuselage, tail, m/s

Greek Letters

$\boldsymbol{\alpha}_w$ torsion velocity vector of the wing, rad/s
 Δ increments in one time step
 $\boldsymbol{\varepsilon}_{\text{ndi}}$ the resulting uncertainty term in NDI control
 $\boldsymbol{\varepsilon}_{\text{indi}}$ the resulting uncertainty term in INDI control
 $\boldsymbol{\eta}$ vector of internal states
 $\boldsymbol{\eta}_w$ vector of generalized coordinates for torsion
 ϕ, θ, ψ Euler angles
 $\boldsymbol{\psi}_w$ torsion displacements of the wing, rad
 $\hat{\boldsymbol{\Psi}}$ resultant of the moment density vector
 $\boldsymbol{\xi}$ vector of external states
 $\boldsymbol{\xi}_w$ vector of generalized coordinates for torsion
 $\boldsymbol{\theta}_f$ Euler angle vector
 $\boldsymbol{\omega}_f$ angular velocity vector of (x_f, y_f, z_f) , rad/s
 $\boldsymbol{\rho}$ relative degree vector
 Γ_ξ ultimate bound of the external states
 Γ_η ultimate bound of the internal states
 Φ shape function matrix of the bending
 Ψ shape function matrix of the torsion
 κ fault indicator
 \mathbf{v} virtual control vector

Acronyms

ABS adaptive backstepping
 AFCS automatic flight control systems
 BS backstepping
 BSMC backstepping sliding mode control
 CAT clear-air turbulence
 FBW fly-by-wire
 FDD fault detection and diagnosis
 FDI fault detection and isolation
 FRTC finite reaching-time continuous
 FTC fault-tolerant control
 GLA gust load alleviation
 HOSMC higher-order sliding mode control
 IBS incremental backstepping
 IBSMC incremental backstepping sliding mode control
 IMU inertia measurement unit
 INDI incremental nonlinear dynamic inversion
 INDI-SMC incremental sliding mode control
 KF Kalman filter

LOC-I	loss of control in-flight
LQR	linear-quadratic regulator
LQG	linear-quadratic Gaussian
LTI	linear time-invariant
MIMO	multi-input and multi-output
MRAC	model reference adaptive control
NASA	national aeronautics and space administration
NDI	nonlinear dynamic inversion
NDI-SMC	sliding mode control based on nonlinear dynamic inversion
NLTV	nonlinear time-varying
OFC	oscillatory failure case
PCH	pseudo-control hedging
PID	proportional-integral-derivative
PSD	power spectral density
RMS	root mean square
SISO	single-input and single-output
SMC	sliding mode control
SMDO	sliding mode disturbance observer
SPM	singular perturbation margin
UAV	unmanned aerial vehicle
VCCTEF	variable camber continuous trailing edge flap



1

INTRODUCTION

1.1. THREATS TO FLIGHT SAFETY

Over the past decades, we have witnessed a swift growth of air transport. Statistical data show that air traffic volume has doubled every 15 years since 1976, and this trend is expected to continue by Airbus's global market forecast [1]. The expansion of air transport not only brings more opportunities to the aviation industry, but also increases the importance of flight safety enhancements.

Using the data of the CAST/ICAO common taxonomy team [2], the causes of aviation fatalities and fatal accidents from 2008 to 2017 are plotted in Fig. 1.1. It can be seen that 25.5% of the fatal accidents are caused by loss of control in-flight (LOC-I). This category also contributes to 49.9% of onboard fatalities. LOC-I is generally related to a significant deviation from the nominal flight envelope, which can be triggered by human behaviors, aircraft malfunctions, external disturbances, etc. [3, 4].

Continuous efforts have been put into reducing the accident rate caused by LOC-I. A statistical analysis conducted by Airbus shows that with the help of fly-by-wire (FBW) technology installed on the fourth generation of civil aircraft, the fatal LOC-I accident rate has been reduced by 75% as compared to the third generation [1]. FBW technology omits the complex and heavy mechanical linkage between the pilot and the hydraulic control system, and makes it possible to enhance flight safety using more advanced automatic flight control systems (AFCS). For new generations of aircraft, the design of AFCS is challenged by many factors, including potential actuator faults and structural damages, atmospheric disturbances, the increase of structural flexibility, and nonlinear dynamics. These factors will be briefly addressed in the following subsections, after which the thesis goal is stated.

1.1.1. ACTUATOR FAULTS AND STRUCTURAL DAMAGES

Many flight accidents were induced by actuator faults and/or structural damages. On October 4th, 1992, the pylon of engine no.3 of a Boeing 747-200F (El Al Cargo Flight LY1862, registration: 4X-AXG) broke, shortly after the takeoff. This structural damage led to loss of both right wing engines, serious damage to the right wing leading edge, and the

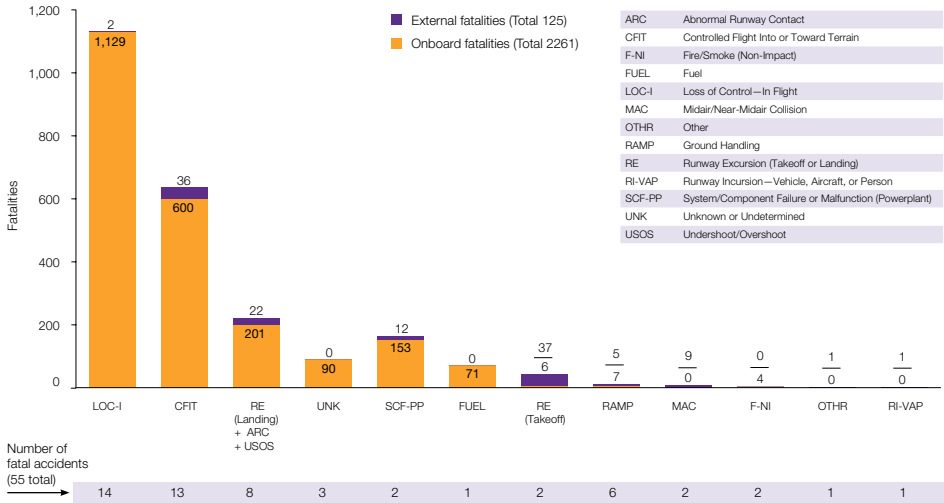


Figure 1.1: Fatalities occurrence categories for worldwide commercial jet fleets from 2008 to 2017 [2].

complete effectiveness loss of outboard ailerons, outboard flaps, spoilers, as well as the inner left and outer right elevators. This aircraft crashed and killed four on-board flight crew and 39 people on the ground [4, 5]. On August 12th 1985, a dome joint of a Boeing 747SR (flight JA8119) broke during flight, which resulted in an explosive decompression. This led to severe damage on the vertical tail and a complete loss of hydraulics. Using differential thrust, the pilots stabilized the aircraft for half an hour, but unfortunately, they did not make it in the end due to crew fatigue [4].



(a) 4X-AXG, photoed on 23th August 1992 at Los Angeles international Airport, © Torsten Maiwald. (b) The Groeneveen and Klein-Kruitberg complexes after the crash of El Al Flight 1862, © Jos Wiersema.

Figure 1.2: Photos about the crash of El Al Flight 1862.

On March 3rd, 1991, shortly after a Boeing 737-200 (United Airlines flight 585) completed its turn onto the final approach course, the aircraft rolled steadily to the right and pitched down until it reached a nearly vertical attitude. This aircraft eventually crashed near the airport [6]. On September 8th, 1994, a Boeing 737-300 (USAir flight 427) encountered a similar accident during its landing phase. This aircraft eventually crashed



Figure 1.3: Pictures of the Boeing 747SR JA8119.

with all 132 people on board killed [7]. The probable cause of these two accidents was “a loss of control of the airplane resulting from the movement of the rudder surface to its blowdown limit” (Ref. [7], Page 295).

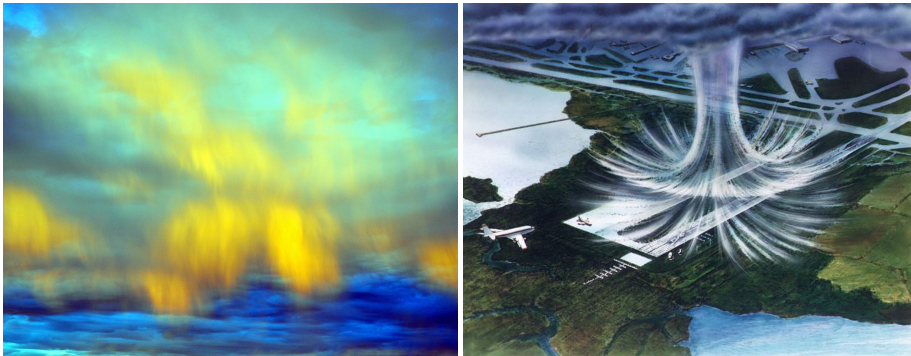
In some cases, the faulty aircraft is still controllable, and some level of performance can still be achieved, which is sufficient to allow the pilot to safely land the aircraft. An investigation showed that the fatal crash of El Al Flight 1862 could have been avoided [8]. A few examples where pilots saved the aircraft and passengers are also known. For example, on November 22th, 2003, pilots successfully landed the DHL Airbus A300B4-203F freighter after it was hit by a surface-to-air missile. On April 12th, 1997, during the take-off of a Lockheed L-1011 aircraft (Delta Air Lines Flight 1080), its left elevator got stuck in a fully upwards position, which made the aircraft pitch up aggressively and nearly caused stall. Luckily, L-1011 has an engine on the vertical tail, and by using differential thrust, the pilots successfully controlled the pitching angle and landed the aircraft [9].

To reduce the accident rate induced by actuator faults and structural damages, many researchers propose to include a “self-repairing” capability in the flight control system, which can reduce the workload of pilots and make full use of the remaining control ability of the faulty aircraft. A closed-loop control system which can tolerate component malfunctions, while maintaining stability and desirable performance, is said to be a fault-tolerant control (FTC) system [4, 10]. A national aeronautics and space administration (NASA) experiment shows that FTC systems can indeed help pilots to control an impaired plane [11, 12]. A bibliographical review of FTC systems can be found in [10].

1.1.2. ATMOSPHERIC DISTURBANCES

Air travel can be very unpleasant and even hazardous due to atmospheric disturbances. Flying an aircraft in the disturbed atmosphere is like cycling on a rough road, which causes fatigue in both structure and human beings. The fatigue in structure can lead to cracks/crushes and even breakages. The passenger ride comfort is compromised, and injuries can also happen. More importantly, the fatigue of pilots and the reduced aircraft handling quality can impair the precise control of flight path needed for safe takeoff and landing, as well as collision avoidance [13, 14].

In history, many flight accidents were directly/indirectly caused by atmospheric disturbances. Twenty-five percent of the 729 accidents reported by the U.S. air carriers from



(a) Downdraft Wind shear clouds illuminate at Twilight over the Mojave Desert, © Jessie Eastland. (b) NASA artist's rendering of a microburst, © NASA.

Figure 1.4: Illustrations for a downdraft windshear and a microburst.

1964 to 1975 are turbulence related [13]. Among these accidents, 115 cases occurred in convective turbulence and 68 in clear-air turbulence (CAT) [15]. In 1972, CAT accidents caused about 23 million dollars' worth of loss to the airlines [15]. One of the critical atmospheric disturbance types is wind shear, which refers to the variation of wind over either horizontal or vertical distances [16]. Twenty-six major civil airplane accidents between 1964 and 1985 were directly caused or contributed to by wind shear, which led to 620 deaths and 200 injuries [17]. These accidents highlight the importance of designing an AFCS that can reduce the effects of atmospheric disturbances.

1.1.3. INCREASE OF STRUCTURAL FLEXIBILITY

On December 17th, 1903, the world witnessed the first successful flight of a heavier-than-air powered aircraft, the Wright Flyer. The lateral control of the Wright Flyer was achieved by making use of the flexible wing structure. That is, the angle of attack was changed *locally* by warping the wing tips [18]. Because of its biplane configuration and relatively low airspeed (maximum speed: 30 mph (48 km/h)), the Wright Flyer did not encounter significant detrimental aeroelastic effects [18].

With the development of aircraft propulsion systems, the maximum airspeed record was constantly broken. At the same time, the wing structures were becoming stiffer and stiffer to shoulder the increasing wing load and to ensure aeroelastic stability. Roll control is normally executed by trailing edge ailerons, which are built independently from the main wing structures. However, stiffer wings lead to a side effect that is very undesirable in aircraft design, namely the increase in structural weight.

Presently, composite materials bring more opportunities to aircraft structural design. They can provide structural strength comparable to metallic alloys, but with reduced structural weight. The Boeing 787 Dreamliner, the first commercial aircraft constructed primarily of composite materials, is designed to be 20% more fuel-efficient than the Boeing 767 [19]. The use of composite materials also brings challenges, including the increase of structural flexibility.

As the wing flexibility increases, the frequency separation between structural and rigid-body modes becomes smaller. Consequently, the usual separation of flight dynamic and aeroelastic analysis becomes less appropriate for gust response predictions and flight control designs. One famous example is the loss of NASA's Helios Prototype Aircraft, shown in Fig. 1.5. This aircraft had a long and slender wing, with aspect ratio 30.9 for enhancing the aerodynamic efficiency [20]. On June 26th, 2003, the Helios Prototype entered moderate air turbulence during a test flight, causing extreme dihedral and leading to an uncontrollable series of pitch oscillations, which resulted in structural breakup and crash of the aircraft [20].

Further research discovered that the instability of the phugoid mode during large dihedral angles was the main reason of the Helios crash [21–23]. Apart from the phugoid mode, the interaction of the structural and rigid-body modes can also lead to instability of other conventional flight dynamic modes [22, 24–26]. These emphasize the necessity of an integrated flight control design for flexible aircraft.



Figure 1.5: Photos of the NASA's Helios, a solar-and fuel-cell-system-powered unmanned aerial vehicle.

1.1.4. NONLINEAR DYNAMICS

The free-flying dynamics of flexible aircraft are nonlinear time-varying (NLTV) [22, 27]. The nonlinearities are contributed to by flight dynamics, aeroelasticity and the inertial couplings between them [27]. For the convenience of analysis and design, the structural vibration dynamics are often described by a series of linear differential equations, and their inertial couplings with rigid-body dynamics are assumed to be negligible [27, 28]. However, these simplifications become invalid for highly flexible aircraft [24, 29–32], whose design becomes a multidisciplinary problem involving intrinsically *nonlinear* structural, aero-, and flight dynamics [30].

Even for a “rigid” aircraft, its free-flying dynamics are also NLTV. Moreover, when the angle of attack is high or when the aircraft is in transonic flight, the nonlinearities in aerodynamics can become influential. In the literature of flight control, it is a common practice to linearize the NLTV system around an equilibrium point, which results in a linear time-invariant (LTI) system. Many control methods are designed based on the LTI model, and the stability of the closed-loop system is analyzed based on the negative definiteness of the eigenvalues. However, this design approach is only valid in the neighborhood of the equilibrium point [33]. In order to expand the applicability of LTI

model-based control, the gain-scheduling method is widely used, where the flight envelope is divided into many smaller operating regimes, and LTI model-based control is designed and tuned for each of them. However, this approach is cumbersome and does not guarantee stability and performance in between operational points.

The dynamic linearization and the gain-scheduling processes are not needed by nonlinear control designs. Stability criteria for these designs are normally defined in the sense of Lyapunov [33]. Since closed-loop stability is of paramount importance in flight control, it will be included in the research goal of this thesis.

1.2. RESEARCH GOAL

The challenges stated in Sec. 1.1 motivate the main research goal of this thesis:

Research Goal

To design a stability-guaranteed nonlinear flight control framework with reduced model dependency and enhanced robustness.

In this thesis, Lyapunov stability criteria are adopted. The robustness to model uncertainties, external disturbances, sudden actuator faults and structural damages are considered, whereas the robustness to sensor faults is out of the scope, and readers are recommended to [10, 34]. Nonlinear control designs with reduced model dependency can simplify the implementation process and reduce cost. To reduce onboard computational load, this thesis also aims at tolerating a wide range of perturbations without using fault detection and diagnosis (FDD) or model identification. Extreme scenarios where these mechanisms become necessary will be discussed in Chapter 8.

Two nonlinear control methods that are frequently used in flight control are nonlinear dynamic inversion (NDI) and backstepping (BS) [33, 35]. Both NDI and BS are model-based control methods, which means that their implementation requires a model of the physical system, and their effectiveness relies on the model accuracy. However, mismatches between the estimated model and the real system dynamics inevitably exist. To enhance the robustness of these model-based control methods to model mismatches, they are augmented with various robust and adaptive mechanisms [35–41]. In contrast to these augmentations, incremental control proposes to improve robustness by fully exploring the sensor measurements.

1.3. INCREMENTAL CONTROL

Incremental control methods include incremental nonlinear dynamic inversion (INDI) [42] and incremental backstepping (IBS) [43]. IBS is an extension of INDI for second-order systems in the strict-feedback form. Incremental control methods were proposed in the aerospace community, and they are referred to as sensor-based approaches.

1.3.1. LITERATURE REVIEW ON INCREMENTAL CONTROL

The idea of INDI can be traced back to the late nineties. In view of the challenges in NDI control, Smith proposed a “simplified” NDI approach in 1998 [44]. This approach is based upon manipulations of the flight dynamic equations and assumptions about the

bandwidth separations. It is found in [44] that the feedback of rotational (angular) acceleration and control surface position can enhance the robustness of NDI to uncertainties in the mathematical model.

The derivations in [44] are further improved in [45, 46]. By virtue of the feedback of accelerations and actuator positions, the control method is shown to accommodate aerodynamic changes *without* the use of stability derivatives [45, 46]. Moreover, a reconfigurable control is developed in [46] using the “simplified” NDI along with sensor failure detection and isolation systems. The aircraft model used in [46] has control redundancy; thus a weighted least squares method is used to allocate the control command. In [47], the “simplified” NDI is referred to as an implicit design of NDI, with which a cascaded aerodynamic angle tracking controller is designed, with its effectiveness demonstrated by numerical simulations.

Inheriting the idea of feeding back angular accelerometers and actuator positions, INDI is first proposed in [42]. The sensor-based control idea of INDI is also shared by [48] and [49]. The derivation of INDI is based on the Taylor series expansion of the system dynamic model and the “time-scale separation” assumption¹. Simulations on an unmanned aerial vehicle (UAV) model show the insensitivity of this method to aerodynamic, center of mass and inertia mismatches [42]. It is also shown in [42] that this method is sensitive to sensor measurement time delays. Therefore, a linear predictive filter is proposed in [42] to predict the angular accelerations.

After its proposal in [42], INDI has been applied to various aerospace systems. In [50], INDI is used to control the angular rate of a spacecraft. In [51], INDI is applied to control the angular rate of an ADS-33 helicopter. The pseudo-control hedging technique [52] is used along with INDI to handle actuator saturations. In [53], numerical simulations show that INDI can tolerate aileron and rudder jamming faults without using online model identification or FDD. Online model identification requires sufficient excitation and selection of thresholds, which can be tricky in practice [53].

INDI also shows promising robustness against external disturbances. In [54], a gust load alleviation control is designed using INDI, which shows better performance and robustness than a linear-quadratic regulator (LQR) control. In [55, 56], it is demonstrated by quadrotor flight tests in a wind tunnel that INDI has better position tracking performance than a PID controller. Recent research in [57] uses INDI along with the primary axis principle [58], which achieves controllable high-speed (over 9 m/s) flight of a quadrotor despite complete loss of a single rotor.

The idea of INDI inspired the proposal of IBS in [43] for second-order nonlinear systems in strict-feedback form. The outer-loop control design of IBS is the same as the standard backstepping control. The differences appear in the inner loop, where the system dynamics are first rewritten in an incremental form, based on which the control increment is designed. Because of the feedback of angular accelerations and actuator positions, numerical simulations using a missile model show that IBS has better robustness against aerodynamic uncertainties than standard backstepping control [43]. This robustness enhancement is also verified by outdoor flight tests on a hexarotor [59].

¹As will be explained in Sec. 1.3.2, this assumption used in INDI control means that the controls can change significantly faster than the states.

1.3.2. CHALLENGES IN INCREMENTAL CONTROL

In spite of the effectiveness of incremental control shown in the literature, challenges and limitations still exist. In this subsection, the derivations of INDI will be briefly reviewed. The same derivations are applicable to the inner-loop IBS control. The limitations of incremental control will then be exposed.

INDI control is derived for the following nonlinear system:

$$\dot{\mathbf{x}} = \mathbf{f}(\mathbf{x}) + \mathbf{G}(\mathbf{x})\mathbf{u}, \quad (1.1)$$

where $\mathbf{f} : \mathbb{R}^n \rightarrow \mathbb{R}^n$, and \mathbf{G} is a nonsingular smooth function mapping $\mathbb{R}^n \rightarrow \mathbb{R}^{n \times m}$. The columns of \mathbf{G} and \mathbf{f} are smooth vector fields. It is further assumed that $m = n$, and the output vector is chosen as $\mathbf{y} = \mathbf{x}$. For this set-up, the input–output relative degree for each control channel equals one, and there are no internal dynamics.

Regarding the applications of incremental control in the literature, the internal dynamics are normally avoided by using a cascaded control structure [42, 50, 51, 53–56, 59–67]. However, the stability of cascaded control structures is not easy to prove because of its dependency on whether there is sufficient time-scale separation between different control loops. Moreover, for under-actuated systems, such as a quadrotor with complete loss of two or more rotors, considering the internal dynamics becomes important.

Denote the sampling interval as Δt ; then the first step of INDI control or inner-loop IBS control is to take the first-order Taylor series expansion of Eq. (1.1) around the condition at $t - \Delta t$ (denoted by subscript 0) as:

$$\dot{\mathbf{x}} = \dot{\mathbf{x}}_0 + \left. \frac{\partial[\mathbf{f}(\mathbf{x}) + \mathbf{G}(\mathbf{x})\mathbf{u}]}{\partial \mathbf{x}} \right|_0 \Delta \mathbf{x} + \mathbf{G}(\mathbf{x}_0)\Delta \mathbf{u} + \mathbf{R}_1, \quad (1.2)$$

where $\Delta \mathbf{x}$ and $\Delta \mathbf{u}$ represent the state and control increments in one sampling time step Δt ; \mathbf{R}_1 represents the higher-order expansion remainder. Although INDI shows effectiveness on external disturbance rejection [54–57, 57] and tolerance to sudden faults [53], these factors are not modeled in Eq. (1.1), and partial derivatives are also not taken with respect to the corresponding variables in Eq. (1.2).

The core step of INDI or inner-loop IBS control is the model simplification based on the so-called “time-scale separation” principle (or assumption). It is noteworthy that this principle is different from the widely accepted time-scale separation between cascaded control loops, which is based on singular perturbation theories. In [42, 50, 51, 53–56, 59–66, 68, 69], the separation concept used in incremental control is described as follows: the controls can change significantly faster than the states, i.e., $\Delta \mathbf{u} \gg \Delta \mathbf{x}$. Therefore, the state-variation-related term and the higher-order terms can be omitted from Eq. (1.2), which yields the simplified incremental dynamics:

$$\dot{\mathbf{x}} \approx \dot{\mathbf{x}}_0 + \mathbf{G}(\mathbf{x}_0)\Delta \mathbf{u} \quad (1.3)$$

This simplification is worth some further discussion; because the plant simplification is made *before* introducing the INDI control inputs, this simplification becomes questionable for unstable plants. Moreover, although the state-variation-related terms and higher-order terms are not used in INDI control design, they should be kept in the closed-loop dynamic equations. Generally speaking, these potential issues have been overlooked in the literature [42, 50, 51, 53–56, 59–66, 68, 69].

Replacing $\dot{\mathbf{x}}$ by a linear virtual control \mathbf{v} , and inverting the dynamics in Eq. (1.3), the INDI or the inner-loop IBS control increment is designed as:

$$\Delta \mathbf{u} = \mathbf{G}^{-1}(\mathbf{x}_0)(\mathbf{v} - \dot{\mathbf{x}}_0) \quad (1.4)$$

This equation defines the control increment $\Delta \mathbf{u}$. The actual control command given to the actuator equals $\mathbf{u} = \mathbf{u}_0 + \Delta \mathbf{u}$, where \mathbf{u}_0 is the measured or estimated control input at the previous time step $t - \Delta t$ [42, 70].

Since Eq. (1.4) is independent of the model of $\mathbf{f}(\mathbf{x})$, it is concluded in [42, 50, 51, 56, 60, 62] that INDI and IBS are robust to the uncertainties in $\mathbf{f}(\mathbf{x})$. However, this conclusion needs further analysis since the omitted terms, which reflect system dynamics, still remain in the closed-loop dynamics. In [42] and [60], it is shown by using linear transfer functions derived from block diagrams that if actuator dynamics are not considered, the model uncertainties in $\mathbf{G}(\mathbf{x})$ do not affect the closed-loop system, and the dynamics from \mathbf{v} to \mathbf{x} become perfectly decoupled integrators. However, stability proofs based on transfer functions are only valid for LTI systems. Moreover, whereas the assumption of $\dot{\mathbf{x}} = \dot{\mathbf{x}}_0$ is made in the block diagram derivations, this is in principle incorrect because in that case, $\Delta \mathbf{u}$ would be zero at all times. Finally, regarding the robustness analysis in [42, 60], the designed control input (Eq. (1.4)) is substituted into the simplified incremental dynamics Eq. (1.3) instead of the actual dynamics, Eq. (1.2) or Eq. (1.1), so the effects of the omitted terms are not considered at all.

In [60], the stability and robustness of the closed-loop system under IBS control considering actuator dynamics are analyzed by formulating the closed-loop system into a state-space form and testing the frozen-time eigenvalues of the time-varying system matrix. However, it has been shown in [71–73] that for linear time-varying systems, the stability criterion based on the negative definiteness of the frozen-time eigenvalues is *neither sufficient nor necessary*. The Lyapunov methods and concepts from nonlinear system perturbation theory are needed for more rigorous stability and robustness analyses of nonlinear time-varying systems.

Although INDI and IBS do not rely on the model of $\mathbf{f}(\mathbf{x})$, they do depend on knowledge of the control effectiveness matrix $\mathbf{G}(\mathbf{x})$. To improve its robustness against uncertainties in $\mathbf{G}(\mathbf{x})$, INDI is augmented with an online least mean squares adaptive filter in [62]. Although this approach works in practice, from a theoretical point of view, due to the separation of control design and model identification, the stability of indirect adaptive control in general cannot be guaranteed.

The uncertainties in $\mathbf{G}(\mathbf{x})$ are also considered in [61], where the IBS method is augmented with three adaptive parameter update laws: tuning functions, immersion and invariance, and least-squares. It is shown by numerical simulations that these augmentations yield comparable effectiveness in improving the robustness of IBS to parametric uncertainties in $\mathbf{G}(\mathbf{x})$. For these adaptive augmentations, the uncertainties need to be parameterized using pre-defined model structures, and the unknown parameters are assumed to be constant or slowly time-varying [61, 74, 75]. This assumption is likely to be invalid when a sudden fault occurs [76]. Apart from the uncertainties in $\mathbf{G}(\mathbf{x})$, the uncertainties under incremental control also contain a state-variation-related term and the high-order terms in Eq. (1.2), as well as the increments of external disturbances [70]. Parameterization for these terms can be tedious due to the difficulties in model struc-

ture selection. Moreover, the high computational load of online parameter update also makes these adaptive augmentations less appropriate for FTC problems.

The challenges exposed in this subsection raise two research questions:

Research Question 1: How can the stability of incremental nonlinear dynamic inversion control be analyzed and expressed?

Research Question 2: How can the concept of incremental backstepping control be improved and how can its robustness be enhanced?

In view of the limitations of using adaptive augmentations to enhance the robustness of incremental control, a promising approach is to robustify it using sliding mode control (SMC). As a special case of variable structure control [77], SMC is invariant (better than robust) to matched uncertainty [77, 78]. The finite-time, or even fixed-time convergence property [77, 79–83] can be achieved in the SMC scheme. The uncertainty parameterization process is also not needed by SMC. In [10], SMC is classified as a passive FTC approach, i.e., it has the ability to tolerate faults without using fault detection and diagnosis, or controller reconfiguration. These advantages have promoted the application of SMC and sliding mode disturbance observers (SMDO) to many aeronautical and space vehicle control problems, where they show benefits in reducing cost in pre-flight design and analysis cycles [84]. To properly define the third research question, these methods will be reviewed in the next section.

1.4. SLIDING MODE CONTROL AND DISTURBANCE OBSERVER

1.4.1. AEROSPACE APPLICATIONS OF SMC

To deal with significant damage to the airframe and actuators, a first-order SMC with an asymptotic observer is proposed in [85]. Simulations on an F-18 aircraft model show that desirable performance can be achieved after a fault occurs, without using FDD [85]. In [86], both actuator and sensor faults of a civil aircraft are considered. For handling the actuator faults, a first-order SMC is designed, which contains a model-based equivalent control estimation and a switching term. The sensor faults are reconstructed online using a sliding model observer. The SMC designed in [86] is augmented by a control allocation technique in [87], and the entire control scheme was verified on TU Delft's research flight simulator SIMONA [4, 86].

In [88], a cascaded reconfigurable sliding mode flight control is designed for an F-16 aircraft. First-order sliding mode is achieved in each loop, using a model-based equivalent control estimation and a boundary-layer approximation for the signum function. The thickness of the boundary layer is reconfigured to account for actuator dynamics, deflection limits, and rate limits. Simulation results show that this control can passively tolerate 50% of rudder and horizontal tail area losses without using online model identification. A similar SMC design is used along with a control allocation method to control a reusable launch vehicle in [89], where simulations show that desirable tracking performance can be achieved in the presence of bounded external disturbances and uncertainties [89]. Similarly, the reconfigurable flight control idea in [88, 89] is applied to

control a tailless aircraft in [90].

The dynamic sliding manifold, which shows benefits in solving the non-minimum phase system tracking problems, is adopted for aeronautical and space vehicle control in [91]. An SMC driven by SMDO framework is designed in [84] with application to a reusable launch vehicle tracking problem. An integral terminal SMC with gain adaptation is applied to a hypersonic gliding vehicle for tolerating actuator faults and model uncertainties [92]. A hypersonic vehicle tracking problem, in the presence of matched and unmatched external disturbances and model uncertainties, is addressed in [93] using a continuous adaptive higher-order SMC.

1.4.2. CHALLENGES IN SLIDING MODE CONTROL

One of the founders of SMC, V. I. Utkin, pointed out that chattering, which is inherent in sliding motions, is the main obstacle for SMC application [94]. Therefore, in the past decades, many researchers have dedicated themselves to reducing the influences of chattering. Since chattering is caused by the discontinuous signum function in SMC, the most widely used approach to reduce its magnitude is to approximate the signum function by other continuous functions [33, 35, 88–91, 95–99]. However, these approximations (and hence compromises) lead to partial loss of robustness [33, 78].

In order to avoid discontinuous control inputs, various higher-order SMC techniques have been proposed. By artificially increasing the input–output relative degree, the discontinuous signum function is “hidden” in the higher-order derivatives of the control input. Because of the integration process, the final control command becomes continuous. However, as pointed out in [78], this branch of methods, including those designed using recursive or nested structures [100–102], cannot totally eliminate chattering.

Unlike the idea of SMC, (higher-order) SMDO observes the disturbances and provides this observation to the control for direct compensation. The relative merits of using SMDO over SMC have been investigated in [103]. Although the observations provided by SMDO are always continuous, the filtering process in first-order SMDO, and the integration process in super-twisting SMDO, can only attenuate instead of totally rejecting chattering in the observations [84].

Since the amplitude of chattering is proportional to the magnitude of discontinuous control [94], one of the research focuses in SMC is on adaptation mechanisms for reducing the discontinuous control gain to its minimum admissible value whilst maintaining the sliding motions and the finite-time convergence property. An SMC adaptation method is proposed in [94] based on the online evaluations of the equivalent control. This method requires knowledge of bounds on the uncertainties and their derivatives. It also calls for the selection of the minimum and maximum allowed adaptive gains. These are not needed for the dual-layer nested adaptive method [78, 104, 105], which can be applied to conventional, super-twisting and higher-order sliding mode schemes.

In spite of the variations of gain adaptation methods in the literature, the sufficient condition for enforcing a sliding motion still requires the switching gain to be larger than the norm of the uncertainty (for first-order methods), or the corresponding norms of the uncertainty derivatives (for higher-order methods) [78, 94, 104, 105]. Therefore, a method that could reduce the uncertainty would be fundamentally beneficial to reducing the minimum possible sliding mode control/observer gains.

1.4.3. A WAY TO REDUCE THE UNCERTAINTY IN SMC

Consider a multi-input/multi-output nonlinear system formulated by:

$$\dot{\mathbf{x}} = \mathbf{f}(\mathbf{x}) + \mathbf{G}(\mathbf{x})\mathbf{u} + \mathbf{d}_x, \quad \mathbf{y} = \mathbf{h}(\mathbf{x}), \quad (1.5)$$

where $\mathbf{f} : \mathbb{R}^n \rightarrow \mathbb{R}^n$ and $\mathbf{h} : \mathbb{R}^n \rightarrow \mathbb{R}^m$ are smooth vector fields. \mathbf{G} is a smooth function mapping $\mathbb{R}^n \rightarrow \mathbb{R}^{n \times m}$, whose columns are smooth vector fields. $\mathbf{d}_x \in \mathbb{R}^n$ represents the external disturbances. Define the vector relative degree of \mathbf{y} with respect to \mathbf{u} as $\boldsymbol{\rho} = [\rho_1, \rho_2, \dots, \rho_m]^T$. Assume $\rho = \sum_{i=1}^m \rho_i = n$; then by differentiating the output, the input–output mapping of the system is given by:

$$\mathbf{y}^{(\boldsymbol{\rho})} = \boldsymbol{\alpha}(\mathbf{x}) + \mathcal{B}(\mathbf{x})\mathbf{u} + \mathbf{d}, \quad (1.6)$$

where $\boldsymbol{\alpha}(\mathbf{x}) = [\mathcal{L}_f^{\rho_1} h_1, \mathcal{L}_f^{\rho_2} h_2, \dots, \mathcal{L}_f^{\rho_m} h_m]^T$, $\mathcal{B}(\mathbf{x}) \in \mathbb{R}^{m \times m}$, $\mathcal{B}_{ij} = \mathcal{L}_{g_j} \mathcal{L}_f^{\rho_i - 1} h_i$, and $\mathbf{d} = [\mathcal{L}_{d_x}^{\rho_1} h_1, \mathcal{L}_{d_x}^{\rho_2} h_2, \dots, \mathcal{L}_{d_x}^{\rho_m} h_m]^T$, with $\mathcal{L}_f^{\rho_i} h_i$, $\mathcal{L}_{d_x}^{\rho_i} h_i$, $\mathcal{L}_{g_j} \mathcal{L}_f^{\rho_i - 1} h_i$ the corresponding Lie derivatives [33]. Assume $\mathcal{B}(\mathbf{x})$ is nonsingular.

For the generic nonlinear system formulated by Eq. (1.5) with input–output mapping given by Eq. (1.6), one approach is to design (higher-order) SMC/SMDO completely independent of the model. In other words, the input–output mapping is written as $\mathbf{y}^{(\boldsymbol{\rho})} = \mathbf{u} + \boldsymbol{\varepsilon}_{\text{free}}$, where $\boldsymbol{\varepsilon}_{\text{free}} = \boldsymbol{\alpha}(\mathbf{x}) + (\mathcal{B}(\mathbf{x}) - \mathbf{I})\mathbf{u} + \mathbf{d}$ is treated as a lumped uncertainty term. This sliding mode design approach is adopted in [106, 107]. However, for many physical systems that do not have sufficiently high control authority, this model-free design approach can be impractical. This is because the resulting uncertainty term $\boldsymbol{\varepsilon}_{\text{free}}$ could have a large norm and variations, which require sufficiently high SMC/SMDO gains for enforcing the sliding modes. Severe variations of the uncertainty term also challenge the online gain adaptation of SMC.

An intuitive approach to reduce the uncertainty is using a preliminary model-based feedback control term to roughly cancel the nonlinearities and couplings. Regarding the dynamics given by Eq. (1.6), the nominal model $\mathbf{y}^{(\boldsymbol{\rho})} = \bar{\boldsymbol{\alpha}}(\mathbf{x}) + \bar{\mathcal{B}}(\mathbf{x})\mathbf{u}$ can be used in the control design. Design the control in the structure of:

$$\mathbf{u}_{\text{ndi-s}} = \bar{\mathcal{B}}^{-1}(\mathbf{x})(\mathbf{v} - \bar{\boldsymbol{\alpha}}(\mathbf{x})) \quad (1.7)$$

Substituting Eq. (1.7) into Eq. (1.6) leads to the dynamics $\mathbf{y}^{(\boldsymbol{\rho})} = \mathbf{v} + \boldsymbol{\varepsilon}_{\text{ndi-s}}$, with $\boldsymbol{\varepsilon}_{\text{ndi-s}} = (\boldsymbol{\alpha} - \bar{\boldsymbol{\alpha}}) + (\mathcal{B} - \bar{\mathcal{B}})\mathbf{u}_{\text{ndi-s}} + \mathbf{d}$. In these new dynamics, after the model-based feedback, the virtual control \mathbf{v} only needs to deal with the remaining uncertainty term $\boldsymbol{\varepsilon}_{\text{ndi-s}}$. With the help of the nominal models $\bar{\boldsymbol{\alpha}}(\mathbf{x})$ and $\bar{\mathcal{B}}(\mathbf{x})$, the norm of the remaining uncertainty, $\|\boldsymbol{\varepsilon}_{\text{ndi-s}}\|$, can be reduced as compared to $\|\boldsymbol{\varepsilon}_{\text{free}}\|$. This reduction of uncertainty is beneficial to robust control in general. Regarding sliding mode control and observation, based on the discussions in Sec. 1.4.2, this uncertainty reduction can reduce the minimum possible sliding mode control/observer gains.

The control structure given by Eq. (1.7) is widely used in the SMC community. Examples include first-order SMC [33, 35, 84, 88, 90, 91, 95, 108–112], higher-order SMC [79, 113–115], SMC driven by a first-order SMDO [84, 116, 117], and SMC driven by a higher-order SMDO [78, 84, 93, 105, 113, 114, 116–118]. Essentially, this control structure is based on feedback linearization, which is also known as NDI in the aerospace community [42, 51, 53].

For model-based control approaches, the effectiveness of uncertainty reduction depends on the model estimation accuracy. However, for complex systems like an aircraft, obtaining accurate models is costly and time-consuming. When a sudden fault occurs, $\|\epsilon_{\text{ndi-s}}\|$ can increase abruptly, which is supported by results in [76, 87, 99, 119]. Consequently, in order to reduce $\|\epsilon_{\text{ndi-s}}\|$ in faulty conditions for gain reduction, online model identification becomes necessary. This process requires sufficient excitation, which can aggravate structural vibration and even make the aircraft fly out of the shrunken (because of the faults) safe flight envelope [120, 121]. Online model identification also requires the selection of model structures and thresholds, which can be tricky in practice [4, 53]. Control methods with high model dependency also complicate the implementation process and increase the onboard computational load.

Ideally, one would design a control method which could simultaneously reduce the model dependency and the resulting uncertainty. These two objectives are contradictory in SMC designs. On one hand, if the model structure in Eq. (1.7) is adopted, then the reduction of model dependency makes $\epsilon_{\text{ndi-s}}$ approach ϵ_{free} , which indicates an *increase* in the resulting uncertainty. On the other hand, it can be seen from the formulation of $\epsilon_{\text{ndi-s}}$ that the reduction of uncertainty requires more accurate model estimations. These observations lead to the third research question of this thesis:

Research Question 3: How can the contradiction between the reduction of model dependency and the reduction of uncertainty in sliding mode control be solved?

A possible approach to solve this contradiction is to introduce other sources of system information. For example, we can “learn” the characteristics of a system from sensor measurements. This is actually the core idea of incremental control. As presented in Sec. 1.3.1, the model dependency of NDI and BS can be reduced in the sensor-based control framework; in spite of their reduced model dependency, INDI and IBS actually show better robustness to model mismatches as compared to NDI and BS [42, 43].

1.5. RESEARCH APPROACH AND CONTRIBUTIONS

In this section, the main research approach of this thesis will be addressed in Sec. 1.5.1, then the main contributions will be summarized in Sec. 1.5.2.

1.5.1. RESEARCH APPROACH AND QUESTIONS

As presented in Sec. 1.2, the main goal of this thesis is to design a nonlinear control framework for uncertain systems. Subsections 1.3.1 and 1.4.1 explained that both incremental control and SMC can deal with model uncertainties, external disturbances and faults. However, these two branches of methods also have their limitations. In view of the limitations presented in Sec. 1.3.2, the main body of this thesis will start with more rigorous analyses for incremental control. Sec. 1.3.2 also showed that incremental control can potentially be robustified by SMC. Furthermore, it has been revealed in Sec. 1.4.3 that the sensor-based control structure is promising in solving the contradiction between the reductions of model dependency and the resulting uncertainty in SMC. These observations inspired the idea to develop a hybrid between SMC and incremental

control, to inherit the advantages and remedy the drawbacks of both approaches.

The proposed hybrid control framework designs the control increment $\Delta \mathbf{u}$. In the literature, there are other control structures, including NDI-based SMC (designs \mathbf{u}) and high-order SMC that artificially increases the relative degree by one order (i.e., designs $\dot{\mathbf{u}}$). All of these three approaches can induce higher-order sliding modes in finite-time. Since $\dot{\mathbf{u}}$ approximately equals $\Delta \mathbf{u} / \Delta t$ when Δt is sufficiently small, an interesting research question emerges:

Research Question 4: What is the relationship between the INDI-based SMC proposed in this thesis, the NDI-based SMC, and higher-order SMC with artificially increased relative degree?

1.5.2. MAIN CONTRIBUTIONS

The main contributions of this thesis can be elaborated from three aspects. First of all, it contributes to incremental control methods:

CONTRIBUTIONS TO INCREMENTAL CONTROL METHODS

- Generalization of incremental control methods for nonlinear uncertain systems with arbitrary input–output relative degrees, without using the time-scale separation assumption or term omissions.
- Lyapunov-based stability analysis of incremental control methods considering the internal dynamics.
- Analysis of the robustness of incremental control methods to model uncertainties, external disturbances, sudden changes in system dynamics using nonlinear system perturbation theory.
- Design of a hybrid control framework that robustifies incremental control methods, which also brings other beneficial properties, including fixed/finite-time convergence in spite of perturbations.

Second of all, this thesis contributes to sliding mode control. This thesis mainly focuses on the control structure; thus the contributions listed below are not constrained by the specific SMC virtual control designs:

CONTRIBUTIONS TO SLIDING MODE CONTROL METHODS

- A solution for the contradiction between the reduction of model dependency and the reduction of uncertainty in sliding mode control.
- Reduction of the minimum possible (higher-order) sliding mode control/observer gains in the hybrid framework, which is beneficial to chattering reduction.
- Comparison of three control structures (NDI-based SMC, higher-order SMC with artificially increased relative degree, and INDI-SMC), which can be used for enforcing higher-order sliding modes.

Generic nonlinear uncertain systems are considered in the control designs and analyses. Therefore, the preceding contributions are applicable to generic nonlinear uncertain systems, not necessarily aerospace systems.

Third of all, this thesis also has contributions in its flight control applications, which are summarized as follows:

CONTRIBUTIONS TO FLIGHT CONTROL

- Verification by numerical simulations and quadrotor flight tests, that the hybrid control framework can help aircraft passively tolerate a wide range of model uncertainties, external disturbances, sudden actuator faults and structural damages.
- Design of an INDI-based integrated flight control law for flexible aircraft, which can control the rigid-body motions, alleviate the gust loads, reduce the wing root bending moment and suppress the elastic modes.

1.6. OUTLINE OF THE THESIS

The main body of this thesis is based on peer-reviewed journal/conference papers. Each chapter of the main body can therefore be read independently. At the beginning of each chapter, there is an introductory paragraph which places the chapter into the context of the full thesis. Figure 1.6 shows a schematic layout of this thesis, where the main body is divided into two parts.

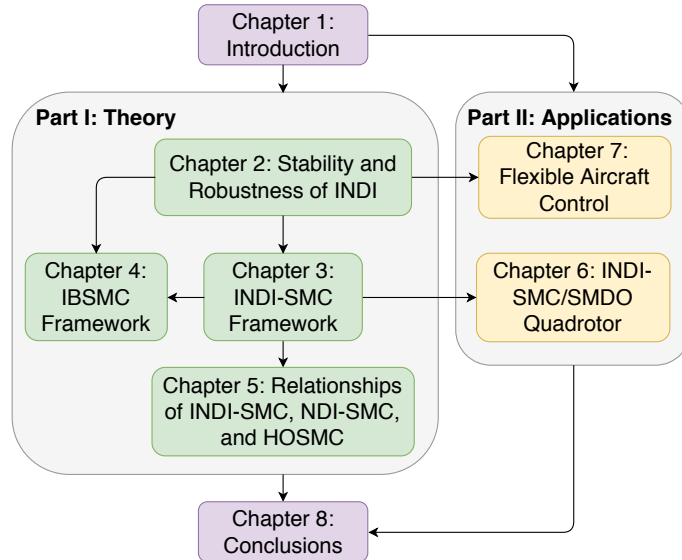


Figure 1.6: Structure of the thesis.

Part I lays emphasis on the theoretical development of the control methods. The derivations and analyses in Part I are applicable to generic nonlinear uncertain systems, not necessarily aerospace systems. Part I starts from Chapter 2, which answers Research

Question 1. It is found in Chapter 2 that an uncertainty term remains in the closed-loop system under INDI control. The properties of this term and a systematic way of compensating for its influences are dealt with in Chapter 3. To answer Research Question 3, a novel control framework which hybridizes INDI with (higher-order) sliding mode controllers/observers is proposed in Chapter 3.

Research Question 2 is answered in Chapter 4, where the stability and robustness of IBS is analyzed. IBS is further hybridized with SMC for robustness enhancement, which is named IBSMC. Research Question 4 is addressed in Chapter 5, where the proposed hybrid control framework is compared with NDI-based SMC methods and a class of higher-order (HO) SMC methods in the literature.

Apart from the theoretical developments, **Part I** also contains some aerospace applications. Chapter 2 handles a rigid aircraft gust load alleviation problem using the reformulated INDI. The control methods proposed in Chapters 3 and 4 are numerically validated via aircraft attitude command tracking problems in the presence of sudden actuator faults and structural damages.

Part II places emphasis on flight control applications. In Chapter 6 the effectiveness of the hybrid control framework proposed in Chapter 3 is verified by flight tests on a partially damaged quadrotor. INDI is used to design an integrated flight control law for flexible aircraft in Chapter 7.

Finally, this thesis is closed by Chapter 8, which presents the conclusions, discussions, and recommendations for future work.

REFERENCES

- [1] Airbus, *A Statistical Analysis of Commercial Aviation Accidents, 1958-2017*, Tech. Rep. (2018).
- [2] *Statistical Summary of Commercial Jet Airplane Accidents, Worldwide Operations, 1959-2017*, Tech. Rep. (Boeing Commercial Airplanes, 2017).
- [3] P. Russell and J. Pardee, *Joint Safety Analysis Team-CAST Approved Final Report Loss of Control JSAT Results and Analysis*, Tech. Rep. (Federal Aviation Administration: Commercial Airline Safety Team, 2000).
- [4] T. Lombaerts, *Fault Tolerant Flight Control, A Physical Model Approach*, Ph.D. thesis, Delft University of Technology (2010).
- [5] H. Smaili, J. Breeman, T. Lombaerts, and O. Stroosma, *A Benchmark for Fault Tolerant Flight Control Evaluation*, (Proceedings of the 7th IFAC Symposium on Fault Detection, Supervision and Safety of Technical Processes, 2009) pp. 241–246.
- [6] *Aircraft Accident Report NTSB/AAR-01/01*, Tech. Rep. (National Transportation Safety Board, 2001).
- [7] *Aircraft Accident Report NTSB/AAR-99/01*, Tech. Rep. (National Transportation Safety Board, 1999).

- [8] J. M. Maciejowski and C. N. Jones, *MPC fault-tolerant flight control case study: flight 1862*, (Proceedings of the 5th IFAC symposium on fault detection, supervision and safety for technical processes, 2003) pp. 121–126.
- [9] F. W. Burcham, T. A. Maine, C. G. Fullerton, and L. D. Webb, *Development and Flight Evaluation of an Emergency Digital Flight Control System Using Only Engine Thrust on an F-15 Airplane*, Tech. Rep. September (NASA Technical Paper, 1996).
- [10] Y. Zhang and J. Jiang, *Bibliographical review on reconfigurable fault-tolerant control systems*, *Annual Reviews in Control* **32**, 229 (2008).
- [11] T. Tucker, *Touchdown : The Development Controlled Aircraft at NASA Dryden*, Tech. Rep. (Monographs in Aerospace History, 1999).
- [12] W. Burcham, A. Maine, and N. Aeronautics, *Emergency Flight Control Using Only Engine Thrust and Lateral Offset : A First Look*, Tech. Rep. (Technical Memorandum NASA/TM-4789, NASA, 1997).
- [13] B. Etkin, *Turbulent Wind and Its Effect on Flight*, *Journal of Aircraft* **18**, 327 (1981).
- [14] B. Etkin, *Dynamics of Atmospheric Flight* (Dover Publications, Toronto, 2005).
- [15] A. I. Brunstein, *Clear air turbulence accidents*, *SAFE Journal* **8** (1978).
- [16] K. R. Hardy, *Wind Shear and Clear Air Turbulence*, *Journal of Air Law and Commerce* **42** (1976).
- [17] *Making the Skies Safer From Windshear*, Tech. Rep. June (NASA Langley Research Center, 1992).
- [18] F. Culick, *Wright Brothers : First Aeronautical Engineers and Test Pilots*, Tech. Rep. (The Society of Experimental Test Pilots, 2001).
- [19] M. Sinnett, *787 No-Bleed Systems: Saving Fuel and Enhancing Operational Efficiencies*, Tech. Rep. (Boeing Company, 2013).
- [20] T. E. Noll, J. M. Brown, M. E. Perez-davis, S. D. Ishmael, G. C. Tiffany, and M. Gaier, *Investigation of the Helios Prototype Aircraft Mishap*, Tech. Rep. January (National Aeronautics and Space Administration, 2004).
- [21] W. Su and C. E. S. Cesnik, *Dynamic Response of Highly Flexible Flying Wings*, *AIAA Journal* **49**, 324 (2011).
- [22] M. J. Patil and D. H. Hodges, *Flight Dynamics of Highly Flexible Flying Wings*, *Journal of Aircraft* **43**, 1790 (2006).
- [23] C.-S. Chang, D. H. Hodges, and M. J. Patil, *Flight Dynamics of Highly Flexible Aircraft*, *Journal of Aircraft* **45**, 538 (2008).
- [24] W. Su, *Coupled Nonlinear Aeroelasticity and Flight Dynamics of Fully Flexible Aircraft*, *Ph.D. thesis*, University of Michigan (2014).

- [25] E. G. Broadbent, J. K. Zbrozek, and E. Huntley, *A Study of Dynamic Aeroelastic Effects on the Stability Control and Gust Response of a Slender Delta Aircraft*, Tech. Rep. 3690 (Aeronautical Research Council Reports And Memoranda, 1972).
- [26] J. Murua, R. Palacios, and J. M. R. Graham, *Applications of the unsteady vortex-lattice method in aircraft aeroelasticity and flight dynamics*, *Progress in Aerospace Sciences* **55**, 46 (2012).
- [27] L. Meirovitch and I. Tuzcu, *National Aeronautics and Space Administration, Langley Research Center*, Tech. Rep. (NASA Langley Research Center, 2003).
- [28] I. Tuzcu, P. Marzocca, E. Cestino, G. Romeo, and G. Frulla, *Stability and Control of a High-Altitude, Long-Endurance UAV*, *Journal of Guidance, Control, and Dynamics* **30**, 713 (2007).
- [29] C. M. Shearer and C. E. Cesnik, *Nonlinear Flight Dynamics of Very Flexible Aircraft*, *Journal of Aircraft* **44**, 1528 (2007).
- [30] R. Palacios, J. Murua, and R. Cook, *Structural and Aerodynamic Models in Nonlinear Flight Dynamics of Very Flexible Aircraft*, *AIAA Journal* **48**, 2648 (2010).
- [31] S. Haghghat, H. H. T. Liu, and J. R. R. A. Martins, *Model-Predictive Gust Load Alleviation Controller for a Highly Flexible Aircraft*, *Journal of Guidance, Control, and Dynamics* **35**, 1751 (2012).
- [32] R. Palacios and C. E. S. Cesnik, *Structural Models for Flight Dynamic Analysis of Very Flexible Aircraft*, *AIAA Structures, Structural Dynamics and Materials Conference*, 1 (2009).
- [33] H. K. Khalil, *Nonlinear Systems* (Prentice-Hall, New Jersey, 2002).
- [34] P. Lu, *Fault diagnosis and fault-tolerant control for aircraft subjected to sensor and actuator faults*, Ph.D. thesis, Delft University and Technology (2016).
- [35] J.-J. E. Slotine and W. Li, *Applied Nonlinear Control* (NJ: Prentice Hall, Englewood Cliffs, 1991).
- [36] A. Astolfi and R. Ortega, *Immersion and invariance: A new tool for stabilization and adaptive control of nonlinear systems*, *IEEE Transactions on Automatic Control* **48**, 590 (2003).
- [37] F. Ikhouane and M. Krstić, *Robustness of the tuning functions adaptive backstepping design for linear systems*, *IEEE Transactions on Automatic Control* **43**, 431 (1998).
- [38] Q. Wang and R. E. Stengel, *Robust nonlinear control of a hypersonic aircraft*, *Journal of Guidance, Control, and Dynamics* **23**, 577 (2000).
- [39] J. S. Brinker and K. a. Wise, *Stability and Flying Qualities Robustness of a Dynamic Inversion Aircraft Control Law*, *Journal of Guidance, Control, and Dynamics* **19**, 1270 (1996).

- [40] J. J. E. Slotine and J. K. Hedrick, *Robust Input-Output Feedback Linearization*, *International Journal Control* **57**, 1133 (1993).
- [41] L. Sonneveldt, Q. P. Chu, and J. A. Mulder, *Nonlinear Flight Control Design Using Constrained Adaptive Backstepping*, *Journal of Guidance, Control, and Dynamics* **30**, 322 (2007).
- [42] S. Sieberling, Q. P. Chu, and J. A. Mulder, *Robust Flight Control Using Incremental Nonlinear Dynamic Inversion and Angular Acceleration Prediction*, *Journal of Guidance, Control, and Dynamics* **33**, 1732 (2010).
- [43] P. Acquatella, E. van Kampen, and Q. P. Chu, *Incremental Backstepping for Robust Nonlinear Flight Control*, *CEAS Conference on Guidance, Navigation, and Control*, 1444 (2013).
- [44] P. Smith, *A Simplified Approach to Nonlinear Dynamic Inversion Based Flight Control*, in *23rd Atmospheric Flight Mechanics Conference* (AIAA, Reston, VA, 1998).
- [45] B. Bacon and A. Ostroff, *Reconfigurable flight control using nonlinear dynamic inversion with a special accelerometer implementation*, in *AIAA Guidance, Navigation, and Control Conference and Exhibit* (American Institute of Aeronautics and Astronautics, Denver, CO, 2000) pp. 1–15.
- [46] B. Bacon, A. Ostroff, and S. Joshi, *Reconfigurable NDI controller using inertial sensor failure detection & isolation*, *IEEE Transactions on Aerospace and Electronic Systems* **37**, 1373 (2001).
- [47] H. B. Chen and S. G. Zhang, *Robust Dynamic Inversion Flight Control Law Design*, in *2nd International Symposium on Systems and Control in Aerospace and Astronautics*, 7 (2008) pp. 1–6.
- [48] K. Youcef-Toumi and O. Ito, *A Time Delay Controller for Systems with Unknown Dynamics*, in *1988 American Control Conference* (IEEE, 1988) pp. 904–913.
- [49] Wu-Chung Su, S. Drakunov, and U. Ozguner, *An $O(T/\text{sup } 2)$ boundary layer in sliding mode for sampled-data systems*, *IEEE Transactions on Automatic Control* **45**, 482 (2000).
- [50] P. Acquatella, W. Falkena, E. van Kampen, and Q. P. Chu, *Robust Nonlinear Spacecraft Attitude Control using Incremental Nonlinear Dynamic Inversion*. in *AIAA Guidance, Navigation, and Control Conference* (American Institute of Aeronautics and Astronautics, Minneapolis, Minnesota, 2012) pp. 1–20.
- [51] P. Simplicio, M. Pavel, E. van Kampen, and Q. P. Chu, *An acceleration measurements-based approach for helicopter nonlinear flight control using Incremental Nonlinear Dynamic Inversion*, *Control Engineering Practice* **21**, 1065 (2013).
- [52] E. Johnson, A. Calise, H. El-Shirbiny, and R. Eysdyk, *Feedback linearization with Neural Network augmentation applied to X-33 attitude control*, *AIAA Guidance, Navigation, and Control Conference and Exhibit*, 1 (2000).

- [53] P. Lu, E. van Kampen, C. de Visser, and Q. P. Chu, *Aircraft fault-tolerant trajectory control using Incremental Nonlinear Dynamic Inversion*, *Control Engineering Practice* **57**, 126 (2016).
- [54] X. Wang, E. van Kampen, and Q. P. Chu, *Gust Load Alleviation and Ride Quality Improvement with Incremental Nonlinear Dynamic Inversion*, in *AIAA Atmospheric Flight Mechanics Conference* (American Institute of Aeronautics and Astronautics, Grapevine, Texas, 2017) pp. 1–21.
- [55] E. J. J. Smeur, G. C. H. E. de Croon, and Q. P. Chu, *Cascaded incremental nonlinear dynamic inversion for MAV disturbance rejection*, *Control Engineering Practice* **73**, 79 (2018), arXiv:1701.07254 .
- [56] E. J. J. Smeur, G. C. H. E. de Croon, and Q. P. Chu, *Gust disturbance alleviation with Incremental Nonlinear Dynamic Inversion*, in *2016 IEEE/RSJ International Conference on Intelligent Robots and Systems (IROS)* (IEEE, 2016) pp. 5626–5631.
- [57] S. Sun, L. Sijbers, X. Wang, and C. de Visser, *High-Speed Flight of Quadrotor Despite Loss of Single Rotor*, *IEEE Robotics and Automation Letters* **3**, 3201 (2018).
- [58] M. W. Mueller and R. D'Andrea, *Stability and control of a quadcopter despite the complete loss of one, two, or three propellers*, *Proceedings - IEEE International Conference on Robotics and Automation* , 45 (2014).
- [59] G. P. Falconi, V. A. Marvakov, and F. Holzapfel, *Fault tolerant control for a hexarotor system using Incremental Backstepping*, *2016 IEEE Conference on Control Applications, CCA 2016* , 237 (2016).
- [60] P. Lu, E. van Kampen, and Q. P. Chu, *Robustness and Tuning of Incremental Backstepping Approach*, in *AIAA Guidance, Navigation, and Control Conference* (American Institute of Aeronautics and Astronautics, Kissimmee, Florida, 2015) pp. 1–15.
- [61] P. van Gils, E. van Kampen, C. C. de Visser, and Q. P. Chu, *Adaptive Incremental Backstepping Flight Control for a High-Performance Aircraft with Uncertainties*, in *AIAA Guidance, Navigation, and Control Conference* (American Institute of Aeronautics and Astronautics, San Diego, California, 2016).
- [62] E. J. J. Smeur, Q. P. Chu, and G. C. H. E. de Croon, *Adaptive Incremental Nonlinear Dynamic Inversion for Attitude Control of Micro Air Vehicles*, *Journal of Guidance, Control, and Dynamics* **39**, 450 (2016).
- [63] F. Grondman, G. Looye, R. O. Kuchar, Q. P. Chu, and E. van Kampen, *Design and Flight Testing of Incremental Nonlinear Dynamic Inversion-based Control Laws for a Passenger Aircraft*, in *2018 AIAA Guidance, Navigation, and Control Conference*, January (American Institute of Aeronautics and Astronautics, Kissimmee, Florida, 2018).
- [64] I. Matamoros and C. C. de Visser, *Incremental Nonlinear Control Allocation for a Tailless Aircraft with Innovative Control Effectors*, in *2018 AIAA Guidance, Navigation, and Control Conference*, January (American Institute of Aeronautics and Astronautics, Kissimmee, Florida, 2018) pp. 1–25.

- [65] W. van Ekeren, G. Looye, R. O. Kuchar, Q. P. Chu, and E. van Kampen, *Design, Implementation and Flight-Tests of Incremental Nonlinear Flight Control Methods*, in *2018 AIAA Guidance, Navigation, and Control Conference*, January (American Institute of Aeronautics and Astronautics, Kissimmee, Florida, 2018) pp. 1–21.
- [66] T. Keijzer, G. Looye, Q. P. Chu, and E. van Kampen, *Design and Flight Testing of Incremental Backstepping based Control Laws with Angular Accelerometer Feedback*, in *AIAA Scitech 2019 Forum*, January (American Institute of Aeronautics and Astronautics, San Diego, California, 2019) pp. 1–25.
- [67] C. Cakiroglu, E. van Kampen, and Q. P. Chu, *Robust Incremental Nonlinear Dynamic Inversion Control Using Angular Accelerometer Feedback*, in *2018 AIAA Guidance, Navigation, and Control Conference*, January (American Institute of Aeronautics and Astronautics, Kissimmee, Florida, 2018).
- [68] Y. Huang, D. M. Pool, O. Stroosma, Q. P. Chu, and M. Mulder, *A Review of Control Schemes for Hydraulic Stewart Platform Flight Simulator Motion Systems*, in *AIAA Modeling and Simulation Technologies Conference* (American Institute of Aeronautics and Astronautics, San Diego, California, 2016) pp. 1–14.
- [69] Y. Huang, D. Pool, O. Stroosma, and Q. P. Chu, *Incremental Nonlinear Dynamic Inversion Control for Hydraulic Hexapod Flight Simulator Motion Systems*, *IFAC-PapersOnLine* **50**, 4294 (2017).
- [70] X. Wang, E. van Kampen, Q. P. Chu, and P. Lu, *Stability Analysis for Incremental Nonlinear Dynamic Inversion Control*, in *2018 AIAA Guidance, Navigation, and Control Conference*, January (American Institute of Aeronautics and Astronautics, Kissimmee, Florida, 2018).
- [71] A. Hodel, M. Whorton, and J. Zhu, *Stability Metrics for Simulation and Flight-Software Assessment and Monitoring of Adaptive Control Assist Compensators*, in *AIAA Guidance, Navigation and Control Conference and Exhibit* (American Institute of Aeronautics and Astronautics, Honolulu, Hawaii, 2008) pp. 1–25.
- [72] X. Yang and J. J. Zhu, *Singular perturbation margin and generalised gain margin for nonlinear time-invariant systems*, *International Journal of Control* **89**, 451 (2016).
- [73] X. Yang and J. J. Zhu, *Singular perturbation margin and generalised gain margin for linear time-invariant systems*, *International Journal of Control* **89**, 451 (2015).
- [74] G. Bartolini, A. Ferrara, L. Giacomini, and E. Usai, *Properties of a combined adaptive/second-order sliding mode control algorithm for some classes of uncertain nonlinear systems*, *IEEE Transactions on Automatic Control* **45**, 1334 (2000).
- [75] B. Cong, X. Liu, and Z. Chen, *Backstepping based adaptive sliding mode control for spacecraft attitude maneuvers*, *Aerospace Science and Technology* **30**, 1 (2013).

- [76] X. Wang and E. van Kampen, *Incremental Backstepping Sliding Mode Fault-Tolerant Flight Control*, in *AIAA Scitech 2019 Forum*, January (American Institute of Aeronautics and Astronautics, San Diego, California, 2019) pp. 1–23.
- [77] C. Edwards and S. K. Spurgeon, *Sliding mode control : theory and applications*, 1st ed. (CRC Press, 1998).
- [78] C. Edwards and Y. B. Shtessel, *Continuous higher order sliding mode control based on adaptive disturbance compensation*, in *2014 13th International Workshop on Variable Structure Systems (VSS)*, Vol. 47 (IEEE, 2014).
- [79] M. Defoort, T. Floquet, A. Kokosy, and W. Perruquetti, *A novel higher order sliding mode control scheme*, *Systems and Control Letters* **58**, 102 (2009).
- [80] S. P. Bhat and D. S. Bernstein, *Geometric homogeneity with applications to finite-time stability*, *Mathematics of Control, Signals, and Systems* **17**, 101 (2005).
- [81] M. Basin, P. Rodriguez-Ramirez, S. X. Ding, T. Daszenies, and Y. Shtessel, *Continuous fixed-time convergent regulator for dynamic systems with unbounded disturbances*, *Journal of the Franklin Institute* **355**, 2762 (2018).
- [82] M. Basin, C. B. Panathula, and Y. Shtessel, *Adaptive uniform finite-/fixed-time convergent second-order sliding-mode control*, *International Journal of Control* **89**, 1777 (2016).
- [83] M. Basin, Y. Shtessel, and F. Aldukali, *Continuous finite- and fixed-time high-order regulators*, *Journal of the Franklin Institute* **353**, 5001 (2016).
- [84] C. E. Hall and Y. B. Shtessel, *Sliding Mode Disturbance Observer-Based Control for a Reusable Launch Vehicle*, *Journal of Guidance, Control, and Dynamics* **29**, 1315 (2006).
- [85] R. A. Hess and S. R. Wells, *Sliding Mode Control Applied to Reconfigurable Flight Control Design*, *Journal of Guidance, Control, and Dynamics* **26**, 452 (2003).
- [86] H. Alwi and C. Edwards, *Fault detection and fault-tolerant control of a civil aircraft using a sliding-mode-based scheme*, *IEEE Transactions on Control Systems Technology* **16**, 499 (2008).
- [87] H. Alwi, C. Edwards, O. Stroosma, and J. A. Mulder, *Fault Tolerant Sliding Mode Control Design with Piloted Simulator Evaluation*, *Journal of Guidance, Control, and Dynamics* **31**, 1186 (2008).
- [88] Y. B. Shtessel, J. M. Buffington, and S. S. Banda, *Multiple Timescale Flight Control Using Reconfigurable Sliding Modes*, *Journal of Guidance, Control, and Dynamics* **22**, 873 (1999).
- [89] Y. Shtessel, C. Hall, and M. Jackson, *Reusable Launch Vehicle Control in Multiple-Time-Scale Sliding Modes*, *Journal of Guidance, Control, and Dynamics* **23**, 1013 (2000).

- [90] Y. Shtessel, J. Buffington, and S. Banda, *Tailless aircraft flight control using multiple time scale reconfigurable sliding modes*, *IEEE Transactions on Control Systems Technology* **10**, 288 (2002).
- [91] Y. B. Shtessel and I. A. Shkolnikov, *Aeronautical and space vehicle control in dynamic sliding manifolds*, *International Journal of Control* **76**, 1000 (2003).
- [92] P. Li, X. Yu, Y. Zhang, and X. Peng, *Adaptive multivariable integral TSMC of a hypersonic gliding vehicle with actuator faults and model uncertainties*, *IEEE/ASME Transactions on Mechatronics* **22**, 2723 (2017).
- [93] P. Yu, Y. Shtessel, and C. Edwards, *Continuous higher order sliding mode control with adaptation of air breathing hypersonic missile*, *International Journal of Adaptive Control and Signal Processing* **30**, 1099 (2016).
- [94] V. I. Utkin and A. S. Poznyak, *Adaptive sliding mode control with application to super-twist algorithm: Equivalent control method*, *Automatica* **49**, 39 (2013).
- [95] M. T. Hamayun, C. Edwards, and H. Alwi, *A fault tolerant control allocation scheme with output integral sliding modes*, *Automatica* **49**, 1830 (2013).
- [96] M. T. Hamayun, C. Edwards, and H. Alwi, *Application of an integral sliding mode FTC for a large transport aircraft*, *Conference on Control and Fault-Tolerant Systems, SysTol'10 - Final Program and Book of Abstracts*, 38 (2010).
- [97] L. Chen, C. Edwards, and H. Alwi, *Integral sliding mode fault-tolerant control allocation for a class of affine nonlinear system*, *International Journal of Robust and Nonlinear Control* **29**, 565 (2019).
- [98] H. Alwi, C. Edwards, and M. T. Hamayun, *Fault tolerant control of a large transport aircraft using an LPV based integral sliding mode controller*, *2013 Conference on Control and Fault-Tolerant Systems (SysTol)*, 637 (2013).
- [99] H. Alwi, *Fault tolerant sliding mode control schemes with aerospace applications*, *Ph.D. thesis*, University of Leicester (2008).
- [100] A. Levant, *Sliding order and sliding accuracy in sliding mode control*, *International Journal of Control* **58**, 1247 (1993).
- [101] A. Levant, *Universal single-input-single-output (SISO) sliding-mode controllers with finite-time convergence*, *IEEE Transactions on Automatic Control* **46**, 1447 (2001).
- [102] A. Levant, *Higher-order sliding modes, differentiation and output-feedback control*, *International Journal of Control* **76**, 924 (2003).
- [103] A. Ferreira, F. J. Bejarano, and L. M. Fridman, *Robust control with exact uncertainties compensation: With or without chattering?* *IEEE Transactions on Control Systems Technology* **19**, 969 (2011).

- [104] C. Edwards and Y. Shtessel, *Adaptive dual-layer super-twisting control and observation*, *International Journal of Control* **89**, 1759 (2016).
- [105] C. Edwards and Y. B. Shtessel, *Adaptive continuous higher order sliding mode control*, *Automatica* **65**, 183 (2016).
- [106] S. Laghrouche, F. Plestan, and A. Glumineau, *Higher order sliding mode control based on integral sliding mode*, *Automatica* **43**, 531 (2007).
- [107] M. Cross and Y. Shtessel, *A Single-Loop High-Order Sliding Mode Controller for a Missile Interceptor*, 2018 15th International Workshop on Variable Structure Systems (VSS), 331 (2018).
- [108] Y. Shtessel, C. Hall, and M. Jackson, *Reusable Launch Vehicle Control in Multiple-Time-Scale Sliding Modes*, *Journal of Guidance, Control, and Dynamics* **23**, 1013 (2000).
- [109] T. Wang, W. Xie, and Y. Zhang, *Sliding mode fault tolerant control dealing with modeling uncertainties and actuator faults*, *ISA Transactions* **51**, 386 (2012).
- [110] Y. Feng, X. Yu, and Z. Man, *Non-singular terminal sliding mode control of rigid manipulators*, *Automatica* **38**, 2159 (2002).
- [111] Y. Wu, X. Yu, and Z. Man, *Terminal sliding mode control design for uncertain dynamic systems*, *Systems & Control Letters* **34**, 281 (1998).
- [112] S. Yu, X. Yu, B. Shirinzadeh, and Z. Man, *Continuous finite-time control for robotic manipulators with terminal sliding mode*, *Automatica* **41**, 1957 (2005).
- [113] M. Sagliano, E. Mooij, and S. Theil, *Adaptive Disturbance-Based High-Order Sliding-Mode Control for Hypersonic-Entry Vehicles*, *Journal of Guidance, Control, and Dynamics* **40**, 521 (2017).
- [114] J. Wang, Q. Zong, R. Su, and B. Tian, *Continuous high order sliding mode controller design for a flexible air-breathing hypersonic vehicle*, *ISA Transactions* **53**, 690 (2014).
- [115] Q. Zong, J. Wang, B. Tian, and Y. Tao, *Quasi-continuous high-order sliding mode controller and observer design for flexible hypersonic vehicle*, *Aerospace Science and Technology* **27**, 127 (2013).
- [116] T. E. Massey and Y. B. Shtessel, *Continuous Traditional and High-Order Sliding Modes for Satellite Formation Control*, *Journal of Guidance, Control, and Dynamics* **28**, 826 (2005).
- [117] L. Besnard, Y. B. Shtessel, and B. Landrum, *Quadrotor vehicle control via sliding mode controller driven by sliding mode disturbance observer*, *Journal of the Franklin Institute* **349**, 658 (2012).
- [118] J. S. Orr and Y. B. Shtessel, *Lunar spacecraft powered descent control using higher-order sliding mode techniques*, *Journal of the Franklin Institute* **349**, 476 (2012).

- [119] X. Wang, E. van Kampen, Q. P. Chu, and P. Lu, *Incremental Sliding-Mode Fault-Tolerant Flight Control*, *Journal of Guidance, Control, and Dynamics* **42**, 244 (2019).
- [120] Y. Zhang, C. C. de Visser, and Q. P. Chu, *Aircraft Damage Identification and Classification for Database-Driven Online Flight-Envelope Prediction*, *Journal of Guidance, Control, and Dynamics* **41**, 1 (2017).
- [121] Y. Zhang, C. C. de Visser, and Q. P. Chu, *Online Physical Model Identification for Database-driven Safe Flight Envelope Prediction of Damaged Aircraft*, in *AIAA Atmospheric Flight Mechanics Conference* (American Institute of Aeronautics and Astronautics, San Diego, California, 2016) pp. 1–11.



I

THEORETICAL DEVELOPMENT



2

STABILITY ANALYSIS FOR INCREMENTAL NONLINEAR DYNAMIC INVERSION CONTROL

The first research question of how to analyze and express the stability of incremental nonlinear dynamic inversion (INDI) control will be addressed in this chapter. As discussed in Chapter 1, although INDI has shown effectiveness in flight control, its derivations and analyses have some limitations. Therefore, this chapter will first reformulate INDI for more general nonlinear systems, without using the time-scale separation assumption or term omissions. Then the stability and robustness of the reformulated INDI will be analyzed using Lyapunov methods and nonlinear system perturbation theory. Finally, this chapter will make analytical and numerical comparisons between the reformulated INDI and the model-based nonlinear dynamic inversion (NDI) control.

This chapter is based on the following article:

Wang, X., van Kampen, E., Chu, Q. P., and Lu, P., "Stability Analysis for Incremental Nonlinear Dynamic Inversion Control", Journal of Guidance, Control, and Dynamics, Vol. 42, No. 5, 2019, pp. 1116-1129. doi:10.2514/1.G003791.

As a sensor-based control method, incremental nonlinear dynamic inversion (INDI) has been applied to various aerospace systems and shown desirable robust performance against aerodynamic model uncertainties. However, its previous derivation based on the time-scale separation principle has some limitations. There is also a need for stability and robustness analysis for INDI. Therefore, this chapter reformulates the INDI control law without using the time-scale separation principle and generalizes it for systems with arbitrary relative degree, with consideration of the internal dynamics. The stability of the closed-loop system in the presence of external disturbances is analyzed using Lyapunov methods and nonlinear system perturbation theories. Moreover, the robustness of the closed-loop system against regular and singular perturbations is analyzed. Finally, this reformulated INDI control law is verified by a Monte-Carlo simulation for an aircraft command tracking problem in the presence of external disturbances and model uncertainties.

2.1. INTRODUCTION

NONLINEAR dynamic inversion (NDI) is a nonlinear control approach that cancels the system nonlinearity by means of feedback, which results into entirely or partly linearized closed-loop system dynamics, to which conventional linear control techniques can then be applied [1, 2]. This method is essentially different from the widely used Jacobian linearization around specific operating points in combination with gain-scheduled linear controllers, whose stability and performance become questionable between operational points. To achieve an exact dynamic cancellation, the NDI control method requires an accurate knowledge of the nonlinear system dynamics. Such a requirement is almost impossible to meet in reality due to model simplifications, computational errors and external disturbances. This main drawback of NDI motivated many control technologies to improve its robustness. One popular approach is combining NDI with linear robust control techniques such as structural singular value (μ) analysis [3, 4] and \mathcal{H}_∞ synthesis. Although these techniques have brought benefits to regular NDI, not all the uncertainties are taken into account or some known nonlinear time-varying (NLTV) dynamics are treated as uncertainties [5]. Therefore, the closed-loop systems can be either marginally or overly conservative in performance and stability robustness [5]. There also exists many attempts on using indirect adaptive control methods to improve the robustness of NDI [6]. Indirect adaptive control methods, in some form or the other, rely on on-line identification, which requires on-line excitation and selection of thresholds. However, the stability of indirect adaptive NDI are not guaranteed [6, 7].

Incremental nonlinear dynamic inversion (INDI) is a sensor-based control method, which requires less model information in both qualitative and quantitative sense, and thus improving the system robustness against model uncertainties. The concept of this method originates from the late nineties and was previously referred to as “simplified NDI” [8] and “modified NDI” [9]. INDI control has been applied to various aerospace systems [7, 10–21]. Regarding its applications on aerospace systems, the INDI method was normally used for the inner-loop angular rate control [7, 10–12, 18–20, 22], where the relative degree for each control channel equals one. The internal dynamics are then avoided by using a cascaded control structure, which is a common practice in flight control system designs [7, 11, 14, 18–20]. However, the stability of cascaded control

structures is not easy to prove because of its dependency on the time-scale separations between different control loops. Also, this cascaded control structure is unsuitable for some problems. For example, it is neither physically meaningful nor practical to separate the higher-order aeroelastic dynamics into cascaded loops.

The existing derivations of the INDI control law are based on the so-called time-scale separation principle, which is actually different from the widely used separations based on singular perturbation theories. In [7, 10–20], this separation concept was claimed as: the controls can change significantly faster than the states. The nonlinear dynamic equations describing the plant dynamics are then simplified into linear incremental dynamic equations by omitting state-variation-related terms and higher-order terms in their Taylor series expansion, based on which the incremental control inputs are designed. This approach is not mathematically rigorous since the plant simplification is made before introducing the INDI control inputs and thus becomes deficient for unstable plants. Moreover, although the state-variation-related terms and higher-order terms are not used in the INDI controller design, they should be kept in the closed-loop dynamic equations and remain influencing the closed-loop system stability and performance, which is also not the case in the literature.

Furthermore, in spite of the numerically verified robustness of INDI to aerodynamic model uncertainties [10, 15, 21], and disturbances [13–15, 21], its previous theoretical stability and robustness proofs have some drawbacks. These previous attempts drew the stability conclusions based on the linear transfer functions derived from block diagrams [10, 13, 14], where inappropriate assumptions are made. The influences of disturbances and uncertainties on the internal dynamics also remain unknown in the literature.

In this chapter, the INDI control in the literature is reformulated for systems with arbitrary relative degree, without using the time-scale separation principle. The stability and robustness of the reformulated INDI is then analyzed using Lyapunov-based methods. Finally, this reformulated INDI is compared with NDI both analytically and numerically, considering model uncertainties and external disturbances.

This chapter is structured as follows: Sec. 2.2 reformulates the INDI control law for three different problems. The stability and robustness issues of INDI are discussed in Sec. 2.3. The effectiveness of the reformulated INDI is numerically verified in Sec. 2.4. Main conclusions are presented in Sec. 2.5.

2.2. REFORMULATIONS OF INCREMENTAL NONLINEAR DYNAMIC INVERSION

In this section, the incremental nonlinear dynamic inversion (INDI) control method will be reformulated for three problems, namely the input–output linearization, output tracking and input-to-state linearization in the presence of external disturbances.

2.2.1. INPUT-OUTPUT LINEARIZATION

Consider a multi-input/multi-output nonlinear system described by

$$\begin{aligned}\dot{\mathbf{x}} &= \mathbf{f}(\mathbf{x}) + \mathbf{G}(\mathbf{x})\mathbf{u} \\ \mathbf{y} &= \mathbf{h}(\mathbf{x})\end{aligned}\quad (2.1)$$

where $\mathbf{f} : \mathbb{R}^n \rightarrow \mathbb{R}^n$ and $\mathbf{h} : \mathbb{R}^n \rightarrow \mathbb{R}^p$ are smooth vector fields. \mathbf{G} is a smooth function mapping $\mathbb{R}^n \rightarrow \mathbb{R}^{n \times m}$, whose columns are smooth vector fields. When $p < m$, which means the number of outputs is smaller than the number of inputs, control of this system via input-output linearization is an overdetermined problem, where a control allocation technique is needed. On the other hand, $p > m$ yields an underdetermined problem. Although a weighted least squares method can be used to solve underdetermined problems, the desired control aims cannot be fully achieved. $p = m$ is assumed in the following derivations.

Denote the elements of \mathbf{h} as h_i , $i = 1, 2, \dots, m$, and the column vectors of the matrix \mathbf{G} as \mathbf{g}_j , $j = 1, 2, \dots, m$, then the Lie derivatives [2] of the function h_i with respect to the vector fields \mathbf{f} and \mathbf{g}_j are defined as

$$\mathcal{L}_f h_i = \frac{\partial h_i}{\partial \mathbf{x}} \mathbf{f}, \quad \mathcal{L}_{\mathbf{g}_j} h_i = \frac{\partial h_i}{\partial \mathbf{x}} \mathbf{g}_j, \quad \mathcal{L}_f^k h_i = \frac{\partial (\mathcal{L}_f^{k-1} h_i)}{\partial \mathbf{x}} \mathbf{f}, \quad \mathcal{L}_{\mathbf{g}_j} \mathcal{L}_f^k h_i = \frac{\partial (\mathcal{L}_f^k h_i)}{\partial \mathbf{x}} \mathbf{g}_j \quad (2.2)$$

The relative degree ρ_i for each output channel i is defined as the smallest integer such that for all $\mathbf{x} \in \mathbb{R}^n$, at least one $j \in \{1, 2, \dots, m\}$ satisfies $\mathcal{L}_{\mathbf{g}_j} \mathcal{L}_f^{\rho_i-1} h_i \neq 0$.

Define the vector relative degree [23] of the system as $\boldsymbol{\rho} = [\rho_1, \rho_2, \dots, \rho_m]^T$, which satisfies

$$\boldsymbol{\rho} = \|\boldsymbol{\rho}\|_1 = \sum_{i=1}^m \rho_i \leq n \quad (2.3)$$

then the output dynamics of the system can be represented as

$$\begin{bmatrix} y_1^{(\rho_1)} \\ y_2^{(\rho_2)} \\ \vdots \\ y_m^{(\rho_m)} \end{bmatrix} = \begin{bmatrix} \mathcal{L}_f^{\rho_1} h_1(\mathbf{x}) \\ \mathcal{L}_f^{\rho_2} h_2(\mathbf{x}) \\ \vdots \\ \mathcal{L}_f^{\rho_m} h_m(\mathbf{x}) \end{bmatrix} + \begin{bmatrix} \mathcal{L}_{\mathbf{g}_1} \mathcal{L}_f^{\rho_1-1} h_1(\mathbf{x}) & \cdots & \mathcal{L}_{\mathbf{g}_m} \mathcal{L}_f^{\rho_1-1} h_1(\mathbf{x}) \\ \mathcal{L}_{\mathbf{g}_1} \mathcal{L}_f^{\rho_2-1} h_2(\mathbf{x}) & \cdots & \mathcal{L}_{\mathbf{g}_m} \mathcal{L}_f^{\rho_2-1} h_2(\mathbf{x}) \\ \vdots & & \vdots \\ \mathcal{L}_{\mathbf{g}_1} \mathcal{L}_f^{\rho_m-1} h_m(\mathbf{x}) & \cdots & \mathcal{L}_{\mathbf{g}_m} \mathcal{L}_f^{\rho_m-1} h_m(\mathbf{x}) \end{bmatrix} \mathbf{u} \quad (2.4)$$

or

$$\mathbf{y}^{(\boldsymbol{\rho})} = \boldsymbol{\alpha}(\mathbf{x}) + \mathcal{B}(\mathbf{x})\mathbf{u} \quad (2.5)$$

If $\rho = n$, then the system given by Eq. (2.1) is full-state feedback linearizable. Otherwise, there are $n - \rho$ internal dynamics unobservable from the output \mathbf{y} . According to the Frobenius theorem [24], $\forall \mathbf{x}_* \in \mathbb{R}^n$, there exist smooth functions $\boldsymbol{\phi}(\mathbf{x}) = [\phi_1(\mathbf{x}), \dots, \phi_{n-\rho}(\mathbf{x})]^T$ defined in a neighborhood D_0 of \mathbf{x}_* such that

$$\frac{\partial \phi_k}{\partial \mathbf{x}} \mathbf{g}_j(\mathbf{x}) = 0, \quad \forall k \in \{1, 2, \dots, n - \rho\}, \quad \forall j \in \{1, 2, \dots, m\}, \quad \forall \mathbf{x} \in D_0 \quad (2.6)$$

Also, $\mathbf{z} = \mathbf{T}(\mathbf{x})$ defined by

$$\begin{aligned}\mathbf{z} &= \mathbf{T}(\mathbf{x}) = [\mathbf{T}_1(\mathbf{x}); \mathbf{T}_2(\mathbf{x})] = [\boldsymbol{\eta}; \boldsymbol{\xi}], \quad \boldsymbol{\eta} = \boldsymbol{\phi}(\mathbf{x}), \quad \boldsymbol{\xi} = [\boldsymbol{\xi}_1; \boldsymbol{\xi}_2; \dots; \boldsymbol{\xi}_m], \\ \boldsymbol{\xi}_i &= [h_i(\mathbf{x}), \mathcal{L}_f h_i(\mathbf{x}), \dots, \mathcal{L}_f^{\rho_i-1} h_i(\mathbf{x})]^T, \quad i = 1, 2, \dots, m\end{aligned}\quad (2.7)$$

is a diffeomorphism on the domain D_0 [2, 24]. $\boldsymbol{\eta}$ and $\boldsymbol{\xi}$ are the state vectors for the internal and external dynamics respectively. Using Eqs. (2.5, 2.6, 2.7), the nonlinear system described by Eq. (2.1) can be transformed into

$$\begin{aligned}\dot{\boldsymbol{\eta}} &= \mathbf{f}_0(\boldsymbol{\eta}, \boldsymbol{\xi}) = \left. \frac{\partial \boldsymbol{\phi}}{\partial \mathbf{x}} \mathbf{f}(\mathbf{x}) \right|_{\mathbf{x}=\mathbf{T}^{-1}(\mathbf{z})} \\ \dot{\boldsymbol{\xi}} &= \mathbf{A}_c \boldsymbol{\xi} + \mathbf{B}_c [\boldsymbol{\alpha}(\mathbf{x}) + \mathcal{B}(\mathbf{x}) \mathbf{u}] \\ \mathbf{y} &= \mathbf{C}_c \boldsymbol{\xi}\end{aligned}\quad (2.8)$$

where $\mathbf{A}_c = \text{diag}\{\mathbf{A}_0^i\}$, $\mathbf{B}_c = \text{diag}\{\mathbf{B}_0^i\}$, $\mathbf{C}_c = \text{diag}\{\mathbf{C}_0^i\}$, $i = 1, 2, \dots, m$, and $(\mathbf{A}_0^i, \mathbf{B}_0^i, \mathbf{C}_0^i)$ is a canonical form representation of a chain of ρ_i integrators.

Assume $\det\{\mathcal{B}(\mathbf{x})\} \neq 0$, otherwise, $p = m$ would still lead to an underdetermined problem. The nonlinear dynamic inversion (NDI) linearization is designed as $\mathbf{u} = \mathcal{B}^{-1}(\mathbf{x})(\mathbf{v} - \boldsymbol{\alpha}(\mathbf{x}))$, where $\mathbf{v} \in \mathbb{R}^m$ is called the pseudo-control input. In the absence of model uncertainties and disturbances, this linearization results in the closed-loop system

$$\begin{aligned}\dot{\boldsymbol{\eta}} &= \mathbf{f}_0(\boldsymbol{\eta}, \boldsymbol{\xi}) \\ \dot{\boldsymbol{\xi}} &= \mathbf{A}_c \boldsymbol{\xi} + \mathbf{B}_c \mathbf{v} \\ \mathbf{y} &= \mathbf{C}_c \boldsymbol{\xi}\end{aligned}\quad (2.9)$$

which indicates this closed-loop system has $n - \rho$ internal dynamics, and m decoupled channels. The input–output mapping for each channel from v_i to y_i is a chain of ρ_i integrators.

NDI linearization however is based on the exact mathematical cancellation of the nonlinear terms $\boldsymbol{\alpha}(\mathbf{x})$ and $\mathcal{B}(\mathbf{x})$. This is almost impossible in practice due to model simplifications, computational errors and external disturbances. One method to reduce the control law model dependency is incremental nonlinear dynamic inversion (INDI), which will be reformulated here.

Taking the first-order Taylor series expansion of Eq. (2.5) around the condition at $t - \Delta t$ (denoted by the subscript 0) as follows:

$$\begin{aligned}\mathbf{y}^{(\rho)} &= \boldsymbol{\alpha}(\mathbf{x}) + \mathcal{B}(\mathbf{x}) \mathbf{u} \\ &= \mathbf{y}_0^{(\rho)} + \left. \frac{\partial [\boldsymbol{\alpha}(\mathbf{x}) + \mathcal{B}(\mathbf{x}) \mathbf{u}]}{\partial \mathbf{x}} \right|_0 \Delta \mathbf{x} + \mathcal{B}(\mathbf{x}_0) \Delta \mathbf{u} + \mathbf{R}_1\end{aligned}\quad (2.10)$$

where $\Delta \mathbf{x}$ and $\Delta \mathbf{u}$ represent the state and control increments in one sampling time step Δt . \mathbf{R}_1 in Eq. (2.10) is the expansion remainder, whose Lagrange form is

$$\mathbf{R}_1 = \frac{1}{2!} \left[\left. \frac{\partial^2 [\boldsymbol{\alpha}(\mathbf{x}) + \mathcal{B}(\mathbf{x}) \mathbf{u}]}{\partial^2 \mathbf{x}} \right|_m \Delta \mathbf{x}^2 + 2 \left. \frac{\partial^2 [\boldsymbol{\alpha}(\mathbf{x}) + \mathcal{B}(\mathbf{x}) \mathbf{u}]}{\partial \mathbf{x} \partial \mathbf{u}} \right|_m \Delta \mathbf{x} \Delta \mathbf{u} \right] \quad (2.11)$$

in which $(\cdot)|_m$ means evaluating (\cdot) at a condition where $\mathbf{x} \in (\mathbf{x}(t - \Delta t), \mathbf{x}(t))$, $\mathbf{u} \in (\mathbf{u}(t - \Delta t), \mathbf{u}(t))$. In Eq. (2.11), \mathbf{R}_1 is not a function of $\Delta \mathbf{u}^2$, since according to Eq. (2.5), $\mathbf{y}^{(\rho)}$ is linear with respect to \mathbf{u} .

Design the incremental control input as

$$\Delta \mathbf{u} = \mathcal{B}^{-1}(\mathbf{x}_0)(\mathbf{v} - \mathbf{y}_0^{(\rho)}) \quad (2.12)$$

where $\mathbf{y}_0^{(\rho)}$ is measured or estimated. The total control command for the actuator is $\mathbf{u} = \mathbf{u}_0 + \Delta \mathbf{u}$. Substituting Eq. (2.12) into Eq. (2.10) results in the input–output mapping of $\mathbf{y}^{(\rho)} = \mathbf{v} + \boldsymbol{\delta}(\mathbf{z}, \Delta t)$, where the perturbation term equals

$$\boldsymbol{\delta}(\mathbf{z}, \Delta t) = \left[\frac{\partial[\boldsymbol{\alpha}(\mathbf{x}) + \mathcal{B}(\mathbf{x})\mathbf{u}]}{\partial \mathbf{x}} \Big|_0 \Delta \mathbf{x} + \mathbf{R}_1 \right] \Big|_{\mathbf{x}=\mathbf{T}^{-1}(\mathbf{z})} \quad (2.13)$$

In the closed-loop system, the values of \mathbf{u} and $\Delta \mathbf{u}$ have already been substituted into the right-hand side of Eq. (2.13), thus $\boldsymbol{\delta}(\mathbf{z}, \Delta t)$ is only denoted as a function of the states \mathbf{z} and the sampling interval. Using the same diffeomorphism $\mathbf{z} = \mathbf{T}(\mathbf{x})$, the closed-loop system dynamics under INDI linearization are given by

$$\begin{aligned} \dot{\boldsymbol{\eta}} &= \mathbf{f}_0(\boldsymbol{\eta}, \boldsymbol{\xi}) \\ \dot{\boldsymbol{\xi}} &= \mathbf{A}_c \boldsymbol{\xi} + \mathbf{B}_c [\mathbf{v} + \boldsymbol{\delta}(\mathbf{z}, \Delta t)] \\ \mathbf{y} &= \mathbf{C}_c \boldsymbol{\xi} \end{aligned} \quad (2.14)$$

which are consistent with Eq. (2.9) except for the perturbation term $\boldsymbol{\delta}(\mathbf{z}, \Delta t)$. The influence of $\boldsymbol{\delta}(\mathbf{z}, \Delta t)$ on system stability and robustness will be elaborated in Sec. 2.3. Although Eq. (2.9) under NDI control seems to be neat, perturbation terms will appear when model uncertainties and external disturbances are considered, which will also be shown in Sec. 2.3. As compared to the conventional NDI control law, the INDI control method is less sensitive to model mismatches, because $\boldsymbol{\alpha}(\mathbf{x})$ is not used in Eq. (2.12). On the other hand, this INDI control law needs the measurement or estimation of $\mathbf{y}_0^{(\rho)}$ and the actuator position \mathbf{u}_0 , this is why INDI control is referred to as a sensor-based approach.

2.2.2. OUTPUT TRACKING

INDI control can also be designed for command tracking problem. Consider the nonlinear plant (Eq. (2.1)) with relative degree $\boldsymbol{\rho} = [\rho_1, \rho_2, \dots, \rho_m]^T$, which can be transformed into the internal and external dynamics given by Eq. (2.8), the output tracking problem requires the output \mathbf{y} to asymptotically track a reference signal $\mathbf{r}(t) = [r_1(t), r_2(t), \dots, r_m(t)]^T$. Assume $r_i(t), i = 1, 2, \dots, m$ and its derivatives up to $r_i^{(\rho_i)}(t)$ are bounded for all t and $r_i^{(\rho_i)}(t)$ is piecewise continuous. Denote the reference and the tracking error vectors as

$$\mathcal{R} = [\mathcal{R}_1; \mathcal{R}_2; \dots; \mathcal{R}_m], \quad \mathcal{R}_i = [r_i, r_i^{(1)}, \dots, r_i^{(\rho_i-1)}]^T, \quad i = 1, 2, \dots, m, \quad \mathbf{e} = \boldsymbol{\xi} - \mathcal{R} \quad (2.15)$$

Using the definitions of the \mathbf{A}_c and \mathbf{B}_c matrices, and the formulation of \mathcal{R} , it can be derived that $\mathbf{A}_c \mathcal{R} - \dot{\mathcal{R}} = -\mathbf{B}_c \mathbf{r}^{(\boldsymbol{\rho})}$, with $\mathbf{r}^{(\boldsymbol{\rho})} = [r_1^{(\rho_1)}, r_2^{(\rho_2)}, \dots, r_m^{(\rho_m)}]^T$. Therefore, Eq. (2.8) can be transformed into

$$\begin{aligned} \dot{\boldsymbol{\eta}} &= \mathbf{f}_0(\boldsymbol{\eta}, \mathbf{e} + \mathcal{R}) \\ \dot{\mathbf{e}} &= \mathbf{A}_c \mathbf{e} + \mathbf{A}_c \mathcal{R} - \dot{\mathcal{R}} + \mathbf{B}_c [\boldsymbol{\alpha}(\mathbf{x}) + \mathcal{B}(\mathbf{x})\mathbf{u}] \\ &= \mathbf{A}_c \mathbf{e} + \mathbf{B}_c [\boldsymbol{\alpha}(\mathbf{x}) + \mathcal{B}(\mathbf{x})\mathbf{u} - \mathbf{r}^{(\boldsymbol{\rho})}] \end{aligned} \quad (2.16)$$

The NDI control for output tracking is designed as

$$\mathbf{u} = \mathcal{B}^{-1}(\mathbf{x})[\mathbf{v} - \boldsymbol{\alpha}(\mathbf{x}) + \mathbf{r}^{(\rho)}] \quad (2.17)$$

When perfect model cancellation is assumed, this NDI control law results in the closed-loop system

$$\dot{\boldsymbol{\eta}} = \mathbf{f}_0(\boldsymbol{\eta}, \mathbf{e} + \mathcal{R}), \quad \dot{\mathbf{e}} = \mathbf{A}_c \mathbf{e} + \mathbf{B}_c \mathbf{v} \quad (2.18)$$

On the other hand, by using Eq. (2.10), the INDI control for output tracking is designed as

$$\Delta \mathbf{u} = \mathcal{B}^{-1}(\mathbf{x}_0)[\mathbf{v} - \mathbf{y}_0^{(\rho)} + \mathbf{r}^{(\rho)}] \quad (2.19)$$

which leads to the closed-loop system as

$$\dot{\boldsymbol{\eta}} = \mathbf{f}_0(\boldsymbol{\eta}, \mathbf{e} + \mathcal{R}), \quad \dot{\mathbf{e}} = \mathbf{A}_c \mathbf{e} + \mathbf{B}_c [\mathbf{v} + \boldsymbol{\delta}(\mathbf{z}, \Delta t)] \quad (2.20)$$

The closed-loop system dynamics given by Eq. (2.14) and Eq. (2.20) are essentially the same. Only the equilibrium point of $\mathbf{z} = [\boldsymbol{\eta}; \boldsymbol{\xi}] = \mathbf{0}$ is shifted to $\mathbf{z}' = [\boldsymbol{\eta}; \mathbf{e}] = \mathbf{0}$, so similar stability and robustness analyses can be made.

2.2.3. INPUT-TO-STATE LINEARIZATION UNDER DISTURBANCE PERTURBATIONS

Consider a special case of input–output linearization by taking the outputs as $y_i = h_i(x) = x_i - x_{i*}$, $i = 1, 2, \dots, m$, or equally $\mathbf{y} = \mathbf{H}(\mathbf{x} - \mathbf{x}_*)$, where \mathbf{H} is a Boolean selection matrix and \mathbf{x}_* is the equilibrium point. This choice of output results in a so-called *symmetrical system* [23] where all m channels have the same relative degree $\rho_i = 1$, and the total relative degree is $\rho = m$. When $m < n$, there are $n - m$ internal dynamics.

Adding the disturbance perturbation $\mathbf{d} \in \mathbb{R}^n$ into the nonlinear plant (Eq. (2.1)) as

$$\begin{aligned} \dot{\mathbf{x}} &= \mathbf{f}(\mathbf{x}) + \mathbf{G}(\mathbf{x})\mathbf{u} + \mathbf{d} \\ \mathbf{y} &= \mathbf{H}(\mathbf{x} - \mathbf{x}_*) \end{aligned} \quad (2.21)$$

Recall Eq. (2.7), since $\rho_i = 1$, the external states are given by $\xi_i = h_i(x) = x_i - x_{i*}$, $i = 1, 2, \dots, m$, with dynamics

$$\dot{\boldsymbol{\xi}} = \dot{\boldsymbol{\xi}} = \bar{\mathbf{f}}(\boldsymbol{\xi}) + \bar{\mathbf{G}}(\boldsymbol{\xi})\mathbf{u} + \mathbf{H}\mathbf{d} \quad (2.22)$$

where $\bar{\mathbf{f}}: \mathbb{R}^m \rightarrow \mathbb{R}^m$, $\bar{\mathbf{G}}: \mathbb{R}^m \rightarrow \mathbb{R}^{m \times m}$ can be calculated by substituting $x_i = \xi_i + x_{i*}$, $i = 1, 2, \dots, m$ into Eq. (2.21). Taking the first-order Taylor series expansion of the external dynamic equations as

$$\begin{aligned} \dot{\boldsymbol{\xi}} &= \bar{\mathbf{f}}(\boldsymbol{\xi}) + \bar{\mathbf{G}}(\boldsymbol{\xi})\mathbf{u} + \mathbf{H}\mathbf{d} \\ &= \dot{\boldsymbol{\xi}}_0 + \left. \frac{\partial [\bar{\mathbf{f}}(\boldsymbol{\xi}) + \bar{\mathbf{G}}(\boldsymbol{\xi})\mathbf{u}]}{\partial \boldsymbol{\xi}} \right|_0 \Delta \boldsymbol{\xi} + \bar{\mathbf{G}}(\boldsymbol{\xi}_0)\Delta \mathbf{u} + \mathbf{H}\Delta \mathbf{d} + \mathbf{R}'_1 \end{aligned} \quad (2.23)$$

In Eq. (2.23), \mathbf{R}'_1 is the expansion remainder which is expressed in its Lagrange form as follows:

$$\mathbf{R}'_1 = \frac{1}{2} \left. \frac{\partial^2 [\bar{\mathbf{f}}(\boldsymbol{\xi}) + \bar{\mathbf{G}}(\boldsymbol{\xi})\mathbf{u}]}{\partial^2 \boldsymbol{\xi}} \right|_m \Delta \boldsymbol{\xi}^2 + \left. \frac{\partial^2 [\bar{\mathbf{f}}(\boldsymbol{\xi}) + \bar{\mathbf{G}}(\boldsymbol{\xi})\mathbf{u}]}{\partial \boldsymbol{\xi} \partial \mathbf{u}} \right|_m \Delta \boldsymbol{\xi} \Delta \mathbf{u} \quad (2.24)$$

in which $(\cdot)|_m$ means evaluating (\cdot) at a condition where $\xi \in (\xi(t - \Delta t), \xi(t))$, $\mathbf{u} \in (\mathbf{u}(t - \Delta t), \mathbf{u}(t))$, and $\mathbf{d} \in (\mathbf{d}(t - \Delta t), \mathbf{d}(t))$. \mathbf{R}'_1 is not a function of $\Delta \mathbf{u}^2$, $\Delta \mathbf{d}^2$, $\Delta \xi \Delta \mathbf{u}$, $\Delta \xi \Delta \mathbf{d}$, which can be examined using Eq. (2.22).

Design the incremental control law as $\Delta \mathbf{u} = \bar{\mathbf{G}}^{-1}(\xi_0)(\mathbf{v} - \dot{\xi}_0)$, the closed-loop external dynamics are formulated by

$$\dot{\xi} = \mathbf{v} + \mathbf{H}\Delta \mathbf{d} + \delta(\xi, \Delta t) \quad (2.25)$$

where $\delta(\xi, \Delta t)$ contains the closed-loop values of \mathbf{R}'_1 and $\frac{\partial[\bar{f}(\xi) + \bar{G}(\xi)\mathbf{u}]}{\partial \xi}|_0 \Delta \xi$ in Eq. (2.23). Analogously, using Eq. (2.6), the internal dynamics under disturbance perturbations are given by

$$\dot{\eta} = \frac{\partial \phi}{\partial \mathbf{x}}(\mathbf{f}(\mathbf{x}) + \mathbf{G}(\mathbf{x})\mathbf{u} + \mathbf{d}) = \frac{\partial \phi}{\partial \mathbf{x}}(\mathbf{f}(\mathbf{x}) + \mathbf{d}) = \mathbf{f}_d(\eta, \xi, \mathbf{d}) \quad (2.26)$$

where $\mathbf{f}_d(\eta, \xi, \mathbf{d}) : \mathbb{R}^{n-\rho} \times \mathbb{R}^\rho \times \mathbb{R}^n \rightarrow \mathbb{R}^{n-\rho}$. Choosing $\phi(\mathbf{x}_*) = \mathbf{0}$, then the diffeomorphism $\mathbf{z} = \mathbf{T}(\mathbf{x}) = [\eta; \xi]$ transforms the equilibrium $\mathbf{x} = \mathbf{x}_*$ into the origin point $\mathbf{z} = [\eta; \xi] = \mathbf{0}$.

When $\mathbf{d} = \mathbf{0}$, the input-to-state linearized closed-loop system dynamics given by Eqs. (2.25, 2.26) are a special case of Eq. (2.14). It can also be observed from Eqs. (2.25, 2.26) that the disturbance \mathbf{d} influences the external dynamics only by its increments $\Delta \mathbf{d}$ while it directly influencing the internal dynamics. Most external disturbances in real life are continuous, thus $\lim_{\Delta t \rightarrow 0} \|\mathbf{d}\|_2 = 0$. In other words, when $\mathbf{d} \neq \mathbf{0}$, $\exists \Delta t, s.t. \|\Delta \mathbf{d}\|_2 < \|\mathbf{d}\|_2$. This is another feature of INDI control, that the main part of the disturbance influences have already been included by previous measurements and compensated by the controller. This control method thus presents improved disturbance rejection ability as verified by simulations [15, 21] and flight tests [13, 14]. This feature of INDI will be further analyzed in Sec. 2.3.

2.3. STABILITY AND ROBUSTNESS ANALYSIS

The stability and robustness of the reformulated INDI control will be analyzed in this section. In the first subsection, the influences of the state-variation-related terms on closed-loop system stability will be discussed. The second subsection discusses the system robustness to regular and singular perturbations.

2.3.1. STABILITY ANALYSIS

In this subsection, the stability of the origin $\mathbf{z} = \mathbf{0}$ of closed-loop system given by Eq. (2.14) under INDI control will be analyzed. Similar conclusions can be drawn for systems modeled by Eq. (2.20) and Eqs. (2.25, 2.26) without disturbances. The closed-loop system under the perturbations of external disturbances and model uncertainties will be analyzed in subsection 2.3.2. The proofs in this section also assume ideal actuators and perfect sensing. The actuator dynamics, nonlinear limits of actuators and the sensing issues will also be discussed in subsection 2.3.2.

Design the pseudo-control $\mathbf{v} = -\mathbf{K}\xi$ such that $\mathbf{A}_c - \mathbf{B}_c\mathbf{K}$ is Hurwitz. As a result, Eq. (2.14) equals

$$\begin{aligned} \dot{\eta} &= \mathbf{f}_0(\eta, \xi) \\ \dot{\xi} &= (\mathbf{A}_c - \mathbf{B}_c\mathbf{K})\xi + \mathbf{B}_c\delta(\mathbf{z}, \Delta t) \end{aligned} \quad (2.27)$$

where the output equation is dropped since it plays no role in the stabilization problem.

Remark 1 The term $\delta(\mathbf{z}, \Delta t)$ in Eq. (2.10) or the term $\delta(\xi, \Delta t)$ in Eq. (2.23) are directly omitted in the literature [7, 10–20] by claiming that the $\Delta \mathbf{z}$ (or $\Delta \xi$) related term is smaller than the $\Delta \mathbf{u}$ related term when the sampling frequency is high, which is referred to as the time-scale separation principle (different from the widely used separation principle based on singular perturbation theory). This statement is not mathematically rigorous and is especially deficient for unstable nonlinear plants because the plant simplifications are made before designing the INDI control inputs. Consequently, the simplified (by omitting terms) incremental dynamic equations fail to adequately model the plant dynamics. Moreover, although these terms are dropped out for the convenience of controller design, they should be kept in the closed-loop system equations and remain influencing the stability and performance, which has been overlooked in the literature.

Considering the following system as the *nominal system*

$$\begin{aligned}\dot{\boldsymbol{\eta}} &= \mathbf{f}_0(\boldsymbol{\eta}, \xi) \\ \dot{\xi} &= (\mathbf{A}_c - \mathbf{B}_c \mathbf{K})\xi\end{aligned}\quad (2.28)$$

whose stability has been extensively proved in the literature, and is listed here for completeness.

Lemma 1 [2] *The origin of Eq. (2.28) is asymptotically stable if the origin of $\dot{\boldsymbol{\eta}} = \mathbf{f}_0(\boldsymbol{\eta}, \mathbf{0})$ is asymptotically stable.*

$\dot{\boldsymbol{\eta}} = \mathbf{f}_0(\boldsymbol{\eta}, \mathbf{0})$ is referred to as the *zero dynamics*, and the nonlinear system is said to be *minimum phase* if its zero dynamics has an asymptotically stable equilibrium point. The definition of asymptotically stable can be found in Appendix A, Definition 4.

Lemma 2 [2] *The origin of Eq. (2.28) is globally asymptotically stable if the system $\dot{\boldsymbol{\eta}} = \mathbf{f}_0(\boldsymbol{\eta}, \xi)$ is input-to-state stable.*

The definitions of globally asymptotically stable and input-to-state stable can be found in Appendix A, Definition 4. The proofs for Lemma 1 and Lemma 2 can be found in [2]. After presenting stability of the *nominal system*, stability of the perturbed system given by Eq. (2.27) will be considered.

Assumption 1 *The partial derivatives of $\boldsymbol{\alpha}(\mathbf{x})$ and $\mathcal{B}(\mathbf{x})$ with respect to \mathbf{x} , up to any order, are bounded.*

Since \mathbf{x} is continuously differentiable (Eq. (2.1)), $\lim_{\Delta t \rightarrow 0} \|\Delta \mathbf{x}\|_2 = 0$. Recall Eq. (2.13), under Assumption 1, the norm value of $\delta(\mathbf{z}, \Delta t)$ can be reduced by increasing the sampling frequency.

Theorem 1 *If $\|\delta(\mathbf{z}, \Delta t)\|_2 \leq \bar{\delta}_\varepsilon$ is satisfied for all $\mathbf{z} \in \mathbb{R}^n$, and $\dot{\boldsymbol{\eta}} = \mathbf{f}_0(\boldsymbol{\eta}, \xi)$ is input-to-state stable, then the state \mathbf{z} of Eq. (2.27) is globally ultimately bounded by a class \mathcal{K} function of $\bar{\delta}_\varepsilon$.*

Proof: Choose the candidate Lyapunov function as $V(\xi) = \xi^T \mathbf{P} \xi$, where $\mathbf{P} = \mathbf{P}^T > 0$ is the solution of the Lyapunov equation $\mathbf{P}(\mathbf{A}_c - \mathbf{B}_c \mathbf{K}) + (\mathbf{A}_c - \mathbf{B}_c \mathbf{K})^T \mathbf{P} = -\mathbf{I}$, then $V(\xi)$ is

positive definite and also satisfies

$$\begin{aligned}\alpha_1(\|\xi\|_2) &\leq V(\xi) \leq \alpha_2(\|\xi\|_2) \\ \alpha_1(\|\xi\|_2) &\triangleq \lambda_{\min}(\mathbf{P})\|\xi\|_2^2, \quad \alpha_2(\|\xi\|_2) \triangleq \lambda_{\max}(\mathbf{P})\|\xi\|_2^2\end{aligned}\quad (2.29)$$

$\lambda_{\min}(\mathbf{P})$, $\lambda_{\max}(\mathbf{P})$ are the minimum and maximum eigenvalues of the \mathbf{P} matrix. α_1, α_2 belong to the class \mathcal{K}_∞ functions (Appendix A, Definition 2). The time derivative of the candidate Lyapunov function is calculated as

$$\begin{aligned}\dot{V} &= \xi^T [\mathbf{P}(\mathbf{A}_c - \mathbf{B}_c \mathbf{K}) + (\mathbf{A}_c - \mathbf{B}_c \mathbf{K})^T \mathbf{P}] \xi + 2\xi^T \mathbf{P} \mathbf{B}_c \delta(\mathbf{z}, \Delta t) \\ &\leq -\|\xi\|_2^2 + 2\|\xi\|_2 \|\mathbf{P} \mathbf{B}_c\|_2 \bar{\delta}_\varepsilon \\ &\leq -\theta_1 \|\xi\|_2^2, \quad \forall \|\xi\|_2 \geq \frac{2\|\mathbf{P} \mathbf{B}_c\|_2 \bar{\delta}_\varepsilon}{1 - \theta_1} \triangleq \mu_1 \bar{\delta}_\varepsilon\end{aligned}\quad (2.30)$$

with constant $\theta_1 \in (0, 1)$. Consequently, for $\forall \xi(t_0) \in \mathbb{R}^p$, there exists a class \mathcal{KL} function (Appendix A, Definition 3) β and finite $T_1 \geq 0$ independent of t_0 such that $\|\xi(t)\|_2$ satisfies [2]

$$\begin{aligned}\|\xi(t)\|_2 &\leq \beta(\|\xi(t_0)\|_2, t - t_0), \quad t_0 \leq \forall t \leq t_0 + T_1 \\ \|\xi(t)\|_2 &\leq \alpha_1^{-1}(\alpha_2(\mu_1 \bar{\delta}_\varepsilon)), \quad \forall t \geq t_0 + T_1 \triangleq t'_0\end{aligned}\quad (2.31)$$

The preceding equations indicate that the external state ξ is bounded for all $t \geq t_0$ and is ultimately bounded by $\Gamma \bar{\delta}_\varepsilon \triangleq \alpha_1^{-1}(\alpha_2(\mu_1 \bar{\delta}_\varepsilon)) = \sqrt{\lambda_{\max}(\mathbf{P})/\lambda_{\min}(\mathbf{P})} \mu_1 \bar{\delta}_\varepsilon$. The definition of ultimate boundedness can be found in Appendix A, Definition 6.

Moreover, by the definition of input-to-state stability (Appendix A, Definition 7), there exists a class \mathcal{KL} function β_0 and a class \mathcal{K} function (Appendix A, Definition 2) γ_0 such that for $\forall \eta(t'_0) \in \mathbb{R}^{n-p}$ and bounded input ξ , the internal state η satisfies

$$\begin{aligned}\|\eta(t)\|_2 &\leq \beta_0(\|\eta(t'_0)\|_2, t - t'_0) + \gamma_0(\sup_{t'_0 \leq \tau \leq t} \|\xi(\tau)\|_2) \\ &= \beta_0(\|\eta(t'_0)\|_2, t - t'_0) + \gamma_0(\Gamma \bar{\delta}_\varepsilon)\end{aligned}\quad (2.32)$$

In addition, because β_0 belongs to class \mathcal{KL} functions, then $\beta_0(\|\eta(t'_0)\|_2, t - t'_0) \leq \theta_2 \bar{\delta}_\varepsilon$, for some finite $T_2 > 0$ and $\theta_2 > 0$. Hence, the state \mathbf{z} satisfies

$$\|\mathbf{z}(t)\|_2 \leq \|\xi(t)\|_2 + \|\eta(t)\|_2 = (\Gamma + \theta_2) \bar{\delta}_\varepsilon + \gamma_0(\Gamma \bar{\delta}_\varepsilon), \quad \forall t \geq t_0 + T_1 + T_2 \quad (2.33)$$

which proves that $\mathbf{z}(t)$ is globally ultimately bounded (Appendix A, Definition 6) by a class \mathcal{K} function of $\bar{\delta}_\varepsilon$. \square

Theorem 1 has no restriction on the values of the initial state and the perturbation bound $\bar{\delta}_\varepsilon$. However, when the internal dynamics $\dot{\eta} = \mathbf{f}_0(\eta, \xi)$ is not input-to-state stable, but only the origin of the zero dynamics $\dot{\eta} = \mathbf{f}_0(\eta, \mathbf{0})$ is exponentially stable (Appendix A, Definition 5), then there will be restrictions on both the initial state, and the perturbations. These phenomena are presented in Theorem 2.

Theorem 2 *If $\|\delta(\mathbf{z}, \Delta t)\|_2 \leq \bar{\delta}_\varepsilon$ is satisfied for all $\mathbf{z} \in \mathbb{R}^n$, and the origin of $\dot{\eta} = \mathbf{f}_0(\eta, \mathbf{0})$ is exponentially stable, then there is a neighborhood D_z of $\mathbf{z} = \mathbf{0}$ and $\varepsilon^* > 0$, such that for every $\mathbf{z}(0) \in D_z$ and $\bar{\delta}_\varepsilon < \varepsilon^*$, the state \mathbf{z} of Eq. (2.27) is ultimately bounded by a class \mathcal{K} function of $\bar{\delta}_\varepsilon$.*

Proof: According to the converse Lyapunov theorem [2], because the origin of $\dot{\boldsymbol{\eta}} = \mathbf{f}_0(\boldsymbol{\eta}, \mathbf{0})$ is exponentially stable, there exists a Lyapunov function $V_2(\boldsymbol{\eta})$ defined in $D_{r_\eta} = \{\boldsymbol{\eta} \in \mathbb{R}^{n-\rho} \mid \|\boldsymbol{\eta}\| < r_\eta\}$ that satisfies the inequalities

$$c_1 \|\boldsymbol{\eta}\|_2^2 \leq V_2(\boldsymbol{\eta}) \leq c_2 \|\boldsymbol{\eta}\|_2^2, \quad \frac{\partial V_2}{\partial \boldsymbol{\eta}} \mathbf{f}_0(\boldsymbol{\eta}, \mathbf{0}) \leq -c_3 \|\boldsymbol{\eta}\|_2^2, \quad \left\| \frac{\partial V_2}{\partial \boldsymbol{\eta}} \right\|_2 \leq c_4 \|\boldsymbol{\eta}\|_2 \quad (2.34)$$

for some positive constants c_1, c_2, c_3, c_4 . Denote

$$\alpha'_1(\|\boldsymbol{\eta}\|_2) \triangleq c_1 \|\boldsymbol{\eta}\|_2^2, \quad \alpha'_2(\|\boldsymbol{\eta}\|_2) \triangleq c_2 \|\boldsymbol{\eta}\|_2^2 \quad (2.35)$$

then α'_1, α'_2 belong to class \mathcal{K}_∞ functions. Furthermore, because \mathbf{f}_0 is continuous and differentiable, there exists a Lipschitz constant L of \mathbf{f}_0 with respect to $\boldsymbol{\xi}$ such that

$$\|\mathbf{f}_0(\boldsymbol{\eta}, \boldsymbol{\xi}) - \mathbf{f}_0(\boldsymbol{\eta}, \mathbf{0})\|_2 \leq L \|\boldsymbol{\xi}\|_2, \quad \forall \|\boldsymbol{\eta}\| < r_\eta \quad (2.36)$$

Choose $V_2(\boldsymbol{\eta})$ as the candidate Lyapunov function for $\dot{\boldsymbol{\eta}} = \mathbf{f}_0(\boldsymbol{\eta}, \boldsymbol{\xi})$, with derivative

$$\begin{aligned} \dot{V}_2(\boldsymbol{\eta}) &= \frac{\partial V_2}{\partial \boldsymbol{\eta}} \mathbf{f}_0(\boldsymbol{\eta}, \mathbf{0}) + \frac{\partial V_2}{\partial \boldsymbol{\eta}} [\mathbf{f}_0(\boldsymbol{\eta}, \boldsymbol{\xi}) - \mathbf{f}_0(\boldsymbol{\eta}, \mathbf{0})] \\ &\leq -c_3 \|\boldsymbol{\eta}\|_2^2 + c_4 L \|\boldsymbol{\eta}\|_2 \|\boldsymbol{\xi}\|_2 \\ &\leq -c_3(1 - \theta_3) \|\boldsymbol{\eta}\|_2^2, \quad \frac{c_4 L \|\boldsymbol{\xi}\|_2}{c_3 \theta_3} \leq \forall \|\boldsymbol{\eta}\|_2 \leq r_\eta \end{aligned} \quad (2.37)$$

with constant $\theta_3 \in (0, 1)$. Denote

$$\mu \triangleq \frac{c_4 L}{c_3 \theta_3} \left(\sup_{t'_0 \leq \tau \leq t} \|\boldsymbol{\xi}(\tau)\|_2 \right) \triangleq \theta_5 \left(\sup_{t'_0 \leq \tau \leq t} \|\boldsymbol{\xi}(\tau)\|_2 \right) \quad (2.38)$$

then

$$\dot{V}_2(\boldsymbol{\eta}) \leq -c_3(1 - \theta_3) \|\boldsymbol{\eta}\|_2^2, \quad \mu \leq \forall \|\boldsymbol{\eta}\|_2 \leq r_\eta, \quad \forall t \geq t'_0 \quad (2.39)$$

Since the conditions for the external states $\boldsymbol{\xi}$ are the same as compared to Theorem 1, Eqs. (2.29, 2.30, 2.31) also hold true in this Theorem. From Eq. (2.31), the supremum of the external state is given by

$$\sup_{t'_0 \leq \tau \leq t} \|\boldsymbol{\xi}(\tau)\|_2 = \alpha_1^{-1}(\alpha_2(\mu_1 \bar{\delta}_\varepsilon)) \quad (2.40)$$

Take $0 < r < r_\eta$ such that $D_r \subset D_{r_\eta}$, according to the boundedness theories [2], if

$$\mu < \alpha_2'^{-1}(\alpha_1'(r)), \quad \|\boldsymbol{\eta}(t'_0)\|_2 \leq \alpha_2'^{-1}(\alpha_1'(r)) \quad (2.41)$$

then there exists a class \mathcal{KL} function β'_0 such that

$$\|\boldsymbol{\eta}(t)\|_2 \leq \beta'_0(\|\boldsymbol{\eta}(t'_0)\|_2, t - t'_0) + \alpha_1'^{-1}(\alpha_2'(\mu)), \quad \forall t \geq t'_0 \quad (2.42)$$

Eq. (2.41) proposes requirements on both the initial condition and the perturbation bound. Using Eqs. (2.38, 2.40, 2.41), the maximum perturbation that the system can sustain is given by

$$\bar{\delta}_\varepsilon < \varepsilon^* \triangleq (1/\mu_1) \alpha_2^{-1}(\alpha_1((1/\theta_5) \alpha_2'^{-1}(\alpha_1'(r)))) \quad (2.43)$$

From Eqs. (2.38, 2.40, 2.42), the normal value of the internal state yields

$$\begin{aligned}\|\boldsymbol{\eta}(t)\|_2 &\leq \beta'_0(\|\boldsymbol{\eta}(t'_0)\|_2, t - t'_0) + \alpha'_1{}^{-1}(\alpha'_2(\theta_5\alpha_1^{-1}(\alpha_2(\mu_1\bar{\delta}_\varepsilon)))) \\ &\leq \theta_6\bar{\delta}_\varepsilon + \theta_5\alpha_1'^{-1}(\alpha'_2(\alpha_1^{-1}(\alpha_2(\mu_1\bar{\delta}_\varepsilon)))), \quad \forall t \geq t_0 + T_1 + T_3\end{aligned}\quad (2.44)$$

for some finite $T_3 > 0$ and $\theta_6 > 0$. Hence, state \mathbf{z} satisfies

$$\begin{aligned}\|\mathbf{z}(t)\|_2 &\leq \|\boldsymbol{\xi}(t)\|_2 + \|\boldsymbol{\eta}(t)\|_2 \\ &= (\Gamma + \theta_6)\bar{\delta}_\varepsilon + \theta_5\alpha_1'^{-1}(\alpha'_2(\alpha_1^{-1}(\alpha_2(\mu_1\bar{\delta}_\varepsilon)))), \quad \forall t \geq t_0 + T_1 + T_3\end{aligned}\quad (2.45)$$

which proves the $\mathbf{z}(t)$ is ultimately bounded by a class \mathcal{K} function of $\bar{\delta}_\varepsilon$. \square

2.3.2. ROBUSTNESS ANALYSIS

DISTURBANCE REJECTION

The INDI control method has promising disturbance rejection ability as has been verified by both simulations [15, 21] and quad-rotor flight tests [13, 14]. However, there is a lack of theoretical proof for the stability of the closed-loop system using INDI control under the perturbation of external disturbances. These issues will be discussed in this subsection.

Normally, the external disturbances are bounded in real life. Denote

$$\bar{d} \triangleq \sup\{\|\mathbf{d}(t)\|_2, \mathbf{d} \in \mathbb{R}^n\}, \quad \forall t \geq t_0 \quad (2.46)$$

which is independent of the sampling interval Δt . Most external disturbances in real life are continuous, thus $\lim_{\Delta t \rightarrow 0} \|\mathbf{d}\|_2 = 0$. Therefore, for a given sampling rate, the supremum of $\|\Delta \mathbf{d}\|_2$ exists. Denote

$$\bar{d}_\varepsilon(\Delta t) \triangleq \sup\{\|\Delta \mathbf{d}(t)\|_2, \Delta \mathbf{d} \in \mathbb{R}^n\}, \quad \forall t \geq t_0 \quad (2.47)$$

As a function of Δt , $\bar{d}_\varepsilon(\Delta t)$ can be reduced by increasing the sampling frequency. Recall the system modeled by Eqs. (2.25, 2.26), and design the pseudo-control as $\mathbf{v} = -\mathbf{K}\boldsymbol{\xi}$ to stabilize the origin $\mathbf{z} = [\boldsymbol{\eta}; \boldsymbol{\xi}] = \mathbf{0}$, the closed-loop system is then given by

$$\begin{aligned}\dot{\boldsymbol{\eta}} &= \mathbf{f}_d(\boldsymbol{\eta}, \boldsymbol{\xi}, \mathbf{d}) \\ \dot{\boldsymbol{\xi}} &= -\mathbf{K}\boldsymbol{\xi} + \mathbf{H}\Delta \mathbf{d} + \boldsymbol{\delta}(\boldsymbol{\xi}, \Delta t)\end{aligned}\quad (2.48)$$

Proposition 1 *If $\|\boldsymbol{\delta}(\boldsymbol{\xi}, \Delta t)\|_2 \leq \bar{\delta}_\varepsilon$ is satisfied for all $\boldsymbol{\xi} \in \mathbb{R}^p$, $\dot{\boldsymbol{\eta}} = \mathbf{f}_d(\boldsymbol{\eta}, \boldsymbol{\xi}, \mathbf{d})$ is continuously differentiable and globally Lipschitz in $(\boldsymbol{\eta}, \boldsymbol{\xi}, \mathbf{d})$, and the origin of $\dot{\boldsymbol{\eta}} = \mathbf{f}_d(\boldsymbol{\eta}, \mathbf{0}, \mathbf{0})$ is globally exponentially stable, then the external state $\boldsymbol{\xi}$ is globally ultimately bounded by a class \mathcal{K} function of $\bar{\delta}_\varepsilon, \bar{d}_\varepsilon$, while the internal state $\boldsymbol{\eta}$ of Eq. (2.48) is globally ultimately bounded by a class \mathcal{K} function of $\bar{d}, \bar{\delta}_\varepsilon, \bar{d}_\varepsilon$.*

Proof: The norm value of the perturbation term in Eq. (2.48) satisfies

$$\|\mathbf{H}\Delta \mathbf{d} + \boldsymbol{\delta}(\boldsymbol{\xi}, \Delta t)\|_2 \leq \|\mathbf{H}\|_2 \|\Delta \mathbf{d}\|_2 + \|\boldsymbol{\delta}(\boldsymbol{\xi}, \Delta t)\|_2 = \bar{d}_\varepsilon + \bar{\delta}_\varepsilon \quad (2.49)$$

where $\|\mathbf{H}\|_2 = 1$ since \mathbf{H} is a Boolean selection matrix. Similar to the proof of Theorem 1, choose the candidate Lyapunov function as $V(\boldsymbol{\xi}) = \boldsymbol{\xi}^T \mathbf{P} \boldsymbol{\xi}$, where $\mathbf{P} = \mathbf{P}^T > 0$ is the solution of the Lyapunov equation $\mathbf{P} \mathbf{K} + \mathbf{K}^T \mathbf{P} = \mathbf{I}$, then the time derivative of $V(\boldsymbol{\xi})$ satisfies

$$\dot{V} \leq -\theta_1 \|\boldsymbol{\xi}\|_2^2, \quad \forall \|\boldsymbol{\xi}\|_2 \geq \frac{2\|\mathbf{P}\|_2(\bar{\delta}_\varepsilon + \bar{d}_\varepsilon)}{1 - \theta_1} \triangleq \mu_2(\bar{\delta}_\varepsilon + \bar{d}_\varepsilon) \quad (2.50)$$

Therefore, $\forall \boldsymbol{\xi}(t_0) \in \mathbb{R}^\rho$, there exists a class \mathcal{KL} function β and $T_4 \geq 0$ independent of t_0 such that $\|\boldsymbol{\xi}(t)\|_2$ satisfies

$$\begin{aligned} \|\boldsymbol{\xi}(t)\|_2 &\leq \beta(\|\boldsymbol{\xi}(t_0)\|_2, t - t_0), & t_0 \leq \forall t \leq t_0 + T_4 \\ \|\boldsymbol{\xi}(t)\|_2 &\leq \alpha_1^{-1}(\alpha_2(\mu_2(\bar{\delta}_\varepsilon + \bar{d}_\varepsilon))), & \forall t \geq t_0 + T_4 \end{aligned} \quad (2.51)$$

In other words, the external state $\boldsymbol{\xi}$ is bounded for all $t \geq t_0$ and ultimately bounded by $\Gamma_\xi \triangleq \alpha_1^{-1}(\alpha_2(\mu_2(\bar{\delta}_\varepsilon + \bar{d}_\varepsilon)))$, which is a class \mathcal{K} function of $\bar{\delta}_\varepsilon$ and \bar{d}_ε .

On the other hand, perturbations directly act on the internal dynamics. Since the origin of $\dot{\boldsymbol{\eta}} = \mathbf{f}_d(\boldsymbol{\eta}, \mathbf{0}, \mathbf{0})$ is globally exponentially stable, Eq. (2.34) is satisfied globally. Moreover, since $\dot{\boldsymbol{\eta}} = \mathbf{f}_d(\boldsymbol{\eta}, \boldsymbol{\xi}, \mathbf{d})$ is continuously differentiable and globally Lipschitz in $(\boldsymbol{\eta}, \boldsymbol{\xi}, \mathbf{d})$, there exists a global Lipschitz constant L such that

$$\|\mathbf{f}_d(\boldsymbol{\eta}, \boldsymbol{\xi}, \mathbf{d}) - \mathbf{f}_d(\boldsymbol{\eta}, \mathbf{0}, \mathbf{0})\|_2 \leq L(\|\boldsymbol{\xi}\|_2 + \|\mathbf{d}\|_2), \quad \forall \boldsymbol{\eta} \in \mathbb{R}^{n-\rho} \quad (2.52)$$

Analogous to the proofs of Theorem 2, Eq. (2.39) is satisfied for $\forall \|\boldsymbol{\eta}\|_2 \geq \mu'$ with $\mu' \triangleq \theta_5(\sup_{t_0+T_4 \leq \tau \leq t} (\|\boldsymbol{\xi}(\tau)\|_2 + \|\mathbf{d}(\tau)\|_2))$, and the internal state $\boldsymbol{\eta}$ satisfies

$$\|\boldsymbol{\eta}(t)\|_2 \leq \beta'_0(\|\boldsymbol{\eta}(t_0 + T_4)\|_2, t - t_0 - T_4) + \theta_5 \alpha_1'^{-1}(\alpha_2'(\Gamma_\xi + \bar{d})), \quad \forall t \geq t_0 + T_4 \quad (2.53)$$

without restrictions on the initial values and the bound of disturbances. Due to the attenuation property of β'_0

$$\begin{aligned} \|\boldsymbol{\eta}(t)\|_2 &\leq [\theta_7 \bar{d} + \theta_5 \alpha_1'^{-1}(\alpha_2'(\bar{d}))] + \theta_5 \alpha_1'^{-1}(\alpha_2'(\alpha_1^{-1}(\alpha_2(\mu_2(\bar{\delta}_\varepsilon + \bar{d}_\varepsilon)))) \triangleq \Gamma_\eta, \\ \forall t &\geq t_0 + T_4 + T_5 \end{aligned} \quad (2.54)$$

for some $\theta_7 > 0$ and finite $T_5 > 0$. The preceding equation indicates that $\boldsymbol{\eta}$ is globally ultimately bounded by a class \mathcal{K} function of $\bar{d}, \bar{\delta}_\varepsilon, \bar{d}_\varepsilon$. \square

Remark 2 These estimations of the ultimate bounds could be conservative for a given perturbation term $\mathbf{H}\Delta\mathbf{d} + \boldsymbol{\delta}(\boldsymbol{\xi}, \Delta t)$, because the term $2\boldsymbol{\xi}^T \mathbf{P} \mathbf{B}_c \boldsymbol{\delta}(\mathbf{z}, \Delta t)$ in Eq. (2.30) can be either positive or negative. Worse-case analyses are done in Eq. (2.30) and Eq. (2.49) by taking the inequality constraints, which may lead to conservative estimations of the ultimate bounds. More accurate ultimate bounds of a perturbed nonlinear system can be obtained via numerical simulations.

The disturbance rejection capability of a control method can be evaluated by the values of the ultimate bounds under prescribed disturbance perturbations. In view of Eqs. (2.51, 2.54), the ultimate bounds Γ_ξ and Γ_η are correlated to:

1. System dynamics: Γ_ξ and Γ_η are functions of $\bar{\delta}_\varepsilon$. Recall Eq. (2.13), $\bar{\delta}_\varepsilon$ can be viewed as a gauge for system dynamics. When system dynamics are fast, which indicates $\|\frac{\partial(\mathbf{A}(x)+\mathcal{B}(x)\mathbf{u})}{\partial x}\|_0$ is large, the sampling frequency should be higher to ensure desired ultimate bounds. This has been verified by many application cases, for rigid airplane control, normally $f_s = 100$ Hz is enough [7, 12, 15, 18–20], while $f_s = 1000$ Hz is needed for flexible aircraft control [21]. $f_s = 512$ Hz is used in Ref. [13, 14] for quadrotor flight control. For the applications on hydraulic systems, $f_s = 5000$ Hz is desirable for controlling the hydraulic forces [16, 17].
2. Disturbance intensity: This can be seen from the expressions for Γ_ξ , Γ_η and definitions of \bar{d} , \bar{d}_ε , that stronger disturbances lead to larger ultimate bounds.
3. \mathbf{K} gains: As shown in Eqs. (2.51, 2.54), both Γ_ξ and Γ_η are monotonically increasing functions of μ_2 . From Eq. (2.50) and the Lyapunov equation, it can be seen that larger \mathbf{K} gains lead to smaller μ_2 , and further resulting in smaller ultimate bounds. Therefore, increasing \mathbf{K} gains is beneficial to releasing the requirement on sampling frequency. However, \mathbf{K} gains are constrained by actuation system limits, high-gain control would also amplify measurement noise.
4. Sampling frequency: Increasing the sampling frequency can reduce the value of both \bar{d}_ε and $\bar{\delta}_\varepsilon$. As discussed in Sec. 2.2, if $\mathbf{d} \neq \mathbf{0}$, $\|\Delta\mathbf{d}\|_2 < \|\mathbf{d}\|_2$ when the sampling interval Δt is sufficiently small. The main part of the disturbances \mathbf{d}_0 can be included by the measurement of $\dot{\xi}_0$, thus only the remaining increment $\Delta\mathbf{d}$ is perturbing ξ . This is one feature that distinguishes INDI from linear-quadratic regulator, proportional-integral and NDI control methods, where normally the disturbances can only be reflected in the measurement of state ξ , which is an integration of $\dot{\xi}_0$. Consequently, these control methods show inferior disturbance rejection ability as compared to the INDI method. In practice, the choice of sampling frequency is constrained by the hardware.
5. Internal dynamics: It can be seen that the first term of Eq. (2.54) cannot be reduced by increasing the sampling frequency, and is a function of \bar{d} . This is because the internal dynamics are uncontrolled by the INDI method. Moreover, being inspired by Theorem 2, when only the origin of $\dot{\eta} = \mathbf{f}_d(\eta, \mathbf{0}, \mathbf{0})$ is ensured to be exponentially stable or \mathbf{f}_d is not globally Lipschitz, constraints on both initial condition and the disturbance intensity need to be imposed. This is presented as Corollary 1. Therefore, the properties of internal dynamics are important for the stability and robustness of the system.

Corollary 1 *If $\|\delta(\xi, \Delta t)\|_2 \leq \bar{\delta}_\varepsilon$ is satisfied for all $\xi \in \mathbb{R}^p$, and the origin of $\dot{\eta} = \mathbf{f}_0(\eta, \mathbf{0}, \mathbf{0})$ is exponentially stable, then there is a neighborhood D_z of $\mathbf{z} = \mathbf{0}$ and $\varepsilon^* > 0$, such that for every $\mathbf{z}(0) \in D_z$ and $(\bar{\delta}_\varepsilon + \bar{d}_\varepsilon) < \varepsilon^*$, the external state ξ in Eq. (2.48) is ultimately bounded by a class \mathcal{K} function of $\bar{\delta}_\varepsilon, \bar{d}_\varepsilon$, while the internal state η in Eq. (2.48) is ultimately bounded by a class \mathcal{K} function of $\bar{d}, \bar{\delta}_\varepsilon, \bar{d}_\varepsilon$.*

The proof of Corollary 1 is similar to the proofs of Proposition 1 and Theorem 2.

ROBUSTNESS TO MODEL UNCERTAINTIES

The model uncertainties considered in this section are classified into the *regular perturbations*, which are defined in the nonlinear system perturbation theories as the perturbations that do not change the order of the nominal system, such as negligible nonlinearities, parametric dispersions and variations [5, 25].

There were few attempts on proving the robustness of the INDI control method to aerodynamics model uncertainties. In Ref. [10], it was shown by using linear transfer functions derived from block diagrams that the model mismatches of the control effectiveness matrix $\mathbf{G}(\mathbf{x})$ (or the generalized $\mathcal{B}(\mathbf{x})$) have no influence on the closed-loop system. However, the assumption of $\dot{\mathbf{x}} = \dot{\mathbf{x}}_0$ is made in the block diagram derivations, which is incorrect since otherwise there will be no $\Delta \mathbf{u}$ term. Moreover, the $\boldsymbol{\delta}(\mathbf{z}, \Delta t)$ term did not show up at all in previous proofs [10, 11, 13]. In view of these reasons, the robustness of INDI to model uncertainties will be rediscussed here.

Considering the nonlinear system with relative degree $\rho \leq n$ transformed into internal and external dynamics given by Eqs. (2.7, 2.8), the nominal INDI control to stabilize the system origin is given by

$$\bar{\mathbf{u}}_{\text{ndi}} = \mathcal{B}^{-1}(\mathbf{x})(\mathbf{v} - \boldsymbol{\alpha}(\mathbf{x})) = \mathcal{B}^{-1}(\mathbf{x})(-\mathbf{K}\mathbf{T}_2(\mathbf{x}) - \boldsymbol{\alpha}(\mathbf{x})) \quad (2.55)$$

which requires the model knowledge of $\boldsymbol{\alpha}$, \mathcal{B} , \mathbf{T}_2 (defined in Eq. (2.7)). When the control law is applied using the approximated model as $\hat{\boldsymbol{\alpha}}$, $\hat{\mathcal{B}}$, $\hat{\mathbf{T}}_2$, the control input is given as

$$\mathbf{u}_{\text{ndi}} = \hat{\mathcal{B}}^{-1}(\mathbf{x})(-\mathbf{K}\hat{\mathbf{T}}_2(\mathbf{x}) - \hat{\boldsymbol{\alpha}}(\mathbf{x})) \quad (2.56)$$

which results in a closed-loop system as

$$\begin{aligned} \dot{\boldsymbol{\eta}} &= \mathbf{f}_0(\boldsymbol{\eta}, \boldsymbol{\xi}) \\ \dot{\boldsymbol{\xi}} &= \mathbf{A}_c \boldsymbol{\xi} + \mathbf{B}_c [\boldsymbol{\alpha}(\mathbf{x}) + \mathcal{B}(\mathbf{x}) \hat{\mathcal{B}}^{-1}(\mathbf{x})(-\mathbf{K}\hat{\mathbf{T}}_2(\mathbf{x}) - \hat{\boldsymbol{\alpha}}(\mathbf{x}))] \\ &= [\mathbf{A}_c \boldsymbol{\xi} - \mathbf{B}_c \mathbf{K} \hat{\mathbf{T}}_2(\mathbf{x})] + \mathbf{B}_c (\boldsymbol{\alpha}(\mathbf{x}) - \hat{\boldsymbol{\alpha}}(\mathbf{x})) + \mathbf{B}_c (\mathcal{B}(\mathbf{x}) \hat{\mathcal{B}}^{-1}(\mathbf{x}) - \mathbf{I})(-\mathbf{K}\hat{\mathbf{T}}_2(\mathbf{x}) - \hat{\boldsymbol{\alpha}}(\mathbf{x})) \\ &= (\mathbf{A}_c - \mathbf{B}_c \mathbf{K}) \boldsymbol{\xi} + \mathbf{B}_c \mathbf{K} (\mathbf{T}_2 - \hat{\mathbf{T}}_2) + \mathbf{B}_c (\boldsymbol{\alpha} - \hat{\boldsymbol{\alpha}}) + \mathbf{B}_c (\mathcal{B} \hat{\mathcal{B}}^{-1} - \mathbf{I})(-\mathbf{K}\hat{\mathbf{T}}_2 - \hat{\boldsymbol{\alpha}}) \\ &\triangleq (\mathbf{A}_c - \mathbf{B}_c \mathbf{K}) \boldsymbol{\xi} + \mathbf{B}_c \boldsymbol{\varepsilon}_{\text{ndi}}(\mathbf{z}) \end{aligned} \quad (2.57)$$

where $\mathbf{I} \in \mathbb{R}^{m \times m}$ is an identity matrix. Using Eq. (2.12), the nominal INDI control for stabilization is given by

$$\Delta \bar{\mathbf{u}}_{\text{ndi}} = \mathcal{B}^{-1}(\mathbf{x}_0)(-\mathbf{K}\mathbf{T}_2(\mathbf{x}) - \mathbf{y}_0^{(\rho)}) \quad (2.58)$$

When applied using estimated models, Eq. (2.58) becomes

$$\Delta \mathbf{u}_{\text{ndi}} = \hat{\mathcal{B}}^{-1}(\mathbf{x}_0)(-\mathbf{K}\hat{\mathbf{T}}_2(\mathbf{x}) - \mathbf{y}_0^{(\rho)}) \quad (2.59)$$

and the closed-loop system dynamics are given by

$$\begin{aligned} \dot{\boldsymbol{\eta}} &= \mathbf{f}_0(\boldsymbol{\eta}, \boldsymbol{\xi}) \\ \dot{\boldsymbol{\xi}} &= (\mathbf{A}_c - \mathbf{B}_c \mathbf{K}) \boldsymbol{\xi} + \mathbf{B}_c \mathbf{K} (\mathbf{T}_2 - \hat{\mathbf{T}}_2) + \mathbf{B}_c \boldsymbol{\delta}(\mathbf{z}, \Delta t) + \mathbf{B}_c (\mathcal{B} \hat{\mathcal{B}}^{-1} - \mathbf{I})(-\mathbf{K}\hat{\mathbf{T}}_2 - \mathbf{y}_0^{(\rho)}) \\ &\triangleq (\mathbf{A}_c - \mathbf{B}_c \mathbf{K}) \boldsymbol{\xi} + \mathbf{B}_c \boldsymbol{\varepsilon}_{\text{ndi}}(\mathbf{z}, \Delta t) \end{aligned} \quad (2.60)$$

The regularly perturbed closed-loop dynamics given by Eqs. (2.57, 2.60) are both in the form of Eq. (2.27). The only difference is the value of the perturbation terms. Therefore, it is straightforward to derive the corollaries of Theorem 1 and Theorem 2 as:

Corollary 2 *If $\|\boldsymbol{\epsilon}_{\text{ndi}/\text{indi}}\|_2 \leq \bar{\epsilon}_{\text{ndi}/\text{indi}}$ is satisfied for all $\mathbf{z} \in \mathbb{R}^n$, and $\dot{\boldsymbol{\eta}} = \mathbf{f}_0(\boldsymbol{\eta}, \boldsymbol{\xi})$ is input-to-state stable, then the states \mathbf{z} of Eq. (2.57) and Eq. (2.60) are globally ultimately bounded by a class \mathcal{K} function of $\bar{\epsilon}_{\text{ndi}}$ and $\bar{\epsilon}_{\text{indi}}$, respectively.*

Corollary 3 *If $\|\boldsymbol{\epsilon}_{\text{ndi}/\text{indi}}\|_2 \leq \bar{\epsilon}_{\text{ndi}/\text{indi}}$ is satisfied for all $\mathbf{z} \in \mathbb{R}^n$, and the origin of $\dot{\boldsymbol{\eta}} = \mathbf{f}_0(\boldsymbol{\eta}, \mathbf{0})$ is exponentially stable, then there is a neighborhood D_z of $\mathbf{z} = \mathbf{0}$ and $\epsilon^* > 0$, such that for every $\mathbf{z}(0) \in D_z$ and $\bar{\epsilon}_{\text{ndi}/\text{indi}} < \epsilon^*$, the states \mathbf{z} of Eq. (2.57) and Eq. (2.60) are ultimately bounded by a class \mathcal{K} function of $\bar{\epsilon}_{\text{ndi}}$ and $\bar{\epsilon}_{\text{indi}}$, respectively.*

Although the closed-loop dynamics given by Eq. (2.57) and Eq. (2.60) have the same form, the perturbation terms $\boldsymbol{\epsilon}_{\text{ndi}}(\mathbf{z})$ and $\boldsymbol{\epsilon}_{\text{indi}}(\mathbf{z}, \Delta t)$ have different properties, which consequently influence the ultimate bounds of the state \mathbf{z} . This will be shown as follows:

The first perturbation term $\mathbf{K}(\mathbf{T}_2 - \hat{\mathbf{T}}_2)$ is identical in $\boldsymbol{\epsilon}_{\text{ndi}}$ (Eq. (2.57)) and $\boldsymbol{\epsilon}_{\text{indi}}$ (Eq. (2.60)). For the second perturbation term, since INDI control $\Delta \mathbf{u}_{\text{indi}}$ is based on the measurements or estimations of $\mathbf{y}_0^{(\rho)}$ instead of the dynamic model $\boldsymbol{\alpha}(\mathbf{x})$, the model uncertainty term $\boldsymbol{\alpha}(\mathbf{x}) - \hat{\boldsymbol{\alpha}}(\mathbf{x})$ in Eq. (2.57) is replaced by $\boldsymbol{\delta}(\mathbf{z}, \Delta t)$ (Eq. (2.60)) under INDI control. The influences of $\|\boldsymbol{\delta}(\mathbf{z}, \Delta t)\|_2$ can become negligible under sufficiently high sampling frequency, while $\|\boldsymbol{\alpha}(\mathbf{x}) - \hat{\boldsymbol{\alpha}}(\mathbf{x})\|_2$ is normally large for aerospace systems, mainly because of the difficulties of modeling the aerodynamics. The last terms of $\boldsymbol{\epsilon}_{\text{ndi}/\text{indi}}$ are mainly caused by the multiplicative uncertainties of the $\mathcal{B}(\mathbf{x})$ matrix, which were incorrectly omitted in the previous literature [10, 11, 13, 14]. Recall Eq. (2.59), the last term of $\boldsymbol{\epsilon}_{\text{indi}}$ can be written as

$$(\mathcal{B}\hat{\mathcal{B}}^{-1} - \mathbf{I})(-\mathbf{K}\hat{\mathbf{T}}_2 - \mathbf{y}_0^{(\rho)}) = (\mathcal{B}\hat{\mathcal{B}}^{-1} - \mathbf{I})\hat{\mathcal{B}}\Delta \mathbf{u}_{\text{indi}} = (\mathcal{B} - \hat{\mathcal{B}})\Delta \mathbf{u}_{\text{indi}} \quad (2.61)$$

Since $\Delta \mathbf{u}_{\text{indi}}$ is a control increment, $\|\mathcal{B} - \hat{\mathcal{B}}^{-1}\|_2 \|\Delta \mathbf{u}_{\text{indi}}\|_2$ can be reduced by increasing the sampling rate. On the contrary, recall Eq. (2.56), the last term of $\boldsymbol{\epsilon}_{\text{ndi}}$ equals

$$(\mathcal{B}\hat{\mathcal{B}}^{-1} - \mathbf{I})(-\mathbf{K}\hat{\mathbf{T}}_2 - \hat{\boldsymbol{\alpha}}) = (\mathcal{B}\hat{\mathcal{B}}^{-1} - \mathbf{I})\hat{\mathcal{B}}\mathbf{u}_{\text{ndi}} = (\mathcal{B} - \hat{\mathcal{B}})\mathbf{u}_{\text{ndi}} \quad (2.62)$$

which depends on the entire control term \mathbf{u}_{ndi} and is independent of Δt . When $\mathbf{u}_{\text{ndi}} \neq \mathbf{0}$, there exists a Δt such that $\|\Delta \mathbf{u}_{\text{indi}}\|_2 < \|\mathbf{u}_{\text{ndi}}\|_2$.

In summary, under sufficiently high sampling frequency, the norm of the closed-loop perturbation terms is smaller under INDI control in the presence of model uncertainties. As a result, according to Corollary 2, when the internal dynamics $\dot{\boldsymbol{\eta}} = \mathbf{f}_0(\boldsymbol{\eta}, \boldsymbol{\xi})$ are input-to-state stable, INDI control will result in smaller ultimate bounds for \mathbf{z} . Moreover, when only the origin of $\dot{\boldsymbol{\eta}} = \mathbf{f}_0(\boldsymbol{\eta}, \mathbf{0})$ is exponentially stable, it is easier for systems under INDI control to fulfill the boundedness condition $\bar{\epsilon}_{\text{ndi}/\text{indi}} < \epsilon^*$ in Corollary 3.

SENSING AND SINGULAR PERTURBATIONS

Based on preceding analyses, INDI control has shown promising inherent robustness to disturbances and regular perturbations without using any additional robust or adaptive

control technique. There are also other sources of perturbations, which increase the order of the system, such as actuator dynamics and higher-order elastic dynamics. These perturbations are classified into *singular perturbations* [5, 25]. Consider the singularly perturbed system model as [2]

$$\dot{\mathbf{x}} = \mathbf{f}(t, \mathbf{x}, \mathbf{z}_p, \epsilon), \quad \epsilon \dot{\mathbf{z}}_p = \mathbf{g}_z(t, \mathbf{x}, \mathbf{z}_p, \epsilon) \quad (2.63)$$

where the perturbed dynamics are decomposed into reduced (slow) and boundary-layer (fast) dynamics. According to the Tikhonov's theorem [2], when the null (quasi) equilibrium states of both the fast and slow dynamics are exponentially stable, there exists a constant $\epsilon_{\max} > 0$ such that the null equilibrium of the singularly perturbed system is exponentially stable for all $\epsilon < \epsilon_{\max}$. This parameter $\epsilon_{\max} > 0$ is referred to as the singular perturbation margin (SPM) in [25], and is equivalent to the phase margin of linear time-invariant systems in the sense of the bijective function [25].

Regarding the aerospace applications of INDI on angular rate control problems, the sensing or estimation of angular accelerations is needed [7, 10–14, 18–20]. Angular accelerometers are already available on the market [22], and a commonly used alternative way to estimate the angular accelerations is to differentiate the filtered angular rate signals [7, 11–14, 18–20]. Consequently, the estimations are lagged owing to the filtering process. Ref. [13, 14, 17, 18] propose to synchronize the input signal with the lagged estimations by imposing the same filter on the input. However, synchronization errors still exist in practice. Based on the preceding discussions, the system is able to sustain sufficiently small lags caused by filtering and actuator dynamics. This proposes an interesting research question of enlarging the singular perturbation margin of the closed-loop system. Possible solutions could be using predictive filters [10] or actuator compensators [26].

2.4. NUMERICAL VALIDATION

Since there have been extensive applications of INDI on aircraft [10, 15, 18–20], helicopter [11], micro air vehicle [13] and spacecraft [12] angular velocity control, this problem will not be repeated here. The numerical example in this section considers a rigid aircraft gust load alleviation (GLA) problem, where the vertical velocity is included in the inner-loop INDI controller. This idea originates from [15], but the old INDI derivation in [15] also has the blemishes mentioned before. Therefore, this GLA problem will be resolved here using the reformulated INDI control. Subsection 2.4.1 presents the aircraft and turbulence models. The INDI flight control is designed in subsection 2.4.2. A command tracking problem in a turbulence field is considered in subsection 2.4.3. The robustness of INDI to model uncertainties and external disturbances will be compared with NDI control in subsection 2.4.4.

2.4.1. AIRCRAFT AND TURBULENCE MODELS

The six-degree-of-freedom rigid aircraft dynamic equations defined in the body frame are given by

$$\dot{\mathbf{V}}_f = -\boldsymbol{\omega} \times \mathbf{V}_f + \frac{\mathbf{F}}{m}, \quad \dot{\boldsymbol{\omega}} = -\mathbf{J}^{-1} \boldsymbol{\omega} \times \mathbf{J} \boldsymbol{\omega} + \mathbf{J}^{-1} \mathbf{M} \quad (2.64)$$

where $\mathbf{V}_f = [V_x, V_y, V_z]^T$ indicates the velocity of the aircraft center of mass (c.m.) relative to the inertial axis expressed in the body axis, and $\boldsymbol{\omega} = [p, q, r]^T$ represents the angular velocity. m is the total mass and \mathbf{J} is the inertia matrix. \mathbf{F} and \mathbf{M} are the total forces and moments, which can be expanded as:

$$\begin{aligned}\mathbf{F} &= \mathbf{F}_a(\mathbf{V}_f, \boldsymbol{\omega}, \mathbf{V}_w) + \mathbf{F}_T(\mathbf{V}_f, \delta_p) + \mathbf{F}_{a_u}(\mathbf{V}_f, \boldsymbol{\omega})\mathbf{u} + \mathbf{F}_G \\ \mathbf{M} &= \mathbf{M}_a(\mathbf{V}_f, \boldsymbol{\omega}, \mathbf{V}_w) + \mathbf{M}_{a_u}(\mathbf{V}_f, \boldsymbol{\omega})\mathbf{u}\end{aligned}\quad (2.65)$$

In the preceding equation, $\mathbf{u} = [\delta_e, \delta_r, \delta_{ar}, \delta_{al}]^T$ denotes the elevator, rudder, right and left aileron deflection angles. \mathbf{F}_a and \mathbf{M}_a denote the aerodynamic forces and moments when $\mathbf{u} = \mathbf{0}$. \mathbf{V}_w is the wind velocity. $\mathbf{F}_{a_u}\mathbf{u}$ and $\mathbf{M}_{a_u}\mathbf{u}$ represent the control forces and moments generated by the aerodynamic control surfaces. \mathbf{F}_T is the thrust, as a function of throttle δ_p . \mathbf{F}_G is the gravitational force.

The aircraft model for simulations is set up using the aerodynamic, inertia and geometric data in [27]. The aerodynamic model is based on the quasi-steady strip theory [27, 28]. This aircraft is abstracted to multiple two dimensional aerodynamic surfaces. There are four aerodynamic control surfaces, each of them contains n_p strips. There are also six aerodynamic surfaces, namely the wing, horizontal and vertical tails, horizontal and vertical lifting surfaces of the fore-fuselage, the engine pylon. Each of these aerodynamic surfaces contains n_k strips. \mathbf{r}_i denotes the distance vector from the c.m. to the aerodynamic center of the i -th strip. The local airspeed of the i -th strip expressed in the body frame is $\mathbf{V}_{a,i} = \mathbf{V}_f + \boldsymbol{\omega} \times \mathbf{r}_i - \mathbf{V}_{w,i}$, where $\mathbf{V}_{w,i}$ is the local wind velocity [29, 30]. In this chapter, $\mathbf{V}_{w,i}$ is calculated in real-time by interpolating the spatial turbulence field at the aerodynamic center of the i -th strip, and then transformed to the body frame. The gust penetration effect [15, 29, 30] is considered since $\mathbf{V}_{w,i}$ depends on the spatial location of the i -th strip. A two dimensional vertical von Kármán turbulence field is presented in Fig. 2.1, in which X_E and Y_E represent the positions in the inertial frame. The turbulence velocity is in unit m/s. The turbulence length scale equals $L_g = 762$ m, and the variance equals $\sigma = 3$ m/s. Fig. 2.1 also shows a sketch map of the aircraft exposed to the turbulence field, the strips on the wing and the horizontal tail are illustrated.

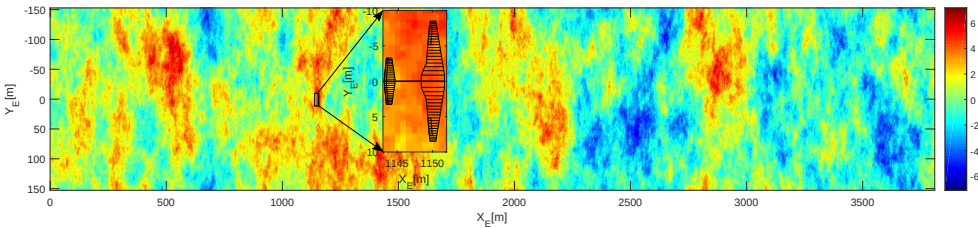


Figure 2.1: A 2D von Kármán vertical turbulence field with $L_g = 762$ m, $\sigma = 3$ m/s.

For the four control surfaces, the distributed force $\mathbf{f}_{u,i}$ on the i -th strip is a function of $\mathbf{V}_{a,i}$, \mathbf{u} and the local derivatives of lift with respect to \mathbf{u} , which is denoted as $C_{L_{u,i}}$. The resultant forces and moments are $\mathbf{F}_{a_u}\mathbf{u} = \sum_i \mathbf{f}_{u,i}$, $\mathbf{M}_{a_u}\mathbf{u} = \sum_i \mathbf{r}_i \times \mathbf{f}_{u,i}$. For the strips on the k -th aerodynamic surface, the distributed force $\mathbf{f}_{a,i}$ depends on the local airspeed

$V_{a,i}$, and the local aerodynamic coefficients. The resultant forces and moments are $F_a = \sum_i \mathbf{f}_{a,i}$, $M_a = \sum_i \mathbf{r}_i \times \mathbf{f}_{a,i}$.

2.4.2. FLIGHT CONTROL DESIGN

Using Eq. (2.65), Eq. (2.64) can be rewritten in the form of $\dot{\mathbf{x}} = \mathbf{f}(\mathbf{x}) + \mathbf{G}(\mathbf{x})\mathbf{u} + \mathbf{d}$ as:

$$\begin{aligned} \begin{bmatrix} \dot{V}_f \\ \dot{\boldsymbol{\omega}} \end{bmatrix} &= \begin{bmatrix} -\boldsymbol{\omega} \times \mathbf{V}_f + \frac{1}{m}(\mathbf{F}_a(\mathbf{V}_f, \boldsymbol{\omega}, \mathbf{0}) + \mathbf{F}_T + \mathbf{F}_G) \\ -\mathbf{J}^{-1}\boldsymbol{\omega} \times \mathbf{J}\boldsymbol{\omega} + \mathbf{J}^{-1}\mathbf{M}_a(\mathbf{V}_f, \boldsymbol{\omega}, \mathbf{0}) \end{bmatrix} + \begin{bmatrix} \frac{1}{m}\mathbf{F}_{a_u} \\ \mathbf{J}^{-1}\mathbf{M}_{a_u} \end{bmatrix} \mathbf{u} \\ &+ \begin{bmatrix} \frac{1}{m}(\mathbf{F}_a(\mathbf{V}_f, \boldsymbol{\omega}, \mathbf{V}_w) - \mathbf{F}_a(\mathbf{V}_f, \boldsymbol{\omega}, \mathbf{0})) \\ \mathbf{J}^{-1}(\mathbf{M}_a(\mathbf{V}_f, \boldsymbol{\omega}, \mathbf{V}_w) - \mathbf{M}_a(\mathbf{V}_f, \boldsymbol{\omega}, \mathbf{0})) \end{bmatrix} \end{aligned} \quad (2.66)$$

where the aerodynamic influences of turbulence are lumped in the disturbance vector \mathbf{d} . Consider an output tracking problem, and choose $\mathbf{y} = \mathbf{H}\mathbf{x} = [V_z, p, q, r]^T$, where \mathbf{H} is a Boolean selection matrix. Based on Eq. (2.5), the vector relative degree of this system equals $\boldsymbol{\rho} = [1, 1, 1, 1]^T$, $\boldsymbol{\alpha}(\mathbf{x}) = \mathbf{H}\mathbf{f}(\mathbf{x})$, $\mathcal{B}(\mathbf{x}) = \mathbf{H}\mathbf{G}(\mathbf{x})$. According to Eq. (2.22), the external states vector $\boldsymbol{\xi} = \mathbf{y}$. There are also two dimensional internal dynamics in this application case. Although the input-to-state stability of the internal dynamics is not easy to prove, the analysis of the origin stability of $\mathbf{f}_d(\boldsymbol{\eta}, \mathbf{0}, \mathbf{0})$ is practical. The two dimensional submanifold for the zero dynamics is given by

$$\mathbf{Z}^* = \{\mathbf{x} \in \mathbb{R}^6, V_z - V_z^* = p = q = r = 0\} \quad (2.67)$$

where V_z^* is the vertical velocity in trim condition. Define $A(t) = \frac{\partial \mathbf{f}_d}{\partial \boldsymbol{\eta}}|_{\boldsymbol{\eta}=\mathbf{0}}$, then $\boldsymbol{\eta} = \mathbf{0}$ is an exponentially stable equilibrium point of \mathbf{f}_d if and only if it is an exponentially stable equilibrium point of the linear system $\dot{\boldsymbol{\eta}} = A(t)\boldsymbol{\eta}$ [2]. This allows the origin stability of the zero dynamics to be easily tested via linearization. The origin of $\boldsymbol{\eta} = \mathbf{f}_d(\boldsymbol{\eta}, \mathbf{0}, \mathbf{0})$ has been tested to be exponentially stable for this model.

Actuator dynamics and limits are considered in this validation. Actuators for aerodynamic control surfaces are modeled as first-order systems with transfer function $A(s) = \frac{-20}{s+20}$. The deflection limits of ailerons, elevator and rudder are $\pm 35^\circ$, $\pm 25^\circ$, $\pm 25^\circ$, respectively. The rate limit for ailerons is $100^\circ/\text{s}$ and is $60^\circ/\text{s}$ for elevator and rudder. Constant throttle δ_p^* is used in the simulations. An additional velocity controller using throttle can be designed if desired. The simulation frequency (difference from the sampling frequency) is 2000 Hz, which is chosen to be sufficiently high to simulate the property of the continuous dynamics in real life. Fig. 2.2 illustrates a block diagram of INDI applied considering actuator dynamics.

2.4.3. COMMAND TRACKING IN A TURBULENCE FIELD

This subsection considers a command tracking problem in the presence of external disturbances. During simulations, the aircraft is flying through the von Kármán turbulence field shown in Fig. 2.1. Symmetrical excitations are assumed in this subsection, namely the local gust velocities $\mathbf{V}_{w,i}$ are interpolated using the spatial locations of the right-hand side strips of the aircraft. $\mathbf{V}_{w,i}$ of the left-hand side strips are assumed to be symmetrical to the right. Asymmetrical excitations will be considered in subsection 2.4.4. Using the flight controller designed in subsection 2.4.2, and referring to Corollary 1, the $\boldsymbol{\eta}$ and reference tracking error \mathbf{e} can then be concluded to be ultimately bounded under

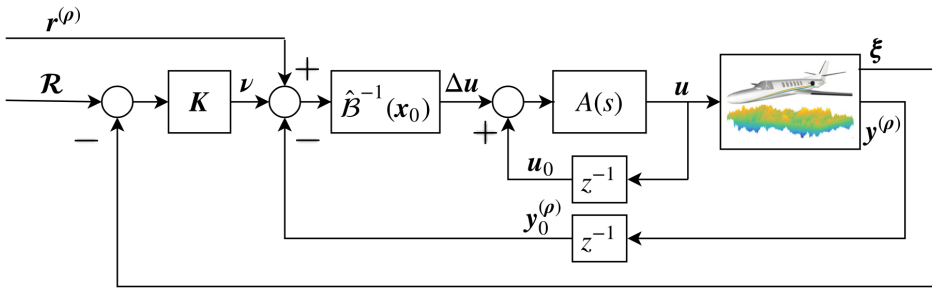


Figure 2.2: The block diagram for a reference tracking problem applied considering actuator dynamics.

small perturbations. Moreover, the ultimate bounds have been proven to be monotonically decreasing functions of K gains and the sampling frequency in subsection 2.3.2. The simulations in this subsection will test the fidelity of these conclusions when actuator dynamics and limits are considered.

Set the references for $[V_z, p, r]^T$ to be their trim values $[V_z^*, 0, 0]^T$, and the reference signal for q is designed as a sinusoid signal with amplitude of $1.5^\circ/\text{s}$ and frequency of 1.5 rad/s . The initial errors are $e(t=0) = [0.5 \text{ m/s}, 0^\circ/\text{s}, 2^\circ/\text{s}, 0^\circ/\text{s}]^T$. Design the gain matrix as $K = a \cdot I_{4 \times 4}$, $a > 0$. In view of Fig. 2.2, there are three sampling processes in this control law, namely the measurement of $y_0^{(\rho)}$, ξ and the actuator position u_0 . The sampling interval Δt will be varied in the subsequent analyses for testing its influences on the ultimate bounds.

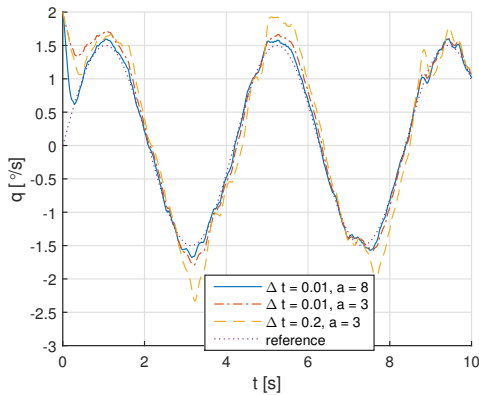


Figure 2.3: Pitch rate tracking responses.

In view of Fig. 2.3 and Fig. 2.4, the aircraft is able to track the pitch rate command using all sets of controller parameters. When $a = 3$, the ultimate bounds for $\Delta t = 0.01 \text{ s}$ are $|e_{V_z}| = 0.23 \text{ m/s}$, $|e_q| = 0.30^\circ/\text{s}$, which degrade into larger ultimate bounds of $|e_{V_z}| = 0.68 \text{ m/s}$, $|e_q| = 0.85^\circ/\text{s}$ when the sampling interval increased into $\Delta t = 0.2 \text{ s}$. Using the same sampling interval $\Delta t = 0.01 \text{ s}$, when the outer loop gains increased from $K = 3 \cdot I_{4 \times 4}$

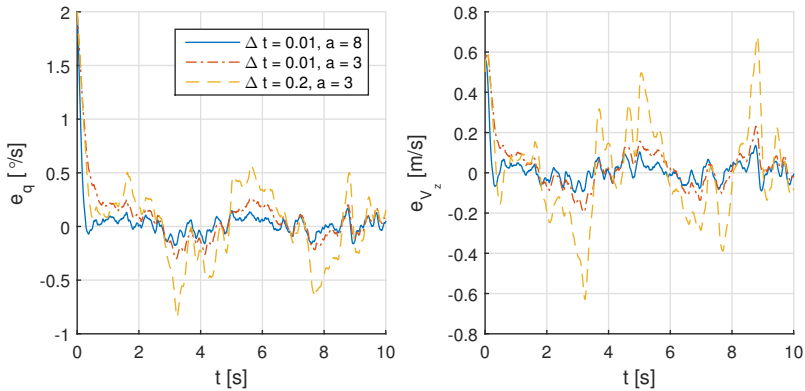


Figure 2.4: Tracking error responses for pitch rate and vertical velocity.

to $\mathbf{K} = 8 \cdot \mathbf{I}_{4 \times 4}$, the closed-loop system responds faster to the errors, which results into smaller ultimate bounds. The control surface deflections are illustrated by Fig. 2.5.

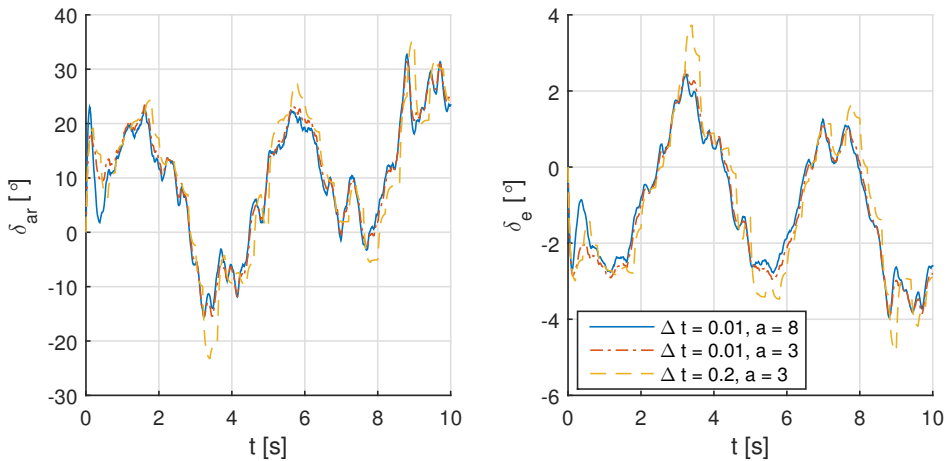


Figure 2.5: Control surface deflections.

Fig. 2.6 shows the ultimate bounds of e_{V_z} and e_q using various controller parameters. The tested sampling intervals varies from $\Delta t = 0.001$ s to $\Delta t = 0.2$ s. As can be seen from Fig. 2.6, in general, for a given gain matrix $\mathbf{K} = a \cdot \mathbf{I}_{4 \times 4}$, the ultimate bounds decrease as the sampling interval decreases. This trend of decrease becomes slower around $\Delta t = 0.12$ s as the contour lines become sparser. Further decreasing the sampling interval does improve the performance but would impose higher requirements on the hardware.

On the other hand, for a given Δt , as a increases from $a = 1$ to $a = 13$, the ultimate bounds decrease first, reaching a minimum around $a \approx 8$, and then show a trend of increase as a further increases. As analyzed before, the ultimate bounds will be smaller for

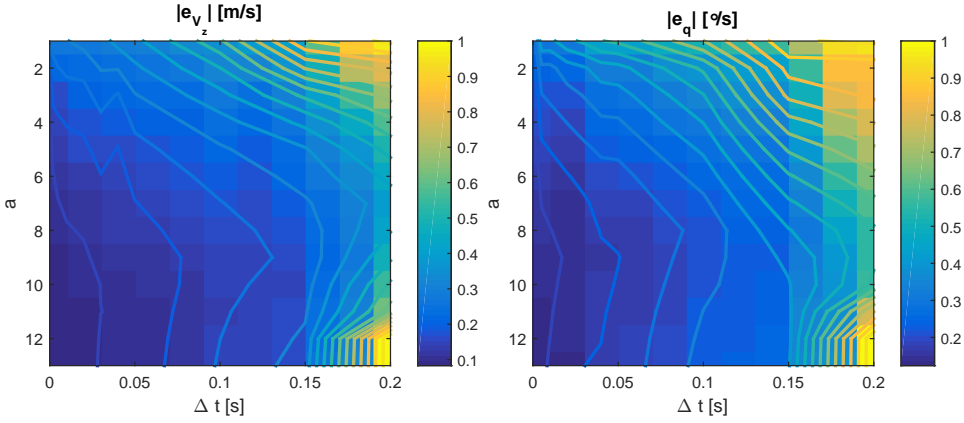


Figure 2.6: The influences of sampling interval and outer-loop gains on the ultimate bounds.

larger \mathbf{K} gains when ideal actuators are applied. However, since actuators have bandwidth, rate and position limits, high-gain control can impose unachievable commands on actuators, which consequently degrades the performance for $a > 8$ and potentially leads to divergence. High-gain control also amplifies the measurement noise in practice.

In summary, simulation results in this subsection verified the ultimate boundedness of the states under INDI control, especially when actuator dynamics and limits are considered. The influences of \mathbf{K} gains and Δt on the ultimate bounds are also verified.

2.4.4. ROBUSTNESS COMPARISONS WITH NONLINEAR DYNAMIC INVERSION

In this subsection, the robustness of the reformulated INDI control will be compared with nonlinear dynamic inversion (NDI) control, in the presence of asymmetrical turbulence excitations and model uncertainties. Eqs. (2.56, 2.58) formulate the NDI and INDI control laws when the estimated models are used. Since $\xi = \mathbf{y} = \mathbf{H}\mathbf{x}$, then $\mathbf{T}_2(\mathbf{x}) = \hat{\mathbf{T}}_2(\mathbf{x}) = \mathbf{H}\mathbf{x}$ in Eqs. (2.56, 2.58). During simulations, the aircraft is gradually flying through the 2D von Kármán turbulence field shown in Fig. 2.1, and the turbulence velocity on each aerodynamic strip is independently interpolated as $\mathbf{V}_{w,i}$. The references for $\xi = [V_z, p, q, r]^T$ are illustrated in Fig. 2.7. The reference for V_z equals its trim value V_z^* . The reference for p is a 3211 signal with magnitude of $5^\circ/\text{s}$ realized by smoothly combined sigmoid functions. The sigmoid function $f(t) = 1/(1 + e^{-t})$ is chosen because of its differentiable property up to any order. The reference for q is a smooth realization of a doublet signal with magnitude of $1.5^\circ/\text{s}$. The reference for r is a sinusoid signal with magnitude of $3^\circ/\text{s}$ and frequency of 1 rad/s. Typical testing signals are chosen as references for comparing the effectiveness and NDI and INDI. In practice, these reference signals are provided by outer-loop controllers for various flight control tasks. For example, the reference for V_z can be designed for load alleviation purposes [15], the reference for r can be designed for minimizing the side-slip angle [10], the references for p and q can be designed for the attitude tracking of ϕ and θ [7], etc. The sampling frequency

used in this subsection is 100 Hz. For fair comparisons, the control gain matrices for both NDI and INDI are identical to $\mathbf{K} = 8 \cdot \mathbf{I}_{4 \times 4}$.

The tracking performance of NDI and INDI in the 2D von Kármán turbulence field (Fig. 2.1) is compared in Figs. 2.7-2.9. Model uncertainties are not introduced in this simulation yet, i.e., $\hat{\boldsymbol{\alpha}} = \boldsymbol{\alpha}$, $\hat{\mathcal{B}} = \mathcal{B}$. However, the disturbance \mathbf{d} as a function of \mathbf{V}_w (Eq. (2.66)) is non-zero. Since the turbulence excitations are asymmetric, lateral states including p and r are also disturbed by \mathbf{d} . In view of Fig. 2.7 and Fig. 2.8, aircraft using INDI control can better track the references in the turbulence field. The rms values of the tracking errors for this simulation case are summarized in the first two rows of Table 2.1, in which INDI shows smaller rms value of errors in all the four controlled channels. These results verify the analyses in subsection 2.3.2, that the ultimate bounds for $\boldsymbol{\xi}$ are only influenced by the disturbance increments $\Delta \mathbf{d}$, and the main influences of \mathbf{d}_0 have been included in the measurements/estimations of $\hat{\boldsymbol{\xi}}_0$. Fig. 2.9 shows the control inputs, where INDI responses more actively for alleviating the turbulence influences. Moreover, the control surface deflection angles are within the limits under both NDI and INDI control.

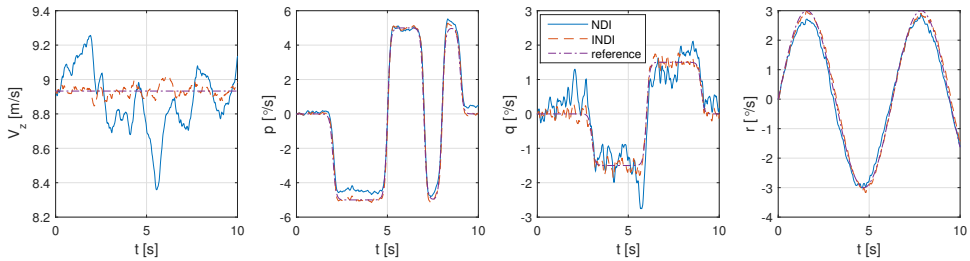


Figure 2.7: Command tracking in a 2D turbulence field.

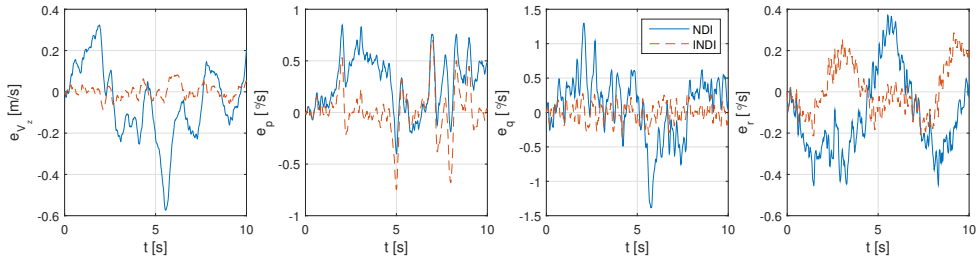


Figure 2.8: Tracking errors in a 2D turbulence field.

Referring to subsection 2.3.2, when implementing the control methods, INDI control only needs the estimated control effectiveness matrix $\hat{\mathcal{B}}$, while NDI requires both $\hat{\boldsymbol{\alpha}}$ and $\hat{\mathcal{B}}$. Recall Eq. (2.66), $\hat{\boldsymbol{\alpha}}$ and $\hat{\mathcal{B}}$ contain the inertia and aerodynamic parameters, whose accurate estimations are very difficult to obtain in practice. Herein, the robustness of NDI and INDI to model uncertainties will be compared. Fig. 2.10-2.12 present the reference tracking responses of the aircraft in the turbulence field (Fig. 2.1). The estimated model $\hat{\mathcal{B}} = 1.3\mathcal{B}$ is used by both NDI and INDI. In other words, both controllers

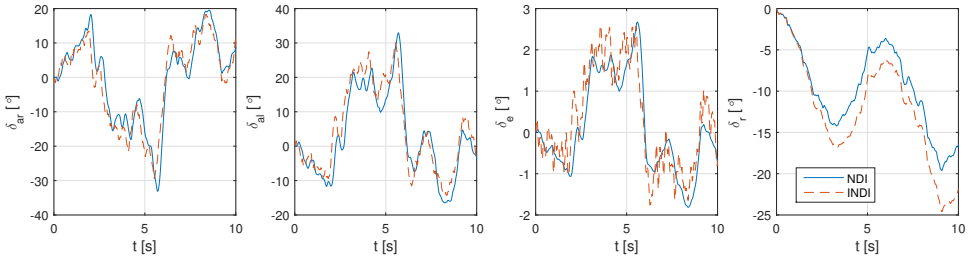


Figure 2.9: Control inputs in the presence of external disturbances.

Table 2.1: RMS values of the tracking errors under NDI and INDI control.

Controllers	rms(e_{V_z}) [m/s]	rms(e_p) [deg/s]	rms(e_q) [deg/s]	rms(e_r) [deg/s]
NDI	0.188	0.387	0.465	0.230
INDI	0.033	0.223	0.130	0.122
NDI uncertain	0.323	0.999	0.564	0.565
INDI uncertain	0.047	0.312	0.155	0.140

overestimate the control effectiveness matrix by 30%. On the other hand, the perfect model $\hat{\alpha} = \alpha$ is used by NDI, even so, the tracking performance of NDI is still inferior than INDI as presented in Fig. 2.10 and Fig. 2.11.

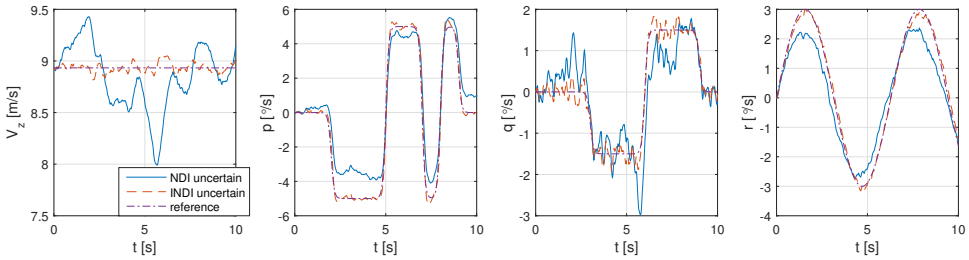


Figure 2.10: Command tracking in a 2D turbulence field with mismatched $\hat{\mathcal{B}}$.

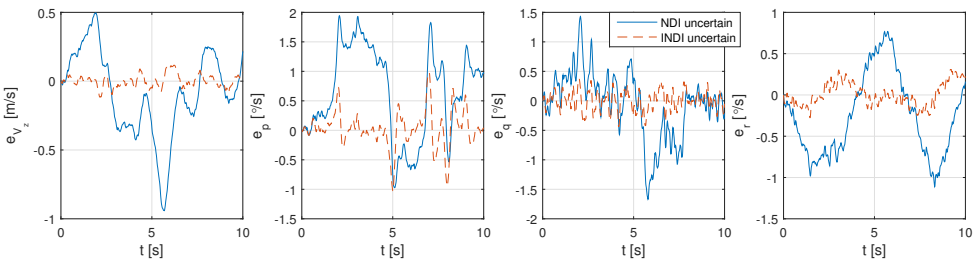


Figure 2.11: Tracking errors in a 2D turbulence field with mismatched $\hat{\mathcal{B}}$.

The rms values of the tracking errors in the presence of external disturbances and model uncertainties are presented in the last two rows of Table 2.1. It can be seen from Fig. 2.10, Fig. 2.11 and Table 2.1 that INDI has better robustness than NDI. When using NDI control, the rms values of the errors in Fig. 2.11 are respectively increased by 71.8%, 158%, 21.3%, 146% as compared to errors in Fig. 2.8. By contrast, INDI is less influenced by the mismatches between $\hat{\mathcal{B}}$ and \mathcal{B} , as the rms values of the errors in Fig. 2.11 are increased by 42.4%, 39.9%, 19.2%, 14.8% as compared to errors in Fig. 2.8. Furthermore, Table 2.1 shows that when mismatched $\hat{\mathcal{B}}$ is used, the rms values of the tracking errors under INDI control are at least three times smaller than the values under NDI control. These results verify the analyses in subsection 2.3.2. In addition, the control surface deflections are illustrated in Fig. 2.12, where both INDI and NDI satisfy the actuator constrains.

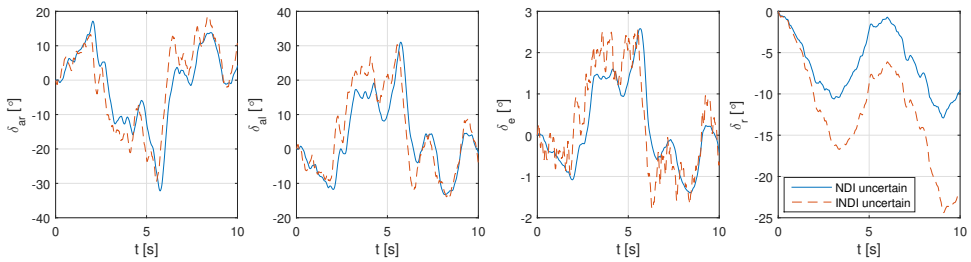


Figure 2.12: Control inputs in the presence of external disturbances and model uncertainties.

The results of a Monte-Carlo simulation containing 1000 samples of uncertain models are presented in Fig. 2.13. Both aerodynamic and inertia uncertainties are added to the estimated models $\hat{\alpha}$ and $\hat{\mathcal{B}}$. As presented in subsection 2.4.1, the aerodynamic model of the present aircraft is based on strip theory. Each of the six aircraft components or the four aerodynamic control surfaces contains n_k/n_p strips with local aerodynamic coefficients. Herein, the slope of lift curve uncertainties for the k -th aircraft component are modeled as normally distributed real numbers as:

$$\Delta_k \sim \mathcal{N}(0, \sigma_k^2), \quad \sigma_k = \frac{0.3}{n_k} \sum_{i=1}^{i=n_k} C_{L\alpha,i} \quad (2.68)$$

which means that for each aircraft component k , the mean value of the slope of lift curve uncertainties equals zero, and the standard deviation σ_k is chosen as 30% of the average $C_{L\alpha}$ value of this component. Analogously, for the p -th aerodynamic control surface:

$$\Delta_p \sim \mathcal{N}(0, \sigma_p^2), \quad \sigma_p = \frac{0.3}{n_p} \sum_{i=1}^{i=n_p} C_{L_u,i} \quad (2.69)$$

Δ_p in the preceding equation represent the uncertainties for the derivatives of lift with respect to \mathbf{u} . The mean value of Δ_p equals zero, and the standard deviation σ_p is chosen as 30% of the average C_{L_u} value of the p -th control surface. It is worth noting that this step up is more elaborate than introducing uncertainties to the conventional stability and control derivatives (e.g., $C_{m\alpha}$, C_{m_q} , $C_{n\beta}$, C_{n_r} , $C_{m\delta_e}$, $C_{n\delta_r}$, etc.), by virtue

of the usage of the strip theory [28]. The uncertainties for mass are assumed to have normal distribution, with $\mu_m = 0$ and σ_m equals 10% of the nominal mass. Normally disturbed uncertainties are also introduced to the inertia parameters J_{xx} , J_{yy} , J_{zz} , J_{xz} . For each of the four parameters, the mean value of uncertain equals zero, and the standard derivation is taken as 25% of the nominal inertia value.

This Monte-Carlo simulation considers the command tracking task in the presence of external disturbance (Fig. 2.1) and model uncertainties. The references for ξ are the same as presented in Fig. 2.7 and Fig. 2.10. Simulation results with $\text{rms}\{e_{V_z}\} > 50$ m/s or $\max\{\text{rms}\{e_p\}, \text{rms}\{e_q\}, \text{rms}\{e_r\}\} > 50^\circ/\text{s}$ are considered as the controller fails to track the commands. Among all the 1000 samples, 31 cases fail under NDI control, while there is no failure case under INDI control. The reason for the failure cases under NDI control can be revealed by Corollary 2 and Corollary 3 that the ultimate boundedness of the states can only be guaranteed if ϵ_{ndi} is bounded. Also, when only the origin of $\dot{\eta} = f_0(\eta, \mathbf{0}, \mathbf{0})$ is guaranteed to be exponentially stable, the uncertainties that NDI can sustain are limited, i.e., $\bar{\epsilon}_{\text{ndi}} < \epsilon^*$ (Corollary 3). However, since ϵ_{ndi} contains both $\alpha - \hat{\alpha}$ and $(\mathcal{B} - \hat{\mathcal{B}}^{-1})\mathbf{u}_{\text{ndi}}$ (Eqs. (2.57), (2.62)), it can become unbounded in severe perturbation circumstances, especially when the actuators have nonlinear constrains.

According to the analyses in subsection 2.3.2, even for the cases that ϵ_{ndi} is bounded, the norm value of ϵ_{ndi} is still larger than that of ϵ_{indi} . As a consequence, the states under NDI control also have larger ultimate bounds in the presence of perturbations. This is verified by the box plots in Fig. 2.13, in which the 31 failure cases under NDI control have been discarded. The interquartile range (IQR) values and the medians of $\text{rms}(e_i)$, $i = V_z, p, q, r$ are summarized in Table 2.2. It can be seen from Fig. 2.13 and Table 2.2 that the robust performance of NDI is significantly degraded by ϵ_{ndi} (Eq. (2.57)). By contrast, INDI is more robust to model uncertainties and disturbances, as IQR $\{\text{rms}(e_i)\}$ using INDI control are at least one order of magnitude smaller than that under NDI control for all $i = V_z, p, q, r$. Furthermore, the median values of $\text{rms}(e_i)$ under INDI control are at least three times smaller than that using NDI control, for all $i = V_z, p, q, r$.

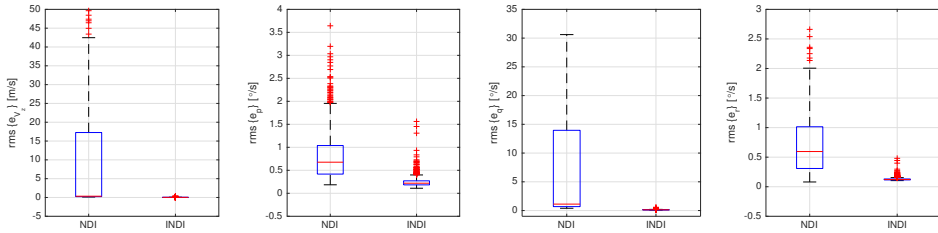


Figure 2.13: Box plots of a Monte-Carlo simulation for robustness comparisons between NDI and INDI.

2.5. CONCLUSIONS

This chapter reformulates the incremental nonlinear dynamic inversion (INDI) control without using the time-scale separation principle, and generalizes it for systems with arbitrary relative degree. Using Lyapunov methods and nonlinear system perturbation

Table 2.2: IQR and median values of $\text{rms}(e_i)$, $i = V_z, p, q, r$ under NDI and INDI control.

Control	Metrics	$i = V_z$ [m/s]	$i = p$ [deg/s]	$i = q$ [deg/s]	$i = r$ [deg/s]
NDI	IQR $\{\text{rms}(e_i)\}$	17.04	0.621	13.27	0.706
	median $\{\text{rms}(e_i)\}$	0.339	0.677	1.119	0.595
INDI	IQR $\{\text{rms}(e_i)\}$	0.014	0.088	0.036	0.016
	median $\{\text{rms}(e_i)\}$	0.032	0.220	0.129	0.122

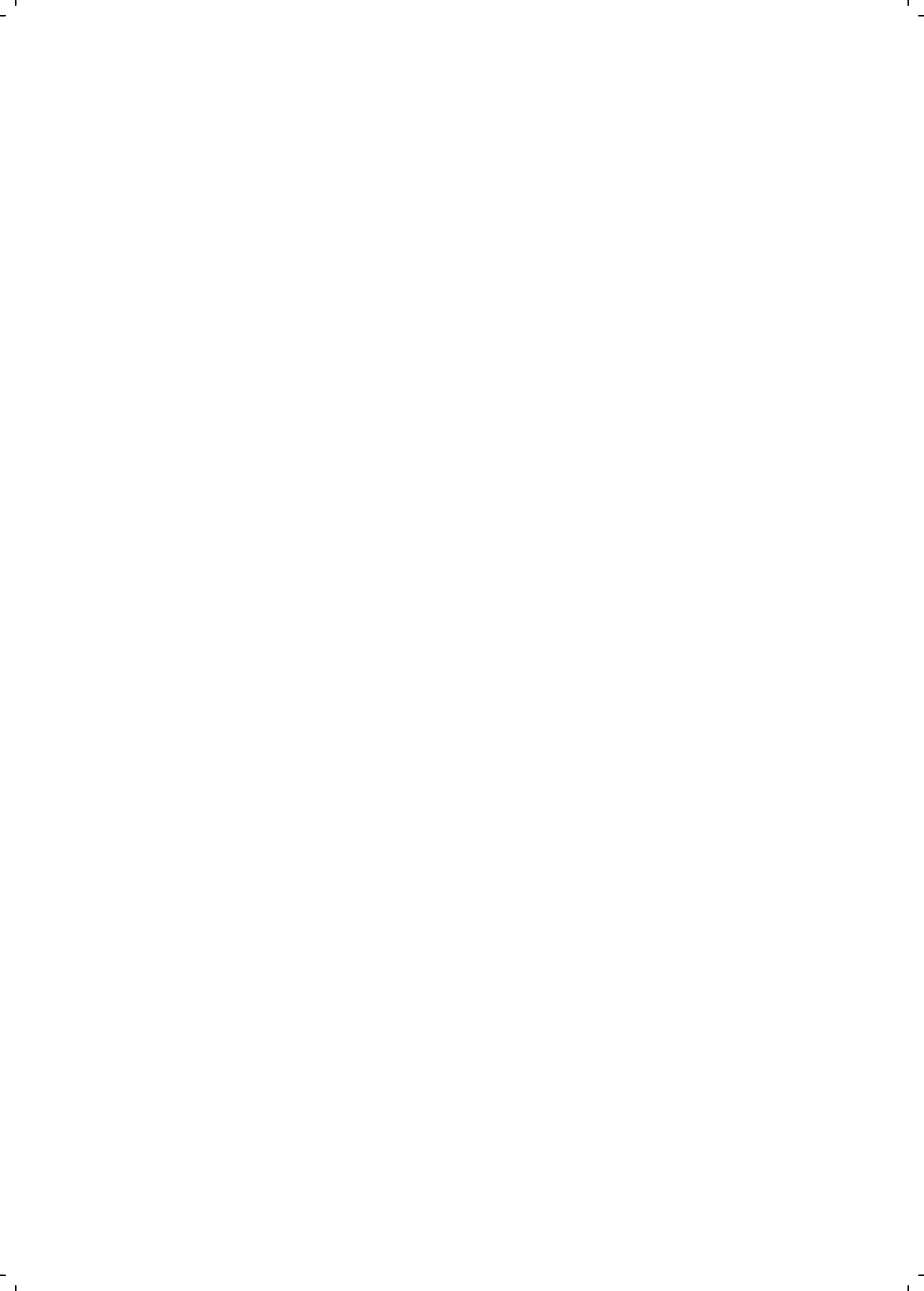
theories, the state of the closed-loop system is proved to be ultimately bounded by a class \mathcal{N} function of the perturbation bounds. There is no restriction on the perturbation value and the initial condition if the internal dynamics are input-to-state stable. Otherwise, corresponding restrictions are needed. Disturbances are shown to directly perturb the internal dynamics while perturbing the external dynamics only by their increments, which contributes to the better disturbance rejection capability of the INDI method. Moreover, INDI is shown to be more robust to regular perturbations than nonlinear dynamic inversion (NDI), without using any additional robust or adaptive techniques. It can also resist certain region of singular perturbations. Finally, numerical comparisons with NDI and a Monte-Carlo simulation demonstrate the effectiveness of the reformulated INDI control, even in the presence of model uncertainties and external disturbances.

REFERENCES

- [1] J.-J. E. Slotine and W. Li, *Applied Nonlinear Control* (NJ: Prentice Hall, Englewood Cliffs, 1991).
- [2] H. K. Khalil, *Nonlinear Systems* (Prentice-Hall, New Jersey, 2002).
- [3] J. Reiner, G. J. Balas, and W. L. Garrard, *Flight control design using Robust dynamic inversion and time-scale separation*, *Automatica* **32**, 1493 (1996).
- [4] H. Lee, S. Reiman, C. Dillon, and H. Youssef, *Robust Nonlinear Dynamic Inversion Control for a Hypersonic Cruise Vehicle*, *AIAA Guidance, Navigation, and Control Conference and Exhibit*, 1 (2007).
- [5] A. Hodel, M. Whorton, and J. Zhu, *Stability Metrics for Simulation and Flight-Software Assessment and Monitoring of Adaptive Control Assist Compensators*, in *AIAA Guidance, Navigation and Control Conference and Exhibit* (American Institute of Aeronautics and Astronautics, Honolulu, Hawaii, 2008) pp. 1–25.
- [6] T. Lombaerts, *Fault Tolerant Flight Control, A Physical Model Approach*, Ph.D. thesis, Delft University of Technology (2010).
- [7] P. Lu, E. van Kampen, C. de Visser, and Q. P. Chu, *Aircraft fault-tolerant trajectory control using Incremental Nonlinear Dynamic Inversion*, *Control Engineering Practice* **57**, 126 (2016).

- [8] P. Smith, *A Simplified Approach to Nonlinear Dynamic Inversion Based Flight Control*, in *23rd Atmospheric Flight Mechanics Conference* (AIAA, Reston, VA, 1998).
- [9] B. Bacon, A. Ostroff, and S. Joshi, *Reconfigurable NDI controller using inertial sensor failure detection & isolation*, *IEEE Transactions on Aerospace and Electronic Systems* **37**, 1373 (2001).
- [10] S. Sieberling, Q. P. Chu, and J. A. Mulder, *Robust Flight Control Using Incremental Nonlinear Dynamic Inversion and Angular Acceleration Prediction*, *Journal of Guidance, Control, and Dynamics* **33**, 1732 (2010).
- [11] P. Simplício, M. Pavel, E. van Kampen, and Q. P. Chu, *An acceleration measurements-based approach for helicopter nonlinear flight control using Incremental Nonlinear Dynamic Inversion*, *Control Engineering Practice* **21**, 1065 (2013).
- [12] P. Acquatella, W. Falkena, E. van Kampen, and Q. P. Chu, *Robust Nonlinear Spacecraft Attitude Control using Incremental Nonlinear Dynamic Inversion*. in *AIAA Guidance, Navigation, and Control Conference* (American Institute of Aeronautics and Astronautics, Minneapolis, Minnesota, 2012) pp. 1–20.
- [13] E. J. J. Smeur, Q. P. Chu, and G. C. H. E. de Croon, *Adaptive Incremental Nonlinear Dynamic Inversion for Attitude Control of Micro Air Vehicles*, *Journal of Guidance, Control, and Dynamics* **39**, 450 (2016).
- [14] E. J. J. Smeur, G. C. H. E. de Croon, and Q. P. Chu, *Gust disturbance alleviation with Incremental Nonlinear Dynamic Inversion*, in *2016 IEEE/RSJ International Conference on Intelligent Robots and Systems (IROS)* (IEEE, 2016) pp. 5626–5631.
- [15] X. Wang, E. van Kampen, and Q. P. Chu, *Gust Load Alleviation and Ride Quality Improvement with Incremental Nonlinear Dynamic Inversion*, in *AIAA Atmospheric Flight Mechanics Conference* (American Institute of Aeronautics and Astronautics, Grapevine, Texas, 2017) pp. 1–21.
- [16] Y. Huang, D. M. Pool, O. Stroosma, Q. P. Chu, and M. Mulder, *A Review of Control Schemes for Hydraulic Stewart Platform Flight Simulator Motion Systems*, in *AIAA Modeling and Simulation Technologies Conference* (American Institute of Aeronautics and Astronautics, San Diego, California, 2016) pp. 1–14.
- [17] Y. Huang, D. Pool, O. Stroosma, and Q. P. Chu, *Incremental Nonlinear Dynamic Inversion Control for Hydraulic Hexapod Flight Simulator Motion Systems*, *IFAC-PapersOnLine* **50**, 4294 (2017).
- [18] F. Grondman, G. Looye, R. O. Kuchar, Q. P. Chu, and E. van Kampen, *Design and Flight Testing of Incremental Nonlinear Dynamic Inversion-based Control Laws for a Passenger Aircraft*, in *2018 AIAA Guidance, Navigation, and Control Conference*, January (American Institute of Aeronautics and Astronautics, Kissimmee, Florida, 2018).

- [19] I. Matamoros and C. C. de Visser, *Incremental Nonlinear Control Allocation for a Tailless Aircraft with Innovative Control Effectors*, in *2018 AIAA Guidance, Navigation, and Control Conference*, January (American Institute of Aeronautics and Astronautics, Kissimmee, Florida, 2018) pp. 1–25.
- [20] W. van Ekeren, G. Looye, R. O. Kuchar, Q. P. Chu, and E. van Kampen, *Design, Implementation and Flight-Tests of Incremental Nonlinear Flight Control Methods*, in *2018 AIAA Guidance, Navigation, and Control Conference*, January (American Institute of Aeronautics and Astronautics, Kissimmee, Florida, 2018) pp. 1–21.
- [21] X. Wang, E. van Kampen, R. De Breuker, and Q. P. Chu, *Flexible Aircraft Gust Load Alleviation with Incremental Nonlinear Dynamic Inversion*, in *2018 AIAA Atmospheric Flight Mechanics Conference*, January (American Institute of Aeronautics and Astronautics, Kissimmee, Florida, 2018) pp. 1–21.
- [22] C. Cakiroglu, E. van Kampen, and Q. P. Chu, *Robust Incremental Nonlinear Dynamic Inversion Control Using Angular Accelerometer Feedback*, in *2018 AIAA Guidance, Navigation, and Control Conference*, January (American Institute of Aeronautics and Astronautics, Kissimmee, Florida, 2018).
- [23] A. L. Fradkov, I. V. Miroshnik, and V. O. Nikiforov, *Nonlinear and Adaptive Control of Complex Systems*, vol. 491 ed., edited by M. Hazewinkel (Springer Netherlands, Dordrecht, 1999).
- [24] A. Isidori, *Nonlinear Control Systems*, 3rd ed. (Springer-Verlag, Berlin, 1995) pp. 257–291.
- [25] X. Yang and J. J. Zhu, *Singular perturbation margin and generalised gain margin for nonlinear time-invariant systems*, *International Journal of Control* **89**, 451 (2016).
- [26] P. Lu, E. van Kampen, and Q. P. Chu, *Robustness and Tuning of Incremental Backstepping Approach*, in *AIAA Guidance, Navigation, and Control Conference* (American Institute of Aeronautics and Astronautics, Kissimmee, Florida, 2015) pp. 1–15.
- [27] L. Meirovitch and I. Tuzcu, *National Aeronautics and Space Administration, Langley Research Center*, Tech. Rep. (NASA Langley Research Center, 2003).
- [28] J. Wright and J. Cooper, *Introduction to Aircraft Aeroelasticity and Loads* (John Wiley & Sons, Washington, DC, 2007) pp. 79–85.
- [29] B. Etkin, *Turbulent Wind and Its Effect on Flight*, *Journal of Aircraft* **18**, 327 (1981).
- [30] B. Etkin, *Dynamics of Atmospheric Flight* (Dover Publications, Toronto, 2005).



3

INCREMENTAL SLIDING MODE FAULT-TOLERANT FLIGHT CONTROL

In Chapter 2, it was found that under incremental nonlinear dynamic inversion (INDI) control, an uncertainty term, ϵ_{indi} , remains in the closed-loop system. The properties (especially the boundedness) of this term will be further explored in this chapter. An approach to compensate for the influences of ϵ_{indi} will also be addressed. It was concluded in Chapter 2 that INDI control is more robust to regular perturbations than is nonlinear dynamic inversion (NDI) control. This inspired the idea of using the sensor-based control structure of INDI to solve the contradiction between the reduction of model dependency and the reduction of uncertainty in sliding mode control. The hybrid of INDI with (higher-order) sliding mode control and sliding mode disturbance observers will be elaborated.

This chapter is based on the following article:

Wang, X., van Kampen, E., Chu, Q. P., and Lu, P., "Incremental Sliding-Mode Fault-Tolerant Flight Control," *Journal of Guidance, Control, and Dynamics*, Vol. 42, No. 2, 2019, pp. 244–259. doi:10.2514/1.G003497.

This chapter proposes a novel control framework that combines the recently reformulated incremental nonlinear dynamic inversion with (higher-order) sliding mode controllers/observers, for generic multi-input/multi-output nonlinear systems, named incremental sliding mode control. As compared to the widely used approach that designs (higher-order) sliding mode controllers/observers based on nonlinear dynamic inversion, the proposed incremental framework can further reduce the uncertainties whilst requiring less model knowledge. Since the uncertainties are reduced in the incremental framework, theoretical analyses demonstrate that the incremental sliding mode control can passively resist a wider range of perturbations with reduced minimum possible control/observer gains. These merits are validated via numerical simulations for aircraft command tracking problems, in the presence of sudden actuator faults and structural damages.

3.1. INTRODUCTION

SAFETY is of paramount importance to aerospace systems. Although air transport remains to be the safest means of transportation, it inevitably suffers from sudden actuator faults, sensor faults and even structural damages. These faults and damages can lead to a non-equilibrium flight accompanied with varied aerodynamic properties, changed inertia properties, new sources of uncertainties and reduced flight control authority. Therefore, fault-tolerant control [1], which is capable of automatically tolerating faults and damages while maintaining stability and desirable performance, is highly demanded.

Fault-tolerant control systems can be classified into passive fault-tolerant control systems and active fault-tolerant control systems [1, 2]. The active fault-tolerant control systems use fault detection and isolation processes to obtain the most up-to-date information of the faulty system. This knowledge is then supplied to reconfigurable mechanisms to redesign the on-board controller. By contrast, the passive fault-tolerant control systems are robust enough to cope with considered faults/damages without any detection or reconfiguration [1]. Being invariant (better than just robust) to matched uncertainties [3, 4], Sliding mode control methods are widely used in passive fault-tolerant control systems [1, 2, 5–11]. A recent flight evaluation demonstrated the effectiveness of a model-based sliding mode controller on solving active actuator fault-tolerant control problems [12].

A well-known obstacle for sliding mode control applications is the chattering phenomenon, caused by high frequency switching of the control input [13, 14]. Although higher-order sliding mode control techniques offer a continuous control signal by artificially increasing the input–output relative degree, chattering is only mitigated instead of being totally eliminated [14]. Another popular approach to alleviate chattering is using approximations of the signum function, such as saturation and sigmoid functions. However, these approximations (and hence compromises) result in partial loss of robustness [15, 16]. On account of the fact that the chattering amplitude is proportional to the magnitude of the discontinuous control, a current research focus is on adaption mechanisms for achieving the minimum possible value of the control gain [13–15, 17]. In spite of the variations of gain adaption methods, the sufficient condition for enforcing a sliding motion still requires the switching gain to be larger than the uncertainty

bound (for first-order sliding mode control), or the corresponding bound for uncertainty derivatives (for higher-order sliding mode control) [13–15, 17].

Many (higher-order) sliding mode disturbance observer designs are based on sliding mode control techniques [18–21]. For these methods, the required switching gain for guaranteeing convergence is a monotonically increasing function of the uncertainty bound, or the corresponding bound for uncertainty derivatives [18–21]. Although the observations provided by disturbance observers are always continuous, the filtering process in first-order sliding mode disturbance observer, and the integration process in super-twisting disturbance observer can only attenuate instead of totally rejecting chattering in the observations [19]. Therefore, a method that could reduce the uncertainty is fundamentally beneficial to reducing the minimum possible gains of both (higher-order) sliding mode controllers and observers.

An intuitive approach to reduce the uncertainty is using a preliminary model-based feedback control term to roughly cancel the nonlinearities and couplings. For nonlinear system control problem, this goal is normally fulfilled by feedback linearization, also known as nonlinear dynamic inversion (NDI) in the aerospace community [22–24]. Examples that use NDI as the baseline control are: first-order sliding mode control [4–6, 10, 11, 16, 19, 25–29], higher-order sliding mode control [30–32], sliding mode control driven by first-order sliding mode disturbance observers [18–20], sliding mode control driven by higher-order sliding mode disturbance observers [14, 15, 18–21, 31–33]. However, side-effects of the model-based approach are also well-known. For instance, pursuing decent models for complex aerospace systems is costly and time-consuming. Model identifications and updates, which are challenging and require sufficient excitations, are also necessary in the presence of faults [24].

In view of the preceding analyses, an interesting research question emerges, i.e., is there a baseline control method that could reduce the uncertainty whilst requiring less model knowledge?

Incremental nonlinear dynamic inversion (INDI) is a sensor-based control approach, which requires less model knowledge than NDI, but has enhanced robustness than both NDI [22, 23], and NDI with model identifications [24]. Numerical simulations [22–24, 34, 35], quadrotor flight tests [36], and passenger aircraft flight tests [37] have consistently demonstrated the robustness and easy implementation of this method, which makes it promising as a baseline control for inducing sliding modes. This chapter follows the recently reformulated INDI in [38], which is more general and more rigorous than INDI in the previous literature [22–24, 34–37]. Research questions still exist for this reformulated INDI. First of all, the property of the remaining uncertainty term after INDI feedback is unclear from the literature. Moreover, there is no explicit model and analysis for the influences of sudden (discontinuous in time) faults on INDI. What is more important is that a compensation method for further improving the robustness of INDI in perturbed circumstances is desired.

The main contribution of this chapter is the hybridization of (higher-order) sliding mode controllers/observers with the reformulated INDI for generic multi-input/multi-output nonlinear systems, named incremental sliding mode control (INDI-SMC), which inherits the advantages and remedies the drawbacks of both methods.

Contributions to the reformulated INDI

In this chapter, the properties (especially the boundedness) of the remaining uncertainty term after INDI feedback will be analyzed. The influences of sudden actuator faults and structural damages on INDI will also be explicitly modeled and analyzed. The robustness enhancement that sliding modes bring to INDI will be proved and numerically verified.

Contributions to (higher-order) sliding mode control

The present chapter introduces an incremental sliding mode control framework, which reduces uncertainty whilst requiring less model knowledge. By virtue of the uncertainty reduction, the minimum possible control/observer gains can be reduced, which is beneficial to chattering alleviation. The advantages of inducing sliding modes based on INDI instead of NDI will be analyzed and numerically validated by aircraft fault-tolerant control problems.

This chapter is organized as follows: The derivations and robustness comparisons between NDI and the reformulated INDI are presented in Sec. 3.2. The INDI-SMC framework is proposed in Sec. 3.3, considering the hybridizations of the reformulated INDI with (higher-order) sliding mode controllers/observers. This INDI-SMC framework is then applied to aircraft flight-tolerant control problems in Sec. 3.4 and compared with NDI, reformulated INDI, and sliding mode control based on NDI in Sec. 3.5. Main conclusions are drawn in Sec. 3.6.

3.2. COMPARISONS BETWEEN NDI AND THE REFORMULATED INDI

3.2.1. PROBLEM FORMULATION

Considering a multi-input/multi-output nonlinear control-affine system described by

$$\dot{\mathbf{x}} = \mathbf{f}(\mathbf{x}) + \mathbf{G}(\mathbf{x})\mathbf{u}, \quad \mathbf{y} = \mathbf{h}(\mathbf{x}), \quad (3.1)$$

where $\mathbf{f} : \mathbb{R}^n \rightarrow \mathbb{R}^n$ and $\mathbf{h} : \mathbb{R}^n \rightarrow \mathbb{R}^m$ are smooth vector fields. \mathbf{G} is a smooth function mapping $\mathbb{R}^n \rightarrow \mathbb{R}^{n \times m}$, whose columns are smooth vector fields. Define the vector relative degree of \mathbf{y} with respect to \mathbf{u} as $\boldsymbol{\rho} = [\rho_1, \rho_2, \dots, \rho_m]^T$. Assume $\rho = \sum_{i=1}^m \rho_i = n$, then by differentiating the output, the input-output mapping of the system is given by

$$\mathbf{y}^{(\boldsymbol{\rho})} = \boldsymbol{\alpha}(\mathbf{x}) + \mathcal{B}(\mathbf{x})\mathbf{u} \quad (3.2)$$

In the preceding equation, $\boldsymbol{\alpha}(\mathbf{x}) = [\mathcal{L}_f^{\rho_1} h_1, \mathcal{L}_f^{\rho_2} h_2, \dots, \mathcal{L}_f^{\rho_m} h_m]^T$, $\mathcal{B}(\mathbf{x}) \in \mathbb{R}^{m \times m}$, $\mathcal{B}_{ij} = \mathcal{L}_{g_j} \mathcal{L}_f^{\rho_i - 1} h_i$, with $\mathcal{L}_f^{\rho_i} h_i$, $\mathcal{L}_{g_j} \mathcal{L}_f^{\rho_i - 1} h_i$ are the corresponding Lie derivatives [16]. Assumed $\det\{\mathcal{B}(\mathbf{x})\} \neq 0$ (before and after faults), which yields a controllable system without control redundancy. Sensor faults are not considered in the present chapter, and the reader is recommended to Ref. [39] for sensor fault detection and fault-tolerant control methods. Define $\boldsymbol{\xi}_i = [h_i, \mathcal{L}_f h_i, \dots, \mathcal{L}_f^{\rho_i - 1} h_i]^T$, $\boldsymbol{\xi} = [\boldsymbol{\xi}_1; \boldsymbol{\xi}_2; \dots; \boldsymbol{\xi}_m]$, $i = 1, 2, \dots, m$, the nonlinear system described by Eq. (3.1) can be transformed into a canonical form as

$$\dot{\boldsymbol{\xi}} = \mathbf{A}_c \boldsymbol{\xi} + \mathbf{B}_c [\boldsymbol{\alpha}(\mathbf{x}) + \mathcal{B}(\mathbf{x})\mathbf{u}], \quad \mathbf{y} = \mathbf{C}_c \boldsymbol{\xi}, \quad (3.3)$$

where $\mathbf{A}_c = \text{diag}\{\mathbf{A}_0^i\}$, $\mathbf{B}_c = \text{diag}\{\mathbf{B}_0^i\}$, $\mathbf{C}_c = \text{diag}\{\mathbf{C}_0^i\}$, $i = 1, 2, \dots, m$, and $(\mathbf{A}_0^i, \mathbf{B}_0^i, \mathbf{C}_0^i)$ is a canonical form representation of a chain of ρ_i integrators. The control object is to make the output \mathbf{y} asymptotically track a reference signal $\mathbf{y}_r(t) = [y_{r_1}(t), y_{r_2}(t), \dots, y_{r_m}(t)]^T$. Assume $y_{r_i}(t)$, $i = 1, 2, \dots, m$, and its derivatives up to $y_{r_i}^{(\rho_i)}(t)$ are bounded for all t and each $y_{r_i}^{(\rho_i)}(t)$ is continuous. Denote the reference and the tracking error vectors as

$$\mathcal{R} = [\mathcal{R}_1; \mathcal{R}_2; \dots; \mathcal{R}_m], \quad \mathcal{R}_i = [y_{r_i}, y_{r_i}^{(1)}, \dots, y_{r_i}^{(\rho_i-1)}]^T, \quad i = 1, 2, \dots, m, \quad \mathbf{e} = \boldsymbol{\xi} - \mathcal{R} \quad (3.4)$$

Using Eq. (3.3), the error dynamics are given by

$$\dot{\mathbf{e}} = \mathbf{A}_c(\mathcal{R} + \mathbf{e}) + \mathbf{B}_c[\boldsymbol{\alpha}(\mathbf{x}) + \mathcal{B}(\mathbf{x})\mathbf{u}] - \dot{\mathcal{R}} = \mathbf{A}_c\mathbf{e} + \mathbf{B}_c[\boldsymbol{\alpha}(\mathbf{x}) + \mathcal{B}(\mathbf{x})\mathbf{u} - \mathbf{y}_r^{(\rho)}] \quad (3.5)$$

where $\mathbf{y}_r^{(\rho)} = [y_{r_1}^{(\rho_1)}, y_{r_2}^{(\rho_2)}, \dots, y_{r_m}^{(\rho_m)}]^T$.

3.2.2. NDI AND THE REFORMULATED INDI

The standard NDI control law for stabilizing \mathbf{e} in Eq. (3.5) is designed as

$$\mathbf{u}_{\text{ndi}} = \bar{\mathcal{B}}^{-1}(\mathbf{x})(\mathbf{v}_c - \bar{\boldsymbol{\alpha}}(\mathbf{x})), \quad \mathbf{v}_c = \mathbf{y}_r^{(\rho)} - \mathbf{K}\mathbf{e}, \quad (3.6)$$

with the gain matrix $\mathbf{K} = \text{diag}\{\mathbf{K}_i\}$, $i = 1, 2, \dots, m$, and $\mathbf{K}_i = [K_{i,0}, K_{i,1}, \dots, K_{i,\rho_i-1}]$ is designed such that $\mathbf{A}_c - \mathbf{B}_c\mathbf{K}$ is Hurwitz. $\mathbf{v}_c \in \mathbb{R}^m$ is called the virtual control. The nominal models \mathcal{B} and $\bar{\boldsymbol{\alpha}}$ are used by NDI, which results in the closed-loop dynamics as

$$\dot{\mathbf{e}} = (\mathbf{A}_c - \mathbf{B}_c\mathbf{K})\mathbf{e} + \mathbf{B}_c\boldsymbol{\varepsilon}_{\text{ndi}} \quad (3.7)$$

where

$$\boldsymbol{\varepsilon}_{\text{ndi}} = (\boldsymbol{\alpha} - \bar{\boldsymbol{\alpha}}) + (\mathcal{B}\bar{\mathcal{B}}^{-1} - \mathbf{I})(\mathbf{v}_c - \bar{\boldsymbol{\alpha}}) = (\boldsymbol{\alpha} - \bar{\boldsymbol{\alpha}}) + (\mathcal{B} - \bar{\mathcal{B}})\mathbf{u}_{\text{ndi}} \quad (3.8)$$

$\boldsymbol{\varepsilon}_{\text{ndi}}$ is the residual cancellation error of NDI caused model uncertainties, external disturbances, faults and damages.

Denote the sampling interval as Δt , and follow the recently reformulated INDI [38], the incremental dynamic equation is then derived by taking the first-order Taylor series expansion of Eq. (3.2) around the condition at $t - \Delta t$ (denoted by the subscript 0) as

$$\begin{aligned} \mathbf{y}^{(\rho)} &= \boldsymbol{\alpha}(\mathbf{x}) + \mathcal{B}(\mathbf{x})\mathbf{u} \\ &= \mathbf{y}_0^{(\rho)} + \left. \frac{\partial[\boldsymbol{\alpha}(\mathbf{x}) + \mathcal{B}(\mathbf{x})\mathbf{u}]}{\partial \mathbf{x}} \right|_0 \Delta \mathbf{x} + \mathcal{B}(\mathbf{x}_0)\Delta \mathbf{u} + \mathbf{R}_1 \end{aligned} \quad (3.9)$$

in which $\Delta \mathbf{x}$ and $\Delta \mathbf{u}$ represent the states and control increments in one sampling time step Δt . \mathbf{R}_1 in Eq. (3.9) is the expansion remainder, whose Lagrange form is

$$\mathbf{R}_1 = \frac{1}{2} \left. \frac{\partial^2[\boldsymbol{\alpha}(\mathbf{x}) + \mathcal{B}(\mathbf{x})\mathbf{u}]}{\partial^2 \mathbf{x}} \right|_m \Delta \mathbf{x}^2 + \left. \frac{\partial^2[\boldsymbol{\alpha}(\mathbf{x}) + \mathcal{B}(\mathbf{x})\mathbf{u}]}{\partial \mathbf{x} \partial \mathbf{u}} \right|_m \Delta \mathbf{x} \Delta \mathbf{u} \quad (3.10)$$

in which $(\cdot)|_m$ means evaluating (\cdot) at a condition where $\mathbf{x} \in (\mathbf{x}(t - \Delta t), \mathbf{x}(t))$, $\mathbf{u} \in (\mathbf{u}(t - \Delta t), \mathbf{u}(t))$. In Eq. (3.10), \mathbf{R}_1 is not a function of $\Delta \mathbf{u}^2$, since according to Eq. (3.2), $\mathbf{y}^{(\rho)}$ is linear with respect to \mathbf{u} .

The incremental control law for stabilizing the error dynamics in Eq. (3.5) is then designed as

$$\Delta \mathbf{u}_{\text{indi}} = \bar{\mathcal{B}}^{-1}(\mathbf{x}_0)(\mathbf{v}_c - \mathbf{y}_0^{(\rho)}), \quad \mathbf{v}_c = \mathbf{y}_r^{(\rho)} - \mathbf{K}\mathbf{e}, \quad (3.11)$$

where \mathbf{K} is kept identical to the gain matrix in Eq. (3.6) for fair comparisons. $\mathbf{y}_0^{(\rho)}$ is measured or estimated. The total control command for actuator is hence $\mathbf{u}_{\text{indi}} = \mathbf{u}_{\text{indi},0} + \Delta \mathbf{u}_{\text{indi}}$ [38]. Substituting Eq. (3.11) into Eqs. (3.5) and (3.9) results in the closed-loop dynamics as

$$\begin{aligned} \dot{\mathbf{e}} &= \mathbf{A}_c \mathbf{e} + \mathbf{B}_c [\mathbf{y}_0^{(\rho)} + \mathcal{B}(\mathbf{x}_0)(\bar{\mathcal{B}}^{-1}(\mathbf{x}_0)(\mathbf{v}_c - \mathbf{y}_0^{(\rho)})) + \boldsymbol{\delta}(\mathbf{x}, \Delta t) - \mathbf{y}_r^{(\rho)}] \\ &\triangleq (\mathbf{A}_c - \mathbf{B}_c \mathbf{K}) \mathbf{e} + \mathbf{B}_c \boldsymbol{\varepsilon}_{\text{indi}} \end{aligned} \quad (3.12)$$

Using Eqs. (3.9, 3.10), $\boldsymbol{\delta}(\mathbf{x}, \Delta t)$ in Eq. (3.12) equals

$$\left[\frac{\partial[\boldsymbol{\alpha}(\mathbf{x}) + \mathcal{B}(\mathbf{x})\mathbf{u}_{\text{indi}}]}{\partial \mathbf{x}} \Big|_0 + \frac{1}{2} \frac{\partial^2[\boldsymbol{\alpha}(\mathbf{x}) + \mathcal{B}(\mathbf{x})\mathbf{u}_{\text{indi}}]}{\partial^2 \mathbf{x}} \Big|_m \Delta \mathbf{x} + \frac{\partial \mathcal{B}(\mathbf{x})}{\partial \mathbf{x}} \Big|_m \Delta \mathbf{u}_{\text{indi}} \right] \Delta \mathbf{x} \quad (3.13)$$

$\boldsymbol{\delta}(\mathbf{x}, \Delta t)$ is only a function of the state vector \mathbf{x} and the sampling interval, since in the closed-loop system, the values of \mathbf{u} and $\Delta \mathbf{u}$ have already been substituted into Eq. (3.13). The closed-loop perturbation term $\boldsymbol{\varepsilon}_{\text{indi}}$ in Eq. (3.12) is further derived as

$$\boldsymbol{\varepsilon}_{\text{indi}} = \boldsymbol{\delta}(\mathbf{x}, \Delta t) + (\mathcal{B}\bar{\mathcal{B}}^{-1} - \mathbf{I})(\mathbf{v}_c - \mathbf{y}_0^{(\rho)}) = \boldsymbol{\delta}(\mathbf{x}, \Delta t) + (\mathcal{B} - \bar{\mathcal{B}})\Delta \mathbf{u}_{\text{indi}} \quad (3.14)$$

As compared to NDI control, this INDI control is less sensitive to model mismatches, because the model information of $\boldsymbol{\alpha}(\mathbf{x})$ is not used in Eq. (3.11). On the other hand, the INDI control law needs the measurement or estimation of $\mathbf{y}_0^{(\rho)}$ and \mathbf{u}_0 ; this is why INDI control is referred to as a sensor-based approach [36, 38].

3.2.3. COMPARISONS BETWEEN $\boldsymbol{\varepsilon}_{\text{ndi}}$ AND $\boldsymbol{\varepsilon}_{\text{indi}}$

Referring to the stability analyses in [38], if $\boldsymbol{\varepsilon}_{\text{ndi}/\text{indi}}$ is bounded by $\bar{\boldsymbol{\varepsilon}}_{\text{ndi}/\text{indi}}$, then the tracking error in Eqs. (3.7, 3.12) is ultimately bounded (Appendix A, Definition 6) by a class \mathcal{K} function (Appendix A, Definition 2) of $\bar{\boldsymbol{\varepsilon}}_{\text{ndi}/\text{indi}}$. Even so, the control performance is inevitable impaired by $\boldsymbol{\varepsilon}_{\text{ndi}/\text{indi}}$.

The formulations for $\boldsymbol{\varepsilon}_{\text{ndi}}$ and $\boldsymbol{\varepsilon}_{\text{indi}}$ are presented by Eqs. (3.8, 3.14). For the reason that INDI is a sensor-based approach, in the sense that the model information of $\boldsymbol{\alpha}$ is obtained by measuring or estimating $\mathbf{y}_0^{(\rho)}$ and \mathbf{u}_0 , the mismatch error $\boldsymbol{\alpha} - \tilde{\boldsymbol{\alpha}}$ in $\boldsymbol{\varepsilon}_{\text{ndi}}$ is accordingly replaced by $\boldsymbol{\delta}(\mathbf{x}, \Delta t)$ in $\boldsymbol{\varepsilon}_{\text{indi}}$. Assume that the partial derivatives of $\boldsymbol{\alpha}(\mathbf{x})$ and $\mathcal{B}(\mathbf{x})$ with respect to \mathbf{x} , up to any order, are bounded. Due to the continuity of \mathbf{x} , $\lim_{\Delta t \rightarrow 0} \|\Delta \mathbf{x}\| = 0$. Therefore, recall Eq. (3.13), the norm value of $\boldsymbol{\delta}(\mathbf{x}, \Delta t)$ term in $\boldsymbol{\varepsilon}_{\text{indi}}$ could become negligible under sufficiently small sampling interval Δt . The insensitivity of INDI to $\boldsymbol{\delta}(\mathbf{x}, \Delta t)$ has been numerically verified in [22–24, 34–36] and flight tested in [37]. The other terms in Eqs. (3.8, 3.14), i.e., $(\mathcal{B} - \bar{\mathcal{B}})\mathbf{u}_{\text{ndi}}$ and $(\mathcal{B} - \bar{\mathcal{B}})\Delta \mathbf{u}_{\text{indi}}$, are caused by the multiplicative uncertainties in the $\mathcal{B}(\mathbf{x})$ matrix.

Theorem 3 *If $\|\mathbf{I} - \mathcal{B}\bar{\mathcal{B}}^{-1}\| \leq \bar{b} < 1$, and if $\|\boldsymbol{\delta}(\mathbf{x}, \Delta t)\| \leq \bar{\delta}$, under sufficiently high sampling frequency f_s , the residual error $\boldsymbol{\varepsilon}_{\text{indi}}$ of INDI given by Eq. (3.14) is ultimately bounded.*

Proof: Recall Eqs. (3.9, 3.11, 3.14), the output dynamics under INDI control can also be written as $\mathbf{y}^{(\rho)} = \mathbf{v}_c + \boldsymbol{\varepsilon}_{\text{indi}}$. Also, at the previous time step $\mathbf{y}_0^{(\rho)} = \mathbf{v}_{c_0} + \boldsymbol{\varepsilon}_{\text{indi}_0}$. Therefore, using Eq. (3.14), $\boldsymbol{\varepsilon}_{\text{indi}}$ can be rewritten as

$$\begin{aligned}\boldsymbol{\varepsilon}_{\text{indi}} &= (\mathcal{B}\bar{\mathcal{B}}^{-1} - \mathbf{I})(\mathbf{v}_c - \mathbf{y}_0^{(\rho)}) + \boldsymbol{\delta} \\ &= (\mathbf{I} - \mathcal{B}\bar{\mathcal{B}}^{-1})\boldsymbol{\varepsilon}_{\text{indi}_0} - (\mathbf{I} - \mathcal{B}\bar{\mathcal{B}}^{-1})(\mathbf{v}_c - \mathbf{v}_{c_0}) + \boldsymbol{\delta} \\ &\triangleq \mathbf{E}\boldsymbol{\varepsilon}_{\text{indi}_0} - \mathbf{E}\Delta\mathbf{v}_c + \boldsymbol{\delta}\end{aligned}\quad (3.15)$$

which can be written in an recursive way as

$$\boldsymbol{\varepsilon}_{\text{indi}}(k) = \mathbf{E}(k)\boldsymbol{\varepsilon}_{\text{indi}}(k-1) - \mathbf{E}(k)\Delta\mathbf{v}_c(k) + \boldsymbol{\delta}(k) \quad (3.16)$$

\mathbf{v}_c is designed to be continuous in time, thus the following equation holds

$$\lim_{\Delta t \rightarrow 0} \|\mathbf{v}_c - \mathbf{v}_{c_0}\| = 0, \quad \forall \mathbf{x} \in \mathbb{R}^n \quad (3.17)$$

Eq. (3.17) also indicates that $\forall \overline{\Delta v}_c > 0, \exists \overline{\Delta t} > 0, s.t.$ for all $0 < \Delta t \leq \overline{\Delta t}, \forall \mathbf{x} \in \mathbb{R}^n, \|\mathbf{v}_c - \mathbf{v}_{c_0}\| \leq \overline{\Delta v}_c$. In other words, there exists a Δt that guarantees the boundedness of $\mathbf{v}_c - \mathbf{v}_{c_0}$. Also, this bound can be further diminished by increasing the sampling frequency. Consequently, Eq. (3.16) satisfies

$$\begin{aligned}\|\boldsymbol{\varepsilon}_{\text{indi}}(k)\| &\leq (\bar{b})^k \|\boldsymbol{\varepsilon}_{\text{indi}}(0)\| + \sum_{j=1}^k (\bar{b})^{k-j+1} \|\Delta\mathbf{v}_c(j)\| + \sum_{j=1}^{k-1} (\bar{b})^{k-j} \|\boldsymbol{\delta}(j)\| + \|\boldsymbol{\delta}(k)\| \\ &\leq (\bar{b})^k \|\boldsymbol{\varepsilon}_{\text{indi}}(0)\| + \overline{\Delta v}_c \sum_{j=1}^k (\bar{b})^{k-j+1} + \bar{\delta} \sum_{j=1}^{k-1} (\bar{b})^{k-j} + \bar{\delta} \\ &= (\bar{b})^k \|\boldsymbol{\varepsilon}_{\text{indi}}(0)\| + \overline{\Delta v}_c \frac{\bar{b} - \bar{b}^{k+1}}{1 - \bar{b}} + \bar{\delta} \frac{1 - \bar{b}^k}{1 - \bar{b}}\end{aligned}\quad (3.18)$$

Since $\bar{b} < 1$, Eq. (3.18) satisfies

$$\|\boldsymbol{\varepsilon}_{\text{indi}}\| \leq \frac{\overline{\Delta v}_c \bar{b} + \bar{\delta}}{1 - \bar{b}}, \quad \text{as } k \rightarrow \infty \quad (3.19)$$

In conclusion, $\boldsymbol{\varepsilon}_{\text{indi}}$ is bounded for all k , and is ultimately bounded by $\frac{\overline{\Delta v}_c \bar{b} + \bar{\delta}}{1 - \bar{b}}$. \square

The boundedness of perturbations is the precondition of many robust control techniques [4]. $\|\mathbf{I} - \mathcal{B}\bar{\mathcal{B}}^{-1}\| \leq \bar{b} < 1$ requires a diagonally dominant structure of $\mathcal{B}\bar{\mathcal{B}}^{-1}$, which excludes unacceptable estimations of \mathcal{B} (e.g., the signs of \mathcal{B} and its estimation $\bar{\mathcal{B}}$ are opposite). Similar requirements can be found in [5, 6, 19, 26, 30]. $f_s = 100$ Hz is a reasonable choice for flight control, as has been verified by both simulations [22–24, 34, 35] and passenger aircraft flight tests [37].

By contrast, as a function of both \mathbf{x} , \mathbf{u}_{ndi} , and being independent of Δt , the residual error of NDI is undetermined under the same conditions. The boundedness of $\boldsymbol{\varepsilon}_{\text{ndi}}$ is normally assumed for the feasibility of sliding mode control designs [5, 6, 19, 26]. However, it will be shown in Sec. 3.5 that even if $\|\mathbf{I} - \mathcal{B}\bar{\mathcal{B}}^{-1}\| \leq \bar{b} < 1$, $\boldsymbol{\varepsilon}_{\text{ndi}}$ has the possibility

to become unbounded in severe damage cases with limited control authority. As a consequence, the NDI based sliding mode controllers can only deal with situations where both the boundedness of $\boldsymbol{\varepsilon}_{\text{ndi}}$ and $\|\mathbf{I} - \mathcal{B}\bar{\mathcal{B}}^{-1}\| \leq \bar{b} < 1$ are satisfied.

One may argue that for some moderate fault and damage cases, $\boldsymbol{\varepsilon}_{\text{ndi}}$ is normally bounded. Even if this is true, by comparing $\boldsymbol{\varepsilon}_{\text{ndi}}$ with $\boldsymbol{\varepsilon}_{\text{indi}}$ under the same fault/damage circumstances, $\boldsymbol{\varepsilon}_{\text{indi}}$ typically has smaller bound, which can be further diminished by increasing f_s . This can be demonstrated by comparing Eq. (3.8) with Eq. (3.14), where $\|\boldsymbol{\delta}(\mathbf{x}, \Delta t)\|$ can become negligible under sufficiently high f_s (Eq. (3.13)), while $\|\boldsymbol{\alpha} - \bar{\boldsymbol{\alpha}}\|$ is normally large in the presence of faults and disturbances, especially for aerospace systems. Moreover, when $\mathbf{u}_{\text{ndi}} \neq \mathbf{0}$, there exists an f_s such that $\|\Delta \mathbf{u}_{\text{indi}}\| < \|\mathbf{u}_{\text{ndi}}\|$. Denote $\bar{\boldsymbol{\varepsilon}}_{\text{ndi}} = \|\boldsymbol{\alpha} - \bar{\boldsymbol{\alpha}}\| + \|\mathcal{B} - \bar{\mathcal{B}}\| \|\mathbf{u}_{\text{ndi}}\| \geq \|\boldsymbol{\varepsilon}_{\text{ndi}}\|$, and $\bar{\boldsymbol{\varepsilon}}_{\text{indi}} = \|\boldsymbol{\delta}(\mathbf{x}, \Delta t)\| + \|\mathcal{B} - \bar{\mathcal{B}}\| \|\Delta \mathbf{u}_{\text{indi}}\| \geq \|\boldsymbol{\varepsilon}_{\text{indi}}\|$, then consequently, in the perturbed conditions that $\|\boldsymbol{\alpha} - \bar{\boldsymbol{\alpha}}\| \neq \mathbf{0}$, $\|\mathcal{B} - \bar{\mathcal{B}}\| \neq \mathbf{0}$, and $\|\mathbf{u}_{\text{ndi}}\| \neq \mathbf{0}$, there exists an f_s such that $\bar{\boldsymbol{\varepsilon}}_{\text{indi}} < \bar{\boldsymbol{\varepsilon}}_{\text{ndi}}$.

The smaller bound of $\boldsymbol{\varepsilon}_{\text{indi}}$ is a useful feature, because for many (higher-order) sliding mode controllers/observers, the required gains for inducing sliding modes are monotonically increasing functions of the perturbation bounds. High control/observer gains are undesirable in practice, because they amplify the measurement noise, excite the unmodeled parasitic dynamics, induce chattering, threaten the actuator rate and/or position limits and potentially lead to divergence. The advantages of the incremental framework will be further demonstrated in Sec. 3.3.

3.3. PROPOSAL OF THE INCREMENTAL SLIDING MODE CONTROL FRAMEWORK

This section proposes a new control approach that hybridizes the reformulated INDI with (higher-order) sliding mode controllers/observers, defined as incremental sliding mode control (INDI-SMC). First, the control frameworks for INDI-SMC and NDI-SMC are presented. Then it will be shown in the following subsections that a wide variety of (higher-order) sliding mode control designs in the literature belong to the NDI-SMC framework, and redesigning them in the new incremental framework is beneficial to chattering reduction and robustness enhancement.

The INDI-SMC framework is proposed as:

$$\Delta \mathbf{u}_{\text{indi-s}} = \bar{\mathcal{B}}^{-1}(\mathbf{x}_0)(\mathbf{v}_c + \mathbf{v}_s - \mathbf{y}_0^{(\rho)}) \quad (3.20)$$

where \mathbf{v}_c is designed for stabilizing the *unperturbed system*, while \mathbf{v}_s can be designed using (higher-order) sliding mode control/observer techniques for perturbation compensations. By contrast, control methods in the literature that are in the form of

$$\mathbf{u}_{\text{ndi-s}} = \bar{\mathcal{B}}^{-1}(\mathbf{x})(\mathbf{v}_c + \mathbf{v}_s - \bar{\boldsymbol{\alpha}}(\mathbf{x})) \quad (3.21)$$

are classified as NDI-SMC.

Design the sliding variable as $\boldsymbol{\sigma}(\mathbf{x}) : \mathbb{R}^n \rightarrow \mathbb{R}^m$, and define the vector relative degree of $\boldsymbol{\sigma}$ with respect to \mathbf{u} as $\mathbf{r} = [r_1, r_2, \dots, r_m]^T$, then the dynamics of the sliding variable $\boldsymbol{\sigma}$ are given by

$$\boldsymbol{\sigma}^{(\mathbf{r})} = \boldsymbol{\alpha}_{\boldsymbol{\sigma}}(\mathbf{x}) + \mathcal{B}_{\boldsymbol{\sigma}}(\mathbf{x})\mathbf{u}, \quad \boldsymbol{\alpha}_{\boldsymbol{\sigma}_i} = \mathcal{L}_f^{r_i} \boldsymbol{\sigma}_i, \quad \mathcal{B}_{\boldsymbol{\sigma}_{ij}} = \mathcal{L}_{g_j} \mathcal{L}_f^{r_i-1} \boldsymbol{\sigma}_i, \quad i, j = 1, 2, \dots, m. \quad (3.22)$$

In the context of sliding mode control, σ is designed such that when the sliding surface $\sigma = \mathbf{0}$ is reached, the system obtains the desirable dynamics, in spite of uncertainties. The following subsections will show how the incremental framework can be used to enforce (higher-order) sliding modes, and its advantages as compared to the NDI-SMC framework.

3.3.1. FIRST-ORDER INCREMENTAL SLIDING MODE CONTROL

In Eq. (3.22), if $r_i = 1$, $i = 1, 2, \dots, m$, control methods that achieve $\sigma = \mathbf{0}$ are referred to as first-order (or conventional) sliding mode control [30, 40]. In order to reduce the switching magnitude, many sliding mode controllers introduce a continuous preliminary feedback component based on the equivalent control method [41]. The equivalent control is defined as the control effort needed to maintain the sliding motion on the surface and is calculated by requiring $\sigma = \dot{\sigma} = \mathbf{0}$ [4, 41]. Recall Eq. (3.22), for first-order sliding mode, $\dot{\sigma} = \alpha_\sigma(\mathbf{x}) + \mathcal{B}_\sigma(\mathbf{x})\mathbf{u}_{\text{eq}} = \mathbf{0}$. By dynamically inverting this nonlinear algebraic equation, the equivalent control \mathbf{u}_{eq} is calculated by

$$\mathbf{u}_{\text{eq}} = -\mathcal{B}_\sigma^{-1}(\mathbf{x})\alpha_\sigma(\mathbf{x}) \quad (3.23)$$

Since \mathbf{u}_{eq} contains uncertainties and disturbances, only the model-based nominal equivalent control $\tilde{\mathbf{u}}_{\text{eq}} = -\tilde{\mathcal{B}}_\sigma^{-1}(\mathbf{x})\tilde{\alpha}_\sigma(\mathbf{x})$ is available for feedback control. The most widely used first-order sliding mode control structure is

$$\mathbf{u} = \tilde{\mathbf{u}}_{\text{eq}} + \mathbf{u}_s = \tilde{\mathcal{B}}_\sigma^{-1}(\mathbf{x})(\mathbf{v}_s - \tilde{\alpha}_\sigma(\mathbf{x})) \quad (3.24)$$

Remark 3 Eq. (3.24) is widely used in sliding mode control techniques regardless of the choice of sliding surface and reaching law. For example, this control structure is adopted using integral-type sliding surfaces [6, 11, 19, 25], linear sliding surfaces [4, 10, 16], dynamic sliding manifolds [26], terminal sliding surfaces [27–29], finite reaching time continuous sliding mode designs [5], etc.

It will be shown by an example that sliding mode control laws designed in the form of Eq. (3.24) are essentially NDI based. Since INDI is able to preserve the benefits of NDI (e.g., decoupling, linearization) while requiring reduced model knowledge, it can also be used in sliding mode control designs. The integral sliding surface is taken as an example, because of its simplicity, strong robustness, and design flexibility.

Design the matrix $\mathbf{D} = \text{diag}\{\mathbf{D}_i\}$, $\mathbf{D}_i = [K_{i,1}, \dots, K_{i,\rho_i-1}, 1]$, $\mathbf{K}_0 = \text{diag}\{K_{i,0}\}$, $\mathbf{K}_{i,0} = [K_{i,0}, 0, \dots, 0]$, $i = 1, 2, \dots, m$, and then design the integral-type sliding variable as

$$\sigma = \mathbf{D}\mathbf{e} - \mathbf{D}\mathbf{e}(t_0) - \int_0^t \mathbf{D}(\mathbf{A}_c - \mathbf{B}_c\mathbf{K})\mathbf{e}d\tau = \mathbf{D}\mathbf{e} - \mathbf{D}\mathbf{e}(t_0) + \int_0^t \mathbf{K}_0\mathbf{e}d\tau \quad (3.25)$$

where \mathbf{K} matrix is the same as used in Eqs. (3.6, 3.11). $\mathbf{D}(\mathbf{A}_c - \mathbf{B}_c\mathbf{K}) = -\mathbf{K}_0$ can be proved by substituting the expressions for \mathbf{D} , \mathbf{K}_0 into Eq. (3.25), and using the condition that $(\mathbf{A}_0^i, \mathbf{B}_0^i, \mathbf{C}_0^i)$ is a canonical form representation of a chain of ρ_i integrators.

Equivalently, Eq. (3.25) can be written as

$$\begin{aligned} \sigma_i &= e_i^{(\rho_i-1)} + K_{i,\rho_i-1}e^{(\rho_i-2)} + K_{i,\rho_i-2}e^{(\rho_i-3)} + \dots + K_{i,1}e^{(0)} + \int_0^t K_{i,0}e_i d\tau \\ &\quad - (e_i^{(\rho_i-1)}(t_0) + K_{i,\rho_i-1}e^{(\rho_i-2)}(t_0) + K_{i,\rho_i-2}e^{(\rho_i-3)}(t_0) + \dots + K_{i,1}e^{(0)}(t_0)) \end{aligned} \quad (3.26)$$

It can be seen from Eq. (3.26) that $\boldsymbol{\sigma}(t_0) = \mathbf{0}$, which means if the initial conditions are known, system dynamics initiate on the sliding surface without a reaching phase. Furthermore, $\dot{\boldsymbol{\sigma}} = \mathbf{0}$ is equal to the desired closed-loop error dynamics as shown by

$$\begin{aligned}\dot{\sigma}_i &= e_i^{(\rho_i)} + K_{i,\rho_i-1} e_i^{(\rho_i-1)} + K_{i,\rho_i-2} e_i^{(\rho_i-2)} + \dots + K_{i,1} e_i^{(1)} + K_{i,0} e_i = 0, \quad i = 1, 2, \dots, m, \\ \dot{\boldsymbol{\sigma}} &= \mathbf{y}^{(\rho)} - \mathbf{y}_r^{(\rho)} + \mathbf{K}\mathbf{e} = \mathbf{0}\end{aligned}\quad (3.27)$$

In the preceding equation, $\mathbf{y}^{(\rho)}$ contains system dynamics, $\mathbf{y}_r^{(\rho)}$ and $\mathbf{K}\mathbf{e}$ are known or measurable. Substituting Eq. (3.2) into Eq. (3.27), control law designed in the form of Eq. (3.24) is

$$\begin{aligned}\dot{\boldsymbol{\sigma}} &= (\boldsymbol{\alpha}(\mathbf{x}) + \mathcal{B}(\mathbf{x})\mathbf{u}) - \mathbf{y}_r^{(\rho)} + \mathbf{K}\mathbf{e} = \mathbf{0} \\ \mathbf{u}_{\text{ndi-s}} &= \bar{\mathbf{u}}_{\text{eq}} + \mathbf{u}_s = \bar{\mathcal{B}}^{-1}(\mathbf{x})(\mathbf{v}_s - \bar{\boldsymbol{\alpha}}(\mathbf{x}) - \mathbf{K}\mathbf{e} + \mathbf{y}_r^{(\rho)})\end{aligned}\quad (3.28)$$

which belongs to NDI-SMC (Eq. (3.21)) with $\mathbf{v}_c = \mathbf{y}_r^{(\rho)} - \mathbf{K}\mathbf{e}$.

By contrast, if the incremental output dynamics (Eq. (3.9)) are substituted into Eq. (3.27), then INDI-SMC (Eq. (3.20)) is designed as

$$\begin{aligned}\dot{\boldsymbol{\sigma}} &= (\mathbf{y}_0^{(\rho)} + \mathcal{B}(\mathbf{x}_0)\Delta\mathbf{u} + \boldsymbol{\delta}(\mathbf{x}, \Delta t)) - \mathbf{y}_r^{(\rho)} + \mathbf{K}\mathbf{e} = \mathbf{0} \\ \Delta\mathbf{u}_{\text{indi-s}} &= \bar{\mathcal{B}}^{-1}(\mathbf{x}_0)(\mathbf{v}_s - \mathbf{y}_0^{(\rho)} - \mathbf{K}\mathbf{e} + \mathbf{y}_r^{(\rho)})\end{aligned}\quad (3.29)$$

As an example, \mathbf{v}_s is designed in the classical way as

$$\mathbf{v}_s = -\mathbf{K}_s \text{sign}(\boldsymbol{\sigma}) = -[K_{s,1} \text{sign}(\sigma_1), K_{s,2} \text{sign}(\sigma_2), \dots, K_{s,m} \text{sign}(\sigma_m)]^T \quad (3.30)$$

where sign represents the signum function, and the switching gains $K_{s,i} > 0$, $i = 1, 2, \dots, m$. If the conditions in Theorem 3 are satisfied, using Eq. (3.14), then the time derivative of the candidate Lyapunov function $V = \frac{1}{2} \boldsymbol{\sigma}^T \boldsymbol{\sigma}$ under the control of Eqs. (3.29, 3.30) is calculated by

$$\begin{aligned}\dot{V} &= \boldsymbol{\sigma}^T \dot{\boldsymbol{\sigma}} = \boldsymbol{\sigma}^T [\mathbf{y}_0^{(\rho)} + \mathcal{B}(\mathbf{x}_0)\bar{\mathcal{B}}^{-1}(\mathbf{x}_0)(\mathbf{v}_s - \mathbf{y}_0^{(\rho)} + \mathbf{v}_c) + \boldsymbol{\delta}(\mathbf{x}, \Delta t) - \mathbf{v}_c] \\ &= \boldsymbol{\sigma}^T [\boldsymbol{\delta}(\mathbf{x}, \Delta t) + (\mathcal{B}\bar{\mathcal{B}}^{-1} - \mathbf{I})(\mathbf{v}_c - \mathbf{y}_0^{(\rho)}) + \mathcal{B}\bar{\mathcal{B}}^{-1}\mathbf{v}_s] \\ &= \boldsymbol{\sigma}^T [\boldsymbol{\varepsilon}_{\text{indi}} - \mathcal{B}\bar{\mathcal{B}}^{-1}\mathbf{K}_s \text{sign}(\boldsymbol{\sigma})] \leq \sum_{i=1}^m (|\sigma_i| |\varepsilon_{\text{indi},i}| + \bar{b} K_{s,i} |\sigma_i| - K_{s,i} |\sigma_i|) \\ &\leq -\eta \sum_{i=1}^m |\sigma_i| = -\eta \boldsymbol{\sigma}^T \text{sign}(\boldsymbol{\sigma}), \quad \forall K_{s,i} \geq \frac{\eta + |\varepsilon_{\text{indi},i}|}{1 - \bar{b}}.\end{aligned}\quad (3.31)$$

where η is a small positive constant. $\dot{V} \leq -\eta \boldsymbol{\sigma}^T \text{sign}(\boldsymbol{\sigma})$ is referred to as the η reaching law and guarantees the sliding surface $\boldsymbol{\sigma} = \mathbf{0}$ is reached in finite time [6–8]. On the sliding surface, the desired error dynamics are achieved, which ensure \mathbf{e} converges to zero.

Reviewing the discussions in subsection 3.2.3, the boundedness of $\boldsymbol{\varepsilon}_{\text{ndi}}$ is undetermined even if the conditions in Theorem 3 are satisfied. For the feasibility of sliding mode control design, assume $\boldsymbol{\varepsilon}_{\text{ndi}}$ is bounded, then similar to the derivations in Eq. (3.31), NDI-SMC given by Eq. (3.28) guarantees the convergence of $\boldsymbol{\sigma}$, when $\mathbf{v}_s = -\mathbf{K}_s \text{sign}(\boldsymbol{\sigma})$, $\forall K_{s,i} \geq (\eta + |\varepsilon_{\text{ndi},i}|)/(1 - \bar{b})$.

Remark 4 First-order sliding mode control that contains a model-based nominal equivalent control term are essentially NDI based, and can be correspondingly designed in the proposed incremental framework. Recall the gain requirement in Eq. (3.31), and the analyses in subsection 3.2.3, this incremental framework is able to passively resist a wider range of perturbations with reduced control gains, because the boundedness condition of $\boldsymbol{\varepsilon}_{\text{indi}}$ is easier to fulfill, and there exists an f_s which makes the bound of $\boldsymbol{\varepsilon}_{\text{indi}}$ smaller than the bound of $\boldsymbol{\varepsilon}_{\text{ndi}}$ under the same perturbation circumstances.

3.3.2. HIGHER-ORDER INCREMENTAL SLIDING MODE CONTROL

The problem of higher-order sliding mode control is equivalent to the finite time stabilization of higher-order integrator chains with bounded nonlinear perturbations [30, 42]. Since NDI is able to reduce the dynamic couplings and nonlinearities by providing a preliminary feedback term based on the nominal model, it is widely used in higher-order sliding mode controllers [30–32].

Consider an output tracking problem for the system described by Eq. (3.1), and choose the sliding variable as $\boldsymbol{\sigma} = \mathbf{y} - \mathbf{y}_r$. Assume the time derivatives of $\sigma_i, \dot{\sigma}_i, \dots, \sigma_i^{(r_i-1)}$ are continuous functions for all $i = 1, 2, \dots, m$, and the manifold defined as

$$\mathcal{S}^r = \{\mathbf{x} | \sigma_i(\mathbf{x}) = \dot{\sigma}_i(\mathbf{x}) = \dots = \sigma_i^{(r_i-1)}(\mathbf{x}) = 0, i = 1, 2, \dots, m.\} \quad (3.32)$$

called the “ r^{th} -order sliding set” [30, 43] is non empty and locally an integral set in the Filippov sense [44], then the motion on \mathcal{S}^r is called the “ r^{th} -order sliding mode” with respect to the sliding variable $\boldsymbol{\sigma}$. It is noteworthy that a r^{th} -order sliding mode can also be established for a system with relative degree $\boldsymbol{\rho}$ less than \mathbf{r} by manually increasing the length of the integrator chains [40]. For clarity, only $\boldsymbol{\rho} = \mathbf{r}$ will be considered in the following derivations.

Recall Eqs. (3.2, 3.5), and define $\mathbf{z} = [\mathbf{z}_1; \mathbf{z}_2; \dots; \mathbf{z}_m]$, $\mathbf{z}_i = [\sigma_i(\mathbf{x}), \mathcal{L}_f \sigma_i(\mathbf{x}), \dots, \mathcal{L}_f^{r_i-1} \sigma_i(\mathbf{x})]^T$, $i = 1, 2, \dots, m$, then the dynamics of the sliding variable $\boldsymbol{\sigma}$ are given by

$$\dot{\mathbf{z}} = \mathbf{A}_c \mathbf{z} + \mathbf{B}_c [\boldsymbol{\alpha}(\mathbf{x}) + \mathcal{B}(\mathbf{x}) \mathbf{u} - \mathbf{y}_r^{(\boldsymbol{\rho})}], \quad \boldsymbol{\sigma}^{(r)} = \mathbf{y}^{(\boldsymbol{\rho})} - \mathbf{y}_r^{(\boldsymbol{\rho})} \quad (3.33)$$

In order to achieve the r^{th} -order sliding mode, Ref. [30] design a higher-order sliding mode controller in the form of Eq. (3.21) as

$$\mathbf{u}_{\text{ndi-s}} = \bar{\mathcal{B}}^{-1}(\mathbf{x})(\mathbf{v}_s + \mathbf{v}_n - \bar{\boldsymbol{\alpha}}(\mathbf{x}) + \mathbf{y}_r^{(\boldsymbol{\rho})}) \quad (3.34)$$

where \mathbf{v}_n is a continuous virtual control to achieve the finite time stabilization of the integrator chains [30, 45]. $\mathbf{v}_c = \mathbf{v}_n + \mathbf{y}_r^{(\boldsymbol{\rho})}$ in Eq. (3.34), which is able to stabilize the *unperturbed system*. It is noteworthy that the formulations for $\boldsymbol{\varepsilon}_{\text{ndi/indi}}$ (Eqs. (3.8, 3.14)) and Theorem 3 are not constrained by the specific \mathbf{v}_c design, they are valid as long as \mathbf{v}_c is continuous in time.

By contrast, using the incremental output dynamics (Eq. (3.9)), the incremental higher-order sliding mode control law is designed in the form of Eq. (3.20) as

$$\Delta \mathbf{u}_{\text{ndi-s}} = \bar{\mathcal{B}}^{-1}(\mathbf{x}_0)(\mathbf{v}_s + \mathbf{v}_n - \mathbf{y}_0^{(\boldsymbol{\rho})} + \mathbf{y}_r^{(\boldsymbol{\rho})}) \quad (3.35)$$

The r^{th} -order sliding mode can then be established by properly designing \mathbf{v}_n and \mathbf{v}_s . As an example, design the augmented sliding variable as $\mathbf{s} = \boldsymbol{\sigma}^{(r-1)} + \mathbf{s}_{au}$, $\dot{\mathbf{s}}_{au} = -\mathbf{v}_n$,

and design \mathbf{v}_s in the classical way as $\mathbf{v}_s = -\mathbf{K}_h \text{sign}(\mathbf{s}) = -[K_{h,1} \text{sign}(s_1), K_{h,2} \text{sign}(s_2), \dots, K_{h,m} \text{sign}(s_m)]^T$, $K_{h,i} > 0$, $i = 1, 2, \dots, m$. When the conditions in Theorem 3 are satisfied, using Eq. (3.14), the time derivative of the candidate Lyapunov function $V_s = \frac{1}{2} \mathbf{s}^T \mathbf{s}$ yields

$$\begin{aligned}
 \dot{V}_s &= \mathbf{s}^T \dot{\mathbf{s}} = \mathbf{s}^T [\mathbf{y}_0^{(\rho)} + \mathcal{B}(\mathbf{x}_0) \bar{\mathcal{B}}^{-1}(\mathbf{x}_0) (\mathbf{v}_s + \mathbf{v}_n - \mathbf{y}_0^{(\rho)} + \mathbf{y}_r^{(\rho)}) + \boldsymbol{\delta}(\mathbf{x}, \Delta t) - \mathbf{y}_r^{(\rho)} - \mathbf{v}_n] \\
 &= \mathbf{s}^T [\boldsymbol{\delta}(\mathbf{x}, \Delta t) + (\mathcal{B} \bar{\mathcal{B}}^{-1} - \mathbf{I})(\mathbf{v}_c - \mathbf{y}_0^{(\rho)}) + \mathcal{B} \bar{\mathcal{B}}^{-1} \mathbf{v}_s] \\
 &= \mathbf{s}^T [\boldsymbol{\varepsilon}_{\text{indi}} - \mathcal{B} \bar{\mathcal{B}}^{-1} \mathbf{K}_h \text{sign}(\mathbf{s})] \leq \sum_{i=1}^m (|s_i| |\boldsymbol{\varepsilon}_{\text{indi},i}| + \bar{b} K_{h,i} |s_i| - K_{h,i} |s_i|) \\
 &\leq -\eta \sum_{i=1}^m |s_i| = -\eta \mathbf{s}^T \text{sign}(\mathbf{s}), \quad \forall K_{h,i} \geq \frac{\eta + |\boldsymbol{\varepsilon}_{\text{indi},i}|}{1 - \bar{b}}. \tag{3.36}
 \end{aligned}$$

Eq. (3.36) proves that when $K_{h,i} \geq (\eta + |\boldsymbol{\varepsilon}_{\text{indi},i}|)/(1 - \bar{b})$, the sliding surface $\mathbf{s} = \mathbf{0}$ will be reached in finite time. On the sliding surface, using the equivalent control method [41], $\boldsymbol{\sigma}^{(r)} = -\boldsymbol{\delta}_{au} = \mathbf{v}_n$, which means the system dynamics are integrator chains with \mathbf{v}_n as an input. Design \mathbf{v}_n using the geometric homogeneity based method introduced in [45], then the r^{th} -order sliding mode is established in finite time.

Analogously, assume $\|\mathbf{I} - \mathcal{B} \bar{\mathcal{B}}^{-1}\| \leq \bar{b} < 1$ and $\boldsymbol{\varepsilon}_{\text{ndi}}$ is bounded, then Eq. (3.34) guarantees the establishment of the r^{th} -order sliding mode in finite time when \mathbf{v}_n ensures finite time convergence of integrator chains, and $\mathbf{v}_s = -\mathbf{K}_h \text{sign}(\mathbf{s})$, $\forall K_{h,i} \geq (\eta + |\boldsymbol{\varepsilon}_{\text{ndi},i}|)/(1 - \bar{b})$.

Remark 5 In view of the gain requirement in Eq. (3.36), similar to the Remark 4, designing a higher-order sliding mode controller in the incremental form enables it to passively resist a wider range of perturbations using lower control gains.

Remark 6 For simplicity, the classical \mathbf{v}_s design using the signum function is adopted in the preceding derivations. To migrate the chattering effects, continuous approximations of the signum function are widely used in the literature [2, 4, 6–9, 12, 16]. Other continuous \mathbf{v}_s designs such as the fast terminal sliding mode-type reaching law [29] can also be used. In spite of the variations of \mathbf{v}_s designs, the relation that larger perturbation bounds require higher control gains consistently holds.

Remark 7 The sliding mode control gains can also be adaptive, which removes the pre-knowledge requirement on the uncertainty bound. Many advanced adaptive sliding mode control methods are aiming for the “as small as possible” gain to migrate the chattering effects [13–15, 17]. Theoretically, the smallest gain that can enforce sliding motion is a monotonically increasing function of the perturbation bound. Since there exists an f_s such that the bound of $\boldsymbol{\varepsilon}_{\text{indi}}$ is smaller as compared to the bound of $\boldsymbol{\varepsilon}_{\text{ndi}}$, the chattering reduction benefit of the incremental framework still holds in the context of adaptive sliding mode control.

3.3.3. FIRST-ORDER INDI-SMC DRIVEN BY FIRST-ORDER SLIDING MODE DISTURBANCE OBSERVERS

An increasingly popular approach is designing sliding mode control in conjunction with sliding mode disturbance observers, known as sliding mode control driven by sliding

mode disturbance observers [14, 15, 18–21, 31–33]. The main idea is using the uncertainty observations in \mathbf{v}_s such that the uncertainties are directly compensated in the framework of Eq. (3.21). This subsection will show the merits of the incremental framework, when a first-order disturbance observer is incorporated. Higher-order sliding mode controllers/observers will be discussed in the next subsection.

Considering the first-order sliding variable Eq. (3.25) with dynamics given by Eq. (3.27) as an example. Ref. [18–21] design sliding model controllers driven by sliding mode disturbance observers in the form of Eq. (3.21), which leads to the closed-loop dynamics:

$$\begin{aligned}\dot{\boldsymbol{\sigma}} &= \mathbf{y}^{(\rho)} - \mathbf{v}_c = (\boldsymbol{\alpha}(\mathbf{x}) + \mathcal{B}(\mathbf{x})\mathbf{u}_{\text{ndi-}s}) - \mathbf{v}_c \\ &= \mathbf{v}_s + ((\boldsymbol{\alpha} - \bar{\boldsymbol{\alpha}}) + (\mathcal{B} - \bar{\mathcal{B}})\mathbf{u}_{\text{ndi-}s}) \triangleq \mathbf{v}_s + \boldsymbol{\varepsilon}_{\text{ndi-}s}\end{aligned}\quad (3.37)$$

in which \mathbf{v}_s contains the perturbation observations, and will be designed later. It is worth noting that the uncertainties in the control effectiveness matrix $\mathcal{B}(\mathbf{x})$ are not considered in [18–21], while they are included in the present chapter.

By contrast, using the incremental framework given by Eq. (3.20) leads to

$$\begin{aligned}\dot{\boldsymbol{\sigma}} &= \mathbf{y}^{(\rho)} - \mathbf{v}_c = (\mathbf{y}_0^{(\rho)} + \mathcal{B}(\mathbf{x}_0)\Delta\mathbf{u}_{\text{ndi-}s} + \boldsymbol{\delta}(\mathbf{x}, \Delta t)) - \mathbf{v}_c \\ &= \mathbf{v}_s + (\boldsymbol{\delta}(\mathbf{x}, \Delta t) + (\mathcal{B} - \bar{\mathcal{B}})\Delta\mathbf{u}_{\text{ndi-}s}) \triangleq \mathbf{v}_s + \boldsymbol{\varepsilon}_{\text{ndi-}s}\end{aligned}\quad (3.38)$$

Proposition 2 *If $\|\mathbf{I} - \mathcal{B}\bar{\mathcal{B}}^{-1}\| \leq \bar{b} < 1$, $\|\boldsymbol{\delta}(\mathbf{x}, \Delta t)\| \leq \bar{\delta}$, and if \mathbf{v}_s is continuous in time, under sufficiently high sampling frequency f_s , the residual error term $\boldsymbol{\varepsilon}_{\text{ndi-}s}$ in Eq. (3.38) is ultimately bounded.*

Proof: The only difference between $\boldsymbol{\varepsilon}_{\text{ndi-}s}$ (Eq. (3.38)) and $\boldsymbol{\varepsilon}_{\text{ndi}}$ (Eq. (3.14)) is the incorporation of \mathbf{v}_s . In the context of sliding mode observer designs, \mathbf{v}_s is always continuous in time. Therefore, analogous to Eq. (3.17) and the subsequent discussions, under sufficiently high f_s , $\Delta\mathbf{v}_s = \mathbf{v}_s - \mathbf{v}_{s_0}$ is bounded. Denote the bound as $\overline{\Delta\mathbf{v}_s}$, then analogous to the proof of Theorem 3, $\boldsymbol{\varepsilon}_{\text{ndi-}s}$ is bounded for all k , and is ultimately bounded by

$$\|\boldsymbol{\varepsilon}_{\text{ndi-}s}\| \leq \frac{\overline{\Delta\mathbf{v}_c}\bar{b} + \overline{\Delta\mathbf{v}_s}\bar{b} + \bar{\delta}}{1 - \bar{b}}\quad (3.39)$$

□

Moreover, since \mathbf{v}_s is continuous in time, similar to the discussions in subsection 3.2.3, under the same perturbation circumstances, there exists an f_s such that $\boldsymbol{\varepsilon}_{\text{ndi-}s}$ has a smaller bound as compared to $\boldsymbol{\varepsilon}_{\text{ndi-}s}$ (Eq. (3.37)). This feature is beneficial to disturbance observations, which will be shown as follows:

Using the first-order sliding mode disturbance observer proposed in [18–21], the auxiliary sliding variable \mathbf{s} is designed as $\mathbf{s} = \boldsymbol{\sigma} + \mathbf{z}_o$, $\dot{\mathbf{z}}_o = -\mathbf{v}_s - \mathbf{v}_o$, with dynamics $\dot{\mathbf{s}} = \boldsymbol{\varepsilon}_{\text{ndi-}s/\text{ndi-}s} - \mathbf{v}_o$ under the control of Eqs. (3.21, 3.20). If \mathbf{s} is stabilized by $\mathbf{v}_o = \mathbf{K}_{ob}\text{sign}(\mathbf{s})$, then the equivalent control exactly equals $\boldsymbol{\varepsilon}_{\text{ndi-}s/\text{ndi-}s}$. This equivalent control can be estimated by low-pass filtering \mathbf{v}_o , consequently, the estimated equivalent control $\hat{\mathbf{v}}_{\text{eq}}$ reconstructs $\boldsymbol{\varepsilon}_{\text{ndi-}s/\text{ndi-}s}$ with a small error proportional to the time constant of the low-pass filter. Finally, designing $\mathbf{v}_s = -\mathbf{K}_\sigma\boldsymbol{\sigma} - \hat{\mathbf{v}}_{\text{eq}}$ with positive definite \mathbf{K}_σ ensures $\boldsymbol{\sigma}$ is bounded by an arbitrary small bound.

Remark 8 The sufficient condition for stabilizing \mathbf{s} is the observer gains $K_{ob,i} > |\epsilon_{\text{ndi-}s/\text{indi-}s}| + \eta$, with a small positive η . Even though the observation term \mathbf{v}_s is continuous, the chattering effects are only attenuated instead of being rejected by the filtering process [19]. Therefore, aiming for the “as small as possible” observer gains is still meaningful. Since there exists an f_s such that $\epsilon_{\text{indi-}s}$ has a smaller bound as compared to $\epsilon_{\text{ndi-}s}$, the incremental framework is beneficial to chattering reduction.

3.3.4. HIGHER-ORDER INDI-SMC DRIVEN BY HIGHER-ORDER SLIDING MODE DISTURBANCE OBSERVERS

This subsection will show how to design a higher-order sliding mode control driven by a higher-order sliding mode disturbance observer in the incremental framework. Following the derivations in subsection 3.3.2, design the sliding variable as $\boldsymbol{\sigma} = \mathbf{y} - \mathbf{y}_r$ and design $\mathbf{v}_c = \mathbf{v}_n + \mathbf{y}_r^{(\rho)}$, then the dynamics of $\boldsymbol{\sigma}$ under the control of Eq. (3.21) is

$$\boldsymbol{\sigma}^{(r)} = \mathbf{y}^{(\rho)} - \mathbf{y}_r^{(\rho)} = \tilde{\boldsymbol{\alpha}}(\mathbf{x}) + \tilde{\mathcal{B}}(\mathbf{x})\mathbf{u}_{\text{ndi-}s} + \boldsymbol{\epsilon}_{\text{ndi-}s} - \mathbf{y}_r^{(\rho)} = \mathbf{v}_n + \mathbf{v}_s + \boldsymbol{\epsilon}_{\text{ndi-}s} \quad (3.40)$$

By contrast, using Eqs. (3.9, 3.38), the dynamics of $\boldsymbol{\sigma}$ under the control of Eq. (3.20) equals

$$\boldsymbol{\sigma}^{(r)} = \mathbf{y}^{(\rho)} - \mathbf{y}_r^{(\rho)} = \mathbf{y}_0^{(\rho)} + \tilde{\mathcal{B}}(\mathbf{x}_0)\Delta\mathbf{u}_{\text{indi-}s} + \boldsymbol{\epsilon}_{\text{indi-}s} - \mathbf{y}_r^{(\rho)} = \mathbf{v}_n + \mathbf{v}_s + \boldsymbol{\epsilon}_{\text{indi-}s} \quad (3.41)$$

The only difference between Eq. (3.40) and Eq. (3.41) is the value of the perturbation terms. Since $\epsilon_{\text{indi-}s}$ has better properties than $\epsilon_{\text{ndi-}s}$, higher-order sliding mode disturbance observers (such as the (adaptive) super-twisting disturbance observer) designed for Eq. (3.40) [14, 15, 18–21, 31–33] can be straightforwardly applied to Eq. (3.41). Design the augmented sliding variable as $\mathbf{s} = \boldsymbol{\sigma}^{(r-1)} + \mathbf{s}_{au}$, $\dot{\mathbf{s}}_{au} = -\mathbf{v}_n$, then $\dot{\mathbf{s}} = \mathbf{v}_s + \boldsymbol{\epsilon}_{\text{ndi-}s/\text{indi-}s}$ for dynamics given by Eqs. (3.40, 3.41). If \mathbf{s} is stabilized by the (adaptive) super-twisting control, then \mathbf{v}_s observes $-\epsilon_{\text{ndi-}s/\text{indi-}s}$ in finite time. Consequently, the closed-loop systems described by Eqs. (3.40, 3.41) behave like *unperturbed systems* in finite time. It is noteworthy that the observation term \mathbf{v}_s provided by (adaptive) super-twisting observer is continuous because of the integration of the signum function.

Remark 9 Theoretically, (adaptive) super-twisting control/observer may be less suitable for resisting sudden (discontinuous in time) on-board faults or damages, since the classical super-twisting control/observer requires bounded $\dot{\epsilon}_{\text{ndi-}s/\text{indi-}s}$, and the adaptive super-twisting requires bounded $\ddot{\epsilon}_{\text{ndi-}s/\text{indi-}s}$ [14, 15, 19]. Nevertheless, many physical processes in reality are at least twice differentiable, which makes the incorporation of (adaptive) super-twisting control/observer possible.

3.3.5. ADVANTAGES OF THE INDI-SMC FRAMEWORK

In this subsection, the NDI (Eq. (3.6)), INDI (Eq. (3.11)), NDI-SMC (Eq. (3.21)), and INDI-SMC (Eq. (3.20)) methods will be compared. The main focus of this chapter is on demonstrating the properties of the incremental framework, instead of specific \mathbf{v}_c and \mathbf{v}_s designs. Therefore, the following comparisons are also independent of \mathbf{v}_c , \mathbf{v}_s , as long as they are kept consistent in the four different control frameworks for fair comparisons.

Fig. 3.1 illustrates the relations of the four control frameworks. When the sliding mode module for calculating \mathbf{v}_s is deactivated, Fig. 3.1 shows the control structure of

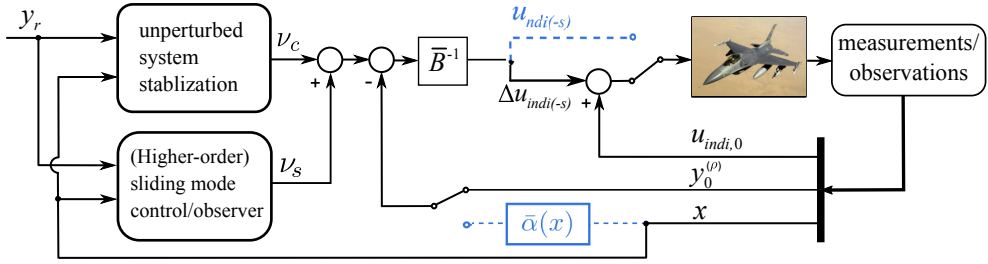


Figure 3.1: Control structures of NDI, INDI, NDI-SMC, and INDI-SMC.

NDI and INDI. To be specific, when the two switches are connected with the blue dashed lines, Fig. 3.1 shows the control structure of NDI, where the nominal model $\bar{\alpha}(x)$ is needed. By contrast, when the two switches are connected with the black solid lines, INDI control presents, which does not need the model $\bar{\alpha}(x)$ but depends on the measurements/estimations of $y_0^{(\rho)}$ and $u_{\text{indi},0}$. Activating the sliding mode module inserts the v_s virtual control for resisting perturbations, which results in the NDI-SMC, and INDI-SMC frameworks. Moreover, INDI and INDI-SMC design the control increments, while NDI and NDI-SMC directly design the total control commands.

By virtue of the incorporation of v_s , the advantage of INDI-SMC over INDI is straightforward, i.e., robustness enhancement. On the other hand, the advantages of the INDI-SMC framework over NDI-SMC are:

1. Less model dependency and lower computational burden.
2. Lower sliding mode control/observer gains required.
3. Improved robustness, since INDI is more robust than NDI.
4. Capability to solve problems that are non-affine in the control.

$\bar{\alpha}(x)$ contains the aerodynamics for aerospace systems, which are difficult to be modeled accurately. Since the incremental framework is independent of $\bar{\alpha}(x)$, the implementation process is simplified, and the computational burden can also be reduced. INDI-SMC also requires lower control and observer gains, mainly because of the better properties of $\epsilon_{\text{indi}(-s)}$. The conditions in Theorem 3 and Proposition 2 ensure the boundedness of $\epsilon_{\text{indi}(-s)}$. By contrast, being independent of Δt , the boundedness of $\epsilon_{\text{ndi}(-s)}$ is not guaranteed under the same conditions. Moreover, in the same fault scenario, there exists an f_s such that $\epsilon_{\text{indi}(-s)}$ has a smaller upper bound as compared to $\epsilon_{\text{ndi}(-s)}$. These properties enable INDI-SMC to passively resist a wider range of perturbations using lower control and observer gains, as compared to NDI-SMC in the literature. In addition, the incremental framework can also deal with non-affine in the control problems, since the incremental dynamic equation (Eq. (3.9)) is derived by taking partial derivative with respect to u . The merits of the incremental sliding mode control framework will be numerically verified in Sec. 3.5.

3.4. FAULT-TOLERANT FLIGHT CONTROL DESIGN

In this section, the nominal six degrees of freedom nonlinear equations of motion of aircraft are given first. Then the actuator faults and structural damages are modeled. After that, the control methods derived in Sec. 3.3 are applied to damaged aircraft fault-tolerant control problems.

3.4.1. NOMINAL EQUATIONS OF MOTION

In the nominal case, the origin of the body-fixed frame is assumed to coincide with the aircraft center of mass (c.m.), and the equations of motion for a rigid aircraft are given by

$$\begin{aligned} \begin{bmatrix} \dot{V} \\ \dot{\omega} \end{bmatrix} &= \begin{bmatrix} m\mathbf{I} & \mathbf{0} \\ \mathbf{0} & \mathbf{J} \end{bmatrix}^{-1} \begin{bmatrix} -m\tilde{\omega}\mathbf{V} + \mathbf{F} \\ -\tilde{\omega}\mathbf{J}\omega + \mathbf{M} \end{bmatrix} \\ \dot{\boldsymbol{\theta}} &= \mathbf{T}(\boldsymbol{\theta})\boldsymbol{\omega} \end{aligned} \quad (3.42)$$

where $\mathbf{V} = [u, v, w]^T$ and $\boldsymbol{\omega} = [p, q, r]^T$ represent the translation and rotational velocities of the body-fixed frame relative to the inertial frame. $\boldsymbol{\theta} = [\phi, \theta, \psi]^T$ contains the Euler angles. m is the total mass and \mathbf{J} represents the inertia matrix. \mathbf{F} and \mathbf{M} are the total force and moment vectors. The $\mathbf{T}(\boldsymbol{\theta})$ matrix links angular velocities $\boldsymbol{\omega}$ to Eulerian velocities $\dot{\boldsymbol{\theta}}$. Bold mark indicates vectors and matrices. $\tilde{(\cdot)}$ denotes the skew-symmetric matrix of the corresponding vector. \mathbf{F} and \mathbf{M} contain aerodynamic, gravitational, and thrust forces and moments. Furthermore, the aerodynamic forces and moments are normally given as functions of the aerodynamic coefficients as

$$\begin{aligned} \mathbf{M}_a &= q_\infty S \mathbf{M}_{bc} \left(\begin{bmatrix} C_l(\beta, r, p) \\ C_m(\alpha, \dot{\alpha}, q) \\ C_n(\beta, r, p) \end{bmatrix} + \begin{bmatrix} C_{l_{\delta_a}}(\alpha, \beta) & 0 & C_{l_{\delta_r}}(\alpha, \beta) \\ 0 & C_{m_{\delta_e}}(\alpha) & 0 \\ C_{n_{\delta_a}}(\alpha, \beta) & 0 & C_{n_{\delta_r}}(\alpha, \beta) \end{bmatrix} \begin{bmatrix} \delta_a \\ \delta_e \\ \delta_r \end{bmatrix} \right) \\ \mathbf{F}_a &= q_\infty S [C_x(\alpha, \beta, q, \delta_e), C_y(\alpha, \beta, p, r, \delta_a, \delta_r), C_z(\alpha, \beta, q, \delta_e)]^T \end{aligned} \quad (3.43)$$

In the preceding equation, α, β represent the angle of attack and the sideslip angle. V is the airspeed, and the dynamic pressure is given by $q_\infty = 0.5\rho V^2$ (ρ is the air density). $\mathbf{M}_{bc} = \text{diag}([b, \bar{c}, b])$, and S, b, \bar{c} are the wing area, wing span and mean aerodynamic chord respectively.

3.4.2. ACTUATOR FAULTS

The actuator faults considered in this chapter are the loss of control surface area and control surface jamming problems. The inertia effects of loss of control surface area are assumed to be negligible, and the aerodynamic effects can be modeled by multiplying the control derivatives with an effectiveness scaling factor, namely, $C'_{ij} = \mu_j C_{ij}$, $i = l, m, n$, $j = \delta_a, \delta_e, \delta_r$, $\mu_j \in [0, 1]$, with $(\cdot)'$ indicating the post-failure condition.

There are two main effects of actuator jamming. One is the influence on control effectiveness, the other is the induced extra forces and moments. If one side of the ailerons or elevators is stuck, the corresponding control derivatives are halved, i.e., $\mu_j = 0.5$, $j = \delta_a, \delta_e$. Jamming faults also introduce new control derivatives such that the decoupling

between longitudinal and lateral controls no longer holds. Specifically, aileron jamming would introduce $C_{m_{\delta_a}}$, and elevator jamming would introduce $C_{l_{\delta_e}}$ and $C_{n_{\delta_e}}$.

Furthermore, extra forces and moments will be induced if control surfaces are jammed at non-neutral positions. If one of the ailerons is jammed at $\delta_{a\Delta}$, the induced force and moment coefficients can be given by

$$\Delta C_l = \frac{1}{2} C_{l_{\delta_a}} \delta_{a\Delta}, \quad \Delta C_n = \frac{1}{2} C_{n_{\delta_a}} \delta_{a\Delta}, \quad \Delta C_y = \frac{1}{2} C_{y_{\delta_a}} \delta_{a\Delta}, \quad \Delta C_z = \frac{\Delta C_l b}{r_{a_y}}, \quad \Delta C_m = -\frac{\Delta C_l b r_{a_x}}{\bar{c} r_{a_y}} \quad (3.44)$$

where $\mathbf{r}_a = [r_{a_x}, r_{a_y}, r_{a_z}]^T$ is the position vector from c.m. to the aerodynamic center of the jammed aileron. Analogously, the induced force and moment coefficients of one-side elevator jamming is calculated by

$$\Delta C_z = -\frac{C_{m_{\delta_e}} \delta_{e\Delta} \bar{c}}{2 r_{e_x}}, \quad \Delta C_m = \frac{1}{2} C_{m_{\delta_e}} \delta_{e\Delta}, \quad \Delta C_l = \frac{\Delta C_z r_{e_y}}{b} \quad (3.45)$$

with $\mathbf{r}_e = [r_{e_x}, r_{e_y}, r_{e_z}]^T$ indicates the position vector from c.m. to the aerodynamic center of the jammed elevator.

3.4.3. STRUCTURAL DAMAGES

There are three main effects of structural damages: the changes of aerodynamic properties, inertia properties, and the control effectiveness [46, 47].

The structural damages may reduce the control effectiveness, and introduce new control derivatives if asymmetric damages are encountered. The methods for modeling these effects have been discussed in the previous subsection.

The structural damages are normally accompanied with mass loss. As a consequence, the center of mass instantaneously shifts to a new location. Since Eq. (3.42) uses c.m. as the reference frame origin O , it should be modified for post-damage cases.

A conventional way to model the dynamics of post-damage aircraft is setting up the EoM on the new c.m. location O' , which is referred to as the CM-Centric method in [47]. Denote the distance vector from O to O' as $\mathbf{r}_{OO'} = [r_{\Delta x}, r_{\Delta y}, r_{\Delta z}]^T$. When using the CM-Centric method, Eq. (3.42) can still be used for post-damage conditions. Consequently, the reference point of moments due to external forces should be transferred to the new c.m. location O' . Furthermore, the inertia tensor needs to be modified with respect to the new point O' using parallel axis theorem. Last but not least, the translational velocity \mathbf{V} in Eq. (3.42) actually refers to the velocity of a new point O' , with the relationship $\mathbf{V}_{O'} = \mathbf{V}_O + \boldsymbol{\omega} \times \mathbf{r}_{OO'}$. As a result, there is a discontinuity in \mathbf{V} if $\boldsymbol{\omega}$ is non-zero at the damage instant, so a trigger logic to reset the integrator of \mathbf{V} is required. This discontinuity and trigger logic are totally avoided by using the non-CM approach [47], which means the frame origin is still fixed on O after damage. The reference frames for moments and inertia tensor are also kept invariant. Additionally, the moment due to gravity $\mathbf{M}_G = \mathbf{r}_{OO'} \times \mathbf{G}$ needs to be added. The equations of motion using non-CM approach is given by [35, 47]

$$\begin{bmatrix} \dot{\mathbf{V}} \\ \dot{\boldsymbol{\omega}} \end{bmatrix} = \begin{bmatrix} m' \mathbf{I} & \tilde{\mathbf{S}}^T \\ \tilde{\mathbf{S}} & \mathbf{J}' \end{bmatrix}^{-1} \begin{bmatrix} -m' \tilde{\boldsymbol{\omega}} \mathbf{V} - \tilde{\boldsymbol{\omega}} \tilde{\mathbf{S}}^T \boldsymbol{\omega} + \mathbf{F}' \\ -\tilde{\mathbf{V}} \tilde{\mathbf{S}}^T \boldsymbol{\omega} - \tilde{\boldsymbol{\omega}} \tilde{\mathbf{S}} \mathbf{V} - \tilde{\boldsymbol{\omega}} \mathbf{J}' \boldsymbol{\omega} + \mathbf{M}' \end{bmatrix} \quad (3.46)$$

$\tilde{(\cdot)}$ in Eq. (3.46) denotes the corresponding skew-symmetric matrix of the vector (\cdot) . $\mathbf{S} = [m' r_{\Delta x}, m' r_{\Delta y}, m' r_{\Delta z}]^T$ is non-zero when using the non-CM approach, which leads to coupled translational and rotational motions.

The aerodynamic characteristics of partially damaged aircraft have been investigated in [46, 48]. It has been found that damages of horizontal stabilizers lead to significant loss in both static and dynamic longitudinal stability. The static derivative C_{m_α} and damping derivative C_{m_q} are approximately linear to the scale of tip loss. An additional rolling moment coefficient due to pitch rate ΔC_{l_q} is induced if geometric asymmetrical damages are imposed on horizontal stabilizers.

Similarly, the damages of vertical tail cause reductions in static and dynamic stability on the directional axis with an approximately linear relationship with the damage scale. These effects are reflected by reductions of C_{n_β} and C_{n_r} .

The tip loss of the wing directly leads to the reduction of the lift slope C_{L_α} . The unequal lift on left and right wings also induces an additional rolling moment coefficient ΔC_{l_α} . For aircraft with positive dihedral angle, C_{l_β} reduces as the wing area lost. The rolling damping coefficient C_{l_p} is also expected to reduce because the wing is the major source of rolling damping. Similar to the effects of asymmetric horizontal stabilizer damage, the asymmetric wing damage would also generate a rolling moment coefficient during pitch motions indicated by ΔC_{l_q} .

The influences of wing, horizontal stabilizer and vertical tail damages on aerodynamic coefficients are summarized in Table 3.1.

Table 3.1: The main influences of structural damages on aerodynamic coefficients.

Damaged component	Changed coefficients	New coefficients
Horizontal stabilizer	C_{m_α}, C_{m_q}	ΔC_{l_q}
Vertical tail	C_{n_β}, C_{n_r}	–
Wing	$C_{L_\alpha}, C_{l_\beta}, C_{l_p}$	$\Delta C_{l_q}, \Delta C_{l_\alpha}$

3.4.4. AIRCRAFT ATTITUDE FAULT-TOLERANT CONTROL DESIGN

Recall Eqs. (3.42, 3.43). the aircraft attitude dynamics can be written in a more compact form as

$$\begin{aligned}\dot{\mathbf{x}}_1 &= \mathbf{f}_1(\mathbf{x}_1)\mathbf{x}_2 \\ \dot{\mathbf{x}}_2 &= \mathbf{f}_2(\mathbf{x}_1, \mathbf{x}_2) + \mathbf{G}_2\mathbf{u}\end{aligned}\quad (3.47)$$

where $\mathbf{x}_1 = [\phi, \theta, \psi]^T$, $\mathbf{x}_2 = [p, q, r]^T$, $\mathbf{u} = [\delta_a, \delta_e, \delta_r]^T$. The plant is perturbed by model uncertainties, damages and failures.

$$\mathbf{f}_2 = \bar{\mathbf{f}}_2 + (\mathbf{f}_{f_2} - \bar{\mathbf{f}}_2)\kappa + \Delta\mathbf{f}_2, \quad \mathbf{G}_2 = \bar{\mathbf{G}}_2 + (\mathbf{G}_{f_2} - \bar{\mathbf{G}}_2)\kappa + \Delta\mathbf{G}_2 \quad (3.48)$$

In Eq. (3.48), $\bar{\mathbf{f}}_2$ and $\bar{\mathbf{G}}_2$ represent the nominal dynamics given by Eq. (3.42). \mathbf{f}_{f_2} and \mathbf{G}_{f_2} denote the new dynamics after sudden actuator faults or structural damages. $\Delta\mathbf{f}_2$ and $\Delta\mathbf{G}_2$ indicate the model uncertainty terms as continuous functions of \mathbf{x} . $\kappa(t) \in [0, 1]$ is a failure indicator, with $\kappa = 1$ denotes post-fault condition, and $\kappa = 0$ denotes the

fault free case. $\kappa(t)$ is designed as a unit step function to indicate the sudden structure breaks and actuator faults during flight. Since the first equation of Eq. (3.47) represents the kinematics of the aircraft attitude, there is no model uncertainty ($\mathbf{f}_1 = \bar{\mathbf{f}}_1$). V, α, β in Eq. (3.43) are viewed as measurable inputs. Choosing $\mathbf{y} = \mathbf{x}_1$, the vector relative degree is then $\boldsymbol{\rho} = [2, 2, 2]^T$. With knowledge only about the nominal model, the controller aims at passively tolerating these faults/damages and model uncertainties. This chapter chooses the attitude control as a demonstrative case for testing the decoupling performance of the controllers. The output and \mathbf{x}_1 can also be chosen as $\mathbf{y} = \mathbf{x}_1 = [\mu, \alpha, \beta]^T$ or $\mathbf{y} = \mathbf{x}_1 = [\phi, \theta, \beta]^T$. Using the kinematic equations for μ, α, β [24], the vector relative degree for these two choices still equals $\boldsymbol{\rho} = [2, 2, 2]^T$. Therefore, the control methods designed in this chapter can be applied straightforwardly.

Using Eqs. (3.8, 3.47), the NDI control input is $\mathbf{u}_{\text{ndi}} = \bar{\mathcal{B}}^{-1}(\mathbf{v}_c - \bar{\boldsymbol{\alpha}})$ (Eq. (3.6)) with residual error

$$\begin{aligned} \boldsymbol{\varepsilon}_{\text{ndi}} &= (\boldsymbol{\alpha} - \bar{\boldsymbol{\alpha}}) + (\mathcal{B}\bar{\mathcal{B}}^{-1} - \mathbf{I})(\mathbf{v}_c - \bar{\boldsymbol{\alpha}}) \\ &= \mathbf{f}_1(\mathbf{f}_2 - \bar{\mathbf{f}}_2) + (\mathbf{f}_1\mathbf{G}_2\bar{\mathbf{G}}_2^{-1}\mathbf{f}_1 - \mathbf{I})(\mathbf{v}_c - \frac{\partial \mathbf{f}_1 \mathbf{x}_2}{\partial \mathbf{x}_1}(\mathbf{f}_1 \mathbf{x}_2) - \mathbf{f}_1 \bar{\mathbf{f}}_2) \end{aligned} \quad (3.49)$$

where $\mathbf{f}_1 = \bar{\mathbf{f}}_1$ is used in the preceding equation. The INDI controller is designed by Eq. (3.11), but since a new variable κ as a discontinuous function of time is incorporated to indicate the sudden faults/damages on-board, $\boldsymbol{\delta}(\mathbf{x}, \Delta t)$ in Eq. (3.13) needs to be augmented by a κ related terms. First, $\boldsymbol{\delta}(\mathbf{x}, \Delta t)$ is augmented by the first-order Taylor series expansion with respect to κ , using Eqs. (3.47, 3.48), this term equals

$$\begin{aligned} \boldsymbol{\eta}_\kappa &= \left. \frac{\partial [\boldsymbol{\alpha} + \mathcal{B}\mathbf{u}]}{\partial \kappa} \right|_0 \Delta \kappa = \frac{\partial [\frac{\partial \mathbf{f}_1 \mathbf{x}_2}{\partial \mathbf{x}_1}(\mathbf{f}_1 \mathbf{x}_2) + \mathbf{f}_1 \mathbf{f}_2 + \mathbf{f}_1 \mathbf{G}_2 \mathbf{u}]}{\partial \kappa} \Big|_0 \Delta \kappa \\ &= \mathbf{f}_1 [(\mathbf{f}_{f_2} - \bar{\mathbf{f}}_2) + (\mathbf{G}_{f_2} - \bar{\mathbf{G}}_2)\mathbf{u}] \Big|_0 \Delta \kappa \end{aligned} \quad (3.50)$$

Since $\kappa(t)$ is a unit step function, then $\Delta \kappa(t)$ is a single square pulse with the magnitude of one and width of Δt . Consequently, this $\boldsymbol{\eta}_\kappa$ term is only non-zero at the failure instant, and at the next time step, the faults/damages have already been reflected in the measurements. This remarkable feature makes the sensor-based INDI a promising approach for fault-tolerant control problems. Recall Eq. (3.50), $\boldsymbol{\eta}_\kappa$ is bounded if at the fault instant t_f , $[(\mathbf{f}_{f_2} - \bar{\mathbf{f}}_2) + (\mathbf{G}_{f_2} - \bar{\mathbf{G}}_2)\mathbf{u}]|_{t=t_f}$ is bounded. This is a reasonable assumption since stricter requirements on the boundedness of $\mathbf{f}_2 - \bar{\mathbf{f}}_2 = (\mathbf{f}_{f_2} - \bar{\mathbf{f}}_2)\kappa + \Delta \mathbf{f}_2$ and $\mathbf{G}_2 - \bar{\mathbf{G}}_2 = (\mathbf{G}_{f_2} - \bar{\mathbf{G}}_2)\kappa + \Delta \mathbf{G}_2$ for all t are often made in the literature [2, 5–10].

Second, $\boldsymbol{\delta}(\mathbf{x}, \Delta t)$ is also augmented by the closed-loop value of the κ -related Taylor series expansion reminder:

$$\begin{aligned} \mathbf{R}_\kappa &= \left. \frac{\partial^2 [\boldsymbol{\alpha} + \mathcal{B}\mathbf{u}]}{\partial^2 \kappa} \right|_m \Delta \kappa^2 + \left. \frac{\partial^2 [\boldsymbol{\alpha} + \mathcal{B}\mathbf{u}]}{\partial \kappa \partial \mathbf{u}} \right|_m \Delta \kappa \Delta \mathbf{u} + \left. \frac{\partial^2 [\boldsymbol{\alpha} + \mathcal{B}\mathbf{u}]}{\partial \kappa \partial \mathbf{x}} \right|_m \Delta \kappa \Delta \mathbf{x} \\ &= \mathbf{f}_1 (\mathbf{G}_{f_2} - \bar{\mathbf{G}}_2) \Big|_m \Delta \mathbf{u} \Delta \kappa + \left. \frac{\partial \mathbf{f}_1 [(\mathbf{f}_{f_2} - \bar{\mathbf{f}}_2) + (\mathbf{G}_{f_2} - \bar{\mathbf{G}}_2)\mathbf{u}]}{\partial \mathbf{x}} \right|_m \Delta \mathbf{x} \Delta \kappa \end{aligned} \quad (3.51)$$

in which $(\cdot)|_m$ means evaluating (\cdot) at a condition where $\mathbf{x} \in (\mathbf{x}(t - \Delta t), \mathbf{x}(t))$, $\mathbf{u} \in (\mathbf{u}(t - \Delta t), \mathbf{u}(t))$, and $\kappa \in (\kappa(t - \Delta t), \kappa(t))$. The $\Delta \kappa^2$ -related term in \mathbf{R}_κ equals zero since system

dynamics are linear with respect to κ (Eqs. (3.47, 3.48)). Since $\Delta\kappa$ converges to zero after the fault occurs, the ultimate bound of $\boldsymbol{\varepsilon}_{\text{indi}(-s)}$ is not influenced by κ . Even though $\boldsymbol{\eta}_\kappa$ only appears at the fault/damage instant, it inevitably degrades the tracking performance of INDI. Therefore, it is meaningful to incorporate \mathbf{v}_s into INDI for robustness enhancement.

3.5. NUMERICAL VALIDATION

In this section, the NDI, INDI, NDI-SMC, and INDI-SMC designed for an aircraft command tracking problem will be compared numerically. The nominal aerodynamic model, thrust model and inertia model are set up adopting the public data of F-16 [49]. The nonlinear dynamic equations of motion before and after failures are given by Eq. (3.42) and Eq. (3.46) respectively. The aerodynamic model and control effectiveness after faults/damages are modeled using the methods in subsection 3.4.2 and subsection 3.4.3. Only the rudder, ailerons and stabilator are considered as inner-loop control variables and they are all modeled as first-order systems with rate and position limits. The bandwidth and limits for the actuators are listed in Table 3.2. A simple proportional-integral thrust control to maintain the airspeed is designed in a separate control loop. This aircraft is initially trimmed at a steady-level flight condition with airspeed $V = 500$ ft/s and altitude $h = 10,000$ ft. The sampling frequency used by the controllers is $f_s = 100$ Hz.

Table 3.2: Limits and bandwidths of actuators.

Actuators	Bandwidth, rad/s	Rate limit, deg/s	Position limit, deg
Ailerons δ_a	20.2	80	± 21.5
Elevators δ_e	20.2	90	± 25
Rudder δ_r	20.2	120	± 30

3.5.1. FLIGHT CONTROL IN THE NOMINAL CASE

The properties of actuators influence the performance of INDI and (higher-order) sliding mode control since both methods need “fast” actuator dynamics. The actuator dynamics are included in some (higher-order) sliding mode controllers [6, 26], which would however increase the relative degree of the overall system. This increase would require higher-order derivatives of the outputs as mentioned in [9]. When the bandwidth of the actuators are sufficiently higher than the system dynamics, the controller can be designed without considering the actuator dynamics, which is a common practice in the literature. This approach is adopted in the present chapter, and the control performance is expected to be improved if faster actuators are used.

The successive tracking references for ϕ, θ, ψ are illustrated in Fig. 3.2, which are smoothly combined sigmoid functions. The sigmoid function $f_r(t) = \frac{1}{1+e^{-t}}$ is chosen because of its differentiable property up to any order.

Remark 10 As discussed in subsection 3.3.5, NDI-SMC or INDI-SMC actually indicates a branch of sliding mode control methods designed using the structure of NDI or INDI, regardless of the sliding order, sliding surface and reaching law designs. Therefore, the

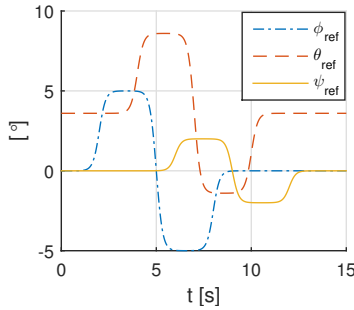


Figure 3.2: Tracking commands.

comparisons are also independent of these factors. Eqs. (3.28, 3.29) with first-order integral-type sliding variable (Eq. (3.25)) are implemented as an example.

The reference tracking controllers using NDI and INDI methods are given by Eqs. (3.6) and (3.11). For fair comparisons, $\mathbf{v}_c = -\mathbf{K}\mathbf{e} + \mathbf{y}_r^{(\rho)}$ for all the four controllers, with the desired error dynamics consistently given by

$$\ddot{e}_i + K_{D,i}\dot{e}_i + K_{P,i}e_i = 0, \quad i = 1, 2, 3. \quad (3.52)$$

The gains are designed as $K_{D,i} = 5.6$, $K_{P,i} = 16$, $i = 1, 2, 3$ to achieve desired second-order error dynamics with natural frequency 4 rad/s and damping ratio 0.7. \mathbf{v}_s is designed in the classical way as $\mathbf{v}_s = -\mathbf{K}_s \text{sign}(\boldsymbol{\sigma})$ with $\mathbf{K}_s = \text{diag}([1, 0.5, 0.3])$. The widely used *boundary-layer method* [2, 4, 6, 9, 16, 25] that replaces the signum functions by saturation functions are also adopted to reduce chattering. The thickness of the boundary layers are $\zeta_i = 0.01$, $i = 1, 2, 3$.

In the nominal condition, namely $\mathbf{f} = \bar{\mathbf{f}}$, $\mathbf{G} = \bar{\mathbf{G}}$, the aircraft responses, tracking errors, and control inputs using the proposed four controllers are illustrated in Fig. 3.3.

As can be seen from Fig. 3.3, all the four controllers are able to make the system track the commands. Owing to the singular perturbations from the actuator dynamics [16, 38], the closed-loop dynamics no longer behave like second-order systems under NDI and INDI controls. The aircraft using INDI control has slightly better performance as compared to that using NDI as can be seen from the tracking error responses. Furthermore, by using both NDI and INDI based sliding mode controllers, the tracking performance is improved without requiring additional control efforts.

3.5.2. FLIGHT CONTROL IN THE PRESENCE OF ACTUATOR FAULTS

In this subsection, the performance of aircraft command tracking in the presence of actuator faults is simulated. The first actuator fault scenario considered is that the rudder suddenly lost 50% of its effectiveness during flight at $t = 7$ s. As can be seen from Fig. 3.4, the rotational and directional tracking performance get noticeably worse from $t = 7$ s under the control of NDI, INDI, and NDI-SMC. The tracking errors under NDI control have the largest rms (root mean square) value. Although the aircraft using

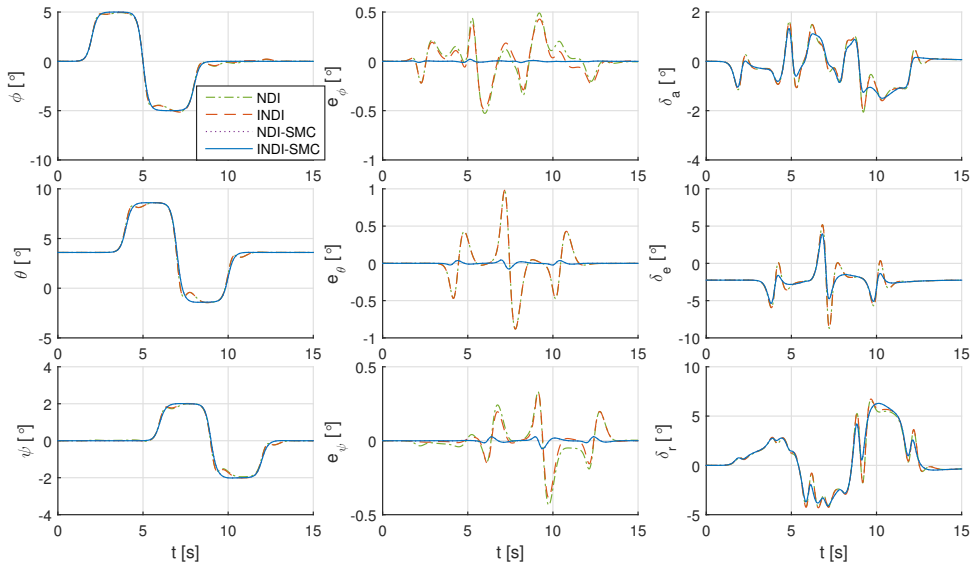


Figure 3.3: Aircraft responses and control inputs under the nominal condition.

NDI-SMC is able to recover from the fault, it presents distinct tracking errors during $t \in [7, 13]$ s. On the other hand, INDI-SMC is able to rapidly recover from the rudder fault with much smaller transition tracking errors.

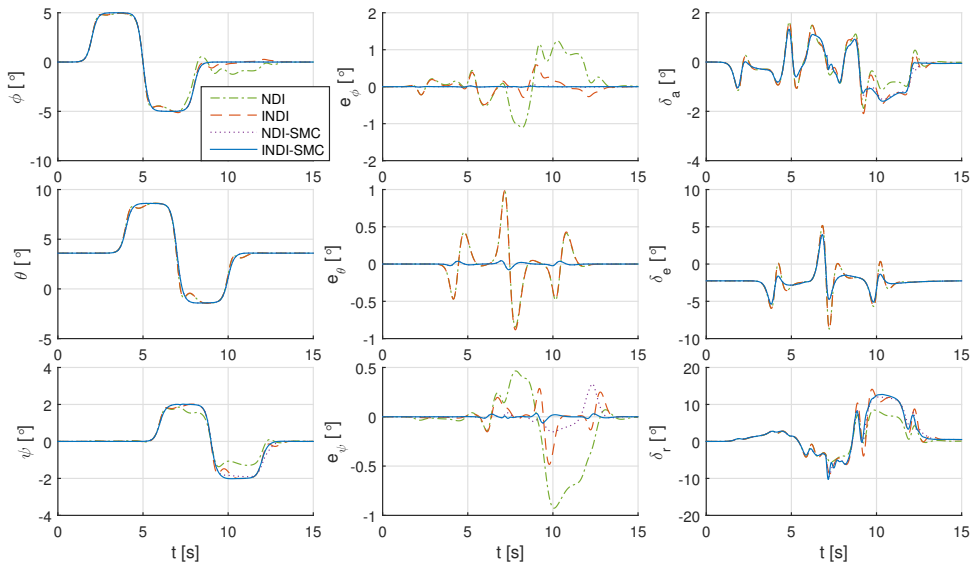


Figure 3.4: Aircraft responses and control inputs under a rudder fault condition ($t = 7$ s).

The second actuator fault scenario considered is when $t = 3$ s, the right aileron runs away with its maximum rate and gets jammed at $\delta_{a\Delta} = 15.05^\circ$. The positive deflections are defined in the conventional way, namely a positive δ_a indicates the right aileron deflects downwards and the left aileron deflects upwards. As discussed in subsection 3.4.2, one side of ailerons stuck at a non-neutral position leads to halved control effectiveness, newly introduced $C_{m\delta_a}$, as well as aerodynamic coefficient increments given by Eq. (3.44). As shown in Fig. 3.5, the aileron jamming induced rolling coefficient ΔC_l makes the aircraft roll to the left from $t = 3$ s under NDI and NDI-SMC control. The coupling effects also make the aircraft yaw to the left under NDI control. ΔC_m makes the aircraft slightly pitch down. NDI control itself shows poor robust performance in this scenario. When combined with sliding mode control, NDI-SMC has improved robustness especially on pitch and yaw channels. However, after fault occurs, the aircraft using NDI-SMC is unable to track the rolling command anymore, and the rudder has a potential to get saturated.

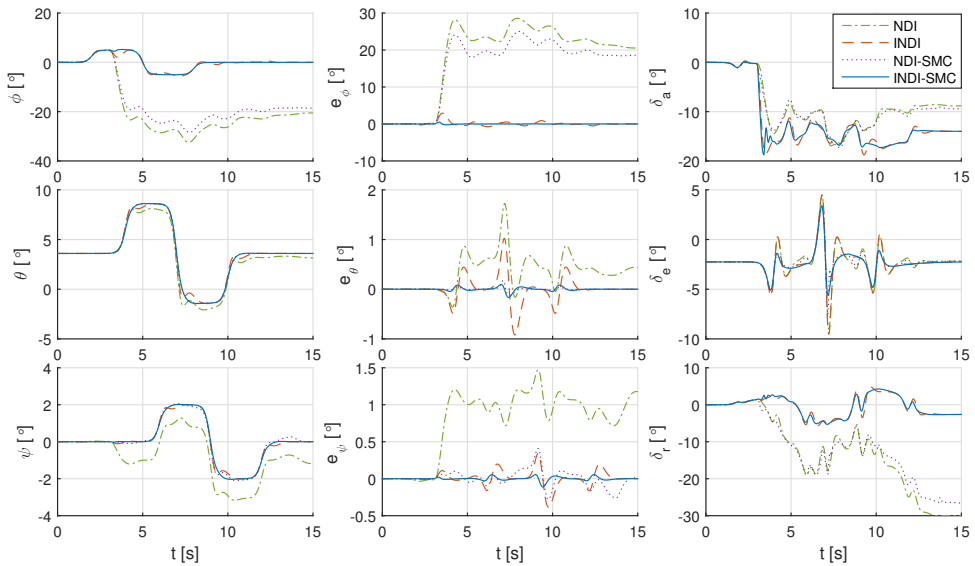


Figure 3.5: Aircraft responses and control inputs under an aileron jamming condition ($t = 3$ s).

On the contrary, aircraft using both INDI and INDI-SMC are able to recover from the aileron fault, and continue to track the commands. In view of Fig. 3.5, the left aileron deflects downwards at -14° and rudder deflects at -2.6° after the commands vanish to re-trim the aircraft. Although the aircraft under INDI control can recover, its ϕ tracking performance degrades. When using the INDI control, the rms value of e_ϕ is 0.17° in the nominal case, but degrades to 0.57° in the presence of fault. By using INDI-SMC, the rms value of e_ϕ is reduced to 0.07° . The aircraft under INDI-SMC also shows better tracking performance in pitch and yaw channels.

The third actuator fault scenario considered in this chapter is the elevator/stabilator jamming problem. At $t = 5$ s, the left stabilator is jammed downwards at $\delta_{e\Delta} = -12.5^\circ$.

Consequently, the stabilator control effectiveness is halved, $C_{l_{\delta_e}}$, $C_{n_{\delta_e}}$ are introduced, and the aerodynamic coefficient increments are given by Eq. (3.45). These coefficient increments cause a positive rolling moment and a negative pitching moment as can be seen from the responses under NDI control in Fig. 3.6.

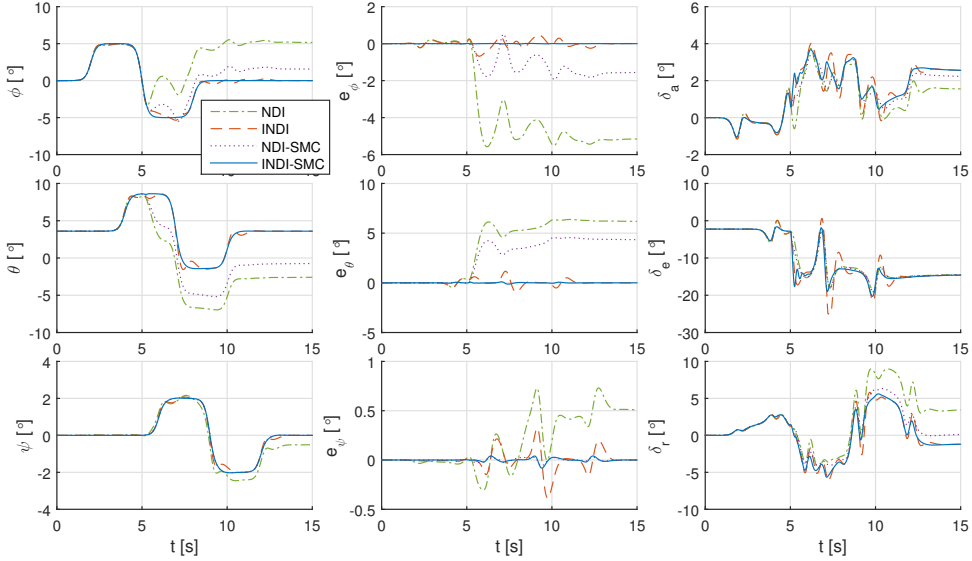


Figure 3.6: Aircraft responses and control inputs under a stabilator jamming condition ($t = 5$ s).

Due to the coupling effects, the yaw angle track performance also deteriorates under NDI control. Even though this deterioration is compensated by NDI-SMC, the roll and pitch angles are still unable to recover from the fault under NDI-SMC control. Aircraft using INDI or INDI-SMC is able to recover from the fault and continue to track the commands. Moreover, the rms of e_θ is diminished from 0.29° under INDI control to 0.02° under INDI-SMC control.

The fourth actuator fault scenario is the combination of the preceding three scenarios with responses shown in Fig. 3.7. Similar phenomena can be observed that NDI and NDI-SMC are unable to recover from the actuator faults, with the yaw angle shows a trend of divergence. Aircraft using INDI or INDI-SMC can recover and continue to track the commands. However, using INDI control, the stabilator gets saturated when $t \in [7.1, 7.4]$ s. By contrast, INDI-SMC shows the highest tracking accuracy before and after faults without actuator saturation.

As analyzed in subsection 3.2.3, the sensor-based INDI control has reduced residual error in the presence of faults/damages as compared to NDI control. The conditions in Theorem 3 lead to a bounded ϵ_{indi} , while the boundedness of ϵ_{ndi} is undetermined under the same conditions. These phenomena are verified via simulations under the fourth actuator fault scenario as shown in Fig. 3.8.

As can be observed from Fig. 3.8, the value of $\|I - \mathcal{B}\bar{\mathcal{B}}^{-1}\|$ for both NDI and INDI show jumps at $t = 3, 5, 7$ s due to successive actuator faults. The variations of $\|I - \mathcal{B}\bar{\mathcal{B}}^{-1}\|$

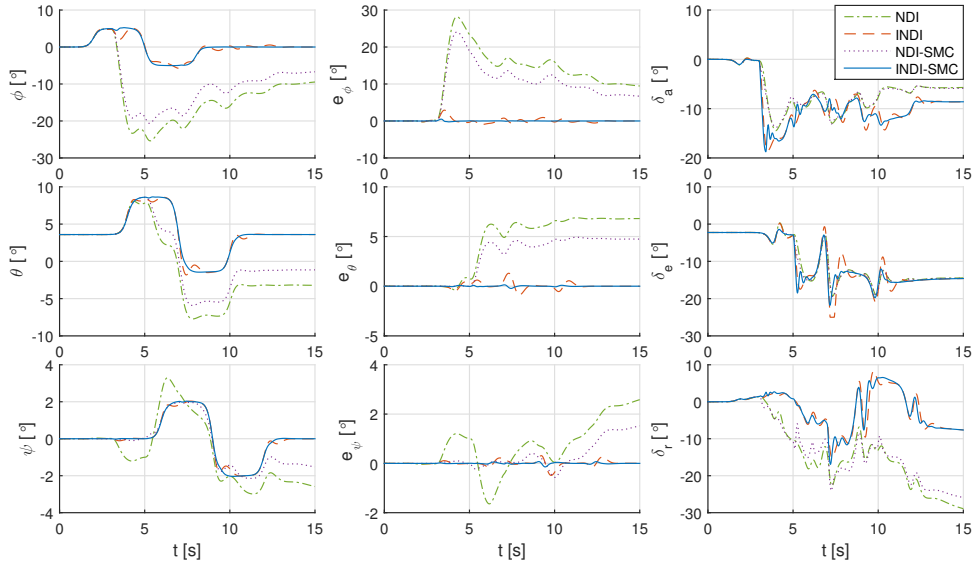


Figure 3.7: Aircraft responses and inputs with aileron, stabilator and rudder faults occur at $t = 3, 5, 7$ s.

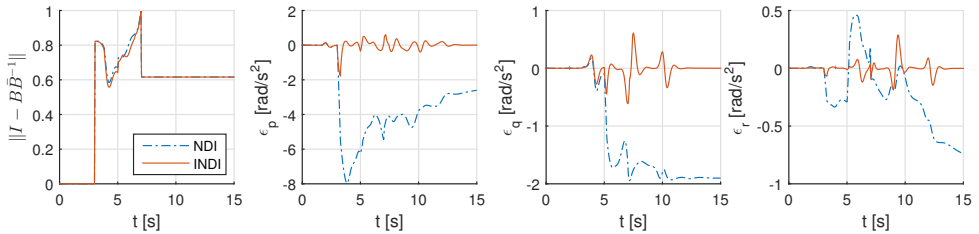


Figure 3.8: Value of $\|I - \mathcal{B}\bar{\mathcal{B}}^{-1}\|$ and the residual errors in the fourth actuator fault scenario.

are because $\mathcal{B}(\mathbf{x})$ is a function of states. $\|I - \mathcal{B}\bar{\mathcal{B}}^{-1}\| \leq \bar{b} < 1$ are satisfied for both NDI and INDI during the entire time history. While the residual errors of INDI remain bounded for all the three control channels, $\epsilon_{\text{ndi},r}$ however shows a trend of divergence. Furthermore, $\|\epsilon_{\text{indi}}\|$ is smaller than $\|\epsilon_{\text{ndi}}\|$ in this scenario. It is noteworthy that $\|\epsilon_{\text{indi}}\|$ can be further diminished by decreasing the sampling interval Δt in practice, while $\|\epsilon_{\text{ndi}}\|$ is independent of Δt .

For the reason that the switching gains of most sliding mode control methods are monotonically increasing functions of perturbation bounds, the smaller and bounded ϵ_{indi} also requires lower control gains. When the same control gains are used for INDI-SMC and NDI-SMC, which is the situation for all the preceding simulations, INDI-SMC shows better performance. One may suppose that improved performance for NDI-SMC can be achieved if the switching gains are increased. This guess is tested by gradually increasing the switching gains of NDI-SMC as $\mathbf{K}_s = c \cdot \text{diag}([1, 0.5, 0.3])$ under the fourth actuator fault scenario, with the simulation results shown in Fig. 3.9.

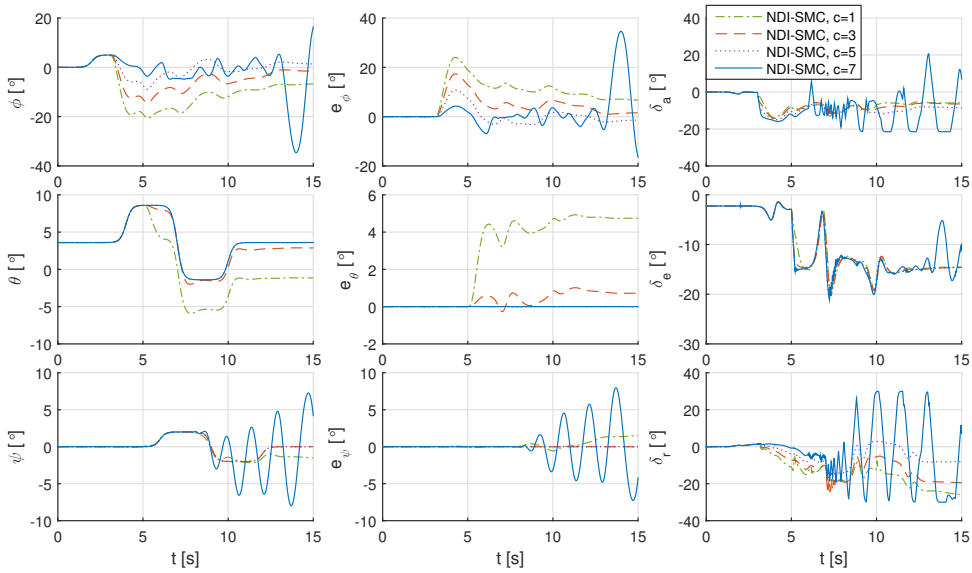


Figure 3.9: Responses using NDI-SMC with gradually increased switching gains.

In view of Fig. 3.9, when the switching gains for NDI-SMC increased from $c = 1$ to $c = 5$, the tracking performance of NDI-SMC is indeed improved. However, the roll angle still has about ten degree's of transition error when $c = 5$. Further increasing the gains to $c = 7$ induces a divergence owing to the rate and position constrains and limited bandwidth of the actuators. The increased switching gains after faults/damages would also amplify the measurement noise in practice. By contrast, the INDI-SMC is able to handle all the considered four actuator fault cases with fixed and lower gains.

3.5.3. FLIGHT CONTROL IN THE PRESENCE OF STRUCTURAL DAMAGES

The aircraft attitude tracking using the proposed four control methods subject to structural damages are simulated in this subsection. The dynamic equations after damages are given by Eq. (3.46). The aerodynamic effects of damages are given in subsection 3.4.3. The inertia properties of this aircraft after damages are calculated by using a model of F-16. In accompany with the specific component breaks, the corresponding control surface is also damaged. Only the nominal model is known by the controllers, and the faults/damages are intended to be tolerated by the controllers.

The first structural damage scenario considered here is the vertical tail damage case. To be specific, half of the vertical tail area is lost at $t = 7$ s. At the same time, 50% of the rudder effectiveness is also lost. The system responses and control inputs are presented in Fig. 3.10.

Fig. 3.10 seems to be similar to Fig. 3.4 at the first glance, but the influences of the forward c.m. shift caused by the vertical tail loss can be seen from the pitch angle tracking error in Fig. 3.10. Under NDI control, the pitch tracking has a steady-state error of 0.21° . The yaw and roll channels also show obvious transition errors under NDI control.

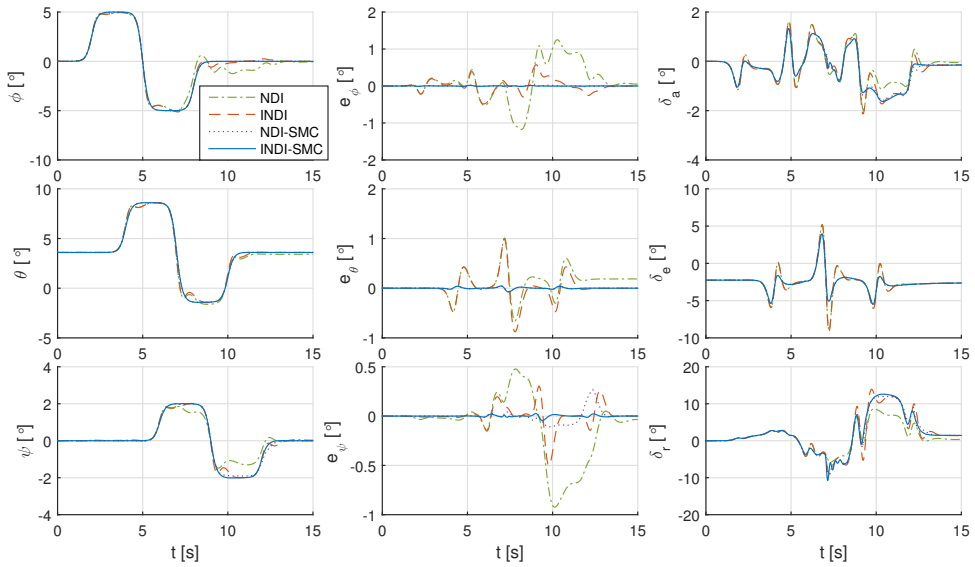


Figure 3.10: Aircraft responses and control inputs under a vertical tail damage condition ($t = 7$ s).

NDI-SMC is able to compensate for the errors in roll and pitch channel, but still shows noticeable e_ψ . INDI-SMC has improved performance as compared to both INDI and NDI-SMC.

The second structural damage scenario simulated here is that at $t = 5$ s, the entire left stabilator is lost, while the right stabilator is still working normally. Accompanying with the left stabilator lost, the c.m. shifts forwards and to the right. The effects of the rolling and pitching moment increments can be seen from the responses under NDI control in Fig. 3.11. The reduced longitudinal damping and stability margin are also influencing the closed-loop system responses. Using NDI control is not enough to make the system recover from this failure. Although NDI-SMC shows improved performance, its convergence speed is slow and still presents small e_θ at $t = 15$ s. Owing to the asymmetrical c.m. shift and the newly induced coefficient ΔC_{lq} , the rms value of e_ϕ increased to 0.18° under INDI control and is reduced by 96% using INDI-SMC.

The third structural damage scenario modeled here is at $t = 3$ s, the right wing lost 25% of its area. At the meanwhile, the right aileron is also lost. The unequal lift on the left and right wing immediately causes a positive rolling moment as can be seen from Fig. 3.12. The coupling effects also cause performance degradations on pitch and yaw channels under NDI and NDI-SMC controls. Using NDI or NDI-SMC, the aircraft is unable to recover from the damage, and the rudder has a potential to get saturated. Both INDI and INDI-SMC are able to make the aircraft recover and continue the tracking missions. The rms value of e_ϕ degrades to 0.51° under INDI control in this scenario, and can be improved into 0.24° using INDI-SMC.

The fourth structural damage scenario is a combination of the preceding three structural damage cases. Specifically, 25% of the right wing breaks at $t = 3$ s, the entire left

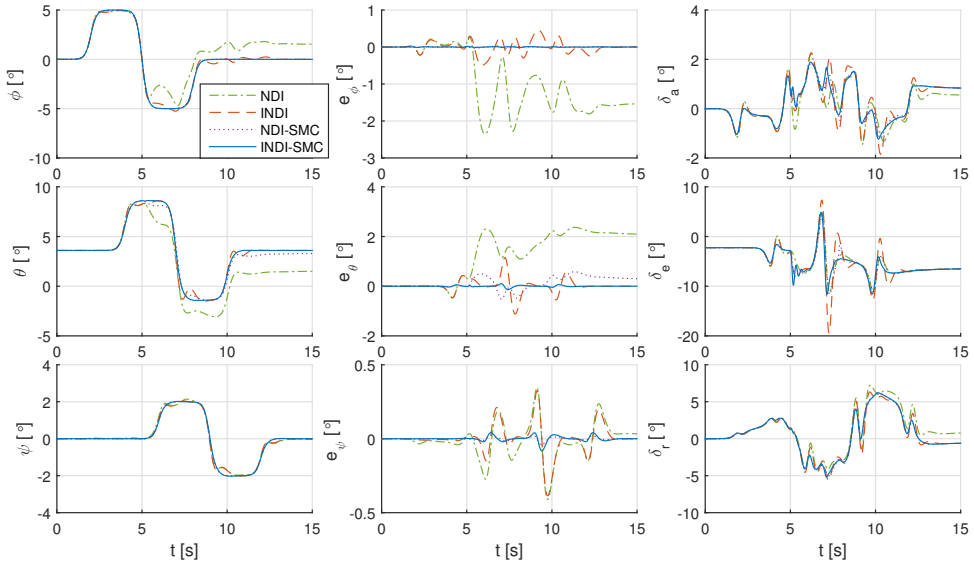


Figure 3.11: Aircraft responses and control inputs under a stabilator damage condition ($t = 5$ s).

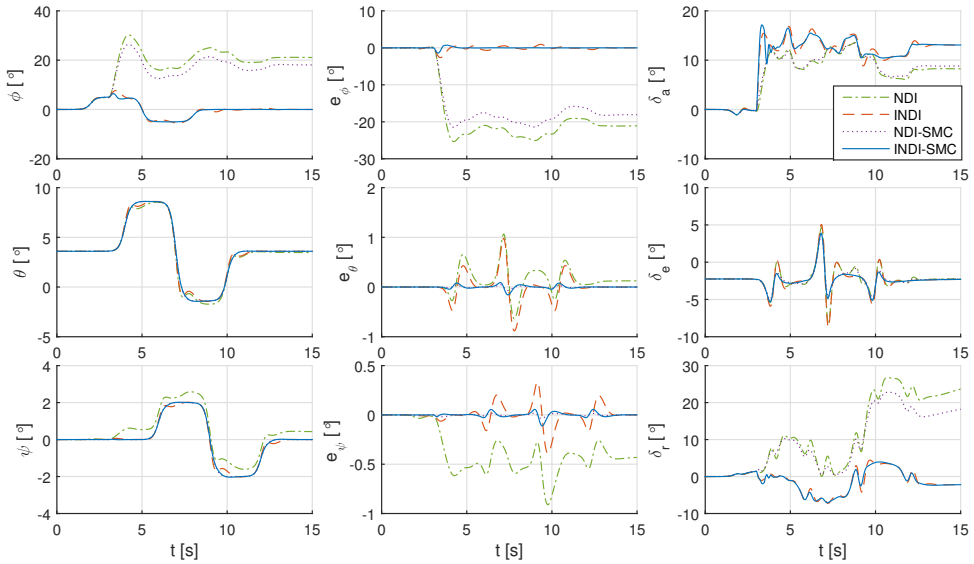


Figure 3.12: Aircraft responses and control inputs under a wing damage condition ($t = 3$ s).

stabilator is lost at $t = 5$ s, and at $t = 7$ s, half area of the vertical tail is lost. The corresponding control surfaces are also lost in accompany with the structural damages. The simulation results are shown in Fig. 3.13, from which it can be seen that both NDI and

NDI-SMC controls are unable to help the aircraft recover from the damages, and the rudder get saturated from $t = 9.6$ s. INDI as well as INDI-SMC can complete the tracking missions in the presence of structural damages. Furthermore, INDI-SMC has the best tracking accuracy.

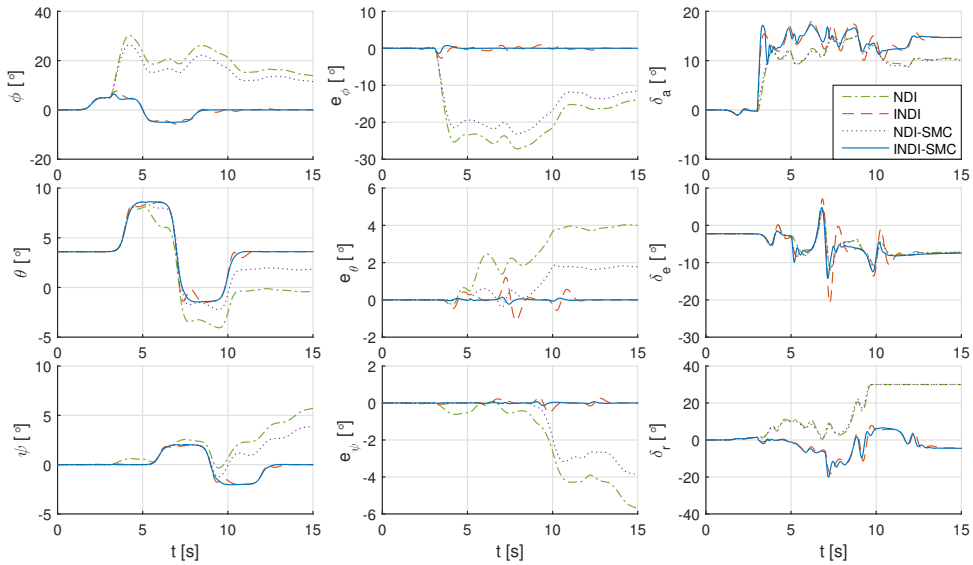


Figure 3.13: Aircraft responses and inputs with wing, stabilator and vertical tail damaged at $t = 3, 5, 7$ s.

The conditions in Theorem 3 are sufficient for a bounded ϵ_{indi} , while the boundedness of ϵ_{ndi} is undetermined under the same conditions (analyses in subsection 3.2.3). This is also verified when the aircraft is subjected to the fourth damage scenario, as illustrated in Fig. 3.14, where $\epsilon_{\text{ndi},r}$ shows a trend of divergence. Furthermore, $\|\epsilon_{\text{indi}}\|$ is smaller than $\|\epsilon_{\text{ndi}}\|$ in Fig. 3.14, which leads to smaller minimum possible gain values for INDI-SMC.

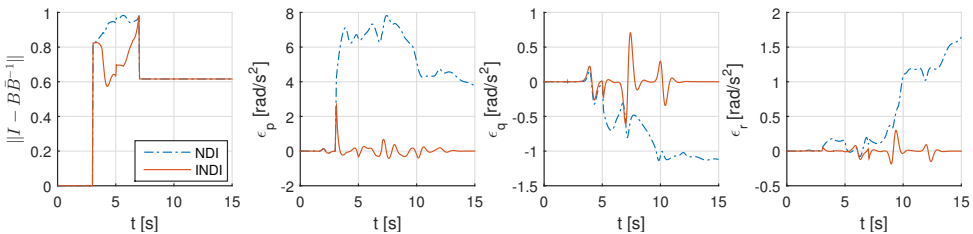


Figure 3.14: Value of $\|I - B\bar{B}^{-1}\|$ and the residual errors in the fourth structural damage scenario.

3.6. CONCLUSIONS

The incremental sliding mode control (INDI-SMC) framework is proposed in this chapter by hybridizing (higher-order) sliding mode controllers/observers with the reformulated incremental nonlinear dynamic inversion (INDI). The incorporations of the sliding mode robustification terms into INDI compensate for the residual errors of INDI, whilst the incremental framework simultaneously reduces the control/observer gains and the model dependency.

It is verified theoretically and numerically that the boundedness conditions for the INDI residual error (ϵ_{indi}) are less strict than those of the nonlinear dynamic inversion (NDI) residual error (ϵ_{ndi}). In severe damage cases, ϵ_{ndi} can become unbounded. Moreover, in the same faults/damages scenario, there exists a sampling frequency which makes the upper bound of ϵ_{indi} smaller than the upper bound of ϵ_{ndi} . These beneficial properties of INDI enable the INDI-SMC framework to passively resist a wider range of perturbations with lower sliding mode control/observer gains, as compared to the widely used way of designing sliding mode control based on NDI.

When applied to passive fault-tolerant flight control problems, the proposed INDI-SMC framework shows better robust performance over NDI, INDI, and the NDI based sliding mode control, in the presence of sudden actuator faults and structural damages, which makes it a promising approach to enhance aircraft survivability in real life.

REFERENCES

- [1] Y. Zhang and J. Jiang, *Bibliographical review on reconfigurable fault-tolerant control systems*, *Annual Reviews in Control* **32**, 229 (2008).
- [2] D. Kim and Y. Kim, *Robust Variable Structure Controller Design for Fault Tolerant Flight Control*, *Journal of Guidance, Control, and Dynamics* **23**, 430 (2000).
- [3] J. Y. Hung, W. Gao, and J. C. Hung, *Variable structure control: a survey*, *IEEE Transactions on Industrial Electronics* **40**, 2 (1993).
- [4] J.-J. E. Slotine and W. Li, *Applied Nonlinear Control* (NJ: Prentice Hall, Englewood Cliffs, 1991).
- [5] Y. Shtessel, J. Buffington, and S. Banda, *Tailless aircraft flight control using multiple time scale reconfigurable sliding modes*, *IEEE Transactions on Control Systems Technology* **10**, 288 (2002).
- [6] Y. B. Shtessel, J. M. Buffington, and S. S. Banda, *Multiple Timescale Flight Control Using Reconfigurable Sliding Modes*, *Journal of Guidance, Control, and Dynamics* **22**, 873 (1999).
- [7] H. Alwi and C. Edwards, *Fault tolerant control using sliding modes with on-line control allocation*, *Automatica* **44**, 1859 (2008).
- [8] H. Alwi, *Fault tolerant sliding mode control schemes with aerospace applications*, Ph.D. thesis, University of Leicester (2008).

- [9] R. A. Hess and S. R. Wells, *Sliding Mode Control Applied to Reconfigurable Flight Control Design*, *Journal of Guidance, Control, and Dynamics* **26**, 452 (2003).
- [10] T. Wang, W. Xie, and Y. Zhang, *Sliding mode fault tolerant control dealing with modeling uncertainties and actuator faults*, *ISA Transactions* **51**, 386 (2012).
- [11] M. T. Hamayun, C. Edwards, and H. Alwi, *A fault tolerant control allocation scheme with output integral sliding modes*, *Automatica* **49**, 1830 (2013).
- [12] L. Chen, H. Alwi, C. Edwards, and M. Sato, *Flight evaluation of an LPV sliding mode controller with online control allocation*, in *2017 IEEE 56th Annual Conference on Decision and Control (CDC)* (IEEE, 2017) pp. 3928–3933.
- [13] V. I. Utkin and A. S. Poznyak, *Adaptive sliding mode control with application to super-twist algorithm: Equivalent control method*, *Automatica* **49**, 39 (2013).
- [14] C. Edwards and Y. B. Shtessel, *Adaptive continuous higher order sliding mode control*, *Automatica* **65**, 183 (2016).
- [15] C. Edwards and Y. B. Shtessel, *Continuous higher order sliding mode control based on adaptive disturbance compensation*, in *2014 13th International Workshop on Variable Structure Systems (VSS)*, Vol. 47 (IEEE, 2014).
- [16] H. K. Khalil, *Nonlinear Systems* (Prentice-Hall, New Jersey, 2002).
- [17] C. Edwards and Y. Shtessel, *Adaptive dual-layer super-twisting control and observation*, *International Journal of Control* **89**, 1759 (2016).
- [18] T. E. Massey and Y. B. Shtessel, *Continuous Traditional and High-Order Sliding Modes for Satellite Formation Control*, *Journal of Guidance, Control, and Dynamics* **28**, 826 (2005).
- [19] C. E. Hall and Y. B. Shtessel, *Sliding Mode Disturbance Observer-Based Control for a Reusable Launch Vehicle*, *Journal of Guidance, Control, and Dynamics* **29**, 1315 (2006).
- [20] L. Besnard, Y. B. Shtessel, and B. Landrum, *Quadrotor vehicle control via sliding mode controller driven by sliding mode disturbance observer*, *Journal of the Franklin Institute* **349**, 658 (2012).
- [21] J. S. Orr and Y. B. Shtessel, *Lunar spacecraft powered descent control using higher-order sliding mode techniques*, *Journal of the Franklin Institute* **349**, 476 (2012).
- [22] S. Sieberling, Q. P. Chu, and J. A. Mulder, *Robust Flight Control Using Incremental Nonlinear Dynamic Inversion and Angular Acceleration Prediction*, *Journal of Guidance, Control, and Dynamics* **33**, 1732 (2010).
- [23] P. Simplício, M. Pavel, E. van Kampen, and Q. P. Chu, *An acceleration measurements-based approach for helicopter nonlinear flight control using Incremental Nonlinear Dynamic Inversion*, *Control Engineering Practice* **21**, 1065 (2013).

- [24] P. Lu, E. van Kampen, C. de Visser, and Q. P. Chu, *Aircraft fault-tolerant trajectory control using Incremental Nonlinear Dynamic Inversion*, *Control Engineering Practice* **57**, 126 (2016).
- [25] Y. Shtessel, C. Hall, and M. Jackson, *Reusable Launch Vehicle Control in Multiple-Time-Scale Sliding Modes*, *Journal of Guidance, Control, and Dynamics* **23**, 1013 (2000).
- [26] Y. B. Shtessel and I. A. Shkolnikov, *Aeronautical and space vehicle control in dynamic sliding manifolds*, *International Journal of Control* **76**, 1000 (2003).
- [27] Y. Feng, X. Yu, and Z. Man, *Non-singular terminal sliding mode control of rigid manipulators*, *Automatica* **38**, 2159 (2002).
- [28] Y. Wu, X. Yu, and Z. Man, *Terminal sliding mode control design for uncertain dynamic systems*, *Systems & Control Letters* **34**, 281 (1998).
- [29] S. Yu, X. Yu, B. Shirinzadeh, and Z. Man, *Continuous finite-time control for robotic manipulators with terminal sliding mode*, *Automatica* **41**, 1957 (2005).
- [30] M. Defoort, T. Floquet, A. Kokosy, and W. Perruquetti, *A novel higher order sliding mode control scheme*, *Systems and Control Letters* **58**, 102 (2009).
- [31] M. Sagliano, E. Mooij, and S. Theil, *Adaptive Disturbance-Based High-Order Sliding-Mode Control for Hypersonic-Entry Vehicles*, *Journal of Guidance, Control, and Dynamics* **40**, 521 (2017).
- [32] J. Wang, Q. Zong, R. Su, and B. Tian, *Continuous high order sliding mode controller design for a flexible air-breathing hypersonic vehicle*, *ISA Transactions* **53**, 690 (2014).
- [33] P. Yu, Y. Shtessel, and C. Edwards, *Continuous higher order sliding mode control with adaptation of air breathing hypersonic missile*, *International Journal of Adaptive Control and Signal Processing* **30**, 1099 (2016).
- [34] P. Acquatella, W. Falkena, E. van Kampen, and Q. P. Chu, *Robust Nonlinear Spacecraft Attitude Control using Incremental Nonlinear Dynamic Inversion*. in *AIAA Guidance, Navigation, and Control Conference* (American Institute of Aeronautics and Astronautics, Minneapolis, Minnesota, 2012) pp. 1–20.
- [35] X. Wang, E. van Kampen, and Q. P. Chu, *Gust Load Alleviation and Ride Quality Improvement with Incremental Nonlinear Dynamic Inversion*, in *AIAA Atmospheric Flight Mechanics Conference* (American Institute of Aeronautics and Astronautics, Grapevine, Texas, 2017) pp. 1–21.
- [36] E. J. J. Smeur, Q. P. Chu, and G. C. H. E. de Croon, *Adaptive Incremental Nonlinear Dynamic Inversion for Attitude Control of Micro Air Vehicles*, *Journal of Guidance, Control, and Dynamics* **39**, 450 (2016).

- [37] F. Grondman, G. Looye, R. O. Kuchar, Q. P. Chu, and E. van Kampen, *Design and Flight Testing of Incremental Nonlinear Dynamic Inversion-based Control Laws for a Passenger Aircraft*, in *2018 AIAA Guidance, Navigation, and Control Conference*, January (American Institute of Aeronautics and Astronautics, Kissimmee, Florida, 2018).
- [38] X. Wang, E. van Kampen, Q. P. Chu, and P. Lu, *Stability Analysis for Incremental Nonlinear Dynamic Inversion Control*, in *2018 AIAA Guidance, Navigation, and Control Conference*, January (American Institute of Aeronautics and Astronautics, Kissimmee, Florida, 2018).
- [39] J. Marzat, H. Piet-Lahanier, F. Damongeot, and E. Walter, *Model-based fault diagnosis for aerospace systems: a survey*, *Proceedings of the Institution of Mechanical Engineers, Part G: Journal of Aerospace Engineering* **226**, 1329 (2012).
- [40] A. Levant, *Higher-order sliding modes, differentiation and output-feedback control*, *International Journal of Control* **76**, 924 (2003).
- [41] V. Utkin, J. Guldner, and J. Shi, *Sliding Mode Control in Electro-Mechanical Systems, Second Edition*, Automation and Control Engineering, Vol. 31 (CRC Press, London, 2009) p. 503.
- [42] S. Laghrouche, F. Plestan, and A. Glumineau, *Higher order sliding mode control based on integral sliding mode*, *Automatica* **43**, 531 (2007).
- [43] A. Levant, *Sliding order and sliding accuracy in sliding mode control*, *International Journal of Control* **58**, 1247 (1993).
- [44] A. F. Filippov, *Matematicheskii Sbornik*, edited by F. M. Arscott, Mathematics and Its Applications, Vol. 18 (Springer Netherlands, Dordrecht, 1988).
- [45] S. P. Bhat and D. S. Bernstein, *Geometric homogeneity with applications to finite-time stability*, *Mathematics of Control, Signals, and Systems* **17**, 101 (2005).
- [46] G. Shah, *Aerodynamic Effects and Modeling of Damage to Transport Aircraft*, in *AIAA Atmospheric Flight Mechanics Conference and Exhibit*, August (American Institute of Aeronautics and Astronautics, Honolulu, Hawaii, 2008) pp. 1–13.
- [47] B. Bacon and I. Gregory, *General Equations of Motion for a Damaged Asymmetric Aircraft*, in *AIAA Atmospheric Flight Mechanics Conference and Exhibit* (American Institute of Aeronautics and Astronautics, Hilton Head, South Carolina, 2007) pp. 1–13.
- [48] Y. Zhang, C. C. de Visser, and Q. P. Chu, *Aircraft Damage Identification and Classification for Database-Driven Online Flight-Envelope Prediction*, *Journal of Guidance, Control, and Dynamics* **41**, 1 (2017).
- [49] L. T. Nguyen, M. E. Ogburn, W. P. Gilbert, K. S. Kibler, P. W. Brown, and P. L. Deal, *NASA Technical Paper 1538*, Tech. Rep. NASA Technical Paper 1538 (1979).



4

INCREMENTAL BACKSTEPPING SLIDING MODE FAULT-TOLERANT FLIGHT CONTROL

In Chapter 3, incremental nonlinear dynamic inversion (INDI) control was hybridized with sliding mode control (SMC) to inherit the advantages and remedy the drawbacks of both approaches. However, for a nonlinear system with high relative degree, the control design based on the input–output mapping can become complicated. If a nonlinear system is in the strict-feedback form, it can be stabilized in a recursive way using backstepping control. Since backstepping control is a model-based approach, researchers have been attempting to combine it with SMC for robustification. In view of the benefits that INDI brings to SMC (shown in Chapter 3), this chapter proposes hybridizing incremental backstepping (IBS) with SMC, which could reduce the model dependency of backstepping while reducing the gain of SMC. Before the hybridization, IBS control will be reformulated for more general systems without using the time-scale separation assumption. The stability and robustness of a closed-loop system under IBS control will also be analyzed using Lyapunov methods.

This chapter is based on the following peer-reviewed conference paper:
Wang, X., van Kampen, E., and Chu, Q. P., “Incremental Backstepping Sliding Mode Fault-Tolerant Flight Control,” AIAA SciTech Guidance Navigation and Control (GNC) conference, 2019, pp. 1–16. doi:10.2514/6.2019-0110.

Fault-tolerant flight control has the potential of improving the aircraft survivability in real life. This chapter proposes an incremental backstepping sliding mode control (IBSMC) framework for multi-input/output nonlinear strict-feedback systems considering model uncertainties, sudden faults, and external disturbances. This approach is a hybridization of the sliding mode control (SMC) and a reformulated incremental backstepping (IBS). By virtue of the benefits contributed by both SMC and IBS, theoretical analyses show that IBSMC has less model dependency and enhanced robustness as compared to backstepping and backstepping hybridized with SMC (BSMC). When applied to aircraft fault-tolerant control problems, numerical simulations demonstrate IBSMC can passively tolerate a wider range of model uncertainties, sudden actuator faults, and sudden structural damages as compared to backstepping and BSMC, using smooth control inputs with lower gains.

4.1. INTRODUCTION

4

SAFETY improvement is a timeless topic in the aerospace community. Over the past few decades, aircraft loss of control has remained one of the key factors of fatal aircraft accidents [1, 2]. Aircraft loss of control is defined to include significant departure from the controlled operational flight envelop, which may be caused by inappropriate crew responses, aircraft impairments, icing, etc. [3]. To prevent loss of control, redundancies and fault tolerant features are strongly recommended in [3]. Fault-tolerant flight control, which is able to automatically maintain the stability and achieve acceptable level of performance in the presence of faults and disturbances with the remaining usable control effectors, is a promising approach to enhance aircraft survivability.

Backstepping is a nonlinear control method, which can globally stabilize the strict-feedback systems through a recursive process [4, 5]. Due to its model-based nature, classical backstepping method is sensitive to model mismatches. Adaptive backstepping (ABS), including immersion and invariance ABS [6], tuning functions ABS [7], can improve the system robustness to parametric uncertainties. However, the uncertainties need to be parameterized using pre-defined model structures, and the unknown parameters are normally required to be constant or slowly time-varying [8–10]. Moreover, when the system has high order, calculations of the virtual control in ABS can become complicate. Tuning the gains in the parameter update law can also be tedious. These issues constrain the applicability of ABS to fault-tolerant flight control problems, since the aerodynamic model structure is difficult to design, especially when structural damages occur. Furthermore, not all the uncertainties and disturbances can be parameterized and meet the slowly time-varying requirement at the same time. The high computational load of ABS is also unfavorable for fault-tolerant flight control.

Sliding mode control (SMC) [4, 5] is a type of variable structure control method featured by its robustness and easy implementation. External disturbances, parametric and nonparametric uncertainties are all incorporated into a lumped uncertainty term by SMC. Only the upper bound of this lumped uncertainty term is needed by conventional first-order SMC methods [11], while the upper bounds of the uncertainty derivatives are required by higher-order SMC methods [12, 13]. These requirements on knowledge of the bounds can further be removed by various adaptive sliding mode control (ASMC) methods [10, 14]. Different from ABS which update the uncertain parameters online,

ASMC directly adapt the control gains according to the distance from the sliding variable to the sliding surface [10, 14].

There have been continuous efforts in combining backstepping techniques with SMC to preserve the merits of both methods [8, 10, 14–17]. For example, a second-order SMC is combined with ABS for feedback linearizable single-input/output (SISO) nonlinear systems that can be transformed into the parametric-pure feedback form and the parametric-strict feedback form in [8], where an SMC virtual control is included at the last step of the ABS design to improve robustness. When the system can only be transformed to the semi-parametric strict feedback form, the SMC virtual control terms are needed in each recursive step to compensate for nonparametric uncertainties [15]. Dynamical ABS and SMC are hybridized in [16] for a class of SISO non-triangular nonlinear systems with unmatched parameterized uncertainties. In [17], integral backstepping is combined with conventional first-order SMC for a quadrotor trajectory control problem. In order to remove the pre-knowledge of the uncertainty bound, backstepping is hybridized with an ASMC method for a spacecraft attitude control problem in [10]. Adaptive fast terminal SMC with nonlinear sliding surface is incorporated into the backstepping framework for controlling the ducted fan engine of a thrust-vectoring aircraft in [14]. In spite of the various SMC designs, the core idea of the combination is consistent in the above methods, that for the recursive steps encounter uncertainties, SMC virtual controls are incorporated into the baseline backstepping virtual control designs to compensate for uncertainties. Regarding the baseline backstepping methods, ABS is less suitable for fault-tolerant flight control as discussed before, while the (integral) backstepping has strong model dependency. A control method that could reduce the model dependency of the baseline backstepping methods without adding extra computational load or impairing robustness is desired.

Incremental backstepping (IBS) is a sensor-based nonlinear control method, which can preserve the benefits of conventional backstepping control, while requiring less model knowledge. IBS was first proposed in [9], which was inspired by the incremental nonlinear dynamic inversion (INDI) method [18]. It has been shown in [19] that INDI has better robustness against regular perturbations than nonlinear dynamic inversion (NDI). The same as INDI, the only model information required by IBS is the control effectiveness matrix. To further improve the robustness of IBS to uncertainties in the control effectiveness matrix, on-line parameter update laws are incorporated into IBS in [9], while the tuning and compensation methods are introduced in [20]. It is shown in [21, 22] that IBS can passively tolerate aircraft actuator jamming fault cases. Flight tests of a fixed-wing UAV under the control of command filtering IBS verified the robustness of this method to model uncertainties and disturbances [23]. Recently, the effectiveness of IBS using the direct measurement of angular accelerometers has been demonstrated by real-world flight tests on a Cessna Citation II aircraft [24]. Although IBS is a promising candidate for fault-tolerant flight control, its previous derivations based on the time-scale separation principle are not mathematically rigorous. The existing stability and robustness analyses for IBS also have limitations. These issues will be addressed in the Sec. 4.2.1.

A hybrid nonlinear control framework named incremental sliding mode control (INDI-SMC) has been proposed in [25]. As a hybridization of SMC and INDI, the INDI-SMC

approach can robustify INDI while reducing the minimum possible gains of SMC. The theoretical developments in [25] have been verified by quadrotor flight tests in [26]. However, the control framework proposed in [25] has some limitations. First of all, when the input–output relative degree is higher than two, the design of INDI-SMC using the input–output mapping can become complicated. Moreover, the SMC reaching law used in [25] is discontinuous, which requires continuous approximations of the signum function for chattering reduction. However, these approximations (hence compromises) lead to partial loss of robustness. Finally, external disturbances are not considered in [25]. These limitations of Ref. [25] will be remedied in this chapter.

Considering the dynamics of aircraft, physical time-scale separations between fast and slow dynamics exist, which allow the controller to be designed in a cascaded way. In the literature, cascaded NDI/INDI are widely used in flight control. However, since the interconnections between loops are assumed to be negligible by cascaded NDI/INDI, they cannot guarantee the closed-loop stability. By contrast, backstepping and IBS are designed in a recursive way, and their closed-loop stability are guaranteed in the Lyapunov sense. Moreover, backstepping control can also stabilize non-minimum phase systems, which can not be solved by NDI/INDI [4]. The matching condition in SMC can also be relaxed in backstepping [4].

The main contribution of this chapter is the proposal of incremental backstepping sliding mode control (IBSMC) framework for multi-input/output nonlinear strict-feedback systems under the perturbations of model uncertainties, on-board sudden faults, and external disturbances. First, the IBS method in the literature is reformulated for more general nonlinear uncertain systems. The new derivation in this chapter does not need the time-scale separation assumption and term omissions. The IBSMC framework is then proposed by incorporating the sliding mode virtual control into the reformulated IBS virtual control designs. As compared to SMC designs hybridized with backstepping (referred to as BSMC in this chapter), theoretical analyses show IBSMC has not only less model dependency, but also enhanced robustness. Moreover, it is analyzed that the switching gains can be reduced by the IBSMC framework, which is beneficial to chattering reduction. These merits are further verified numerically by an aircraft fault-tolerant control problem in the presence of model uncertainties, on-board sudden actuator faults and structural damages.

The derivations and analytical comparisons are presented in Sec. 4.2. A fault-tolerant flight control problem is presented in Sec. 4.3 and Sec. 4.4. Main conclusions are drawn in Sec. 4.5.

4.2. INCREMENTAL BACKSTEPPING SLIDING MODE CONTROL

Consider a multi-input/output nonlinear uncertain system formulated by:

$$\begin{aligned}
 \dot{\mathbf{x}}_1 &= \mathbf{f}_1(\mathbf{x}_1) + \mathbf{G}_1(\mathbf{x}_1)\mathbf{x}_2 \\
 \dot{\mathbf{x}}_2 &= \mathbf{f}_2(\mathbf{x}_1, \mathbf{x}_2) + \mathbf{G}_2(\mathbf{x}_1, \mathbf{x}_2)\mathbf{x}_3 \\
 &\vdots \\
 \dot{\mathbf{x}}_n &= \mathbf{f}_n(\mathbf{x}_1, \mathbf{x}_2, \dots, \mathbf{x}_n, \kappa(t)) + \mathbf{G}_n(\mathbf{x}_1, \mathbf{x}_2, \dots, \mathbf{x}_n, \kappa(t))\mathbf{u} + \mathbf{d} \\
 \mathbf{y} &= \mathbf{x}_1
 \end{aligned} \tag{4.1}$$

where $\mathbf{x} = [\mathbf{x}_1^T, \mathbf{x}_2^T, \dots, \mathbf{x}_n^T]^T$ is the state vector, with $\mathbf{x}_i \in \mathbb{R}^m$, $i = 1, 2, \dots, n$. $\mathbf{u} \in \mathbb{R}^m$, $\mathbf{y} \in \mathbb{R}^m$ are the system input, output vectors. $\mathbf{f}_i \in \mathbb{R}^m$, $i = 1, 2, \dots, n-1$ is a set of smooth vector fields. $\mathbf{G}_i \in \mathbb{R}^{m \times m}$, $i = 1, 2, \dots, n-1$ is a set of smooth function mappings. The columns of each \mathbf{G}_i are smooth vector fields. Assume \mathbf{G}_i , $i = 1, 2, \dots, n-1$ are nonsingular. \mathbf{f}_i , \mathbf{G}_i , $i = 1, 2, \dots, n-1$ are known dynamics. $\mathbf{d} \in \mathbb{R}^m$ represents external disturbance vector. $\mathbf{f}_n \in \mathbb{R}^m$, $\mathbf{G}_n \in \mathbb{R}^{m \times m}$ are perturbed by uncertainties and on-board faults, which are modeled as:

$$\mathbf{f}_n = \bar{\mathbf{f}}_n + (\mathbf{f}_f - \bar{\mathbf{f}}_n)\kappa(t) + \Phi_n\boldsymbol{\theta} + \boldsymbol{\eta}_f(\mathbf{x}, t), \quad \mathbf{G}_n = \bar{\mathbf{G}}_n + (\mathbf{G}_f - \bar{\mathbf{G}}_n)\kappa(t) + \Psi_n\boldsymbol{\theta} + \boldsymbol{\eta}_G(\mathbf{x}, t) \quad (4.2)$$

where $\kappa(t) \in \mathbb{R}$ is designed as a step input to model the sudden fault at $t = t_f$ during flight. Specifically, $t < t_f$, $\kappa = 0$ indicates the fault-free case, and $t \geq t_f$, $\kappa = 1$ denotes post-fault condition. $\bar{\mathbf{f}}_n$ and $\bar{\mathbf{G}}_n$ are the nominal models used for controller design, while \mathbf{f}_f and \mathbf{G}_f denoting the post-fault dynamics. $\bar{\mathbf{f}}_n$, $\bar{\mathbf{G}}_n$ as well as the columns of $\bar{\mathbf{G}}_n$, \mathbf{G}_f are smooth vector fields. $\Phi_n\boldsymbol{\theta}$ and $\Psi_n\boldsymbol{\theta}$ represent parametric uncertainties, where the parameter vector $\boldsymbol{\theta} \in \mathbb{R}^p$ is not necessarily constant nor slow time-varying. $\Phi_n(\mathbf{x}), \Psi_n(\mathbf{x}) \in \mathbb{R}^{m \times p}$, whose columns are known smooth vector fields. $\boldsymbol{\eta}_f, \boldsymbol{\eta}_G \in \mathbb{R}^m$ are smooth vector fields denoting nonparametric uncertainties. Assume $\mathbf{G}_n(\mathbf{x}, \kappa)$ is nonsingular for all t . It will be shown in Sec. 4.3 that a class of aerospace system dynamics can be described by Eqs. (4.1, 4.2).

4.2.1. REFORMULATION AND ROBUSTNESS ANALYSIS FOR INCREMENTAL BACKSTEPPING

In order to reduce the model dependency of backstepping, the incremental backstepping (IBS) control was proposed in [27], and has been used for solving many flight control problems [9, 20–24, 27]. However, the existing derivations and robustness analyses of IBS have some limitations:

The core step of the existing IBS derivations is the model simplification based on the time-scale separation principle, which claims that the controls can change significantly faster than the states [9, 20–23, 27]. Based on this principle or assumption, when the sampling frequency is high, the state variation related nonlinear terms and higher-order terms are omitted from the Taylor series expansion of the nonlinear plant, which results in the simplified incremental dynamics used for controller design. This plant simplification is not mathematically rigorous since the states of an open-loop unstable plant may change faster than the controls. Furthermore, although the higher-order terms and state variation related terms are not used by the IBS control, they still exist in the closed-loop dynamics and remain influencing the closed-loop system stability and performance. These issues have been overlooked in the literature.

The existing robustness analyses of IBS also need improvements. It is straightforward concluded in [20], that systems under IBS control are robust to the uncertainties in system dynamics $\mathbf{f}_n(\mathbf{x})$, because the model of $\mathbf{f}_n(\mathbf{x})$ is not used in IBS designs. This statement is deficient since the influences of $\mathbf{f}_n(\mathbf{x})$ still remain in the closed-loop system, although its model is not used by the controller. Moreover, Ref. [20] concludes if ideal actuators are used, the inner-loop system dynamics under IBS control is a single integrator, even when the control effectiveness matrix contains uncertainties. This conclusion is also defective because it is proved by using linear transfer functions derived

from block diagrams, where the inappropriate condition $\dot{\mathbf{x}}_n = \dot{\mathbf{x}}_{n,0}$ is used. Last but not least, in [20], the stability and robustness of the closed-loop system under IBS control considering actuator dynamics are analyzed by formulating the closed-loop system into a state-space form, and testing the frozen-time eigenvalues of the time-varying system matrix. However, it has been proved in [28] that for linear time varying systems, the stability criterion based on the negative definiteness of the frozen-time eigenvalues is neither sufficient nor necessary.

Although the robustness of IBS to sudden actuator jamming faults has been numerically evaluated in [22], there is a lack of explicit theoretical analyses for the influences of sudden (discontinuous in time) faults on IBS. In addition, IBS in the literature is only derived for systems whose relative degree equals two.

In view of these limitations of the existing IBS derivations, before the proposal of incremental backstepping sliding mode control (IBSMC), the IBS control will be reformulated for more general systems (Eq. (4.1)) without using the time-scale separation principle. The stability of the closed-loop system will be analyzed using Lyapunov methods.

Denote the sampling interval as Δt . Taking the first-order Taylor series expansion for the dynamics of \mathbf{x}_n around the condition at $t - \Delta t$ (denoted by the subscript 0) as:

$$\begin{aligned} \dot{\mathbf{x}}_n = & \dot{\mathbf{x}}_{n,0} + \frac{\partial[\mathbf{f}_n(\mathbf{x}, \kappa) + \mathbf{G}_n(\mathbf{x}, \kappa)\mathbf{u}]}{\partial \mathbf{u}} \Big|_0 \Delta \mathbf{u} + \frac{\partial[\mathbf{f}_n(\mathbf{x}, \kappa) + \mathbf{G}_n(\mathbf{x}, \kappa)\mathbf{u}]}{\partial \mathbf{x}} \Big|_0 \Delta \mathbf{x} \\ & + \frac{\partial[\mathbf{f}_n(\mathbf{x}, \kappa) + \mathbf{G}_n(\mathbf{x}, \kappa)\mathbf{u}]}{\partial \kappa} \Big|_0 \Delta \kappa + \Delta \mathbf{d} + \mathbf{R}_1 \end{aligned} \quad (4.3)$$

where $\Delta \mathbf{x} = \mathbf{x} - \mathbf{x}_0$, $\Delta \mathbf{u} = \mathbf{u} - \mathbf{u}_0$, respectively denote the variations of states and control inputs in one incremental time step. $\Delta \mathbf{d} = \mathbf{d} - \mathbf{d}_0$ denotes the variations of the external disturbances \mathbf{d} in Δt , while $\Delta \kappa = \kappa - \kappa_0$ denotes the changes of the fault indicator κ . \mathbf{R}_1 in Eq. (4.3) is the expansion remainder, whose Lagrange form is

$$\begin{aligned} \mathbf{R}_1 = & \frac{1}{2} \frac{\partial^2[\mathbf{f}_n + \mathbf{G}_n \mathbf{u}]}{\partial^2 \mathbf{x}} \Big|_m \Delta \mathbf{x}^2 + \frac{\partial^2[\mathbf{f}_n + \mathbf{G}_n \mathbf{u}]}{\partial \mathbf{x} \partial \mathbf{u}} \Big|_m \Delta \mathbf{x} \Delta \mathbf{u} \\ & + \frac{\partial^2[\mathbf{f}_n + \mathbf{G}_n \mathbf{u}]}{\partial \mathbf{x} \partial \kappa} \Big|_m \Delta \mathbf{x} \Delta \kappa + \frac{\partial^2[\mathbf{f}_n + \mathbf{G}_n \mathbf{u}]}{\partial \mathbf{u} \partial \kappa} \Big|_m \Delta \mathbf{u} \Delta \kappa \end{aligned} \quad (4.4)$$

in which $(\cdot)|_m$ means evaluating (\cdot) at a condition where $\mathbf{x} \in (\mathbf{x}(t - \Delta t), \mathbf{x}(t))$, $\mathbf{u} \in (\mathbf{u}(t - \Delta t), \mathbf{u}(t))$, $\mathbf{d} \in (\mathbf{d}(t - \Delta t), \mathbf{d}(t))$, and $\kappa \in (\kappa(t - \Delta t), \kappa(t))$. In Eq. (4.4), \mathbf{R}_1 is not a function of $\Delta \mathbf{u}^2$, $\Delta \mathbf{d}^2$, $\Delta \kappa^2$, nor $\Delta \mathbf{u} \Delta \mathbf{d}$, $\Delta \mathbf{d} \Delta \kappa$, which can be examined using Eqs. (4.1, 4.2). Eq. (4.3) is referred to as the incremental dynamic equation (without any term omission).

Consider an output tracking problem and denote the reference vector as $\mathbf{y}_r = [y_{r_1}, y_{r_2}, \dots, y_{r_m}]^T$. Assume the derivatives of $y_{r_i}(t)$, $i = 1, 2, \dots, m$, up to $y_{r_i}^{(n)}(t)$ are continuous bounded functions, IBS is recursively reformulated as:

Step 1:

Define the error variable as $\mathbf{z}_1 = \mathbf{x}_1 - \mathbf{y}_r$, recall Eq. (4.1), then $\dot{\mathbf{z}}_1 = \mathbf{f}_1 + \mathbf{G}_1 \mathbf{x}_2 - \dot{\mathbf{y}}_r$. This subsystem can be stabilized with respect to a candidate Lyapunov function $V_1(\mathbf{z}_1) = \frac{1}{2} \mathbf{z}_1^T \mathbf{z}_1$, if \mathbf{x}_2 equals its desired value $\mathbf{x}_{2,d}$, which is designed as:

$$\mathbf{x}_{2,d} = \boldsymbol{\phi}_1(\mathbf{x}_1) = \mathbf{G}_1^{-1}(-\mathbf{f}_1 - \mathbf{K}_1 \mathbf{z}_1 + \dot{\mathbf{y}}_r) \quad (4.5)$$

where \mathbf{K}_1 is a positive definite diagonal gain matrix. If $\mathbf{x}_2 = \mathbf{x}_{2,d}$, substituting Eq. (4.5) into Eq. (4.1) leads to $\dot{V}_1(\mathbf{z}_1) = -\mathbf{z}_1^T \mathbf{K}_1 \mathbf{z}_1 \leq 0$.

Step k ($2 \leq k \leq n-1$):

Define the tracking error of \mathbf{x}_k as $\mathbf{z}_k = \mathbf{x}_k - \mathbf{x}_{k,d}$, where $\mathbf{x}_{k,d} = \boldsymbol{\phi}_{k-1}(\mathbf{x}_1, \dots, \mathbf{x}_{k-1})$ is the desired value for \mathbf{x}_k designed in *Step k-1*. By using Eq. (4.1), the dynamics of \mathbf{z}_k is given by $\dot{\mathbf{z}}_k = \mathbf{f}_k + \mathbf{G}_k \mathbf{x}_{k+1} - \dot{\boldsymbol{\phi}}_{k-1}(\mathbf{x}_1, \dots, \mathbf{x}_{k-1})$. Design the desired value for \mathbf{x}_{k+1} as:

$$\mathbf{x}_{k+1,d} = \boldsymbol{\phi}_k(\mathbf{x}_1, \dots, \mathbf{x}_k) = \mathbf{G}_k^{-1}(-\mathbf{f}_k - \mathbf{K}_k \mathbf{z}_k + \dot{\boldsymbol{\phi}}_{k-1} - \mathbf{G}_{k-1}^T \mathbf{z}_{k-1}) \quad (4.6)$$

When $\mathbf{x}_{k+1} = \mathbf{x}_{k+1,d}$, by substituting Eq. (4.6) into Eq. (4.1), the time derivative of a candidate Lyapunov function $V_k(\mathbf{z}_1, \dots, \mathbf{z}_k) = \frac{1}{2} \sum_{i=1}^k \mathbf{z}_i^T \mathbf{z}_i$ is derived as:

$$\dot{V}_k = -\sum_{i=1}^{k-1} \mathbf{z}_i^T \mathbf{K}_i \mathbf{z}_i + \mathbf{z}_{k-1}^T \mathbf{G}_{k-1} \mathbf{z}_k + \mathbf{z}_k^T (-\mathbf{K}_k \mathbf{z}_k - \mathbf{G}_{k-1}^T \mathbf{z}_{k-1}) = -\sum_{i=1}^k \mathbf{z}_i^T \mathbf{K}_i \mathbf{z}_i \leq 0 \quad (4.7)$$

Step n:

Different from the above steps, model uncertainties, faults, and disturbances appear in the last step. Define the tracking error of \mathbf{x}_n as $\mathbf{z}_n = \mathbf{x}_n - \mathbf{x}_{n,d} = \mathbf{x}_n - \boldsymbol{\phi}_{n-1}$. Using Eq. (4.3), the dynamics of \mathbf{z}_n are given as:

$$\begin{aligned} \dot{\mathbf{z}}_n &= \dot{\mathbf{x}}_{n,0} + \mathbf{G}_n(\mathbf{x}_0, \kappa_0) \Delta \mathbf{u} + \left. \frac{\partial[\mathbf{f}_n(\mathbf{x}, \kappa) + \mathbf{G}_n(\mathbf{x}, \kappa) \mathbf{u}]}{\partial \mathbf{x}} \right|_0 \Delta \mathbf{x} \\ &\quad + \left. \frac{\partial[\mathbf{f}_n(\mathbf{x}, \kappa) + \mathbf{G}_n(\mathbf{x}, \kappa) \mathbf{u}]}{\partial \kappa} \right|_0 \Delta \kappa + \Delta \mathbf{d} + \mathbf{R}_1 - \dot{\boldsymbol{\phi}}_{n-1} \end{aligned} \quad (4.8)$$

Design the IBS control increment as:

$$\Delta \mathbf{u}_{\text{ibs}} = \bar{\mathbf{G}}_n^{-1}(-\dot{\mathbf{x}}_{n,0} - \mathbf{K}_n \mathbf{z}_n + \dot{\boldsymbol{\phi}}_{n-1} - \mathbf{G}_n^T \mathbf{z}_{n-1}) \triangleq \bar{\mathbf{G}}_n^{-1}(\mathbf{v}_c - \dot{\mathbf{x}}_{n,0}) \quad (4.9)$$

where $\dot{\mathbf{x}}_{n,0}$ instead of the nominal model $\bar{\mathbf{f}}_n$ (Eq. (4.22)) is used by the controller. The total control command vector for actuators is $\mathbf{u}_{\text{ibs}} = \mathbf{u}_{\text{ibs},0} + \Delta \mathbf{u}_{\text{ibs}}$. In practice, $\dot{\mathbf{x}}_{n,0}$ and $\mathbf{u}_{\text{ibs},0}$ can be either estimated [23, 29] or directly measured [24, 30].

Considering a candidate Lyapunov function $V_n = \frac{1}{2} \sum_{i=1}^n \mathbf{z}_i^T \mathbf{z}_i$, then substituting Eq. (4.9) into Eq. (4.8) yields:

$$\dot{V}_n = -\sum_{i=1}^n \mathbf{z}_i^T \mathbf{K}_i \mathbf{z}_i + \mathbf{z}_n^T (\boldsymbol{\delta}(\mathbf{x}, \kappa, \Delta t) + (\mathbf{G}_n \bar{\mathbf{G}}_n^{-1} - \mathbf{I})(\mathbf{v}_c - \dot{\mathbf{x}}_{n,0}) + \Delta \mathbf{d}) \triangleq -\sum_{i=1}^n \mathbf{z}_i^T \mathbf{K}_i \mathbf{z}_i + \mathbf{z}_n^T \boldsymbol{\varepsilon}_{\text{ibs}} \quad (4.10)$$

where $\mathbf{I} \in \mathbb{R}^{m \times m}$ is an identity matrix. $\boldsymbol{\delta}(\mathbf{x}, \kappa, \Delta t)$ in Eq. (4.10) denotes the *closed-loop* values of the variations in Eq. (4.8), specifically

$$\boldsymbol{\delta}(\mathbf{x}, \kappa, \Delta t) \triangleq \left[\left. \frac{\partial[\mathbf{f}(\mathbf{x}, \kappa) + \mathbf{G}(\mathbf{x}, \kappa) \mathbf{u}]}{\partial \mathbf{x}} \right|_0 \Delta \mathbf{x} + \left. \frac{\partial[\mathbf{f}(\mathbf{x}, \kappa) + \mathbf{G}(\mathbf{x}, \kappa) \mathbf{u}]}{\partial \kappa} \right|_0 \Delta \kappa + \mathbf{R}_1 \right] \Big|_{\mathbf{u}=\mathbf{u}_{\text{indi}}} \quad (4.11)$$

In view of Eq. (4.10), the closed-loop system is perturbed by $\boldsymbol{\varepsilon}_{\text{ibs}}$, in which $\boldsymbol{\delta}(\mathbf{x}, \kappa, \Delta t)$ contains the influences of sudden faults, state-variation-related terms and higher-order terms. The term caused by control effectiveness matrix mismatches presents in $\boldsymbol{\varepsilon}_{\text{ibs}}$ even without considering actuator dynamics. The characteristics of $\boldsymbol{\varepsilon}_{\text{ibs}}$ will be further analyzed in Sec. 4.2.4.

4.2.2. PROPOSAL OF INCREMENTAL BACKSTEPPING SLIDING MODE CONTROL

As shown in Sec. 4.2.1, the closed-loop system under IBS control is perturbed by $\boldsymbol{\varepsilon}_{\text{ibs}}$ when considering faults, uncertainties and disturbances. The influences of $\boldsymbol{\varepsilon}_{\text{ibs}}$ were also observed in the real-world flight tests of a fixed-wing UAV [23]. $\boldsymbol{\delta}(\mathbf{x}, \kappa, \Delta t)$ and $\Delta \mathbf{d}$ are not easy to be parametrized, so it is less appropriate to use ABS. Instead, IBSMC will be proposed in this subsection to compensate for the influences of $\boldsymbol{\varepsilon}_{\text{ibs}}$. The control increment of IBSMC is designed as:

$$\Delta \mathbf{u}_{\text{ibsmc}} = \tilde{\mathbf{G}}_n^{-1} (\mathbf{v}_c + \mathbf{v}_s - \dot{\mathbf{x}}_{n,0}) \quad (4.12)$$

where \mathbf{v}_c is the continuous IBS virtual control, which is identical to \mathbf{v}_c in Eq. (4.9). The SMC virtual control \mathbf{v}_s can be designed using any SMC technique. In this chapter, the finite reaching-time continuous (FRTC) SMC method [31, 32] is adopted. This method not only achieves finite-time convergence to the sliding surface, but also has enhanced robustness to noise and disturbances as compared to the boundary-layer approximation for the signum function [4, 11, 31]. Design the sliding surface as $\boldsymbol{\sigma} = \mathbf{z}_n = \mathbf{0}$, and design \mathbf{v}_s as:

$$\begin{aligned} \mathbf{v}_s &= -\mathbf{K}_s \text{sig}(\boldsymbol{\sigma})^\gamma = -[K_{s,1} |\sigma_1|^{\gamma_1} \text{sign}(\sigma_1), K_{s,2} |\sigma_2|^{\gamma_2} \text{sign}(\sigma_2), \dots, K_{s,m} |\sigma_m|^{\gamma_m} \text{sign}(\sigma_m)]^T, \\ i &= 1, 2, \dots, m \end{aligned} \quad (4.13)$$

where $K_{s,i} > 0$, $\gamma_i \in (0, 1)$. It is noteworthy that $|\sigma_i|^{\gamma_i} \text{sign}(\sigma_i)$ is a continuous function of σ_i without any approximation. Assume $\|\mathbf{I} - \mathbf{G}_n \tilde{\mathbf{G}}_n^{-1}\| \leq \bar{b} < 1$, and $\boldsymbol{\varepsilon}_{\text{ibs}}$ (Eq. (4.10)) is bounded, then by using Eq. (4.10), the time derivative of $V_n = \frac{1}{2} \sum_{i=1}^n \mathbf{z}_i^T \mathbf{z}_i$ using IBSMC is calculated by:

$$\begin{aligned} \dot{V}_n &= -\sum_{i=1}^n \mathbf{z}_i^T \mathbf{K}_i \mathbf{z}_i + \mathbf{z}_n^T (\boldsymbol{\varepsilon}_{\text{ibs}} - \mathbf{G}_n \tilde{\mathbf{G}}_n^{-1} \mathbf{K}_s \text{sig}(\boldsymbol{\sigma})^\gamma) \\ &\leq -\sum_{i=1}^n \mathbf{z}_i^T \mathbf{K}_i \mathbf{z}_i + \sum_{i=1}^m (|\sigma_i| |\boldsymbol{\varepsilon}_{\text{ibs},i}| + \bar{b} K_{s,i} |\sigma_i|^{\gamma_i+1} - K_{s,i} |\sigma_i|^{\gamma_i+1}) \\ &\leq -\sum_{i=1}^n \mathbf{z}_i^T \mathbf{K}_i \mathbf{z}_i - \sum_{i=1}^m \rho_i |\sigma_i|, \quad \forall |\sigma_i| \geq \left(\frac{\rho_i + |\boldsymbol{\varepsilon}_{\text{ibs},i}|}{(1-\bar{b})K_{s,i}} \right)^{\frac{1}{\gamma_i}}, \quad \forall \rho_i > 0 \end{aligned} \quad (4.14)$$

Eq. (4.14) proves the ultimate bound [4] of σ_i equals $\left(\frac{\rho_i + |\boldsymbol{\varepsilon}_{\text{ibs},i}|}{(1-\bar{b})K_{s,i}} \right)^{\frac{1}{\gamma_i}}$, whose size can be made arbitrarily small when $K_{s,i} > \frac{\rho_i + |\boldsymbol{\varepsilon}_{\text{ibs},i}|}{(1-\bar{b})}$, and if γ_i is arbitrarily small. Define $\mathbf{z} = [\mathbf{z}_1^T, \mathbf{z}_1^T, \dots, \mathbf{z}_n^T]^T$, since $V_n = \frac{1}{2} \|\mathbf{z}\|_2^2$, and $\boldsymbol{\sigma} = \mathbf{z}_n$, Eq. (4.14) also proves \mathbf{z} is uniformly ultimately bounded [4, 29].

4.2.3. OTHER SLIDING SURFACE DESIGNS

The sliding variable $\boldsymbol{\sigma}$ is not necessarily equal to \mathbf{z}_n , it can also be a linear or nonlinear function of \mathbf{z}_i . For example, design $\boldsymbol{\sigma}$ in the following form:

$$\boldsymbol{\sigma} = \mathbf{z}_n + \mathbf{C}_{n-1} \mathbf{z}_{n-1} + \mathbf{C}_{n-2} \mathbf{z}_{n-2} + \dots + \mathbf{C}_1 \mathbf{z}_1 \quad (4.15)$$

Design a candidate Lyapunov function as follows:

$$V = \frac{1}{2} \sum_{i=1}^{n-1} \mathbf{z}_i^T \mathbf{z}_i + \frac{1}{2} \boldsymbol{\sigma}^T \boldsymbol{\sigma} \quad (4.16)$$

Reviewing Sec. 4.2.1 and 4.2.2, the closed-loop system dynamics are given as:

$$\begin{aligned} \dot{\mathbf{z}}_1 &= \mathbf{f}_1 + \mathbf{G}_1 \mathbf{x}_{2,d} - \dot{\mathbf{y}}_r + \mathbf{G}_1 \mathbf{z}_2 = -\mathbf{K}_1 \mathbf{z}_1 + \mathbf{G}_1 \mathbf{z}_2 \\ \dot{\mathbf{z}}_i &= \mathbf{f}_i + \mathbf{G}_i \mathbf{x}_{i+1,d} - \dot{\boldsymbol{\phi}}_{i-1} + \mathbf{G}_i \mathbf{z}_{i+1} \\ &= -\mathbf{K}_i \mathbf{z}_i - \mathbf{G}_{i-1}^T \mathbf{z}_{i-1} + \mathbf{G}_i \mathbf{z}_{i+1}, \quad 2 \leq i \leq n-1 \end{aligned} \quad (4.17)$$

Using Eqs. (4.15, 4.17), the dynamics of the sliding variable are derived as:

$$\dot{\boldsymbol{\sigma}} = \mathbf{C}_1(-\mathbf{K}_1 \mathbf{z}_1 + \mathbf{G}_1 \mathbf{z}_2) + \sum_{i=2}^{n-1} \mathbf{C}_i(-\mathbf{K}_i \mathbf{z}_i - \mathbf{G}_{i-1}^T \mathbf{z}_{i-1} + \mathbf{G}_i \mathbf{z}_{i+1}) + \dot{\mathbf{z}}_n \quad (4.18)$$

The derivative of the candidate Lyapunov function (Eq. (4.16)) is derived using Eqs. (4.15), (4.17), (4.18), and (4.8) as:

$$\begin{aligned} \dot{V} &= -\sum_{i=1}^{n-1} \mathbf{z}_i^T \mathbf{K}_i \mathbf{z}_i + \mathbf{z}_{n-1}^T \mathbf{G}_{n-1} \mathbf{z}_n + \boldsymbol{\sigma}^T \dot{\boldsymbol{\sigma}} \\ &= -\sum_{i=1}^{n-1} \mathbf{z}_i^T \mathbf{K}_i \mathbf{z}_i - \mathbf{z}_{n-1}^T \mathbf{G}_{n-1} (\mathbf{C}_{n-1} \mathbf{z}_{n-1} + \dots + \mathbf{C}_1 \mathbf{z}_1) + \mathbf{z}_{n-1}^T \mathbf{G}_{n-1} \boldsymbol{\sigma} \\ &\quad + \boldsymbol{\sigma}^T [\mathbf{C}_1(-\mathbf{K}_1 \mathbf{z}_1 + \mathbf{G}_1 \mathbf{z}_2) + \sum_{i=2}^{n-1} \mathbf{C}_i(-\mathbf{K}_i \mathbf{z}_i - \mathbf{G}_{i-1}^T \mathbf{z}_{i-1} + \mathbf{G}_i \mathbf{z}_{i+1}) \\ &\quad + (\dot{\mathbf{x}}_{n,0} + \mathbf{G}_n(\mathbf{x}_0, \kappa_0) \Delta \mathbf{u} + \Delta \mathbf{d} + \boldsymbol{\delta}(\mathbf{x}, \kappa, \Delta t) - \dot{\boldsymbol{\phi}}_{n-1})] \end{aligned} \quad (4.19)$$

An SMC virtual control term \mathbf{v}_s is needed to compensator for the uncertainties, faults and disturbances present in $\dot{\mathbf{z}}_n$. Design the IBSMC input as:

$$\begin{aligned} \Delta \mathbf{u}_{\text{ibsmc}} &= \bar{\mathbf{G}}_n^{-1} (-\dot{\mathbf{x}}_{n,0} + \dot{\boldsymbol{\phi}}_{n-1} - \mathbf{G}_{n-1}^T \mathbf{z}_{n-1} - \mathbf{C}_1(-\mathbf{K}_1 \mathbf{z}_1 + \mathbf{G}_1 \mathbf{z}_2) \\ &\quad - \sum_{i=2}^{n-1} \mathbf{C}_i(-\mathbf{K}_i \mathbf{z}_i - \mathbf{G}_{i-1}^T \mathbf{z}_{i-1} + \mathbf{G}_i \mathbf{z}_{i+1}) - \mathbf{K}_c \boldsymbol{\sigma} + \mathbf{v}_s) \\ &\triangleq \bar{\mathbf{G}}_n^{-1} (\mathbf{v}'_c + \mathbf{v}_s - \dot{\mathbf{x}}_{n,0}) \end{aligned} \quad (4.20)$$

where \mathbf{K}_c is a positive definite gain matrix. Analogous to the preceding control designs, \mathbf{v}_s can be designed using any SMC technique. As an example, following the classical way as $\mathbf{v}_s = -\mathbf{K}_s \text{sign}(\boldsymbol{\sigma})$, where \mathbf{K}_s is a positive definite diagonal gain matrix. Assume $\|\mathbf{I} - \mathbf{G}_n \bar{\mathbf{G}}_n^{-1}\| \leq \bar{b} < 1$, and $\boldsymbol{\epsilon}'_{\text{ibs}} = \boldsymbol{\delta}(\mathbf{x}, \kappa, \Delta t) + (\mathbf{G}_n \bar{\mathbf{G}}_n^{-1} - \mathbf{I})(\mathbf{v}'_c - \dot{\mathbf{x}}_{n,0}) + \Delta \mathbf{d}$ is bounded, then

substituting Eq. (4.20) into Eq. (4.19) results in:

$$\begin{aligned}
\dot{V} &= -\sum_{i=1}^{n-1} \mathbf{z}_i^T \mathbf{K}_i \mathbf{z}_i - \mathbf{z}_{n-1}^T \mathbf{G}_{n-1} (\mathbf{C}_{n-1} \mathbf{z}_{n-1} + \dots + \mathbf{C}_1 \mathbf{z}_1) + \boldsymbol{\sigma}^T (\boldsymbol{\varepsilon}'_{\text{ibs}} - \mathbf{K}_c \boldsymbol{\sigma} - \mathbf{G}_n \bar{\mathbf{G}}_n^{-1} \mathbf{K}_s \text{sign}(\boldsymbol{\sigma})) \\
&\leq -[\mathbf{z}_1^T, \mathbf{z}_2^T, \dots, \mathbf{z}_{n-1}^T] \begin{bmatrix} \mathbf{K}_1 & \mathbf{0} & \dots & \mathbf{0} \\ \mathbf{0} & \mathbf{K}_2 & \dots & \mathbf{0} \\ \vdots & \vdots & \ddots & \vdots \\ \mathbf{G}_{n-1} \mathbf{C}_1 & \mathbf{G}_{n-1} \mathbf{C}_2 & \dots & \mathbf{G}_{n-1} \mathbf{C}_{n-1} + \mathbf{K}_{n-1} \end{bmatrix} \begin{bmatrix} \mathbf{z}_1 \\ \mathbf{z}_2 \\ \vdots \\ \mathbf{z}_{n-1} \end{bmatrix} \\
&\quad - \boldsymbol{\sigma}^T \mathbf{K}_c \boldsymbol{\sigma} + \sum_{i=1}^m (|\sigma_i| |\varepsilon'_{\text{ibs},i}| + \bar{b} K_{s,i} |\sigma_i| - K_{s,i} |\sigma_i|) \\
&\leq -[\mathbf{z}_1^T, \mathbf{z}_2^T, \dots, \mathbf{z}_{n-1}^T] \mathbf{Q} [\mathbf{z}_1^T, \mathbf{z}_2^T, \dots, \mathbf{z}_{n-1}^T]^T - \boldsymbol{\sigma}^T \mathbf{K}_c \boldsymbol{\sigma} \\
&\quad - \sum_{i=1}^m \rho_i |\sigma_i|, \quad \forall K_{s,i} \geq \frac{\rho_i + |\varepsilon'_{\text{ibs},i}|}{1 - \bar{b}}, \quad \forall \rho_i > 0
\end{aligned} \tag{4.21}$$

4

$\dot{V} \leq 0$ if \mathbf{Q} is a positive definite matrix, which can be achieved by properly choosing the gain matrices \mathbf{C}_i and \mathbf{K}_i . If the positive definiteness of \mathbf{Q} is achieved, then according to Barbalat's Lemma [5], \mathbf{z}_i , $i = 1, 2, \dots, n-1$, and $\boldsymbol{\sigma}$ converge to zero in spite of the perturbation of $\boldsymbol{\varepsilon}'_{\text{ibs}}$.

4.2.4. COMPARISONS BETWEEN BSMC AND IBSMC

For the nonlinear dynamics in Eq. (4.1), the standard backstepping control input is design as:

$$\mathbf{u}_{\text{bs}} = \bar{\mathbf{G}}_n^{-1} (-\bar{\mathbf{f}}_n - \mathbf{K}_n \mathbf{z}_n + \dot{\boldsymbol{\phi}}_{n-1} - \mathbf{G}_{n-1}^T \mathbf{z}_{n-1}) \triangleq \bar{\mathbf{G}}_n^{-1} (\mathbf{v}_c - \bar{\mathbf{f}}_n) \tag{4.22}$$

where $\boldsymbol{\phi}_{n-1}$ is the same as in Eq. (4.6). As a model-based control approach, the nominal models $\bar{\mathbf{f}}_n$ and $\bar{\mathbf{G}}_n$ are used by backstepping in Eq. (4.22). Substituting Eq. (4.22) into Eq. (4.1) yields:

$$\dot{V}_n = -\sum_{i=1}^n \mathbf{z}_i^T \mathbf{K}_i \mathbf{z}_i + \mathbf{z}_n^T (\mathbf{f}_n - \bar{\mathbf{f}}_n + (\mathbf{G}_n \bar{\mathbf{G}}_n^{-1} - \mathbf{I})(\mathbf{v}_c - \bar{\mathbf{f}}_n) + \mathbf{d}) \triangleq -\sum_{i=1}^n \mathbf{z}_i^T \mathbf{K}_i \mathbf{z}_i + \mathbf{z}_n^T \boldsymbol{\varepsilon}_{\text{bs}} \tag{4.23}$$

$\boldsymbol{\varepsilon}_{\text{bs}}$ in the above equation indicates the uncertain vector that remains in the closed-loop system. If $\boldsymbol{\varepsilon}_{\text{bs}}$ is bounded, then \mathbf{z}_i , $i = 1, 2, \dots, n$, can be proved to be ultimately bounded by class \mathcal{K} functions of $\boldsymbol{\varepsilon}_{\text{bs}}$ [4, 29]. If $\boldsymbol{\varepsilon}_{\text{bs}}$ is unbounded in severe damage cases, \mathbf{z}_i , $i = 1, 2, \dots, n$ will also become unbounded.

To improve the robustness of backstepping control, earlier research suggests combining SMC with backstepping [8, 10, 14–17]. The main idea of this combination is to use an SMC virtual control input to compensate for the uncertain term $\boldsymbol{\varepsilon}_{\text{bs}}$. Specially, the hybrid BSMC input is designed in the following structure:

$$\mathbf{u}_{\text{bsmc}} = \bar{\mathbf{G}}_n^{-1} (\mathbf{v}_c + \mathbf{v}_s - \bar{\mathbf{f}}_n) \tag{4.24}$$

where \mathbf{v}_s is the SMC virtual control input, which can be designed using any SMC technique.

After reviewing the BSMC approach, it will be analytically compared with the IBSMC proposed in Sec. 4.2.2. The main focus of the comparisons are on the control structure, thus the conclusions drawn in this subsection are not constrained by the specific SMC virtual control design. In other words, the sliding variable can be any function of \mathbf{z}_i . The \mathbf{v}_s in Eqs. (4.24, 4.12) can be designed using any SMC technique, as long as the same SMC method is consistently used by BSMC and IBSMC for fair comparisons.

The first difference between BSMC and IBSMC can be revealed by Eqs. (4.24, 4.12), where the nominal model $\bar{\mathbf{f}}_n$ is used by BSMC, while the measurements or estimations of $\dot{\mathbf{x}}_{n,0}$ and \mathbf{u}_0 are needed by IBSMC. Consequently, IBSMC has less model dependency than BSMC, but is more sensitive to sensing issues (e.g., sensor noise, delays, etc.).

In the presence of model uncertainties, sudden faults, and external disturbances, different perturbation terms exist in BSMC and IBSMC, namely $\boldsymbol{\varepsilon}_{bs}$ in Eq. (4.23) and $\boldsymbol{\varepsilon}_{ibs}$ in Eq. (4.10). These two perturbation terms have different properties. Actually, $\boldsymbol{\varepsilon}_{ibs}$ is in a similar form with $\boldsymbol{\varepsilon}_{indi}$ in [26], expect two differences: 1) $\boldsymbol{\varepsilon}_{ibs}$ contains \mathbf{G}_n while $\boldsymbol{\varepsilon}_{indi}$ in [26] uses \mathbf{G} ; 2) $\boldsymbol{\varepsilon}_{ibs}$ distinguishes the parametric and nonparametric uncertainties in \mathbf{f}_n and \mathbf{G}_n , which is not the case in $\boldsymbol{\varepsilon}_{indi}$. Based on the similarities between $\boldsymbol{\varepsilon}_{indi}$ and $\boldsymbol{\varepsilon}_{ibs}$, the following corollary of the Theorem 2 in [26] is proposed:

Corollary 4 *If $\|\mathbf{I} - \mathbf{G}_n \bar{\mathbf{G}}_n^{-1}\| \leq \bar{b} < 1$ for all t , and if $\|\boldsymbol{\delta}(\mathbf{x}, \kappa, \Delta t)\| \leq \bar{\delta}$, under sufficiently high sampling frequency, $\boldsymbol{\varepsilon}_{ibs}$ given by Eq. (4.10) is bounded for all t , and is ultimately bounded by $\frac{\Delta v_c \bar{b} + \bar{\delta} + \Delta \bar{d}}{1 - \bar{b}}$, where Δv_c and $\Delta \bar{d}$ are the upper bounds of $\Delta \mathbf{v}_c$ and $\Delta \mathbf{d}$ in Eq. (4.10), respectively.*

Moreover, $\boldsymbol{\varepsilon}_{bs}$ (4.23) is in a similar form with $\boldsymbol{\varepsilon}_{ndi}$ in [26]. Therefore, analogous to the comparisons of $\boldsymbol{\varepsilon}_{ndi}$ and $\boldsymbol{\varepsilon}_{indi}$ in [26], the following conclusions are drawn for $\boldsymbol{\varepsilon}_{bs}$ and $\boldsymbol{\varepsilon}_{ibs}$:

1. The conditions in Corollary 4 guarantee a bounded $\boldsymbol{\varepsilon}_{ibs}$, while the boundedness of $\boldsymbol{\varepsilon}_{bs}$ is undetermined in the same conditions.
2. Even if both $\boldsymbol{\varepsilon}_{bs}$ and $\boldsymbol{\varepsilon}_{ibs}$ are bounded, if the sampling frequency is sufficient high, the upper bound of $\boldsymbol{\varepsilon}_{ibs}$ is smaller than that of $\boldsymbol{\varepsilon}_{bs}$, before and after a fault occurs.
3. $\boldsymbol{\varepsilon}_{ibs}$ has smaller variations in different fault cases, while $\boldsymbol{\varepsilon}_{bs}$ is more fault-case dependent.

The smaller bound of $\boldsymbol{\varepsilon}_{ibs}$ can fundamentally release the control effort of SMC because for most SMC designs, the required SMC gains are monotonically increasing functions of the uncertainty bounds. As a consequence, inheriting the robustness of both IBS and SMC, IBSMC is able to attain better robustness using not only reduced model information, but also reduced SMC gains (beneficial to chattering reduction). These conclusions will be numerically validated in Sec. 4.4. A reasonable choice of the sampling frequency depends on the specific system characteristics and hardware constraints [29]. It has been proved by flight tests that 50~100 Hz is suitable for airplane flight control [23, 24, 30].

4.3. FAULT-TOLERANT FLIGHT CONTROL SYSTEM DESIGN

In this section, the control methods derived for generic nonlinear uncertain systems (Eq. (4.1) in Sec. 4.2) will be applied to fault-tolerant flight control problems. The six-degree-of-freedom dynamics for rigid-aircraft with and without structural damage can be found in [25]. However, the flight control design in [25] has some limitations. First, the attitude control in [25] enforces the aircraft to track independent roll, pitch and heading angle commands. This can be impractical because normally the side-slip angle should be stabilized to zero during maneuvers for minimizing the side force. Moreover, the actuator fault scenarios considered in [25] only include partial loss of control effectiveness and solid jamming. For these two types of fault, the fault-induced disturbing force and moment coefficients are constant. Time-varying disturbing coefficients are more challenging for control design. In view of these limitations, the flight control design in this chapter will minimize the side-slip angle. The solid oscillatory failure case (OFC), which induces time-varying disturbing coefficients will also be modeled and evaluated in simulations.

4

The solid OFC is mainly caused by electronic components in fault mode generating spurious sinusoidal signals, which propagate through the servo-loop control, and lead to control surface oscillations [33]. “Solid” means the spurious sinusoidal signals substitute instead of being added to (“liquid” OFC) the normal control signal [33]. If one-side of elevator or aileron has solid OFC, the corresponding control derivatives are halved, namely $C'_{ij} = \mu_j C_{ij}$, $i = l, m, n$, $j = \delta_a, \delta_e, \delta_r$, $\mu_j = 0.5$, with $(\cdot)'$ indicating the post-fault condition. Asymmetric actuator faults also invalidate the decoupling between lateral and longitudinal controls. Specially, $C_{m\delta_a}$ will be introduced by asymmetric aileron fault, while $C_{l\delta_e}$ and $C_{n\delta_e}$ will be introduced by asymmetric elevator fault. Furthermore, time-varying disturbing force and moment coefficients ($\tilde{C}_x, \tilde{C}_y, \tilde{C}_z, \tilde{C}_l, \tilde{C}_m, \tilde{C}_n$) will be induced by solid OFC. These coefficients are proportional to the control derivatives and control surface positions, thus they are also spurious sinusoidal signals.

This section considers an aircraft attitude control problem, where the controlled attitude angles are chosen as $\mathbf{y} = \mathbf{x}_1 = [\phi, \theta, \beta]^T$. ϕ , θ and β are the roll, pitch angles and side-slip angle. Their kinematics can be found in [34]. Choose \mathbf{x}_2 equals the angular rate $\boldsymbol{\omega} = [p, q, r]^T$, and \mathbf{u} equals the deflections of aileron δ_a , elevator δ_e and rudder δ_r , then the aircraft attitude dynamics [34] are written in a more compact form:

$$\begin{aligned}\dot{\mathbf{x}}_1 &= \mathbf{f}_1(\mathbf{x}_1) + \mathbf{G}_1(\mathbf{x}_1)\mathbf{x}_2 \\ \dot{\mathbf{x}}_2 &= \mathbf{f}_2(\mathbf{x}_1, \mathbf{x}_2) + \mathbf{G}_2(\mathbf{x}_1, \mathbf{x}_2)\mathbf{u}\end{aligned}\quad (4.25)$$

In the presence of faults, model uncertainties and disturbances, the kinematics of \mathbf{x}_1 are unaffected while the dynamics of \mathbf{x}_2 are perturbed. Therefore, the aircraft attitude dynamics modeled by Eq. (4.25) belong to Eq. (4.1), so the controllers designed in Sec. 4.2 can then be directly applied to this control problem.

4.4. NUMERICAL VALIDATION

In this section, the robustness of BS, BSMC and IBSMC will be numerically evaluated by evaluating their ability of passively tolerating faults and uncertainties. “Passive” means these control methods are not aware of the faults and uncertainties, and consistently

use the model estimated in the nominal condition. The nominal aerodynamic, thrust and inertia models are set up using the public data of F-16 [35]. It is noteworthy that this aerodynamic data for pitching moment coefficient is non-affine in δ_e , which results in insolvable control problem for BS and BSMC. By contrast, IBSMC and IBS are able to solve non-affine in the control problems, because Eq. (4.3) takes partial derivatives with respect to \mathbf{u} . For fair comparisons, an affine in δ_e model approximated using polynomial functions [9] are consistently used by all the controllers. The dynamics of rudder, ailerons and stabilators are all modeled as first-order systems. The bandwidth and limits for the actuators can be found in Table 2 of Ref. [25]. A simple proportional-integral thrust control is designed in a separate control loop to maintain airspeed. This aircraft is initially trimmed at a steady level flight condition with airspeed $V = 500$ ft/s and altitude $h = 10,000$ ft. The sampling frequency is $f_s = 100$ Hz.

The main focus of this chapter is on the comparisons of different control structures, which is independent of specific \mathbf{v}_c and \mathbf{v}_s designs. For fair comparisons, gain matrices $\mathbf{K}_1 = \text{diag}([2, 2, 2])$ (in Eq. (4.5)), and $\mathbf{K}_2 = \text{diag}([5, 5, 5])$ (in Eqs. (4.22, 4.9)) are consistently used by all the controllers. The \mathbf{v}_s for BSMC and IBSMC are both designed using FRTC SMC method, with $\boldsymbol{\sigma} = \mathbf{z}_n$. The SMC parameters used by both BSMC and IBSMC (in Eq. (4.14)) are $\mathbf{K}_s = \text{diag}([0.5, 0.5, 0.1])$ and $\gamma_i = 0.3$, $i = 1, 2, 3$. The control performance with varied \mathbf{K}_s and γ_i will also be analyzed in the following contexts.

4.4.1. FLIGHT CONTROL IN THE NOMINAL CASE

The references for ϕ and θ are smoothly combined sigmoid functions as continuous and differentiable realizations of 3211 signals. As can be seen from Fig. 4.1, $|\phi_r| = 20^\circ$, and $|\theta_r - \theta_*| = 15^\circ$, where θ_* is the pitch angle in the trim condition. $\beta_r = 0^\circ$ to minimize the side force during maneuvers.

Fig. 4.1 shows that all the three controllers, BS, BSMC and IBSMC are able to steer the aircraft to follow the commands. Only small tracking errors present in transition phases, and they are all ultimately bounded. The control surface deflections are smooth, and IBSMC has slightly better performance than BS and BSMC.

4.4.2. FLIGHT CONTROL IN THE PRESENCE OF MODEL UNCERTAINTIES

In this subsection, the robustness of the controllers to uncertainties will be evaluated. The attitude references are the same as references in the nominal case. Parametric uncertainties are added to the nonlinear system. Specifically, the inertia parameters $J_{xx}, J_{yy}, J_{zz}, J_{xz}$, the damping coefficients $C_{y_r}, C_{y_p}, C_{n_r}, C_{n_p}, C_{l_r}, C_{l_p}, C_{z_q}, C_{m_q}, C_{x_q}$, the control effectiveness $C_{l_{\delta_a}}, C_{l_{\delta_r}}, C_{n_{\delta_a}}, C_{n_{\delta_r}}, C_{y_{\delta_a}}, C_{y_{\delta_r}}$, and the coefficients $C_x(\alpha, \delta_e, M)$, $C_z(\alpha, \delta_e, M)$, $C_m(\alpha, \delta_e, M)$, $C_y(\alpha, \beta, M)$, $C_l(\alpha, \beta, M)$, $C_n(\alpha, \beta, M)$ are multiplied with random combinations of scaling factors, which are in the range of $[0.2, 2]$. The aircraft responses in the presence of uncertainties are shown in Fig. 4.2, from which it can be seen IBSMC has the best tracking performance. Furthermore, the tracking errors using all these three controllers are ultimately bounded. In view of Fig. 4.3, $\|\mathbf{I} - \mathbf{G}_n \tilde{\mathbf{G}}_n^{-1}\| < 1$ is satisfied in this simulation case, and the bound of $\boldsymbol{\epsilon}_{\text{ibs}}$ is smaller than that of $\boldsymbol{\epsilon}_{\text{bs}}$. These results verify the analyses in Sec. 4.2.4.

For the responses shown in Fig. 4.2, the \mathbf{v}_s for BSMC and IBSMC are identically designed using FRTC SMC, with the same parameters \mathbf{K}_s and γ_i . It can be seen from

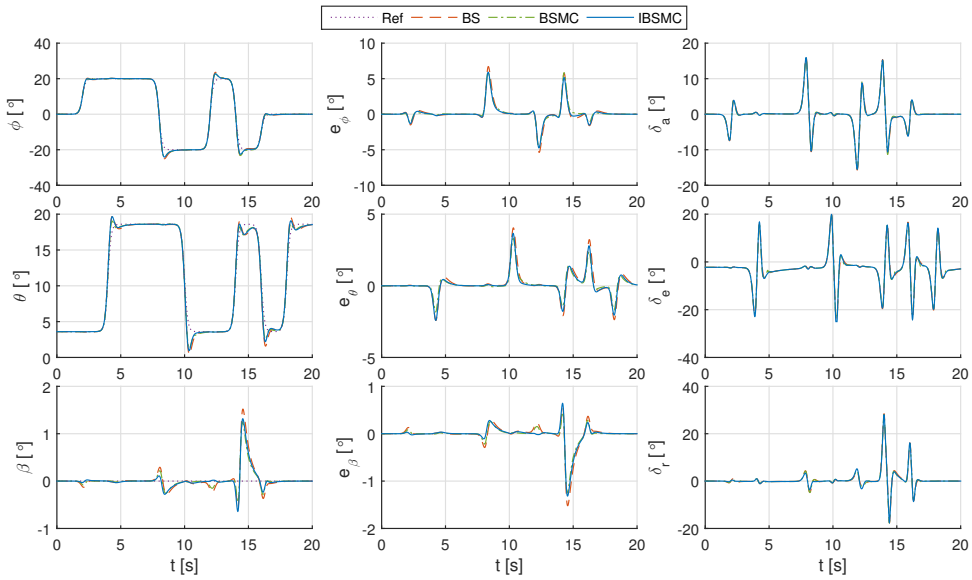


Figure 4.1: Aircraft responses and control inputs in the nominal condition.

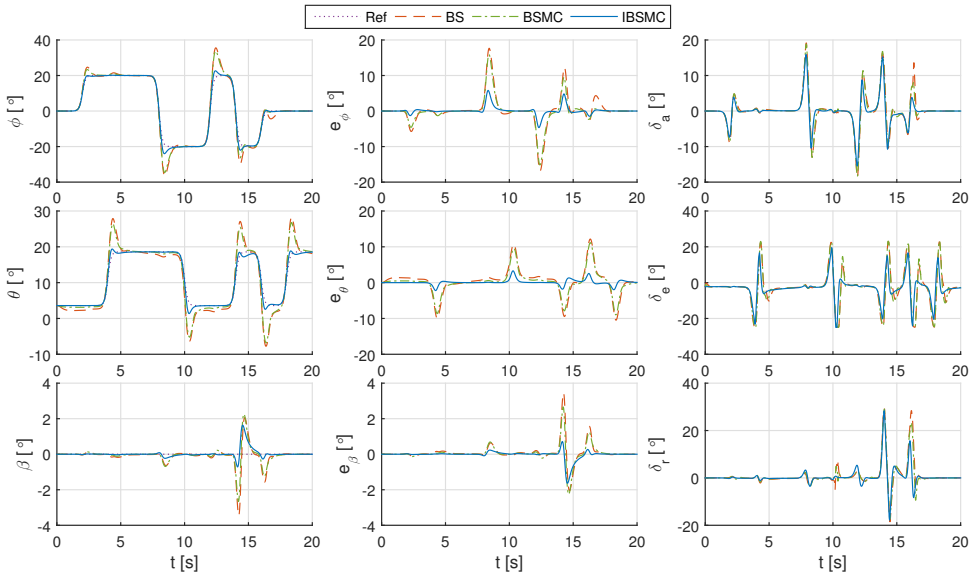


Figure 4.2: Aircraft responses and control inputs in the presence of model uncertainties.

Fig. 4.2 that BSMC using these parameters only brings limited performance improvements to standard backstepping. Recall Eq. (4.14), the ultimate bound of σ_i can be reduced by increasing $K_{s,i}$ and reducing γ_i . The \mathbf{v}_s in Eq. (4.13) using difference pa-

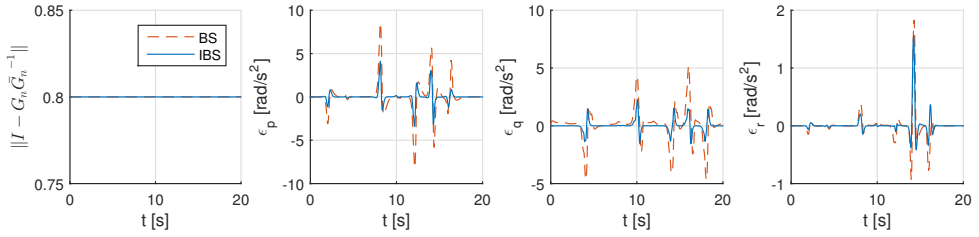


Figure 4.3: Responses of $\|I - G_n \bar{G}_n^{-1}\|$ and ϵ_{bs} , ϵ_{ibs} in the presence of model uncertainties.

rameters are illustrated in Fig. 4.4.

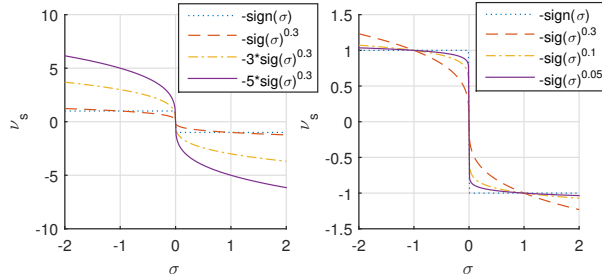


Figure 4.4: The FRTC SMC input \mathbf{v}_s (Eq. (4.13)) with different parameters.

Fig. 4.5 illustrates the influences of SMC gains on the tracking performance of BSMC, where the gain matrix \mathbf{K}_s is multiplied with successively increased coefficient $c = 1, 3, 5$, while $\gamma_i = 0.3$ is consistently used. As can be seen from the left subplot of Fig. 4.4, the increased gains amplify the control effort of \mathbf{v}_s , which can consequently improve the tracking performance of BSMC as verified by Fig. 4.5. However, high-gain control not only amplifies the measurement noise in practice, but can also impose unachievable commands on actuators. Since actuators have limited bandwidth and nonlinear constraints, high-gain control would induce oscillations and potential instabilities, which is verified in Fig. 4.5 for the $c = 5$ case. Moreover, BSMC using five-times higher gains than IBSMC still has inferior robust performance than IBSMC, which can be seen by comparing Fig. 4.5 with Fig. 4.2.

The ultimate bound of σ_i can also be reduced by diminishing γ_i (Eq. (4.14)). As shown by Eq. (4.13) and the right subplot of Fig. 4.4, $\text{sig}(\sigma)^\gamma = |\sigma|^\gamma \text{sign}(\sigma)$ becomes steeper near $\sigma = 0$ as γ approaches zero, which can speed up the convergence near the sliding surface. This is verified by the tracking performance of BSMC using varies γ shown in Fig. 4.6. However, if $\gamma = 0$, then $\text{sig}(\sigma)^\gamma = \text{sign}(\sigma)$, which means although the \mathbf{v}_s designed by Eq. (4.13) is continuous, chattering would present in practice if γ is too small. This phenomenon is verified in Fig. 4.6 by the $\gamma = 0.05$ case. Therefore, trade-offs should be made between performance and chattering reduction. Furthermore, the performance of IBSMC is better than BSMC with all the tested γ values, which can be seen by comparing Fig. 4.6 with Fig. 4.2.

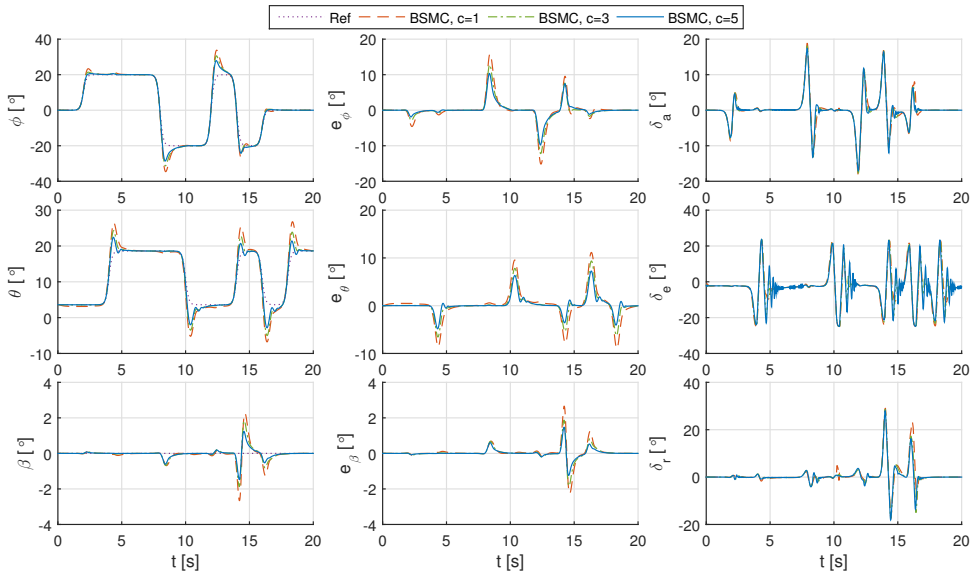


Figure 4.5: The influences of SMC gains on the tracking performance of BSMC.

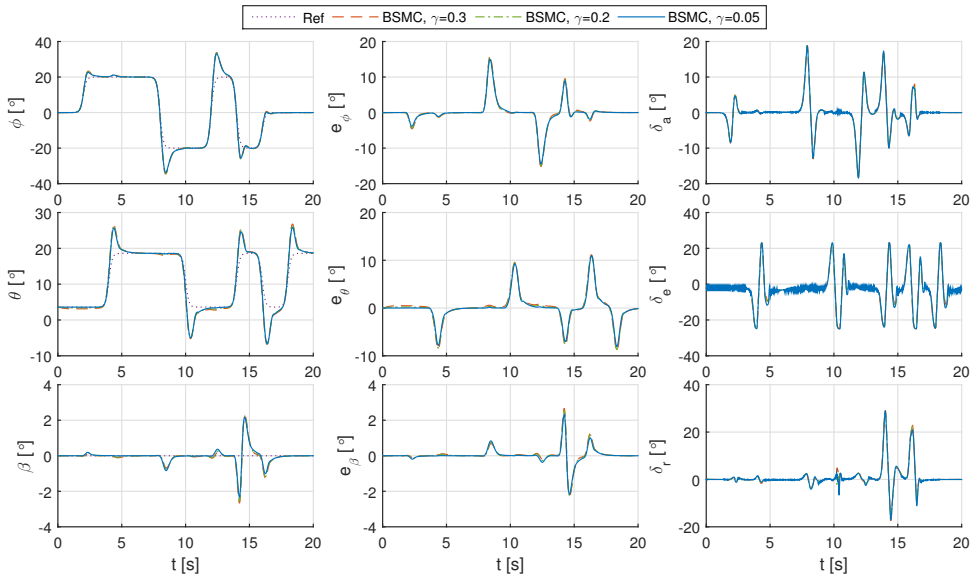


Figure 4.6: The influences of SMC parameter γ on the tracking performance of BSMC.

4.4.3. FLIGHT CONTROL IN THE PRESENCE OF ACTUATOR FAULTS

In this subsection, the robustness of BS, BSMC, and IBSMC will be evaluated by their abilities of passively resisting the left stabilator solid OFC fault. This fault is introduced

from $t = 5$ s. Based on the modeling method in Sec. 4.3, the post-fault deflection of the left stabilator is modeled as $\delta_{e,l} = 10\sin(2(t-5))$ ($^\circ$), $t \geq 5$ s. The right stabilator is still under control. Because of the fault, $C_{m\delta_e}$ is halved, and new control derivatives $C_{l\delta_e}$ and $C_{n\delta_e}$ are induced. The disturbing coefficients caused by the solid OFC significantly deteriorate the tracking performance of backstepping, as shown in Fig. 4.7. IB-SMC shows the best performance over backstepping and BSMC in all the three channels. $\|I - G_n \tilde{G}_n^{-1}\| < 1$ is satisfied in this scenario as shown in Fig. 4.8. It is also illustrated in Fig. 4.8 that the bound of ϵ_{ibs} is smaller than that of ϵ_{bs} . Because of the smaller perturbation bound, when the same SMC gains are used, the ultimate bound of z_i using IBSMC has smaller ultimate bound, which is verified by Fig. 4.7.

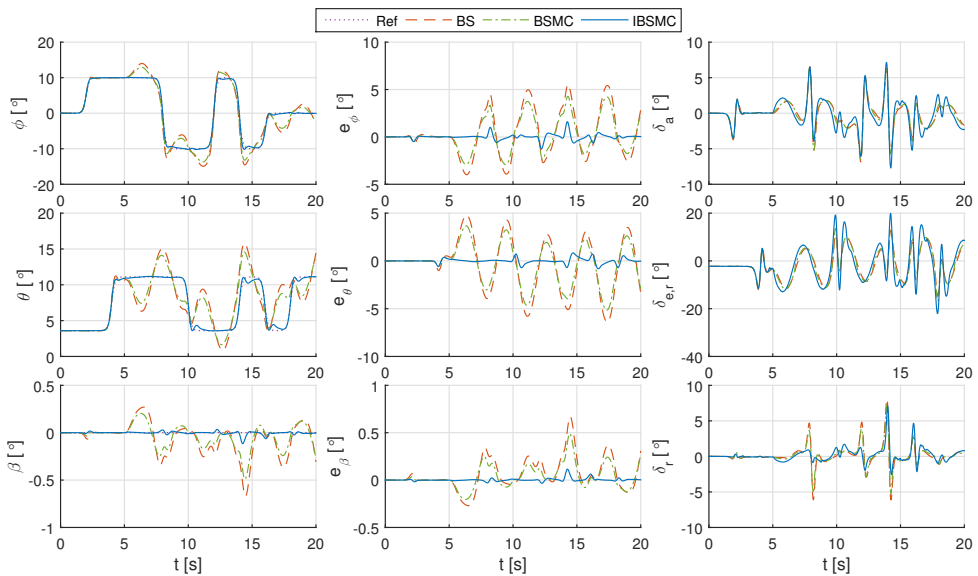


Figure 4.7: Aircraft responses and control inputs with a stabilator solid OFC fault occurs at $t = 5$ s.

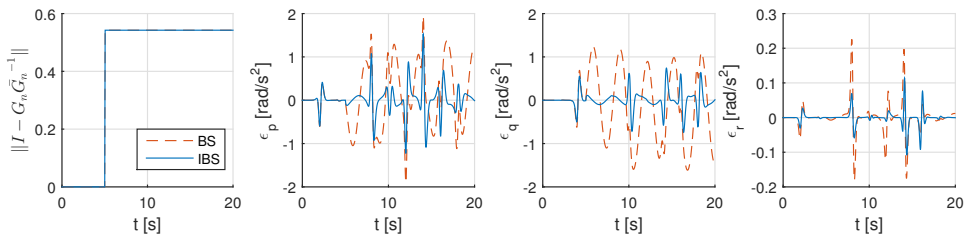


Figure 4.8: Responses of $\|I - G_n \tilde{G}_n^{-1}\|$ and ϵ_{bs} , ϵ_{ibs} with a stabilator solid OFC fault occurs at $t = 5$ s.

4.4.4. FLIGHT CONTROL IN THE PRESENCE OF STRUCTURAL DAMAGES

In this subsection, the robustness of BS, BSMC, and IBSMC will be evaluated by their abilities of passively resisting structural damages. The damaged aircraft is unable to execute severe maneuvers, because of its shrunken flight envelop. Therefore, the attitude references are halved in this subsection as compared to the nominal case, namely, $|\phi_r| = 10^\circ$, $|\theta_r - \theta_*| = 7.5^\circ$, $\beta_r = 0^\circ$. The influences of structural damages are modeled using methods in [25].

During simulations, the right wing lost 25% of its area at $t = 3$ s. Afterwards, the entire left stabilator is lost at $t = 5$ s. Subsequently, one half area of the vertical tail is lost at $t = 7$ s. Accompanying with the structural damages, the corresponding control surfaces are also lost. The aircraft responses and control inputs using BS, BSMC, and IBSMC are shown in Fig. 4.9, from which it can be seen IBSMC has the best tracking accuracy. Although the tracking errors using BSMC and BS are ultimately bounded, remarkable performance deteriorations present. The conclusion that ϵ_{ibbs} has smaller bound than ϵ_{bs} is further verified in Fig. 4.10, which consequently leads to the better robustness of IBSMC.

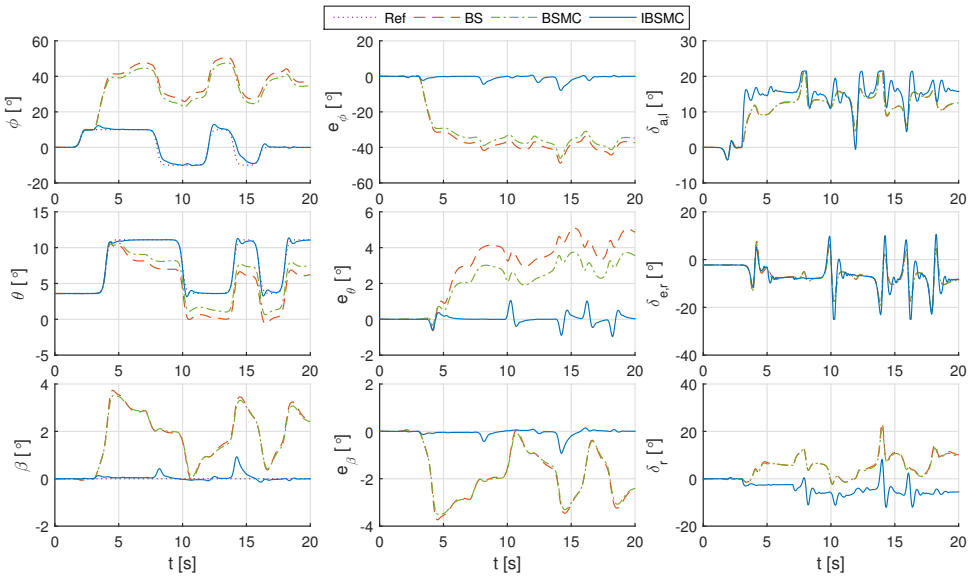


Figure 4.9: Aircraft responses and control inputs with wing, stabilator and vertical tail damaged at $t = 3, 5, 7$ s.

Analogous to the discussions in Sec. 4.4.2, the performance of BSMC can be improved by reducing γ and increasing \mathbf{K}_s . It has been shown in Fig. 4.6 that chattering effects would present as γ approaching zero. Fig. 4.11 shows the tracking responses of an aircraft using BSMC in the second structural damage scenario with gradually increased gains $\mathbf{K}_s = c \cdot \text{diag}([0.5, 0.5, 0.1])$. It can be seen from Fig. 4.11 that high-gain BSMC can indeed enhance the tracking performance, but will cause oscillations owing to the actuator limits, and will also amplify measurement noise in practice. By contrast, IBSMC with much lower SMC gains is able to provide satisfactory tracking performance in spite

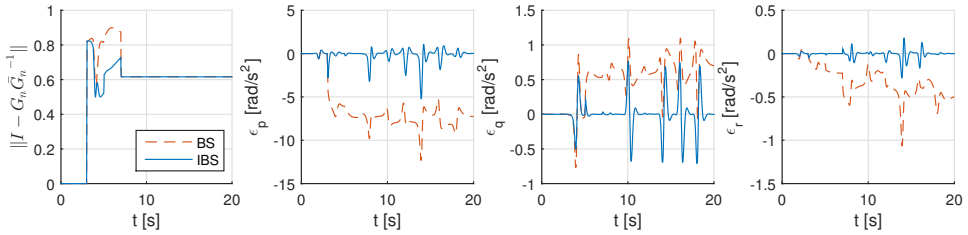


Figure 4.10: Responses of $\|I - G_n \tilde{G}_n^{-1}\|$, ϵ_{bs} , ϵ_{ibs} with wing, stabilator and vertical tail damaged at $t = 3, 5, 7$ s.

of structural damages, as illustrated in Fig. 4.9.

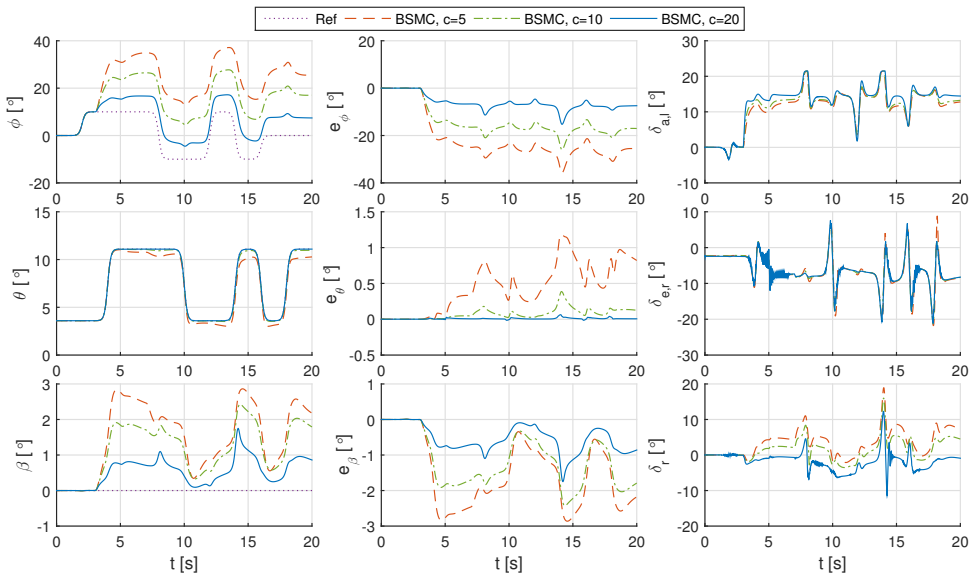


Figure 4.11: The influences of the SMC gains on the tracking performance of BSMC in a structural damage scenario.

4.5. CONCLUSIONS

This chapter proposes an incremental backstepping sliding mode control (IBSMC) framework for multi-input/output nonlinear strict-feedback systems under the perturbations of model uncertainties, sudden faults, and external disturbances. Inheriting the merits of both incremental backstepping (IBS) and sliding mode control (SMC), this hybrid framework has both lower model dependency and enhanced robustness than backstepping and SMC hybridized with backstepping (BSMC). Moreover, the SMC gains needed by IBSMC are lower than that of BSMC, which is beneficial to chattering reduction and migrating the effects of measurement noise. In addition, tuning of IBSMC is straightforward, and is easier than adaptive backstepping.

For solving the aircraft fault-tolerant control problem, the SMC virtual controls in BSMC and IBSMC are consistently designed using the finite reaching-time continuous SMC method. Numerical simulations verify that IBSMC has better robustness over backstepping and BSMC, in the presence of model uncertainties, sudden actuator faults and structural damages. In conclusion, easier implementation, reduced model dependency, and enhanced robustness make the proposed IBSMC framework promising for enhancing aircraft survivability in real life.

REFERENCES

- [1] *Statistical Summary of Commercial Jet Airplane Accidents, Worldwide Operations, 1959-2016*, Tech. Rep. (Boeing Commercial Airplanes, 2015).
- [2] *Annual Safety Review 2017*, Tech. Rep. (European Aviation Safety Agency, 2017).
- [3] P. Russell and J. Pardee, *Joint Safety Analysis Team-CAST Approved Final Report Loss of Control JSAT Results and Analysis*, Tech. Rep. (Federal Aviation Administration: Commercial Airline Safety Team, 2000).
- [4] H. K. Khalil, *Nonlinear Systems* (Prentice-Hall, New Jersey, 2002).
- [5] J.-J. E. Slotine and W. Li, *Applied Nonlinear Control* (NJ: Prentice Hall, Englewood Cliffs, 1991).
- [6] A. Astolfi and R. Ortega, *Immersion and invariance: A new tool for stabilization and adaptive control of nonlinear systems*, *IEEE Transactions on Automatic Control* **48**, 590 (2003).
- [7] F. Ikhouane and M. Krstić, *Robustness of the tuning functions adaptive backstepping design for linear systems*, *IEEE Transactions on Automatic Control* **43**, 431 (1998).
- [8] G. Bartolini, A. Ferrara, L. Giacomini, and E. Usai, *Properties of a combined adaptive/second-order sliding mode control algorithm for some classes of uncertain nonlinear systems*, *IEEE Transactions on Automatic Control* **45**, 1334 (2000).
- [9] P. van Gils, E. van Kampen, C. C. de Visser, and Q. P. Chu, *Adaptive Incremental Backstepping Flight Control for a High-Performance Aircraft with Uncertainties*, in *AIAA Guidance, Navigation, and Control Conference* (American Institute of Aeronautics and Astronautics, San Diego, California, 2016).
- [10] B. Cong, X. Liu, and Z. Chen, *Backstepping based adaptive sliding mode control for spacecraft attitude maneuvers*, *Aerospace Science and Technology* **30**, 1 (2013).
- [11] Y. B. Shtessel, J. M. Buffington, and S. S. Banda, *Multiple Timescale Flight Control Using Reconfigurable Sliding Modes*, *Journal of Guidance, Control, and Dynamics* **22**, 873 (1999).
- [12] C. E. Hall and Y. B. Shtessel, *Sliding Mode Disturbance Observer-Based Control for a Reusable Launch Vehicle*, *Journal of Guidance, Control, and Dynamics* **29**, 1315 (2006).

- [13] M. Sagliano, E. Mooij, and S. Theil, *Adaptive Disturbance-Based High-Order Sliding-Mode Control for Hypersonic-Entry Vehicles*, *Journal of Guidance, Control, and Dynamics* **40**, 521 (2017).
- [14] S. B. Fazeli Asl and S. S. Moosapour, *Adaptive backstepping fast terminal sliding mode controller design for ducted fan engine of thrust-vectoring aircraft*, *Aerospace Science and Technology* **71**, 521 (2017).
- [15] A. J. Koshkouei, A. Zinober, and S. Sheffield, *Adaptive Sliding Backstepping Control of Nonlinear Semi-Strict Feedback Form Systems*, *Mediterranean Conference on Control and Automation*, 2376 (1999).
- [16] J. C. Scarratt, A. Zinober, R. E. Mills, M. Rios-Bolivar, A. Ferrara, and L. Giacomini, *Dynamical Adaptive First and Second-Order Sliding Backstepping Control of Nonlinear Nontriangular Uncertain Systems*, *Journal of Dynamic Systems, Measurement, and Control* **122**, 746 (2000).
- [17] Z. Jia, J. Yu, Y. Mei, Y. Chen, Y. Shen, and X. Ai, *Integral backstepping sliding mode control for quadrotor helicopter under external uncertain disturbances*, *Aerospace Science and Technology* **68**, 299 (2017).
- [18] S. Sieberling, Q. P. Chu, and J. A. Mulder, *Robust Flight Control Using Incremental Nonlinear Dynamic Inversion and Angular Acceleration Prediction*, *Journal of Guidance, Control, and Dynamics* **33**, 1732 (2010).
- [19] X. Wang, E. van Kampen, Q. P. Chu, and P. Lu, *Stability Analysis for Incremental Nonlinear Dynamic Inversion Control*, *Journal of Guidance, Control, and Dynamics* (2019), 10.2514/1.G003791.
- [20] P. Lu, E. van Kampen, and Q. P. Chu, *Robustness and Tuning of Incremental Backstepping Approach*, in *AIAA Guidance, Navigation, and Control Conference* (American Institute of Aeronautics and Astronautics, Kissimmee, Florida, 2015) pp. 1–15.
- [21] P. Lu and E. van Kampen, *Active Fault-Tolerant Control System using Incremental Backstepping Approach*, in *AIAA Guidance, Navigation, and Control Conference*, January (American Institute of Aeronautics and Astronautics, Kissimmee, Florida, 2015) pp. 1–17.
- [22] P. Lu, E. van Kampen, C. C. de Visser, and Q. P. Chu, *Framework for Simultaneous Sensor and Actuator Fault-Tolerant Flight Control*, *Journal of Guidance, Control, and Dynamics* **40**, 1 (2017).
- [23] W. van Ekeren, G. Looye, R. O. Kuchar, Q. P. Chu, and E. van Kampen, *Design, Implementation and Flight-Tests of Incremental Nonlinear Flight Control Methods*, in *2018 AIAA Guidance, Navigation, and Control Conference*, January (American Institute of Aeronautics and Astronautics, Kissimmee, Florida, 2018) pp. 1–21.
- [24] T. Keijzer, G. Looye, Q. P. Chu, and E. van Kampen, *Design and Flight Testing of Incremental Backstepping based Control Laws with Angular Accelerometer Feedback*, in *AIAA Scitech 2019 Forum*, January (American Institute of Aeronautics and Astronautics, San Diego, California, 2019) pp. 1–25.

- [25] X. Wang, E. van Kampen, Q. P. Chu, and P. Lu, *Incremental Sliding-Mode Fault-Tolerant Flight Control*, *Journal of Guidance, Control, and Dynamics* **42**, 244 (2019).
- [26] X. Wang, S. Sun, E. van Kampen, and Q. P. Chu, *Quadrotor Fault Tolerant Incremental Sliding Mode Control driven by Sliding Mode Disturbance Observers*, *Aerospace Science and Technology* **87**, 417 (2019).
- [27] P. Acquatella, E. van Kampen, and Q. P. Chu, *Incremental Backstepping for Robust Nonlinear Flight Control*, *CEAS Conference on Guidance, Navigation, and Control*, 1444 (2013).
- [28] A. Hodel, M. Whorton, and J. Zhu, *Stability Metrics for Simulation and Flight-Software Assessment and Monitoring of Adaptive Control Assist Compensators*, in *AIAA Guidance, Navigation and Control Conference and Exhibit* (American Institute of Aeronautics and Astronautics, Honolulu, Hawaii, 2008) pp. 1–25.
- [29] X. Wang, E. van Kampen, Q. P. Chu, and P. Lu, *Stability Analysis for Incremental Nonlinear Dynamic Inversion Control*, in *2018 AIAA Guidance, Navigation, and Control Conference*, January (American Institute of Aeronautics and Astronautics, Kissimmee, Florida, 2018).
- [30] F. Grondman, G. Looye, R. O. Kuchar, Q. P. Chu, and E. van Kampen, *Design and Flight Testing of Incremental Nonlinear Dynamic Inversion-based Control Laws for a Passenger Aircraft*, in *2018 AIAA Guidance, Navigation, and Control Conference*, January (American Institute of Aeronautics and Astronautics, Kissimmee, Florida, 2018).
- [31] M. Brown, Y. Shtessel, and J. Buffington, *Finite reaching time continuous sliding mode control with enhanced robustness*, in *AIAA Guidance, Navigation, and Control Conference and Exhibit*, August (American Institute of Aeronautics and Astronautics, Denver, CO, 2000).
- [32] Y. Shtessel, J. Buffington, and S. Banda, *Tailless aircraft flight control using multiple time scale reconfigurable sliding modes*, *IEEE Transactions on Control Systems Technology* **10**, 288 (2002).
- [33] P. Goupil, *Oscillatory failure case detection in the A380 electrical flight control system by analytical redundancy*, *IFAC Proceedings Volumes (IFAC-PapersOnline)* **17**, 681 (2007).
- [34] B. Etkin, *Dynamics of Atmospheric Flight* (Dover Publications, Toronto, 2005).
- [35] L. T. Nguyen, M. E. Ogburn, W. P. Gilbert, K. S. Kibler, P. W. Brown, and P. L. Deal, *NASA Technical Paper 1538*, Tech. Rep. NASA Technical Paper 1538 (1979).

5

COMPARISONS OF THREE CONTROL STRUCTURES FOR INDUCING HIGHER-ORDER SLIDING MODES

In Chapter 3, the incremental sliding mode control (INDI-SMC), as a hybridization of incremental nonlinear dynamic inversion (INDI) and sliding mode control (SMC) was proposed. This hybrid framework designs the control increment $\Delta \mathbf{u}$, and can be used to achieve higher-order sliding modes in finite time. In the literature, there are also other control structures for enforcing higher-order sliding modes. A widely adopted approach is to use the control structure of nonlinear dynamic inversion (NDI) to directly design \mathbf{u} . Another approach is to artificially increase the input-output relative degree and design the higher-order derivatives of \mathbf{u} . Based on these observations, this chapter will make analytical and numerical comparisons among these three different control structures that can be used for inducing higher-order sliding modes.

This chapter is based on the following peer-reviewed conference paper:
Wang, X., van Kampen, E., Chu, Q. P., "Comparisons of Three Control Structures for Inducing Higher-Order Sliding Modes", European Control Conference, IEEE, Naples, Italy, 2019, pp. 1-8.

For mitigating the chattering effect in the sliding mode control (SMC), many adaptation mechanisms have been proposed to reduce the switching gains. However, less attention is paid to the control structure, which influences the resulting uncertainty term and determines the minimum possible gains. This chapter compares three control structures for inducing higher-order sliding modes in finite time: nonlinear dynamic inversion (NDI) based SMC, higher-order sliding mode control (HOSMC) with artificially increased relative degree, and the recently proposed incremental nonlinear dynamic inversion (INDI) based SMC. The latter two control structures have reduced model dependency as compared to NDI-SMC. Moreover, their nominal control increments are found to be approximately equivalent if the sampling interval is sufficiently small and if their gains satisfy certain conditions. Under the same circumstances, the norm value of the resulting uncertainty using INDI-SMC is several orders of magnitude smaller than those using other control structures. For maintaining the sliding modes, the minimum possible gains required by HOSMC approximately equal those needed by INDI-SMC divided by the sampling interval. Nevertheless, these two approaches have comparable chattering degrees, which are effectively reduced as compared to NDI-SMC. The analytical results are verified by numerical simulations.

5.1. INTRODUCTION

5

FEATURED by its invariance to the matched uncertainty and its finite time convergence property, sliding mode control (SMC) is a useful approach for stabilizing perturbed systems. However, many SMC methods suffer from the chattering phenomenon, which is the high frequency switching in the control signal. Although continuous approximations of the signum function and a class of higher-order sliding mode control (HOSMC) techniques can mitigate the chattering effect, it is shown in [1] that none of these methods can totally eliminate chattering.

In view of the fact that the chattering amplitude is proportional to the discontinuous switching gain [2], a recent research focus in the SMC community is on adapting the switching gains to their minimum possible values whilst maintaining the sliding modes and the finite-time convergence property [1–4]. An adaptation mechanism for the super-twisting algorithm based on direct measurements of the equivalent control is presented in [2]. A dual-layer nested adaptive method is proposed in [4] and further developed in [1, 3], which can be applied to super-twisting, conventional (first-order), and higher-order sliding mode schemes. These methods are derived for the sliding variable dynamics, which contain a lumped uncertainty term and decoupled control inputs. However, the real system dynamics usually have coupled control inputs, and are perturbed by both additive and multiplicative uncertainties. Converting the real coupled system dynamics to the decoupled sliding variable dynamics is an important intermediate step which has been overlooked in the literature. This issue is influential because different control structures used for this conversion will result in different closed-loop uncertainty terms which are crucial to the minimum possible values of the sliding mode control/observer gains.

Feedback linearization, which is also known as nonlinear dynamic inversion (NDI) in the aerospace community [5–7] is a widely used control structure for solving nonlin-

ear system sliding mode control problems. A recent review of NDI based SMC with various sliding orders and virtual control designs can be found in [8]. It is also shown in [8] that SMC which contains a model-based estimation of the equivalent control [1, 2] is essentially NDI based. However, the NDI control structure has a contradiction between the reduction of uncertainty and model dependency. To be specific, reducing the model dependency of NDI is beneficial to complex system (such as an airplane) control implementations, but would increase the norm of the remaining uncertainties in the sliding variable dynamics, which eventually requires higher sliding mode control/observer gain for perturbation compensations.

In order to solve this contradiction, recent research proposes to use the control structure of incremental nonlinear dynamic inversion (INDI) for inducing sliding modes [8]. INDI is a so-called, sensor-based control approach developed in the aerospace community, which designs the control increment $\Delta \mathbf{u}$ in one sampling interval Δt [5]. The idea of INDI can be traced back to the late nineties, when it was found in [9] that the feedback of angular acceleration and control surface position can enhance the robustness of NDI to model uncertainties. Inheriting this idea, INDI was first proposed in [6], and has shown promising effectiveness on fault-tolerant flight control [7], helicopter control [10], flexible aircraft control [11], and high-speed control of a damaged quadrotor with complete loss of a single rotor [12], in the past decade. A recent research generalized INDI for generic nonlinear uncertain systems with arbitrary relative degree, without using the time-scale separation assumption [5]. It is found in [5], that part of the system dynamics and external disturbances are contained in the output derivatives and control inputs at the previous time step. Therefore, feeding back their latest samples/estimations can improve the robustness of NDI to regular perturbations while reducing its model dependency. This analytical conclusion is verified by real-world passenger airplane flight tests in [13, 14]. The sensor-based control idea of INDI is also shared by [15, 16], where the signals at the previous time step are used to estimate disturbance. Different from [15, 16], the only model information required by INDI is the estimation of the control effectiveness matrix. By virtue of the sensor-based nature of INDI, SMC using the control structure of INDI instead of NDI can simultaneously reduce the control model dependency and uncertainties remaining in the sliding variable dynamics [8], which is beneficial to chattering reduction.

Another strategy for chattering mitigation is artificially increasing the input–output relative degree, and designing the higher-order derivatives of the control input [17, 18]. The actual control input is then integrated from the designed control derivatives. Because of this integration process, the high frequency chattering can be smoothed. Although this strategy is widely used, the property of the resulting uncertainty term and its influences on the minimum possible SMC gains remain unclear in the literature. In this chapter, particular interest is paid to HOSMC which artificially increases the relative degree by one order (designs $\dot{\mathbf{u}}$). Since $\dot{\mathbf{u}}$ approximately equals $\Delta \mathbf{u}/\Delta t$ when Δt is sufficiently small, an interesting research question emerges: is there any relationship between the INDI-SMC and HOSMC with artificially increased relative degree, although these two methods originate from completely different ideas?

The main contributions of this chapter are the comparisons among three different control structures that can be used for inducing higher-order sliding modes. These

three control structures are NDI-SMC and HOSMC with artificially increased relative degree developed in the SMC community, and the INDI-SMC recently proposed in the aerospace community. The comparisons are mainly in three aspects: 1) model dependency and the required signals for implementation; 2) the relationships of the nominal controls; 3) the properties of the resulting uncertainty terms and their influences on the minimum possible values of the sliding mode control/observer gains.

This chapter is structured as follows: The three control structures will be presented in Sec. 5.2, analytically compared in Sec. 5.3, and numerically compared in Sec. 5.4. Main conclusions are drawn in Sec. 5.5.

5.2. THREE CONTROL STRUCTURES FOR INDUCING HIGHER-ORDER SLIDING MODES

Consider a multi-input/multi-output nonlinear control-affine system

$$\dot{\mathbf{x}} = \mathbf{f}(\mathbf{x}) + \mathbf{G}(\mathbf{x})\mathbf{u} + \mathbf{d}_x, \quad \mathbf{y} = \mathbf{h}(\mathbf{x}), \quad (5.1)$$

where $\mathbf{f} : \mathbb{R}^n \rightarrow \mathbb{R}^n$ and $\mathbf{h} : \mathbb{R}^n \rightarrow \mathbb{R}^m$ are smooth vector fields. \mathbf{G} is a smooth function mapping $\mathbb{R}^n \rightarrow \mathbb{R}^{n \times m}$, whose columns are smooth vector fields. $\mathbf{d}_x \in \mathbb{R}^n$ represents external disturbances. Boldfaces indicate vectors and matrices.

5

Assumption 2 *The vector relative degree of \mathbf{y} with respect to \mathbf{u} denoted as $\mathbf{r} = [r_1, r_2, \dots, r_m]^T$ is constant and known, and the corresponding internal dynamics are stable.*

By differentiating the output, the input–output mapping of the system is given by

$$\mathbf{y}^{(\mathbf{r})} = \boldsymbol{\alpha}(\mathbf{x}) + \mathcal{B}(\mathbf{x})\mathbf{u} + \mathbf{d}, \quad (5.2)$$

where $\mathbf{y}^{(\mathbf{r})} = [y_1^{(r_1)}, \dots, y_m^{(r_m)}]^T$, $\mathcal{B}(\mathbf{x}) \in \mathbb{R}^{m \times m}$, $\mathcal{B}_{ij} = \mathcal{L}_{g_j} \mathcal{L}_f^{r_i-1} h_i$, $\boldsymbol{\alpha}(\mathbf{x}) = [\mathcal{L}_f^{r_1} h_1, \dots, \mathcal{L}_f^{r_m} h_m]^T$, $\mathbf{d} = [\mathcal{L}_{d_x}^{r_1} h_1, \dots, \mathcal{L}_{d_x}^{r_m} h_m]^T$, with $\mathcal{L}_f^{r_i} h_i$, $\mathcal{L}_{d_x}^{r_i} h_i$, $\mathcal{L}_{g_j} \mathcal{L}_f^{r_i-1} h_i$ the corresponding Lie derivatives. The control effectiveness matrix $\mathcal{B}(\mathbf{x})$ is nonsingular under *Assumption 2*.

The control objective is to make the output \mathbf{y} track a reference signal $\mathbf{y}_c(t) = [y_{c_1}(t), \dots, y_{c_m}(t)]^T$. Assume $y_{c_i}(t)$, $i = 1, \dots, m$, and its derivatives up to $y_{c_i}^{(r_i+1)}(t)$ are bounded for all t . Choose the sliding variable as $\boldsymbol{\sigma} = \mathbf{y} - \mathbf{y}_c$.

Definition 1 [17, 18] *Consider the nonlinear system given by Eq. (5.1) and the sliding variable $\boldsymbol{\sigma}$, assume the time derivatives of $\sigma_i, \dot{\sigma}_i, \dots, \sigma_i^{(r_i-1)}$ are continuous functions for all $i = 1, \dots, m$. The manifold defined as*

$$\mathcal{S}^r = \{\mathbf{x} | \sigma_i(\mathbf{x}) = \dot{\sigma}_i(\mathbf{x}) = \dots = \sigma_i^{(r_i-1)}(\mathbf{x}) = 0, i = 1, \dots, m\} \quad (5.3)$$

is called the “ \mathbf{r}^{th} -order sliding set” [18, 19]. If this sliding set is non empty and locally an integral set in the Filippov sense [20], then the motion on \mathcal{S}^r is called the “ \mathbf{r}^{th} -order sliding mode” with respect to the sliding variable $\boldsymbol{\sigma}$.

In the following subsections, three control structures for inducing the \mathbf{r}^{th} -order sliding mode will be presented.

5.2.1. NONLINEAR DYNAMIC INVERSION BASED CONTROL

The estimated system dynamics $\mathbf{y}^{(r)} = \bar{\boldsymbol{\alpha}}(\mathbf{x}) + \bar{\mathcal{B}}(\mathbf{x})\mathbf{u}$ are used for control design, which bring both additive uncertainties $\boldsymbol{\alpha} - \bar{\boldsymbol{\alpha}} + \mathbf{d}$, and multiplicative uncertainties $\mathcal{B} - \bar{\mathcal{B}}$. For inducing the r^{th} -order sliding mode, the nonlinear dynamic inversion (NDI) control structure is adopted in [18, 21] as:

$$\mathbf{u}_{\text{ndi-s}} = \bar{\mathcal{B}}^{-1}(\mathbf{x})(\mathbf{v}_n + \mathbf{v}_s + \mathbf{y}_c^{(r)} - \bar{\boldsymbol{\alpha}}(\mathbf{x})) \quad (5.4)$$

where $\mathbf{y}_c^{(r)} = [y_{c_1}^{r_1}, y_{c_2}^{r_2}, \dots, y_{c_m}^{r_m}]^T$. \mathbf{v}_n and \mathbf{v}_s are two virtual control terms. This control structure will be abbreviated as NDI-SMC in the subsequent context. Using Eq. (5.4), the dynamics of $\boldsymbol{\sigma}$ are

$$\begin{aligned} \boldsymbol{\sigma}^{(r)} &= \mathbf{y}^{(r)} - \mathbf{y}_c^{(r)} = \bar{\boldsymbol{\alpha}}(\mathbf{x}) + \bar{\mathcal{B}}(\mathbf{x})\mathbf{u}_{\text{ndi-s}} + \boldsymbol{\varepsilon}_{\text{ndi-s}} - \mathbf{y}_c^{(r)} \\ &= \mathbf{v}_n + \mathbf{v}_s + \boldsymbol{\varepsilon}_{\text{ndi-s}} \end{aligned} \quad (5.5)$$

where

$$\begin{aligned} \boldsymbol{\varepsilon}_{\text{ndi-s}} &= (\boldsymbol{\alpha} - \bar{\boldsymbol{\alpha}}) + (\mathcal{B}\bar{\mathcal{B}}^{-1} - \mathbf{I})(\mathbf{v}_n + \mathbf{v}_s + \mathbf{y}_c^{(r)} - \bar{\boldsymbol{\alpha}}) \\ &= (\boldsymbol{\alpha} - \bar{\boldsymbol{\alpha}}) + (\mathcal{B} - \bar{\mathcal{B}})\mathbf{u}_{\text{ndi-s}} + \mathbf{d} \end{aligned} \quad (5.6)$$

$\boldsymbol{\varepsilon}_{\text{ndi-s}}$ in Eq. (5.6) is the closed-loop uncertainty term caused by model uncertainties, external disturbances, actuator faults, structural damage, etc [8]. If \mathbf{v}_s can compensate for $\boldsymbol{\varepsilon}_{\text{ndi-s}}$, and if the nominal virtual control \mathbf{v}_n can stabilize the unperturbed r^{th} -order integrator chains [18, 22], then the r^{th} -order sliding mode can be established by Eq. (5.4).

5.2.2. INCREMENTAL SLIDING MODE CONTROL

Incremental sliding mode control (INDI-SMC) is a recently proposed control framework [8], which can simultaneously reduce the model dependency and the minimum possible switching gains of NDI-SMC. Denote the sampling interval as Δt . To begin with, the incremental dynamic equation is derived by taking the first-order Taylor series expansion of Eq. (5.2) around the condition at $t - \Delta t$ (denoted by subscript 0) as

$$\mathbf{y}^{(r)} = \mathbf{y}_0^{(r)} + \mathcal{B}(\mathbf{x}_0)\Delta\mathbf{u} + \Delta\mathbf{d} + \left. \frac{\partial[\boldsymbol{\alpha}(\mathbf{x}) + \mathcal{B}(\mathbf{x})\mathbf{u}]}{\partial\mathbf{x}} \right|_0 \Delta\mathbf{x} + \mathbf{R}_1 \quad (5.7)$$

where $\Delta\mathbf{x} = \mathbf{x} - \mathbf{x}_0$, $\Delta\mathbf{u} = \mathbf{u} - \mathbf{u}_0$, $\Delta\mathbf{d} = \mathbf{d} - \mathbf{d}_0$ respectively denote the variations of states, control inputs and external disturbances in one incremental time step. \mathbf{R}_1 in Eq. (5.7) is the expansion remainder, whose Lagrange form is

$$\mathbf{R}_1 = \frac{1}{2} \left. \frac{\partial^2[\boldsymbol{\alpha}(\mathbf{x}) + \mathcal{B}(\mathbf{x})\mathbf{u}]}{\partial^2\mathbf{x}} \right|_m \Delta\mathbf{x}^2 + \left. \frac{\partial^2[\boldsymbol{\alpha}(\mathbf{x}) + \mathcal{B}(\mathbf{x})\mathbf{u}]}{\partial\mathbf{x}\partial\mathbf{u}} \right|_m \Delta\mathbf{x}\Delta\mathbf{u} \quad (5.8)$$

in which $(\cdot)|_m$ means evaluating (\cdot) at a condition where $\mathbf{x} \in (\mathbf{x}(t - \Delta t), \mathbf{x}(t))$, $\mathbf{u} \in (\mathbf{u}(t - \Delta t), \mathbf{u}(t))$, and $\mathbf{d} \in (\mathbf{d}(t - \Delta t), \mathbf{d}(t))$. In Eq. (5.8), \mathbf{R}_1 is not a function of $\Delta\mathbf{u}^2$, $\Delta\mathbf{d}^2$, $\Delta\mathbf{u}\Delta\mathbf{d}$. This can be examined using Eq. (5.2), where $\mathbf{y}^{(\rho)}$ is linear with respect to both \mathbf{u} and \mathbf{d} .

Based on Eq. (5.7), the INDI-SMC framework is proposed as [8]

$$\Delta\mathbf{u}_{\text{ndi-s}} = \bar{\mathcal{B}}^{-1}(\mathbf{x}_0)(\mathbf{v}_n + \mathbf{v}_s + \mathbf{y}_c^{(r)} - \mathbf{y}_0^{(r)}) \quad (5.9)$$

The total control command vector for the actuators is $\mathbf{u}_{\text{ndi-s}} = \mathbf{u}_{\text{ndi-s},0} + \Delta\mathbf{u}_{\text{ndi-s}}$.

Remark 11 $\mathbf{u}_{\text{indi-}s,0}$ denotes the latest sampled actuator position vector, instead of the control command given to the actuator at the previous time step. The flight tests in [23] shows that this sensing process can mitigate the influences of actuator dynamics. If actuator dynamics are not considered, $\mathbf{u}_{\text{indi-}s} = \sum \Delta \mathbf{u}_{\text{indi-}s}$, which is essentially a numerical integration process.

As compared to the NDI based control structure (Eq. (5.4)), INDI-SMC is independent of the model information $\bar{\mathbf{a}}(\mathbf{x})$, which simplifies the implementation process. Only the estimation of the control effectiveness ($\bar{\mathcal{B}}$) is needed by INDI-SMC. The calculation of the partial derivatives in Eq. (5.7) is not needed for control implementation. It will be shown later that the multiplications of these partial derivatives with $\Delta \mathbf{x}$ are treated as perturbations in the closed-loop system. This approach also inherits the sensor-based nature of INDI, since the measurements/estimations of $\mathbf{y}_0^{(r)}$ and $\mathbf{u}_{\text{indi-}s,0}$ are needed. For some physical systems, including aircraft, $\mathbf{y}_0^{(r)}$ and $\mathbf{u}_{\text{indi-}s,0}$ can be directly measured [13, 14].

Finally, substituting the control input (Eq. (5.9)) into Eq. (5.7), and using the definition of $\boldsymbol{\sigma}$, the resulting closed-loop dynamics are

$$\begin{aligned}\boldsymbol{\sigma}^{(r)} &= \mathbf{y}^{(r)} - \mathbf{y}_c^{(r)} = \mathbf{y}_0^{(r)} + \bar{\mathcal{B}}(\mathbf{x}_0) \Delta \mathbf{u}_{\text{indi-}s} + \boldsymbol{\varepsilon}_{\text{indi-}s} - \mathbf{y}_c^{(r)} \\ &= \mathbf{v}_n + \mathbf{v}_s + \boldsymbol{\varepsilon}_{\text{indi-}s}\end{aligned}\quad (5.10)$$

where

$$\boldsymbol{\varepsilon}_{\text{indi-}s} = \left. \frac{\partial(\boldsymbol{\alpha}(\mathbf{x}) + \mathcal{B}(\mathbf{x})\mathbf{u}_{\text{indi-}s})}{\partial \mathbf{x}} \right|_0 \Delta \mathbf{x} + \mathbf{R}_1|_{\mathbf{u}=\mathbf{u}_{\text{indi-}s}} + (\mathcal{B} - \bar{\mathcal{B}})|_0 \Delta \mathbf{u}_{\text{indi-}s} + \Delta \mathbf{d} \quad (5.11)$$

in which $(\mathcal{B} - \bar{\mathcal{B}})|_0$ denotes $\mathcal{B}(\mathbf{x}_0) - \bar{\mathcal{B}}(\mathbf{x}_0)$. $\mathbf{R}_1|_{\mathbf{u}=\mathbf{u}_{\text{indi-}s}}$ means substituting $\mathbf{u} = \mathbf{u}_{\text{indi-}s}$ into the remainder \mathbf{R}_1 in Eq. (5.8). It can be seen that Eq. (5.10) is in the same form as Eq. (5.5), thus the r^{th} -order sliding mode can be achieved by properly designing \mathbf{v}_n and \mathbf{v}_s . However, the NDI and INDI based control structures result in different closed-loop perturbation terms: $\boldsymbol{\varepsilon}_{\text{ndi-}s}$ and $\boldsymbol{\varepsilon}_{\text{indi-}s}$. The properties of these two terms, and their influences on the minimum possible gains will be elaborated in Sec. 5.3.2 and Sec. 5.3.3.

5.2.3. HIGHER-ORDER SLIDING MODE CONTROL WITH ARTIFICIALLY INCREASED RELATIVE DEGREE

Consider artificially increasing r_i by one order for all $i = 1, \dots, m$. Dynamically extend Eq. (5.2) as

$$\mathbf{y}^{(r+1)} = \frac{\partial(\boldsymbol{\alpha}(\mathbf{x}) + \mathcal{B}(\mathbf{x})\mathbf{u})}{\partial \mathbf{x}} \dot{\mathbf{x}} + \mathcal{B}(\mathbf{x})\dot{\mathbf{u}} + \dot{\mathbf{d}} \quad (5.12)$$

Design the control derivative in the structure of

$$\dot{\mathbf{u}}_{\text{ho-}s} = \bar{\mathcal{B}}^{-1}(\mathbf{x})(\mathbf{v}'_n + \mathbf{v}'_s + \mathbf{y}_c^{(r+1)}) \quad (5.13)$$

which is referred to as HOSMC with artificially increased r . This control structure results in

$$\begin{aligned}\boldsymbol{\sigma}^{(r+1)} &= \mathbf{y}^{(r+1)} - \mathbf{y}_c^{(r+1)} = \bar{\mathcal{B}}(\mathbf{x})\dot{\mathbf{u}}_{\text{ho-}s} + \boldsymbol{\varepsilon}_{\text{ho-}s} - \mathbf{y}_c^{(r+1)} \\ &= \mathbf{v}'_n + \mathbf{v}'_s + \boldsymbol{\varepsilon}_{\text{ho-}s}\end{aligned}\quad (5.14)$$

where

$$\boldsymbol{\varepsilon}_{\text{ho-}s} = \frac{\partial(\boldsymbol{\alpha}(\mathbf{x}) + \mathcal{B}(\mathbf{x})\mathbf{u}_{\text{ho-}s})}{\partial \mathbf{x}} \dot{\mathbf{x}} + (\mathcal{B} - \bar{\mathcal{B}})\dot{\mathbf{u}}_{\text{ho-}s} + \dot{\mathbf{d}} \quad (5.15)$$

It is noteworthy that the $\mathbf{y}_c^{(r+1)}$ term is viewed as uncertainty by [24], and is not used in Eq. (5.13). It is suggested in this chapter to include this term in Eq. (5.13) as a known term. In view of Eq. (5.14), the $\mathbf{r} + 1^{th}$ -order sliding mode can be induced if \mathbf{v}'_s can compensate for $\boldsymbol{\varepsilon}_{\text{ho-}s}$, and if the nominal virtual control \mathbf{v}'_n can achieve the stabilization of the $\mathbf{r} + 1^{th}$ -order unperturbed integrator chains [18, 22].

The actual control is integrated from Eq. (5.13) and can be further derived as

$$\begin{aligned} \mathbf{u}_{\text{ho-}s} &= \int_0^t \dot{\mathbf{u}}_{\text{ho-}s} = \int_0^{t-\Delta t} \dot{\mathbf{u}}_{\text{ho-}s} + \int_{t-\Delta t}^t \dot{\mathbf{u}}_{\text{ho-}s} \\ &\approx \mathbf{u}_{\text{ho-}s,0} + \dot{\mathbf{u}}_{\text{ho-}s}(t)\Delta t \end{aligned} \quad (5.16)$$

which means the control increment of $\mathbf{u}_{\text{ho-}s}$ in Δt approximately equals

$$\Delta \mathbf{u}_{\text{ho-}s} \approx \dot{\mathbf{u}}_{\text{ho-}s}(t)\Delta t = \bar{\mathcal{B}}^{-1}(\mathbf{x})(\mathbf{v}'_n + \mathbf{v}'_s + \mathbf{y}_c^{(r+1)})\Delta t \quad (5.17)$$

The control increment of $\mathbf{u}_{\text{ho-}s}$ is derived in Eqs. (5.16) and (5.17) for the convenience of comparison with Eq. (5.9). As compared to $\Delta \mathbf{u}_{\text{indi-}s}$ in Eq. (5.9), $\mathbf{u}_{\text{ho-}s}$ is also independent of the model information $\bar{\boldsymbol{\alpha}}(\mathbf{x})$. However, the $\mathbf{y}_c^{(r+1)}$ term used in Eq. (5.17) is not needed by INDI-SMC (Eq. (5.9)). Other similarities and differences between this method and INDI-SMC will be further explored in Sec. 5.3.

5.3. ANALYTICAL COMPARISONS

In this section, the three control structures presented in Sec. 5.2 will be analytically compared. The nominal control parts will be considered in 5.3.1. The properties of the perturbation terms will be compared in 5.3.2. The perturbation compensations and minimum possible gain requirements will be discussed in 5.3.3.

5.3.1. COMPARISONS OF THE NOMINAL CONTROL

This subsection considers the nominal case where the perturbation terms in Eqs. (5.5), (5.10), and (5.14) all equal to zero. The virtual controls \mathbf{v}_s and \mathbf{v}'_s for perturbation compensation are also zero. Under this circumstance, the closed-loop dynamics using NDI-SMC and INDI-SMC become \mathbf{r}^{th} -order integrator chains with the nominal virtual control \mathbf{v}_n as an input, namely $\boldsymbol{\sigma}^{(r)} = \mathbf{v}_n$. Analogously, using the control structure of HOSMC with artificially increased \mathbf{r} , $\boldsymbol{\sigma}^{(r+1)} = \mathbf{v}'_n$ according to Eq. (5.14). Three approaches of the nominal dynamics stabilization will be discussed.

ASYMPTOTIC STABILIZATION

It is classical to stabilize the unperturbed integrator chains asymptotically by linear virtual controls. For NDI and INDI based SMC, \mathbf{v}_n in Eqs. (5.4, 5.9) is consistently designed as:

$$\mathbf{v}_n = -\mathbf{K}_{r-1}\boldsymbol{\sigma}^{(r-1)} - \mathbf{K}_{r-2}\boldsymbol{\sigma}^{(r-2)} \dots - \mathbf{K}_0\boldsymbol{\sigma} \quad (5.18)$$

where the positive definite diagonal gain matrices $\mathbf{K}_{r-1} = \text{diag}\{K_{r-1,i}\}, \dots, \mathbf{K}_0 = \text{diag}\{K_{0,i}\}$, $i = 1, \dots, m$ are designed such that the r^{th} - order polynomials $p^{r_i} + K_{r-1,i}p^{r_i-1} + \dots + K_{0,i}$ are Hurwitz.

Analogously, for asymptotically stabilizing the $r + 1^{\text{th}}$ - order integrator chains, \mathbf{v}'_n in Eq. (5.17) is designed as:

$$\mathbf{v}'_n = -\mathbf{K}'_r \boldsymbol{\sigma}^{(r)} - \mathbf{K}'_{r-1} \boldsymbol{\sigma}^{(r-1)} - \mathbf{K}'_{r-2} \boldsymbol{\sigma}^{(r-2)} \dots - \mathbf{K}'_0 \boldsymbol{\sigma} \quad (5.19)$$

where $\mathbf{K}'_r = \text{diag}\{K'_{r,i}\}, \dots, \mathbf{K}'_0 = \text{diag}\{K'_{0,i}\}$, $i = 1, \dots, m$ are designed such that the $r + 1^{\text{th}}$ - order polynomials $p^{r_i+1} + K'_{r,i}p^{r_i} + K'_{r-1,i}p^{r_i-1} \dots + K'_{0,i}$ are Hurwitz.

Using the definition of the sliding variable, $\boldsymbol{\sigma}^{(r)} = \mathbf{y}^{(r)} - \mathbf{y}_c^{(r)}$ in Eq. (5.19). Therefore, the nominal control part $\bar{\mathcal{B}}^{-1}(\mathbf{x}_0)(\mathbf{v}_n + \mathbf{y}_c^{(r)} - \mathbf{y}_0^{(r)})$ in Eq. (5.9) approximately equals the nominal control increment $\bar{\mathcal{B}}^{-1}(\mathbf{x})\mathbf{v}'_n \Delta t$ in Eq. (5.17) if

1. $\bar{\mathcal{B}}^{-1}(\mathbf{x}_0) \approx \bar{\mathcal{B}}^{-1}(\mathbf{x})$
2. $\mathbf{y}^{(r)} \approx \mathbf{y}_0^{(r)}$
3. $\mathbf{K}'_r = \frac{\mathbf{I}_m}{\Delta t}$, $\mathbf{K}'_{r-1} = \frac{\mathbf{K}_{r-1}}{\Delta t}$, ..., $\mathbf{K}'_0 = \frac{\mathbf{K}_0}{\Delta t}$.

where \mathbf{I}_m is an m dimensional identity matrix. Using the continuity of \mathbf{x} , $\lim_{\Delta t \rightarrow 0} \|\mathbf{x} - \mathbf{x}_0\| = 0$. Therefore, the first condition can be satisfied when Δt is sufficiently small. $\mathbf{y}_0^{(r)}$ used by Eq. (5.9) represents the value of $\mathbf{y}^{(r)}$ at the previous time step, which can be directly measured [5, 14] or estimated [13, 23]. For HOSMC, $\mathbf{y}^{(r)}$ is normally numerically differentiated from \mathbf{y} using, for example, sliding mode differentiator [17, 24]. Although based on different ideas, $\mathbf{y}^{(r)}$ and $\mathbf{y}_0^{(r)}$ become close under sufficiently small Δt . The last gain condition can be derived by comparing Eq. (5.9) with Eq. (5.17), and comparing Eq. (5.18) with Eq. (5.19).

FINITE TIME STABILIZATION

The unperturbed integrator chains can also be stabilized in finite time using nonlinear continuous virtual controls.

Proposition 3 Consider the unperturbed integrator chain set $\boldsymbol{\sigma}^{(r)} = \mathbf{v}_n$, there exists $\epsilon_i \in (0, 1)$, $i = 1, \dots, m$, such that for every $\alpha_i \in (1 - \epsilon_i, 1)$, the r^{th} - order sliding mode is established in finite time by

$$\begin{aligned} \mathbf{v}_n &= [v_{n,1}, v_{n,2}, \dots, v_{n,m}]^T \\ v_{n,i} &= -K_{r-1,i} |\sigma_i^{(r_i-1)}|^{\alpha_{r_i,i}} \text{sign}(\sigma_i^{(r_i-1)}) - \dots - K_{0,i} |\sigma_i|^{\alpha_{1,i}} \text{sign}(\sigma_i), \quad i = 1, \dots, m \end{aligned} \quad (5.20)$$

where $\mathbf{K}_{r-1} = \text{diag}\{K_{r-1,i}\}, \dots, \mathbf{K}_0 = \text{diag}\{K_{0,i}\}$, and their elements are chosen such that the r^{th} - order polynomials $p^{r_i} + K_{r-1,i}p^{r_i-1} + K_{r-2,i}p^{r_i-2} \dots + K_{0,i}$ are Hurwitz. The scalars $\alpha_{1,i}, \dots, \alpha_{r_i,i}$ satisfy

$$\alpha_{k-1,i} = \frac{\alpha_{k,i} \alpha_{k+1,i}}{2\alpha_{k+1,i} - \alpha_{k,i}}, \quad k = 2, \dots, r_i, \quad i = 1, \dots, m \quad (5.21)$$

with $\alpha_{r_i+1,i} = 1$, $\alpha_{r_i,i} = \alpha_i$.

Proof: Using *Definition 1*, this proposition is essentially a multi-input/multi-output generalization of the Proposition 8.1 in [22]. \square

Using *Proposition 3*, there exists $\epsilon'_i \in (0, 1)$, $i = 1, \dots, m$, such that for every $\alpha'_i \in (1 - \epsilon'_i, 1)$, the $\mathbf{r} + 1$ th- order sliding mode is established in finite time by

$$\begin{aligned} \mathbf{v}'_n &= [v'_{n,1}, v'_{n,2}, \dots, v'_{n,m}]^T \\ v'_{n,i} &= -K'_{r,i} |\sigma_i^{(r_i)}|^{\alpha'_{i+1,i}} \text{sign}(\sigma_i^{(r_i)}) - \dots - K'_{0,i} |\sigma_i|^{\alpha'_{1,i}} \text{sign}(\sigma_i), \quad i = 1, \dots, m \end{aligned} \quad (5.22)$$

The gain choices are the same as in Eq. (5.19). The scalars $\alpha'_{1,i}, \dots, \alpha'_{r_i+1,i}$ satisfy

$$\alpha'_{k-1,i} = \frac{\alpha'_{k,i} \alpha'_{k+1,i}}{2\alpha'_{k+1,i} - \alpha'_{k,i}}, \quad k = 2, \dots, r_i + 1, \quad i = 1, \dots, m \quad (5.23)$$

with $\alpha'_{r_i+2,i} = 1$, $\alpha'_{r_i+1,i} = \alpha'_i$.

Comparing Eq. (5.20) with Eq. (5.22), the nominal control part $\bar{\mathcal{B}}^{-1}(\mathbf{x}_0)(\mathbf{v}_n + \mathbf{y}_c^{(r)} - \mathbf{y}_0^{(r)})$ in Eq. (5.9) approximately equals the nominal control increment $\bar{\mathcal{B}}^{-1}(\mathbf{x})\mathbf{v}'_n \Delta t$ in Eq. (5.17) if

1. $\bar{\mathcal{B}}^{-1}(\mathbf{x}_0) \approx \bar{\mathcal{B}}^{-1}(\mathbf{x})$
2. $\mathbf{y}^{(r)} \approx \mathbf{y}_0^{(r)}$
3. $\mathbf{K}'_r = \frac{\mathbf{I}_m}{\Delta t}$, $\mathbf{K}'_{r-1} = \frac{\mathbf{K}_{r-1}}{\Delta t}$, \dots , $\mathbf{K}'_0 = \frac{\mathbf{K}_0}{\Delta t}$.
4. $\alpha'_{r_i,i} = \alpha_{r_i,i}$, \dots , $\alpha'_{1,i} = \alpha_{1,i}$.
5. $\epsilon_i \ll 1$, $\alpha'_{r_i+1,i} = \frac{2\alpha'_{r_i,i}}{1 + \alpha'_{r_i,i}}$.

As discussed in subsection 5.3.1, the first two conditions can be satisfied using sufficiently small Δt . If the third and fourth conditions are satisfied, $v_{n,i}$ in Eq. (5.20) exactly equals $v'_{n,i} + K'_{r,i} |\sigma_i^{(r_i)}|^{\alpha'_{i+1,i}} \text{sign}(\sigma_i^{(r_i)})$ in Eq. (5.22) multiplied with Δt . If $\alpha'_{r_i+1,i} = 1$, then $|\sigma_i^{(r_i)}|^{\alpha'_{i+1,i}} \text{sign}(\sigma_i^{(r_i)}) = \sigma_i^{(r_i)} = y_i^{(r_i)} - y_{c_i}^{(r_i)}$, which means the first terms in Eq. (5.22), multiplied with Δt , approximate $\mathbf{y}_c^{(r)} - \mathbf{y}_0^{(r)}$ in Eq. (5.9), under the second and third conditions. In order to enforce the finite time convergence, the fifth condition is proposed, in which $\alpha'_{r_i+1,i}$ satisfies Eq. (5.23), while $\alpha'_{r_i+1,i}$ and $\alpha'_{r_i,i} = \alpha_{r_i,i}$ are sufficiently close to one by requiring $\epsilon_i \ll 1$.

Remark 12 The unperturbed integral chains can also be stabilized in fixed-time using continuous \mathbf{v}_n and \mathbf{v}'_n [25]. Analogous conditions can be derived which make $\bar{\mathcal{B}}^{-1}(\mathbf{x}_0)(\mathbf{v}_n + \mathbf{y}_c^{(r)} - \mathbf{y}_0^{(r)})$ in Eq. (5.9) and $\bar{\mathcal{B}}^{-1}(\mathbf{x})\mathbf{v}'_n \Delta t$ in Eq. (5.17) approximately equal.

5.3.2. COMPARISONS OF THE PERTURBATION TERMS

$\epsilon_{\text{ndi-s}}$ (Eq. (5.6)) and $\epsilon_{\text{indi-s}}$ (Eq. (5.11)) have been compared in [8, 26]. The main conclusions are summarized as follows:

1. The boundedness conditions for $\epsilon_{\text{ndi-s}}$ are stricter than those of $\epsilon_{\text{indi-s}}$.

2. Even if $\boldsymbol{\varepsilon}_{\text{ndi-}s}$ is bounded, under the same perturbation circumstance, there exists a Δt such that the upper bound of $\boldsymbol{\varepsilon}_{\text{indi-}s}$ is smaller than that of $\boldsymbol{\varepsilon}_{\text{ndi-}s}$.
3. $\boldsymbol{\varepsilon}_{\text{indi-}s}$ has less variations in different fault scenarios, while $\boldsymbol{\varepsilon}_{\text{ndi-}s}$ is more fault-case dependent.

By virtue of these properties, the INDI-SMC framework is able to passively resist a wide range of uncertainties with lower sliding mode control/observer gains, as compared to the widely used NDI-SMC framework.

The properties of $\boldsymbol{\varepsilon}_{\text{ho-}s}$ will be addressed here. Using Eq. (5.15), the first-order approximation of $\boldsymbol{\varepsilon}_{\text{ho-}s}$ equals

$$\boldsymbol{\varepsilon}_{\text{ho-}s} \approx \frac{\partial(\boldsymbol{\alpha}(\mathbf{x}) + \mathcal{B}(\mathbf{x})\mathbf{u}_{\text{ho-}s})}{\partial \mathbf{x}} \frac{\Delta \mathbf{x}}{\Delta t} + (\mathcal{B} - \bar{\mathcal{B}}) \frac{\Delta \mathbf{u}_{\text{ho-}s}}{\Delta t} + \frac{\Delta \mathbf{d}}{\Delta t} \quad (5.24)$$

Therefore, in comparison with Eq. (5.11), $\boldsymbol{\varepsilon}_{\text{ho-}s}(t)\Delta t \approx \boldsymbol{\varepsilon}_{\text{indi-}s}(t)$, $\dot{\boldsymbol{\varepsilon}}_{\text{ho-}s}(t)\Delta t \approx \dot{\boldsymbol{\varepsilon}}_{\text{indi-}s}(t)$ if $\mathbf{u}_{\text{ho-}s}(t) \approx \mathbf{u}_{\text{indi-}s}(t)$. Although $\mathbf{u}_{\text{ho-}s}$ and $\mathbf{u}_{\text{indi-}s}$ are designed using different control structures, their nominal increments are approximately equivalent if the conditions in Sec. 5.3.1 are satisfied. Moreover, based-on the equivalent control concept [2, 27], the required average control to maintain the sliding mode is identical in spite of the control structures. To be specific, once the $\mathbf{r} + 1$ th-order sliding mode is achieved by HOSMC, $\boldsymbol{\sigma}^{\mathbf{r}} \equiv \mathbf{0}$, thus $\mathbf{u}_{\text{ho-}s} \equiv \mathcal{B}^{-1}(\mathbf{y}_c^{(\mathbf{r})} - \boldsymbol{\alpha} - \mathbf{d})$ according to Eq. (5.2). This value is also what $\mathbf{u}_{\text{indi-}s}$ must take on average to maintain the \mathbf{r} th-order sliding mode [27]. In other words, once the \mathbf{r} th and $\mathbf{r} + 1$ th-order sliding modes are respectively achieved by INDI-SMC and HOSMC, the condition $\mathbf{u}_{\text{ho-}s} \approx \mathbf{u}_{\text{indi-}s}$ is satisfied.

5.3.3. PERTURBATION COMPENSATIONS AND THE MINIMUM POSSIBLE GAINS

The three control structures discussed in Sec. 5.2 result in different closed-loop perturbation terms, which have different properties Eq. (5.3.2). It will be shown in this subsection that the minimum possible gains in \mathbf{v}_s and \mathbf{v}'_s are determined by the norms of these perturbation terms.

FIRST-ORDER PERTURBATION COMPENSATION

For stabilizing the perturbed dynamics in Eqs. (5.5, 5.10), design an auxiliary sliding variable as $\mathbf{s} = \boldsymbol{\sigma}^{(\mathbf{r}-1)} - \int \mathbf{v}_n$, then $\dot{\mathbf{s}} = \mathbf{v}_s + \boldsymbol{\varepsilon}_{\text{ndi-}s/\text{indi-}s}$ under the control of NDI and INDI based SMC. These dynamics can be stabilized using a first-order SMC as $\mathbf{v}_s = -\mathbf{K}_s \text{sign}(\mathbf{s}) = -[K_{s,1} \text{sign}(s_1), \dots, K_{s,m} \text{sign}(s_m)]^T$. The sufficient condition to enforce a sliding motion in finite time is that $K_{s,i}(t) > \eta + |\boldsymbol{\varepsilon}_{\text{ndi-}s/\text{indi-}s,i}(t)|$, which coincides with the time-varying minimum possible gain requirement in [1]. η is a small positive design constant for satisfying the η -reachability condition [1, 27].

When the sliding surface $\mathbf{s} = \mathbf{0}$ is reached, the equivalent closed-loop dynamics [18, 27] become $\boldsymbol{\sigma}^{(\mathbf{r})} = \mathbf{v}_n$, which recover the nominal condition despite the presence of perturbations. Using the \mathbf{v}_n designed in Sec. 5.3.1, the \mathbf{r} th-order sliding mode with respect to $\boldsymbol{\sigma}$ is achieved.

Analogously, for HOSMC with artificially increased \mathbf{r} , design an auxiliary sliding variable as $\mathbf{s}' = \boldsymbol{\sigma}^{(\mathbf{r})} - \int \mathbf{v}'_n$, then $\dot{\mathbf{s}}' = \mathbf{v}'_s + \boldsymbol{\varepsilon}_{\text{ho-}s}$ using Eq. (5.14). \mathbf{s}' can be stabilized at zero in finite time by $\mathbf{v}'_s = -\mathbf{K}'_s \text{sign}(\mathbf{s}') = -[K'_{s,1} \text{sign}(s'_1), \dots, K'_{s,m} \text{sign}(s'_m)]^T$, with $K'_{s,i}(t) >$

$\eta + |\varepsilon_{\text{ho-}s,i}(t)|$ for all t . As a result, within finite time, $\boldsymbol{\sigma}^{(r+1)} = \mathbf{v}'_n$ on the sliding surface $\mathbf{s}' = \mathbf{0}$. Using \mathbf{v}'_n designed in Sec. 5.3.1 ensures the establishment of the $r + 1^{\text{th}}$ -order sliding mode with respect to $\boldsymbol{\sigma}$.

Since there exists a Δt , such that the bound of $\varepsilon_{\text{indi-}s}$ is smaller than that of $\varepsilon_{\text{ndi-}s}$ (5.3.2), the minimum possible gains needed by INDI-SMC are lower than those required by NDI-SMC. Moreover, it has been shown in 5.3.2 that once the sliding modes are achieved, $\varepsilon_{\text{ho-}s}(t)\Delta t \approx \varepsilon_{\text{indi-}s}(t)$. Therefore, for maintaining the sliding modes, the minimum possible value of $\mathbf{K}'_s(t)$ approximately equals $\mathbf{K}_s(t)$ used by INDI-SMC divided by Δt .

Remark 13 Although $\mathbf{K}'_s(t)$ used by HOSMC with artificially increased r should be several orders of magnitude higher than $\mathbf{K}_s(t)$ used by INDI-SMC, the chattering magnitudes of these two methods are comparable since \mathbf{v}'_s is multiplied with Δt in $\Delta \mathbf{u}_{\text{ho-}s}$ (Eq. (5.17)).

SUPER-TWISTING OBSERVER

In this subsection, \mathbf{v}_s and \mathbf{v}'_s will be designed by a super-twisting observer. The classical fixed-gain super-twisting observer will be designed first, then the observer with time-varying gain will be discussed.

Assumption 3 *The time derivatives of $\varepsilon_{\text{ndi-}s}(t)$ (Eq. (5.6)), $\varepsilon_{\text{indi-}s}(t)$ (Eq. (5.11)), $\varepsilon_{\text{ho-}s}(t)$ (Eq. (5.15)) are bounded. Denote their upper-bounds as: $|\dot{\varepsilon}_{\text{ndi-}s,i}(t)| < \bar{\varepsilon}_{\text{ndi-}s,i}$, $|\dot{\varepsilon}_{\text{indi-}s,i}(t)| < \bar{\varepsilon}_{\text{indi-}s,i}$, $|\dot{\varepsilon}_{\text{ho-}s,i}(t)| < \bar{\varepsilon}_{\text{ho-}s,i}$.*

Use the same auxiliary sliding variables \mathbf{s} and \mathbf{s}' as in 5.3.3, and design

$$\mathbf{v}_s = -\boldsymbol{\lambda}|\mathbf{s}|^{1/2}\text{sign}(\mathbf{s}) - \boldsymbol{\beta} \int \text{sign}(\mathbf{s}) \quad (5.25)$$

where $\boldsymbol{\lambda} = \text{diag}\{\lambda_i\}$, $\lambda_i = 1.5\bar{\varepsilon}_{\text{ndi-}s/\text{indi-}s,i}^{1/2}$, $\boldsymbol{\beta} = \text{diag}\{\beta_i\}$, $\beta_i = 1.1\bar{\varepsilon}_{\text{ndi-}s/\text{indi-}s}$, $i = 1, \dots, m$, then $\mathbf{s} = \dot{\mathbf{s}} = \mathbf{0}$ is established in finite time [4]. On the sliding surfaces, $\mathbf{v}_s(t)$ observes $-\varepsilon_{\text{ndi-}s/\text{indi-}s}(t)$ according to Eqs. (5.5, 5.10), thus the unperturbed dynamics $\boldsymbol{\sigma}^{(r)} = \mathbf{v}_n$ are recovered in finite time. Analogously, \mathbf{s}' is stabilized in finite time by

$$\mathbf{v}'_s = -\boldsymbol{\lambda}'|\mathbf{s}'|^{1/2}\text{sign}(\mathbf{s}') - \boldsymbol{\beta}' \int \text{sign}(\mathbf{s}') \quad (5.26)$$

where $\boldsymbol{\lambda}' = \text{diag}\{\lambda'_i\}$, $\lambda'_i = 1.5\bar{\varepsilon}_{\text{ho-}s,i}^{1/2}$, $\boldsymbol{\beta}' = \text{diag}\{\beta'_i\}$, $\beta'_i = 1.1\bar{\varepsilon}_{\text{ho-}s,i}$, $i = 1, \dots, m$, then \mathbf{v}'_s observes $-\varepsilon_{\text{ho-}s}$ in finite time. Consequently, the unperturbed dynamics $\boldsymbol{\sigma}^{(r+1)} = \mathbf{v}'_n$ are achieved in finite time. Adopting \mathbf{v}'_n designed in 5.3.1 enforces the $r + 1^{\text{th}}$ -order sliding mode with respect to $\boldsymbol{\sigma}$.

Once the sliding modes are achieved $\dot{\varepsilon}_{\text{ho-}s}(t)\Delta t \approx \dot{\varepsilon}_{\text{indi-}s}(t)$ according to the analyses in 5.3.2. Therefore, in view of the gain conditions, $\boldsymbol{\lambda}'$ approximately equals $\boldsymbol{\lambda}$ used by INDI-SMC divided by $\sqrt{\Delta t}$ to maintain the sliding mode. Moreover, $\boldsymbol{\beta}'$ approximately equals $\boldsymbol{\beta}$ used by INDI-SMC divided by Δt .

The super-twisting observers designed by Eqs. (5.25, 5.26) use fixed gain matrices. Although the discontinuous signum functions have been integrated, the chattering effects can not be totally eliminated [1, 2]. This issue inspires some recent researches to

use time-varying $\beta(t)$ and $\beta'(t)$ for mitigating the chattering effects. Different adaptation mechanisms are proposed in [1–3] which make $\beta_i(t)$ and $\beta'_i(t)$ as low as possible, whilst still guaranteeing that $\beta_i(t) > |\dot{\epsilon}_{\text{ndi-s/indi-s},i}(t)|$, $\beta'_i(t) > |\dot{\epsilon}_{\text{ho-s},i}(t)|$, $i = 1, \dots, m$. In view of these conditions, for maintaining the sliding modes, the minimum possible value of $\beta'(t)$ still approximately equals $\beta(t)$ used by INDI-SMC divided by Δt .

Remark 14 When the super-twisting observers are used, the chattering magnitude of HOSMC with artificially increased r is similar with that of INDI-SMC, because \mathbf{v}'_s will be multiplied with Δt in Eq. (5.17).

Remark 15 The influences of control structures on the minimum possible control/observer gain values are not restricted to the two preceding $\mathbf{v}_s/\mathbf{v}'_s$ designs. This is because for most sliding mode control/observer designs, the minimum possible gains are positively correlated with the norms of the closed-loop uncertainties or the norms of the corresponding derivatives.

5.4. NUMERICAL COMPARISONS

Consider a nonlinear control-affine system:

$$\ddot{x} = \dot{x} + 3x + x^2 + 10u + d \quad (5.27)$$

where the external disturbance $d = 0.5 \sin(10t)$. The control aim is making the output $y = x$ track the reference signal $y_c = 5 \sin(t)$ in finite time. The relative degree r of the system equals two. As compared to Eq. (5.2), $\alpha = \dot{x} + 3x + x^2$, $\mathcal{B} = 10$ for this system. Assume the estimated model used for control design is $\tilde{\alpha} = x + 0.5x^2$, $\tilde{\mathcal{B}} = 15$, which has mismatches with the plant. The disturbance d is unknown by the controllers. Design the sliding variable as $\sigma = y - y_c$. The initial conditions are: $y(t=0) = 2$, $\dot{y}(t=0) = 0$. The sampling frequency is $f_s = 1000$ Hz ($\Delta t = 0.001$ s).

Using Eqs. (5.4, 5.9, 5.13), the control inputs using the three discussed control structures are

$$u_{\text{ndi-s}} = (1/15)(v_n + v_s + \ddot{y}_c - (x + 0.5x^2)) \quad (5.28)$$

$$\Delta u_{\text{indi-s}} = (1/15)(v_n + v_s + \ddot{y}_c - \ddot{y}_0) \quad (5.29)$$

$$\dot{u}_{\text{ho-s}} = (1/15)(v'_n + v'_s + \ddot{y}_c) \quad (5.30)$$

v_n in Eqs. (5.28, 5.29) are designed using *Proposition 3* with the control parameters $K_0 = 16$, $K_1 = 6.4$, $\alpha_2 = 0.98$. α_1 is calculated using Eq. (5.21) as $\alpha_1 = 0.96$. Design v'_n using Eq. (5.22, 5.23), while satisfying the five conditions in subsection 5.3.1, then the nominal control increment $\tilde{\mathcal{B}}^{-1}(x)\mathbf{v}'_n\Delta t$ in Eq. (5.17) becomes close to the nominal control increment of INDI-SMC (Eq. (5.9)). Explicitly, $K'_0 = 16/\Delta t$, $K'_1 = 6.4/\Delta t$, $K'_2 = 1/\Delta t$, $\alpha'_2 = 0.98$, $\alpha'_1 = 0.96$, $\alpha'_3 = 0.99$. v_s and v'_s are designed using the super-twisting observer in 5.3.3, their gain selection issues will be addressed later on.

Evolutions of the output, and the derivatives of σ using three different control structures are shown in Fig. 5.1. It can be seen that the 2^{nd} -order sliding mode with respect to σ is achieved within finite time by both INDI-SMC and INDI-SMC despite the presence

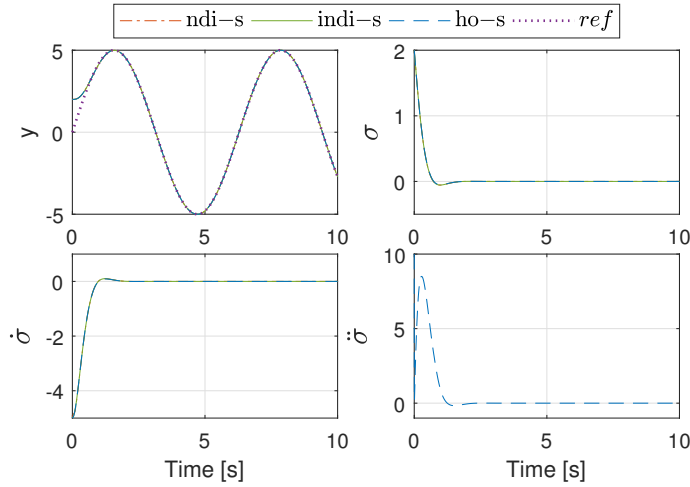


Figure 5.1: Evolutions of the output y , and the derivatives of σ .

of the disturbance and model mismatches. The 3^{rd} -order sliding mode is also established by HOSMC within finite time. Because the control parameters are chosen correspondingly, similar transient responses are present, with $|\sigma_{ndi-s} - \sigma_{indi-s}| < 0.020$ and $|\sigma_{indi-s} - \sigma_{ho-s}| < 0.007$ throughout the entire time history.

As discussed in subsection 5.3.2, the three considered control structures result in different perturbation terms. The evolutions of these terms are shown in the left subplot of Fig. 5.2, from which it can be seen that ε_{ndi-s} (Eq. (5.6)) is quite different from $\varepsilon_{indi-s}/\Delta t$ (Eq. (5.11)) and ε_{ho-s} (Eq. (5.15)). This difference can be revealed by comparing the formulations of the uncertainty terms, where it can be found that only ε_{ndi-s} contains $\alpha - \bar{\alpha}$. Worse $\bar{\alpha}$ estimation would result in increased $|\varepsilon_{ndi-s}|$. The upper bound of ε_{indi-s} is three orders of magnitude smaller than that of ε_{ndi-s} and ε_{ho-s} . Except for rare time instances where $\varepsilon_{ndi-s} = 0$, while $\varepsilon_{indi-s} \neq 0$, $|\varepsilon_{indi-s}(t)| < |\varepsilon_{ndi-s}(t)|$ throughout the entire time history. This inequality is beneficial to chattering reduction, since the time-varying minimum possible switching gain is determined by the absolute value of the uncertainty (subsection 5.3.3).

Moreover, for all $t \in (0, 10]$, $|\varepsilon_{indi-s}/\Delta t - \varepsilon_{ho-s}| < 1.24$, which verifies the analyses in Sec. 5.3.2. As a consequence, $K'_s(t)$ used by HOSMC should be three orders of magnitude higher than $K_s(t)$ used by INDI-SMC if v_s and v'_s are designed using the first-order SMC (5.3.3). Nevertheless, these two methods will lead to comparable chattering magnitude according to Remark 13.

The evolutions of the uncertainty derivatives are shown in the right subplot of Fig. 5.2. $\dot{\varepsilon}_{ndi-s}$ has quite different responses as compared to $\dot{\varepsilon}_{indi-s}/\Delta t$ and $\dot{\varepsilon}_{ho-s}$. For all $t \in (0, 10]$, $|\dot{\varepsilon}_{indi-s}/\Delta t - \dot{\varepsilon}_{ho-s}| < 2.51$, which verifies the analyses in subsection 5.3.2. In this simulation case, $\bar{\varepsilon}_{ndi-s} = 120$, $\bar{\varepsilon}_{ho-s} = 350$, while $\bar{\varepsilon}_{indi-s}$ is only 0.35. Using the gain conditions imposed on Eqs. (5.25, 5.26), the super-twisting observations are illustrated in Fig. 5.3. All the three observers converge within 0.3 seconds, after which the nominal dynamics are recovered, thus the higher-order sliding modes are established in spite of perturba-

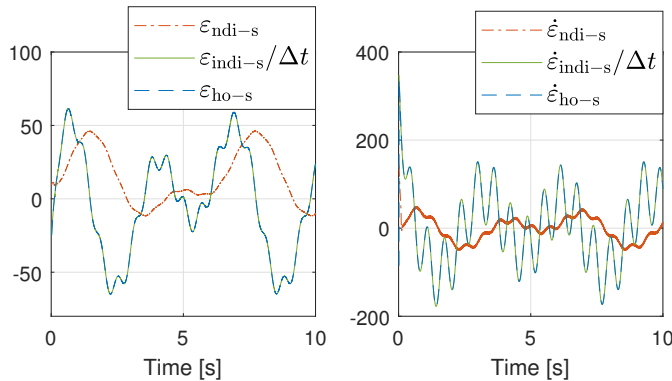


Figure 5.2: Evolutions of the uncertainties (left) and their derivatives (right).

tions as shown in Fig. 5.1.

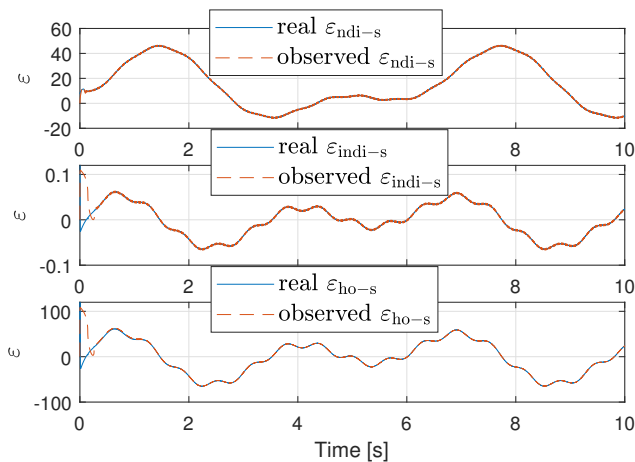


Figure 5.3: The real and observed (via super-twisting observers) uncertainties.

Even though the observations provided by the super-twisting observers are continuous, chattering is only attenuated instead of being totally rejected by the integration in Eqs. (5.25, 5.26) [1]. This is verified by Fig. 5.4, where the NDI-SMC control input has a chattering magnitude of about 0.06. By contrast, because of the three orders of magnitude smaller observer gains, $u_{\text{indi-s}}$ is much smoother, which is verified by Fig. 5.4 in both time and frequency domains. The right subplot of Fig. 5.4 illustrates the Welch's power spectral density estimation of the control inputs (using the Matlab command "pwelch"). It can also be observed from Fig. 5.4 that although HOSMC has even higher observer gains than NDI-SMC, the chattering magnitude of $u_{\text{ho-s}}$ is comparable with that of $u_{\text{ndi-s}}$. This has been explained by Remark 14 and is verified by Fig. 5.4. Furthermore, because the five conditions in subsection 5.3.1 are satisfied, HOSMC with artificially increased r and INDI-SMC provide similar control inputs as $|u_{\text{indi-s}} - u_{\text{ho-s}}| < 0.014$

for all $t \in (0, 10)$ s.

It can be seen from the evolutions of the uncertainty derivatives that once the sliding modes are established, the gains determined by the upper bounds can be conservative. As argued in subsection 5.3.1, even if the observer gains are adapted, their minimum possible values are still constrained by the norms of the uncertainty derivatives. In view of the right subplot of Fig. 5.2, INDI-SMC has the smallest minimum possible observer gains among all the three discussed control structures.

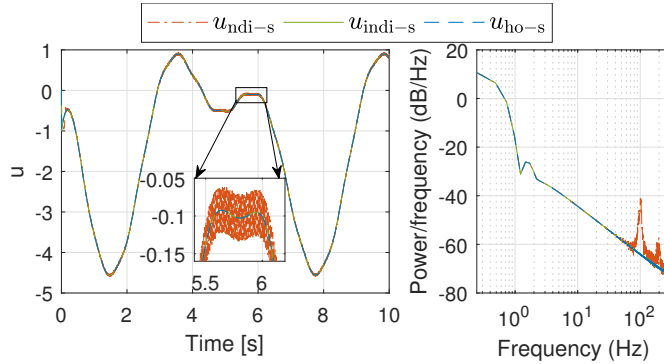


Figure 5.4: Control inputs in the time (left) and the frequency (right) domains.

In view of the preceding results, when the five conditions in 5.3.1 are satisfied, INDI-SMC and HOSMC with artificially increased r have similar performance and chattering magnitude. Their resulting uncertainties, uncertainty derivatives, and the minimum possible gains are directly connected by Δt . A natural research question would be: what if the conditions in 5.3.1 are unsatisfied? This is tested by a case where the previously used K'_0 and K'_1 are multiplied with 0.3, with the results shown in Fig. 5.5.

In this case, Fig. 5.5 shows that the transient responses of INDI-SMC and HOSMC no long resemble each other. Since K'_0 and K'_1 are reduced, it takes longer (six seconds) for HOSMC to converge. However, once the sliding modes are enforced, $u_{\text{ho-s}} \approx u_{\text{indi-s}}$. Furthermore, $\epsilon_{\text{ho-s}}(t) \approx \epsilon_{\text{indi-s}}(t)/\Delta t$, $\dot{\epsilon}_{\text{ho-s}}(t) \approx \dot{\epsilon}_{\text{indi-s}}(t)/\Delta t$ after $t = 6$ s in Fig. 5.5. These results verify the analyses in subsection 5.3.2.

5.5. CONCLUSIONS

In this chapter, three control structures for inducing higher-order sliding modes: nonlinear dynamic inversion based sliding mode control (abbreviated to NDI-SMC, which designs $u_{\text{nda-s}}$), incremental sliding mode control (indicated as INDI-SMC, which designs $\Delta u_{\text{indi-s}}$), and higher-order sliding mode control (HOSMC) with artificially increased relative degree by one order (designs $u_{\text{ho-s}}$) are compared analytically and numerically. $u_{\text{nda-s}}$ needs both the estimations of system dynamics and control effectiveness for control implementation, while only the estimated control effectiveness is needed by $\Delta u_{\text{indi-s}}$ and $u_{\text{ho-s}}$. Nevertheless, $\Delta u_{\text{indi-s}}$ depends on the measurements/estimations of the output derivatives, while $u_{\text{ho-s}}$ relies on the numerically differentiated output derivatives and the higher-order derivatives of the tracking commands.

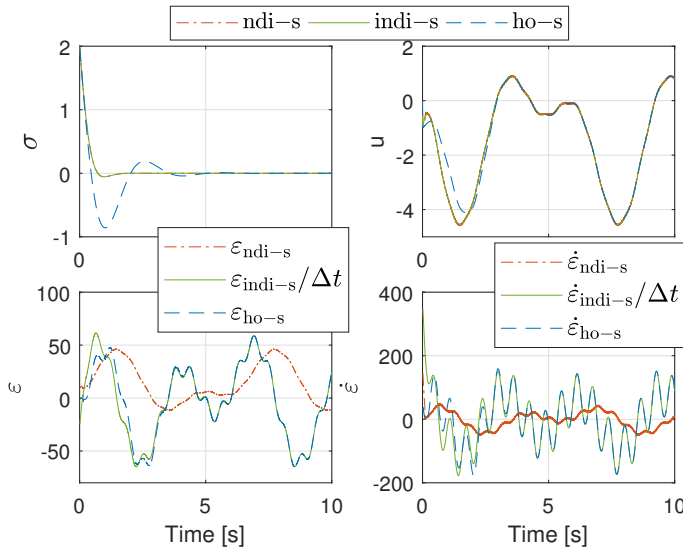


Figure 5.5: A test case in which the conditions in 5.3.1 are not satisfied.

5

Although the considered HOSMC and INDI-SMC originate from completely different ideas, their nominal control increments are found to be approximately equivalent if the sampling interval Δt is sufficiently small and if their control parameters satisfy the conditions presented in subsection 5.3.1. When these conditions are satisfied, similar transient responses and control performance are achieved by HOSMC and INDI-SMC. Otherwise, although their transient responses would be different, once the higher-order sliding modes are achieved, the control efforts needed to maintain the sliding modes become the same.

In the presence of external disturbances and model uncertainties, these three control structures result in different closed-loop uncertainty terms, namely ϵ_{ndi-s} , ϵ_{indi-s} and ϵ_{ho-s} . It is verified in this chapter that there exists a Δt such that $\|\epsilon_{indi-s}(t)\| < \|\epsilon_{ndi-s}(t)\|$ almost everywhere. Moreover, it is found that once the sliding modes are enforced, $\epsilon_{ho-s}(t)\Delta t \approx \epsilon_{indi-s}(t)$, $\dot{\epsilon}_{ho-s}(t)\Delta t \approx \dot{\epsilon}_{indi-s}(t)$. For most sliding mode control/observer designs, the minimum possible gains are determined by the norms of the uncertainty terms or the norms of the corresponding derivatives. Therefore, for maintaining the sliding modes, the minimum possible gains required by HOSMC approximately equal those needed by INDI-SMC divided by Δt . Even so, these two control structures lead to comparable chattering magnitudes, which are efficaciously reduced as compared to NDI-SMC.

REFERENCES

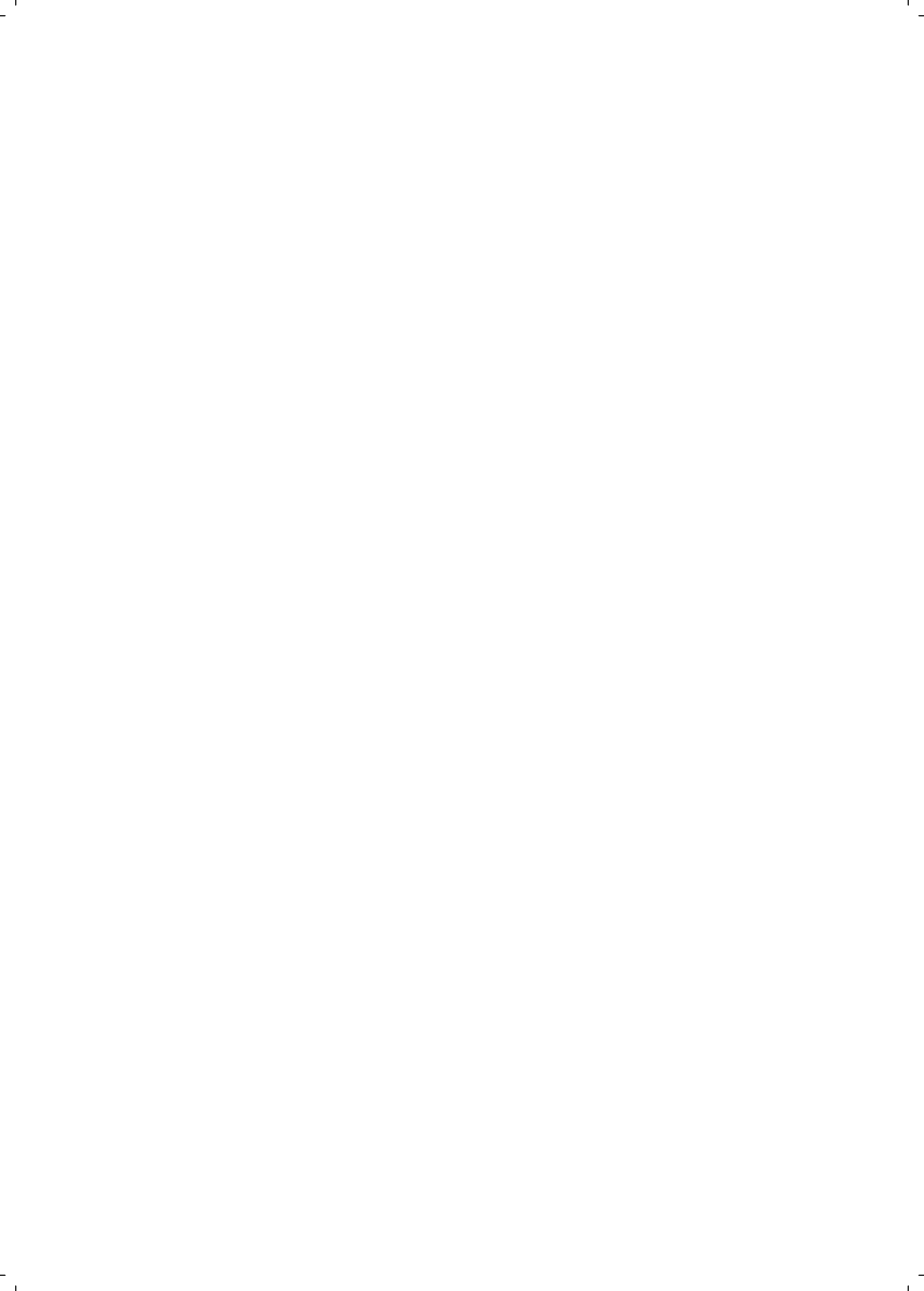
- [1] C. Edwards and Y. B. Shtessel, *Adaptive continuous higher order sliding mode control*, *Automatica* **65**, 183 (2016).
- [2] V. I. Utkin and A. S. Poznyak, *Adaptive sliding mode control with application to*

- super-twist algorithm: Equivalent control method*, *Automatica* **49**, 39 (2013).
- [3] C. Edwards and Y. Shtessel, *Adaptive dual-layer super-twisting control and observation*, *International Journal of Control* **89**, 1759 (2016).
- [4] C. Edwards and Y. B. Shtessel, *Continuous higher order sliding mode control based on adaptive disturbance compensation*, in *2014 13th International Workshop on Variable Structure Systems (VSS)*, Vol. 47 (IEEE, 2014).
- [5] X. Wang, E. van Kampen, Q. P. Chu, and P. Lu, *Stability Analysis for Incremental Nonlinear Dynamic Inversion Control*, *Journal of Guidance, Control, and Dynamics* (2019), 10.2514/1.G003791.
- [6] S. Sieberling, Q. P. Chu, and J. A. Mulder, *Robust Flight Control Using Incremental Nonlinear Dynamic Inversion and Angular Acceleration Prediction*, *Journal of Guidance, Control, and Dynamics* **33**, 1732 (2010).
- [7] P. Lu, E. van Kampen, C. de Visser, and Q. P. Chu, *Aircraft fault-tolerant trajectory control using Incremental Nonlinear Dynamic Inversion*, *Control Engineering Practice* **57**, 126 (2016).
- [8] X. Wang, E. van Kampen, Q. P. Chu, and P. Lu, *Incremental Sliding-Mode Fault-Tolerant Flight Control*, *Journal of Guidance, Control, and Dynamics* **42**, 244 (2019).
- [9] P. Smith, *A Simplified Approach to Nonlinear Dynamic Inversion Based Flight Control*, in *23rd Atmospheric Flight Mechanics Conference* (AIAA, Reston, VA, 1998).
- [10] P. Simplício, M. Pavel, E. van Kampen, and Q. P. Chu, *An acceleration measurements-based approach for helicopter nonlinear flight control using Incremental Nonlinear Dynamic Inversion*, *Control Engineering Practice* **21**, 1065 (2013).
- [11] X. Wang, E. van Kampen, Q. P. Chu, and R. De Breuker, *Flexible Aircraft Gust Load Alleviation with Incremental Nonlinear Dynamic Inversion*, *Journal of Guidance, Control, and Dynamics*, 1 (2019).
- [12] S. Sun, L. Sijbers, X. Wang, and C. de Visser, *High-Speed Flight of Quadrotor Despite Loss of Single Rotor*, *IEEE Robotics and Automation Letters* **3**, 3201 (2018).
- [13] F. Grondman, G. Looye, R. O. Kuchar, Q. P. Chu, and E. van Kampen, *Design and Flight Testing of Incremental Nonlinear Dynamic Inversion-based Control Laws for a Passenger Aircraft*, in *2018 AIAA Guidance, Navigation, and Control Conference*, January (American Institute of Aeronautics and Astronautics, Kissimmee, Florida, 2018).
- [14] T. Keijzer, G. Looye, Q. P. Chu, and E. van Kampen, *Design and Flight Testing of Incremental Backstepping based Control Laws with Angular Accelerometer Feedback*, in *AIAA Scitech 2019 Forum*, January (American Institute of Aeronautics and Astronautics, San Diego, California, 2019) pp. 1–25.

- [15] Wu-Chung Su, S. Drakunov, and U. Ozguner, *An $O(T/\sup 2l)$ boundary layer in sliding mode for sampled-data systems*, *IEEE Transactions on Automatic Control* **45**, 482 (2000).
- [16] R. Morgan and U. Ozguner, *A decentralized variable structure control algorithm for robotic manipulators*, *IEEE Journal on Robotics and Automation* **1**, 57 (1985).
- [17] A. Levant, *Higher-order sliding modes, differentiation and output-feedback control*, *International Journal of Control* **76**, 924 (2003).
- [18] M. Defoort, T. Floquet, A. Kokosy, and W. Perruquetti, *A novel higher order sliding mode control scheme*, *Systems and Control Letters* **58**, 102 (2009).
- [19] A. Levant, *Sliding order and sliding accuracy in sliding mode control*, *International Journal of Control* **58**, 1247 (1993).
- [20] A. F. Filippov, *Matematicheskii Sbornik*, edited by F. M. Arscott, Mathematics and Its Applications, Vol. 18 (Springer Netherlands, Dordrecht, 1988).
- [21] J. Wang, Q. Zong, R. Su, and B. Tian, *Continuous high order sliding mode controller design for a flexible air-breathing hypersonic vehicle*, *ISA Transactions* **53**, 690 (2014).
- [22] S. P. Bhat and D. S. Bernstein, *Geometric homogeneity with applications to finite-time stability*, *Mathematics of Control, Signals, and Systems* **17**, 101 (2005).
- [23] E. J. J. Smeur, Q. P. Chu, and G. C. H. E. de Croon, *Adaptive Incremental Nonlinear Dynamic Inversion for Attitude Control of Micro Air Vehicles*, *Journal of Guidance, Control, and Dynamics* **39**, 450 (2016).
- [24] P. Yu, Y. Shtessel, and C. Edwards, *Continuous higher order sliding mode control with adaptation of air breathing hypersonic missile*, *International Journal of Adaptive Control and Signal Processing* **30**, 1099 (2016).
- [25] M. Basin, Y. Shtessel, and F. Aldukali, *Continuous finite- and fixed-time high-order regulators*, *Journal of the Franklin Institute* **353**, 5001 (2016).
- [26] X. Wang, S. Sun, E. van Kampen, and Q. P. Chu, *Quadrotor Fault Tolerant Incremental Sliding Mode Control driven by Sliding Mode Disturbance Observers*, *Aerospace Science and Technology* **87**, 417 (2019).
- [27] V. Utkin, J. Guldner, and J. Shi, *Sliding Mode Control in Electro-Mechanical Systems, Second Edition*, Automation and Control Engineering, Vol. 31 (CRC Press, London, 2009) p. 503.

II

FLIGHT CONTROL APPLICATIONS



6

QUADROTOR FAULT-TOLERANT INCREMENTAL SLIDING MODE CONTROL DRIVEN BY SLIDING MODE DISTURBANCE OBSERVERS

In Chapter 3, the incremental sliding mode control (INDI-SMC), which hybridizes the incremental nonlinear dynamic inversion (INDI) and sliding mode control (SMC) was proposed. The effectiveness of this hybrid control will be evaluated by quadrotor flight tests in this chapter. The derivations in Chapter 3 will also be improved. Specifically, the influences of external disturbances and sudden actuator faults will be considered in both derivations and robustness analysis. In this chapter, SMC driven by sliding mode disturbance observers (SMDO) will be implemented. It will be shown that the reduced model dependency of INDI-SMC/SMDO and its smaller uncertainty variations can simplify the implementation process. Furthermore, this chapter will confirm that a wide range of actuator faults and external disturbances can be passively tolerated by INDI-SMC/SMDO, with reduced and fixed control and observer gains.

This chapter is based on the following article:

Wang, X., Sun, S., van Kampen, E., and Chu, Q.P., "Quadrotor Fault-Tolerant Incremental Sliding Mode Control Driven by Sliding Mode Disturbance Observers," *Aerospace Science and Technology*, Vol. 87, 2019, pp. 417–430. doi:10.1016/j.ast.2019.03.001.

This chapter proposes an incremental sliding mode control driven by sliding mode disturbance observers (INDI-SMC/SMDO), with application to a quadrotor fault tolerant control problem. By designing the SMC/SMDO based on the control structure of the sensor-based incremental nonlinear dynamic inversion (INDI), instead of the model-based nonlinear dynamic inversion (NDI) in the literature, the model dependency of the controller and the uncertainties in the closed-loop system are simultaneously reduced. This allows INDI-SMC/SMDO to passively resist a wider variety of faults and external disturbances using continuous control inputs with lower control and observer gains. When applied to a quadrotor, both numerical simulations and real-world flight tests demonstrate that INDI based SMC/SMDO has better performance and robustness over NDI based SMC/SMDO, in the presence of model uncertainties, wind disturbances, and sudden actuator faults. Moreover, the implementation process is simplified because of the reduced model dependency and smaller uncertainty variations of INDI-SMC/SMDO. Therefore, the proposed control method can be easily implemented to improve the performance and survivability of quadrotors in real life.

6.1. INTRODUCTION

CHARACTERIZED by mechanical simplicity, high maneuverability, and task adaptability, autonomous quadrotors have attracted considerable interests in academic and industrial communities. A recent research revealed the usage of quadrotors has a potential for reducing the greenhouse gas emissions and energy consumption [1]. Due to the lack of redundancies, rotor failures have high impacts on quadrotor safety. To make widespread applications of quadrotors possible in the future, improving their reliability while maintaining affordability becomes more and more important.

Being invariant (better than just robust) to matched uncertainties [2, 3], sliding mode control (SMC) is a promising candidate to fulfill this goal. A variety of SMC methods have been proposed for quadrotors to resist external disturbances and to cope with faults [4–14]. In spite of the varieties in SMC designs, for most SMC algorithms, the required control gains are positively correlated with uncertainty bounds (for first-order SMC), or the bounds of uncertainty derivatives (for higher-order SMC). However, high-gain SMC methods are problematic, they amplify the measurement noise, excite unmodeled dynamics, and aggravate the well-known chattering phenomenon [15]. On account of these side-effects, one of the research focuses in the SMC community is on achieving the minimum possible value of the SMC gains [15–18].

Two effective approaches can be used to reduce the SMC gains. One is using a continuous model-based preliminary feedback control term to roughly cancel the nonlinearities and dynamic couplings, such that only the remaining uncertainties need to be compensated by SMC. Regrading nonlinear control problems, this feedback term is commonly derived by dynamically inverting nonlinear algebraic equations, namely, by using nonlinear dynamic inversion (NDI). Examples can be given for both first-order [4–9, 12, 19] and higher-order [11, 13, 20, 21] sliding mode control methods. The other approach is incorporating the uncertainty estimations, for example by using sliding mode disturbance observers (SMDO), such that only the estimation errors need to be dealt with by SMC [8, 13, 19, 22]. Although these two approaches have their advantages, it is

impractical and tedious to pursue a perfect model. Moreover, the switching gains used in SMDO still need to be larger than the uncertainty bounds or their derivatives [8, 13, 19, 22]. Even though continuity can be retained by using a filtering process in the equivalent control estimations of SMDO, the high-frequency switching component can only be attenuated instead of being totally rejected [19]. Therefore, it is valuable to design a control method which could fundamentally reduce the control efforts of SMC/SMDO whilst requiring less model knowledge.

Incremental nonlinear dynamic inversion (INDI) is a sensor-based control method, which not only has less model dependency, but also obtains better robustness as compared to the NDI control [23, 24]. INDI was initially proposed in [25], and has been successfully applied on the angular rate control [26] and position control [27] problems of quadrotors. Flight tests on a CS-25 certified passenger aircraft demonstrate that INDI outperforms NDI, in the presence of model uncertainties, sensor noises, and real-world disturbances [23]. Recently, this INDI control method was reformulated in [24] to broaden its applicability. The stability and robustness of this method are also analyzed in [24] using Lyapunov methods and the nonlinear system perturbation theories. It has been proved in [24] that for a nonlinear system with stable internal dynamics, if the remaining regular perturbation term in INDI is bounded, then the states will be ultimately bounded by a class \mathcal{K} function of the regular perturbation bound. Although the ultimate bound of the states can be reduced by increasing the sampling frequency and the control gains, these two approaches have practical limitations.

A nonlinear control framework named incremental sliding mode control (INDI-SMC), which hybridizes the reformulated INDI with SMC was proposed in [28]. This hybridization inherits the advantages and remedies the drawbacks of both methods. On the one hand, by introducing a SMC term into INDI, the influences of the remaining regular perturbation term can be compensated. On the other hand, by designing SMC based on the sensor-based INDI control framework, the model dependency and the minimum possible control gains of SMC can simultaneously be reduced. Nevertheless, Ref. [28] still has some limitations. First of all, the influences of sudden faults were not explicitly considered in the control derivations and the stability analyses. Also, the external disturbances were not included in the control derivations, analyses and simulation tests. Finally, only a classical first-order SMC hybridized with INDI was numerically verified in [28], whilst the consequences of incorporating SMDO have not been demonstrated yet. These issues will be dealt with in the present chapter.

The main contributions of this chapter are the proposal of incremental sliding mode control driven by sliding mode disturbance observers (INDI-SMC/SMDO), and its application to a quadrotor fault tolerant control problem. Apart from its lower model dependency, the proposed method also has improved robustness and performance as compared to SMC/SMDO designs based on NDI in the literature. Moreover, by virtue of the sensor-based characteristic of INDI, the control objectives can be achieved using lower switching gains, which effectively mitigates the chattering effects of SMC. Furthermore, a wider range of disturbances and faults can be passively resisted without gain adaptation. Finally, the effectiveness of this method is verified by both numerical simulations and real-world flight tests.

The structure of this chapter is as follows: Sec. 6.2 proposes the INDI-SMC/SMDO

method and analyzes its stability and robustness. Theoretical comparisons with NDI based SMC/SMDO are also conducted in Sec. 6.2. Both the NDI and INDI based SMC/SMDO methods are applied to a quadrotor fault tolerant control problem in Sec. 6.3. The effectiveness of the proposed INDI-SMC/SMDO method is demonstrated by simulations in Sec. 6.4 and by flight tests in Sec. 6.5. Main conclusions are drawn in Sec. 6.6.

6.2. INCREMENTAL SLIDING MODE CONTROL DRIVEN BY SLIDING MODE DISTURBANCE OBSERVERS

Consider a nonlinear multi-input/multi-output control-affine system:

$$\dot{\mathbf{x}} = \mathbf{f}(\mathbf{x}, \kappa(t)) + \mathbf{G}(\mathbf{x}, \kappa(t))\mathbf{u} + \mathbf{d}(t), \quad \mathbf{y} = \mathbf{x}, \quad (6.1)$$

where $\mathbf{x} \in \mathcal{R}^n$, $\mathbf{u} \in \mathcal{R}^n$, $\mathbf{f}(\mathbf{x}, \kappa(t)) \in \mathcal{R}^n$, $\mathbf{G}(\mathbf{x}, \kappa(t)) = [\mathbf{g}_1, \mathbf{g}_2, \dots, \mathbf{g}_n] \in \mathcal{R}^{n \times n}$, $\mathbf{g}_i \in \mathcal{R}^n$, $i = 1, 2, \dots, n$. $\mathbf{d} \in \mathcal{R}^n$ represents the bounded external disturbances. To indicate the sudden fault at $t = t_f$ during flight, $\kappa(t) \in \mathcal{R}$ is designed as a step function, with $t < t_f$, $\kappa = 0$ indicates the fault-free case and $t \geq t_f$, $\kappa = 1$ denotes the post-fault condition. \mathbf{f} and \mathbf{G} are expanded as:

$$\mathbf{f} = \bar{\mathbf{f}} + (\mathbf{f}_f - \bar{\mathbf{f}})\kappa + \hat{\mathbf{f}}, \quad \mathbf{G} = \bar{\mathbf{G}} + (\mathbf{G}_f - \bar{\mathbf{G}})\kappa + \hat{\mathbf{G}} \quad (6.2)$$

In the preceding equation, $\bar{\mathbf{f}}$, $\bar{\mathbf{G}}$ are the nominal dynamics used for controller design, \mathbf{f}_f , \mathbf{G}_f denote the post-fault dynamics, and $\hat{\mathbf{f}}$, $\hat{\mathbf{G}}$ represent the model uncertainties as continuous functions of \mathbf{x} .

Assumption 4 $\mathbf{G}(\mathbf{x}, \kappa(t))$ in Eq. (6.1) is nonsingular for all t .

6

Assumption 4 constrains the damage intensity considered in the present chapter. If $\mathbf{G}(\mathbf{x}, \kappa(t))$ becomes singular because of faults, subspace control strategies need to be used. For example, a subspace control strategy is used in conjunction with incremental nonlinear dynamic inversion (INDI) in [29] for achieving the high speed flight (over 9 m/s) of a damaged quadrotor with complete loss of a single rotor.

The control aim is to design a continuous sliding mode control (SMC) input that achieves decoupled asymptotic output tracking $\mathbf{y}_c - \mathbf{y} = \mathbf{e} \rightarrow \mathbf{0}$, in the presence of model uncertainties, external disturbances, and sudden faults. The output reference \mathbf{y}_c should be differentiable with continuous $\dot{\mathbf{y}}_c$. In the context of the sliding mode control, the sliding variable $\boldsymbol{\sigma}$ is designed such that when $\boldsymbol{\sigma} = \mathbf{0}$ is reached, the desired error dynamics are achieved. For fair comparisons, a sliding variable designed as

$$\boldsymbol{\sigma} = \mathbf{e} + \mathbf{K}_c \int \mathbf{e} dt \quad (6.3)$$

will be consistently used in this chapter. $\mathbf{K}_c = \text{diag}\{K_{c_i}\}$, $i = 1, 2, \dots, n$, and K_{c_i} are chosen to achieve desired error dynamics.

In subsection 6.2.1, SMC/sliding mode disturbance observers (SMDO) based on the control structure of NDI will be introduced first as a benchmark, then INDI-SMC/SMDO will be proposed in subsection 6.2.2. These two control approaches will be compared analytically in subsection 6.2.3.

6.2.1. NDI-SMC/SMDO

Using Eq. (6.1), the dynamics of the sliding variable in Eq. (6.3) are given by:

$$\begin{aligned}\dot{\sigma} &= \dot{e} + \mathbf{K}_c e = (\dot{y}_c + \mathbf{K}_c e - \dot{\bar{f}}) + (\bar{f} - \mathbf{f} - \mathbf{d}) - \bar{\mathbf{G}}\mathbf{u} - (\mathbf{G} - \bar{\mathbf{G}})\mathbf{u} \\ &\triangleq \bar{\Psi} + \Delta\Psi - \bar{\mathbf{G}}\mathbf{u} - \Delta\mathbf{G}\mathbf{u}\end{aligned}\quad (6.4)$$

in which $\Delta\Psi$ and $\Delta\mathbf{G}$ are unavailable for controller design. It is noteworthy that $\Delta\mathbf{G}$ represents the multiplicative uncertainties in the control effectiveness matrix, which was not considered in Ref. [8, 19].

In order to reduce the control gains, SMC can be used along with SMDO, which can estimate bounded uncertainties. SMDO designs are independent of the model structure, only the bounds of uncertainties are needed by the classical SMDO designs, and the bounds of the uncertainty derivatives are required by the higher-order SMDO (e.g., Super-twisting SMDO [8, 19, 22]) designs. This chapter designs a classical SMDO as an example, where the auxiliary sliding variables are introduced as:

$$\mathbf{s} = \boldsymbol{\sigma} + \mathbf{z}, \quad \dot{\mathbf{z}} = -\bar{\Psi} + \bar{\mathbf{G}}\mathbf{u} - \mathbf{v}_o \quad (6.5)$$

Substituting Eq. (6.4) into Eq. (6.5) yields:

$$\dot{\mathbf{s}} = (\Delta\Psi - \Delta\mathbf{G}\mathbf{u}) - \mathbf{v}_o \triangleq -\boldsymbol{\varepsilon}_{\text{ndi}} - \mathbf{v}_o \quad (6.6)$$

Denote the control input as \mathbf{u}_{ndi} , then using Eqs. (6.2, 6.4), $\boldsymbol{\varepsilon}_{\text{ndi}}$ in Eq. (6.6) is rewritten as:

$$\boldsymbol{\varepsilon}_{\text{ndi}} = -\Delta\Psi + \Delta\mathbf{G}\mathbf{u}_{\text{ndi}} = [\hat{\mathbf{f}} + \hat{\mathbf{G}}\mathbf{u}_{\text{ndi}} + \mathbf{d}] + \kappa[(\mathbf{f}_f - \bar{\mathbf{f}}) + (\mathbf{G}_f - \bar{\mathbf{G}})\mathbf{u}_{\text{ndi}}] \quad (6.7)$$

Assumption 5 For all $\mathbf{x} \in \mathcal{R}^n$, $\kappa \in \mathcal{R}$, and bounded external disturbance $\mathbf{d} \in \mathcal{R}^n$, $\boldsymbol{\varepsilon}_{\text{ndi}}$ in Eq. (6.7) is bounded.

The boundedness of the perturbations is the precondition of many robust control methods. For example, Assumption 5 is made in [19, 30–33]. Design \mathbf{v}_o as:

$$\mathbf{v}_o = \mathbf{K}_s \text{Sign}(\mathbf{s}) = [K_{s,1} \text{sign}(s_1), K_{s,2} \text{sign}(s_2), \dots, K_{s,n} \text{sign}(s_n)]^T, \quad K_{s,i} \geq \eta + |\boldsymbol{\varepsilon}_{\text{ndi},i}| \quad (6.8)$$

where η is a small positive constant. Then \mathbf{s} is stabilized at zero in finite time. This can be proved by introducing a candidate Lyapunov function $V_1 = \frac{1}{2} \mathbf{s}^T \mathbf{s}$. Using Eqs. (6.6, 6.8), the time derivative of V_1 is:

$$\dot{V}_1 = \mathbf{s}^T \dot{\mathbf{s}} = \mathbf{s}^T (-\boldsymbol{\varepsilon}_{\text{ndi}} - \mathbf{v}_o) \leq \sum_{i=1}^n |s_i| |\boldsymbol{\varepsilon}_{\text{ndi},i}| - K_{s,i} |s_i| \leq -\eta \sum_{i=1}^n |s_i| \quad (6.9)$$

$\mathbf{s}^T \dot{\mathbf{s}} \leq -\eta \sum_{i=1}^n |s_i|$ is referred to as the η reaching law, which ensures $s_i = 0$ is reached in finite time $t_{r,i} \leq |s_i(0)|/\eta$ [18, 19]. Therefore, in view of Eq. (6.6), the equivalent control [2, 19] $\mathbf{v}_{\text{eq},i}$ estimates exactly $-\boldsymbol{\varepsilon}_{\text{ndi},i}$, $\forall t_i \geq t_{r,i}$. One way to obtain \mathbf{v}_{eq} is filtering \mathbf{v}_o as $\hat{\mathbf{v}}_{\text{eq},i}(s) = G_{LPF}(s) \mathbf{v}_{o,i}(s)$, in which s is a Laplace variable and $G_{LPF}(s)$ is the transfer function of a low-pass filter. When first-order low-pass filters with time constant τ_i are used, $\hat{\mathbf{v}}_{\text{eq}}$ estimates $-\boldsymbol{\varepsilon}_{\text{ndi}}$ with a small estimation error proportional to τ_i , i.e.,

$|\varepsilon_{\text{ndi},i} - \hat{v}_{\text{eq},i}| < \mathcal{O}(\tau_i)$. Using $\|\cdot\|$ to denote the 2-norm of a vector, then $\|\varepsilon_{\text{ndi}} + \hat{v}_{\text{eq}}\| < \mathcal{O}(\boldsymbol{\tau}) \triangleq \|\mathcal{O}(\tau_1), \dots, \mathcal{O}(\tau_n)\|^T$. As presented in [19], τ_i can be taken very small, and its lower boundary is the sampling interval of the onboard computer.

Following the SMDO design, the continuous SMC/SMDO control input that asymptotically stabilizes $\boldsymbol{\sigma}$ is designed as:

$$\mathbf{u}_{\text{ndi}} = \bar{\mathbf{G}}^{-1}(\bar{\Psi} + \mathbf{K}_\sigma \boldsymbol{\sigma} + \hat{\mathbf{v}}_{\text{eq}}) \quad (6.10)$$

where $\mathbf{K}_\sigma = \text{diag}\{K_{\sigma,i}\}$, $K_{\sigma,i} > 0$. Substituting Eqs. (6.6, 6.10) into Eq. (6.4) leads to $\dot{\boldsymbol{\sigma}} = -\mathbf{K}_\sigma \boldsymbol{\sigma} + [\Delta\Psi - \Delta\mathbf{G}\mathbf{u}_{\text{ndi}}] - \hat{\mathbf{v}}_{\text{eq}} = -\mathbf{K}_\sigma \boldsymbol{\sigma} - (\varepsilon_{\text{ndi}} + \hat{\mathbf{v}}_{\text{eq}})$. Introducing a candidate Lyapunov function $V_2 = \boldsymbol{\sigma}^T \mathbf{P} \boldsymbol{\sigma}$, where $\mathbf{P} = \mathbf{P}^T > 0$ is the solution of the Lyapunov equation $\mathbf{P}\mathbf{K}_\sigma + \mathbf{K}_\sigma^T \mathbf{P} = \mathbf{I}$. $\mathbf{I} \in \mathcal{R}^{n \times n}$ is an identity matrix. Then when $t > \max\{t_{r,i}\}$, the time derivative of V_2 is:

$$\begin{aligned} \dot{V}_2 &= -\boldsymbol{\sigma}^T [\mathbf{P}\mathbf{K}_\sigma + \mathbf{K}_\sigma^T \mathbf{P}] \boldsymbol{\sigma} - 2\boldsymbol{\sigma}^T \mathbf{P} (\varepsilon_{\text{ndi}} + \hat{\mathbf{v}}_{\text{eq}}) \\ &< -\|\boldsymbol{\sigma}\|^2 + 2\|\boldsymbol{\sigma}\| \|\mathbf{P}\| \mathcal{O}(\boldsymbol{\tau}) \\ &\leq -\gamma \|\boldsymbol{\sigma}\|^2, \quad \forall \|\boldsymbol{\sigma}\| \geq \frac{2\|\mathbf{P}\| \mathcal{O}(\boldsymbol{\tau})}{1-\gamma} \end{aligned} \quad (6.11)$$

with constant $\gamma \in (0, 1)$. Eq. (6.11) proves that under Assumptions 4 and 5, the NDI-SMC/SMDO control law given by Eq. (6.10), in which $\hat{\mathbf{v}}_{\text{eq}}$ is observed using a SMDO with gain condition given in Eq. (6.8) ensures that the state $\boldsymbol{\sigma}$ is ultimately bounded by a class \mathcal{K} function [24, 34] of $\mathcal{O}(\boldsymbol{\tau})$. Theoretically, this ultimate bound can be made arbitrarily small [19, 31] by reducing τ_i and increasing $K_{\sigma,i}$.

6

Remark 16 The control input given by Eq. (6.10) is essentially based on the control structure of nonlinear dynamic inversion (NDI), whose virtual control now contains three parts: the classical NDI virtual control $\dot{\mathbf{y}}_c + \mathbf{K}_c \mathbf{e}$, the SMC virtual control $\mathbf{K}_\sigma \boldsymbol{\sigma}$, and the SMDO virtual control $\hat{\mathbf{v}}_{\text{eq}}$. Therefore, Eq. (6.10) is referred to as NDI based SMC driven by SMDO in this chapter, which is abbreviated to NDI-SMC/SMDO.

Remark 17 Many other SMC/SMDO designs in the literature also contain a preliminary feedback term using NDI to reduce the control efforts of SMC/SMDO. For example, adaptive fuzzy gain-scheduling SMC [12], first-order SMC using the equivalent control estimated from the nominal model [4, 6–9, 19], adaptive SMC [5], higher-order SMC [20–22], adaptive super-twisting SMC [11], modified super-twisting SMC using a higher-order sliding mode observer [13].

One well-known drawback of NDI is its model dependency, which consequently reduces its robustness to model uncertainties, on-board faults and external disturbances. SMC/SMDO is able to observe and compensate for bounded perturbations, as shown in Eqs. (6.9, 6.10). Even though the SMC/SMDO control input designed by Eq. (6.10) is continuous, the high-frequency switchings of \mathbf{v}_o are only attenuated by filtering, instead of being totally rejected [19]. In other words, the $\hat{\mathbf{v}}_{\text{eq}}$ term in Eq. (6.10) is still oscillating. A method that can simultaneously reduce the model dependency of NDI and mitigate the side effects of SMC/SMDO would be beneficial.

6.2.2. INDI-SMC/SMDO

INDI-SMC/SMDO aims to reduce the model dependency, and improve the robustness of NDI-SMC/SMDO, without using high control/observer gains. Denote the sampling interval as Δt . To begin with, the incremental dynamic equation is derived by taking the first-order Taylor series expansion of Eq. (6.1) around the condition at $t - \Delta t$ (denoted by the subscript 0) as:

$$\begin{aligned} \dot{\mathbf{y}} = & \dot{\mathbf{y}}_0 + \mathbf{G}(\mathbf{x}_0, \kappa_0)\Delta\mathbf{u} + \left. \frac{\partial[\mathbf{f}(\mathbf{x}, \kappa) + \mathbf{G}(\mathbf{x}, \kappa)\mathbf{u}]}{\partial\mathbf{x}} \right|_0 \Delta\mathbf{x} \\ & + \left. \frac{\partial[\mathbf{f}(\mathbf{x}, \kappa) + \mathbf{G}(\mathbf{x}, \kappa)\mathbf{u}]}{\partial\kappa} \right|_0 \Delta\kappa + \Delta\mathbf{d} + \mathbf{R}_1 \end{aligned} \quad (6.12)$$

In the above equation, $\Delta\mathbf{x} = \mathbf{x} - \mathbf{x}_0$, $\Delta\mathbf{u} = \mathbf{u} - \mathbf{u}_0$, respectively denote the variations of states and control inputs in one incremental time step Δt . $\Delta\kappa = \kappa - \kappa_0$ denotes the changes of the fault indicator κ , while $\Delta\mathbf{d} = \mathbf{d} - \mathbf{d}_0$ denotes the variations of the external disturbances \mathbf{d} in Δt . $\dot{\mathbf{y}}_0$ is the latest sampled output derivative vector. If $\dot{\mathbf{y}}_0$ cannot be measured, it can be estimated from the sampled outputs. The approaches of obtaining $\dot{\mathbf{y}}_0$ for control implementation will be further discussed in Sec. 6.5. \mathbf{R}_1 in Eq. (6.12) is the expansion remainder, using Eqs. (6.1, 6.2), the Lagrange form of the remainder is

$$\begin{aligned} \mathbf{R}_1 = & \frac{1}{2} \left. \frac{\partial^2[\mathbf{f} + \mathbf{G}\mathbf{u}]}{\partial^2\mathbf{x}} \right|_m \Delta\mathbf{x}^2 + \left. \frac{\partial\mathbf{G}}{\partial\mathbf{x}} \right|_m \Delta\mathbf{x}\Delta\mathbf{u} + (\mathbf{G}_f - \bar{\mathbf{G}})|_m \Delta\mathbf{u}\Delta\kappa \\ & + \left. \frac{\partial[(\mathbf{f}_f - \bar{\mathbf{f}}) + (\mathbf{G}_f - \bar{\mathbf{G}})\mathbf{u}]}{\partial\mathbf{x}} \right|_m \Delta\mathbf{x}\Delta\kappa \end{aligned} \quad (6.13)$$

in which $(\cdot)|_m$ means evaluating (\cdot) at a condition where $\mathbf{x} \in (\mathbf{x}(t - \Delta t), \mathbf{x}(t))$, $\mathbf{u} \in (\mathbf{u}(t - \Delta t), \mathbf{u}(t))$, $\mathbf{d} \in (\mathbf{d}(t - \Delta t), \mathbf{d}(t))$, and $\kappa \in (\kappa(t - \Delta t), \kappa(t))$. In Eq. (6.13), \mathbf{R}_1 is not a function of $\Delta\mathbf{u}^2$, $\Delta\mathbf{d}^2$, $\Delta\kappa^2$, nor the coupling terms $\Delta\mathbf{x}\Delta\mathbf{d}$, $\Delta\kappa\Delta\mathbf{d}$, $\Delta\mathbf{u}\Delta\mathbf{d}$. This can be examined using Eqs. (6.1, 6.2). As compared to the incremental dynamic equations derived in [24, 28], Eq. (6.12) takes partial derivatives with respect to both κ and \mathbf{d} .

The same sliding variable σ in Eq. (6.3) is also used by INDI-SMC/SMDO for fair comparisons. However, the controller will be designed based on Eq. (6.12) instead of Eq. (6.1). The dynamics of σ are then derived as:

$$\begin{aligned} \dot{\sigma} = & \dot{\mathbf{e}} + \mathbf{K}_c\mathbf{e} = [\dot{\mathbf{y}}_c + \mathbf{K}_c\mathbf{e} - \dot{\mathbf{y}}_0] - \bar{\mathbf{G}}\Delta\mathbf{u} - (\mathbf{G} - \bar{\mathbf{G}})\Delta\mathbf{u} \\ & - \left[\left. \frac{\partial[\mathbf{f}(\mathbf{x}, \kappa) + \mathbf{G}(\mathbf{x}, \kappa)\mathbf{u}]}{\partial\mathbf{x}} \right|_0 \Delta\mathbf{x} + \left. \frac{\partial[\mathbf{f}(\mathbf{x}, \kappa) + \mathbf{G}(\mathbf{x}, \kappa)\mathbf{u}]}{\partial\kappa} \right|_0 \Delta\kappa + \Delta\mathbf{d} + \mathbf{R}_1 \right] \\ \triangleq & \bar{\Psi}' + \Delta\Psi' - \bar{\mathbf{G}}\Delta\mathbf{u} - \Delta\mathbf{G}\Delta\mathbf{u} \end{aligned} \quad (6.14)$$

Design an auxiliary sliding variable $\mathbf{s}' = \sigma + \mathbf{z}'$, $\dot{\mathbf{z}}' = -\bar{\Psi}' + \bar{\mathbf{G}}\Delta\mathbf{u} - \mathbf{v}'_o$, then by using Eq. (6.14), the dynamics of \mathbf{s}' are:

$$\dot{\mathbf{s}}' = (\Delta\Psi' - \Delta\mathbf{G}\Delta\mathbf{u}) - \mathbf{v}'_o \triangleq -\boldsymbol{\varepsilon}_{\text{indi}} - \mathbf{v}'_o \quad (6.15)$$

$\boldsymbol{\varepsilon}_{\text{indi}}$ in Eq. (6.15) is the lumped perturbation term in INDI-SMC/SMDO. Denote the control input as \mathbf{u}_{indi} , which will be designed in Theorem 4. The control input in one

incremental time step is denoted as $\Delta \mathbf{u}_{\text{indi}}$. Using Eq. (6.2), the *closed-loop* values of the perturbations in Eq. (6.14) are further derived as:

$$\begin{aligned} \boldsymbol{\delta}(\mathbf{x}, \kappa, \Delta t) &\triangleq \left[\frac{\partial[\mathbf{f}(\mathbf{x}, \kappa) + \mathbf{G}(\mathbf{x}, \kappa)\mathbf{u}]}{\partial \mathbf{x}} \Big|_0 \Delta \mathbf{x} + \frac{\partial[\mathbf{f}(\mathbf{x}, \kappa) + \mathbf{G}(\mathbf{x}, \kappa)\mathbf{u}]}{\partial \kappa} \Big|_0 \Delta \kappa + \mathbf{R}_1 \right] \Big|_{\mathbf{u}=\mathbf{u}_{\text{indi}}} \\ &= \boldsymbol{\delta}_b(\mathbf{x}, \Delta \kappa, \Delta t) + \boldsymbol{\delta}_d(\mathbf{x}, \Delta t)\kappa_0 + \boldsymbol{\delta}_\kappa(\mathbf{x})\Delta \kappa \end{aligned} \quad (6.16)$$

in which

$$\begin{aligned} \boldsymbol{\delta}_b(\mathbf{x}, \Delta \kappa, \Delta t) &= \frac{\partial[\bar{\mathbf{f}} + \hat{\mathbf{f}} + (\bar{\mathbf{G}} + \hat{\mathbf{G}})\mathbf{u}_{\text{indi}}]}{\partial \mathbf{x}} \Big|_0 \Delta \mathbf{x} + \mathbf{R}_1 \Big|_{\mathbf{u}=\mathbf{u}_{\text{indi}}} \\ \boldsymbol{\delta}_d(\mathbf{x}, \Delta t) &= \frac{\partial[(\mathbf{f}_f - \bar{\mathbf{f}}) + (\mathbf{G}_f - \bar{\mathbf{G}})\mathbf{u}_{\text{indi}}]}{\partial \mathbf{x}} \Big|_0 \Delta \mathbf{x} \\ \boldsymbol{\delta}_\kappa(\mathbf{x}) &= [(\mathbf{f}_f - \bar{\mathbf{f}}) + (\mathbf{G}_f - \bar{\mathbf{G}})\mathbf{u}_{\text{indi}}] \Big|_0 \end{aligned} \quad (6.17)$$

Therefore, recall Eq. (6.14), $\boldsymbol{\varepsilon}_{\text{indi}}$ in Eq. (6.15) is written as:

$$\boldsymbol{\varepsilon}_{\text{indi}} = -\Delta \boldsymbol{\Psi}' + \Delta \mathbf{G} \Delta \mathbf{u}_{\text{indi}} = [\boldsymbol{\delta}_b + \hat{\mathbf{G}} \Delta \mathbf{u}_{\text{indi}} + \Delta \mathbf{d}] + \kappa_0 \boldsymbol{\delta}_d + \kappa (\mathbf{G}_f - \bar{\mathbf{G}}) \Delta \mathbf{u}_{\text{indi}} + \boldsymbol{\delta}_\kappa \Delta \kappa \quad (6.18)$$

For a bounded $\boldsymbol{\varepsilon}_{\text{indi}}$, design \mathbf{v}'_o in Eq. (6.15) as:

$$\mathbf{v}'_o = \mathbf{K}'_s \text{Sign}(\mathbf{s}') = [K'_{s,1} \text{sign}(s'_1), K'_{s,2} \text{sign}(s'_2), \dots, K'_{s,n} \text{sign}(s'_n)]^T, \quad K'_{s,i} \geq \eta + |\varepsilon_{\text{indi},i}| \quad (6.19)$$

where η is a small positive constant.

Theorem 4 For system described by Eqs. (6.1, 6.2), and the sliding variable $\boldsymbol{\sigma}$ in Eq. (6.3), if the INDI-SMC/SMDO control is designed as

$$\Delta \mathbf{u}_{\text{indi}} = \bar{\mathbf{G}}^{-1} (\bar{\boldsymbol{\Psi}}' + \mathbf{K}'_\sigma \boldsymbol{\sigma} + \hat{\mathbf{v}}'_{\text{eq}}) \quad (6.20)$$

where $\bar{\boldsymbol{\Psi}}'$ is defined in Eq. (6.14), $\mathbf{K}'_\sigma = \text{diag}\{K'_{\sigma,i}\}$, $K'_{\sigma,i} > 0$, and $\hat{\mathbf{v}}'_{\text{eq}}$ is low-pass filtered from \mathbf{v}'_o in Eq. (6.19), then under Assumption 4, for a bounded $\boldsymbol{\varepsilon}_{\text{indi}}$ (Eq. (6.18)), $\boldsymbol{\sigma}$ will be ultimately bounded by an arbitrarily small bound.

Proof: Chose a candidate Lyapunov function $V_3 = \frac{1}{2} \mathbf{s}'^T \mathbf{s}'$, and use Eqs. (6.15, 6.19) lead to:

$$\dot{V}_3 = \mathbf{s}'^T \dot{\mathbf{s}}' = \mathbf{s}'^T (-\boldsymbol{\varepsilon}_{\text{indi}} - \mathbf{v}'_o) \leq \sum_{i=1}^n |s'_i| |\varepsilon_{\text{indi},i}| - K'_{s,i} |s'_i| \leq -\eta \sum_{i=1}^n |s'_i| \quad (6.21)$$

Therefore, according to the η reaching law [18, 19], the sliding surfaces $s'_i = 0$, $i = 1, 2, \dots, n$ are reached in finite time $t'_{r,i} \leq |s'_i(0)|/\eta$. On the sliding surfaces, using Eq. (6.15), the equivalent control [2, 19] $\mathbf{v}'_{\text{eq},i}$ equals $-\varepsilon_{\text{indi},i}$. This equivalent control can be estimated by filtering \mathbf{v}'_o as $\hat{\mathbf{v}}'_{\text{eq},i}(s) = G_{LPF}(s) \mathbf{v}'_{o,i}(s)$, where $G_{LPF}(s)$ is the transfer function of a low-pass filter. Consequently, $\hat{\mathbf{v}}'_{\text{eq},i}$ estimates $-\varepsilon_{\text{indi},i}$ in finite time with a small estimation error proportional to the time constant of the filter, i.e., $|\varepsilon_{\text{indi},i} - \hat{\mathbf{v}}'_{\text{eq},i}| < \mathcal{O}(\tau_i)$. In a vector form, $\|\boldsymbol{\varepsilon}_{\text{indi}} + \hat{\mathbf{v}}'_{\text{eq}}\| < \mathcal{O}(\boldsymbol{\tau}) \triangleq \|\mathcal{O}(\tau_1), \dots, \mathcal{O}(\tau_n)\|^T$.

Use the observed perturbation term $\hat{\mathbf{v}}'_{\text{eq}}$, and substitute Eqs. (6.18, 6.20) into Eq. (6.14) result in:

$$\dot{\boldsymbol{\sigma}} = -\mathbf{K}'_{\sigma}\boldsymbol{\sigma} + [\Delta\Psi' - \Delta\mathbf{G}\Delta\mathbf{u}_{\text{indi}}] - \hat{\mathbf{v}}'_{\text{eq}} = -\mathbf{K}'_{\sigma}\boldsymbol{\sigma} - (\boldsymbol{\varepsilon}_{\text{indi}} + \hat{\mathbf{v}}'_{\text{eq}}) \quad (6.22)$$

Introducing a candidate Lyapunov function $V_4 = \boldsymbol{\sigma}^T \mathbf{P}' \boldsymbol{\sigma}$, where $\mathbf{P}' = \mathbf{P}'^T > 0$ is the solution of the Lyapunov equation $\mathbf{P}' \mathbf{K}'_{\sigma} + \mathbf{K}'_{\sigma T} \mathbf{P}' = \mathbf{I}$. Then when $t > \max\{t'_{r,i}\}$, the time derivative of V_4 is:

$$\begin{aligned} \dot{V}_4 &= -\boldsymbol{\sigma}^T [\mathbf{P}' \mathbf{K}'_{\sigma} + \mathbf{K}'_{\sigma T} \mathbf{P}'] \boldsymbol{\sigma} - 2\boldsymbol{\sigma}^T \mathbf{P}' (\boldsymbol{\varepsilon}_{\text{indi}} + \hat{\mathbf{v}}'_{\text{eq}}) \\ &< -\|\boldsymbol{\sigma}\|^2 + 2\|\boldsymbol{\sigma}\| \|\mathbf{P}'\| \mathcal{O}(\boldsymbol{\tau}) \\ &\leq -\gamma \|\boldsymbol{\sigma}\|^2, \quad \forall \|\boldsymbol{\sigma}\| \geq \frac{2\|\mathbf{P}'\| \mathcal{O}(\boldsymbol{\tau})}{1-\gamma} \end{aligned} \quad (6.23)$$

with constant $\gamma \in (0, 1)$. Eq. (6.23) proves $\boldsymbol{\sigma}$ is ultimately bounded by a class \mathcal{K} function [24, 34] of $\mathcal{O}(\boldsymbol{\tau})$. In theory, this ultimate bound can be made arbitrarily small [19, 31] by reducing τ_i and increasing $\mathbf{K}'_{\sigma,i}$. \square

The total control command of INDI-SMC/SMDO is $\mathbf{u}_{\text{indi}} = \mathbf{u}_{\text{indi}|0} + \Delta\mathbf{u}_{\text{indi}}$, where $\Delta\mathbf{u}_{\text{indi}}$ is designed as Eq. (6.20), $\mathbf{u}_{\text{indi}|0}$ is the latest sampled \mathbf{u}_{indi} . If $\mathbf{u}_{\text{indi}|0}$ is not directly measurable, it can also be estimated online [35]. In view of Eqs. (6.14, 6.20), the control law designed using the structure of INDI does not require the model information of \mathbf{f} . Even through the model dependency of INDI-SMC/SMDO is reduced, its robustness is enhanced by virtue of its sensor-based structure [24, 28, 36]. This distinguishes INDI-SMC/SMDO from Ref. [37, 38], where the nominal model of \mathbf{f} is still needed. The sensor-based structure also has lower computation load than the online dynamic reconstruction using neural networks [39]. Apart from its reduced model dependency, other benefits of using the INDI control structure in SMC/SMDO designs will be further explored.

For both NDI and INDI based SMC/SMDO, the boundedness of the perturbation term is the precondition of controller design. The boundedness of $\boldsymbol{\varepsilon}_{\text{ndi}}$ for all t is assumed in Assumption 5. Instead of making a similar assumption for $\boldsymbol{\varepsilon}_{\text{indi}}$, it will be shown in Theorem 5 that some less strict conditions can guarantee the boundedness of $\boldsymbol{\varepsilon}_{\text{indi}}$.

Assumption 6 $\boldsymbol{\delta}_{\kappa}(\mathbf{x})$ in Eq. (6.17) is bounded by $\bar{\delta}_{\kappa}$ for $t_f \leq t < t_f + \Delta t$.

Assumption 6 is less strict than Assumption 5. It can be seen from Eq. (6.7) and Eq. (6.17) that the $\kappa[(\mathbf{f}_f - \hat{\mathbf{f}}) + (\mathbf{G}_f - \hat{\mathbf{G}})\mathbf{u}_{\text{ndi}}]$ term contained in $\boldsymbol{\varepsilon}_{\text{ndi}}$ corresponds to $\boldsymbol{\delta}_{\kappa}(\mathbf{x})$ in $\boldsymbol{\varepsilon}_{\text{indi}}$. However, only the boundedness of $\boldsymbol{\delta}_{\kappa}(\mathbf{x})$ for a short time interval Δt is needed in Assumption 6, while the boundedness of the entire $\boldsymbol{\varepsilon}_{\text{ndi}}$ for all t is required in Assumption 5. Since $\kappa(t)$ is a step function to indicate a sudden fault, $\Delta\kappa$ is a single square pulse with magnitude of one and width of Δt . Consequently, the term $\boldsymbol{\delta}_{\kappa}(\mathbf{x})\Delta\kappa$ is only non-zero during a short time interval $t_f \leq t < t_f + \Delta t$. After $t = t_f + \Delta t$, the main influences of the fault have already been included by the measurements/estimations at the latest sampled condition.

Assumption 7 In Eq. (6.17), $\|\boldsymbol{\delta}_b(\mathbf{x}, \Delta\kappa, \Delta t)\| \leq \bar{\delta}_b$, while $\|\boldsymbol{\delta}_d(\mathbf{x}, \Delta t)\| \leq \bar{\delta}_d$.

Since \mathbf{x} is continuously differentiable, $\lim_{\Delta t \rightarrow 0} \|\Delta \mathbf{x}\| = 0$. Then if the partial derivatives of \mathbf{f} and \mathbf{G} in Eq. (6.1) with respect to \mathbf{x} , up to any order, are bounded, according to the expressions in Eq. (6.17), the norm values of $\boldsymbol{\delta}_b$ and $\boldsymbol{\delta}_d$ can be reduced by increasing the sampling frequency.

Theorem 5 *If $\|\mathbf{I} - \mathbf{G}\bar{\mathbf{G}}^{-1}\| \leq \bar{b} < 1$ for all t , under Assumptions 6 and 7, for sufficiently high sampling frequency, $\boldsymbol{\varepsilon}_{\text{indi}}$ given by Eq. (6.18) is ultimately bounded.*

Proof: Using Eqs. (6.14, 6.18, 6.20), $\boldsymbol{\varepsilon}_{\text{indi}}$ is written as

$$\begin{aligned}\boldsymbol{\varepsilon}_{\text{indi}} &= \boldsymbol{\delta}(\mathbf{x}, \kappa, \Delta t) + \Delta \mathbf{d} + \Delta \mathbf{G}\bar{\mathbf{G}}^{-1}(\bar{\Psi}' + \mathbf{K}'_{\sigma}\boldsymbol{\sigma} + \hat{\mathbf{v}}'_{\text{eq}}) \\ &= \boldsymbol{\delta}(\mathbf{x}, \kappa, \Delta t) + \Delta \mathbf{d} + (\mathbf{G}\bar{\mathbf{G}}^{-1} - \mathbf{I})((\dot{\mathbf{y}}_c + \mathbf{K}_c \mathbf{e}) + \mathbf{K}'_{\sigma}\boldsymbol{\sigma} + \hat{\mathbf{v}}'_{\text{eq}} - \dot{\mathbf{y}}_0)\end{aligned}\quad (6.24)$$

Define the lumped virtual control term as $\mathbf{v} = (\dot{\mathbf{y}}_c + \mathbf{K}_c \mathbf{e}) + \mathbf{K}'_{\sigma}\boldsymbol{\sigma} + \hat{\mathbf{v}}'_{\text{eq}}$, which contains three parts: the classical INDI virtual control $\dot{\mathbf{y}}_c + \mathbf{K}_c \mathbf{e}$, the SMC virtual control $\mathbf{K}'_{\sigma}\boldsymbol{\sigma}$, and the observation term $\hat{\mathbf{v}}'_{\text{eq}}$. These three terms are all continuous in time.

Using the definition $\boldsymbol{\sigma} = \mathbf{e} + \mathbf{K}_c \int \mathbf{e} dt$, $\mathbf{e} = \mathbf{y}_c - \mathbf{y}$, and the closed-loop dynamics given by Eq. (6.22), then

$$\dot{\boldsymbol{\sigma}} = -\mathbf{K}'_{\sigma}\boldsymbol{\sigma} - (\boldsymbol{\varepsilon}_{\text{indi}} + \hat{\mathbf{v}}'_{\text{eq}}) = \dot{\mathbf{y}}_c - \dot{\mathbf{y}} + \mathbf{K}_c \mathbf{e}\quad (6.25)$$

Therefore

$$\dot{\mathbf{y}} = (\dot{\mathbf{y}}_c + \mathbf{K}_c \mathbf{e}) + \mathbf{K}'_{\sigma}\boldsymbol{\sigma} + \hat{\mathbf{v}}'_{\text{eq}} + \boldsymbol{\varepsilon}_{\text{indi}} = \mathbf{v} + \boldsymbol{\varepsilon}_{\text{indi}}\quad (6.26)$$

Eq. (6.26) is valid for all t , thus for the previous time step, $\dot{\mathbf{y}}_0 = \mathbf{v}_0 + \boldsymbol{\varepsilon}_{\text{indi}_0}$. Substituting this equation into Eq. (6.24) yields:

$$\begin{aligned}\boldsymbol{\varepsilon}_{\text{indi}} &= \boldsymbol{\delta}(\mathbf{x}, \kappa, \Delta t) + \Delta \mathbf{d} + (\mathbf{G}\bar{\mathbf{G}}^{-1} - \mathbf{I})(\mathbf{v} - \dot{\mathbf{y}}_0) \\ &= (\mathbf{I} - \mathbf{G}\bar{\mathbf{G}}^{-1})\boldsymbol{\varepsilon}_{\text{indi}_0} - (\mathbf{I} - \mathbf{G}\bar{\mathbf{G}}^{-1})(\mathbf{v} - \mathbf{v}_0) + \boldsymbol{\delta}(\mathbf{x}, \kappa, \Delta t) + \Delta \mathbf{d} \\ &\triangleq \mathbf{E}\boldsymbol{\varepsilon}_{\text{indi}_0} - \mathbf{E}\Delta \mathbf{v} + \boldsymbol{\delta}(\mathbf{x}, \kappa, \Delta t) + \Delta \mathbf{d}\end{aligned}\quad (6.27)$$

which can be written in a recursive way as:

$$\boldsymbol{\varepsilon}_{\text{indi}}(k) = \mathbf{E}(k)\boldsymbol{\varepsilon}_{\text{indi}}(k-1) - \mathbf{E}(k)\Delta \mathbf{v}(k) + \boldsymbol{\delta}(k) + \Delta \mathbf{d}(k)\quad (6.28)$$

k in the above equation indicates the k -th time step. Since $\Delta \kappa$ is only non-zero for $t_f \leq t < t_f + \Delta t$, then $\boldsymbol{\delta}_{\kappa} \Delta \kappa$ is bounded under Assumption 6. Recall Eq. (6.16), then under Assumptions 6 and 7, $\|\boldsymbol{\delta}(\mathbf{x}, \kappa, \Delta t)\| \leq \|\boldsymbol{\delta}_b(\mathbf{x}, \Delta \kappa, \Delta t)\| + \|\boldsymbol{\delta}_d(\mathbf{x}, \Delta t)\| \cdot 1 + \|\boldsymbol{\delta}_{\kappa}(\mathbf{x}) \Delta \kappa\| \leq \bar{\delta}_b + \bar{\delta}_d + \bar{\delta}_{\kappa} \triangleq \bar{\delta}$.

Furthermore, \mathbf{v} is designed to be continuous in time, thus

$$\lim_{\Delta t \rightarrow 0} \|\mathbf{v} - \mathbf{v}_0\| = 0, \quad \forall \mathbf{x} \in \mathcal{R}^n\quad (6.29)$$

which also indicates that $\forall \overline{\Delta v} > 0, \exists \overline{\Delta t} > 0, s.t.$ for all $0 < \Delta t \leq \overline{\Delta t}, \forall \mathbf{x} \in \mathbb{R}^n, \|\mathbf{v} - \mathbf{v}_0\| \leq \overline{\Delta v}$. In other words, there exists a Δt that guarantees the boundedness of $\mathbf{v} - \mathbf{v}_0$. Also, this bound can be further diminished by increasing the sampling frequency. In addition, for a bounded disturbance vector \mathbf{d} , its increment in one time step $\Delta \mathbf{d}$ is also

bounded. Denote this bound as $\overline{\Delta d}$. Using these bounds, and recall the condition $\|E\| = \|I - G\bar{G}^{-1}\| \leq \bar{b} < 1$ in this theorem, Eq. (6.28) satisfies:

$$\begin{aligned}
 \|\boldsymbol{\varepsilon}_{\text{indi}}(k)\| &\leq (\bar{b})^k \|\boldsymbol{\varepsilon}_{\text{indi}}(0)\| + \sum_{j=1}^k (\bar{b})^{k-j+1} \|\Delta \mathbf{v}(j)\| + \sum_{j=1}^{k-1} (\bar{b})^{k-j} \|\boldsymbol{\delta}(j) + \Delta \mathbf{d}(j)\| + \|\boldsymbol{\delta}(j) + \Delta \mathbf{d}(j)\| \\
 &\leq (\bar{b})^k \|\boldsymbol{\varepsilon}_{\text{indi}}(0)\| + \overline{\Delta v} \sum_{j=1}^k (\bar{b})^{k-j+1} + (\bar{\delta} + \overline{\Delta d}) \sum_{j=1}^{k-1} (\bar{b})^{k-j} + (\bar{\delta} + \overline{\Delta d}) \\
 &= (\bar{b})^k \|\boldsymbol{\varepsilon}_{\text{indi}}(0)\| + \overline{\Delta v} \frac{\bar{b} - \bar{b}^{k+1}}{1 - \bar{b}} + (\bar{\delta} + \overline{\Delta d}) \frac{1 - \bar{b}^k}{1 - \bar{b}}
 \end{aligned} \tag{6.30}$$

Since $\bar{b} < 1$, Eq. (6.30) satisfies:

$$\|\boldsymbol{\varepsilon}_{\text{indi}}\| \leq \frac{\bar{b}\overline{\Delta v} + \bar{\delta} + \overline{\Delta d}}{1 - \bar{b}}, \quad \text{as } k \rightarrow \infty \tag{6.31}$$

In conclusion, $\boldsymbol{\varepsilon}_{\text{indi}}$ is bounded for all k , and is ultimately bounded by $\frac{\bar{b}\overline{\Delta v} + \bar{\delta} + \overline{\Delta d}}{1 - \bar{b}}$. \square

Remark 18 Theorem 5 in this chapter improves the Theorem 1 in [28] in three aspects: 1) consideration of the external disturbances \mathbf{d} ; 2) consideration of the sudden faults, as $\boldsymbol{\delta}(\mathbf{x}, \kappa, \Delta t)$ is a function of the fault indicator κ ; 3) the virtual control \mathbf{v} in this chapter also includes the contributions from SMC and SMDO, while the \mathbf{v}_c in [28] only considers the classical INDI virtual control term.

Remark 19 Theorem 5 proves that a diagonally dominate structure of $G\bar{G}^{-1}$, a sufficiently high sampling frequency, as well as Assumptions 6 and 7 guarantee a bounded $\boldsymbol{\varepsilon}_{\text{indi}}$. This bound can also be further diminished by increasing the sampling frequency. By contrast, $\boldsymbol{\varepsilon}_{\text{ndi}}$ is independent of Δt , and its boundedness is undetermined under the same conditions. Therefore, for the feasibility of the NDI-SMC/SMDO design, the stricter Assumption 5 needs to be imposed.

6.2.3. COMPARISONS BETWEEN NDI AND INDI BASED SMC/SMDO

A block diagram is shown by Fig. 6.1, in which two switches are used to transform between NDI and INDI based SMC/SMDO. When these switches are connected to black solid lines, the INDI-SMC/SMDO control structure is activated, where the controller uses the measurements/estimations of $\hat{\mathbf{y}}_0$ and $\mathbf{u}_{\text{indi}}|_0$. On the contrary, when the switches are connected to blue dashed lines, the NDI-SMC/SMDO control structure is activated, which depends on the model $\mathbf{f}(\mathbf{x})$. This block diagram mainly illustrates the control structures, so the gain matrices \mathbf{K}_σ , \mathbf{K}_s can be different for these two approaches.

As can be seen from the derivations of NDI and INDI based SMC/SMDO and Fig. 6.1, the same SMC/SMDO design is used to compensate for different perturbations, $\boldsymbol{\varepsilon}_{\text{ndi}}$ and $\boldsymbol{\varepsilon}_{\text{indi}}$. The properties of these perturbations are crucial to the stability and robustness of the closed-loop systems. As discussed in subsection 6.2.2, $\boldsymbol{\varepsilon}_{\text{indi}}$ is bounded when the conditions in Theorem 5 are satisfied, while the boundedness of $\boldsymbol{\varepsilon}_{\text{ndi}}$ is undetermined under the same conditions. Moreover, it has been proved in [28] that there exists a Δt such that $\boldsymbol{\varepsilon}_{\text{indi}}$ has smaller bound as compared to $\boldsymbol{\varepsilon}_{\text{ndi}}$. This feature of the incremental framework is fundamentally beneficial to reducing the switching gains in SMC [28].

exists a Δt that ensures $\|(\mathbf{G}_f - \tilde{\mathbf{G}})\|\Delta \mathbf{u}_{\text{indi}}\| < \|(\mathbf{G}_f - \tilde{\mathbf{G}})\|\mathbf{u}_{\text{ndi}}\|$, when $\mathbf{u}_{\text{ndi}} \neq \mathbf{0}$. Moreover, system using the INDI control structure is only perturbed by δ_d instead of $\mathbf{f}_f - \tilde{\mathbf{f}}$. Consequently, after the fault occurs, if $\mathbf{d} \neq \mathbf{0}$, $\mathbf{u}_{\text{ndi}} \neq \mathbf{0}$, there exists a Δt , such that the upper bound of ϵ_{indi} is smaller than that of ϵ_{ndi} .

In summary, there exists a sampling interval Δt , such that in the perturbed circumstances, if $\mathbf{u}_{\text{ndi}} \neq \mathbf{0}$, the upper bound of ϵ_{indi} is smaller than that of ϵ_{ndi} , before and after the fault. Also, the upper bound of ϵ_{indi} can be further diminished by decreasing Δt . These properties of ϵ_{indi} can fundamentally reduce the control efforts of SMC/SMDO, because for most SMC and SMDO methods, the required switching gains are monotonically increasing functions of the uncertainty bounds. As a consequence, the SMC/SMDO designs based on the incremental control structure can achieve better performance and robustness using not only less model information but also reduced gains, as compared to those NDI based methods. The robustness of the incremental control structure is contributed by its sensor-based characteristic, that the uncertainties can be reduced by fully exploiting the measurements.

It is worth noting that ϵ_{indi} also has smaller variations in different fault cases, while the augmented uncertainty term $(\mathbf{f}_f - \tilde{\mathbf{f}}) + (\mathbf{G}_f - \tilde{\mathbf{G}})\mathbf{u}_{\text{ndi}}$ in ϵ_{ndi} is more fault-case dependent. Therefore, INDI-SMC/SMDO has the potential of passively resisting a wider range of perturbations, while gain adjustments may be required by NDI-SMC/SMDO in different fault scenarios.

The above analyses are conducted for generic nonlinear systems. The condition of “sufficiently high sampling frequency” may sound strict, but actually it is not difficult to find a reasonable Δt in practice. Further discussions about the selections of Δt can be found in [24]. In the following two sections, the benefits of INDI-SMC/SMDO will be demonstrated via both simulations and flight tests for a quadrotor fault tolerant control problem.

6.3. QUADROTOR FAULT-TOLERANT FLIGHT CONTROL

In order to compare the performance and robustness of NDI and INDI based SMC/SMDO, a quadrotor attitude control problem in the presence of model uncertainties, wind disturbances, and actuator faults will be considered in this section. The position control of quadrotors can be designed in the same way.

6.3.1. QUADROTOR MODEL

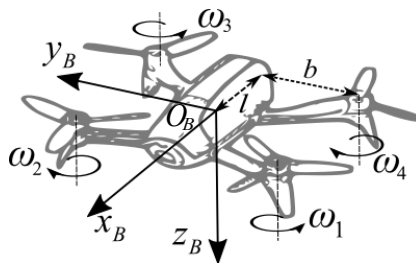


Figure 6.2: A Bebop 2 quadrotor and axes definition.

A Parrot Bebop 2 quadrotor is shown in Fig. 6.2. Denote the body frame as (O_B, X_B, Y_B, Z_B) , where O_B coincides with the aircraft center of mass, and $O_B X_B Z_B$ represents the aircraft symmetrical plane. The distances to each of the rotors along the $O_B X_B$ and $O_B Y_B$ axes are respectively given by l and b . The rotation rates of the four rotors are denoted by $\boldsymbol{\omega} = [\omega_1, \omega_2, \omega_3, \omega_4]^T$. The orientation of the vehicle is described by Euler angles $\boldsymbol{\theta} = [\phi, \theta, \psi]^T$. Assume $\theta \in (-\frac{\pi}{2}, \frac{\pi}{2})$, $\phi \in (-\frac{\pi}{2}, \frac{\pi}{2})$. Expressing the angular rate of the quadrotor in the body frame as $\boldsymbol{\Omega} = [p, q, r]^T$, then the kinematic equations for the Euler angles are:

$$\dot{\boldsymbol{\theta}} = \mathbf{R}_\theta(\boldsymbol{\theta})\boldsymbol{\Omega} \quad (6.32)$$

in which $\mathbf{R}_\theta(\boldsymbol{\theta})$ can be found in [40]. The quadrotor rotational dynamics are given by:

$$\mathbf{I}_v(\kappa)\dot{\boldsymbol{\Omega}} + \boldsymbol{\Omega} \times \mathbf{I}_v(\kappa)\boldsymbol{\Omega} = \mathbf{M}_c(\boldsymbol{\omega}^2, \kappa) + \mathbf{M}_a(\boldsymbol{\Omega}, \mathbf{V}_a, \kappa) + \mathbf{M}_r(\boldsymbol{\omega}, \dot{\boldsymbol{\omega}}, \boldsymbol{\Omega}, \mathbf{I}_{r_{zz}}(\kappa)) \quad (6.33)$$

where $\mathbf{I}_v(\kappa)$ is the inertia matrix of the whole quadrotor, $\mathbf{M}_a(\boldsymbol{\Omega}, \mathbf{V}_a, \kappa)$ is the aerodynamic moment vector, \mathbf{V}_a is the quadrotor airspeed, $\mathbf{M}_c(\boldsymbol{\omega}^2, \kappa)$ is the control moment vector. $\mathbf{M}_r(\boldsymbol{\omega}, \dot{\boldsymbol{\omega}}, \boldsymbol{\Omega}, \mathbf{I}_{r_{zz}}(\kappa))$ contains two parts: the gyroscopic moments of the rotors (as a function of $\boldsymbol{\omega}$, $\boldsymbol{\Omega}$, rotor inertia vector $\mathbf{I}_{r_{zz}}(\kappa)$), and also the spin-up torque of the rotors (as a function of $\dot{\boldsymbol{\omega}}$ and $\mathbf{I}_{r_{zz}}(\kappa)$). For the rotor failure cases considered in the present chapter, the fault indicator κ is introduced to \mathbf{I}_v , $\mathbf{I}_{r_{zz}}$, \mathbf{M}_c , \mathbf{M}_a in Eq. (6.33). On the one hand, rotor failures directly lead to changes in the rotor inertia $\mathbf{I}_{r_{zz}}$ and the inertia matrix of the whole quadrotor \mathbf{I}_v . On the other hand, rotor failures modify the aerodynamic properties of the vehicle, thus the aerodynamic moment \mathbf{M}_a and the control moment \mathbf{M}_c are also functions of κ .

The thrust and reactive torque of the rotors are approximately proportional to $\boldsymbol{\omega}^2$ [26, 41], and the proportionality coefficients are respectively denoted by k_i , λ_i , $i = 1, 2, 3, 4$. Therefore, using the geometry parameters shown in Fig. 6.2, \mathbf{M}_c and the total thrust T can be modeled by:

$$\begin{pmatrix} \mathbf{M}_c \\ T \end{pmatrix} = \begin{pmatrix} -bk_1 & bk_2 & bk_3 & -bk_4 \\ lk_1 & lk_2 & -lk_3 & -lk_4 \\ \lambda_1 & -\lambda_2 & \lambda_3 & -\lambda_4 \\ k_1 & k_2 & k_3 & k_4 \end{pmatrix} \boldsymbol{\omega}^2 \triangleq \mathbf{G}_m(\kappa)\boldsymbol{\omega}^2 \quad (6.34)$$

The spin-up torque in \mathbf{M}_r was neglected by most publications about quadrotor control, but it was shown in Ref. [26] via flight tests that this term is influential to the yaw channel control. However, if \mathbf{M}_r is incorporated into the controller design, the system dynamics become $\dot{\mathbf{x}} = \mathbf{f}(\mathbf{x}, \kappa) + \mathbf{G}(\mathbf{x}, \boldsymbol{\omega}, \dot{\boldsymbol{\omega}}, \boldsymbol{\omega}^2, \kappa)$, which is not affine in $\boldsymbol{\omega}$. Actually, because the incremental dynamic equation is derived by taking partial derivatives with respect to \mathbf{u} (Eq. (6.12)), the INDI control structure can also deal with non-affine in the control systems, as also shown in [24, 26]. In spite of this benefit of INDI, for fair comparisons with NDI-SMC/SMDO, \mathbf{M}_r is viewed as uncertainty in this chapter, and will be observed by a SMDO. Consequently, the dynamic model for controller design becomes affine in $\boldsymbol{\omega}^2$.

6.3.2. CONTROLLER DESIGN

The control objective is quadrotor attitude command tracking, i.e., $\boldsymbol{\theta} = [\phi, \theta, \psi]^T \rightarrow \boldsymbol{\theta}_c$. Considering the natural time-scale separation of the quadrotor dynamics [8, 26, 27], the

control law can be designed using two nested control loops. An alternative way is taking $\mathbf{y} = \boldsymbol{\theta}$, which makes the relative degree of \mathbf{y} with respect to $\boldsymbol{\omega}^2$ equals two. Non-cascaded controllers can then be designed analogous to Eqs. (6.10, 6.20) [24]. Since these two approaches are analogous, and the cascaded control structure is more widely used in aerospace systems, this chapter also designs the controllers in a cascaded way.

The inner-loop controller will be separately designed using NDI and INDI based SM-C/SMDO methods, aiming at $\boldsymbol{\Omega} \rightarrow \boldsymbol{\Omega}_c$, $T \rightarrow T_c$, where $\boldsymbol{\Omega}_c$ and T_c will be provided by the outer-loop controllers. In view of Eqs. (6.33, 6.34), the inner-loop dynamics are written as:

$$\begin{pmatrix} \dot{\boldsymbol{\Omega}} \\ T/m \end{pmatrix} = \begin{pmatrix} -\mathbf{I}_v^{-1}(\boldsymbol{\Omega} \times \mathbf{I}_v \boldsymbol{\Omega} - \mathbf{M}_a) \\ 0 \end{pmatrix} + \begin{pmatrix} \mathbf{I}_v^{-1} & \mathbf{0}_{3 \times 1} \\ \mathbf{0}_{1 \times 3} & 1/m \end{pmatrix} \mathbf{G}_m \boldsymbol{\omega}^2 + \begin{pmatrix} \mathbf{d}_1 + \mathbf{I}_v^{-1} \mathbf{M}_r \\ d_2 \end{pmatrix} \quad (6.35)$$

in which $\mathbf{d}_1 \in \mathcal{R}^3$, $d_2 \in \mathcal{R}$ represent external disturbances.

Remark 20 In Ref. [4, 5, 7, 9–12, 14], the control input vector is taken as $\mathbf{u} = [\mathbf{M}_c, T]^T$. This choice is deficient because only the uncertainties of \mathbf{I}_v can be considered in the controller designs. However, it is more difficult to estimate \mathbf{G}_m owing to the aerodynamic effects. Furthermore, actuator faults have the largest influences on \mathbf{G}_m . In addition, for real-life implementations, $\mathbf{u} = [\mathbf{M}_c, T]^T$ still needs to be converted into rotor speed commands. Therefore, this chapter takes $\mathbf{u} = \boldsymbol{\omega}^2$, and the rotor speed command vector is accordingly $\sqrt{\mathbf{u}}$.

Define $\mathbf{x} = [\boldsymbol{\Omega}, \int (T/m) dt]^T$, then Eq. (6.35) can be expressed in the form of Eq. (6.1). Following the procedures in subsection 6.2.1, the inner-loop control using NDI-SMC/SMDO is designed by Eq. (6.10). On the other hand, the INDI-SMC/SMDO controller is designed using the incremental dynamic equation, which is derived as:

$$\begin{pmatrix} \dot{\boldsymbol{\Omega}} \\ T/m \end{pmatrix} = \begin{pmatrix} \dot{\boldsymbol{\Omega}}_0 \\ T_0/m \end{pmatrix} + \begin{pmatrix} \boldsymbol{\delta}(\boldsymbol{\Omega}, \mathbf{V}_a, \kappa, \Delta t) \\ 0 \end{pmatrix} + \begin{pmatrix} \mathbf{I}_v^{-1} & \mathbf{0}_{3 \times 1} \\ \mathbf{0}_{1 \times 3} & 1/m \end{pmatrix} \mathbf{G}_m \Delta \boldsymbol{\omega}^2 + \begin{pmatrix} \Delta \mathbf{d}_1 + \boldsymbol{\delta}_{M_r} \\ \Delta d_2 \end{pmatrix} \quad (6.36)$$

where

$$\begin{aligned} \boldsymbol{\delta}(\boldsymbol{\Omega}, \mathbf{V}_a, \kappa, \Delta t) &= \left. \frac{\partial [\mathbf{I}_v^{-1}(-\boldsymbol{\Omega} \times \mathbf{I}_v \boldsymbol{\Omega} + \mathbf{M}_a)]}{\partial \boldsymbol{\Omega}} \right|_0 \Delta \boldsymbol{\Omega} + \left. \frac{\partial [\mathbf{I}_v^{-1}(-\boldsymbol{\Omega} \times \mathbf{I}_v \boldsymbol{\Omega} + \mathbf{M}_a + \mathbf{M}_c)]}{\partial \kappa} \right|_0 \Delta \kappa \\ &\quad + \left. \frac{\partial [\mathbf{I}_v^{-1} \mathbf{M}_a]}{\partial \mathbf{V}_a} \right|_0 \Delta \mathbf{V}_a + \mathbf{R}'_1 \end{aligned} \quad (6.37)$$

and with $\boldsymbol{\delta}_{M_r}$ representing the variations of $\mathbf{I}_v^{-1} \mathbf{M}_r$ in one incremental time step. \mathbf{R}'_1 is the Taylor's expansion remainder of Eq. (6.36). According to the physical time-scale separations of quadrotor dynamics, the variations of velocities are slower than the variations of angular rates. Also, since \mathbf{V}_a is a continuous function of time, $\|\Delta \mathbf{V}_a\|$ vanishes to zero as Δt approaches zero. Following the procedures in subsection 6.2.2, the inner-loop control using INDI-SMC/SMDO is then designed by Eq. (6.20).

After the design of the inner-loop controllers using both NDI and INDI based SM-C/SMDO, the outer-loop controllers are designed to provide the commands $\boldsymbol{\Omega}_c$ and T_c . $\boldsymbol{\Omega}_c$ is designed to achieve attitude control: $\boldsymbol{\theta} \rightarrow \boldsymbol{\theta}_c$, while T_c is designed to control height: $h \rightarrow h_c$.

Recall Eq. (6.32), since there is no model uncertainty in this kinematic equation, a simple NDI controller can be adopted. Design the virtual control as $\mathbf{v}_{att} = \dot{\boldsymbol{\theta}}_c + \mathbf{K}_{att}(\boldsymbol{\theta}_c - \boldsymbol{\theta})$, $\mathbf{K}_{att} = \text{diag}\{K_{att_i}\}$, $K_{att_i} > 0$, $i = 1, 2, 3$, then the reference for the angular rates is designed as $\boldsymbol{\Omega}_c = \mathbf{R}_\theta^{-1}(\boldsymbol{\theta})\mathbf{v}_{att}$. $\mathbf{R}_\theta(\boldsymbol{\theta})$ is invertible when $\theta \in (-\frac{\pi}{2}, \frac{\pi}{2})$.

For the height control, define the position vector as $\mathbf{P} = [x, y, -h]^T$, then its dynamics are given as:

$$\ddot{\mathbf{P}} = \mathbf{g} + \mathbf{R}_{IB}(\mathbf{F}_a + \mathbf{T})/m \quad (6.38)$$

where $\mathbf{g} = [0, 0, g]^T$ is the gravitational acceleration vector, \mathbf{R}_{IB} is the rotational matrix from the body frame to the inertial frame. \mathbf{F}_a is the aerodynamic force vector expressed in the body frame, and $\mathbf{T} = [0, 0, -T]^T$ is the thrust vector. Denote the z component of $\ddot{\mathbf{P}}$ as a_z , and assume the aerodynamic force in the $O_B Z_B$ direction is negligible as compared to thrust, then the last row of Eq. (6.38) is written as $a_z = g - (\cos\theta\cos\phi)T/m$. Design the command for a_z as $a_{z_c} = -\ddot{h}_c - K_d(\dot{h}_c - \dot{h}) - K_p(h_c - h)$, $K_d > 0$, $K_p > 0$, then the command for thrust is accordingly given by $(T_c/m) = (g - a_{z_c})/(\cos\theta\cos\phi)$.

At this point, the height, attitude, and angular rate controllers have been completely designed. In order to enforce the natural time-scale separations in the closed-loop system, the gain matrices \mathbf{K}_c , \mathbf{K}_{att} , need to fulfill $\min(K_{c_i}) > \max(K_{att_i})$ for roll, pitch, and yaw control channels.

6.4. NUMERICAL VALIDATIONS

In this section, the controllers designed in Sec. 6.2 and Sec. 6.3 will be evaluated in the Matlab/Simulink environment. Two models for a Parrot Bebop quadrotor are set up. One high fidelity model identified from wind tunnel test data [41] is used for simulations. Another simplified model, which excludes aerodynamic effects, gyroscopic moments and spin-up torque, is used by the controllers. It is worth noting that neglecting these factors in quadrotor control design is a common practice. The actuator dynamics are modeled as first-order low-pass filters with time constants of 0.02 s. The maximum and minimum rotational speed of the rotors are 12000 revolutions per minute (rpm) and 3000 rpm respectively. The controller sampling frequency is 500 Hz.

Three perturbation sources are evaluated: model uncertainties, wind disturbances and sudden actuator faults during flight.

For the model uncertainties, the inertia matrix $\bar{\mathbf{I}}_v$ used by on-board controllers equals 70% of the nominal \mathbf{I}_v . The mismatch between \mathbf{I}_v and $\bar{\mathbf{I}}_v$ brings model uncertainties to both \mathbf{f} and \mathbf{G} . The \mathbf{G}_m matrix used for simulations is time varying because k_i , λ_i , $i = 1, 2, 3, 4$ are influenced by the aerodynamic conditions (airspeed, air density, etc.). However, for the simplicity of implementation, constant $\bar{\mathbf{G}}_m$ matrix evaluated at the hover condition is used by the controllers, which brings model mismatches even without actuator fault.

Remark 21 The pure INDI control designed for a quadrotor in Ref. [26] identifies the time varying control effectiveness matrix during flight. This system identification based adaption is a modular approach, whose stability cannot be ensured. The usage of constant control effectiveness matrix in this chapter is simpler, and the corresponding uncertainties can be compensated by SMC/SMDO.

The airspeed V_a of a quadrotor equals $V - V_w$ [40], where V is the ground speed, and V_w denotes the velocity of the atmosphere relative to the inertial frame. In this chapter, V_w is considered as the “1-cos” gust [42]. As shown in Fig. 6.3, gusts are added along the x and y directions of the inertial frame. The maximum gust velocity equals 3 m/s. Since the airspeed V_a contains V_w , the dynamic pressure and the angle of attack of the rotor system are influenced by V_w . Consequently, the thrust, in-plane forces, and moments on each rotor are affected by V_w . As mentioned in Sec. 6.3, these aerodynamic effects caused by V_w are viewed as external disturbances. For more details about the influences of atmospheric disturbances on the quadrotors, readers are recommended to Ref. [29].

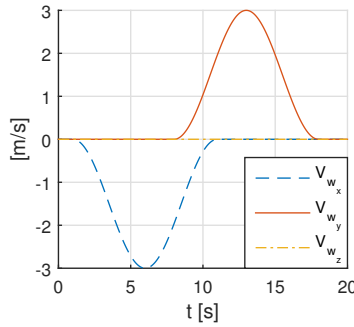


Figure 6.3: Wind disturbances.

Finally, to model a sudden fault of the i -th rotor during flight, for $t \geq t_f$, the corresponding effectiveness in \mathbf{G}_m is scaled in the simulation model, i.e., $k_i' = \mu_i k_i$, $\lambda_i' = \mu_i \lambda_i$, $\mu_i \in (0, 1]$. However, in spite of faults, constant \mathbf{G}_m matrix is consistently used by both controllers.

The attitude commands are smoothly combined sigmoid functions (shown in Fig. 6.4 and Fig. 6.8) as continuous realizations of doublet signals. These commands on different channels have phase shifts with each other, in which way the decoupling performance of the controllers can be evaluated. The height command is $h = 1$ m. The initial conditions are $\phi(t=0) = 0^\circ$, $\theta(t=0) = 0^\circ$, $\psi(t=0) = 0^\circ$, $h(t=0) = 0$ m.

The main focus of this chapter is on the comparisons between NDI and INDI based SMC/SMDO designs, so the outer-loop controllers are kept identical. The gains used by the outer-loop controllers are: $K_p = 10$, $K_d = 5$, $\mathbf{K}_{att} = \text{diag}([2, 2, 1])$, $\mathbf{K}_c = \text{diag}([8, 8, 6])$. Trade-offs should be made when tuning the inner-loop parameters: \mathbf{K}_σ , \mathbf{K}_s , and the filter time constants τ_i . High \mathbf{K}_σ gains can accelerate the convergence of σ , but will amplify measurement noise at the meanwhile. Trade-offs also exist in tuning the filter parameters in SMDO. Specifically, high cut-off frequency introduces more chattering and noise into $\hat{\mathbf{v}}_{\text{eq}}$, but low cut-off frequency increases the observation errors $\mathcal{O}(\tau_i)$. For fair comparison, $\mathbf{K}_\sigma = \text{diag}([0.5, 0.5, 0.5, 1])$, and $\boldsymbol{\tau} = [0.05, 0.05, 0.08, 0.05]^T$ are used by both NDI and INDI based SMC/SMDO controllers. The filter time constant in the yaw channel is larger for suppressing the oscillations caused by the spin-up torque.

The gain requirements presented in Eqs. (6.8, 6.19) are the minimum possible gains for enforcing sliding motions [15–18]. Since $\boldsymbol{\varepsilon}_{\text{ndi}}$ and $\boldsymbol{\varepsilon}_{\text{indi}}$ are time-varying, the minimum possible gains are also time-varying. The dual layer nested adaptive methodology

in [18] can be used to adjust the gains online. In subsection 6.2.3, it has been shown that there exists a Δt , such that the upper bound of ϵ_{indi} is smaller than that of ϵ_{ndi} , in the presence of model uncertainties, wind disturbances, and sudden faults. Moreover, ϵ_{indi} also has smaller variations in different fault cases. Because of these merits, the required \mathbf{K}_s gains for INDI-SMC/SMDO are lower and need less adjustments. For the simplicity of implementation, constant \mathbf{K}_s gains will be used by both NDI and INDI based SMC/SMDO. In the following two subsections, the robustness and chattering magnitude of the two methods will be compared.

6.4.1. SIMULATION RESULTS OF NDI-SMC/SMDO

Fig. 6.4 illustrates the tracking performance of NDI-SMC/SMDO. In all of the three different cases, model uncertainties and wind disturbances are incorporated, while the degree of actuator faults varies. Without loss of generality, sudden effectiveness losses are imposed on the third rotor at $t = 5$ s, which are reflected by the abrupt tracking overshoots in Fig. 6.4. Regardless of these overshoots, the quadrotor using NDI-SMC/SMDO control is able to recover from faults within seconds, and resist the perturbations of model uncertainties and wind disturbances at the same time. However, the tracking and decoupling performance of this controller indeed deteriorates with the increases of fault degree.

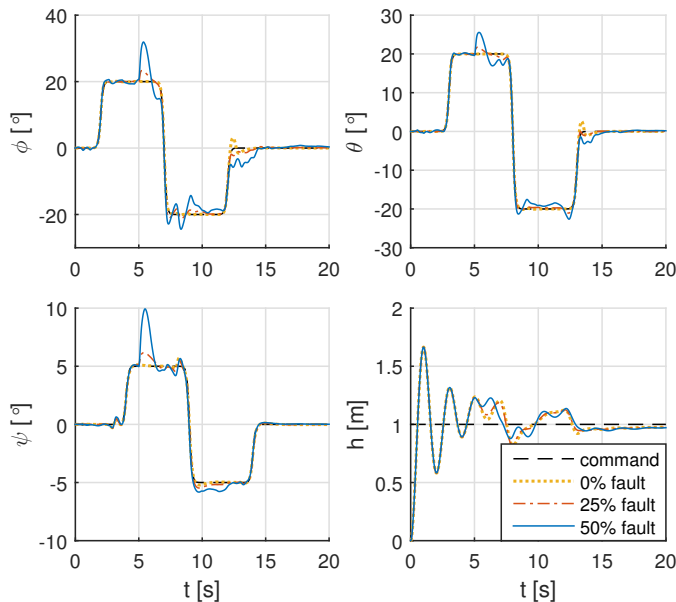


Figure 6.4: Quadrotor responses under NDI-SMC/SMDO control.

The responses of the sliding variables σ are shown in Fig. 6.5, as consistent with the analyses in Sec. 6.2, σ asymptotically converges to the sliding surface. Additionally, $\|\sigma\|$ distinctly increases after the actuator fault occurs, and $\|\sigma\|$ is positively correlated to the fault degree. It can also be observed from Fig. 6.5 that the auxiliary sliding variable s

converges in finite time under perturbations. The high frequency switchings of \mathbf{s} (which is normal [19]) will not influence the continuity of \mathbf{u} because of the filtering process in SMDO.

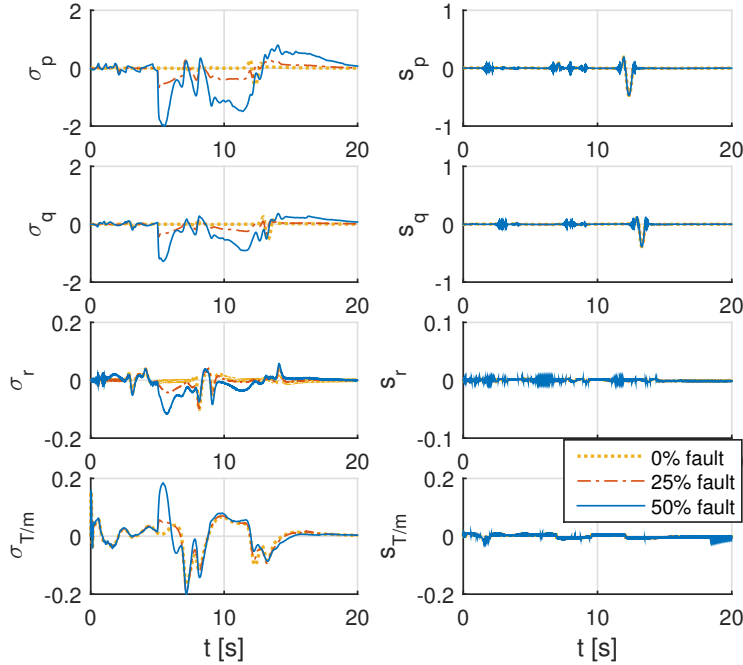


Figure 6.5: Responses of sliding variables under NDI-SMC/SMDO control.

One core parameter that guarantees the convergence of \mathbf{s} is \mathbf{K}_s . As proved by Eqs. (6.8) and (6.9), the elements of \mathbf{K}_s need to be larger than the uncertainty bounds. In view of Eq. (6.7) and the discussions in subsection 6.2.3, the uncertain term $\boldsymbol{\varepsilon}_{\text{ndi}}$ is influenced by all the three perturbation sources. Moreover, owing to the term $(\mathbf{f}_f - \hat{\mathbf{f}}) + (\mathbf{G}_f - \hat{\mathbf{G}})\mathbf{u}_{\text{ndi}}$, $\|\boldsymbol{\varepsilon}_{\text{ndi}}\|$ varies significantly for different fault cases. This is verified by Fig. 6.6, which presents abrupt increases of $\|\boldsymbol{\varepsilon}_{\text{ndi}}\|$ after $t = 5$ s, and also strong correlations of $\|\boldsymbol{\varepsilon}_{\text{ndi}}\|$ with the fault degree. As a consequence, the \mathbf{K}_s used in NDI-SMC/SMDO must be adapted or manually adjusted in different scenarios. For the simulation cases shown in Fig. 6.6, $\mathbf{K}_s = \text{diag}([4, 5, 3, 8])$ is used when no actuator fault occurs. To guarantee the convergence of \mathbf{s} , \mathbf{K}_s needs to be increased to $\text{diag}([50, 40, 4, 10])$ for the '25% fault' case, and be further raised to $\text{diag}([150, 90, 5, 12])$ when half of the rotor effectiveness is lost. These gain increases induce a side effect, chattering. As illustrated by Fig. 6.6, the oscillation magnitudes of $\hat{\mathbf{v}}_{\text{eq}}$ increase with the rise of \mathbf{K}_s .

Furthermore, in view of Eq. (6.10), an increase of \mathbf{K}_s will lead to the oscillations in the control input. It can be seen from Fig. 6.7 that even though filtered by the actuator dynamics, the measured (without noise in simulations) rotor speeds are still oscillating. In addition, ω_3 in Fig. 6.7 increases after $t = 5$ s to compensate for the effectiveness loss.

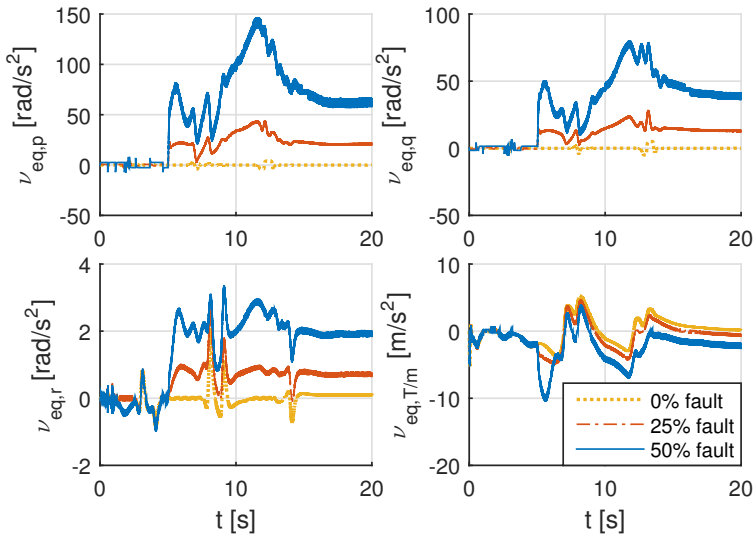


Figure 6.6: Observed uncertainties $\hat{\mathbf{v}}_{eq}$ under NDI-SMC/SMDO control.

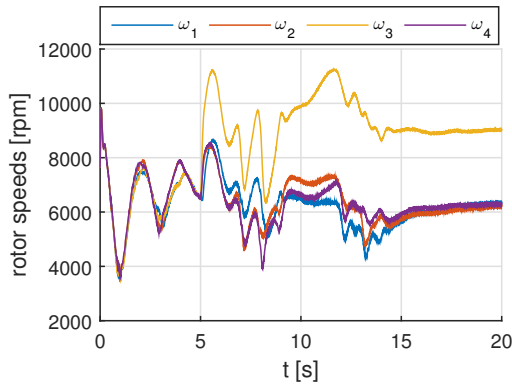


Figure 6.7: Measured rotor speeds under NDI-SMC/SMDO control in the '50% fault' case.

6.4.2. SIMULATION RESULTS OF INDI-SMC/SMDO

In this subsection, the same fault scenarios will be used to test the effectiveness of INDI-SMC/SMDO.

When comparing Fig. 6.8 with Fig. 6.4, obvious tracking performance improvements of INDI based control can be observed. The effectiveness of INDI-SMC/SMDO is hardly influenced by the perturbations, and only small ripples appear after $t = 5$ s.

The responses of the sliding variables in Fig. 6.9 also show improvements when compared to the responses in Fig. 6.5. Specifically, $|\sigma_p|$, $|\sigma_q|$ under INDI-SMC/SMDO are one order of magnitude smaller than the values using NDI-SMC/SMDO control. Moreover, σ in Fig. 6.9 has a higher convergence rate, and smaller variations. The auxiliary sliding variable \mathbf{s} also shows smaller fluctuations in Fig. 6.9.

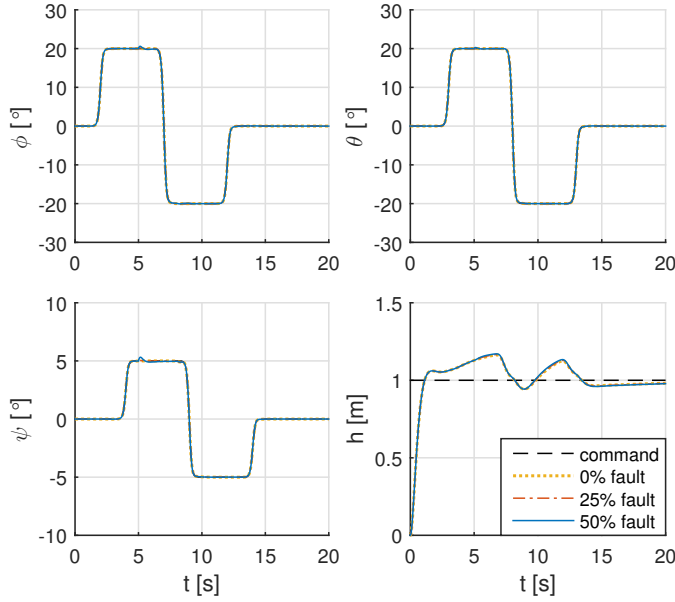


Figure 6.8: Quadrotor responses under INDI-SMC/SMDO control.

The main reason for the performance and robustness improvements of INDI based SMC/SMDO can be seen from Fig. 6.10. Since \mathbf{s} in both Fig. 6.5 and Fig. 6.9 converges, $\hat{\mathbf{v}}_{eq}$ in Fig. 6.6 and Fig. 6.10 can respectively estimate $-\boldsymbol{\varepsilon}_{ndi}$ and $-\boldsymbol{\varepsilon}_{indi}$. According to the analyses in subsection 6.2.3, the upper bound of $\boldsymbol{\varepsilon}_{indi}$ is smaller than that of $\boldsymbol{\varepsilon}_{ndi}$, in the presence of faults, model uncertainties and disturbances. This is verified by comparing Fig. 6.10 with Fig. 6.6, where $|v_{eq,p}|$ and $|v_{eq,q}|$ are two orders of magnitude smaller under INDI based SMC/SMDO control than NDI based in the ‘50% fault’ case. Also, $|v_{eq,r}|$ and $|v_{eq,T/m}|$ are one order of magnitude smaller under INDI-SMC/SMDO control. Furthermore, as illustrated in Fig. 6.10, since $\boldsymbol{\delta}_\kappa(\mathbf{x})\Delta\kappa$ is only non-zero for $t_f \leq t < t_f + \Delta t$ (subsection 6.2.3), $\boldsymbol{\varepsilon}_{indi}$ has comparable bounds before and after a sudden fault. Furthermore, according to Eq. (6.18), after a fault occurs, the term $\boldsymbol{\delta}_d + (\mathbf{G}_f - \bar{\mathbf{G}})\Delta\mathbf{u}_{indi}$ is added to $\boldsymbol{\varepsilon}_{indi}$, which also has smaller changes in different fault cases as verified by Fig. 6.10.

These beneficial properties of $\boldsymbol{\varepsilon}_{indi}$ allow a lower and fixed gain matrix $\mathbf{K}_s = \text{diag}([2, 2, 0.5, 1])$ to be used for resisting all the tested perturbations, which simplifies the implementation process, and fundamentally reduces the chattering effects of SMC/SMDO. As can be seen by comparing Fig. 6.10 with Fig. 6.6, the uncertainty observations $\hat{\mathbf{v}}_{eq}$ are much smoother when using INDI-SMC/SMDO. The rotor speeds in Fig. 6.11 are also much smoother than those shown in Fig. 6.7.

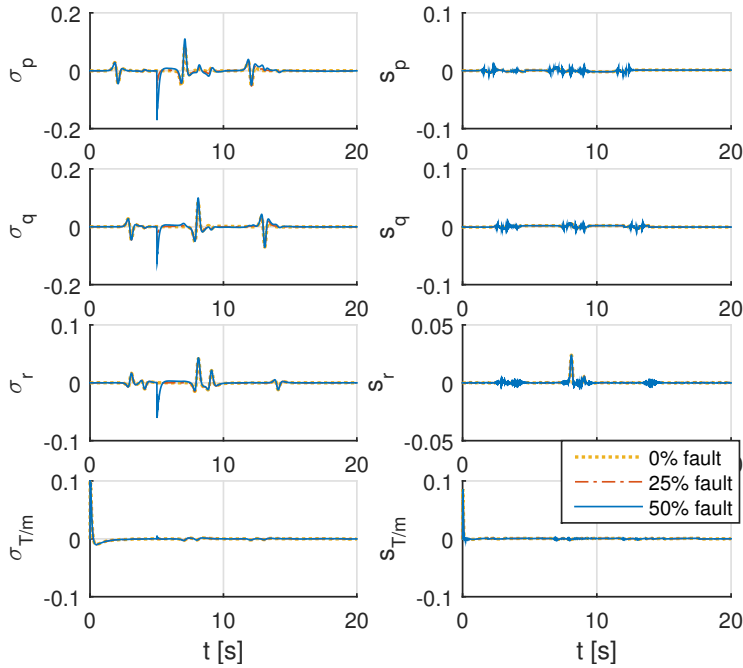


Figure 6.9: Responses of sliding variables under INDI-SMC/SMDO control.

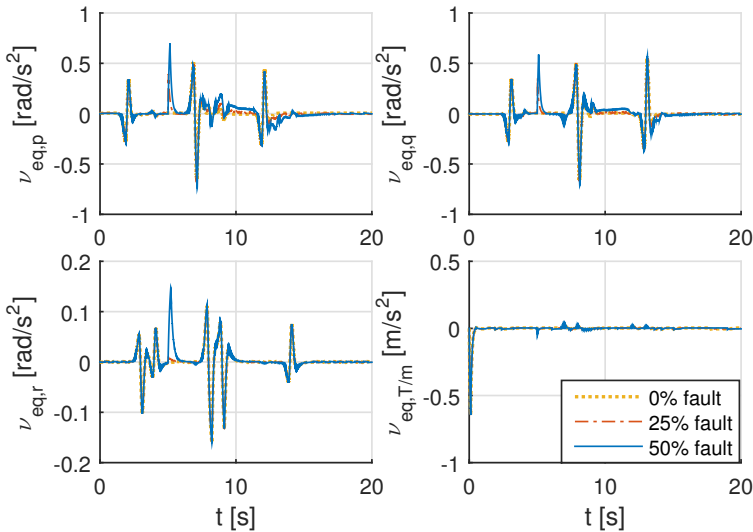


Figure 6.10: Observed uncertainties $\hat{\nu}_{eq}$ under INDI-SMC/SMDO control.

6.5. EXPERIMENTAL VALIDATIONS

6.5.1. EXPERIMENTAL SETUP

The performance and robustness of the proposed INDI-SMC/SMDO controller are further validated via flight tests. These experiments are conducted using a Parrot Bebop

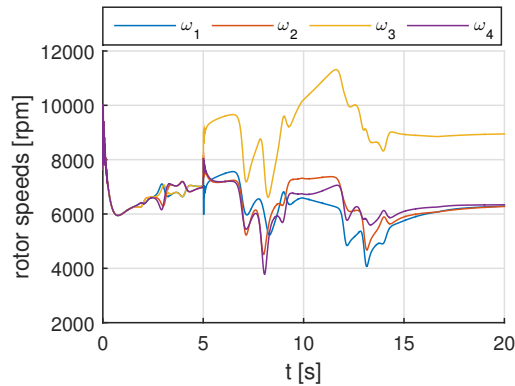


Figure 6.11: Measured rotor speeds under INDI-SMC/SMDO control in the '50% fault' case.

2 quadrotor as shown in Fig. 6.12. The control laws are executed on-board using an open-source autopilot software, Paparazzi, which is able to read the MPU 6050 inertia measurement unit (IMU) measurements and drive the motors at 512 Hz. The position and attitude are measured by external motion capture system (OptiTrack) in 120 Hz and transmitted to the on-board controller via Wi-Fi.



Figure 6.12: A Bebop 2 quadrotor with one damaged rotor.

Some practical issues should be considered before implementing the INDI-SMC/SMDO control law. The first issue is the way of obtaining $\mathbf{\Omega}_0$ when applying Eqs. (6.20, 6.36) in the inner-loop. The feasibility of directly measuring $\mathbf{\Omega}_0$ via angular accelerometers has been demonstrated in Ref. [43]. Another simple way is estimating $\mathbf{\Omega}_0$ from gyroscope measurements using a wash-out filter [26]. To deal with the corresponding lag, the input signal should be synchronized with the estimations. Since this way of estimation and synchronization has been verified via both passenger aircraft and quadrotor flight tests [23, 26, 27], it is also adopted in the present flight tests. T_0/m in Eq. (6.36) is calculated from the specific force measured by linear accelerometers. The rotor speed $u_{\text{indi}i0}$ is measured by the Brushless DC Motor Driver of the Bebop2 quadrotor.

The outer-loop controllers used in flight tests are identical with the simulated controllers. For the inner-loop, \mathbf{K}_σ is still equal to $\text{diag}([0.5, 0.5, 0.5, 1])$, while $\boldsymbol{\tau}$ is increased to $[0.1, 0.1, 0.17, 0.1]^T$ for attenuating the measurement noise. An estimated constant control effectiveness matrix $\bar{\mathbf{G}}$ is used by both NDI and INDI based controllers. The nominal model $\bar{\mathbf{f}}$ used by NDI-SMC/SMDO is a hover model which excludes aerodynamic effects, gyroscopic moments and spin-up torque. As shown in Eqs. (6.14, 6.20), INDI-SMC/SMDO does not need the model information $\bar{\mathbf{f}}$.

Both controllers are evaluated in two scenarios: with and without actuator faults. Even if four unbroken rotors are equipped, model mismatches still exist, which become more conspicuous when airspeed increases during maneuvers. For the faulty configuration, the diameter of the right rear rotor disk (third) is reduced by 5 cm as shown by Fig. 6.12, which approximately reduce its effectiveness by 55% according to flight test results.

6.5.2. FLIGHTS WITHOUT ACTUATOR FAULT

The SMDO gain matrix $\mathbf{K}_s = \text{diag}([20, 20, 1, 1])$ is used by INDI-SMC/SMDO in flight tests. The \mathbf{K}_s used by NDI-SMC/SMDO is first tuned to be identical to the INDI based, as denoted by ‘NDI-S/S’ in the subsequent figures, then it is increased to ensure the convergence of \mathbf{s} as denoted by ‘NDI-S/S-HG’.

Fig. 6.13 illustrates the responses of a quadrotor tracking a filtered doublet pitch angle command. When using INDI-SMC/SMDO control, the quadrotor performs the best with smallest overshoots and tracking errors. Although NDI based SMC/SMDO control using the same \mathbf{K}_s is able to follow the command, large transition errors are present. This performance deterioration is mainly caused by model uncertainties. As also shown by Fig. 6.14, ‘NDI-S/S’, which uses the same \mathbf{K}_s as ‘INDI-S/S’, is unable to adequately observe the uncertainties in pitch, yaw and thrust channels. The large variations of $\boldsymbol{\epsilon}_{\text{ndi}}$ can only be observed when \mathbf{K}_s is raised to $\text{diag}([20, 50, 20, 10])$, as shown by the high-gain ‘NDI-S/S-HG’ in Fig. 6.14. This high-gain controller performs better than the low-gain ‘NDI-S/S’, but is still inferior than INDI based SMC/SMDO as illustrated by Fig. 6.13.

It can also be seen from Fig. 6.14 that the observed uncertainties under INDI based control have smaller variations. Increasing the switching gains in NDI-SMC/SMDO can better observe $\boldsymbol{\epsilon}_{\text{ndi}}$, but consequently cause severe oscillations, especially in pitch and yaw channels.

The responses of the sliding variables are presented in Fig. 6.15. As is consistent with the above analyses, using the same \mathbf{K}_s with INDI based control is insufficient for NDI-SMC/SMDO, because s_r diverges, and s_q, s_T are absent from the sliding surfaces for about two seconds. Moreover, σ_r under low-gain NDI based control also diverges. High-gain NDI-SMC/SMDO can enforce the convergence of $\boldsymbol{\sigma}$ and \mathbf{s} . However, severe oscillations in s_q are present, and the convergence of $\sigma_q, \sigma_{T/m}$ is still slower than the response under INDI-SMC/SMDO control.

6.5.3. FLIGHTS WITH ACTUATOR FAULT

This subsection presents the flight test results of NDI and INDI based SMC/SMDO controllers applied to a quadrotor with one damaged rotor (Fig. 6.12). As verified by simulations, INDI based SMC/SMDO is able to passively tolerate actuator faults and model

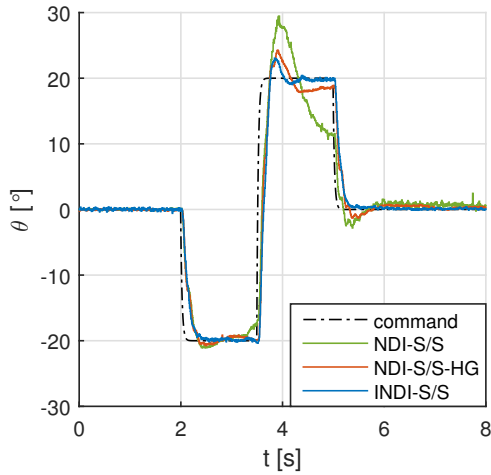
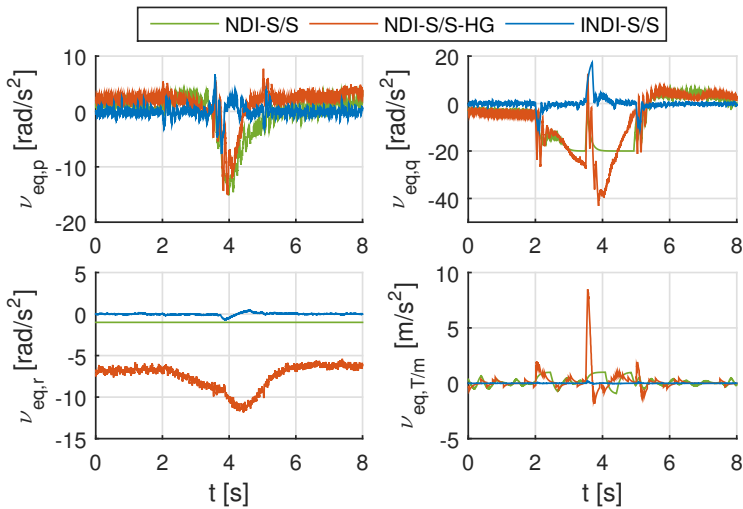


Figure 6.13: Quadrotor tracking responses without actuator fault.

Figure 6.14: Observed uncertainties $\hat{\mathbf{v}}_{eq}$ without actuator fault.

uncertainties, thus the same SMDO gain matrix $\mathbf{K}_s = \text{diag}([20, 20, 1, 1])$ is still used by the faulty quadrotor. However, this gain matrix is insufficient for NDI based SMC/SMDO, even without actuator fault, as shown in the previous subsection. Therefore, in this subsection, it is going to be evaluated whether NDI based SMC/SMDO can passively resist the actuator fault without gain adjustment. Namely, $\mathbf{K}_s = \text{diag}([20, 50, 20, 10])$ is used by NDI based controller first, as denoted by ‘NDI-S/S-HG’ in the subsequent figures.

Fig. 6.16 shows that although the faulty quadrotor can follow the trend of command without gain adjustment, its performance deteriorates. Recall from Eq. (6.7) that ac-

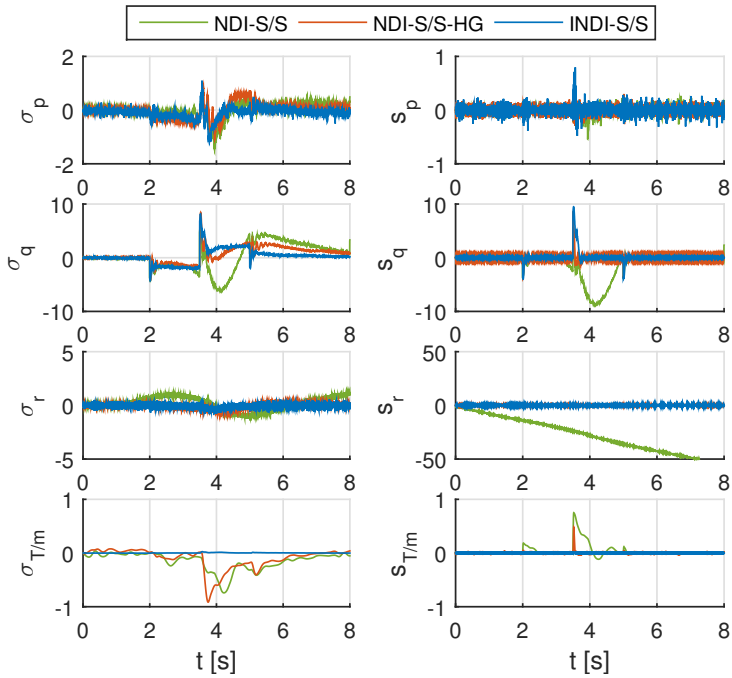


Figure 6.15: Sliding variable responses without actuator fault.

6

tuator faults introduce $(\mathbf{f}_f - \bar{\mathbf{f}}) + (\mathbf{G}_f - \bar{\mathbf{G}})\mathbf{u}_{\text{ndi}}$ into $\boldsymbol{\varepsilon}_{\text{ndi}}$. This term causes large variations in $\|\boldsymbol{\varepsilon}_{\text{ndi}}\|$ after fault occurs because \mathbf{u}_{ndi} is far from zero for trimming the quadrotor. Therefore, as exposed by Fig. 6.17, the gain matrix tuned for the fault-free case is insufficient, which leads to saturations in the observed uncertainties in the pitch and roll channels. In order to fully observe the uncertainties, \mathbf{K}_s needs to be increased to $\text{diag}([80, 100, 20, 10])$ according to the flight test results. This very high gain control case is denoted by ‘NDI-S/S-VHG’ in Fig. 6.16-6.19. This controller with even higher switching gains can better observe $-\boldsymbol{\varepsilon}_{\text{ndi}}$ as shown in Fig. 6.17, and consequently improve the tracking performance as illustrated in Fig. 6.16.

On the contrary, INDI-SMC/SMDO is able to tolerate the actuator fault passively *without any* gain adjustment. In view of Fig. 6.17, the observed $-\boldsymbol{\varepsilon}_{\text{indi}}$ has much smaller oscillations as compared to the observed $-\boldsymbol{\varepsilon}_{\text{ndi}}$. Moreover, as shown in Fig. 6.16, INDI-SMC/SMDO performs the best with smallest transition errors. Analogous to the above analyses, when using NDI-SMC/SMDO control without gain adjustment, s_p diverges and s_q is absence from the sliding surface throughout the maneuvering time period, as illustrated by Fig. 6.18. Even though without gain adaption, the sliding variables $\boldsymbol{\sigma}$ and \mathbf{s} under INDI-SMC/SMDO control have the highest convergence rates and lightest oscillations among all the tested controllers.

Reducing the switching gains is crucial for chattering reduction of SMC/SMDO methods. As verified by both simulations and flight tests, the filtering process in SMDO can only attenuate instead of rejecting the oscillations in $\hat{\mathbf{v}}_{\text{eq}}$. Therefore, the lower gains

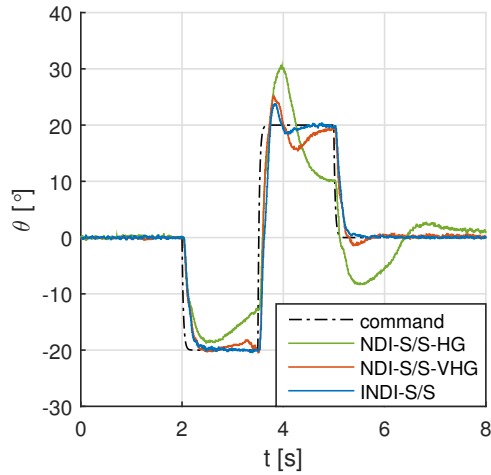


Figure 6.16: Quadrotor tracking responses with actuator fault.

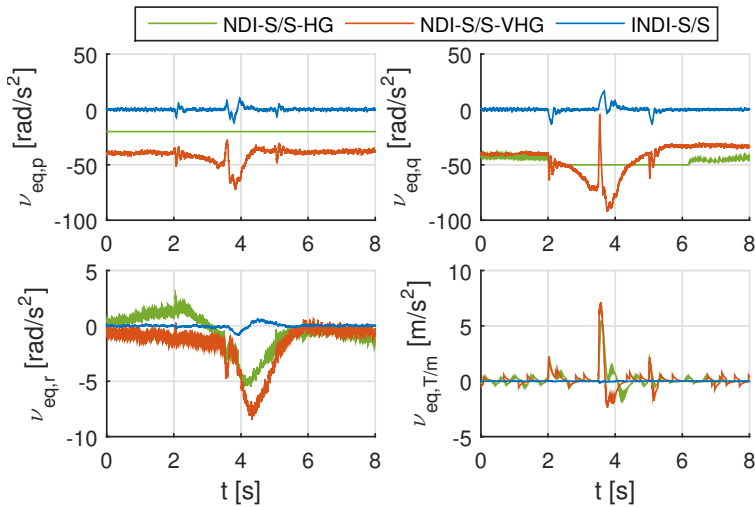


Figure 6.17: Observed uncertainties $\hat{\mathbf{v}}_{eq}$ with actuator fault.

used by INDI-SMC/SMDO also lead to lighter oscillations in $\hat{\mathbf{v}}_{eq}$ (Fig. 6.10, 6.14, 6.17) and in the rotor speeds (Fig. 6.11).

The rotor speeds under the control of very-high-gain NDI-SMC/SMDO and INDI-SMC/SMDO are shown in Fig. 6.19. The first rotor get saturated at 3000 rpm for 0.3 s under NDI-SMC/SMDO control, while the rotor speeds are within limits using INDI-SMC/SMDO. Owing to the measurement noise, the chattering reduction advantage of INDI based SMC/SMDO becomes less obvious in Fig. 6.19, where the rotor speeds using NDI and INDI based controllers seem to have comparable oscillations.

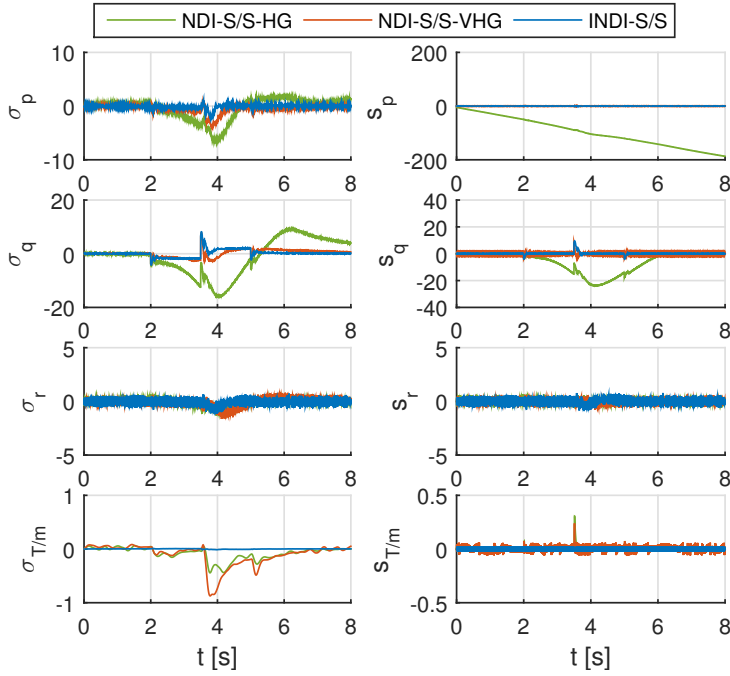


Figure 6.18: Sliding variable responses with actuator fault.

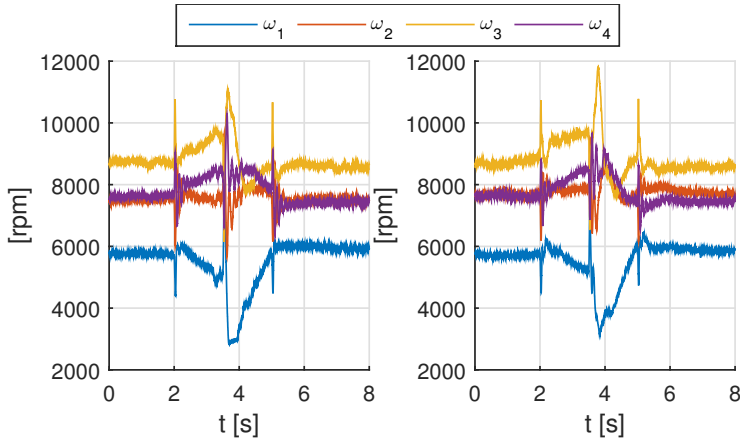


Figure 6.19: Rotor speeds using NDI (left) and INDI (right) based SMC/SMDO in the faulty condition.

The reason behind this phenomenon can be better revealed in the frequency domain. Divide \mathbf{u}_{ndi} (Eq. (6.10)) into $\mathbf{u}_{\text{ndi},s} = \bar{\mathbf{G}}^{-1}(\mathbf{K}_\sigma \boldsymbol{\sigma} + \hat{\mathbf{v}}_{\text{eq}})$ (the contributions of SMC/S-MDO), and $\mathbf{u}_{\text{ndi},c} = \bar{\mathbf{G}}^{-1}\bar{\boldsymbol{\Psi}}$ (the contributions of the traditional NDI). Also, \mathbf{u}_{indi} (Eq. (6.20)) is divided into $\mathbf{u}_{\text{indi},s} = \bar{\mathbf{G}}^{-1}(\mathbf{K}'_\sigma \boldsymbol{\sigma} + \hat{\mathbf{v}}'_{\text{eq}})$ and $\mathbf{u}_{\text{indi},c} = \mathbf{u}_{\text{indi}|_0} + \bar{\mathbf{G}}^{-1}\bar{\boldsymbol{\Psi}}'$. The power spec-

tral densities (PSD) of u_{ndi,s_i} and u_{indi,s_i} , $i = 1, 2, 3, 4$ for the four rotors are illustrated in the left subplot of Fig. 6.20, where it can be seen that $P_{uu,\text{indi},s}$ is lower than $P_{uu,\text{ndi},s}$ in most frequency ranges. This verifies that the control efforts of SMC/SMDO is indeed released using the INDI control structure, and the chattering is reduced in $u_{\text{indi},s}$. On the other hand, INDI-SMC/SMDO is contributed more by $u_{\text{indi},c}$, which has less model dependency than $u_{\text{ndi},c}$ but relies more on sensor measurements. The corresponding measurement noise in $u_{\text{indi},c}$ conceals the benefit of $u_{\text{indi},s}$ in high frequency range, and leads to a comparable PSD of the overall u_{indi} and u_{ndi} as illustrated by the right subplot of Fig. 6.20. The noise level in $u_{\text{indi},c}$ can be reduced by using better sensors, which can be easier than perfecting the model used by NDI-SMC/SMDO.

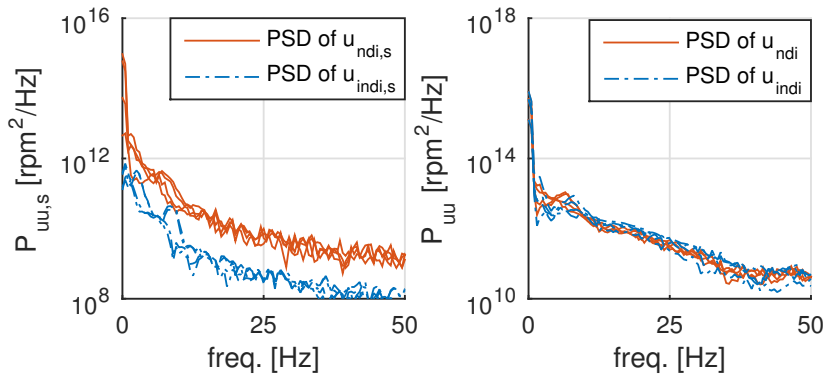


Figure 6.20: The left subplot presents the PSD of $u_{\text{ndi},s}$, $u_{\text{indi},s}$, while the right shows the PSD of u_{ndi} , u_{indi} .

6.6. CONCLUSIONS

A control method named INDI-SMC/SMDO, which designs the sliding mode control (SMC) driven by sliding mode disturbance observers (SMDO) based on the control structure of incremental nonlinear dynamics inversion (INDI) is proposed in this chapter. By virtue of the sensor-based characteristic of INDI, SMC/SMDO designs based on INDI require less model knowledge than designs based on nonlinear dynamics inversion (NDI). In the presence of model uncertainties, external disturbances and sudden faults, it has been shown both analytically and numerically that the perturbation terms under NDI and INDI based SMC/SMDO control (ϵ_{ndi} and ϵ_{indi}) have different properties. First of all, the boundedness of ϵ_{indi} is guaranteed when the conditions in Theorem 5 are satisfied, while the boundedness of ϵ_{ndi} is undetermined under the same conditions. More importantly, there exists a sampling frequency that makes the upper bound of ϵ_{indi} is smaller than that of ϵ_{ndi} , which can fundamentally reduce the control efforts of SMC/SMDO because for most SMC and SMDO designs, there is a positive correlation between the required switching gains and the uncertainty bounds. ϵ_{indi} is also proved to have smaller variations in different fault circumstances, while ϵ_{ndi} is more fault-case dependent. These merits of ϵ_{indi} allow INDI-SMC/SMDO to use reduced and fixed gains for resisting a wider variety of faults and disturbances, while the gains for NDI based SMC/SMDO are higher and require adjustments in different scenarios. Finally, the advantages

of INDI-SMC/SMDO are demonstrated by both numerical simulations and real-world quadrotor flight tests. In conclusion, easier implementation, reduced model dependency, improved performance and robustness make the proposed INDI-SMC/SMDO a promising method for enhancing aircraft safety in real life.

REFERENCES

- [1] J. K. Stolaroff, C. Samaras, E. R. O'Neill, A. Lubers, A. S. Mitchell, and D. Ceperley, *Energy use and life cycle greenhouse gas emissions of drones for commercial package delivery*, *Nature Communications* **9**, 409 (2018).
- [2] J.-J. E. Slotine and W. Li, *Applied Nonlinear Control* (NJ: Prentice Hall, Englewood Cliffs, 1991).
- [3] J. Y. Hung, W. Gao, and J. C. Hung, *Variable structure control: a survey*, *IEEE Transactions on Industrial Electronics* **40**, 2 (1993).
- [4] R. Xu and U. Ozguner, *Sliding Mode Control of a Quadrotor Helicopter*, *Proceedings of the 45th IEEE Conference on Decision and Control*, 4957 (2006).
- [5] D. Lee, H. J. Kim, and S. Sastry, *Feedback linearization vs. adaptive sliding mode control for a quadrotor helicopter*, *International Journal of Control, Automation and Systems* **7**, 419 (2009).
- [6] F. Sharifi, M. Mirzaei, B. W. Gordon, and Y. Zhang, *Fault Tolerant Control of A Quadrotor UAV Using Sliding Mode Control*, *2010 Conference on Control and Fault-Tolerant Systems (SysTol)*, 239 (2010).
- [7] T. Li, Y. Zhang, and B. W. Gordon, *Passive and active nonlinear fault-tolerant control of a quadrotor unmanned aerial vehicle based on the sliding mode control technique*, *Special Issue Article Proc IMechE Part I: J Systems and Control Engineering* **227**, 12 (2012).
- [8] L. Besnard, Y. B. Shtessel, and B. Landrum, *Quadrotor vehicle control via sliding mode controller driven by sliding mode disturbance observer*, *Journal of the Franklin Institute* **349**, 658 (2012).
- [9] A. R. Merheb, H. Noura, and F. Bateman, *Design of Passive Fault-Tolerant Controllers of a Quadrotor Based on Sliding Mode Theory*, *International Journal of Applied Mathematics and Computer Science* **25**, 561 (2015).
- [10] A. Modirrousta and M. Khodabandeh, *A novel nonlinear hybrid controller design for an uncertain quadrotor with disturbances*, *Aerospace Science and Technology* **45**, 294 (2015).
- [11] S. Rajappa, C. Masone, H. H. Bulthoff, and P. Stegagno, *Adaptive Super Twisting Controller for a quadrotor UAV*, *Proceedings - IEEE International Conference on Robotics and Automation 2016-June*, 2971 (2016).

- [12] Y. Yang and Y. Yan, *Attitude regulation for unmanned quadrotors using adaptive fuzzy gain-scheduling sliding mode control*, *Aerospace Science and Technology* **54**, 208 (2016).
- [13] F. Mu, M. Bonilla, and E. S. Espinoza, *Robust Trajectory Tracking for Unmanned Aircraft Systems Using High Order Sliding Mode Controllers-Observers*, in *2017 International Conference on Unmanned Aircraft Systems (ICUAS)* (Miami, Florida, 2017).
- [14] Z. Jia, J. Yu, Y. Mei, Y. Chen, Y. Shen, and X. Ai, *Integral backstepping sliding mode control for quadrotor helicopter under external uncertain disturbances*, *Aerospace Science and Technology* **68**, 299 (2017).
- [15] V. I. Utkin and A. S. Poznyak, *Adaptive sliding mode control with application to super-twist algorithm: Equivalent control method*, *Automatica* **49**, 39 (2013).
- [16] C. Edwards and Y. B. Shtessel, *Continuous higher order sliding mode control based on adaptive disturbance compensation*, in *2014 13th International Workshop on Variable Structure Systems (VSS)*, Vol. 47 (IEEE, 2014).
- [17] C. Edwards and Y. Shtessel, *Adaptive dual-layer super-twisting control and observation*, *International Journal of Control* **89**, 1759 (2016).
- [18] C. Edwards and Y. B. Shtessel, *Adaptive continuous higher order sliding mode control*, *Automatica* **65**, 183 (2016).
- [19] C. E. Hall and Y. B. Shtessel, *Sliding Mode Disturbance Observer-Based Control for a Reusable Launch Vehicle*, *Journal of Guidance, Control, and Dynamics* **29**, 1315 (2006).
- [20] P. M. Tiwari, S. Janardhanan, and M. Un Nabi, *Attitude control using higher order sliding mode*, *Aerospace Science and Technology* **54**, 108 (2016).
- [21] M. Defoort, T. Floquet, A. Kokosy, and W. Perruquetti, *A novel higher order sliding mode control scheme*, *Systems and Control Letters* **58**, 102 (2009).
- [22] T. E. Massey and Y. B. Shtessel, *Continuous Traditional and High-Order Sliding Modes for Satellite Formation Control*, *Journal of Guidance, Control, and Dynamics* **28**, 826 (2005).
- [23] F. Grondman, G. Looye, R. O. Kuchar, Q. P. Chu, and E. van Kampen, *Design and Flight Testing of Incremental Nonlinear Dynamic Inversion-based Control Laws for a Passenger Aircraft*, in *2018 AIAA Guidance, Navigation, and Control Conference*, January (American Institute of Aeronautics and Astronautics, Kissimmee, Florida, 2018).
- [24] X. Wang, E. van Kampen, Q. P. Chu, and P. Lu, *Stability Analysis for Incremental Nonlinear Dynamic Inversion Control*, *Journal of Guidance, Control, and Dynamics* (2019), 10.2514/1.G003791.

- [25] S. Sieberling, Q. P. Chu, and J. A. Mulder, *Robust Flight Control Using Incremental Nonlinear Dynamic Inversion and Angular Acceleration Prediction*, *Journal of Guidance, Control, and Dynamics* **33**, 1732 (2010).
- [26] E. J. J. Smeur, Q. P. Chu, and G. C. H. E. de Croon, *Adaptive Incremental Nonlinear Dynamic Inversion for Attitude Control of Micro Air Vehicles*, *Journal of Guidance, Control, and Dynamics* **39**, 450 (2016).
- [27] E. J. J. Smeur, G. C. H. E. de Croon, and Q. P. Chu, *Gust disturbance alleviation with Incremental Nonlinear Dynamic Inversion*, in *2016 IEEE/RSJ International Conference on Intelligent Robots and Systems (IROS)* (IEEE, 2016) pp. 5626–5631.
- [28] X. Wang, E. van Kampen, Q. P. Chu, and P. Lu, *Incremental Sliding-Mode Fault-Tolerant Flight Control*, *Journal of Guidance, Control, and Dynamics* **42**, 244 (2019).
- [29] S. Sun, L. Sijbers, X. Wang, and C. de Visser, *High-Speed Flight of Quadrotor Despite Loss of Single Rotor*, *IEEE Robotics and Automation Letters* **3**, 3201 (2018).
- [30] Y. B. Shtessel, J. M. Buffington, and S. S. Banda, *Multiple Timescale Flight Control Using Reconfigurable Sliding Modes*, *Journal of Guidance, Control, and Dynamics* **22**, 873 (1999).
- [31] Y. Shtessel, J. Buffington, and S. Banda, *Tailless aircraft flight control using multiple time scale reconfigurable sliding modes*, *IEEE Transactions on Control Systems Technology* **10**, 288 (2002).
- [32] Y. B. Shtessel and I. A. Shkolnikov, *Aeronautical and space vehicle control in dynamic sliding manifolds*, *International Journal of Control* **76**, 1000 (2003).
- [33] V. Utkin and J. Shi, *Integral sliding mode in systems operating under uncertainty conditions*, *Proceedings of 35th IEEE Conference on Decision and Control* **4**, 1 (1996).
- [34] H. K. Khalil, *Nonlinear Systems* (Prentice-Hall, New Jersey, 2002).
- [35] P. Acquatella, E. van Kampen, and Q. P. Chu, *Incremental Backstepping for Robust Nonlinear Flight Control*, *CEAS Conference on Guidance, Navigation, and Control* , 1444 (2013).
- [36] X. Wang and E. van Kampen, *Incremental Backstepping Sliding Mode Fault-Tolerant Flight Control*, in *AIAA Scitech 2019 Forum*, January (American Institute of Aeronautics and Astronautics, San Diego, California, 2019) pp. 1–23.
- [37] X. Shao, Q. Meng, J. Liu, and H. Wang, *RISE and disturbance compensation based trajectory tracking control for a quadrotor UAV without velocity measurements*, *Aerospace Science and Technology* **74**, 145 (2018).
- [38] X. Shao, J. Liu, H. Cao, C. Shen, and H. Wang, *Robust dynamic surface trajectory tracking control for a quadrotor UAV via extended state observer*, *International Journal of Robust and Nonlinear Control* **28**, 2700 (2018).

- [39] Y. Song, L. He, D. Zhang, J. Qian, and J. Fu, *Neuroadaptive Fault-Tolerant Control of Quadrotor UAVs: A More Affordable Solution*, *IEEE Transactions on Neural Networks and Learning Systems*, 1 (2018).
- [40] B. Etkin, *Dynamics of Atmospheric Flight* (Dover Publications, Toronto, 2005).
- [41] S. Sun, R. Schilder, and C. C. de Visser, *Identification of Quadrotor Aerodynamic Model from High Speed Flight Data*, in *2018 AIAA Atmospheric Flight Mechanics Conference*, January (American Institute of Aeronautics and Astronautics, Kissimmee, Florida, 2018) pp. 1–23.
- [42] X. Wang, E. van Kampen, and Q. P. Chu, *Gust Load Alleviation and Ride Quality Improvement with Incremental Nonlinear Dynamic Inversion*, in *AIAA Atmospheric Flight Mechanics Conference* (American Institute of Aeronautics and Astronautics, Grapevine, Texas, 2017) pp. 1–21.
- [43] C. Cakiroglu, E. van Kampen, and Q. P. Chu, *Robust Incremental Nonlinear Dynamic Inversion Control Using Angular Accelerometer Feedback*, in *2018 AIAA Guidance, Navigation, and Control Conference*, January (American Institute of Aeronautics and Astronautics, Kissimmee, Florida, 2018).



7

FLEXIBLE AIRCRAFT GUST LOAD ALLEVIATION WITH INCREMENTAL NONLINEAR DYNAMIC INVERSION

As discussed in Chapter 1, an integrated flight control design considering both rigid-body and aeroelastic dynamics becomes more and more important with the increase of structural flexibility. In view of Chapters 2 and 3, the inherent robustness of incremental nonlinear dynamic inversion (INDI) makes it a promising candidate for flexible aircraft control. Therefore, this chapter designs a multi-objective INDI control law for free-flying flexible aircraft; in the process, it demonstrates how to make trade-offs among different control objectives in the framework of INDI. Practical issues, including the online estimations of elastic states and state derivatives, will also be considered.

This chapter is based on the following article:

Wang, X., van Kampen, E., Chu, Q. P., "Flexible Aircraft Gust Load Alleviation with Incremental Nonlinear Dynamic Inversion," *Journal of Guidance, Control, and Dynamics*, 2019, pp. 1–16. doi:10.2514/1.G003980.

In this chapter, a controller based on incremental nonlinear dynamic inversion (INDI) is designed for the flexible aircraft gust load alleviation (GLA) problem. First, a flexible aircraft model that captures both inertia and aerodynamic coupling effects between flight dynamics and structural dynamics is presented. Then, an INDI GLA controller is designed for this aircraft model based on sensor measurements and the Kalman filter online estimation. Besides, the fifth order Padé approximation is used to model the pure time delay in the state estimation. Furthermore, simulations of the flexible aircraft flying through various spatial turbulence and gust fields demonstrate the effectiveness of the proposed controller on rigid-body motion regulation, vertical load alleviation, wing root bending moment reduction and elastic modes suppression. Additionally, numerical perturbation tests and a Monte Carlo study show the robustness of the proposed controller to aerodynamic model uncertainties.

7.1. INTRODUCTION

WHILE enjoying the benefits provided by light-weight composite materials, aircraft designers are facing the challenges of the accompanying greater structural flexibility. As the structural flexibility increases, not only do the interactions between aerodynamics and structural dynamics become significant, the coupling effects between rigid-body dynamics and structural dynamics are also non-negligible [1–4]. When a flexible aircraft encounters atmospheric disturbances, both the rigid-body and flexible modes are excited, which reduces pilot handling qualities, degrades passenger ride quality, introduces extra structural loads, and shortens the structural fatigue life. Traditionally, the flight control and structural vibration suppression are performed separately, and notch filters are used to avoid interactions between them. This design approach may be less appropriate for modern flexible aircraft. Instead, an integrated control design, which simultaneously accounts for rigid-body and aeroelastic control, can lead to better overall performance.

The free-flying dynamics of flexible aircraft are nonlinear and time-varying (NLTV) [2, 5]. The nonlinearities are contributed to by flight dynamics, aeroelasticity and the inertial couplings between them [2]. Even for a rigid aircraft, when the angle of attack is high or when the aircraft is in transonic flight, the aerodynamics are nonlinear. Under the small deformation assumption, the structural vibration dynamics are described by a series of second-order linear differential equations, and their inertial couplings with rigid-body dynamics are negligible. These can be invalid for highly flexible aircraft, for which the consideration of nonlinearity in flight control design becomes important [6, 7].

In the literature of flexible aircraft flight control, it is a common practice to linearize the NLTV system around an equilibrium point, and then execute a model reduction procedure. Based on the resulting low-order and linear time-invariant (LTI) system, the linear-quadratic Gaussian (LQG) method is used for gust load alleviation (GLA) in [8, 9], and for flutter suppression in [10, 11]. Although both linear-quadratic regulator (LQR) and the Kalman filter are optimal, as their combination, LQG does not automatically ensure good robustness properties. Linear robust control can improve the robustness of a closed-loop system. An H_∞ robust controller is designed in [12] for reducing the wing root bending moment of a very flexible aircraft. In [7], a mixed norm H_2/H_∞ control is used to alleviate the gust load of a flexible aircraft. However, it is commented in [13]

that LTI model based robust control could be either marginal or overly conservative in performance and stability robustness. Moreover, to ensure desirable handling qualities over the entire flight envelope, controllers based on LTI models need to be used along with the gain scheduling method, which can be cumbersome and does not guarantee stability robustness [14].

Flexible aircraft control designs considering nonlinearities do exist in the literature. In [15], the nonlinear dynamic inversion (NDI) method is used to control a high altitude long endurance highly flexible aircraft. Since NDI design uses a nonlinear model, it can be applied in the absence of gain scheduling. Nonetheless, the robustness of NDI is impaired by its model dependency. An adaptive backstepping (ABS) control is designed for an aeroservoelastic system in [16], where the plant is parameterized using pre-defined model structures. However, the unknown parameters are assumed to be constant or slowly time-varying in ABS design [17], which limits its applicability. Furthermore, not all the uncertainties and external disturbances can be parameterized, and even if they can, tuning of the resulting design can be tedious. An LTI aeroservoelastic system augmented by a nonlinear perturbation term is regulated by a model reference adaptive control (MRAC) in [16], where it was assumed that the perturbation satisfies the matching condition and can be parameterized into the multiplication of regressors and constant parameters. The reference model used in [16] is also LTI, thus, model updates are necessary when the flight condition changes or when a fault occurs. Because the flight envelope shrinks in faulty conditions [18], enforcing the system to track an LTI model designed in the nominal case can lead to instability. Last but not least, dynamic equations need to be solved for the parameter adaptation in MRAC, which requires high computational resources, especially for a high-order aeroservoelastic system.

Incremental nonlinear dynamic inversion (INDI) is a nonlinear sensor-based control approach. After its proposal in [19], its effectiveness has been demonstrated by real-world flight tests on a tail-sitter UAV [20], quadrotors [21–23], and even a CS-25 certified passenger aircraft [24]. The stability and robustness of INDI is analyzed in [25] using Lyapunov methods and nonlinear system perturbation theory. As compared to LTI model-based control methods, the gain scheduling technique is not needed by INDI. The uncertainty parameterization process is also omitted in INDI, which removes slowly time-varying parameter assumption and eliminates the tedious model structure selection procedure. INDI has less model dependency than NDI, ABS and MRAC, which simplifies its implementation process. The tuning of INDI is straightforward [26]. Being independent of the dynamic parameter update laws, INDI also has lower computational cost.

Although the model dependency of INDI is reduced, its robustness is enhanced by the feedback of output derivatives. The robustness of INDI to model uncertainties has been analyzed in [25], and evaluated in [19, 27]. By virtue of its sensor-based nature, INDI is able to passively tolerate a wide range of actuator faults and structural damages without using any additional robust or adaptive techniques [28]. As analyzed in [25], INDI also has inherent robustness to external disturbances. The wind-tunnel tests in [21] show that under the INDI control, a damaged quadrotor with complete loss of a single rotor can resist over 9 m/s of wind disturbance. A rigid aircraft GLA problem is considered in [29], where INDI outperforms the LQR control. These merits of INDI inspired

the idea of using it to solve the flexible aircraft GLA problem, which has not been addressed in the literature. Due to the complexity of aeroservoelastic systems, several research questions emerge: How to conduct a reasonable model simplification based on the characteristics of flexible aircraft? How to make trade-offs among different control objectives in the framework of INDI? How to obtain the state derivatives of flexible aircraft? How is the robustness of the control to state estimation errors, external disturbances, sudden faults and model uncertainties? These questions will be answered in this chapter.

The main contributions of this chapter are as follows: 1) an integrated nonlinear control law for flexible aircraft aiming at rigid-body motion regulation, gust load alleviation, wing root bending moment reduction and elastic mode suppression; 2) an online optimal state observer with a Padé approximation to model the pure time delay; 3) theoretical analyses and numerical validations for the robustness of the proposed control to external disturbances, sudden faults and model uncertainties.

The rest of the chapter is organized as follows: Sec. 7.2 presents the models for flexible aircraft and turbulence fields. Sec. 7.3 derives the INDI GLA control law with the simulation results shown and discussed in Sec. 7.4. The main conclusions are drawn in Sec. 7.5.

7.2. FLEXIBLE AIRCRAFT AND GUST MODELS

7.2.1. FLEXIBLE AIRCRAFT EQUATIONS OF MOTION

In order to capture both aerodynamic and inertial coupling effects between the rigid-body and structural dynamics of free-flying flexible aircraft, the dynamic equations derived in quasi-coordinates [2] are adopted in this chapter. The flexible wings are modeled as cantilever beams undergoing bending and torsional deformations. The remaining components, namely fuselage and empennage (horizontal and vertical tails) are assumed to be rigid. A set of body-fixed axes (O_i, x_i, y_i, z_i) with $i = f, w, e$, are attached to the undeformed aircraft as shown by Fig. 7.1. Generic Lagrangian equations of motion in quasi-coordinates are given in Eq. (7.1) [2].

7

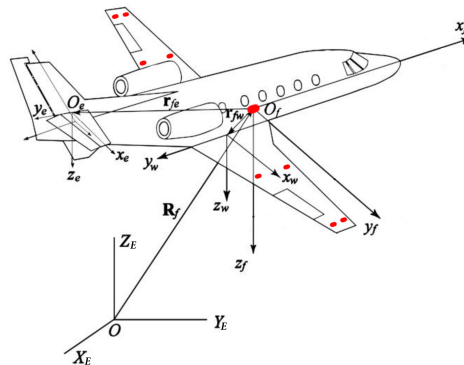


Figure 7.1: Coordinate system definition [2].

$$\begin{aligned}
\frac{d}{dt} \left(\frac{\partial L}{\partial \mathbf{V}_f} \right) + \tilde{\boldsymbol{\omega}}_f \frac{\partial L}{\partial \mathbf{V}_f} - \mathbf{C}_f \frac{\partial L}{\partial \mathbf{R}_f} &= \mathbf{F} \\
\frac{d}{dt} \left(\frac{\partial L}{\partial \boldsymbol{\omega}_f} \right) + \tilde{\mathbf{V}}_f \frac{\partial L}{\partial \mathbf{V}_f} + \tilde{\boldsymbol{\omega}}_f \frac{\partial L}{\partial \boldsymbol{\omega}_f} - \mathbf{E}_f^{-T} \frac{\partial L}{\partial \boldsymbol{\theta}_f} &= \mathbf{M} \\
\frac{\partial}{\partial t} \left(\frac{\partial \hat{L}}{\partial \mathbf{v}_w} \right) - \frac{\partial \hat{L}}{\partial \mathbf{u}_w} + \frac{\partial \hat{\mathcal{F}}_{uw}}{\partial \dot{\mathbf{u}}_w} + \mathcal{L} \mathbf{u}_w &= \hat{\mathbf{U}} \\
\frac{\partial}{\partial t} \left(\frac{\partial \hat{L}}{\partial \boldsymbol{\alpha}_w} \right) + \frac{\partial \hat{\mathcal{F}}_{\alpha w}}{\partial \dot{\boldsymbol{\psi}}_w} + \mathcal{H} \boldsymbol{\psi}_w &= \hat{\boldsymbol{\Psi}}
\end{aligned} \tag{7.1}$$

In Eq. (7.1), $L = \mathcal{T} - \mathcal{V}$ represents the Lagrangian energy for the whole aircraft. \mathbf{V}_f and $\boldsymbol{\omega}_f$ represent the (x_f, y_f, z_f) axes translational and rotational velocities, while \mathbf{R}_f and $\boldsymbol{\theta}_f$ indicate the position and Euler angles of the (x_f, y_f, z_f) axes relative to (X_E, Y_E, Z_E) . \mathbf{F} and \mathbf{M} are the total forces and moments, while $\hat{\mathbf{U}}$ and $\hat{\boldsymbol{\Psi}}$ are the resultant of force and moment density vectors. $\mathbf{C}_f(\phi, \theta, \psi)$ is the rotation transformation matrix from inertial axes (X_E, Y_E, Z_E) to (x_f, y_f, z_f) , and the $\mathbf{E}_f(\phi, \theta)$ matrix links angular velocities $\boldsymbol{\omega}_f$ to Eulerian velocities $\dot{\boldsymbol{\theta}}_f$. (\cdot) indicates the volume density of energy terms and $(\tilde{\cdot})$ refers to the skew-symmetric matrix of a vector. \mathcal{L} and \mathcal{H} are matrices of stiffness differential operators, with \mathcal{F}_{uw} and $\mathcal{F}_{\alpha w}$ represent the Rayleigh dissipation function densities. \mathbf{u}_w and $\mathbf{v}_w = \dot{\mathbf{u}}_w$ represent elastic bending displacement and velocity vectors, while $\boldsymbol{\psi}_w$ and $\boldsymbol{\alpha}_w = \dot{\boldsymbol{\psi}}_w$ represent elastic torsion angle and angular velocity vectors. The Galerkin method is used to discretize the flexible displacements in modal form as

$$\begin{aligned}
\mathbf{u}_w(\mathbf{r}_w, t) &= \boldsymbol{\Phi}(\mathbf{r}_w) \mathbf{q}(t), \quad \dot{\mathbf{q}}(t) = \mathbf{s}(t), \\
\boldsymbol{\psi}_w(\mathbf{r}_w, t) &= \boldsymbol{\Psi}(\mathbf{r}_w) \boldsymbol{\xi}_w(t), \quad \dot{\boldsymbol{\xi}}_w(t) = \boldsymbol{\eta}_w(t),
\end{aligned} \tag{7.2}$$

where $\boldsymbol{\Phi}(\mathbf{r}_w)$ and $\boldsymbol{\Psi}(\mathbf{r}_w)$ are bending and torsion shape function matrices respectively. \mathbf{r}_{fw} and \mathbf{r}_{fe} represent relative distances of component axes. \mathbf{C}_w and \mathbf{C}_e refer to the coordinates transformation matrices. The velocities of an infinitesimal mass element dm on the wing, $\bar{\mathbf{v}}_w$, the fuselage, $\bar{\mathbf{v}}_f$, and the tail, $\bar{\mathbf{v}}_e$, can be expressed as

$$\begin{aligned}
\bar{\mathbf{v}}_w(\mathbf{r}_w, t) &= \mathbf{C}_w \mathbf{V}_f + \mathbf{C}_w \tilde{\mathbf{r}}_{fw}^T \boldsymbol{\omega}_f + (\tilde{\mathbf{r}}_w + \widetilde{\boldsymbol{\Phi} \mathbf{q}})^T \mathbf{C}_w \boldsymbol{\omega}_f + \tilde{\mathbf{r}}_w^T \boldsymbol{\Psi} \boldsymbol{\eta} + \boldsymbol{\Phi} \mathbf{s} \\
\bar{\mathbf{v}}_f(\mathbf{r}_f, t) &= \mathbf{V}_f + \tilde{\mathbf{r}}_f^T \boldsymbol{\omega}_f \\
\bar{\mathbf{v}}_e(\mathbf{r}_e, t) &= \mathbf{V}_f + (\tilde{\mathbf{r}}_{fe} + \widetilde{\mathbf{C}_e^T \mathbf{r}_e})^T \boldsymbol{\omega}_f
\end{aligned} \tag{7.3}$$

Using Eq. (7.3), the total kinetic energy of the aircraft is

$$\mathcal{T} = \sum_i \mathcal{T}_i = \frac{1}{2} \mathbf{V}^T \mathbf{M} \mathbf{V}, \quad \mathcal{T}_i = \frac{1}{2} \int \bar{\mathbf{v}}_i^T \bar{\mathbf{v}}_i dm_i, \quad i = f, w, e \tag{7.4}$$

in which $\mathbf{V} = [\mathbf{V}_f^T \boldsymbol{\omega}_f^T \mathbf{s}^T \boldsymbol{\eta}_w^T]^T$, \mathbf{M} is the system mass matrix varies with deformations

given as

$$\begin{aligned} \mathbf{M}_{st} &= \begin{bmatrix} m\mathbf{I}_{3 \times 3} & \tilde{\mathbf{S}}^T & \mathbf{C}_w^T \int \Phi dm_w & \mathbf{C}_w^T \int \tilde{\mathbf{r}}_w^T \Psi dm_w \\ \tilde{\mathbf{S}} & \mathbf{J} & \mathbf{C}_w^T \int (\tilde{\mathbf{r}}_w + \widetilde{\Phi} \mathbf{q}) \Phi dm_w & \mathbf{C}_w^T \int (\tilde{\mathbf{r}}_w + \widetilde{\Phi} \mathbf{q}) \tilde{\mathbf{r}}_w^T \Psi dm_w \\ \text{symmetric} & & \int \Phi^T \Phi dm_w & \int \Phi^T \tilde{\mathbf{r}}_w^T \Psi dm_w \\ & & \int \Psi^T \tilde{\mathbf{r}}_w^T \Phi dm_w & \int \Psi^T \tilde{\mathbf{r}}_w \tilde{\mathbf{r}}_w^T \Psi dm_w \end{bmatrix} \\ &= \begin{bmatrix} \mathbf{M}_{rr} & \mathbf{M}_{re} \\ \mathbf{M}_{er} & \mathbf{M}_{ee} \end{bmatrix} \end{aligned} \quad (7.5)$$

with $\tilde{\mathbf{S}}$ represents the matrix of first moment of area, and \mathbf{J} represents moment of inertia of the deformed aircraft, defined as

$$\begin{aligned} \tilde{\mathbf{S}} &= \int \tilde{\mathbf{r}}_f dm_f + \int \tilde{\mathbf{r}}_{fe} dm_e + \int \mathbf{C}_e^T \tilde{\mathbf{r}}_e \mathbf{C}_e dm_e + \int \tilde{\mathbf{r}}_{fw} dm_w + \int \mathbf{C}_w^T (\tilde{\mathbf{r}}_w + \widetilde{\Phi} \mathbf{q})^T \mathbf{C}_w dm_w \\ \mathbf{J} &= \int \tilde{\mathbf{r}}_f^T \tilde{\mathbf{r}}_f dm_f + \int [\mathbf{C}_w \tilde{\mathbf{r}}_{fw}^T + (\tilde{\mathbf{r}}_w + \widetilde{\Phi} \mathbf{q})^T \mathbf{C}_w]^T [\mathbf{C}_w \tilde{\mathbf{r}}_{fw} + (\tilde{\mathbf{r}}_w + \widetilde{\Phi} \mathbf{q})^T \mathbf{C}_w] dm_w \\ &+ \int [\mathbf{C}_e \tilde{\mathbf{r}}_{fe}^T + \tilde{\mathbf{r}}_e^T \mathbf{C}_e]^T [\mathbf{C}_e \tilde{\mathbf{r}}_{fe} + \tilde{\mathbf{r}}_e^T \mathbf{C}_e] dm_e \end{aligned} \quad (7.6)$$

The linear momentum of the aircraft $\mathbf{p} = [\mathbf{p}_{V_f}^T \mathbf{p}_{\omega_f}^T \mathbf{p}_{uw}^T \mathbf{p}_{\psi w}^T]^T$ can be calculated as

$$\mathbf{p} = \frac{\partial \mathcal{T}}{\partial \mathbf{V}} = \mathbf{M}_{st} \mathbf{V} \quad (7.7)$$

For the model in present chapter, potential energy is purely due to wing deformation strain energy, which can be expressed as

$$\mathcal{V} = \frac{1}{2} (\mathbf{q}^T \mathcal{K}_{uw} \mathbf{q} + \boldsymbol{\xi}_w^T \mathcal{K}_{\psi w} \boldsymbol{\xi}_w), \quad \mathcal{K}_{uw} = \int EI (\Phi'')^T \Phi'' dx, \quad \mathcal{K}_{\psi w} = \int GJ (\Psi')^T \Psi' dx \quad (7.8)$$

where EI and GJ refer to the bending and torsion stiffness respectively. Assume structural damping matrices $\mathcal{C}_{uw}, \mathcal{C}_{\psi w}$ are respectively proportional to $\mathcal{K}_{uw}, \mathcal{K}_{\psi w}$. Substituting Eqs. (7.2, 7.4, 7.7, 7.8) into Eq. (7.1), the system dynamics can be expressed in discrete form as [2]

$$\begin{aligned} \dot{\mathbf{p}}_{V_f} &= -\tilde{\boldsymbol{\omega}}_f \mathbf{p}_{V_f} + \mathbf{F} \\ \dot{\mathbf{p}}_{\omega_f} &= -\tilde{\mathbf{V}}_f \mathbf{p}_{V_f} - \tilde{\boldsymbol{\omega}}_f \mathbf{p}_{\omega_f} + \mathbf{M} \\ \dot{\mathbf{p}}_{uw} &= \frac{\partial \mathcal{T}}{\partial \mathbf{q}} - \mathcal{K}_{uw} \mathbf{q} - \mathcal{C}_{uw} \mathbf{s} + \mathbf{Q} \\ \dot{\mathbf{p}}_{\psi w} &= -\mathcal{K}_{\psi w} \boldsymbol{\xi}_w - \mathcal{C}_{\psi w} \boldsymbol{\eta}_w + \boldsymbol{\Theta} \end{aligned} \quad (7.9)$$

where $\frac{\partial \mathcal{T}}{\partial \mathbf{q}} = \frac{\partial \tilde{\mathbf{v}}_w^T}{\partial \mathbf{q}} \frac{\partial \mathcal{T}}{\partial \tilde{\mathbf{v}}_w} = \widetilde{\Phi \mathbf{C}_w \boldsymbol{\omega}_f}^T \int \tilde{\mathbf{v}}_w dm_w$ includes Coriolis and centrifugal forces of the wing. Eq. (7.9) includes the translational, rotational, bending and torsion dynamic equations. The kinematic equations of the aircraft are given as

$$\dot{\mathbf{R}}_f = \mathbf{C}_f^T \mathbf{V}_f, \quad \dot{\boldsymbol{\theta}}_f = \mathbf{E}_f^{-1} \boldsymbol{\omega}_f \quad (7.10)$$

The generalized forces on the right-hand side of Eq. (7.9) can be obtained by means of virtual work. They are listed here for completeness [2].

$$\begin{aligned}
 \mathbf{F} &= \int_{D_f} [\mathbf{f}_f + \mathbf{F}_E \delta(\mathbf{r} - \mathbf{r}_E)] dD_f + \mathbf{C}_w^T \int_{D_w} \mathbf{f}_w dD_w + \mathbf{C}_e^T \int_{D_e} \mathbf{f}_e dD_e \\
 \mathbf{M} &= \int_{D_f} \tilde{\mathbf{r}}_f [\mathbf{f}_f + \mathbf{F}_E \delta(\mathbf{r} - \mathbf{r}_E)] dD_f + \int_{D_w} [\tilde{\mathbf{r}}_{fw} \mathbf{C}_w^T + \mathbf{C}_w^T (\tilde{\mathbf{r}}_w + \widetilde{\Phi} \mathbf{q})] \mathbf{f}_w dD_w \\
 &\quad + \int_{D_e} [\tilde{\mathbf{r}}_{fe} \mathbf{C}_e^T + \mathbf{C}_e^T \tilde{\mathbf{r}}_e] \mathbf{f}_e dD_e \\
 \mathbf{Q} &= \int_{D_w} \Phi^T \mathbf{f}_w dD_w, \quad \Theta = \int_{D_w} \Psi^T \tilde{\mathbf{r}}_w \mathbf{f}_w dD_w
 \end{aligned} \tag{7.11}$$

$\mathbf{f}_f, \mathbf{f}_w, \mathbf{f}_e$ in Eq. (7.11) are distributed forces acting on the fuselage, wing and empennage. They contain the aerodynamic, gravitational and control forces. The aerodynamic forces are calculated based on quasi-steady strip theory, and the local airspeed on each strip is perturbed by motions and gusts. δ represents the Dirac delta function. \mathbf{F}_E indicates the thrust and \mathbf{r}_E represents the engine position.

The main feature of the modeling approach in [2] is that the flight dynamics and structural dynamics are coupled both inertially and aerodynamically. The aerodynamic couplings can be seen from the right-hand side of Eq. (7.9) where the generalized forces $\mathbf{F}, \mathbf{M}, \mathbf{Q}, \Theta$ are functions of both the rigid-body and elastic states. The inertial couplings reflect on Eq. (7.5), where the off-diagonal blocks of the mass matrix $\mathbf{M}_{er}, \mathbf{M}_{re}$ are non-zero. Also, in the rigid-body mass matrix \mathbf{M}_{rr} , $\tilde{\mathbf{S}}$ and \mathbf{J} are functions of deformations as shown in Eq. (7.6). These inertial coupling effects can be considerable for highly flexible aircraft.

7.2.2. UNSTEADY AERODYNAMIC MODELS

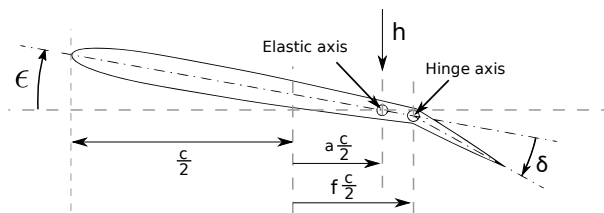


Figure 7.2: A 2D airfoil with a trailing edge flap.

In this chapter, the unsteady aerodynamics of the wing and tails are modeled using the modified strip theory. In this approach, the considered lifting surface is discretized into a series of undeformable strips. The aerodynamic force and moment on each strip are calculated using its steady-flow aerodynamic properties and the unsteady aerodynamic theories for a 2D airfoil. Considering a 2D airfoil exposed to disturbed atmosphere with three degrees of freedom: heave h , pitching around the elastic axis ϵ , and a flap deflection δ . The geometric parameters and the positive directions of movements are indicated in Fig. 7.2. It is worth noting that h and ϵ contain the contributions from

both rigid-body and structural motions. In incompressible flow, the sectional lift coefficient and pitching moment coefficient around the elastic axis are formulated as

$$\begin{aligned} C_L &= C_L^{c,he} + C_L^{nc,he} + C_L^{c,\delta} + C_L^{nc,\delta} + C_L^{c,g} \\ C_m &= C_m^{c,he} + C_m^{nc,he} + C_m^{c,\delta} + C_m^{nc,\delta} + C_m^{c,g} \end{aligned} \quad (7.12)$$

In Eq. (7.12), the superscripts c and nc respectively indicates the circulatory and noncirculatory contributions. The circulatory terms are caused by the vorticity in the flow, which is time-history dependent. The noncirculatory terms result from the change in momentum of the surrounding air caused by the airfoil motions and flap deflections. In incompressible flow, the noncirculatory contributions are instant and not subject to a time-history effect [30]. The superscripts he , δ , and g respectively denotes the contributions from the airfoil motions, flap deflections and atmospheric disturbances. Using the expressions of Theodorsen [31], the circulatory terms due to airfoil motions are:

$$C_L^{c,he} = C_{L_\alpha}^{SF} C(k) \alpha_{3/4}, \quad C_m^{c,he} = \left(\frac{1}{4} + \frac{a}{2} \right) C_L^{c,he} \quad (7.13)$$

where $C_{L_\alpha}^{SF}$ is the lift curve slope in steady flow, which includes a compressibility correction using the Prandtl-Glauert factor. It is noteworthy that Theodorsen considers thin airfoils, thus the lift curve slope $C_{L_\alpha}^{SF}$ is assumed to be 2π [31]. In this chapter, more general expressions are used. $\alpha_{3/4} = \epsilon + \frac{\dot{h}}{V} + \frac{c}{2V} \left(\frac{1}{2} - a \right) \dot{\epsilon}$ is the angle of attack at the three quarter chord. $C(k)$ is the Theodorsen's function, where $k = \frac{\omega c}{2V}$ is the reduced frequency [31]. For an airfoil with lift curve slope $C_{L_\alpha}^{SF}$ in steady flow, the noncirculatory coefficients due to airfoil motions are [31]:

$$\begin{aligned} C_L^{nc,he} &= \frac{C_{L_\alpha}^{SF}}{2\pi} \frac{c}{4V} \left(\dot{\epsilon} + \frac{\ddot{h}}{V} - a \frac{c}{2V} \ddot{\epsilon} \right) \\ C_m^{nc,he} &= -\frac{C_{L_\alpha}^{SF}}{2\pi} \frac{c}{8V} \left(\left(\frac{1}{2} - a \right) \dot{\epsilon} - a \frac{\ddot{h}}{V} + \frac{c}{2V} \left(\frac{1}{8} + a^2 \right) \ddot{\epsilon} \right) \end{aligned} \quad (7.14)$$

7

The circulatory terms contributed by flap deflections also have time-history effects, they are given as

$$C_L^{c,\delta} = C_{L_\alpha}^{SF} C(k) \left(\frac{T_{10}}{\pi} \delta + \frac{T_{11}}{2\pi} \frac{c}{2V} \dot{\delta} \right), \quad C_m^{c,\delta} = \left(\frac{1}{4} + \frac{a}{2} \right) C_L^{c,\delta} \quad (7.15)$$

where T_{10} and T_{11} are constant geometric parameters depending on the hinge position [31]. The noncirculatory terms contributed by the flap are functions of δ , $\dot{\delta}$ and $\ddot{\delta}$. Their specific expressions can be found in [31]. $C(k)$ in Eq. (7.15) is the same as used in Eq. (7.13), which depends on the reduced frequency k . However, this formulation is less suitable for simulating aircraft maneuvers under random turbulence excitations in the time-domain. Wagner's function, which gives the lift response to a step change in angle of attack due to airfoil motions, is the time-domain counterpart of Theodorsen's function [32]. An exponential approximation of Wagner's function is $\phi(\tau) = 1 - 0.165e^{-0.0455\tau} - 0.335e^{-0.3\tau}$, where $\tau = 2Vt/c$ is a non-dimensional time variable [33]. On the other hand, the unsteady responses of an airfoil to a unit sharp-edged gust is given by the Küssner's function, which is exponentially approximated as $\psi_g(\tau) = 1 - 0.5e^{-0.13\tau} - 0.5e^{-\tau}$ [32].

Both $\phi(\tau)$ and $\psi_g(\tau)$ are in the form of $f(\tau) = 1 - a_1 e^{-b_1 \tau} - a_2 e^{-b_2 \tau}$. Using the Duhamel's integral, a system that has an indicial response function $f(\tau)$ can be realized in the control canonical form as:

$$\begin{aligned} \begin{bmatrix} \dot{x}_{a_1} \\ \dot{x}_{a_2} \end{bmatrix} &= \begin{bmatrix} 0 & 1 \\ -\left(\frac{2V}{c}\right)^2 b_1 b_2 & -\left(\frac{2V}{c}\right)(b_1 + b_2) \end{bmatrix} \begin{bmatrix} x_{a_1} \\ x_{a_2} \end{bmatrix} + \begin{bmatrix} 0 \\ 1 \end{bmatrix} u \\ y &= \left[(a_1 + a_2) b_1 b_2 \left(\frac{2V}{c}\right)^2, (a_1 b_1 + a_2 b_2) \left(\frac{2V}{c}\right) \right] \begin{bmatrix} x_{a_1} \\ x_{a_2} \end{bmatrix} \\ &\quad + (1 - a_1 - a_2) u \end{aligned} \quad (7.16)$$

Substituting the parameters of $\phi(\tau)$ into Eq. (7.16), and choosing $u = \alpha_{3/4} + \left(\frac{T_{10}}{\pi} \delta + \frac{T_{11}}{2\pi} \frac{c}{2V} \dot{\delta}\right)$, then based on Eqs. (7.13, 7.15), the circulatory lift coefficient caused by arbitrary airfoil motions and flap deflections is $C_L^{c,he} + C_L^{c,\delta} = C_{L\alpha}^{SF} y$. The corresponding circulatory moment coefficient equals $C_{L\alpha}^{SF} y$ multiplied with $\frac{1}{4} + \frac{a}{2}$ (Eq. (7.13) and Eq. (7.15)).

On the other hand, considering the airfoil encounters an arbitrary vertical gust input $w_g(t)$ on the leading edge. Substituting the parameters of $\psi_g(\tau)$ into Eq. (7.16), then the gust induced lift coefficient $C_L^{c,g}$ equals $C_{L\alpha}^{SF} y$ when the input u equals $\text{atan}(w_g(t)/V)$. Analogously, $C_m^{c,g}$ in Eq. (7.12) equals $(\frac{1}{4} + \frac{a}{2}) C_L^{c,g}$. x_{a_1} and x_{a_2} in Eq. (7.16) are known as the aerodynamic lag states. In view of the preceding derivations, four aerodynamic lag states are needed by each strip. Two of them are used for modeling the time-history dependent effects caused by motions and flap deflections, and the other two are used to model unsteady gust responses.

This chapter considers viscous flow, and the sectional drag coefficient is modeled as $C_D = C_{D_0} + k_D (C_L^{c,he} + C_L^{c,\delta} + C_L^{c,g})^2$. C_{D_0} is the drag coefficient corresponding to zero lift. Only the circulatory part of the lift contributes to the quadratic drag [32]. Using the sectional aerodynamic coefficients C_L, C_D, C_m , the distributed aerodynamic forces and moments can be calculated.

7.2.3. GUST AND TURBULENCE MODELS

Two methods are often used to model atmospheric disturbances, namely the stochastic continuous turbulence and the deterministic discrete gust. The continuous turbulence is often simplified into a stationary, homogeneous, isotropic stochastic process with Gaussian distribution. The power spectral density of the two commonly used turbulence models, Dryden (denoted by subscript D_w) and von Kármán models (denoted by subscript v_{Kw}) are respectively given by [34]

$$\Phi_{Dw}(\omega) = \sigma^2 \frac{L_g}{\pi V} \frac{1 + 3\left(\frac{L_g \omega}{V}\right)^2}{\left[1 + \left(\frac{L_g \omega}{V}\right)^2\right]^2}, \quad \Phi_{vKw}(\omega) = \sigma^2 \frac{L_g}{\pi V} \frac{1 + \frac{8}{3}\left(a \frac{L_g \omega}{V}\right)^2}{\left[1 + \left(a \frac{L_g \omega}{V}\right)^2\right]^{\frac{11}{6}}} \quad (7.17)$$

where ω is the angular frequency, L_g is the turbulence scale length, σ is the turbulence intensity. Constant $a = 1.339$, and V is the aircraft speed. While von Kármán model better fits available experimental and theoretical data, especially in high frequency range [35], its irrational spectra requires approximate difference equations to generate turbulence velocities in the time domain. As an alternative, it can be realized in the two dimensional

spatial domain based on the 2D von Kármán spectrum [35]

$$S_{w_g w_g}(\Omega_x, \Omega_y) = \frac{4\sigma^2 (aL_g)^4}{9\pi} \frac{\Omega_x^2 + \Omega_y^2}{[1 + (a\Omega_x L_g)^2 + (a\Omega_y L_g)^2]^{7/3}} \quad (7.18)$$

where Ω_x and Ω_y are the spatial frequencies along the X_E and Y_E directions. The vertical turbulence velocity w_g as a function of the spatial position (X_E, Y_E) is calculated as

$$w_g(X_E, Y_E) = \mathcal{F}^{-2} \left\{ \sqrt{S_{w_g w_g}(\Omega_x, \Omega_y)} \mathcal{F}^2 \{w_n(X_E, Y_E)\} \right\} \quad (7.19)$$

in which $w_n(X_E, Y_E)$ represents the 2D Gauss white noise generated in the spatial domain. \mathcal{F}^{-2} represents the 2D inverse Fourier transform, while \mathcal{F}^2 denotes the 2D Fourier transform. For more details about this 2D realization, readers are recommended to [36]. In this chapter, the external disturbances are assumed to be symmetrical to the aircraft (O_f, x_f, y_f) plane, while the turbulence velocities vary along the wing span. For example, a realization of the 2D symmetrical von Kármán moderate turbulence field with $L_g = 762$ m and $\sigma = 1.5$ m/s is shown in Fig. 7.3. This realization can be verified by comparing the covariance function of the simulated field with its theoretical values [35].

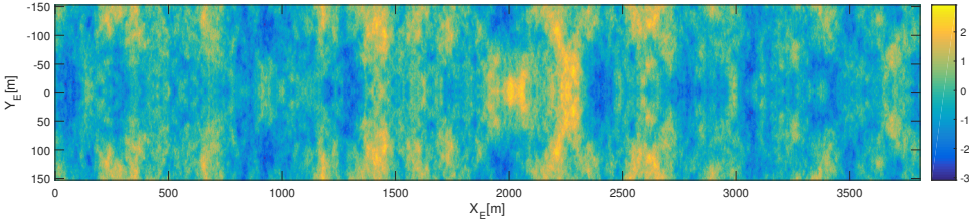


Figure 7.3: A 2D symmetrical von Kármán vertical turbulence field ($L_g = 762$ m, $\sigma = 1.5$ m/s).

The rational spectra of the Dryden model allow it to be directly realized in the time domain, by passing a white noise through a filter given by Eq. (7.20). This filter will be used in the state estimation process (Sec. 7.3.3).

$$H_{Dw}(s) = \sigma \sqrt{\frac{L_g}{\pi V}} \frac{1 + \frac{\sqrt{3}L_g}{V} s}{(1 + \frac{L_g}{V} s)^2} \quad (7.20)$$

The “1-cos” gust model can more precisely capture the solitary gust feature, as compared to the sharp-edged and the ramped gust models. A “1-cos” gust is defined as Eq. (7.21) and can be broadened into a symmetric w_{g_s} and an asymmetric w_{g_a} gust field as described by Eq. (7.22).

$$w_g = \frac{w_m}{2} \left(1 - \cos \frac{2\pi X_E}{\lambda_x}\right), \quad (7.21)$$

$$w_{g_s} = \frac{w_m}{4} \left(1 - \cos \frac{2\pi X_E}{\lambda_x}\right) \left(1 - \cos \frac{2\pi Y_E}{\lambda_y}\right) b$$

$$w_{g_a} = \frac{w_m}{2} \left(1 - \cos \frac{2\pi X_E}{\lambda_x}\right) \sin \frac{2\pi Y_E}{\lambda_y} \quad (7.22)$$

where w_m represents the maximum gust velocity and λ_x , λ_y refer to the gust lengths in X_E , Y_E directions, respectively. An example of a symmetric gust field is given by Fig. 7.4, in which the parameters of the first gust w_{g1} is $\lambda_{x1} = \lambda_{y1} = 100$ m, $w_{m1} = 5$ m/s and of the second gust w_{g2} is $\lambda_{x2} = \lambda_{y2} = 180$ m, $w_{m2} = 5$ m/s.

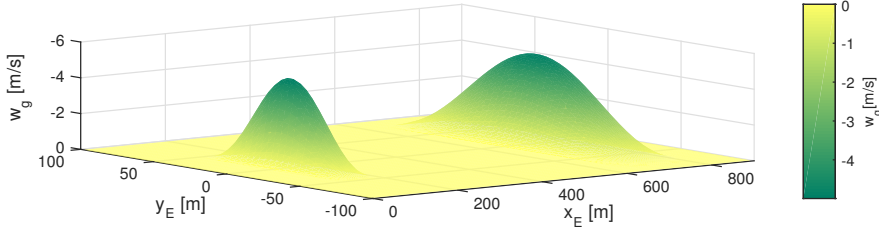


Figure 7.4: A 2D symmetrical “1-cos” vertical gust field.

During time-domain simulations, the flexible aircraft flies through the 2D spatial turbulence and gust fields. For each aerodynamic strip, the local vertical gust velocity w_g is independently interpolated using the spacial location of the airfoil leading edge. In this way, the gust penetration effect [35] is naturally captured. In short, this effect means that the gust met by the wings at the current time instant will only be encountered by the tail after a short time period.

7.3. FLEXIBLE AIRCRAFT GUST LOAD ALLEVIATION CONTROL

7.3.1. INCREMENTAL NONLINEAR DYNAMIC INVERSION CONTROL

Considering a nonlinear control-affine system:

$$\dot{\mathbf{x}} = \mathbf{f}(\mathbf{x}, \kappa(t)) + \mathbf{G}(\mathbf{x}, \kappa(t))\mathbf{u} + \mathbf{d}(t) \quad (7.23)$$

where \mathbf{d} represents a bounded external disturbance vector. To indicate a sudden fault at $t = t_f$ during flight, $\kappa(t) \in \mathbb{R}$ is designed as a step function, with $t < t_f$, $\kappa = 0$ indicates the fault-free case and $t \geq t_f$, $\kappa = 1$ denotes the post-fault condition.

Expanding \mathbf{f} and \mathbf{G} as:

$$\mathbf{f} = \bar{\mathbf{f}} + (\mathbf{f}_f - \bar{\mathbf{f}})\kappa + \hat{\mathbf{f}}, \quad \mathbf{G} = \bar{\mathbf{G}} + (\mathbf{G}_f - \bar{\mathbf{G}})\kappa + \hat{\mathbf{G}} \quad (7.24)$$

where $\bar{\mathbf{f}}$, $\bar{\mathbf{G}}$ are the nominal dynamics used for controller design, \mathbf{f}_f , \mathbf{G}_f denote the post-fault dynamics, and $\hat{\mathbf{f}}$, $\hat{\mathbf{G}}$ represent the model uncertainties as continuous functions of \mathbf{x} . Taking the first-order Taylor series expansion of Eq. (7.23) around the condition at $t - \Delta t$ (denoted by the subscript 0) as:

$$\begin{aligned} \dot{\mathbf{x}} = & \dot{\mathbf{x}}_0 + \mathbf{G}(\mathbf{x}_0, \kappa_0)\Delta\mathbf{u} + \left. \frac{\partial[\mathbf{f}(\mathbf{x}, \kappa) + \mathbf{G}(\mathbf{x}, \kappa)\mathbf{u}]}{\partial\mathbf{x}} \right|_0 \Delta\mathbf{x} \\ & + \left. \frac{\partial[\mathbf{f}(\mathbf{x}, \kappa) + \mathbf{G}(\mathbf{x}, \kappa)\mathbf{u}]}{\partial\kappa} \right|_0 \Delta\kappa + \Delta\mathbf{d} + \mathbf{R}_1 \end{aligned} \quad (7.25)$$

In the above equation, $\Delta\mathbf{x} = \mathbf{x} - \mathbf{x}_0$, $\Delta\mathbf{u} = \mathbf{u} - \mathbf{u}_0$, respectively denote the variations of states and control inputs in one incremental time step Δt . $\Delta\kappa = \kappa - \kappa_0$ denotes the

changes of the fault indicator κ , while $\Delta \mathbf{d} = \mathbf{d} - \mathbf{d}_0$ denotes the variations of the external disturbances \mathbf{d} in Δt . \mathbf{R}_1 in Eq. (7.25) is the expansion remainder, using Eqs. (7.23, 7.24), the Lagrange form of the remainder is

$$\begin{aligned} \mathbf{R}_1 = & \frac{1}{2} \frac{\partial^2 [\mathbf{f} + \mathbf{G}\mathbf{u}]}{\partial^2 \mathbf{x}} \Big|_m \Delta \mathbf{x}^2 + \frac{\partial \mathbf{G}}{\partial \mathbf{x}} \Big|_m \Delta \mathbf{x} \Delta \mathbf{u} + (\mathbf{G}_f - \bar{\mathbf{G}}) \Big|_m \Delta \mathbf{u} \Delta \kappa \\ & + \frac{\partial [(\mathbf{f}_f - \bar{\mathbf{f}}) + (\mathbf{G}_f - \bar{\mathbf{G}})\mathbf{u}]}{\partial \mathbf{x}} \Big|_m \Delta \mathbf{x} \Delta \kappa \end{aligned} \quad (7.26)$$

in which $(\cdot)|_m$ means evaluating (\cdot) at a condition where $\mathbf{x} \in (\mathbf{x}(t - \Delta t), \mathbf{x}(t))$, $\mathbf{u} \in (\mathbf{u}(t - \Delta t), \mathbf{u}(t))$, $\mathbf{d} \in (\mathbf{d}(t - \Delta t), \mathbf{d}(t))$, and $\kappa \in (\kappa(t - \Delta t), \kappa(t))$. In Eq. (7.26), \mathbf{R}_1 is not a function of $\Delta \mathbf{u}^2$, $\Delta \mathbf{d}^2$, $\Delta \kappa^2$, nor the coupling terms $\Delta \mathbf{x} \Delta \mathbf{d}$, $\Delta \kappa \Delta \mathbf{d}$, $\Delta \mathbf{u} \Delta \mathbf{d}$, which can be examined using Eqs. (7.23, 7.24).

Using the nominal system control effectiveness matrix $\bar{\mathbf{G}}(\mathbf{x})$ to design the INDI control increment as $\Delta \mathbf{u} = \bar{\mathbf{G}}^{-1}(\mathbf{x})(\mathbf{v} - \dot{\mathbf{x}}_0)$, where \mathbf{v} is the virtual control. Then based on Eq. (7.25), the closed-loop system dynamics under INDI control are:

$$\dot{\mathbf{x}} = \dot{\mathbf{x}}_0 + \mathbf{G} \bar{\mathbf{G}}^{-1}(\mathbf{v} - \dot{\mathbf{x}}_0) + \Delta \mathbf{d} + \boldsymbol{\delta}(\mathbf{x}, \kappa, \Delta t) \quad (7.27)$$

where $\boldsymbol{\delta}(\mathbf{x}, \kappa, \Delta t)$ indicates the closed-loop value of the perturbations, specifically

$$\boldsymbol{\delta}(\mathbf{x}, \kappa, \Delta t) = \left[\frac{\partial [\mathbf{f}(\mathbf{x}, \kappa) + \mathbf{G}(\mathbf{x}, \kappa)\mathbf{u}]}{\partial \mathbf{x}} \Big|_0 \Delta \mathbf{x} + \frac{\partial [\mathbf{f}(\mathbf{x}, \kappa) + \mathbf{G}(\mathbf{x}, \kappa)\mathbf{u}]}{\partial \kappa} \Big|_0 \Delta \kappa + \mathbf{R}_1 \right] \Big|_{\mathbf{u}=\mathbf{u}_{\text{indi}}} \quad (7.28)$$

Based on Eqs. (7.27, 7.28), the closed-loop dynamics are written as

$$\dot{\mathbf{x}} = \mathbf{v} + [(\mathbf{G} - \bar{\mathbf{G}})\Delta \mathbf{u} + \Delta \mathbf{d} + \boldsymbol{\delta}(\mathbf{x}, \kappa, \Delta t)] \triangleq \mathbf{v} + \boldsymbol{\varepsilon}_{\text{indi}} \quad (7.29)$$

$\boldsymbol{\varepsilon}_{\text{indi}}$ in Eq. (7.29) is a nonlinear perturbation term remaining in the closed-loop system, which is caused by model mismatches, external disturbances and sudden faults. If the conditions in Theorem 5 of Chapter 6 are satisfied, the perturbation term $\boldsymbol{\varepsilon}_{\text{indi}}$ is ultimately bounded.

The virtual control \mathbf{v} can be designed for different control purposes (e.g. command tracking, state stabilization, etc. [25]). Considering a command tracking problem, where the first-order time derivative of the reference vector \mathbf{x}_{ref} is assumed to be bounded and piecewise continuous.

Proposition 4 *If $\|\boldsymbol{\varepsilon}_{\text{indi}}\| \leq \bar{\varepsilon}_{\text{indi}}$ for all $\mathbf{x} \in \mathbb{R}^n$, design $\mathbf{v} = \dot{\mathbf{x}}_{\text{ref}} + \mathbf{K}_p(\mathbf{x}_{\text{ref}} - \mathbf{x})$, where \mathbf{K}_p is a positive definite gain matrix, then the tracking error $\mathbf{e} = \mathbf{x}_{\text{ref}} - \mathbf{x}$ for the system given by Eq. (7.29) is globally ultimately bounded by a class \mathcal{K} function of $\bar{\varepsilon}_{\text{indi}}$.*

Proof: The definitions for global ultimate boundedness and the class \mathcal{K} function can be found in Appendix A, Definition 6, Definition 2. This Proposition can be proved considering a candidate Lyapunov function $V = (\mathbf{x}_{\text{ref}} - \mathbf{x})^T (\mathbf{x}_{\text{ref}} - \mathbf{x})$, and using Lemma A.3 and Proposition B.1 in [25]. \square

The INDI control is featured by its robustness to model mismatches and reduced model dependency. For rigid aircraft control, the estimated control effectiveness matrix

$\tilde{\mathbf{G}}$ is the only model information needed by INDI. Even though the controller is independent of $\mathbf{f}(\mathbf{x})$, its robustness is improved by the feedback of $\dot{\mathbf{x}}_0$. In the presence of model uncertainties, external disturbances, sudden faults and even structural damages, $\boldsymbol{\varepsilon}_{\text{indi}}$ has a smaller bound than the bound on the remaining perturbation term in nonlinear dynamic inversion control [28]. As a consequence, the ultimate bound of the tracking errors under INDI control is also smaller (Proposition 4).

7.3.2. INDI FOR FLEXIBLE AIRCRAFT GLA

The flexible aircraft dynamics given by Eqs. (7.9, 7.10) coupled with unsteady aerodynamics (Sec. 7.2.2) are nonlinear and of high order. For an aircraft model with m_e elastic modes and n_a aerodynamic strips, there are 6 kinematic states, 6 states for \mathbf{p}_{V_f} and \mathbf{p}_{ω_f} , m_e states for \mathbf{p}_{uw} and $\mathbf{p}_{\psi w}$, m_e states for \mathbf{q} and $\boldsymbol{\xi}_w$ in Eq. (7.2), and $4n_a$ aerodynamic lag states (Sec. 7.2.2). In order to reduce the computational load of the on-board controller, and also to ensure the observability of the system, it is beneficial to reduce the number of states in the model used for control design. Therefore, a reduced-order nonlinear flexible aircraft model is established, whose kinematic and dynamic equations are still given by Eqs. (7.9, 7.10), but only the first $m'_e < m_e$ structural modes are included. The dynamics of the remaining $m_e - m'_e$ modes are viewed as singular perturbations [14, 25] to the system. This is reasonable since the high frequency structural modes are more damped, and are less coupled with the rigid-body modes. The gust related $2n_a$ aerodynamic lag states are not needed in this reduced-order model, since gust inputs are viewed as external disturbances by the controller, and are uncorrelated with system dynamics. The other $2n_a$ aerodynamic lag states related to motions are also viewed as singular perturbations to the system [14, 25]. The noncirculatory aerodynamic terms do not increase the order of the system, thus they are viewed as regular perturbations [25, 37]. This process reduces the number of states from $12 + 2m_e + 4n_a$ to $12 + 2m'_e$, and also reduces the model information available to the controller. The characteristics of the full and reduced-order models will be compared in Sec. 7.4.1. The reduced-order model will be used to design the INDI GLA control law. This control law will be validated using the full-order model in Sec. 7.4.4.

Define the rigid-body states as $\mathbf{x}_r = [\mathbf{V}_f^T \boldsymbol{\omega}_f^T]^T$, and the elastic states as $\mathbf{x}_e = \mathbf{H}[\mathbf{q}^T \boldsymbol{\xi}_w^T]^T$. \mathbf{H} is a boolean selection matrix to choose part of the structural modes for control. Considering the dynamics of the reduced-order model (Eq. (7.9)), and taking the first-order Taylor series expansion as:

$$\begin{aligned} \dot{\mathbf{p}}_{V_f} &= \dot{\mathbf{p}}_{V_{f0}} + \left(-\frac{\partial \tilde{\boldsymbol{\omega}}_f \mathbf{p}_{V_f}}{\partial \mathbf{x}_r} \Big|_0 \Delta \mathbf{x}_r - \frac{\partial \tilde{\boldsymbol{\omega}}_f \mathbf{p}_{V_f}}{\partial \dot{\mathbf{x}}_e} \Big|_0 \Delta \dot{\mathbf{x}}_e + \frac{\partial \mathbf{F}}{\partial \mathbf{x}_r} \Big|_0 \Delta \mathbf{x}_r \right) + \frac{\partial \mathbf{F}}{\partial \mathbf{x}_e} \Big|_0 \Delta \mathbf{x}_e + \frac{\partial \mathbf{F}}{\partial \dot{\mathbf{x}}_e} \Big|_0 \Delta \dot{\mathbf{x}}_e \\ &\quad + \frac{\partial \mathbf{F}}{\partial \mathbf{u}} \Big|_0 \Delta \mathbf{u} \triangleq \dot{\mathbf{p}}_{V_{f0}} + \mathbf{K}_r + \mathbf{K}_e + \mathbf{K}_{de} + \mathbf{K}_u + \boldsymbol{\varepsilon}_1 \\ \dot{\mathbf{p}}_{\omega_f} &= \dot{\mathbf{p}}_{\omega_{f0}} + \left(-\frac{\partial \tilde{\mathbf{V}}_f \mathbf{p}_{V_f} + \tilde{\boldsymbol{\omega}}_f \mathbf{p}_{\omega_f}}{\partial \mathbf{x}_r} \Big|_0 \Delta \mathbf{x}_r - \frac{\partial \tilde{\mathbf{V}}_f \mathbf{p}_{V_f} + \tilde{\boldsymbol{\omega}}_f \mathbf{p}_{\omega_f}}{\partial \dot{\mathbf{x}}_e} \Big|_0 \Delta \dot{\mathbf{x}}_e + \frac{\partial \mathbf{M}}{\partial \mathbf{x}_r} \Big|_0 \Delta \mathbf{x}_r \right) \\ &\quad + \frac{\partial \mathbf{M}}{\partial \mathbf{x}_e} \Big|_0 \Delta \mathbf{x}_e + \frac{\partial \mathbf{M}}{\partial \dot{\mathbf{x}}_e} \Big|_0 \Delta \dot{\mathbf{x}}_e + \frac{\partial \mathbf{M}}{\partial \mathbf{u}} \Big|_0 \Delta \mathbf{u} \triangleq \dot{\mathbf{p}}_{\omega_{f0}} + \mathbf{W}_r + \mathbf{W}_e + \mathbf{W}_{de} + \mathbf{W}_u + \boldsymbol{\varepsilon}_2 \end{aligned}$$

$$\begin{aligned}
\dot{\mathbf{p}}_{uw} &= \dot{\mathbf{p}}_{uw_0} - \mathcal{K}_{uw}\Delta\mathbf{q} - \mathcal{C}_{uw}\Delta\mathbf{s} + \left(\frac{\partial\mathbf{Q}}{\partial\mathbf{x}_r} \Big|_0 \Delta\mathbf{x}_r + \frac{\partial(\frac{\partial\mathcal{F}}{\partial\mathbf{q}})}{\partial\mathbf{x}_r} \Big|_0 \Delta\mathbf{x}_r + \frac{\partial(\frac{\partial\mathcal{F}}{\partial\mathbf{q}})}{\partial\mathbf{x}_e} \Big|_0 \Delta\mathbf{x}_e + \frac{\partial(\frac{\partial\mathcal{F}}{\partial\mathbf{q}})}{\partial\dot{\mathbf{x}}_e} \Big|_0 \Delta\dot{\mathbf{x}}_e \right) \\
&\quad + \frac{\partial\mathbf{Q}}{\partial\mathbf{x}_e} \Big|_0 \Delta\mathbf{x}_e + \frac{\partial\mathbf{Q}}{\partial\dot{\mathbf{x}}_e} \Big|_0 \Delta\dot{\mathbf{x}}_e + \frac{\partial\mathbf{Q}}{\partial\mathbf{u}} \Big|_0 \Delta\mathbf{u} \triangleq \dot{\mathbf{p}}_{uw_0} + \mathbf{U}_q + \mathbf{U}_s + \mathbf{U}_r + \mathbf{U}_e + \mathbf{U}_{de} + \mathbf{U}_u + \boldsymbol{\varepsilon}_3 \\
\dot{\mathbf{p}}_{\psi w} &= \dot{\mathbf{p}}_{\psi w_0} - \mathcal{K}_{\psi w}\Delta\boldsymbol{\xi}_w - \mathcal{C}_{\psi w}\Delta\boldsymbol{\eta}_w + \frac{\partial\boldsymbol{\Theta}}{\partial\mathbf{x}_r} \Big|_0 \Delta\mathbf{x}_r + \frac{\partial\boldsymbol{\Theta}}{\partial\mathbf{x}_e} \Big|_0 \Delta\mathbf{x}_e + \frac{\partial\boldsymbol{\Theta}}{\partial\dot{\mathbf{x}}_e} \Big|_0 \Delta\dot{\mathbf{x}}_e + \frac{\partial\boldsymbol{\Theta}}{\partial\mathbf{u}} \Big|_0 \Delta\mathbf{u} \\
&\triangleq \dot{\mathbf{p}}_{\psi w_0} + \mathbf{Y}_\xi + \mathbf{Y}_\eta + \mathbf{Y}_r + \mathbf{Y}_e + \mathbf{Y}_{de} + \mathbf{Y}_u + \boldsymbol{\varepsilon}_4
\end{aligned} \tag{7.30}$$

In the above equations, the control vector is defined as $\mathbf{u} = [\delta_{a_s}, \delta_{a_a}, \delta_e, \delta_r]^T$. δ_{a_s} and δ_{a_a} respectively denote the symmetrical and asymmetrical aileron deflections. δ_e indicates the elevator deflections while δ_r represents the rudder deflections. $\boldsymbol{\varepsilon}_i$, $i = 1, 2, 3, 4$ includes the $\Delta\kappa$ related terms, the disturbance variations $\Delta\mathbf{d}$, and the higher-order terms in Eq. (7.25).

Since INDI uses the information of discrete samples, its performance is influenced by the sampling frequency, which is constrained by the hardware in practice. For a given Δt , the value of $\boldsymbol{\delta}(\mathbf{x}, \kappa, \Delta t)$ in Eq. (7.27) depends on the specific system dynamics. It has been proved in [25] that for faster system dynamics, Δt should be smaller to ensure a desirable ultimate bound. This also makes sense from a physical point of view that the characteristics of rapidly changing dynamics can only be captured by using high sampling frequency. For flexible aircraft dynamics, the variations of elastic states are typically faster than the rigid-body states. In Eq. (7.30), partial derivatives are separately taken with respect to \mathbf{x}_r , \mathbf{x}_e and $\dot{\mathbf{x}}_e$. Although the state variation related terms can all be viewed as perturbations, in which way the only model information used by the control is $\bar{\mathbf{G}}(\mathbf{x})$ (Eq. (7.29)), for relaxing the requirement on the sampling frequency, while maintaining the control performance, it is chosen in this chapter to include the terms related to the elastic state variations in control design. Nevertheless, since the rigid-body states have slower dynamics, the $\Delta\mathbf{x}_r$ related terms are viewed as perturbations by the controller.

The complexity of the control can be further reduced by analyzing the physics of the flexible aircraft. Although the mass matrix of the flexible aircraft is a function of the elastic states, it is still diagonally dominant. Consequently, in the translational and rotational equations, the partial derivatives of the nonlinear coupling terms with respect to $\dot{\mathbf{x}}_e$ can become less significant in Δt . Moreover, the partial derivatives of the Coriolis and centrifugal forces with respect to \mathbf{x}_e and $\dot{\mathbf{x}}_e$ have limited effects on the wing bending dynamics. Therefore, these terms are also viewed as perturbations by the controller. The specific expressions of these partial derivatives can be found in [38]. For simplicity, the incremental terms in the translational, rotational, bending and torsion dynamic equations are respectively denoted by \mathbf{K} , \mathbf{W} , \mathbf{U} , \mathbf{Y} in Eq. (7.30). Based on the above analyses, in one incremental time step Δt , the \mathbf{K}_r , \mathbf{W}_r , \mathbf{U}_r , \mathbf{Y}_r terms are less influential, thus they are viewed as perturbations by the controller. The feasibility of this simplification will

be verified in Sec. 7.4.2. Consequently, Eq. (7.30) is simplified into the following form:

$$\begin{aligned}
 \begin{bmatrix} \dot{\mathbf{p}}_{V_f} \\ \dot{\mathbf{p}}_{\omega_f} \\ \dot{\mathbf{p}}_{uw} \\ \dot{\mathbf{p}}_{\psi w} \\ \dot{\mathbf{q}} \\ \dot{\boldsymbol{\xi}}_w \end{bmatrix} &= \begin{bmatrix} \dot{\mathbf{p}}_{V_{f_0}} \\ \dot{\mathbf{p}}_{\omega_{f_0}} \\ \dot{\mathbf{p}}_{uw_0} \\ \dot{\mathbf{p}}_{\psi w_0} \\ \dot{\mathbf{q}}_0 \\ \dot{\boldsymbol{\xi}}_{w,0} \end{bmatrix} + \begin{bmatrix} \mathbf{0} & \frac{\partial \mathbf{F}}{\partial \mathbf{s}} & \frac{\partial \mathbf{F}}{\partial \boldsymbol{\eta}_w} & \frac{\partial \mathbf{F}}{\partial \mathbf{q}} & \frac{\partial \mathbf{F}}{\partial \boldsymbol{\xi}_w} \\ -\mathcal{C}_{uw} + \frac{\partial \mathbf{Q}}{\partial \mathbf{s}} & \frac{\partial \mathbf{M}}{\partial \mathbf{s}} & \frac{\partial \mathbf{M}}{\partial \boldsymbol{\eta}_w} & \frac{\partial \mathbf{M}}{\partial \mathbf{q}} & \frac{\partial \mathbf{M}}{\partial \boldsymbol{\xi}_w} \\ \mathbf{0} & \frac{\partial \boldsymbol{\Theta}}{\partial \mathbf{s}} & -\mathcal{C}_{\psi w} + \frac{\partial \boldsymbol{\Theta}}{\partial \boldsymbol{\eta}_w} & \frac{\partial \boldsymbol{\Theta}}{\partial \mathbf{q}} & -\mathcal{K}_{\psi w} + \frac{\partial \boldsymbol{\Theta}}{\partial \boldsymbol{\xi}_w} \\ \mathbf{0} & & \mathbf{I} & & \mathbf{0} \end{bmatrix} \begin{bmatrix} \Delta \mathbf{s} \\ \Delta \boldsymbol{\eta}_w \\ \Delta \mathbf{q} \\ \Delta \boldsymbol{\xi}_w \end{bmatrix} \\
 &+ \begin{bmatrix} \frac{\partial \mathbf{F}}{\partial \delta_{as}} & \frac{\partial \mathbf{F}}{\partial \delta_{aa}} & \frac{\partial \mathbf{F}}{\partial \delta_e} & \frac{\partial \mathbf{F}}{\partial \delta_r} \\ \frac{\partial \mathbf{M}}{\partial \delta_{as}} & \frac{\partial \mathbf{M}}{\partial \delta_{aa}} & \frac{\partial \mathbf{M}}{\partial \delta_e} & \frac{\partial \mathbf{M}}{\partial \delta_r} \\ \frac{\partial \mathbf{Q}}{\partial \delta_{as}} & \frac{\partial \mathbf{Q}}{\partial \delta_{aa}} & \mathbf{0} & \mathbf{0} \\ \frac{\partial \boldsymbol{\Theta}}{\partial \delta_{as}} & \frac{\partial \boldsymbol{\Theta}}{\partial \delta_{aa}} & \mathbf{0} & \mathbf{0} \\ \mathbf{0} & \mathbf{0} & \mathbf{0} & \mathbf{0} \end{bmatrix} \begin{bmatrix} \Delta \delta_{as} \\ \Delta \delta_{aa} \\ \Delta \delta_e \\ \Delta \delta_r \end{bmatrix} + \boldsymbol{\varepsilon} \quad (7.31)
 \end{aligned}$$

where \mathbf{I} and $\mathbf{0}$ are the identity matrix and zero matrix. $\boldsymbol{\varepsilon}$ is the augmented perturbation term. In view of Eq. (7.31), the partial derivatives of the generalized forces with respect to \mathbf{x}_e and $\dot{\mathbf{x}}_e$ contribute to aerodynamic stiffness and damping respectively. Furthermore, the control surface deflections directly lead to acceleration variations.

For the convenience of the virtual control design, define $\mathbf{x} = [\mathbf{p}_{V_f}^T \mathbf{p}_{\omega_f}^T \mathbf{p}_{uw}^T \mathbf{p}_{\psi w}^T \mathbf{q}^T \boldsymbol{\xi}_w^T]^T$. Velocities and deformations can also be used as states as $\mathbf{x}_V = [\mathbf{V}_f^T \boldsymbol{\omega}_f^T \mathbf{s}^T \boldsymbol{\eta}_w^T \mathbf{q}^T \boldsymbol{\xi}_w^T]^T$, with a simple transformation of $\mathbf{x} = \mathbf{M}_s \mathbf{x}_V$, $\mathbf{M}_s = \text{diag}([\mathbf{M}_{st}, \mathbf{I}])$. Recall Eq. (7.31), the system dynamic equation is represented as

$$\dot{\mathbf{x}} = \dot{\mathbf{x}}_0 + \boldsymbol{\Gamma}|_0 \Delta \mathbf{x}_V + \boldsymbol{\Upsilon}|_0 \Delta \mathbf{u} + \boldsymbol{\varepsilon} \quad (7.32)$$

The above equation is different from the incremental dynamic equation for rigid aircraft [19, 26, 27, 29] since the $\Delta \mathbf{x}_V$ related term still remains. $\Delta \mathbf{x}_V \approx \mathbf{M}_s^{-1}|_0 \Delta \mathbf{x} + \Delta(\mathbf{M}_s^{-1}) \mathbf{x}_0 + \Delta(\mathbf{M}_s^{-1}) \Delta \mathbf{x}$, where $\Delta(\mathbf{M}_s^{-1})$ is caused by the off-diagonal variations of $\Delta \mathbf{q}$. Since the mass matrix is diagonally dominant [38], the terms containing $\Delta(\mathbf{M}_s^{-1})$ and the higher-order terms can be viewed as perturbations. $\boldsymbol{\varepsilon}'$ is used to combine these terms with the $\boldsymbol{\varepsilon}$ in Eq. (7.31). Denote $\mathbf{A}_e \triangleq (\boldsymbol{\Gamma} \mathbf{M}_s^{-1})|_0$, $\mathbf{B}_e \triangleq \boldsymbol{\Upsilon}|_0$, Eq. (7.31) is then simplified to

$$\dot{\mathbf{x}} = \dot{\mathbf{x}}_0 + \mathbf{A}_e \Delta \mathbf{x} + \mathbf{B}_e \Delta \mathbf{u} + \boldsymbol{\varepsilon}' \quad (7.33)$$

The main control aim of this chapter is load alleviation, so a reference model is designed to generate references for the states and state derivatives for load control purposes. The internal loads, also known as “stress resultants” are caused by the externally applied forces and moments. The strategy of this controller is to use control surface deflections to compensate for the load variations caused by perturbations, so that the generalized forces are retained at their nominal values \mathbf{F}_* , \mathbf{M}_* , \mathbf{Q}_* , $\boldsymbol{\Theta}_*$. The subscript $(\cdot)_*$ indicates the nominal trimmed condition. Expanding the total force as the nominal

force \mathbf{F}_* , the forces variations due to aerodynamic uncertainties $\Delta\mathbf{F}_a$, caused by atmospheric disturbances $\Delta\mathbf{F}_d$, and generated by control inputs $\Delta\mathbf{F}_c$ as

$$\mathbf{F} = \mathbf{F}_* + \Delta\mathbf{F}_a + \Delta\mathbf{F}_d + \Delta\mathbf{F}_c \quad (7.34)$$

The moment \mathbf{M} , and the generalized elastic forces \mathbf{Q} and Θ in Eq. (7.9) can also be expanded in this form. In order to retain the forces and moments at their nominal values, the desired forces generated by the control surfaces should be

$$\begin{aligned} \Delta\mathbf{F}_c &= -\Delta(\mathbf{F}_a + \mathbf{F}_d), & \Delta\mathbf{M}_c &= -\Delta(\mathbf{M}_a + \mathbf{M}_d) \\ \Delta\mathbf{Q}_c &= -\Delta(\mathbf{Q}_a + \mathbf{Q}_d), & \Delta\Theta_c &= -\Delta(\Theta_a + \Theta_d) \end{aligned} \quad (7.35)$$

Recall Eq. (7.9), in order to satisfy the above equations, assuming the Coriolis and centrifugal forces are small, then the virtual control $\mathbf{v}_{rm} = [\mathbf{v}_{\mathbf{P}_{V_f}}^T \ \mathbf{v}_{\mathbf{P}_{\omega_f}}^T \ \mathbf{v}_{\mathbf{P}_{u_w}}^T \ \mathbf{v}_{\mathbf{P}_{\psi_w}}^T \ \mathbf{v}_q^T \ \mathbf{v}_\xi^T]^T$ can be designed as

$$\begin{aligned} \mathbf{v}_{\mathbf{P}_{V_f}} &= -\tilde{\omega}_f \mathbf{P}_{V_f} + \mathbf{F}_* \\ \mathbf{v}_{\mathbf{P}_{\omega_f}} &= -\tilde{V}_f \mathbf{P}_{V_f} - \tilde{\omega}_f \mathbf{P}_{\omega_f} + \mathbf{M}_* \\ \mathbf{v}_{\mathbf{P}_{u_w}} &= -\mathcal{H}_{uw} \mathbf{q} - \mathcal{C}_{uw} \mathbf{s} + \mathbf{Q}_* = -\mathcal{H}_{uw} (\mathbf{q} - \mathbf{q}_*) - \mathcal{C}_{uw} (\mathbf{s} - \mathbf{s}_*) \\ \mathbf{v}_{\mathbf{P}_{\psi_w}} &= -\mathcal{H}_{\psi w} \boldsymbol{\xi}_w - \mathcal{C}_{\psi w} \boldsymbol{\eta}_w + \Theta_* = -\mathcal{H}_{\psi w} (\boldsymbol{\xi}_w - \boldsymbol{\xi}_{w,*}) - \mathcal{C}_{\psi w} (\boldsymbol{\eta}_w - \boldsymbol{\eta}_{w,*}) \\ \mathbf{v}_q &= \mathbf{0}, \quad \mathbf{v}_\xi = \mathbf{0} \end{aligned} \quad (7.36)$$

If the nominal condition is steady level flight, then $\mathbf{F}_* = \mathbf{M}_* = \mathbf{s}_* = \boldsymbol{\eta}_{w,*} = \mathbf{0}$. The nominal condition can also be constant speed climb and decent, level turn, etc. The desired $\dot{\mathbf{q}}$, $\dot{\boldsymbol{\xi}}_w$ are all equal to zero. The reference for states are obtained by integrating the virtual control as

$$\mathbf{x}_{rm} = \mathbf{x}_{rm*} + \int_0^t \mathbf{v}_{rm} \, d\tau \quad (7.37)$$

7

A proportional virtual control term \mathbf{v}_p is added to minimize the reference tracking errors as

$$\mathbf{v} = \mathbf{v}_{rm} + \mathbf{v}_p = \mathbf{v}_{rm} + \mathbf{K}_p (\mathbf{x}_{rm} - \mathbf{x}) \quad (7.38)$$

where \mathbf{K}_p is a positive definite gain matrix (the same as in Proposition 4). Using Eq. (7.33), and based on Sec. 7.3.1, the INDI GLA control law is designed as:

$$\Delta\mathbf{u} = (\mathbf{B}_e^T \mathbf{W} \mathbf{B}_e)^{-1} \mathbf{B}_e^T \mathbf{W} (\mathbf{v} - \dot{\mathbf{x}}_0 - \mathbf{A}_e \Delta\mathbf{x}) \quad (7.39)$$

For the reason that the number of control variables is less than the number of states, the weighted least squares method is used in the present INDI control law. The weighting matrix \mathbf{W} is chosen as a positive definite matrix, which can be tuned based on the control priority. The total control command for the actuator is $\mathbf{u} = \Delta\mathbf{u} + \mathbf{u}_0$, where \mathbf{u}_0 is the sampled actuator position vector [25]. A block diagram is illustrated in Fig. 7.5, where z^{-1} represents one time step delay, $T_s/(z-1)$ is a discretized integrator using the forward Euler method, PID represents a proportional-integral-derivative regulator.

model is available for the observer design. Linearize the reduced-order model around the equilibrium point, the resulting dynamics are written as

$$\begin{bmatrix} \dot{\mathbf{x}}_r \\ \dot{\mathbf{x}}_e \\ \dot{\mathbf{x}}_e \end{bmatrix} = \begin{bmatrix} \mathbf{A}_{rr} & \mathbf{A}_{re} \\ \mathbf{A}_{er} & \mathbf{A}_{ee} \end{bmatrix} \begin{bmatrix} \mathbf{x}_r \\ \mathbf{x}_e \\ \mathbf{x}_e \end{bmatrix} + \begin{bmatrix} \mathbf{B}_r \\ \mathbf{B}_{el} \end{bmatrix} \mathbf{u} + \begin{bmatrix} \mathbf{w}_r \\ \mathbf{w}_e \end{bmatrix}$$

$$\mathbf{y}_V = [\mathbf{C}_r \quad \mathbf{C}_{el}] [\mathbf{x}_r \quad \mathbf{x}_e \quad \mathbf{x}_e]^T + \mathbf{D}_V \mathbf{u} + \mathbf{v} \quad (7.42)$$

The process noise $[\mathbf{w}_r^T \quad \mathbf{w}_e^T]^T$ contains the model errors and external disturbances. For GLA problems, it is common to augment the linear system models with the Dryden turbulence model as a prior knowledge of the process noise [10, 40]. In reality, however, the turbulence spectrum is usually unknown. In order to get a satisfactory state estimation while making the controller be capable of handling a broad range of disturbances, the Dryden model is augmented into the system model with parametric uncertainties. These uncertain parameters can be modeled as random walks and be estimated online. Recalling Eq. (7.20), the state-space realization of the Dryden spectrum can be given by

$$\begin{aligned} \dot{\mathbf{x}}_w &= \mathbf{A}_g \mathbf{x}_w + \mathbf{B}_g \mathbf{n} \\ \mathbf{w}_{g_w} &= \mathbf{C}_g \mathbf{x}_w \end{aligned} \quad (7.43)$$

where \mathbf{n} is the Gaussian white noise. In view of Fig. 7.3, the gust velocity varies on each strip. However, for maintaining the observation efficiency, the gust velocities are assumed to be uniformly distributed on the wing \mathbf{w}_{g_w} and the tail \mathbf{w}_{g_H} in the observation process. Also, the gust penetration effect is roughly modeled as a time shift ζ from the wing to the tail in the observation process. In other words, the current gust velocities on the tail equal the gust velocities on the wing ζ seconds ago, i.e. $\mathbf{w}_{g_H} = e^{-\zeta s} \mathbf{w}_{g_w}$. The pure time delay $e^{-\zeta s}$ is approximated using the fifth order Padé approximation in the Laplace domain, which can be realized in the time domain as

$$\begin{aligned} \mathbf{w}_{g_H} &= e^{-\zeta s} \mathbf{w}_{g_w} \approx H(\zeta s) \mathbf{w}_{g_w} \\ \dot{\mathbf{x}}_\zeta &= \mathbf{A}_\zeta \mathbf{x}_\zeta + \mathbf{B}_\zeta \mathbf{w}_{g_w} = \mathbf{A}_\zeta \mathbf{x}_\zeta + \mathbf{B}_\zeta \mathbf{C}_g \mathbf{x}_w, \quad \mathbf{w}_{g_H} = \mathbf{C}_\zeta \mathbf{x}_\zeta \end{aligned} \quad (7.44)$$

The influences of gust on the elastic modes are modeled as $\mathbf{w}_e = \mathbf{E}_w \mathbf{w}_{g_w} + \mathbf{E}_H \mathbf{w}_{g_H} + \mathbf{d}_e$, with \mathbf{d}_e represents the aircraft and turbulence model errors. Since the rigid states \mathbf{x}_r can be directly measured, they are treated as inputs to the elastic state estimation equation. In summary, the integrated linear model for Kalman filter estimation is written as

$$\begin{bmatrix} \dot{\mathbf{x}}_e \\ \dot{\mathbf{x}}_e \\ \dot{\mathbf{x}}_w \\ \dot{\mathbf{x}}_\zeta \end{bmatrix} = \begin{bmatrix} \mathbf{A}_{ee} & \mathbf{E}_w \mathbf{C}_g & \mathbf{E}_H \mathbf{C}_\zeta \\ \mathbf{0} & \mathbf{A}_g & \mathbf{0} \\ \mathbf{0} & \mathbf{B}_\zeta \mathbf{C}_g & \mathbf{A}_\zeta \end{bmatrix} \begin{bmatrix} \mathbf{x}_e \\ \mathbf{x}_e \\ \mathbf{x}_w \\ \mathbf{x}_\zeta \end{bmatrix} + \begin{bmatrix} \mathbf{B}_{el} & \mathbf{A}_{er} \\ \mathbf{0} & \mathbf{0} \\ \mathbf{0} & \mathbf{0} \end{bmatrix} \begin{bmatrix} \mathbf{u} \\ \mathbf{x}_r \end{bmatrix}$$

$$+ \begin{bmatrix} \mathbf{0} \\ \mathbf{B}_g \\ \mathbf{0} \end{bmatrix} \mathbf{n} + \begin{bmatrix} \mathbf{d}_e \\ \mathbf{0} \\ \mathbf{0} \end{bmatrix}$$

$$\mathbf{y}_V = [\mathbf{C}_{el} \quad \mathbf{0} \quad \mathbf{0}] [\dot{\mathbf{x}}_e \quad \mathbf{x}_e \quad \mathbf{x}_w \quad \mathbf{x}_\zeta]^T$$

$$+ [\mathbf{D}_V \quad \mathbf{C}_r] [\mathbf{u} \quad \mathbf{x}_r]^T + \mathbf{v} \quad (7.45)$$

which is written in a more compact form as

$$\begin{aligned}\dot{\mathbf{x}}_{kf} &= \mathbf{A}_{kf}\mathbf{x}_{kf} + \mathbf{B}_{kf}\mathbf{u}_{kf} + \mathbf{G}_{kf}\mathbf{n} + \mathbf{d}_{kf} \\ \mathbf{y}_{kf} &= \mathbf{C}_{kf}\mathbf{x}_{kf} + \mathbf{D}_{kf}\mathbf{u}_{kf} + \mathbf{v}\end{aligned}\quad (7.46)$$

The measurement noise covariance matrix is $\mathbf{R}_{kf} = E\{\mathbf{v}\mathbf{v}^T\}$, which is set based on the realistic noise level of the sensors. The process noise covariance matrix is chosen as $\mathbf{Q}_{kf} = E\{\mathbf{G}_{kf}\mathbf{n}\mathbf{n}^T\mathbf{G}_{kf}^T\} + \mathbf{Q}_d$, where \mathbf{Q}_d is an additive matrix tuned to account for the aircraft and turbulence model errors. The effectiveness of this state estimation approach will be shown in Sec. 7.4.3.

7.4. SIMULATION RESULTS AND DISCUSSIONS

The effectiveness of the proposed controller on gust load alleviation, and its robustness to model uncertainties and actuator faults will be evaluated in this section. A nonlinear full-order benchmark flexible aircraft validation model is set up using the geometry, inertia and stiffness data published in [2]. The dynamics of this aircraft have been discussed in Sec. 7.2. Each side of the wing model contains five bending modes and five torsion modes. The eigenfunctions of a uniform cantilever beam and a uniform clamped-free shaft are used as the bending shape functions $\Phi(\mathbf{r}_w)$ and the torsion shape functions $\Psi(\mathbf{r}_w)$ respectively. The rest of the aircraft components are assumed to be rigid. Different from the quasi-steady strip theory used in [2], modified strip theory (Sec. 7.2.2) is adopted in this chapter. This validation model uses the steady-flow lift curve slope ($C_{L\alpha}^{SF}$ in Eq. (7.13)) provided by [2]. These values are corrected using the Prandtl-Glauert factor to consider compressibility. The distributed forces on the right and left lifting surfaces are calculated independently, in which way the lateral flight dynamic modes can be considered.

All the control surface actuator dynamics are modeled as first-order systems with time constant 0.02 s. The deflection limits of ailerons, elevator and rudder are $\pm 30^\circ$, $\pm 20^\circ$, $\pm 20^\circ$ respectively. The rate limits for ailerons are $100^\circ/\text{s}$ and are $60^\circ/\text{s}$ for the elevator and rudder. The sampling frequency is $f_s = 1000$ Hz for capturing the high frequency elastic modes. For the load cases considered in this chapter, the variations of the airspeed are within ± 0.2 m/s in the open-loop responses, thus constant throttle is assumed in the subsequent simulations. A simple proportional-integral-derivative throttle controller can always be used if the airspeed has large deviations.

7.4.1. TRIM AND MODEL ANALYSIS

In order to analyze the couplings between the structural and rigid-body dynamics, a quasi-rigid aircraft model [2, 29] is set up. This quasi-rigid aircraft assumes infinitely high wing stiffness, and its kinematic equations are equal to Eq. (7.10). The dynamics of this quasi-rigid aircraft is described by the first two equations of Eq. (7.9), and all the elastic motion related terms are set to be zero. The resulting six degrees of freedom equations become identical to the conventional rigid-aircraft dynamic equations expressed in the body-fixed frame when O_f is coincide with the center of mass. Quasi-steady aerodynamics are used by this quasi-rigid aircraft model.

The full-order flexible aircraft model contains 20 elastic modes (10 for each wing),

and 97 aerodynamic strips, thus referring to Sec. 7.3.2, the total number of states equals 440. As presented in Sec. 7.3.2, a reduced-order nonlinear flexible aircraft model is used for control design. This model only includes the first 3 structural modes on each wing, coupled with quasi-steady aerodynamics, thus the total number of states is reduced to 24. The unsteady aerodynamic effects are viewed as perturbations to the controller (Sec. 7.3.2). The control designed using the reduced-order model will be implemented on the full-order model to evaluate its effectiveness.

Using the distributed inertia and stiffness data in [2], the natural frequency of the first wing elastic mode is 36.4 rad/s, which may not be representative for a very flexible aircraft. In order to evaluate the genericity of the proposed controller, a more flexible aircraft model is set up, which reduces the bending and torsion stiffness of the benchmark flexible aircraft model by 80%. Consequently, the natural frequency of the first wing elastic mode becomes 16.34 rad/s (2.6 Hz). The structural damping matrices \mathcal{C}_{uw} and $\mathcal{C}_{\psi w}$ are assumed to be proportional to the stiffness matrices in [2]. Therefore, these damping matrices are also reduced by 80% in this more flexible aircraft model.

The quasi-rigid aircraft, the full-order benchmark flexible aircraft, the reduced-order flexible aircraft, and the flexible with 80% reduced stiffness are all trimmed at a steady level flight condition, with $h_* = 25,000$ ft, $V_{E_*} = 127$ m/s, $M_{a_*} = 0.41$. The steady level flight trim constraints are given by

$$\begin{aligned}\dot{\mathbf{R}}_{f_*} &= [V_{E_*} \ 0 \ 0]^T, \quad \boldsymbol{\theta}_{f_*} = [0 \ \theta_* \ 0]^T, \quad \mathbf{V}_{f_*} = \mathbf{C}_f(\boldsymbol{\theta}_*)\dot{\mathbf{R}}_{f_*}, \\ \boldsymbol{\omega}_{f_*} &= \mathbf{0}, \quad \alpha_* = \theta_*, \quad \beta_* = 0, \quad \mathbf{s}_* = \mathbf{0}, \quad \boldsymbol{\eta}_{w,*} = \mathbf{0}\end{aligned}\quad (7.47)$$

In view of the symmetric characteristic of the steady level flight condition, asymmetric states and control inputs are automatically set to be zero. The trim solutions for the considered flight condition satisfying Eq. (7.47) are summarized in Table 7.1.

Table 7.1: Trim solutions for four aircraft models.

	α_* [°]	δ_{e_*} [°]	F_{E_*} [N]	\mathbf{q}_* [mm]	$\boldsymbol{\xi}_{w,*}$ [°]
Quasi-rigid	4.03	-3.71	2809	-	-
Full-order Flexible	3.98	-3.61	2782	[-34.96, 4.36, -0.36, 0.01, -0.03] ^T	[0.114, -0.020, 0.008, -0.003, 0.002] ^T
Reduced-order Flexible	3.98	-3.61	2782	[-34.29, 3.63] ^T	0.114
Full-order Flexible with Reduced Stiffness	3.76	-3.23	2675	[-183.41, 23.57, -2.03, 0.07, -0.14] ^T	[0.588, -0.111, 0.043, -0.014, 0.009] ^T

F_{E_*} and δ_{e_*} in Table 7.1 respectively represents the thrust and elevator deflection in the trim condition. For the present models, the wing elastic axis is coincide with the unswept wing beam, thus the bending and torsion modes are decoupled. Also, the aerodynamic center of the wing is in front of the elastic axis. Consequently, in the trim condition, the wing is bending upwards with a nose-up torsional angle. Because of this nose-up twist, α_* of the flexible aircraft are smaller than that of the quasi-rigid aircraft.

The trim solutions of the reduced-order and full-order flexible aircraft are close to each other. Moreover, the flexible aircraft with reduced stiffness has larger deformations than the benchmark flexible aircraft, which can be seen from the values of \mathbf{q}_* and $\xi_{w,*}$ in Table 7.1.

An eigenvalue analysis is performed to show the characteristics of the four models. Fig. 7.6 compares the poles of the quasi-rigid aircraft, and two flexible aircraft. Due to the coupling effects, the rigid mode poles of the flexible aircraft deviate from the poles of the quasi-rigid aircraft. For all the models, there are four poles in the origin for X_E, Y_E, Z_E, ψ . The reduced-order model is able to maintain the low frequency characteristics of the full-order system. As can be seen from Fig. 7.6, the poles of the reduced-order model are in agreement with that of the full-order model in the low frequency range. The distinctions between these two models increase as frequency increases.

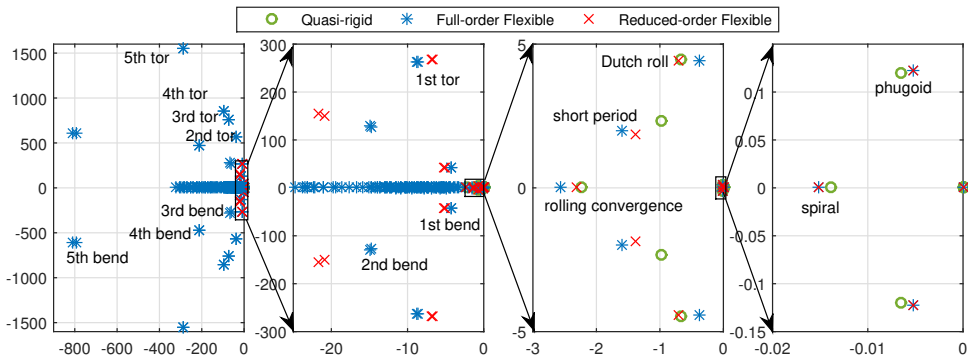


Figure 7.6: Eigenvalues of the quasi-rigid, full and reduced-order flexible aircraft models.

Fig. 7.7 compares the poles of the quasi-rigid, benchmark flexible and the flexible aircraft with reduced stiffness. It can be observed that the elastic modes of the flexible aircraft with 80% reduced stiffness have reduced frequency and higher damping ratio. For example, as the stiffness reduces, the first bending mode frequency reduces from 42.5 rad/s to 23.1 rad/s, while the damping ratio increases from 0.101 to 0.153. Besides, the frequency of the first torsion mode reduces from 263 rad/s to 115 rad/s, while the damping ratio increases from 0.029 to 0.033. As the wing flexibility increases, the couplings between the structural and rigid-body dynamics become more prominent. In view of the third subplot of Fig. 7.7, the benchmark full-order flexible aircraft has higher short-period damping ratio than the quasi-rigid aircraft, which coincides with the results in [41, 42]. When 80% of the wing stiffness is reduced, the pair of complex conjugate short-period poles merges to become two real poles. The disappearance of the conventional oscillatory short period mode caused by the wing flexibility was also reported in [5, 43, 44]. The dominant pitching pole of the more flexible aircraft is -0.783, which is expected to move to the unstable region as the wing stiffness further reduces [44]. The reduction of wing stiffness also induces an unstable phugoid mode, which is observed from the fourth subplot of Fig. 7.7. This phenomenon is in agreement with the results in [5, 43, 45]. In addition, the lateral flight dynamic modes are also influenced by the wing flexibility. These couplings between the rigid-body and structural dynamics high-

light the necessity of an intergrated controller, which can simultaneously consider the aeroelastic and flight dynamic control objectives.

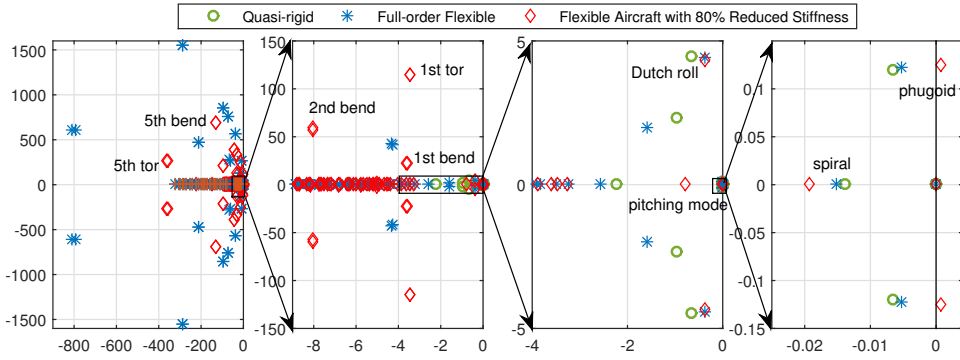


Figure 7.7: Eigenvalues of the quasi-rigid, full-order flexible aircraft, and a flexible aircraft with 80% reduced stiffness.

7.4.2. VALIDATION OF THE MODEL SIMPLIFICATION

According to the analysis in Sec. 7.3.2, the \mathbf{K}_r , \mathbf{W}_r , \mathbf{U}_r , \mathbf{Y}_r terms in Eq. (7.30) are less influential in one incremental time step, thus they are viewed as perturbations by the controller. To validate this process, the values of the terms in Eq. (7.30) will be numerically compared in this subsection.

The benchmark flexible aircraft is initially trimmed in a steady level flight condition. 1° step elevator δ_e , rudder δ_r , symmetric δ_{as} and asymmetric δ_{aa} aileron deflection commands are separately given to the aircraft. In one incremental time step $\Delta t = 0.001$ s, the norm value of the terms in Eq. (7.30) are shown in Fig. 7.8. For clarity, only the terms in the translational, rotational, and the right wing vibration equations are shown in the figure. The left wing vibrations are exactly symmetrical or asymmetrical to the right wing.

7

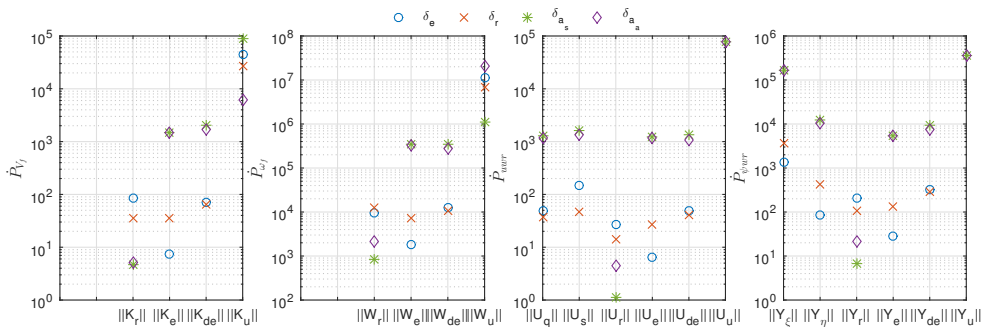


Figure 7.8: Norm value of the terms in Eq. (7.30) in one incremental time step.

It can be seen from Fig. 7.8 that the elevator (δ_e blue circles) and rudder (δ_r red cross)

deflections directly lead to translational and rotational acceleration variations, because $\|\mathbf{K}_u\|$ and $\|\mathbf{W}_u\|$ are at least two orders of magnitude larger than $\|\mathbf{K}_r\|$, $\|\mathbf{K}_e\|$, $\|\mathbf{K}_{de}\|$, $\|\mathbf{W}_r\|$, $\|\mathbf{W}_e\|$, $\|\mathbf{W}_{de}\|$. δ_e and δ_a do not directly influence the generalized elastic forces \mathbf{Q} and Θ , thus $\|\mathbf{U}_u\| = \|\mathbf{Y}_u\| = 0$. Even so, the elevator and rudder deflections indirectly excite bending and torsion motions due to the coupling effects, as $\|\mathbf{U}_q\|$, $\|\mathbf{U}_s\|$, $\|\mathbf{U}_r\|$, $\|\mathbf{U}_e\|$, $\|\mathbf{U}_{de}\|$, $\|\mathbf{Y}_\xi\|$, $\|\mathbf{Y}_\eta\|$, $\|\mathbf{Y}_r\|$, $\|\mathbf{Y}_e\|$, $\|\mathbf{Y}_{de}\|$ are nonzero.

The symmetric aileron (δ_{a_s} green asterisks) deflections directly lead to translational ($\|\mathbf{K}_u\|$), bending ($\|\mathbf{U}_u\|$) and torsion ($\|\mathbf{Y}_u\|$) accelerations, as well as small pitching accelerations ($\|\mathbf{W}_u\|$). The \mathbf{u} related terms are about 40, 4, 40 times larger than the \mathbf{x}_e and $\dot{\mathbf{x}}_e$ related terms in the translational, rotational, bending equations respectively. $\|\mathbf{Y}_\xi\|$ is comparable with $\|\mathbf{Y}_u\|$ because the wing torsion modes have higher frequency and smaller damping ratio than the bending modes (Fig. 7.6). Nevertheless, under δ_{a_s} deflections, $\|\mathbf{K}_r\|$, $\|\mathbf{W}_r\|$, $\|\mathbf{U}_r\|$, $\|\mathbf{Y}_r\|$ are at least two orders of magnitude smaller than the remaining terms.

The term values under the asymmetric aileron (δ_{a_a} purple diamonds) excitation show similar phenomena as under δ_{a_s} excitation. Namely, the \mathbf{x}_e and $\dot{\mathbf{x}}_e$ related terms have comparable variations as compared to the \mathbf{u} related terms, while $\|\mathbf{K}_r\|$, $\|\mathbf{W}_r\|$, $\|\mathbf{U}_r\|$, $\|\mathbf{Y}_r\|$ are at least two orders of magnitude smaller than the remaining terms. The simulation results in this subsection further verify the feasibility of viewing \mathbf{K}_r , \mathbf{W}_r , \mathbf{U}_r , \mathbf{Y}_r as perturbations in the control design process (Sec. 7.3.2).

7.4.3. STATE ESTIMATION RESULTS AND DISCUSSIONS

The method presented in Sec. 7.3.3 will be used to estimate the elastic states \mathbf{x}_e and $\dot{\mathbf{x}}_e$ while the flexible aircraft flying through a 2D von Kármán turbulence field (Fig. 7.3). The parameters of the turbulence field are $L_g = 762$ m, $\sigma = 1.5$ m/s. The measurement noise \mathbf{v} is modeled as white noise with standard deviation of 0.03 m/s². The turbulence parameters used by the Dryden model are $L_g = 800$ m, $\sigma = 1.8$ m/s, which are chosen to be different from the actual turbulence field for including the parametric uncertainties. As mentioned in Sec. 7.3.3, these uncertain parameters can be modeled as random walk and be estimated online. In this research, by tuning the process noise covariance matrix \mathbf{Q}_{kf} , the Kalman filter already shows satisfactory results without directly estimating these uncertain parameters.

Fig. 7.9 illustrates the real and estimated deformation velocities of the first, second bending modes and the first torsion mode. As can be seen from Figs. 7.9 and 7.10, the Kalman filter online estimation converges within 0.02 s. The estimation errors are all within the posterior estimate standard deviation boundary.

The deformation accelerations $\ddot{\mathbf{x}}_e$ can be reconstructed from linear accelerometer measurements. As an alternative, $\ddot{\mathbf{x}}_e$ can also be obtained by passing $\dot{\mathbf{x}}_e$ through a “washout” filter: $s\omega_n^2/(s^2 + 2\zeta_n\omega_n s + \omega_n^2)$. The estimation results of the deformation accelerations are shown in Fig. 7.11, where only small disagreements between the real and estimated values present. Fig. 7.12 shows the estimated generalized elastic displacements \mathbf{x}_e . Different from the elastic velocity and acceleration estimations, perceptible errors present in the displacement estimations. The reason behind this can be revealed by Eq. (7.41), in which the accelerometer measurements are less correlated with \mathbf{x}_e . The only term in Eq. (7.41) that contains \mathbf{x}_e is $\widetilde{\Phi}\mathbf{q}^T \mathbf{C}_w \dot{\omega}_f$, whose z component is almost zero

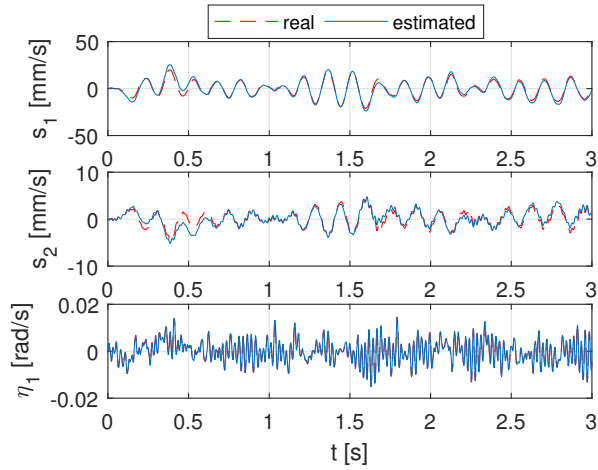


Figure 7.9: Real and estimated deformation velocities.

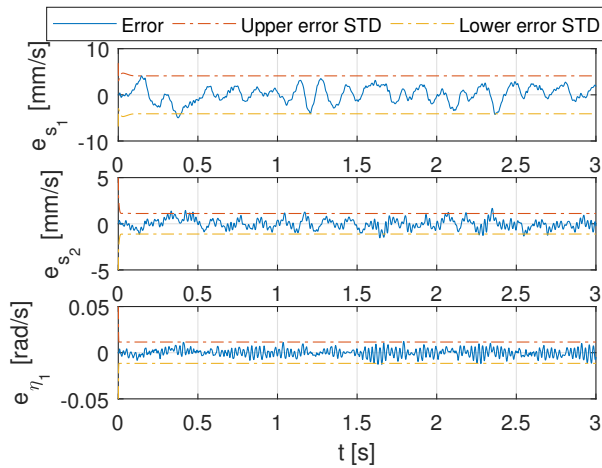


Figure 7.10: Deformation velocity estimation errors.

under small deformations. As a consequence, the estimation of \mathbf{x}_e has to depend more on the linearized reduced-order model, which is different from the nonlinear full-order dynamics. Nevertheless, it will be shown in Sec. 7.4.4 that these estimation errors can be tolerated by the INDI control.

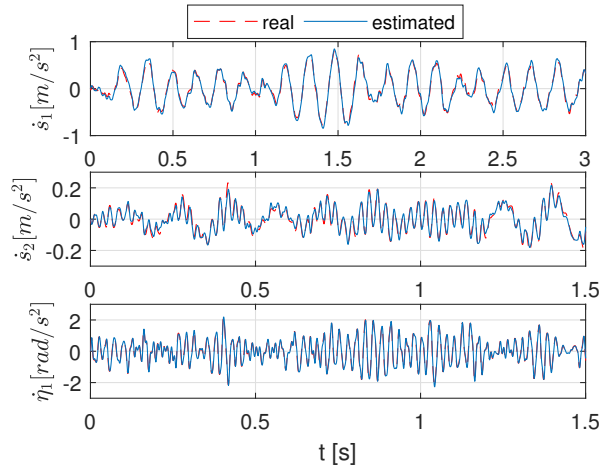


Figure 7.11: Real and estimated deformation accelerations.

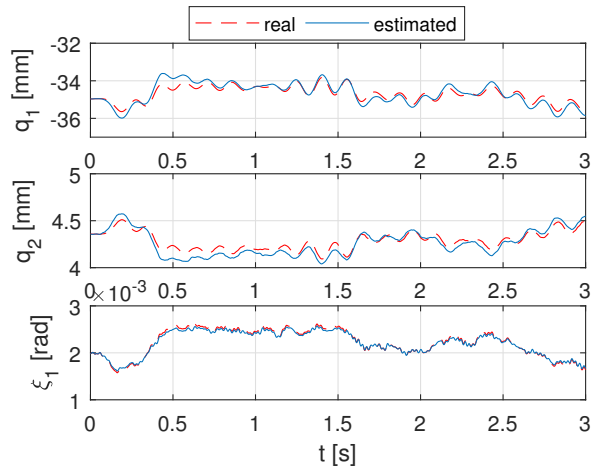


Figure 7.12: Real and estimated deformations.

7.4.4. INDI GLA SIMULATION RESULTS AND DISCUSSIONS

In this subsection, the INDI GLA control law derived in Sec. 7.3.2 will be validated by the benchmark full-order nonlinear flexible aircraft model. This aircraft flies through both a continuous turbulence field (Fig. 7.3) and a discrete gust field (Fig. 7.4). The deviation

of the vertical load factor from its nominal value $\tilde{n}_z = n_z - n_{z*}$, and the derivation of the wing root bending moment $\tilde{M}_r = M_r - M_{r*}$ are chosen as two performance metrics.

Figs. 7.13-7.17 illustrate the dynamic responses of the flexible aircraft flying through a von Kármán turbulence field (Fig. 7.3), in which “Open” means responses without control. “INDI” means the closed-loop responses of the system under INDI GLA control, where the states and their derivatives are assumed to be available. “KF” refers to the closed-loop system responses, when the estimated elastic states and their derivatives are used by the controller. The root mean square (rms) value as well as the peaks of \tilde{n}_z and \tilde{M}_r are summarized in Table 7.2. It can be seen from Fig. 7.13 and Table 7.2 that the proposed INDI GLA controller effectively alleviates both the vertical load and the wing root bending moment. Because of the unsteady aerodynamic effects, the load responses in Fig. 7.13 are smoother than the results in [38] where quasi-steady aerodynamics are used. INDI is able to tolerate the state estimation errors (Sec. 7.4.3) since the closed-loop responses using the estimated states only have small deteriorations as compared to the ideal case.

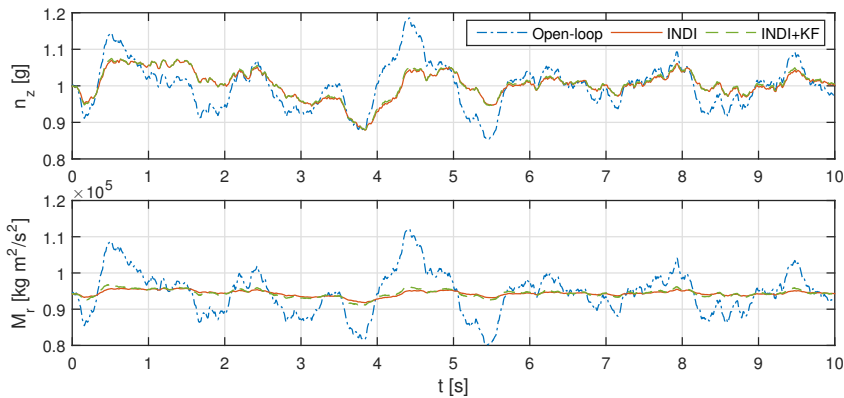


Figure 7.13: Vertical load factor and wing root bending moment responses under turbulence excitation.

7

Table 7.2: The maximum and rms values of the load deviations under turbulence excitation.

	$\max(\tilde{n}_z)$ [g]	$\hat{\sigma}(\tilde{n}_z)$ [g]	$\max(\tilde{M}_r)$ [N·m]	$\hat{\sigma}(\tilde{M}_r)$ [N·m]
Open	0.186	0.0616	1.80×10^4	6.04×10^3
INDI	0.072 (61.3%)	0.0386 (37.4%)	1.63×10^3 (90.9%)	815 (86.5%)
KF	0.074 (60.1%)	0.0392 (36.4%)	2.71×10^3 (84.9%)	1.08×10^3 (82.2%)

Fig. 7.15 shows the responses of the generalized elastic displacements, namely the first bending q_{r_1} , second bending q_{r_2} , and the first torsion ξ_{r_1} modes of the right wing. For this flexible aircraft configuration, only one set of aileron is available on the wing, which aims at wing bending and torsion modes suppression, vertical load control and roll rate control at the same time. However, according to the controllability analysis, this configuration is unable to achieve a decoupled control for all its missions. For example,

in the presence of an upwash gust, the wing lift increases, which results in load increment, upward bending and nose-up torsion of the wing as can be seen in Figs. 7.18-7.20. The symmetric up deflections of ailerons would alleviate the wing load and the bending deformation, but would degrade the torsion deformation because the aerodynamic center of the aileron is behind the wing elastic axis. Since the torsion stiffness is normally larger than the bending stiffness, the vertical load and bending mode control are weighted heavier in Eq. (7.39). Consequently, as shown in Fig. 7.14, the bending modes of the flexible wing are successfully suppressed, while the torsion deformations have reasonable increments. There are a couple of ways to improve the torsion responses. The fundamental solution would be adding control surfaces (e.g. inboard ailerons, flap-erons, spoilers, etc.) to achieve a synergetic control with the outboard ailerons. Novel control surfaces like the variable camber continuous trailing edge flap (VCCTEF) developed in NASA Ames [9, 11] are beneficial to elastic wing controls. It is noteworthy that from the control design point of view, increasing the number of control surfaces only expands the dimension of the \mathbf{B}_e matrix (Eq. (7.33)). Stiffening the wing box or increasing the control weights on the torsion motion are also possible approaches.

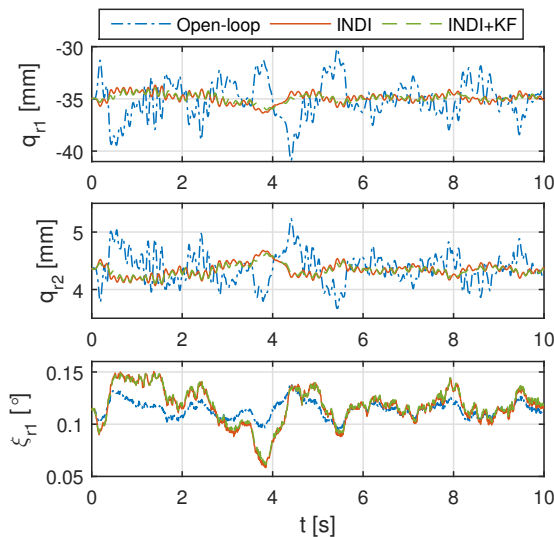


Figure 7.14: Generalized displacements under turbulence excitation.

The wing-tip bending and torsion deformations are illustrated in Fig. 7.15. When using the INDI control, the rms of $z_{\text{tip}} - z_{\text{tip}^*}$ is reduced by 72.6% while rms $(\phi_{\text{tip},r} - \phi_{\text{tip},r}^*)$ is increased by 33% owing to the lack of control surface numbers. Moreover, the rms of pitch rate is suppressed from 0.37 deg/s to 0.07 deg/s. The control inputs are illustrated in Fig. 7.17, where the left aileron deflections δ_{al} equal the right δ_{ar} in the symmetric turbulence field.

The dynamic responses of the flexible aircraft in a symmetric “1 – cos” gust field (Fig. 7.4) are illustrated in Figs. 7.18-7.21. As shown in Fig. 7.18 and Table 7.3. The vertical load factor and wing root bending moment are alleviated by over 36% and 86% re-

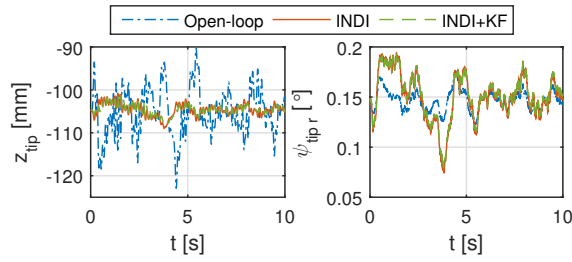


Figure 7.15: Wing-tip bending and torsion deformations under turbulence excitation.

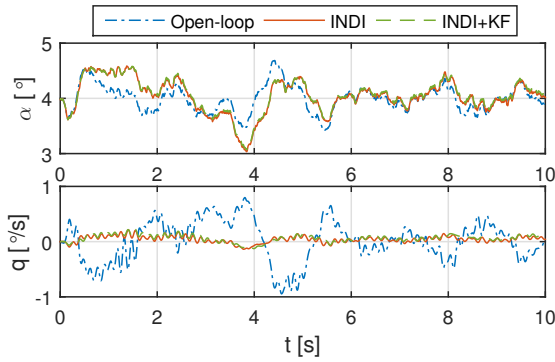


Figure 7.16: Rigid-body state responses.

7

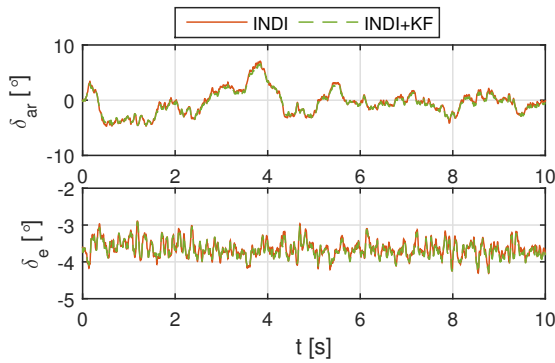


Figure 7.17: Control inputs using INDI.

spectively. In the presence of upwash gusts, the ailerons deflect upward symmetrically to alleviate the wing load as shown in Fig. 7.22. Analogous to the responses under turbulence excitations, the bending modes are suppressed while the torsion modes have acceptable increments in this gust field, as shown in Fig. 7.19 and Fig. 7.20. In view of Fig. 7.21, the peak of pitch rate q is reduced by 82.7%.

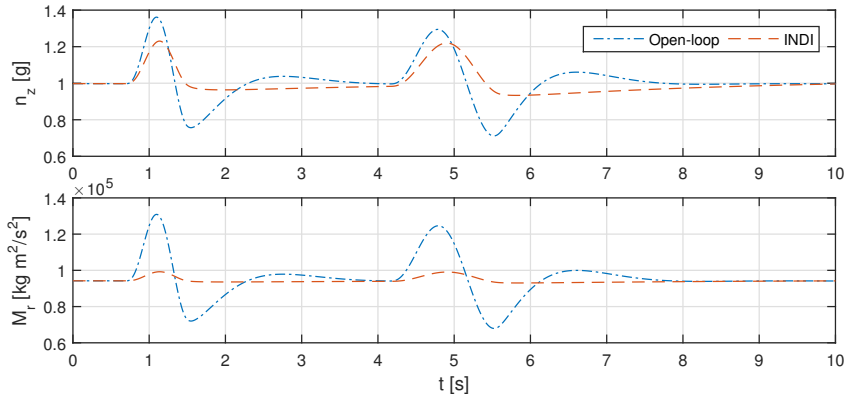


Figure 7.18: Vertical load factor and wing root bending moment responses under gust excitation.

Table 7.3: The maximum and rms values of the load deviations under gust excitation.

	$\max(\tilde{n}_z)$ [g]	$\hat{\sigma}(\tilde{n}_z)$ [g]	$\max(\tilde{M}_r)$ [N·m]	$\hat{\sigma}(\tilde{M}_r)$ [N·m]
Open	0.362	0.113	3.67×10^4	1.10×10^4
INDI	0.231 (36.2%)	0.070 (38.1%)	5.10×10^3 (86.1%)	1.50×10^3 (86.4%)

7.4.5. VALIDATION BY A MORE FLEXIBLE AIRCRAFT MODEL

As discussed in Sec. 7.4.1, the benchmark aircraft may not be representative for a very flexible aircraft, thus a more flexible aircraft model which reduces the stiffness of the benchmark aircraft by 80% is also used to validate the proposed controller. It has been shown in Fig. 7.7 that the increase of flexibility changes both the rigid-body and elastic modes of the benchmark flexible aircraft. The normal control design routine for this more flexible aircraft would be: 1) build a nonlinear reduced-order flexible aircraft model; 2) identify the \mathbf{A}_e and \mathbf{B}_e matrices in Eq. (7.39); 3) re-tune the control parameters \mathbf{K}_p in Eq. (7.38). In view of the analyses in Sec. 7.3.1, the INDI control is robust to model mismatches by virtue of its sensor-based nature. Therefore, to simplify the implementation process and to assess the robustness of this control, the controller designed for the benchmark aircraft is directly applied to this more flexible aircraft model without modifying the \mathbf{A}_e , \mathbf{B}_e , \mathbf{K}_p matrices. During simulations, this more flexible aircraft flies through the 2D turbulence filed shown in Fig. 7.3 for ten seconds. The results are presented in Figs. 7.23-7.27, in which “MF” represents “More Flexible”. As illustrated in Fig. 7.23, in spite of the model mismatches and the nonoptimal control gains, the

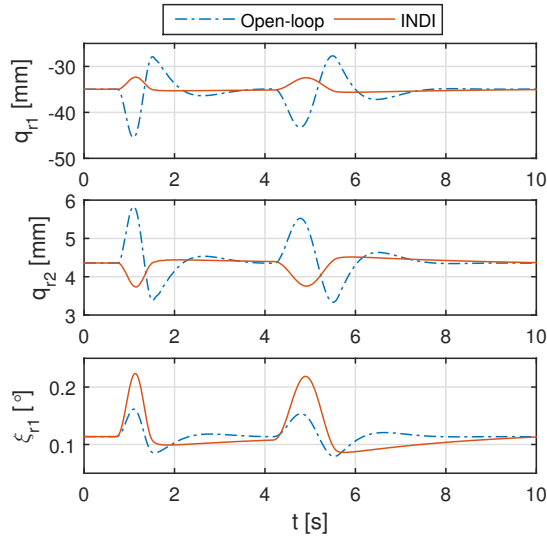


Figure 7.19: Generalized displacements under gust excitation.

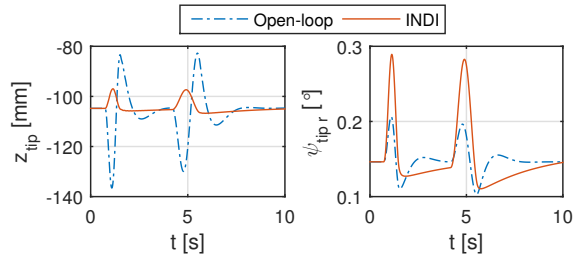


Figure 7.20: Wing-tip bending and torsion deformations under gust excitation.

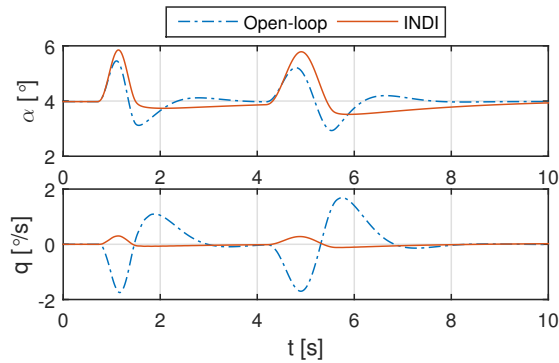


Figure 7.21: Rigid-body state responses to gust.

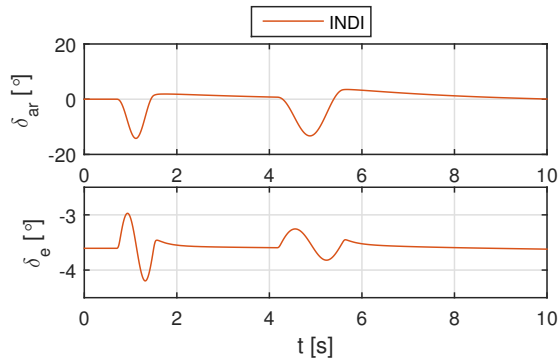


Figure 7.22: Control inputs in a gust field.

maximum value of $n_z - n_{z*}$ is still reduced by 36.8%. Moreover, the maximum and rms values of the wing root bending moment deviations are respectively reduced by 84.7% and 78.3%. The performance of this control can be further improved by using more accurate \mathbf{A}_e , \mathbf{B}_e matrices and optimizing the control gains.

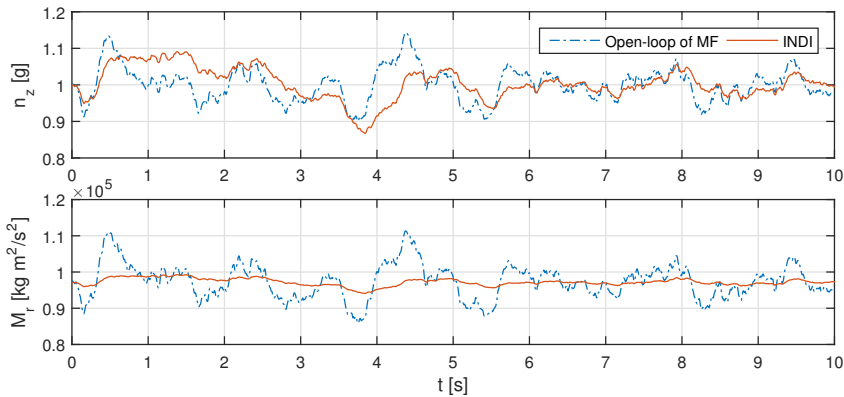


Figure 7.23: Load responses of a more flexible aircraft under turbulence excitation.

The generalized displacements and the wing-tip deformations are shown in Figs. 7.24 and 7.25. When compared to the open-loop responses of the benchmark flexible aircraft (Figs. 7.14 and 7.15), this more flexible aircraft has higher vibration magnitude and reduced vibration frequency in the turbulence field. Fig. 7.25 shows that the wing-tip of this more flexible aircraft bends up by 551 mm in the trim condition, and oscillates in the range of $[-606, -508]$ mm under turbulence excitations. The INDI control can reduce the rms of $z_{tip} - z_{tip*}$ by 70.3%. The pitch rate magnitude of this more flexible aircraft doubles the value of the benchmark aircraft (Fig. 7.16). When INDI is applied, the magnitude of q is reduced from 2.5 deg/s to 0.5 deg/s. The control surface deflections are illustrated in Fig. 7.27.

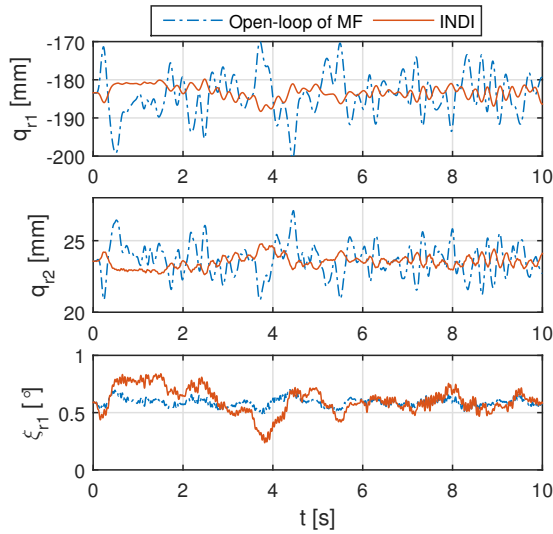


Figure 7.24: Generalized displacements of the more flexible aircraft.

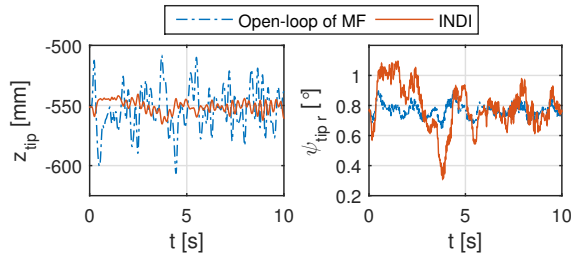


Figure 7.25: Wing-tip bending and torsion deformations of the more flexible aircraft.

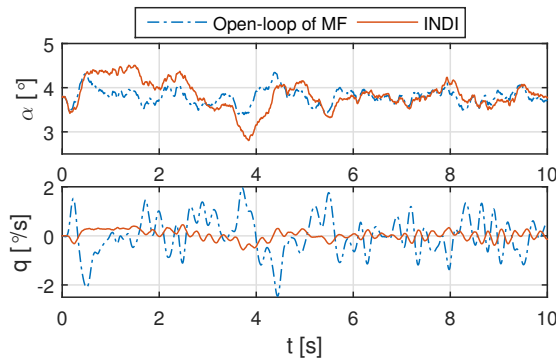


Figure 7.26: Rigid-body state responses.

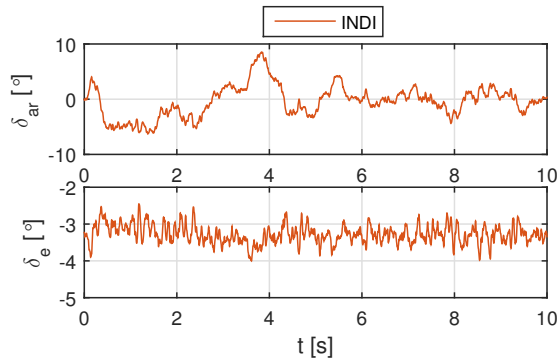


Figure 7.27: Control inputs using INDI.

7.4.6. TOLERANCE TO ACTUATOR FAULTS

The INDI control can passively tolerate actuator sudden faults provided \mathbf{GG}^{-1} remains diagonally dominant in the post-fault condition [28, 46]. In practice, the tolerance of the control to actuator faults is also constrained by the rate and position limits of the actuators. In this subsection, a command-filtered actuator compensator is used to handle the actuator nonlinear constrains. The core idea of this technique is that the command given to the actuator is passed through a command filter first, which considers the nonlinear constrains and bandwidth of the actuator. When the actuator limits are reached, instead of enforcing the actuator to follow the physically unachievable command, an actuator compensator can guarantee the output of the command filter being tracked. For more details of this technique, readers are recommended to [47]. The pseudo-control hedging (PCH) technique can also be used to deal with actuator constrains [48, 49]. Real-world flight tests have demonstrated the applicability of the combination of PCH and INDI [24].

This subsection will test the robustness of the proposed INDI GLA control to actuator partial loss of effectiveness. When an actuator fault occurs, the circulatory and noncirculatory aerodynamic coefficients related to control deflections in Eqs. (7.12, 7.15) are scaled. However, the control is not aware of the fault, and still uses the \mathbf{B}_e matrix estimated in the nominal case.

Fig. 7.28 shows the load responses of the benchmark flexible aircraft with partial loss of control effectiveness. The label $\sigma_{\Delta M_r}$ is an abbreviation for the rms value of $M_r - M_{r_s}$. During simulations, this aircraft flies through the turbulence field shown in Fig. 7.3 for ten seconds, and all the considered actuator faults occur at $t = 0$ s. As shown in Fig. 7.28, without changing any control parameter, this controller is able to passively tolerate both ailerons simultaneously lose 50% of their effectiveness. When the fault percentage is larger than 50%, the effectiveness of the control is limited by the rate constrains of the ailerons. The command-filtered actuator compensator can still guarantee the stability, while the load alleviation performance inevitably decreases with the increase of fault severity.

Apart from load alleviation, a more important mission of the elevator is to trim the aircraft. As shown in Table 7.1, the elevator trim angle δ_{e^*} is nonzero in the considered

flight condition. As a consequence, when the elevator partially loses its effectiveness, its deflection angle should increase timely to re-trim the aircraft. It can be observed from Fig. 7.28 that this controller can passively tolerate up to 80% of the elevator effectiveness loss. For more severe cases, the position limit of the elevator is reached, and a re-trim becomes physically impossible.

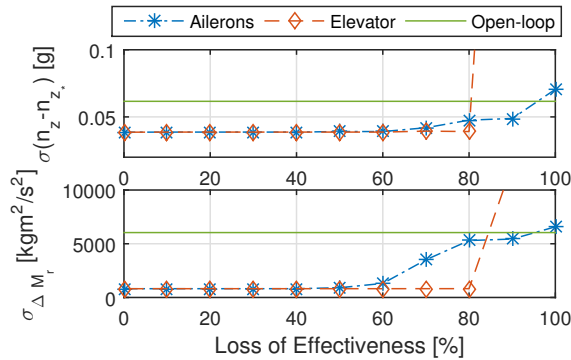


Figure 7.28: rms values of the load deviations in the presence of actuator effectiveness loss.

A more comprehensive fault case is illustrated in Fig. 7.29, where the elevator suddenly loses half of its effectiveness at $t = 1$ s, following which 50% of the right aileron effectiveness is also lost at $t = 3$ s. This asymmetrical fault case challenges the lateral re-trim ability of this controller. The same as claimed before, neither the model nor the control parameter is modified after the faults occur. In view of Fig. 7.29, after the elevator fault occurs, the mean value of δ_e doubles in 0.5 second to re-trim the aircraft. The deflection angle of the right (δ_{ar}) and left (δ_{al}) ailerons are equal before $t = 3$ s (the positive sign is defined as: right aileron deflects downwards, and left upwards). After $t = 3$ s, the magnitude of δ_{ar} increases to compensate for its effectiveness loss. The lateral states p and r are hardly influenced by the faults. As compared to the open-loop responses (Figs. 7.13 and 7.16), the rms of q and $M_r - M_{r^*}$ are respectively reduced by 80.6% and 86.4% in spite of the faults.

7

7.4.7. ROBUSTNESS TO AERODYNAMIC MODEL UNCERTAINTIES

As analyzed in Sec. 7.3.1, the INDI control is designed via a sensor-based approach, namely a part of the dynamic model is replaced by sensor measurements, which improves the robustness of this controller to model mismatches. Regarding flight control, a large proportion of the model mismatches is caused by the difficulties in estimating the aerodynamic coefficients. In view of this, the robustness of the proposed INDI GLA control law to aerodynamic model uncertainties will be evaluated in this subsection.

The flexible aircraft model used in this chapter contains k lifting surfaces, namely the fuselage (fu), engine pylon (p), wings (w), horizontal tail (ht) and vertical tail (vt). Each aircraft component is divided into n_k strips and steady-flow lift curve slope of each strip ($C_{L\alpha}^{SF}$ in Eq. (7.13)) adopts the tabular data in [2]. In this subsection, this model is augmented by the uncertain parameters $\Delta C_{L\alpha}^{SF}$ for robustness validations. It is remark-

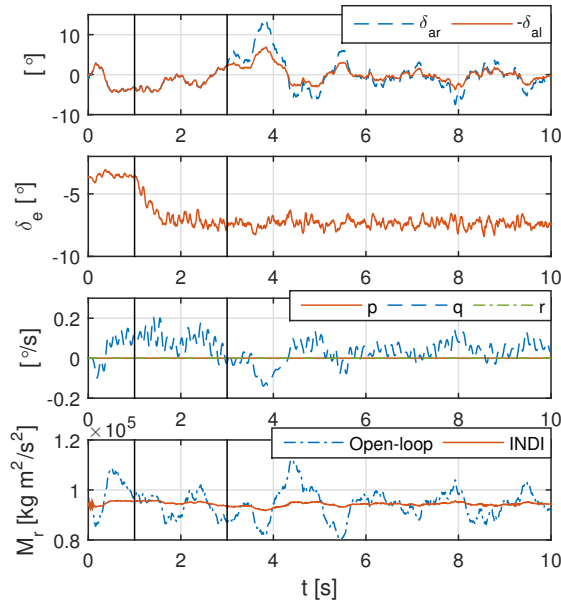


Figure 7.29: Half of the elevator and the right aileron effectiveness are successively lost at $t = 1$ s, and $t = 3$ s.

able that for the wings and tails, the incorporation of $\Delta C_{L\alpha}^{SF}$ also changes the control effectiveness because $C_L^{c,\delta}$ is a function of $C_{L\alpha}^{SF}$ (Eq. (7.15)). A Monte Carlo simulation containing one thousand uncertain aerodynamic models is conducted, where $\Delta C_{L\alpha}^{SF}$ is modeled by

$$\Delta C_{L\alpha k}^{SF} \triangleq \{\Delta C_{L\alpha k}^{SF} \in \mathbb{R} | \Delta C_{L\alpha k}^{SF} = N(0, \sigma_k^2)\}, \quad \sigma_k = \frac{\rho_k}{n_k} \sum_{i=1}^{i=n_k} C_{L\alpha i}^{SF}, \quad k = fu, p, w, ht, vt. \quad (7.48)$$

For each lifting surface k , the mean value of the uncertainty is zero and the standard deviation σ_k is chosen as ρ_k times the average $C_{L\alpha}^{SF}$ of this lifting surface. The perturbation range is chosen as $\rho_{ht} = \rho_{vt} = 0.3$, $\rho_{fu} = \rho_p = 0.2$, $\rho_w = 0.1$. As shown in Fig. 7.30, among all the 1000 samples, the median value of the vertical load factor derivation $n_z - n_{z^*}$ under INDI GLA control is 0.0435 g, which is alleviated by 29.4% as compared to the open-loop value 0.0616 g (Table 7.2). The interquartile range of $n_z - n_{z^*}$ is only 0.015 g. Moreover, the rms of the wing root bending moment deviations using INDI GLA control is lower than the open-loop value 6405 N·m for all the tested samples. The few larger rms of load variations are caused by dramatic wing lift coefficient perturbations and long-term actuator saturations. This Monte Carlo simulation further verifies the robustness of the proposed controller to aerodynamic model uncertainties.

7.5. CONCLUSIONS

In this chapter, an incremental nonlinear dynamic inversion (INDI) gust load alleviation (GLA) control law is designed for flexible aircraft. A high-order flexible aircraft validation

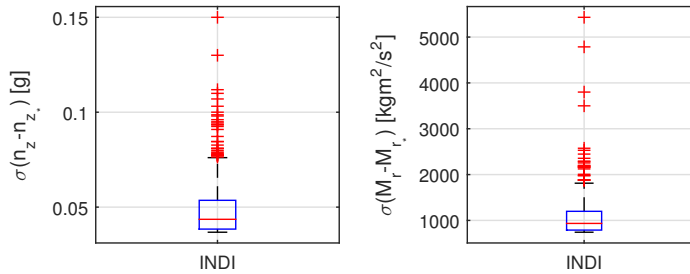


Figure 7.30: Box plot of a Monte Carlo simulation of the closed-loop system subjects to model uncertainties.

model is set up, which considers unsteady aerodynamics and encompasses both inertia and aerodynamic couplings between rigid-body and structural dynamics. This flexible aircraft model is compared with a quasi-rigid aircraft model from the perspective of the trim and eigenvalue solutions. The coupling effects lead to different trim solutions for these two models, and also distinguish the rigid-body modes of the flexible aircraft from the modes of the quasi-rigid aircraft. As the wing stiffness reduces, the coupling effects become more prominent. The phugoid mode becomes unstable if the wing stiffness is reduced by 80%.

In order to simplify the implementation process and reduce the on-board computational load, a reduced-order model is used for control and observer designs. By virtue of its sensor-based nature, INDI only needs part of the reduced-order model information. INDI can guarantee the globally ultimate boundedness of the tracking errors in the presence of bounded perturbations (Proposition 4). Due to the lack of control surfaces, the weighted-least squares method is used along with INDI to make trade-offs among different control objectives. It is shown that the elastic states and their derivatives can be observed from accelerometer measurements using a Kalman filter along with a Padé approximation for modelling the pure time delay.

7

Time domain simulations of a full-order flexible aircraft model flying through various 2D spatial turbulence and gust fields verify that the proposed INDI GLA controller can effectively regulate the rigid-body motions, alleviate the gust loads, reduce the wing root bending moment, and suppress the wing bending modes. The INDI GLA control designed for the benchmark flexible aircraft also shows effectiveness on another more flexible aircraft model without control parameter adjustment. The robustness of the proposed controller is also verified in faulty conditions. It can tolerate sudden actuator faults without using any additional fault detection/estimation method, unless a re-trim becomes physically unachievable. Moreover, a Monte Carlo study demonstrates the robustness of the proposed controller to aerodynamic model uncertainties. In conclusion, less model dependency, easy implementation, reduced computational cost, and robustness to external disturbances, sudden faults and model uncertainties, make the proposed INDI control law promising for alleviating the gust loads of flexible aircraft in real life.

REFERENCES

- [1] L. Meirovitch and I. Tuzcu, *Time Simulations of the Response of Maneuvering Flexible Aircraft*, *Journal of Guidance, Control, and Dynamics* **27**, 814 (2004).
- [2] L. Meirovitch and I. Tuzcu, *National Aeronautics and Space Administration, Langley Research Center*, Tech. Rep. (NASA Langley Research Center, 2003).
- [3] M. R. Waszak and D. K. Schmidt, *Flight Dynamics of Aeroelastic Vehicles*, *Journal of Aircraft* **25**, 563 (1988).
- [4] C. Xie, L. Yang, Y. Liu, and C. Yang, *Stability of Very Flexible Aircraft with Coupled Nonlinear Aeroelasticity and Flight Dynamics*, *Journal of Aircraft* **55**, 1 (2017).
- [5] M. J. Patil and D. H. Hodges, *Flight Dynamics of Highly Flexible Flying Wings*, *Journal of Aircraft* **43**, 1790 (2006).
- [6] S. Haghghat, H. H. T. Liu, and J. R. R. A. Martins, *Model-Predictive Gust Load Alleviation Controller for a Highly Flexible Aircraft*, *Journal of Guidance, Control, and Dynamics* **35**, 1751 (2012).
- [7] W. Fan, H. H. Liu, and R. Kwong, *Gust Load Alleviation Control for a Flexible Aircraft with Loss of Control Effectiveness*, in *AIAA Guidance, Navigation, and Control Conference* (American Institute of Aeronautics and Astronautics, Grapevine, Texas, 2017) pp. 1–16.
- [8] M. Dillsaver, C. Cesnik, and I. Kolmanovsky, *Gust Load Alleviation Control for Very Flexible Aircraft*, in *AIAA Atmospheric Flight Mechanics Conference* (American Institute of Aeronautics and Astronautics, Portland, Oregon, 2011) pp. 1–18.
- [9] Y. Ferrier, N. T. Nguyen, E. Ting, D. Chaparro, X. Wang, C. C. de Visser, and Q. P. Chu, *Active Gust Load Alleviation of High-Aspect Ratio Flexible Wing Aircraft*, in *2018 AIAA Guidance, Navigation, and Control Conference*, January (American Institute of Aeronautics and Astronautics, Kissimmee, Florida, 2018) pp. 1–36.
- [10] B. S. Liebst, W. L. Garrard, and J. A. Farm, *Design of a multivariable flutter suppression/gust load alleviation system*, *Journal of Guidance, Control, and Dynamics* **11**, 220 (1988).
- [11] N. T. Nguyen, S. Sweil, and E. Ting, *Adaptive Linear Quadratic Gaussian Optimal Control Modification for Flutter Suppression of Adaptive Wing*, in *AIAA Infotech @ Aerospace* (American Institute of Aeronautics and Astronautics, Kissimmee, Florida, 2015) pp. 1–23.
- [12] R. G. Cook, R. Palacios, and P. Goulart, *Robust Gust Alleviation and Stabilization of Very Flexible Aircraft*, *AIAA Journal* **51**, 330 (2013).
- [13] A. Hodel, M. Whorton, and J. Zhu, *Stability Metrics for Simulation and Flight-Software Assessment and Monitoring of Adaptive Control Assist Compensators*, in *AIAA Guidance, Navigation and Control Conference and Exhibit* (American Institute of Aeronautics and Astronautics, Honolulu, Hawaii, 2008) pp. 1–25.

- [14] H. K. Khalil, *Nonlinear Systems* (Prentice-Hall, New Jersey, 2002).
- [15] R. J. Caverly, A. R. Girard, I. V. Kolmanovskiy, and J. R. Forbes, *Nonlinear Dynamic Inversion of a Flexible Aircraft*, *IFAC-PapersOnLine* **49**, 338 (2016).
- [16] A. Tewari, *JohnWiley & Sons Ltd* (JohnWiley & Sons Ltd, Chennai, India, 2016).
- [17] L. Sonneveldt, Q. P. Chu, and J. A. Mulder, *Nonlinear Flight Control Design Using Constrained Adaptive Backstepping*, *Journal of Guidance, Control, and Dynamics* **30**, 322 (2007).
- [18] Y. Zhang, C. C. de Visser, and Q. P. Chu, *Aircraft Damage Identification and Classification for Database-Driven Online Flight-Envelope Prediction*, *Journal of Guidance, Control, and Dynamics* **41**, 1 (2017).
- [19] S. Sieberling, Q. P. Chu, and J. A. Mulder, *Robust Flight Control Using Incremental Nonlinear Dynamic Inversion and Angular Acceleration Prediction*, *Journal of Guidance, Control, and Dynamics* **33**, 1732 (2010).
- [20] E. J. J. Smeur, M. Bronz, and G. C. H. E. de Croon, *Incremental control and guidance of hybrid aircraft applied to the Cyclone tailsitter UAV*, (2018), arXiv:1802.00714 .
- [21] S. Sun, L. Sijbers, X. Wang, and C. de Visser, *High-Speed Flight of Quadrotor Despite Loss of Single Rotor*, *IEEE Robotics and Automation Letters* **3**, 3201 (2018).
- [22] E. J. J. Smeur, Q. P. Chu, and G. C. H. E. de Croon, *Adaptive Incremental Nonlinear Dynamic Inversion for Attitude Control of Micro Air Vehicles*, *Journal of Guidance, Control, and Dynamics* **39**, 450 (2016).
- [23] E. J. J. Smeur, G. C. H. E. de Croon, and Q. P. Chu, *Cascaded incremental nonlinear dynamic inversion for MAV disturbance rejection*, *Control Engineering Practice* **73**, 79 (2018), arXiv:1701.07254 .
- [24] F. Grondman, G. Looye, R. O. Kuchar, Q. P. Chu, and E. van Kampen, *Design and Flight Testing of Incremental Nonlinear Dynamic Inversion-based Control Laws for a Passenger Aircraft*, in *2018 AIAA Guidance, Navigation, and Control Conference*, January (American Institute of Aeronautics and Astronautics, Kissimmee, Florida, 2018).
- [25] X. Wang, E. van Kampen, Q. P. Chu, and P. Lu, *Stability Analysis for Incremental Nonlinear Dynamic Inversion Control*, *Journal of Guidance, Control, and Dynamics* (2019), 10.2514/1.G003791.
- [26] P. Lu, E. van Kampen, C. de Visser, and Q. P. Chu, *Aircraft fault-tolerant trajectory control using Incremental Nonlinear Dynamic Inversion*, *Control Engineering Practice* **57**, 126 (2016).
- [27] P. Simplicio, M. Pavel, E. van Kampen, and Q. P. Chu, *An acceleration measurements-based approach for helicopter nonlinear flight control using Incremental Nonlinear Dynamic Inversion*, *Control Engineering Practice* **21**, 1065 (2013).

- [28] X. Wang, E. van Kampen, Q. P. Chu, and P. Lu, *Incremental Sliding-Mode Fault-Tolerant Flight Control*, *Journal of Guidance, Control, and Dynamics* **42**, 244 (2019).
- [29] X. Wang, E. van Kampen, and Q. P. Chu, *Gust Load Alleviation and Ride Quality Improvement with Incremental Nonlinear Dynamic Inversion*, in *AIAA Atmospheric Flight Mechanics Conference* (American Institute of Aeronautics and Astronautics, Grapevine, Texas, 2017) pp. 1–21.
- [30] J. Wright and J. Cooper, *Introduction to Aircraft Aeroelasticity and Loads* (John Wiley & Sons, Washington, DC, 2007) pp. 79–85.
- [31] T. Theodorsen, *General Theory of Aerodynamic Instability and the Mechanism of Flutter*, Tech. Rep. (NACA Technical Report No. 496, 1935).
- [32] R. Bisplinghoff, R. Ashley, H., and Halfman, *Aeroelasticity* (Addison-Wesley Publishing Company, 1955).
- [33] R. T. Jones, *Operational treatment of the nonuniform-lift theory in airplane dynamics*, Tech. Rep. (Technical Note 667, NACA, 1938).
- [34] *U.S. Military Specification MIL-F-8785C* (1980).
- [35] B. Etkin, *Dynamics of Atmospheric Flight* (Dover Publications, Toronto, 2005).
- [36] W. Van Staveren, *Thesis PhD*, Ph.D. thesis, Delft University of Technology (2003).
- [37] X. Yang and J. J. Zhu, *Singular perturbation margin and generalised gain margin for nonlinear time-invariant systems*, *International Journal of Control* **89**, 451 (2016).
- [38] X. Wang, E. van Kampen, R. De Breuker, and Q. P. Chu, *Flexible Aircraft Gust Load Alleviation with Incremental Nonlinear Dynamic Inversion*, in *2018 AIAA Atmospheric Flight Mechanics Conference*, January (American Institute of Aeronautics and Astronautics, Kissimmee, Florida, 2018) pp. 1–21.
- [39] C. Cakiroglu, E. van Kampen, and Q. P. Chu, *Robust Incremental Nonlinear Dynamic Inversion Control Using Angular Accelerometer Feedback*, in *2018 AIAA Guidance, Navigation, and Control Conference*, January (American Institute of Aeronautics and Astronautics, Kissimmee, Florida, 2018).
- [40] C. Nam, Y. Kim, and J. Layton, *Active Aeroelastic Wing Design for Gust Load Alleviation and Flutter Suppression*, in *38th Structures, Structural Dynamics, and Materials Conference* (American Institute of Aeronautics and Astronautics, Kissimmee, Florida, 1997) pp. 729–737.
- [41] M. Natella, X. Wang, and R. De Breuker, *The Effects of Aeroelastic Tailoring on Flight Dynamic Stability*, in *2018 AIAA/ASCE/AHS/ASC Structures, Structural Dynamics, and Materials Conference*, January (Kissimmee, Florida, 2018).
- [42] G. Avanzini, F. Nicassio, and G. Scarselli, *Reduced-Order Short-Period Model of Flexible Aircraft*, *Journal of Guidance, Control, and Dynamics* **40**, 2017 (2017).

- [43] W. Su, *Coupled Nonlinear Aeroelasticity and Flight Dynamics of Fully Flexible Aircraft*, Ph.D. thesis, Univertisy of Michigan (2014).
- [44] E. G. Broadbent, J. K. Zbrozek, and E. Huntley, *A Study of Dynamic Aeroelastic Effects on the Stability Control and Gust Response of a Slender Delta Aircraft*, Tech. Rep. 3690 (Aeronautical Research Council Reports And Memoranda, 1972).
- [45] J. Murua, R. Palacios, and J. M. R. Graham, *Applications of the unsteady vortex-lattice method in aircraft aeroelasticity and flight dynamics*, *Progress in Aerospace Sciences* **55**, 46 (2012).
- [46] X. Wang, S. Sun, E. van Kampen, and Q. P. Chu, *Quadrotor Fault Tolerant Incremental Sliding Mode Control driven by Sliding Mode Disturbance Observers*, *Aerospace Science and Technology* **87**, 417 (2019).
- [47] P. Lu, E. van Kampen, and Q. P. Chu, *Robustness and Tuning of Incremental Backstepping Approach*, in *AIAA Guidance, Navigation, and Control Conference* (American Institute of Aeronautics and Astronautics, Kissimmee, Florida, 2015) pp. 1–15.
- [48] E. N. Johnson and A. J. Calise, *Pseudo-Control Hedging : a New Method for Adaptive Control*, Advances in Navigation Guidance and Control Technology Workshop (2000).
- [49] E. Johnson, A. Calise, H. El-Shirbiny, and R. Eysdyk, *Feedback linearization with Neural Network augmentation applied to X-33 attitude control*, *AIAA Guidance, Navigation, and Control Conference and Exhibit*, 1 (2000).

8

CONCLUSIONS AND RECOMMENDATIONS

This dissertation has been dedicated to enhancing flight safety through advanced automatic flight control systems. At the beginning of this dissertation, some challenges in flight control design were posed: actuator faults and structural damages, atmospheric disturbances, increase of structural flexibility, and the nonlinear dynamics. In view of these challenges, the main research goal was proposed as:

Research Goal

To design a stability-guaranteed nonlinear flight control framework with reduced model dependency and enhanced robustness.

To achieve this research goal, four research questions were raised in Chapter 1. These questions have been addressed in the four chapters of Part I, and their answers will be presented in Sec. 8.1.1. The theories and methods developed in Part I have shown effectiveness on solving various flight control problems in Part I and Part II. The main findings and conclusions through implementations will be summarized in Sec. 8.1.2. Moreover, the final conclusions will be drawn in Sec. 8.1.3. Finally, the limitations of this thesis and recommendations for future work will be presented in Sec. 8.2.

8.1. CONCLUSIONS

8.1.1. ANSWERS TO RESEARCH QUESTIONS

Two promising methods to control uncertain nonlinear systems: incremental control and sliding mode control (SMC) were reviewed in Sec. 1.3.1 and Sec. 1.4.1. However, as has been exposed in Sec. 1.3.2 and Sec. 1.4.2, these two approaches also have their limitations. In view of these limitations, three research questions were proposed:

Research Question 1: How can the stability of incremental nonlinear dynamic inversion control be analyzed and expressed?

This research question is addressed in Chapter 2, where incremental nonlinear dynamic inversion (INDI) control is first generalized for uncertain nonlinear systems with arbitrary input–output relative degree. The new derivations in Chapter 2 do not need the time-scale separation assumption or term omissions.

It is then found in Chapter 2 that even in the absence of model uncertainties and external disturbances, perturbations still remain in the closed-loop system under INDI control. These perturbations contain a state-variation-related term and higher-order terms of the first-order Taylor series expansion of system dynamics. It is shown that, if the partial derivatives of system dynamics with respect to state, up to any order, are bounded, the norm value of the entire perturbation term can be reduced by increasing the sampling frequency.

Moreover, it is proven in Chapter 2 that, if the internal dynamics are input-to-state stable, the state under INDI control is globally ultimately bounded by a class \mathcal{K} function of the perturbation bound. Input-to-state stable is a relatively strict condition. If only the origin of the zero dynamics is exponentially stable, then the closed-loop system under INDI control is only locally ultimately bounded by a class \mathcal{K} function of the perturbation bound. “Locally” means that not only the initial state should be in the neighborhood of the origin, the bound of the perturbation should also be sufficiently small.

Furthermore, in the presence of external disturbances, it is proven that under INDI control, the internal states are directly perturbed by the disturbances, whereas the external states are only perturbed by the increments of the disturbances. By virtue of the sensor-based nature of INDI, the main influences of external disturbances are included in the measurements/estimations of the output derivatives.

Finally, INDI control is shown to be more robust to regular perturbations than nonlinear dynamic inversion (NDI) control, without using any additional robust or adaptive techniques. A certain region of singular perturbations can also be resisted by INDI.

Chapter 2 shows that a part of the input–output mapping of a nonlinear system is included in the estimated or measured output derivatives. This system information contained in sensor measurements can be used to solve the third research question:

Research Question 3: How can the contradiction between the reduction of model dependency and the reduction of uncertainty in sliding mode control be solved?

It has been demonstrated in Chapter 2 that in spite of its reduced model dependency, INDI has better robustness against regular perturbations than NDI. Nevertheless, the properties of the regular-perturbation-induced uncertainty term ϵ_{indi} remain unknown in Chapter 2. In view of this, Chapter 3 shows that a diagonally dominant structure of $\mathcal{B}\bar{\mathcal{B}}^{-1}$ (the real control effectiveness matrix multiplied with the inverse of its estimation) and a sufficiently high sampling frequency are needed for the boundedness of

ϵ_{indi} . The sufficient conditions for the boundedness of ϵ_{indi} are less strict than those of the regular-perturbation-induced uncertainty term ϵ_{ndi} in NDI control. Numerical simulations show that ϵ_{ndi} can become unbounded in severe damage cases, especially when the actuators have position and rate limits. Furthermore, under the same regular perturbation circumstance, there exists a sampling frequency which makes the upper bound of ϵ_{indi} smaller than that of ϵ_{ndi} .

The reduced model dependency and the smaller bound of ϵ_{indi} make INDI a promising substitution of NDI in (higher-order) SMC and sliding mode disturbance observer (SMDO) designs. The hybridization of INDI with SMC/SMDO inherits the advantages and remedies the drawbacks of both approaches. The incorporation of SMC/SMDO into INDI not only robustifies INDI, but also brings fixed/finite-time convergence. The design of SMC/SMDO using the sensor-based control structure of INDI allows the hybrid control to passively resist a wide range of perturbations with lower sliding mode control/observer gains. Simulation results verify that the model dependency and the resulting uncertainty can be simultaneously reduced in the hybrid control framework.

The developments in Chapters 2 and 3 help to answer the second research question:

Research Question 2: How can the concept of incremental backstepping control be improved and how can its robustness be enhanced?

In Chapter 4, IBS control is generalized for higher-order nonlinear uncertain systems in the strict-feedback form, without using the time-scale assumption or term omissions. Then it is found that in the presence of regular perturbations, the system under IBS control is perturbed by an uncertainty term ϵ_{ibs} . This term is in a similar form as ϵ_{indi} . Analogous to the proofs in Chapter 3, the boundedness conditions for ϵ_{ibs} are presented in Chapter 4. It is also shown that there exists a sampling frequency which ensures that ϵ_{ibs} has a smaller upper bound than the uncertainty term under backstepping control (ϵ_{bs}). The smaller upper bound of ϵ_{ibs} motivated the hybridization of the reformulated IBS with SMC, named IBSMC. The robustness of IBS is enhanced in the hybrid framework, because the SMC virtual control can compensate for the influences of ϵ_{ibs} . Furthermore, as compared to backstepping sliding mode control in the literature, the proposed IBSMC framework can simultaneously reduce the model dependency and the minimum possible SMC gains. In addition, for nonlinear systems in the strict-feedback form, the recursive IBSMC design is simpler than INDI-SMC (which depends on the input–output mapping) proposed in Chapter 3.

The INDI-SMC framework proposed in Chapter 3 can induce both first- and higher-order sliding modes. In the literature, higher-order sliding modes can also be achieved by other control structures. This leads to the last research question of this thesis:

Research Question 4: What is the relationship between the INDI-based SMC proposed in this thesis, the NDI-based SMC, and higher-order SMC with artificially increased relative degree?

In Chapter 5, analytical and numerical comparisons are made among INDI-SMC, NDI-SMC, and HOSMC which artificially increases the relative degree by one order. All of them can be used to induce higher-order sliding modes in finite time. It is found that only the estimated control effectiveness matrix is needed by the considered HOSMC and INDI-SMC, while NDI-SMC has higher model dependency. The implementation of INDI-SMC requires the measurements/estimations of the output derivatives, while the considered HOSMC uses the numerically differentiated output derivatives as well as the higher-order derivatives of the tracking commands.

Furthermore, although the considered HOSMC and INDI-SMC originate from completely different ideas, their nominal control increments are found to be approximately equivalent if the sampling interval Δt is sufficiently small, and if their control parameters satisfy certain conditions (presented in Sec. 5.3.1). Once these conditions are satisfied, the considered HOSMC and INDI-SMC lead to similar transient responses and control performance.

In the presence of external disturbances and model uncertainties, different closed-loop uncertainty terms appear, namely $\epsilon_{\text{ndi-s}}$, $\epsilon_{\text{indi-s}}$ and $\epsilon_{\text{ho-s}}$. It is found in Chapter 5 that once the sliding modes are enforced, $\epsilon_{\text{ho-s}}(t)\Delta t \approx \epsilon_{\text{indi-s}}(t)$, and also $\dot{\epsilon}_{\text{ho-s}}(t)\Delta t \approx \dot{\epsilon}_{\text{indi-s}}(t)$. As a consequence, for maintaining the sliding modes, the minimum possible gains required by the considered HOSMC approximately equal those needed by INDI-SMC divided by Δt . Although the switching gains needed by the considered HOSMC are several orders of magnitude higher than those of INDI-SMC, these two control structures lead to comparable chattering magnitudes, which are effectively reduced as compared to NDI-SMC.

8.1.2. IMPLEMENTATION FINDINGS AND CONCLUSIONS

The main findings through applying the theories developed in Part I to flight control will be summarized in this subsection.

In Chapter 2, the generalized INDI control is used to drive a rigid aircraft to track references in various spacial turbulence fields. As compared to NDI control, better tracking performance is achieved by the generalized INDI control. Moreover, the influences of sampling interval and virtual control gains on the ultimate bounds are verified. Finally, a Monte-Carlo simulation shows that the generalized INDI control is less sensitive to external disturbances and model uncertainties than NDI control.

In Chapter 3, INDI-SMC is used to solve aircraft fault-tolerant control problems. Numerical simulations confirm that INDI-SMC has better performance over NDI, INDI and NDI-SMC, in the presence of sudden actuator faults and structural damages. A wide range of perturbations can be passively tolerated by INDI-SMC, without using online model identification or fault detection and diagnosis (FDD). Moreover, the minimum possible gains needed by INDI-SMC are lower than those of NDI-SMC, which is beneficial to chattering reduction. Similar conclusions are also drawn in Chapter 4 where, in spite of its reduced model dependency and reduced gains, IBSMC enhances the tracking performance of an aircraft in the presence of model uncertainties, sudden actuator faults and structural damages.

In Chapter 6, the SMC hybridized with incremental control framework is validated by quadrotor flight tests. The derivations in Chapter 3 are also improved by explicitly

considering sudden (discontinuous in time) faults and external disturbances. It is verified in Chapter 6 that in the presence of model uncertainties, actuator faults and external disturbances, there exists a sampling frequency such that the upper bound of ϵ_{indi} is smaller than that of ϵ_{ndi} , both before and after a fault occurs. Chapter 6 also shows that the main influences of faults can be included in the output derivatives, thus ϵ_{indi} still varies around zero after a fault occurs. Last but not least, ϵ_{indi} has smaller variations in different fault cases, while ϵ_{ndi} is more fault-case dependent and even has abrupt changes when a sudden fault occurs.

Both simulations and real-world flight tests demonstrate that these beneficial properties of INDI-SMC allow a quadrotor to passively resist a wide range of perturbations with lower and fixed control/observer gains. By contrast, the gains used by the model-based SMC/SMDO design are higher and must be adapted or manually adjusted in different scenarios. The implementation process of INDI-SMC is also simplified because of its reduced model dependency and smaller uncertainty variations. In addition, the onboard computational load of INDI-SMC is reduced in the considered scenarios since online model identification and dynamic parameter update laws are not used.

In Chapter 7, a model analysis demonstrates the influences of structural flexibility on rigid-body modes. For the considered aircraft model, as its wing stiffness reduces, the pair of complex conjugate short-period poles merges to become two real poles; the phugoid mode also moves to the unstable region. These phenomena further verify the necessity of an integrated flight control design for flexible aircraft.

An INDI-based integrated flight control is designed for flexible aircraft in Chapter 7. Time domain simulations of a full-order flexible aircraft model flying through various two-dimensional spatial turbulence and gust fields verify that the proposed INDI controller can effectively regulate rigid-body motions, alleviate gust loads, reduce the wing root bending moment, and suppress the wing elastic modes.

8.1.3. FINAL CONCLUSIONS

In conclusion, the incremental sliding mode control framework and the incremental backstepping sliding mode control framework proposed in this thesis:

1. have guaranteed stability in the Lyapunov sense;
2. have reduced model dependency as compared to NDI, BS, NDI-SMC and BSMC;
3. have lower computational load than ABS and MRAC;
4. have reduced sliding mode control and observer gains, which is beneficial to chattering reduction; and
5. have enhanced robustness to model uncertainties, external disturbances, sudden actuator faults and structural damages.

These benefits can reduce the cost in aircraft design and certification cycles. Although the two hybrid control frameworks are developed with the goal of enhancing aviation safety, they are also applicable to generic nonlinear uncertain systems, including robotic manipulators, hydraulic systems, etc. Moreover, this thesis builds a bridge between the flight control community and the sliding mode control community, which can open-up cooperation and opportunities. More importantly, we believe the proposed control frameworks can reduce the loss of control in-flight accident rate in reality, and boost a widespread usage of flying robots.

8.2. LIMITATIONS AND RECOMMENDATIONS

The limitations of this thesis and recommendations for future work will be discussed from three aspects:

INCREMENTAL CONTROL

Regarding the influences of external disturbances on INDI, only the symmetrical system is considered in Chapter 2. For more general systems, not only the external disturbances \mathbf{d} , but also the higher-order derivatives of \mathbf{d} will appear in the input–output mapping. Therefore, the robustness analysis for more general systems should consider other issues, including the differentiability and smoothness of \mathbf{d} , the boundedness of the higher-order derivatives of \mathbf{d} , etc. These are recommended as future work.

As shown in [1–4], phase margin is only applicable to stability analysis of linear time-invariant systems. To analyze the robustness of nonlinear time-varying systems against singular perturbations (actuator dynamics, sensor dynamics, higher-order elastic dynamics, etc.), more advanced theories including singular perturbation margin (SPM) [2, 3] are needed. Since the SPM theory is still under development, the discussions in Chapter 2 have some limitations. Using more advanced mathematical tools to analyze the robustness of INDI against singular perturbations is a valuable research direction.

After analyzing the stability margin of a nonlinear system against singular perturbations, it is interesting to find approaches to enlarge the SPM. An initial thought would be to include some “predictive” feature in the closed-loop, such as using a predictive filter [5]. This research direction is also recommended.

Because the core idea of incremental control is to replace a part of the model by sensor measurements, this control approach is inevitably more sensitive to sensing issues, such as sensor dynamics, transport delay, measurement noise, etc. Although real-world implementations have demonstrated the effectiveness of incremental control even in the presence of these issues [6–9], a more rigorous theoretical analysis using advanced stability criteria for the robustness of incremental control to these issues is needed.

The stability and robustness analyses presented in Chapter 2, and the analyses for the uncertainty term ϵ_{indi} in Chapters 3 and 6 can also help to analyze other incremental-model-based control approaches, including incremental approximate dynamic programming [10], incremental model-based heuristic dynamic programming [11], etc. These are recommended as future work.

8

FLEXIBLE AIRCRAFT CONTROL

Although more emphases of Chapter 7 are put on the control design, the flexible aircraft model used in Chapter 7 can be improved. First of all, the bending and torsion stiffness of the benchmark flexible aircraft model are reduced by 80% for the validations in Chapter 7. More realistic flexible aircraft data can increase the reliability of the proposed controller. Moreover, strip theory has higher fidelity on high-aspect-ratio aircraft. For the aircraft model used in Chapter 7, strip theory is not the best choice. More importantly, due to the lack of control surfaces, the weighted-least squares method is used along with INDI to make trade-offs among different control objectives. Therefore, the effectiveness of the proposed controller can be improved if more control surfaces are available. More advanced trailing edge design concepts including the variable camber

continuous trailing edge flap (VCCTEF) proposed in NASA Ames [12–14] and the Smart X concept proposed in TU Delft are recommended.

Although only INDI is applied to flexible aircraft flight control in this thesis, INDI-SMC and IBSMC can also be used. These hybrid control methods further robustify the incremental control, as verified in Chapters 3 and 4.

INCREMENTAL SLIDING MODE CONTROL

This thesis has shown that the hybridization of incremental control and SMC can passively tolerate a wide range of faults and disturbances. “Passive” means that neither FDD nor controller reconfiguration is needed [15]. However, in some extreme cases, these mechanisms become necessary. This can be explained using Theorem 3 in Chapter 3, in which one of the sufficient conditions for the boundedness of ϵ_{indi} is $\|I - \mathcal{B}\mathcal{B}^{-1}\| \leq \bar{b} < 1$. If this condition becomes invalid because of faults, FDD and controller reconfiguration become necessary. This is not only applicable to INDI-SMC, but also holds for any robust control that takes the boundedness of uncertainty as a pre-condition.

One illuminative example is quadrotor flight control where tracking of three decoupled attitude angles can be achieved by a healthy quadrotor (Chapter 6), while only a reduced attitude control can be achieved by a quadrotor with complete loss of a single rotor [9]. The switching of control strategies when one or more rotors are completely lost needs the incorporation of FDD. Nevertheless, the circumstances that require FDD and controller reconfiguration are reduced with the help of INDI-SMC. Therefore, the false alarm rate of FDD and the onboard computational load can be reduced; the design and implementation processes can be simplified as well. These will be addressed in a following publication of the author.

It has been shown in Chapter 6 that a wide range of perturbations can be tolerated by INDI-SMC with lower and fixed control/observer gains, while the gains needed by NDI-SMC are higher and must be adapted or manually adjusted in different fault cases. Although using fixed gains can reduce the onboard computational load (Chapter 6), in theory the SMC gains can only be reduced to their minimum possible values when gain adaptations are used. Even so, because of the lower bound and smaller variations of ϵ_{indi} (Chapter 6), the gain adaptation rate is supposed to be reduced by INDI-SMC. The verification of this deduction is recommended as future work.

Since incremental control utilizes the previous sample to reduce the remaining perturbation, it is meaningful to derive and analyze the control algorithms purely in discrete time. The discrete-time sliding mode control has been addressed in [16, 17] for sampled-data linear systems with matched uncertainties. The idea of estimating the disturbances using one-step delayed sample in incremental control is also adopted by [16, 17]. A recently submitted paper [18] generalizes the methods in [16, 17] to linear sampled-data multi-input/output systems with matched uncertainties. It can also enhance the sliding accuracy while alleviating possible high-gain control effort. However, stability-guaranteed sliding mode control design for sampled-data nonlinear systems with both matched and unmatched uncertainties remains challenging, where advanced mathematically tools such as Taylor-Lie series discretization [19] or the Adomian decomposition [20] are needed.

Finally, the theories in Part I are developed for generic nonlinear uncertain systems, it is therefore suggested to apply them to other physical systems.

REFERENCES

- [1] A. Hodel, M. Whorton, and J. Zhu, *Stability Metrics for Simulation and Flight-Software Assessment and Monitoring of Adaptive Control Assist Compensators*, in *AIAA Guidance, Navigation and Control Conference and Exhibit* (American Institute of Aeronautics and Astronautics, Honolulu, Hawaii, 2008) pp. 1–25.
- [2] X. Yang and J. J. Zhu, *Singular perturbation margin and generalised gain margin for nonlinear time-invariant systems*, *International Journal of Control* **89**, 451 (2016).
- [3] X. Yang and J. J. Zhu, *Singular perturbation margin and generalised gain margin for linear time-invariant systems*, *International Journal of Control* **89**, 451 (2015).
- [4] X. Yang, X. Wang, C. Xie, and J. J. Zhu, *On structural property metrics for Model Error of linear systems*, in *2016 American Control Conference (ACC)*, 3 (IEEE, Boston, MA, 2016) pp. 1148–1153.
- [5] S. Sieberling, Q. P. Chu, and J. A. Mulder, *Robust Flight Control Using Incremental Nonlinear Dynamic Inversion and Angular Acceleration Prediction*, *Journal of Guidance, Control, and Dynamics* **33**, 1732 (2010).
- [6] T. Keijzer, G. Looye, Q. P. Chu, and E. van Kampen, *Design and Flight Testing of Incremental Backstepping based Control Laws with Angular Accelerometer Feedback*, in *AIAA Scitech 2019 Forum*, January (American Institute of Aeronautics and Astronautics, San Diego, California, 2019) pp. 1–25.
- [7] F. Grondman, G. Looye, R. O. Kuchar, Q. P. Chu, and E. van Kampen, *Design and Flight Testing of Incremental Nonlinear Dynamic Inversion-based Control Laws for a Passenger Aircraft*, in *2018 AIAA Guidance, Navigation, and Control Conference*, January (American Institute of Aeronautics and Astronautics, Kissimmee, Florida, 2018).
- [8] W. van Ekeren, G. Looye, R. O. Kuchar, Q. P. Chu, and E. van Kampen, *Design, Implementation and Flight-Tests of Incremental Nonlinear Flight Control Methods*, in *2018 AIAA Guidance, Navigation, and Control Conference*, January (American Institute of Aeronautics and Astronautics, Kissimmee, Florida, 2018) pp. 1–21.
- [9] S. Sun, L. Sijbers, X. Wang, and C. de Visser, *High-Speed Flight of Quadrotor Despite Loss of Single Rotor*, *IEEE Robotics and Automation Letters* **3**, 3201 (2018).
- [10] Y. Zhou, E. van Kampen, and Q. P. Chu, *Incremental Approximate Dynamic Programming for Nonlinear Adaptive Tracking Control with Partial Observability*, *Journal of Guidance, Control, and Dynamics* **41**, 2554 (2018).
- [11] Y. Zhou, *Online reinforcement learning control for aerospace systems*, Ph.D. thesis, Delft University of Technology (2018).
- [12] N. T. Nguyen, S. Sweil, and E. Ting, *Adaptive Linear Quadratic Gaussian Optimal Control Modification for Flutter Suppression of Adaptive Wing*, in *AIAA Infotech@Aerospace* (Kissimmee, Florida, 2015) pp. 1–23.

- [13] E. A. Tal, N. T. Nguyen, and E. Ting, *Comparison of Unsteady Aerodynamics Approximations for Time-Domain Representation of Frequency-Independent Aeroelastic State-Space Models*, in *56th AIAA/ASCE/AHS/ASC Structures, Structural Dynamics, and Materials Conference*, January (American Institute of Aeronautics and Astronautics, Kissimmee, Florida, 2015).
- [14] N. T. Nguyen, E. Ting, D. Chaparro, M. C. Drew, and S. S.-M. Swei, *Multi-Objective Flight Control for Drag Minimization and Load Alleviation of High-Aspect Ratio Flexible Wing Aircraft*, in *58th AIAA/ASCE/AHS/ASC Structures, Structural Dynamics, and Materials Conference*, January (American Institute of Aeronautics and Astronautics, Grapevine, Texas, 2017).
- [15] Y. Zhang and J. Jiang, *Bibliographical review on reconfigurable fault-tolerant control systems*, *Annual Reviews in Control* **32**, 229 (2008).
- [16] Wu-Chung Su, S. Drakunov, and U. Ozguner, *An $O(T/\sup 2)$ boundary layer in sliding mode for sampled-data systems*, *IEEE Transactions on Automatic Control* **45**, 482 (2000).
- [17] T. Nguyen, W.-c. Su, and Z. Gajic, *Output Feedback Sliding Mode Control for Sampled-Data Systems*, **55**, 1684 (2010).
- [18] T. Nguyen, C. Edwards, V. Azimi, and W.-c. Su, *On the Control Effort in Output Feedback Sliding Mode Control of Sampled-Data Systems*, [arXiv:arXiv:1904.06489v1](https://arxiv.org/abs/1904.06489v1).
- [19] N. Kazantzis, K. T. Chong, J. H. Park, and A. G. Parlos, *Control-Relevant Discretization of Nonlinear Systems With Time-Delay Using Taylor-Lie Series*, *Journal of Dynamic Systems, Measurement, and Control* **127**, 153 (2005).
- [20] Y. Zhang, K. T. Chong, N. Kazantzis, and A. Parlos, *Discretization of nonlinear input-driven dynamical systems using the Adomian Decomposition Method*, *Applied Mathematical Modelling* **36**, 5856 (2012).



A

DEFINITIONS USED IN NONLINEAR CONTROL THEORY

In this thesis, some definitions in nonlinear control theory are frequently used. For readers' convenience, they are summarized in this appendix. All the definitions are transcribed from Chapter 4 of Hassan K Khalil's book: "Nonlinear Systems" [1].

Definition 2 A continuous function $\alpha: [0, a) \rightarrow [0, \infty)$ is said to belong to class \mathcal{K} if it is strictly increasing and $\alpha(0) = 0$. It is said to belong to class \mathcal{K}_∞ if $a = \infty$ and $\alpha(r) \rightarrow \infty$ as $r \rightarrow \infty$.

Definition 3 A continuous function $\beta: [0, a) \times [0, \infty) \rightarrow [0, \infty)$ is said to belong to class \mathcal{KL} if, for each fixed s , the mapping $\beta(r, s)$ belongs to class \mathcal{K} with respect to r and, for each fixed r , the mapping $\beta(r, s)$ is decreasing with respect to s and $\beta(r, s) \rightarrow 0$ as $s \rightarrow \infty$.

For the system

$$\dot{x} = f(t, x) \tag{A.1}$$

where $f: [0, \infty) \times D \rightarrow \mathbb{R}^n$ is piecewise continuous in t and locally Lipschitz in x on $[0, \infty) \times D$, and $D \subset \mathbb{R}$ is a domain that contains the origin $x = 0$.

Definition 4 The equilibrium point $x = 0$ of (A.1) is

- stable if, for each $\varepsilon > 0$, there is $\delta = \delta(\varepsilon, t_0) > 0$ such that

$$\|x(t_0)\| < \delta \Rightarrow \|x(t)\| < \varepsilon, \quad \forall t \geq t_0 \geq 0 \tag{A.2}$$

- uniformly stable if, for each $\varepsilon > 0$, there is $\delta = \delta(\varepsilon) > 0$, independent of t_0 , such that (A.2) is satisfied.
- asymptotically stable if it is stable and there is a positive constant $c = c(t_0)$ such that $x(t) \rightarrow 0$ as $t \rightarrow \infty$, for all $\|x(t_0)\| < c$.

- *uniformly asymptotically stable if it is uniformly stable and there is a positive constant c , independent of t_0 , such that for all $\|x(t_0)\| < c$, $x(t) \rightarrow 0$ as $t \rightarrow \infty$, uniformly in t_0 ; that is, for each $\eta > 0$, there is $T = T(\eta) > 0$ such that*

$$\|x(t)\| < \eta, \quad \forall t \geq t_0 + T(\eta), \quad \forall \|x(t_0)\| < c \quad (\text{A.3})$$

- *globally uniformly asymptotically stable if it is uniformly stable, $\delta(\varepsilon)$ can be chosen to satisfy $\lim_{\varepsilon \rightarrow \infty} \delta(\varepsilon) = \infty$, and for each pair of positive numbers η and c , there is $T = T(\eta, c) > 0$ such that*

$$\|x(t)\| < \eta, \quad \forall t \geq t_0 + T(\eta, c), \quad \forall \|x(t_0)\| < c \quad (\text{A.4})$$

Definition 5 *The equilibrium point $x = 0$ of (A.1) is exponentially stable if there exist positive constants c, k , and λ such that*

$$\|x(t)\| \leq k\|x(t_0)\|e^{-\lambda(t-t_0)}, \quad \forall \|x(t_0)\| < c \quad (\text{A.5})$$

and globally exponentially stable if (A.5) is satisfied for any initial state $x(t_0)$.

Definition 6 *The solutions of (A.1) are*

- *uniformly bounded if there exists a positive constant c , independent of $t_0 \geq 0$, and for every $a \in (0, c)$, there is $\beta = \beta(a) > 0$, independent of t_0 , such that*

$$\|x(t_0)\| \leq a \Rightarrow \|x(t)\| \leq \beta, \quad \forall t \geq t_0 \quad (\text{A.6})$$

- *globally uniformly bounded if (A.6) holds for arbitrarily large a .*
- *uniformly ultimately bounded with ultimate bound b if there exist positive constant b and c , independent of $t_0 \geq 0$, and for every $a \in (0, c)$, there is $T = T(a, b) \geq 0$, independent of t_0 , such that*

$$\|x(t_0)\| \leq a \Rightarrow \|x(t)\| \leq b, \quad \forall t \geq t_0 + T \quad (\text{A.7})$$

- *globally uniformly ultimately bounded if (A.7) holds for arbitrarily large a .*

It is noteworthy that for autonomous systems, the word “uniformly” can be dropped, since the solution only depends on $t - t_0$.

Consider the system

$$\dot{x} = f(t, x, u) \quad (\text{A.8})$$

where $f: [0, \infty) \times \mathbb{R}^n \times \mathbb{R}^m \rightarrow \mathbb{R}^n$ is piecewise continuous in t and locally Lipschitz in x and u . The input $u(t)$ is a piecewise continuous, bounded function of t for all $t \geq 0$.

Definition 7 *The system (A.8) is said to be input-to-state stable if there exist a class $\mathcal{K}\mathcal{L}$ function β and a class \mathcal{K} function γ such that for any initial state $x(t_0)$ and any bounded input $u(t)$, the solution $x(t)$ exists for all $t \geq t_0$ and satisfies*

$$\|x(t)\| \leq \beta(\|x(t_0)\|, t - t_0) + \gamma\left(\sup_{t_0 \leq \tau \leq t} \|u(\tau)\|\right) \quad (\text{A.9})$$

REFERENCES

- [1] H. K. Khalil, *Nonlinear Systems* (Prentice-Hall, New Jersey, 2002).

ACKNOWLEDGEMENTS

This dissertation is the result of four years of my exploration in Delft, the Netherlands, with sparkling moments and memorable experiences. At the end of this journey, I would like to express my sincerest gratitude to many people “traveled” with me. Without your accompany, this journey would be much more rough and rocky.

My first thank goes to my promotor, Prof. Max Mulder for giving me the opportunity to explore in Delft. I still remember our first Skype interview in 2015, which was interrupted by the internet disconnection for more than three times. In spite of these interruptions, you were so patient and kindly helped me to overcome my nervousness. Thanks for giving me the opportunity to be a teaching assistant in one of your courses, from which I learned many skills. Your persistence and enthusiasm deeply inspired me. I am truly grateful for your high-level guidance, and your valuable suggestions on my research work.

I would like to thank my co-promotor, Dr. Erik-Jan van Kampen. Thanks for helping me to focus when I was distracted by too many possible approaches, and for providing creative options when I was stuck. Thanks for bearing my immature English skills for four years, and revising my manuscripts word by word. Thanks for advertising my research work and introducing me to other researchers. I really appreciate the relaxing and flexible research environment that you provided. Your way of effectively arranging time and overcome procrastination also gives me a valuable lesson.

My deep appreciation also goes to my supervisor Dr. Qiping Chu. Thanks for bringing INDI to my world! I am inspired by your enthusiasm in scientific research. Discussions with you are always pleasant and fruitful. I am impressed by your colorful life experiences which you shared with us in the coffee corner. I have learned a lot from you, not only about how to do research but also a placid attitude towards life.

My gratitude also goes out to Dr. Peng Lu. In my first year of Ph.D. research, Peng gave me a lot of help. Your rigorousness and persistence in research inspired me. Peng is also a co-author of two journal papers of mine. Before the review process started, he has already left Delft. However, he could have Skype meetings with me for hours in spite of the time differences, which I deeply appreciate. Also, I would like to thank you and your wife Dr. Xiang Li for inviting me for dinner in Leiden.

I cherish the opportunity to work with my colleagues in C&S. I would like to acknowledge Dr. Yingzhi Huang, my INDI brother. Since our research topics are related, we had many discussions on the methodology and applications of INDI. Thanks for sharing me with many relevant papers and your opinions towards them. Special thanks also to my office mates in room 3.21: Emmanuel Sunil, Junzi Sun, and Wei Fu, you guys have made this little working place so cozy and special. I am so happy that at this moment, all of you have got your ideal job! Best wishes for your career and personal life! Thanks for lending books to me, dear Dyah Jatiningrum. Wish you and your family all the best! Yvonne Ferrier and Isabelle El-Hajj, thanks for choosing me as your thesis supervisor, I hope that I

have helped you in some way.

During my Ph.D. journey, I have had a fortune of working with people in the Smart and Aeroelastic Structures Lab in TU Delft. Special thanks to Dr. Roeland de Breuker. Thanks for introducing me to the wonderful world of aeroelasticity! I appreciate your effort on helping me make connections with your Ph.D. students: Mario Natella, Tigran Mkhoyan, Jurij Sodja, Paul Lancelot, Darwin Rajpal, etc. I learnt a lot from you and your students. Dear Mario, how could I express my thanks towards you? You helped me to overcome my anxiousness and depressions along the journey. Deriving the nonlinear dynamic equations with you is one of the most enjoyable and exciting experiences in the past four years. All the best to your start-up company! I will remember Tigran not only by his impressive research, but also by his hand-made artistic jewelry. Both Mario and Tigran are examples that a creative person not only succeeds in research. To Jurij and Paul, for the discussions, suggestions and patient explanations.

I will miss Delft enormously because of the lovely people I met here. Thanks, Dr. Daan Pool, for arranging the basketball games in Delft and the road trip along the Pacific Coast Highway. Dear Dirk, I was so happy to give presentations with you at four a.m. Dutch time in San Diego. Although none of us won the final competition, it was still a memorable experience. Your funny MEMEs in the group emails made my days. Thanks Dr. Henry Tol for inviting us to your home in Volendam, the cheesecake made by your wife was very tasty. Thanks Jaime, Tommaso, Ewoud, Tao, Ye, Yingzhi for skating and hanging out with me. I will also remember the talks in the coffee corner with Prof. Bob Mulder, Dr. Coen de Visser, Dr. Clark Borst, Dr. Guido de Croon, Dr. Joost Ellerbroek, Dr. Marilena Pavel, Prof. Jacco Hoekstra, Dr. Rene van Paassen, Olaf, Ferdinand, Andries, Christophe, Kasper, Ivan, Kimberly, Kirk, Annemarie, Shuo, Isabel, Julia, Sarah, Mario, Neno, Jelmer, Tom, Daniel, Paolo, Ezgi, Matej, Kevin, Anne, Christian, Diana, Shushuai, Sophie, Ye Zhou, Hann Woei, Bertine, Tim, Bo, Ying, Yingfu.

This journey will also be cherished because of the “off-curricular” activities. Sincere thanks to all the friends I made here in Delft. Thanks Junzi for preparing the dinner for Chinese Spring Festival Eve for three consecutive years. To sweet and lovely Ye Zhang for all the colorful memories, which I will cherish throughout my life. To Yingzhi, Gehua, Wei, Ye Zhou, Ying, Shuo, Chuan, Linfeng, Shushuai, Riming, Hao, Hongzhi, Dan, Ziqiao, Feijia, Xiaodong for the countless gatherings, movies, drinks, dinners, road trips, and your kind encouragements. Gratitude to the best roommate I have ever met: the adorable and adventurous Anouk Rossen. Thanks for taking me to pole fitness, Jiu-jitsu and yoga. Thanks for teaching me Dutch, Japanese, Para Para Dance, and baking, for free. Best wishes for your new Ph.D. journey in Tokyo.

This thesis is also contributed by some people outside of TU Delft. I would like to thank Prof. Jim Zhu, an expert in nonlinear control theory and a dedicated teacher. He flies from Ohio to Beihang every winter since 2013 for teaching Chinese students nonlinear control theories. He has the magic to teach the dull mathematical theories in a vivid way, which enormously inspired my interest. I am also highly grateful for the help of Dr. Xiaojing Yang, a student of Prof. Jim Zhu. Actually, it was Xiaojing, who opened a window of the bigger world for me and encouraged me to pursue a Ph.D. degree abroad. My life would be totally different if I did not talk with you in 2014. I also appreciate the help of Dr. Ligu Sun, who graduated from C&S in 2015. He sketched a beautiful Delft in

my mind through our talks in Beijing. I would also like to thank the aeroelastic experts: Prof. Changchuan Xie, Yang Meng, Lan Yang from Beihang, as well as Dr. Shuo Zhang from Beijing Institute of Technology, for your generous help.

I gratefully acknowledge the China Scholarship Council for the financial support.

Special thanks to my boyfriend, Sihao Sun, for being part of my life. Last but not least, my deepest gratitude goes to my beloved parents, Haicong Liu and Zhengping Wang. I cherish every moment that we spent together. Thank you so much for your support, encouragement and unconditional love!

Xuerui Wang
Delft, May 2019



CURRICULUM VITÆ

Xuerui WANG

11-11-1992 Born in Qingyang, Gansu, China

EDUCATION

2015-2019 Ph.D. in Aerospace Engineering
Delft University of Technology, the Netherlands
Thesis: Incremental Sliding Mode Flight Control
Promotor: Prof. dr. M. Mulder

2014-2015 Ph.D. in Aerospace Engineering
Beijing University of Aeronautics and Astronautics, China

2010-2014 B.Sc. in Aerospace Engineering
Beijing University of Aeronautics and Astronautics, China
Thesis: Landing Safety in the Presence of Gust Disturbances

AWARDS

2019 AIAA SciTech GNC conference best student paper finalist
2014 Distinguished undergraduate student
2013 The third place in European Air Cargo Challenge (ACC)



LIST OF PUBLICATIONS

JOURNAL PAPERS:

6. **X. Wang**, E. van Kampen, Q. P. Chu, and P. Lu, *Stability Analysis for Incremental Nonlinear Dynamic Inversion Control*, Journal of Guidance, Control, and Dynamics, Vol. 42, No. 5, 2019, pp. 1116-1129. doi:10.2514/1.G003791.
5. **X. Wang**, E. van Kampen, Q. P. Chu, and R. De Breuker, *Flexible Aircraft Gust Load Alleviation with Incremental Nonlinear Dynamic Inversion*, Journal of Guidance, Control, and Dynamics, 2019, pp. 1–18. doi:10.2514/1.G003980.
4. **X. Wang**, E. van Kampen, Q. P. Chu, and P. Lu, *Incremental Sliding Mode Fault-Tolerant Flight Control*, Journal of Guidance, Control, and Dynamics, Vol. 42, No. 2, 2019, pp. 244–259. doi:10.2514/1.G003497.
3. **X. Wang**, S. Sun, E. van Kampen, and Q. P. Chu, *Quadrotor Fault-Tolerant Incremental Sliding Mode Control Driven by Sliding Mode Disturbance Observers*, Aerospace Science and Technology, Vol. 87, 2019, pp. 417–430. doi:10.1016/j.ast.2019.03.001.
2. S. Sun, L. Sijbers, **X. Wang**, and C. C. de Visser, *High-Speed Flight of Quadrotor despite Loss of Single Rotor*, IEEE Robotics and Automation Letters, Vol. 3, No. 4, 2018, pp. 3201–3207. doi:10.1109/LRA.2018.2851028.
1. S. Sun, **X. Wang**, Q. P. Chu, and C. C. de Visser, *Robust Nonlinear Control of a Quadrotor with Complete Loss of Double Diagonal Rotors*, IEEE Transactions on Robotics (T-RO), 2019 (under review).

PEER-REVIEWED CONFERENCE PAPERS:

8. **X. Wang**, E. van Kampen, and Q. P. Chu, *Comparisons of Three Control Structures for Inducing Higher-Order Sliding Modes*, European Control Conference (ECC), IEEE, Naples, Italy, 2019, pp. 1-8.
7. X. Yang, **X. Wang**, C. Xie, and J. J. Zhu, *On structural property metrics for Model Error of linear systems*, 2016 American Control Conference (ACC), Vol. 2016-July, IEEE, 2016, pp. 1148–1153. doi:10.1109/ACC.2016.7525070.
6. **X. Wang**, and E. van Kampen, *Incremental Backstepping Sliding Mode Fault-Tolerant Flight Control*, 2019 AIAA Guidance, Navigation, and Control Conference, American Institute of Aeronautics and Astronautics, San Diego, California, 2019, pp. 1–23. doi:10.2514/6.2019-0110 (**Nominated for Best Student Paper Award**).
5. **X. Wang**, E. van Kampen, Q. P. Chu, and P. Lu, *Stability Analysis for Incremental Nonlinear Dynamic Inversion Control*, 2018 AIAA Guidance, Navigation, and Control Conference, American Institute of Aeronautics and Astronautics, Kissimmee, Florida, 2018, pp. 1–16. doi:10.2514/6.2018-1115.

4. **X. Wang**, E. van Kampen, R. De Breuker, and Q. P. Chu, *Flexible Aircraft Gust Load Alleviation with Incremental Nonlinear Dynamic Inversion*, 2018 AIAA Atmospheric Flight Mechanics Conference, American Institute of Aeronautics and Astronautics, Kissimmee, Florida, 2018, pp. 1–21. doi:10.2514/6.2018-0774.
3. M. Natella, **X. Wang**, and R. De Breuker, *The Effects of Aeroelastic Tailoring on Flight Dynamic Stability*, 2018 AIAA/ASCE/AHS/ASC Structures, Structural Dynamics, and Materials Conference, Kissimmee, Florida, 2018. doi:10.2514/6.2018-0191.
2. Y. Ferrier, N. T. Nguyen, E. Ting, D. Chaparro, **X. Wang**, C. C. de Visser, and Q. P. Chu, *Active Gust Load Alleviation of High-Aspect Ratio Flexible Wing Aircraft*, 2018 AIAA Guidance, Navigation, and Control Conference, American Institute of Aeronautics and Astronautics, Kissimmee, Florida, 2018, pp. 1–36. doi:10.2514/6.2018-0620.
1. **X. Wang**, E. van Kampen, and Q. P. Chu, *Gust Load Alleviation and Ride Quality Improvement with Incremental Nonlinear Dynamic Inversion*, AIAA Atmospheric Flight Mechanics Conference, American Institute of Aeronautics and Astronautics, Grapevine, Texas, 2017, pp. 1–21. doi:10.2514/6.2017-1400.

